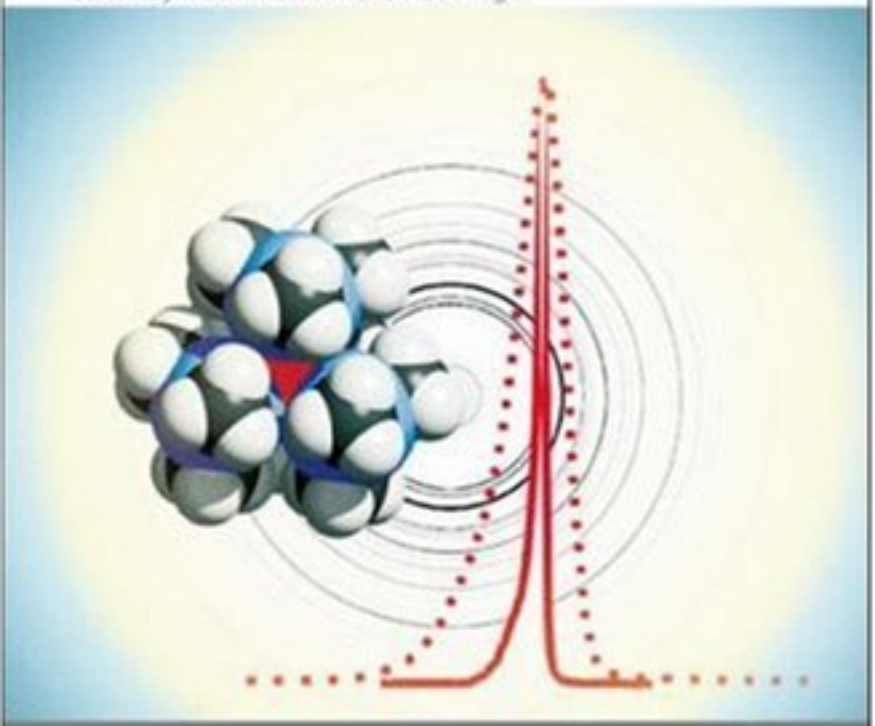
# Powder Diffraction

## Theory and Practice

Edited by R E Dinnebier and S J L Billinge



RSC Publishing

# Powder Diffraction
## Theory and Practice

# Dedication

This book is dedicated to our wives and children: Natalia, Alexander, Maximilian, Debby, Ian, Isabel, and Sophie.

# Powder Diffraction
## Theory and Practice

Edited by

**Robert E. Dinnebier**
*Max-Planck Institute for Solid State Research, Stuttgart, Germany*

**Simon J. L. Billinge**
*Department of Physics and Astronomy, Michigan State University, USA*

RSC Publishing

ISBN: 978 0 85404 231 9

A catalogue record for this book is available from the British Library

© The Royal Society of Chemistry 2008

*All rights reserved*

*Apart from fair dealing for the purposes of research for non commercial purposes or for private study, criticism or review, as permitted under the Copyright, Designs and Patents Act 1988 and the Copyright and Related Rights Regulations 2003, this publication may not be reproduced, stored or transmitted, in any form or by any means, without the prior permission in writing of The Royal Society of Chemistry, or in the case of reproduction in accordance with the terms of licences issued by the Copyright Licensing Agency in the UK, or in accordance with the terms of the licences issued by the appropriate Reproduction Rights Organization outside the UK. Enquiries concerning reproduction outside the terms stated here should be sent to The Royal Society of Chemistry at the address printed on this page.*

Published by The Royal Society of Chemistry,
Thomas Graham House, Science Park, Milton Road,
Cambridge CB4 0WF, UK

Registered Charity Number 207890

For further information see our web site at www.rsc.org

# Preface

Knowledge of the atomic scale geometrical structure of matter is a prerequisite for understanding and predicting the properties of technologically and scientifically important materials. The geometrical structure of a material does not only consist of the time and space averaged periodic conformation of atoms in an idealized crystal lattice but also the microstructure caused by imperfections, dislocations, and all kinds of disorder that often are responsible for interesting properties of the material under investigation.

The most frequently used technique for the determination of crystal structures is single crystal analysis. However, if no single crystals of suitable size and quality are available, powder diffraction is the nearest alternative. Furthermore, single crystal analysis does not provide information on the bulk material and is not a routinely used technique for the determination of microstructural properties. Neither is it often used to characterize disorder in materials. Studies of macroscopic stresses in components, both residual from processing and *in situ* under load, are studied by powder diffraction, as is the texture of polycrystalline samples. Powder diffraction remains to this day a crucial tool in the characterization of materials, with increasing importance and breadth of application as instrumentation, methods, data analysis and modeling become more powerful and quantitative.

The powder diffraction pattern contains a wealth of information in addition to the pure crystal structure, as can be seen in Figure 1.

Although, the powder method was developed as early as 1916 by Debye and Scherrer, for more than 50 years its use was almost exclusively limited to qualitative and semi-quantitative phase analysis and macroscopic stress measurements. The main reason for this can be found in what is known as the principal problem of powder diffraction: accidental and systematic peak overlap caused by a projection of three-dimensional reciprocal space on to the one-dimensional $2\theta$ axis, leading to a strongly reduced information content compared to a single crystal data set. However, despite the loss of angular information, often sufficient information resides in the 1D dataset to reconstruct the 3D structure. Indeed, quantitative analysis of the pattern using modern computers and software yields the wealth of additional information about the sample structure that is illustrated in Figure 1. Modern

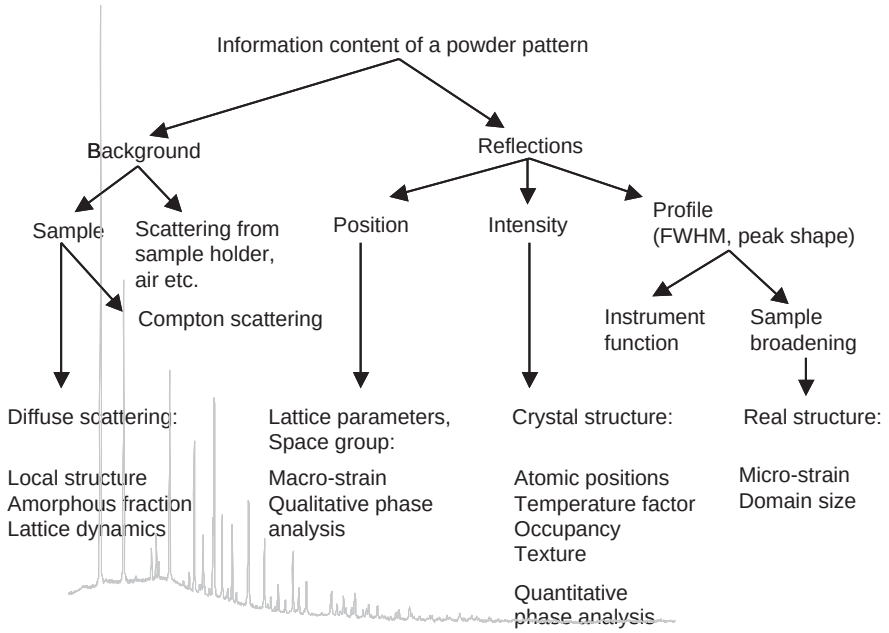



**Figure 1** General information content of a powder diffraction pattern.

instrumentation and sources are yielding data of unprecedented quality and modern analysis methods continue to increase our ability to harvest useful information from the data. The powder diffraction technique has never contributed to materials research in more diverse and important ways than now as we approach its centenary.

This book is an advanced introductory text about modern methods and applications of powder diffraction in research. A strong working knowledge of diffraction and crystallography is assumed. This book does not present a basic introduction to crystallography and diffraction from crystals, which is available in many introductory texts and other books, such as the excellent *Fundamentals of Powder Diffraction* by Pecharsky and Zavalij (Kluwer Academic Publishers, Boston, 2003). This book presents a broad overview of current methods and applications, including their theory and practice, with useful information on getting started in these methods. The book is written by renowned experts in the respective techniques.

The current excitement in powder diffraction is in quantitative analysis of the data. The book is laid out in a way that facilitates understanding the information content of the data, as well as best practices for collecting and analyzing data for quantitative analysis. After a very brief overview of the basic theory of diffraction from crystals and powders, data collection strategies are described, including X-ray, neutron and electron diffraction setups using modern-day apparatus including synchrotron sources. Data corrections that are essential

for quantitative analysis are then introduced, before we move to a discussion of the analysis methods themselves.

The major breakthrough in the value of the powder method as a quantitative tool was the development of the Rietveld method in 1969, a technique for crystal structure refinement which, for the first time, made use of the entire powder pattern instead of analyzing individual, non-overlapped, Bragg reflections separately. This approach minimizes the impact of overlapped and degenerate peaks by calculating the entire powder pattern of a crystalline model, including various experimental and sample dependent peak-broadening effects. Parameters in the model such as atomic positions, lattice parameters, and experimental factors that affect peak-shape and background are varied, using a least-squares approach, until the agreement between the calculated and measured diffraction profiles are optimized. This is a refinement method: a good initial guess at, or knowledge of, the structure is required and this model is refined by small adjustments. The approach has proved to be enormously successful with rapidly increasing numbers of Rietveld refined structures reported in the literature. The method was quickly extended from reactor neutron data, with its nice Gaussian line-profiles and lack of atomic form-factor, to in-house X-ray powder diffraction, synchrotron powder diffraction and time-of-flight neutron data from pulsed spallation sources, and to refinements of incommensurate and magnetic structures.

At each stage, great effort and ingenuity is needed in finding optimal experimental conditions and in understanding and analyzing the resulting line-shapes. A consequence of this is that the rich informational content of the line-shapes was recognized, giving birth to modern line-profile fitting of whole-patterns. Here the line-profile is calculated from first-principles taking into account sample state such as particle size distributions, inhomogeneous strains and texture, as well as experimental setup and aberrations. There is a nice feedback effect that better profile descriptions result in more accurate Bragg-peak intensities resulting in more detailed structure refinements.

Similar to the line-profile story, the rich information content of the background has come to be recognized. Rather than subtracting a parameterized background and discarding it, as is done in a conventional Rietveld refinement, careful corrections can be made for experimental effects such as Compton scattering, fluorescence, multiple scattering and scattering from sample environments. The resulting "background" beneath and between the Bragg peaks of the corrected data is information-rich diffuse scattering from the sample, which encodes information about the local structure and how it deviates from the average crystal structure in the form of defects and correlated lattice dynamics (phonons). Total scattering methods that include both the Bragg and diffuse components are only now being fully appreciated with quantitative analyses in real space using the atomic pair distribution function (PDF) method, and in reciprocal-space with Monte Carlo simulated annealing type modeling.

Beginning in the early 1980s, roughly 10 years after the development of Rietveld refinement, some *ab initio* determinations of crystal structures from

powder diffraction data began to appear. These used single crystal methods but the Bragg-peak intensities were extracted, with difficulty, from the overlapped powder data. This is possible for sufficiently simple structures, with sufficiently high-quality data. Nowadays, with the data quality from synchrotron X-ray sources coupled with excellent algorithms, either direct methods or global optimization methods in direct space, determination of even complex crystal structures from powder diffraction data is becoming a routine method in almost all branches of natural sciences and engineering. The success rate mainly depends on three parameters: choice of measurement device, pattern profile description and structure solving algorithms. It is becoming increasingly evident that the use of highly monochromatic parallel beam synchrotron radiation is a must to reach an accuracy in the atomic parameters, which allows for the interpretation of bonding conditions and reaction mechanisms. In some cases, even details like rotational disorder can be extracted from powder diffraction data if maximum entropy methods are combined with high-resolution synchrotron data.

Powder diffraction measurements are generally straightforward to carry out (there is no sample alignment!) and can be quick, especially with parallel collection approaches such as 1D and 2D detectors. Parallel data collection makes non-ambient parametric studies possible, where parameters such as temperature, pressure, electric or magnetic field or flow-gas compositions are varied and the state of the sample (including phase composition, structure, local structure, particle size distribution and strain *etc*.) is monitored quantitatively under changing conditions. New two-dimensional detectors in combination with synchrotron radiation require very short exposure times and enable structure determinations and refinements in a time-resolved fashion during chemical reactions *in situ*, or after a perturbation. These developments are opening up new fields for the powder method.

The use of synchrotron radiation goes far beyond crystal structure determination: Quantitative detection of small amounts of polymorphic phases is of great interest for pharmaceutical research and in the concrete business. The tunability of wavelength over a large energy range can be used for anomalous dispersion experiments or for depth profiling of thin films or artificial limbs to name just a few. The future of powder diffraction is exciting. Rather than the technique being made redundant, as some people expected, by synchrotron-based single-crystal studies on micron-sized crystals (microcrystallography), the ease and broad applicability of structure determination and refinement with powders is threatening some traditional domains of the single-crystal technique. Figure 2 illustrates the relationship between single crystal and powder diffraction in the sphere of structure solution.

In reality, the two techniques are highly complementary, have their own strengths and weaknesses and domains of applicability, and one will never supercede the other. However, the domain where powder diffraction is having an impact is certainly growing and diversifying. We hope that this book will help students and other researchers participate in this future.

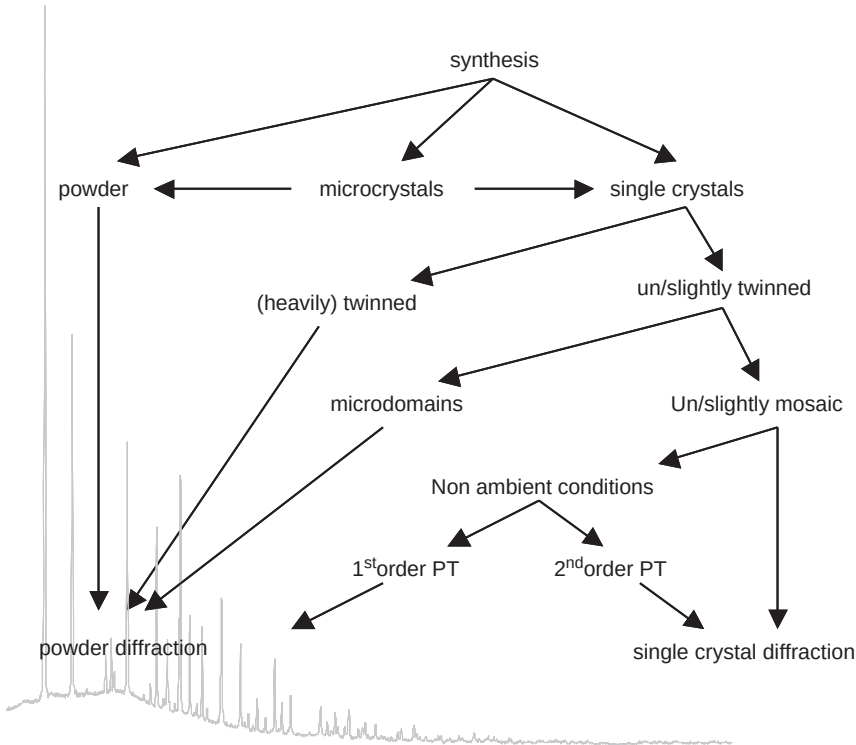



**Figure 2** Illustration of the relationship between the domains of applicability of the powder and single crystal methods in the area of structure solution.

## ACKNOWLEDGEMENTS

We would like to thank all authors for their time and effort spent in writing high quality, up-to-date contributions. Truly, without them this book would not exist on two levels, not only did they write the chapters but they contributed seminally to the developments they describe.

Robert E. Dinnebier
Stuttgart, Germany

Simon J. L. Billinge
East Lansing, Michigan

# Contents

**Chapter 1 Principles of Powder Diffraction**
*Robert E. Dinnebier and Simon J. L. Billinge*

1.1 Introduction 1
1.2 Fundamentals 1
1.3 Derivation of the Bragg Equation 3
1.4 The Bragg Equation in the Reciprocal Lattice 6
1.5 The Ewald Construction 11
1.6 Taking Derivatives of the Bragg Equation 15
1.7 Bragg's Law for Finite Size Crystallites 17
Bibliography 19

**Chapter 2 Experimental Setups**
*Jeremy Karl Cockcroft and Andrew N. Fitch*

2.1 Introduction 20
2.2 Sources of X-ray Radiation 21
2.2.1 Laboratory X-ray Sources 21
2.2.2 Synchrotron X-ray Sources 25
2.3 X-ray Optics 29
2.3.1 Filters 29
2.3.2 Monochromators 29
2.3.3 Mirrors 30
2.4 X-ray Detectors 31
2.4.1 Point Detectors 31
2.4.2 Linear Detectors 31
2.4.3 Area Detectors 32
2.4.4 Detector Calibration 33
2.5 Laboratory Instrumental Configurations 33
2.5.1 Reflection Geometry 33
2.5.2 Transmission Geometry 36

2.6 Synchrotron Instrumental Configurations 37
2.6.1 Pre-sample Optics 37
2.6.2 Parallel-beam Instruments 38
2.6.3 Debye–Scherrer Geometry Instruments 40
2.7 Measurements 41
2.7.1 Sample Holders 41
2.7.2 Standard Samples 43
2.7.3 Data Acquisition 44
2.8 Energy Dispersive Powder X-ray Diffraction 45
2.9 Powder Neutron Diffraction 46
2.9.1 Properties of the Neutron 46
2.9.2 Sources of Neutrons 48
2.9.3 Detection of Neutrons 49
2.9.4 Monochromatic Techniques 50
2.9.5 Time-of-Flight Techniques 53
References 56

**Chapter 3 The Intensity of a Bragg Reflection**
*R. B. Von Dreele and J. Rodriguez-Carvajal*

3.1 Introduction 58
3.2 Single Atom Scattering Theory 58
3.2.1 X-ray Scattering 58
3.2.2 Neutron Scattering 62
3.3 Scattering from a Crystal Lattice 63
3.3.1 Thermal Motion Effects 65
3.3.2 The Lorentz Factor 66
3.3.3 Scattering from a Modulated Crystal Lattice 67
3.3.4 Neutron Magnetic Moment Scattering 71
3.4 Scattering from a Polycrystalline Powder 83
3.4.1 Friedel Pair Overlap 84
3.4.2 Reflection Multiplicity 84
3.4.3 Texture Effects 84
3.4.4 Absorption Effects 86
Acknowledgements 87
References 87

**Chapter 4 General Data Reduction**
*Rudolf Allmann*

4.1 Introduction 89
4.2 Elimination of Fake Reflections (Outliers) 90
4.3 Fitting and Subtraction of Background 91
4.4 Data Smoothing 93

4.4.1 Smoothing by Sliding Polynomials (Savitzky–Golay Method) 93
4.4.2 Digital Low Pass Filters 96
4.5 $K\alpha_2$-Stripping 100
4.6 Peak Search Algorithms 105
4.6.1 Trend-oriented Peak Search 105
4.6.2 Peak Search by Second Derivatives 107
4.6.3 Peak Search with a Predefined Peak Shape 110
4.7 Profile Fitting and Profile Shape Functions 111
4.8 Detection and Correction of Systematic Errors 119
4.8.1 External Standards 126
4.8.2 Internal Standards 127
4.8.3 Correction Together with the Refinement of Lattice Constants 130
References 131

**Chapter 5 The Profile of a Bragg Reflection for Extracting Intensities**
*Armel Le Bail*

5.1 Introduction 134
5.2 Overview of Contributions to the Peak Profile Function 135
5.3 Instrumental Aberrations 136
5.3.1 Largest Size Effect Ever Detected 137
5.3.2 Monte Carlo Ray-tracing 138
5.4 Sample Broadening 141
5.4.1 Crystallite Size 142
5.4.2 Lattice Strain 146
5.4.3 Anisotropic Sample Broadening: Faulting 148
5.5 Individual Peak Fitting and Line Profile Analysis 151
5.5.1 Peak Fitting for Intensity/Position Extraction – With or without Cell Knowledge 152
5.5.2 Using Individual Peaks for Size/Distortion Extraction 152
5.5.3 Further Approximations 152
5.6 Whole Powder Pattern Decomposition (WPPD) – No Structure 153
5.6.1 No Cell Restraint 153
5.6.2 Cell-restrained Whole Powder Pattern Decomposition 153
5.6.3 Main Applications of WPPD 156
5.7 Conclusions 158
References 159

**Chapter 6 Instrumental Contributions to the Line Profile in X-Ray Powder Diffraction. Example of the Diffractometer with Bragg–Brentano Geometry**
*Alexander Zuev*

6.1 Introduction 166
6.2 Contributions to the Observed Profile 169
6.3 General Description of the Method 171
6.4 Basic Equations 173
6.4.1 Vector Equation of a Cone 173
6.4.2 Equation of a Conic 173
6.5 Diffractometer with Bragg–Brentano Geometry 175
6.5.1 Coordinate Systems for Bragg–Brentano Geometry 175
6.5.2 Equation of a Conic in the Receiving Slit Plane (Coordinate System *CS*) 176
6.5.3 Equation of a Conic in the Sample Surface Plane (Coordinate System *CS*) 177
6.5.4 Case of the Degenerated Cone ($2\theta = 90^\circ$) 177
6.5.5 Intersections of the Conic and Receiving Slit Boundary 178
6.5.6 Angle Between Two Planes 178
6.6 Application of the Method 179
6.6.1 Some Illustrative Examples of the Conic in the Receiving Slit Plane 179
6.6.2 Specific Instrumental Function 182
6.6.3 Total Instrumental Profile 192
6.7 About Misalignment, Soller Slits, Monochromator 194
6.7.1 Misalignment 194
6.7.2 Soller Slits 194
6.7.3 Monochromator 196
6.8 Plane Crystal Monochromator in the Diffracted Beam 197
6.8.1 Setting of the Monochromator 197
6.8.2 Reflection Cones 198
6.8.3 Intersection of the Diffraction and Reflection Conics in the Receiving Slit Plane 199
6.9 Effect of the Plane Monochromator on Instrumental Function 200
6.9.1 Equatorial Aberration in the Presence of the Monochromator 200
6.9.2 Axial Aberration in the Presence of the Monochromator 201
6.9.3 Total Instrumental Function in the Presence of the Monochromator 201

6.10 Conclusions 201
Acknowledgements 203
References 203

**Chapter 7 Indexing and Space Group Determination**
*Angela Altomare, Carmelo Giacovazzo and Anna Moliterni*

7.1 The Crystalline Lattice in Powder Diffraction 206
7.2 Indexing of a Powder Pattern 211
7.2.1 Introduction 211
7.2.2 Figures of Merit 213
7.2.3 Geometrical Ambiguities 214
7.2.4 Historical Indexing Programs 214
7.2.5 Evolved Indexing Programs 217
7.3 Space Group Determination 220
7.3.1 Introduction 220
7.3.2 The DASH Procedure 221
7.3.3 The EXPO2004 Procedure 222
References 225

**Chapter 8 Crystal Structure Determination**
*Rocco Caliandro, Carmelo Giacovazzo and Rosanna Rizzi*

8.1 Introduction 227
8.2 The Patterson Function 228
8.3 Direct Methods 230
8.3.1 Scaling of the Observed Intensities and Normalization of the Structure Factors 232
8.3.2 Estimate of Structure Invariants 233
8.3.3 Tangent Formula 238
8.3.4 A Typical Direct Methods Procedure 239
8.3.5 Figure of Merit 239
8.3.6 Completion of the Crystal Structure and Preliminary Refinement 240
8.3.7 Solving Crystal Structures from Powder Neutron Data 242
8.4 Direct-space Techniques 243
8.4.1 Grid Search Methods 245
8.4.2 Monte Carlo Methods 245
8.4.3 Simulated Annealing Techniques 249
8.4.4 Genetic Algorithm Techniques 252
8.4.5 Hybrid Approaches 254
8.4.6 Application to Real Structures 257
8.4.7 Crystal Structure Prediction 258

8.5 Conclusions and Outlook 260
Symbols and Notation 261
References 261

**Chapter 9 Rietveld Refinement**
*R. B. Von Dreele*

9.1 Introduction 266
9.2 Rietveld Theory 268
9.2.1 Least Squares 268
9.3 Constraints and Restraints 271
9.3.1 Introduction 271
9.3.2 Rigid Body Refinement 271
9.3.3 Rigid Body Refinement of $Fe[OP(C_6H_5)_3]_4Cl_2FeCl_4$ 274
9.3.4 Stereochemical Restraint Refinement 277
9.3.5 Protein Powder Refinements 279
Acknowledgement 280
References 280

**Chapter 10 The Derivative Difference Minimization Method**
*Leonid A. Solovyov*

10.1 Introduction 282
10.2 Derivative Difference Minimization Principle 283
10.3 DDM Decomposition Procedure 285
10.4 Results and Discussion 288
10.4.1 Tests on Simulated and Real Data 288
10.4.2 Applications of DDM 291
10.5 Conclusions 295
References 295

**Chapter 11 Quantitative Phase Analysis**
*Ian C. Madsen and Nicola V. Y. Scarlett*

11.1 Introduction 298
11.2 Phase Analysis 299
11.3 Mathematical Basis 300
11.3.1 Reference Intensity Ratio (RIR) Methods 303
11.3.2 Rietveld-based Methods 304
11.4 Factors Limiting Accuracy 308
11.4.1 Particle Statistics 308
11.4.2 Preferred Orientation 310

11.4.3 Microabsorption 312
11.4.4 Precision, Accuracy and the Calculation of Error 314
11.5 Examples of QPA *via* Powder Diffraction 315
11.5.1 Application in Mineralogical Systems 315
11.5.2 Applications in Industrial Systems 322
11.6 Summary 326
Acknowledgements 326
Appendix A: Derivation of Errors in Rietveld-based Quantitative Phase Analysis 327
Relative Phase Abundances 327
Absolute Phase Abundances 327
Amorphous Content 328
References 329

**Chapter 12 Microstructural Properties: Texture and Macrostress Effects**
*Nicolae C. Popa*

12.1 Texture 332
12.1.1 The Orientation Distribution Function and the Pole Distributions 332
12.1.2 Two Goals in Texture Analysis 335
12.1.3 Dollase–March Model 337
12.1.4 The Spherical Harmonics Approach 339
12.2 Macroscopic Strain and Stress 348
12.2.1 Elastic Strain and Stress in a Crystallite – Mathematical Background 349
12.2.2 Strain and Stress in Polycrystalline Samples 352
12.2.3 Status of the Strain/Stress Analysis by Diffraction 355
12.2.4 Strain/Stress in Isotropic Samples – Classical Approximations 357
12.2.5 Hydrostatic Pressure in Isotropic Polycrystals 363
12.2.6 The Macroscopic Strain/Stress by Spherical Harmonics 365
References 373

**Chapter 13 Microstructural Properties: Lattice Defects and Domain Size Effects**
*Paolo Scardi*

13.1 Introduction 376
13.2 Origin of Line Broadening 377

13.2.1 Size Broadening 377
13.2.2 Strain Broadening 381
13.2.3 Other Sources of Line Broadening 384
13.3 Traditional *versus* Innovative Methods 387
13.3.1 Integral Breadth Methods 387
13.3.2 Fourier Methods 389
13.3.3 Profile Fitting and Traditional LPA Methods 394
13.3.4 Whole Powder Pattern Modelling 395
13.4 WPPM: Examples of Application 396
13.4.1 Heavily Deformed Metal Powders 396
13.4.2 Nanocrystalline Cerium Oxide Powder 402
Acknowledgements 405
List of Principal Symbols 405
Appendix: Fourier Transforms of Profile Components 407
Instrumental Profile (IP) 407
Domain Size (S) 407
Faulting (F) 408
Dislocations (D) 408
Anti-phase Domain Boundaries (APB) 410
Stoichiometry Fluctuation (C) 410
References 411

**Chapter 14 Two-dimensional Diffraction Using Area Detectors**
*Bernd Hinrichsen, Robert E. Dinnebier and Martin Jansen*

14.1 Two-dimensional Detectors 414
14.1.1 CCD Detectors 415
14.1.2 Imaging Plate Detectors 416
14.1.3 Flat Panel Detectors 416
14.1.4 Hybrid Pixel Detectors 417
14.2 Diffraction Geometry 418
14.2.1 Resolution and FWHM in Two-dimensional Diffraction 419
14.2.2 Diffraction Angle Transformation 422
14.2.3 Incident Angle and Ray Distance Calculations 426
14.2.4 General Transformations 426
14.3 Intensity Corrections 429
14.3.1 Lorentz Corrections 430
14.3.2 Polarization Correction 434
14.3.3 Incident Angle Correction 435
References 437

**Chapter 15 Powder Diffraction under Non-ambient Conditions**
*Poul Norby and Ulrich Schwarz*

15.1 Introduction 439
15.2 *In Situ* Powder Diffraction 440
15.2.1 Techniques and Instrumentation 442
15.3 Powder Diffraction at High Pressure 450
15.3.1 Introduction 450
15.3.2 The Diamond Anvil Cell 451
15.3.3 Pressure Media 453
15.3.4 Diffraction Measurements 454
15.3.5 Pressure Measurement 457
15.3.6 Thermodynamic Considerations 459
Selected Reviews 461
*In-situ* diffraction 461
High-pressure Diffraction 461
References 462

**Chapter 16 Local Structure from Total Scattering and Atomic Pair Distribution Function (PDF) Analysis**
*Simon Billinge*

16.1 Introduction 464
16.2 Theory 470
16.2.1 Single Component Systems 470
16.2.2 Multicomponent Systems 473
16.3 Experimental Methods 479
16.4 Structural Modeling 481
16.4.1 Model Independent Structural Information from the PDF 481
16.4.2 Modeling the PDF 482
16.4.3 Modeling Total Scattering in Reciprocal Space 485
16.4.4 Emerging Modeling Approaches 486
References 491

**Chapter 17 Computer Software for Powder Diffraction**
*Lachlan M. D. Cranswick*

17.1 Introduction 494
17.2 Finding and Testing Software 494
17.2.1 Locating New Software 494
17.2.2 Selecting Software 495
17.2.3 Re-locating Software on the Internet 495

17.3 Available Software 495
17.3.1 Third-party Diffractometer Control Software 495
17.3.2 Phase Identification and Search-match Software 496
17.3.3 Crystal Structure Databases 498
17.3.4 Powder Data Conversion 500
17.3.5 Structure Data Conversion and Transformation 503
17.3.6 Powder Diffraction Pattern Viewing and Processing 504
17.3.7 Peak Finding and Peak Profiling 510
17.3.8 Powder Indexing 510
17.3.9 Space Group Assignment 521
17.3.10 Space Group Information Software and Databases 521
17.3.11 Unit Cell Refinement 522
17.3.12 Full Profile Fitting (Pawley, Le Bail) 523
17.3.13 Texture Analysis Software 528
17.3.14 Size Strain Analysis 528
17.3.15 Single Crystal Suites useful to Powder Diffraction 530
17.3.16 Powder Diffraction Suites 531
17.3.17 Structure Solution Software Specifically for Powder Diffraction 531
17.3.18 Structure Solution Using Single Crystal Software 534
17.3.19 2D to 3D Molecular Model Generation 534
17.3.20 Single Crystal Refinement Programs and Helper Programs to Assist in Building up the Structure 538
17.3.21 Rietveld Structure Refinement 541
17.3.22 Pair Distribution Function Software 541
17.3.23 Hydrogen Placement Using Single Crystal and Ancillary Software 541
17.3.24 Free Standing Powder and Single Crystal Fourier Map Generation and Display Software 541
17.3.25 Quantitative Phase Analysis 548
17.3.26 Powder Pattern Calculation 548
17.3.27 Structure Validation 548
17.3.28 Crystallographic Structure Visualization: During Structure Solution and Refinement 554

17.3.29 Visualization and Photo Realistic Rendering of Crystal Structures 555
17.3.30 Miscellaneous Resources 562
Appendix 1: Internet links for Cited Software and Resources 562

**Subject Index** 571

CHAPTER 1

# Principles of Powder Diffraction

ROBERT E. DINNEBIER[a] AND SIMON J. L. BILLINGE[b]

[a] Max-Planck-Institute for Solid State Research, Heisenbergstrasse 1, D-70569 Stuttgart, Germany; [b] Department of Physics and Astronomy, 4268 Biomed. Phys. Sci. Building, Michigan State University, East Lansing, MI 48824, USA

## 1.1 INTRODUCTION

This chapter presents some very basic results about the geometry of diffraction from crystals. This is developed in much greater detail in many textbooks but a concise statement of the basic concepts greatly facilitates the understanding of the advanced later chapters so we reproduce it here for the convenience of the reader. Since the results are so basic, we do not make any attempt to reference the original sources. The bibliography at the end of the chapter lists a selection of some of our favorite introductory books on powder diffraction.

## 1.2 FUNDAMENTALS

X-rays are electromagnetic (em) waves with a much shorter wavelength than visible light, typically on the order of 1 Å ($=1\times10^{-10}$ m). The physics of em-waves is well understood and excellent introductions to the subject are found in every textbook on optics. Here we briefly review the results most important for understanding the geometry of diffraction from crystals. Classical em-waves can be described by a sine wave that repeats periodically every $2\pi$ radians. The spatial length of each period is the wavelength $\lambda$. If two identical waves are not coincident, they are said to have a "phase shift" with respect to each other (Figure 1.1). This is either measured as a linear shift, $\Delta$ on a length scale, in the units of the wavelength, or equivalently as a phase shift, $\delta\phi$ on an angular scale, such that:

$$\frac{\Delta}{\lambda}=\frac{\delta\varphi}{2\pi}\Rightarrow\delta\varphi=\frac{2\pi}{\lambda}\Delta \tag{1}$$

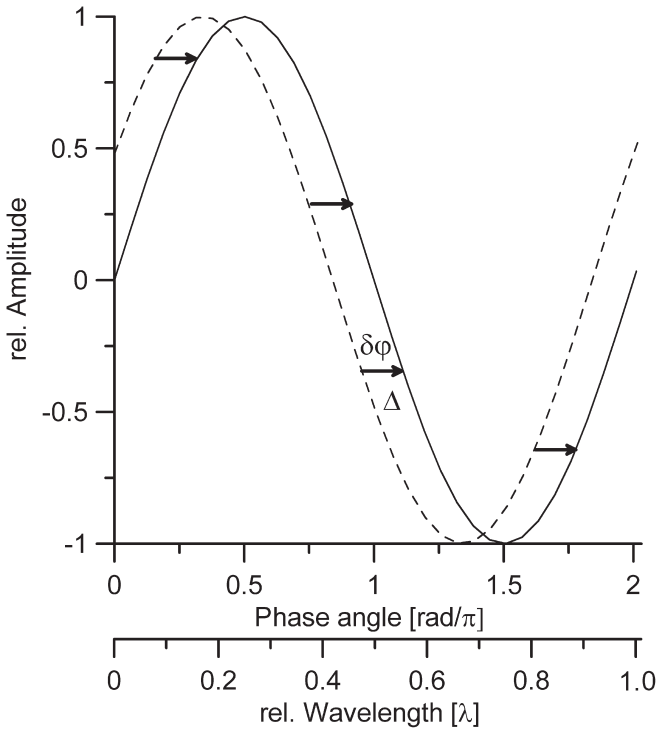



**Figure 1.1** Graphical illustration of the phase shift between two sine waves of equal amplitude.

The detected intensity, $I$, is the square of the amplitude, $A$, of the sine wave. With two waves present, the resulting amplitude is not just the sum of the individual amplitudes but depends on the phase shift $\delta\varphi$. The two extremes occur when $\delta\varphi = 0$ (constructive interference), where $I = (A_1 + A_2)^2$, and $\delta\varphi = \pi$ (destructive interference), where $I = (A_1 - A_2)^2$. In general, $I = [A_1 + A_2 \exp(i\delta\varphi)]^2$. When more than two waves are present, this equation becomes:

$$I = \left[\sum_j A_j \exp(i\varphi_j)\right]^2, \tag{2}$$

where the sum is over all the sine-waves present and the phases, $\phi_j$ are measured with respect to some origin.

X-ray diffraction involves the measurement of the intensity of X-rays scattered from electrons bound to atoms. Waves scattered at atoms at different positions arrive at the detector with a relative phase shift. Therefore, the measured intensities yield information about the relative atomic positions (Figure 1.2).

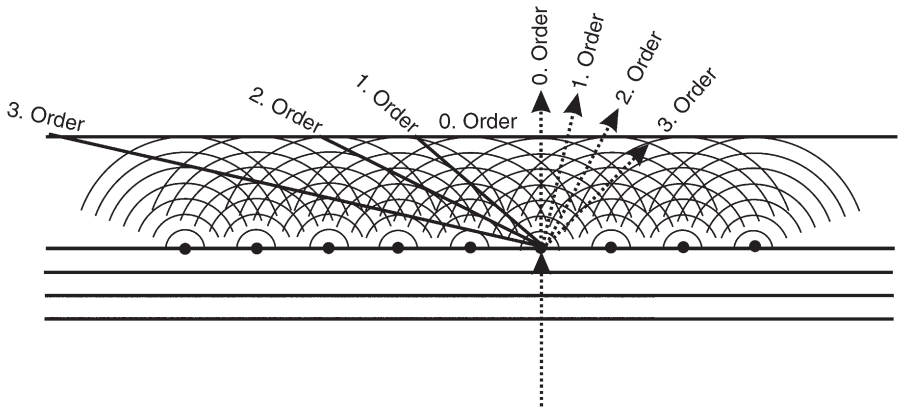



**Figure 1.2** Scattering of a plane wave by a one dimensional chain of atoms. Wave front and wave vectors of different orders are given. Dashed lines indicate directions of incident and scattered wave propagation. The labeled orders of diffraction refer to the directions where intensity maxima occur due to constructive interference of the scattered waves.

In the case of X-ray diffraction, the Fraunhofer approximation is used to calculate the detected intensities. This is a far-field approximation, where the distance, $L_1$, from the source to the place where scattering occurs (the sample), and then on to the detector, $L_2$, is much larger than the separation, $D$, of the scatterers. This is an excellent approximation, since in this case $D/L_1 \approx D/L_2 \approx 10^{-10}$. The Fraunhofer approximation greatly simplifies the mathematics. The incident X-rays form a wave such that the constant phase wave front is a plane wave. X-rays scattered by single electrons are outgoing spherical waves that again appear as plane waves in the far-field. This allows us to express the intensity of diffracted X-rays using Equation (2).

The phases $\varphi_j$ introduced in Equation (2), and therefore the measured intensity $I$, depend on the position of the atoms, $j$, and the directions of the incoming and the scattered plane waves (Figure 1.2). Since the wave-vectors of the incident and scattered waves are known, we can infer the relative atomic positions from the detected intensities.

From optics we know that diffraction only occurs if the wavelength is comparable to the separation of the scatterers. In 1912, Friedrich, Knipping and Max von Laue performed the first X-ray diffraction experiment using single crystals of copper sulfate and zinc sulfite, proving the hypothesis that X-rays are em-waves of very short wavelength, on the order of the separation of the atoms in a crystalline lattice. Four years later (1916), Debye and Scherrer reported the first powder diffraction pattern with a procedure that is named after them.

## 1.3 DERIVATION OF THE BRAGG EQUATION

The easiest access to the structural information in powder diffraction is *via* the well-known Bragg equation (W. L. Bragg, 1912), which describes the principle

of X-ray diffraction in terms of a reflection of X-rays by sets of lattice planes. Lattice planes are crystallographic planes, characterized by the index triplet *hkl*, the so-called Miller indices. Parallel planes have the same indices and are equally spaced, separated by the distance $d_{hkl}$. Bragg analysis treats X-rays like visible light being reflected by the surface of a mirror, with the X-rays being specularly reflected at the lattice planes. In contrast to the lower energy visible light, the X-rays penetrate deep inside the material where additional reflections occur at thousands of consecutive parallel planes. Since all X-rays are reflected in the same direction, superposition of the scattered rays occurs. From Figure 1.3 it follows that the second wave travels a longer distance *PN* before and *NQ* after reflection occurs. Constructive interference occurs only if $\Delta = PN + NQ$ is a multiple $n = 0, \pm 1, \pm 2, \ldots$ of the wavelength $\lambda$:

$$\Delta = n\lambda \tag{3}$$

In all other cases, destructive interference results since it is always possible to find a deeper plane, *p*, for which the relation $p\Delta = n\lambda$ with $n = \pm 1/2, \pm 3/2, \ldots$ (*i.e.*, perfect destructive interference) exactly holds. Thus, sharp intensity maxima emerge from the sample only at the special angles where Equation (3) holds, with no intensity in between. As can be easily seen from Figure 1.3, geometrically:

$$\Delta = 2d \sin\theta \tag{4}$$

where *d* is the interplanar spacing of parallel lattice planes and $2\theta$ is the diffraction angle, the angle between the incoming and outgoing X-ray beams. Combining Equations (3) and (4) we get:

$$n\lambda = 2d \sin\theta \tag{5}$$

the famous Bragg equation.

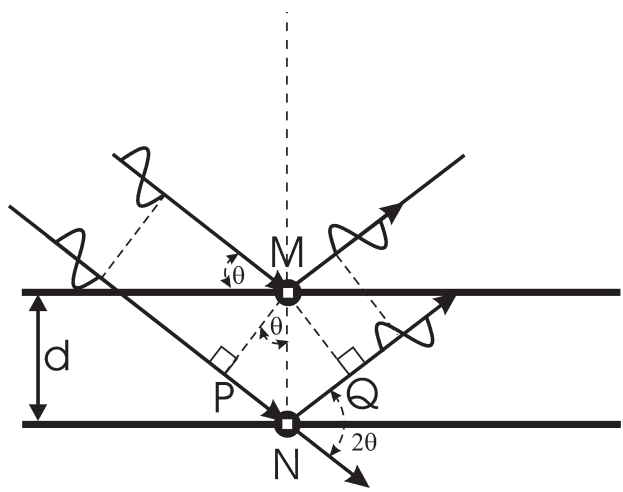



**Figure 1.3** Illustration of the geometry used for the simplified derivation of Bragg's law.

This simplified derivation of the Bragg equation, although leading to the correct solution, has a serious drawback. In reality the X-rays are not reflected by planes but are scattered by electrons bound to the atoms. Crystal planes are not like shiny optical mirrors, but contain discrete atoms separated by regions of much lower electron intensity, and, in general, atoms in one plane will not lie exactly above atoms in the plane below. How is it then that the simplified picture shown in Figure 1.3 results in the correct result? A more general description (Bloss, 1971) shows that Equation (5) is also valid, if the atom of the lower lattice plane in Figure 1.3 is shifted by an arbitrary amount parallel to the plane (Figure 1.4).

The phase shift can immediately be deduced from Figure 1.4 as:

$$\begin{aligned} n\lambda &= MN\cos(180^\circ - (\alpha+\theta)) + MN\cos(\alpha-\theta) \\ &= MN[-\cos(\alpha+\theta) + \cos(\alpha-\theta)] \end{aligned} \tag{6}$$

From any textbook on trigonometry we know that:

$$\begin{aligned} \cos(\alpha+\theta) &= \cos\alpha\cos\theta - \sin\alpha\sin\theta \\ \cos(\alpha-\theta) &= \cos\alpha\cos\theta + \sin\alpha\sin\theta \end{aligned} \tag{7}$$

Therefore Equation (7) becomes:

$$n\lambda = MN[2\sin\alpha\sin\theta] \tag{8}$$

with:

$$d = MN\sin\alpha \tag{9}$$

from which the already known Bragg equation follows:

$$n\lambda = 2d\sin\theta \tag{10}$$

Another equivalent, and highly useful, expression of the Bragg equation is:

$$Ed = \frac{6.199}{\sin\theta} \quad \text{with} \quad \lambda[\text{Å}] = \frac{12.398}{E[\text{keV}]} \tag{11}$$

with the energy $E$ of the X-rays in keV.

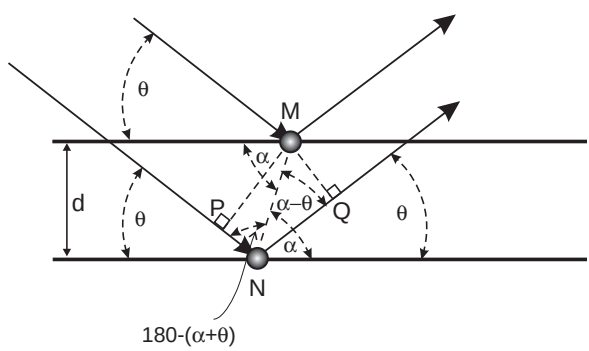



**Figure 1.4** Illustration of the geometry in the general case where scattering takes place at the position of atoms in consecutive planes.

To derive the Bragg equation, we used an assumption of specular reflection, which is borne out by experiment. For crystalline materials, destructive interference completely destroys intensity in all directions except where Equation (5) holds. This is no longer true for disordered materials where diffracted intensity can be observed in all directions away from reciprocal lattice points, known as diffuse scattering, as discussed in Chapter 16.

## 1.4 THE BRAGG EQUATION IN THE RECIPROCAL LATTICE

As a prerequisite, the so-called reciprocal lattice needs to be introduced. Notably, it is not the intention of this book to reproduce basic crystallographic knowledge but, for completeness, some important formalism that recurs throughout the book is briefly presented.

The reciprocal lattice was invented by crystallographers as a simple and convenient representation of the physics of diffraction by a crystal. It is an extremely useful tool for describing all kinds of diffraction phenomena occurring in powder diffraction (Figure 1.5).

Imagine that besides the "normal" crystal lattice with the lattice parameters $a$, $b$, $c$, $\alpha$, $\beta$, $\gamma$, and the volume $V$ of the unit cell, a second lattice with lattice parameters of $a^*$, $b^*$, $c^*$, $\alpha^*$, $\beta^*$, $\gamma^*$, and the volume $V^*$, and with the same origin, exists such that:

$$\begin{gathered}\mathbf{a}\cdot\mathbf{b}^* = \mathbf{a}\cdot\mathbf{c}^* = \mathbf{b}\cdot\mathbf{c}^* = \mathbf{a}^*\cdot\mathbf{b} = \mathbf{a}^*\cdot\mathbf{c} = \mathbf{b}^*\cdot\mathbf{c} = 0^{\dagger} \\ \mathbf{a}\cdot\mathbf{a}^* = \mathbf{b}\cdot\mathbf{b}^* = \mathbf{c}\cdot\mathbf{c}^* = 1\end{gathered} \tag{12}$$

This is known as the reciprocal lattice, which exists in so-called reciprocal space. As we will see, it turns out that the points in the reciprocal lattice are related to the vectors defining the crystallographic planes. There is one point in the reciprocal lattice for each crystallographic plane, *hkl*. For now, just consider $h$, $k$ and $l$ to be integers that index a point in the reciprocal lattice. A reciprocal lattice vector $\mathbf{h}_{\mathrm{hkl}}$ is the vector from the origin of reciprocal space to the (*hkl*) reciprocal lattice point:[‡]

$$\mathbf{h}_{hkl} = h\mathbf{a}^* + k\mathbf{b}^* + l\mathbf{c}^*;\ h,k,l \in Z \tag{13}$$

The length of the reciprocal base vectors is defined according to:

$$\mathbf{a}^* = x(\mathbf{b}\times\mathbf{c}) \tag{14}$$

where the scale factor $x$ can easily be deduced using Equation (12) as:

$$\mathbf{a}^*\mathbf{a} = x(\mathbf{b}\times\mathbf{ca}) = xV \Rightarrow x = \frac{1}{V} \tag{15}$$

[†] Vectors are in bold.

[‡] The reciprocal lattice is a commonly used construct in solid state physics, but with a different normalization: $\mathbf{a}\ \mathbf{a}^*\quad 2\pi$.

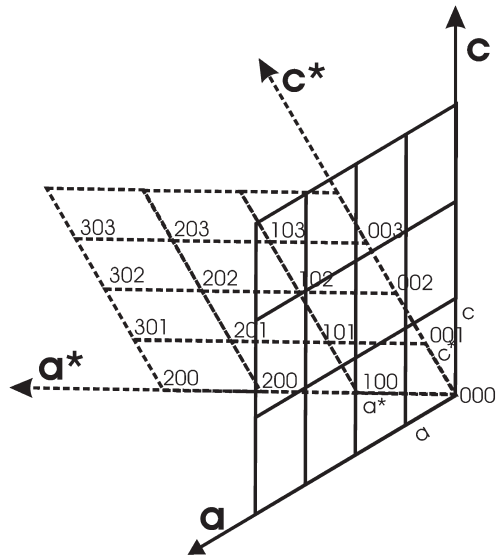



**Figure 1.5** Two dimensional monoclinic lattice and its corresponding reciprocal lattice.

leading to:

$$\mathbf{a}^* = \frac{1}{V}(\mathbf{b} \times \mathbf{c}),\ \mathbf{b}^* = \frac{1}{V}(\mathbf{c} \times \mathbf{a}),\ \mathbf{c}^* = \frac{1}{V}(\mathbf{a} \times \mathbf{b}), \tag{16}$$

and vice versa:

$$\mathbf{a} = \frac{1}{V^*}(\mathbf{b}^* \times \mathbf{c}^*),\ \mathbf{b} = \frac{1}{V^*}(\mathbf{c}^* \times \mathbf{a}^*),\ \mathbf{c} = \frac{1}{V^*}(\mathbf{a}^* \times \mathbf{b}^*) \tag{17}$$

The relationship between the reciprocal and the real lattice parameters is:

$$\begin{aligned}
a^* &= \frac{bc\sin\alpha}{V}, \\
b^* &= \frac{ac\sin\beta}{V}, \\
c^* &= \frac{ab\sin\gamma}{V}, \\
\cos\alpha^* &= \frac{\cos\beta\cos\gamma - \cos\alpha}{\sin\beta\sin\gamma}, \\
\cos\beta^* &= \frac{\cos\beta\cos\gamma - \cos\alpha}{\sin\beta\sin\gamma}, \\
\cos\alpha^* &= \frac{\cos\beta\cos\gamma - \cos\alpha}{\sin\beta\sin\gamma}, \\
V &= abc\sqrt{1 + 2\cos\alpha\cos\beta\cos\gamma - \cos^2\alpha - \cos^2\beta - \cos^2\gamma}
\end{aligned} \tag{18}$$

Equation (18) simplifies considerably for higher symmetry crystal systems.

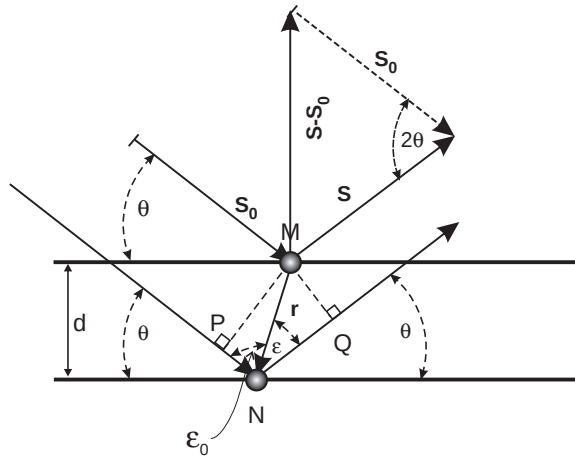



**Figure 1.6** Illustration of the important wave and scattering vectors in the case of elastic Bragg scattering.

We now rederive Bragg's law using vector notation. The wave vectors of the incoming and outgoing beams are given by $\mathbf{s}_0$ and $\mathbf{s}$, respectively (Figure 1.6). They point in the direction of propagation of the wave and their length depends on $\lambda$. For elastic scattering (no change in wavelength on scattering), $\mathbf{s}_0$ and $\mathbf{s}$ have the same length.

We define the scattering vector as:

$$\mathbf{h} = (\mathbf{s} - \mathbf{s}_0) \tag{19}$$

which for a specular reflection is always perpendicular to the scattering plane. The length of $\mathbf{h}$ is given by:

$$\frac{h}{s} = 2\sin\theta \tag{20}$$

Comparison with the formula for the Bragg equation [Equation (5)]:

$$\frac{n\lambda}{d} = 2\sin\theta \tag{21}$$

we get:

$$\frac{n\lambda}{d} = \frac{h}{s} \tag{22}$$

Setting the magnitude of $\mathbf{s}$ to $1/\lambda$, we get the Bragg equation in terms of the magnitude of the scattering vector $h$:

$$h = \frac{n}{d} \tag{23}$$

This shows that diffraction occurs when the magnitude of the scattering vector $\mathbf{h}$ is an integral number of reciprocal lattice spacings $1/d$. We define a vector $\mathbf{d}^*$

perpendicular to the lattice planes with length $1/d$. Since **h** is perpendicular the scattering plane, this leads to:

$$\mathbf{h} = n\mathbf{d}^* \tag{24}$$

Diffraction can occur at different scattering angles $2\theta$ for the same crystallographic plane, giving the different orders $n$ of diffraction. For simplicity, the number $n$ will be incorporated in the indexing of the lattice planes, where:

$$d^*_{nh,nk,nl} = nd^*_{hkl} \tag{25}$$

*e.g.*, $d^*_{222} = 2d^*_{111}$ and we get an alternative expression for Bragg's equation:

$$\mathbf{h} = \mathbf{d}^*_{hkl} \tag{26}$$

The vector $\mathbf{d}^*_{hkl}$ points in a direction perpendicular to a real space lattice plane. We would like to express this vector in terms of reciprocal space basis vectors **a***, **b***, **c***.

First we define $\mathbf{d}_{hkl}$ in terms of real space basis vectors **a**, **b**, **c**. Referring to Figure 1.7, we can define that:

$$\mathbf{OA} = \frac{1}{h}\mathbf{a},\ \mathbf{OB} = \frac{1}{k}\mathbf{b},\ \mathbf{OC} = \frac{1}{l}\mathbf{c} \tag{27}$$

with $h$, $k$, and $l$ being integers as required by the periodicity of the lattice. These three integers are the Miller indices that provide a unique definition for the set of parallel planes.

The plane perpendicular vector $\mathbf{d}_{hkl}$ originates on one plane and terminates on the next parallel plane. Therefore, $\mathbf{OA} \cdot \mathbf{d} = (OA)d\cos\alpha$. From Figure 1.7 we see that, geometrically, $(OA)\cos\alpha = d$. Substituting, we get $\mathbf{OA} \cdot \mathbf{d} = d^2$. Combining with Equation (27) leads to:

$$\frac{1}{h}\mathbf{a} \cdot \mathbf{d} = d^2 \tag{28}$$

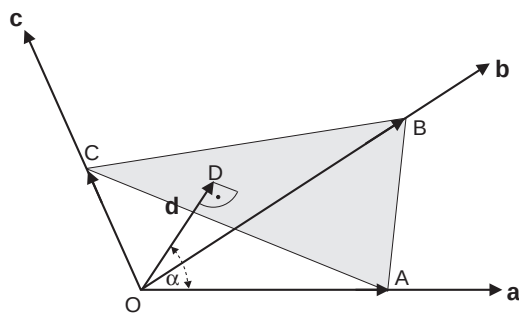



**Figure 1.7** Geometrical description of a lattice plane in terms of real space basis vectors.

and consequently:

$$h = \mathbf{a} \cdot \frac{\mathbf{d}}{d^2},\ k = \mathbf{b} \cdot \frac{\mathbf{d}}{d^2},\ l = \mathbf{c} \cdot \frac{\mathbf{d}}{d^2} \tag{29}$$

By definition, $h$, $k$, and $l$ are divided by their largest common integer to be Miller indices. The vector $\mathbf{d}^*_{hkl}$, from Bragg's Equation (26) points in the plane normal direction parallel to $\mathbf{d}$ but with length $1/d$. We can now write $\mathbf{d}^*_{hkl}$ in terms of the vector $\mathbf{d}$:

$$\mathbf{d}^*_{hkl} = \frac{\mathbf{d}}{d^2} \tag{30}$$

which gives:

$$\mathbf{d}^*_{hkl} = h\mathbf{a} + k\mathbf{b} + l\mathbf{c} \tag{31}$$

or written in terms of the reciprocal basis:

$$\mathbf{d}^*_{hkl} = h\mathbf{a}^* + k\mathbf{b}^* + l\mathbf{c}^* \tag{32}$$

which was obtained using:

$$\begin{aligned} \mathbf{d}^*_{hkl} \cdot \mathbf{a}^* &= h\mathbf{a} \cdot \mathbf{a}^* + k\mathbf{b} \cdot \mathbf{a}^* + l\mathbf{c} \cdot \mathbf{a}^* = h \\ \mathbf{d}^*_{hkl} \cdot \mathbf{b}^* &= h\mathbf{a} \cdot \mathbf{b}^* + k\mathbf{b} \cdot \mathbf{b}^* + l\mathbf{c} \cdot \mathbf{b}^* = k \\ \mathbf{d}^*_{hkl} \cdot \mathbf{c}^* &= h\mathbf{a} \cdot \mathbf{c}^* + k\mathbf{b} \cdot \mathbf{c}^* + l\mathbf{c} \cdot \mathbf{c}^* = l \end{aligned} \tag{33}$$

Comparing Equation (32) with Equation (13) proves the identity of $\mathbf{d}^*_{hkl}$ and the reciprocal lattice vectorh $\mathbf{h}_{hkl}$. Bragg's equation, Equation (26), can be restated as:

$$\mathbf{h} = \mathbf{h}_{hkl} \tag{34}$$

In other words, diffraction occurs whenever the scattering vector $\mathbf{h}$ equals a reciprocal lattice vector $\mathbf{h}_{hkl}$. This powerful result is visualized in the useful Ewald construction that is described below.

Useful equivalent variations of the Bragg equation are:

$$|\mathbf{h}| = |\mathbf{s} - \mathbf{s}_0| = \frac{2\sin\theta}{\lambda} = \frac{1}{d} \tag{35}$$

and:

$$|\mathbf{Q}| = \frac{4\pi\sin\theta}{\lambda} = \frac{2\pi}{d} \tag{36}$$

The vector $\mathbf{Q}$ is the physicist's equivalent of the crystallographer's $\mathbf{h}$. The physical meaning of $\mathbf{Q}$ is the momentum transfer on scattering and differs from the scattering vector $\mathbf{h}$ by a factor of $2\pi$.

## 1.5 THE EWALD CONSTRUCTION

The Bragg equation shows that diffraction occurs when the scattering vector equals a reciprocal lattice vector. The scattering vector depends on the geometry of the experiment whereas the reciprocal lattice is determined by the orientation and the lattice parameters of the crystalline sample. Ewald's construction combines these two concepts in an intuitive way. A sphere of radius $1/\lambda$ is constructed and positioned in such a way that the Bragg equation is satisfied, and diffraction occurs, whenever a reciprocal lattice point coincides with the surface of the sphere (Figure 1.8).

The recipe for constructing Ewald's sphere[§] is as follows (Figure 1.8):

1. Draw the incident wave vector $\mathbf{s}_0$. This points in the direction of the incident beam with length $1/\lambda$.
2. Draw a sphere centered on the tail of this vector with radius $1/\lambda$. The incident wave vector $\mathbf{s}_0$ defines the radius of the sphere. The scattered wave vector $\mathbf{s}$, also of length $1/\lambda$, points in a direction from the sample to the detector. This vector is drawn also starting from the center of the sphere and also terminates at a point on the surface. The scattering vector $\mathbf{h} = \mathbf{s} - \mathbf{s}_0$ completes the triangle from the tip of $\mathbf{s}$ to the tip of $\mathbf{s}_0$, both lying on the surface of the sphere.
3. Draw the reciprocal lattice with the origin lying at the tip of $\mathbf{s}_0$.
4. Find all the places on the surface of the sphere, where reciprocal lattice points lie.

This construction places a reciprocal lattice point at one end of $\mathbf{h}$. By definition, the other end of $\mathbf{h}$ lies on the surface of the sphere. Thus, Bragg's law is only satisfied, when another reciprocal lattice point coincides with the surface of the sphere. Diffraction is emanating from the sample in these directions. To detect the diffracted intensity, one simply moves the detector to the right position. Any vector between two reciprocal lattice points has the potential to produce a Bragg peak. The Ewald sphere construction additionally indicates which of these possible reflections satisfy experimental constraints and are therefore experimentally accessible.

Changing the orientation of the crystal reorients the reciprocal lattice bringing different reciprocal lattice points on to the surface of the Ewald sphere. An ideal powder contains individual crystallites in all possible orientations with equal probability. In the Ewald construction, every reciprocal lattice point is smeared out onto the surface of a sphere centered on the origin of reciprocal space. This is illustrated in Figure 1.9. The orientation of the $\mathbf{d}^*_{hkl}$ vector is lost and the three-dimensional vector space is reduced to one dimension of the modulus of the vector $\mathbf{d}^*_{hkl}$.

These spherical shells intersect the surface of the Ewald sphere in circles. Figure 1.10 shows a two-dimensional projection. Diffracted beams emanate

[§] For practical reasons, plots of the Ewald "sphere" are circular cuts through the sphere and the corresponding slice of reciprocal space.

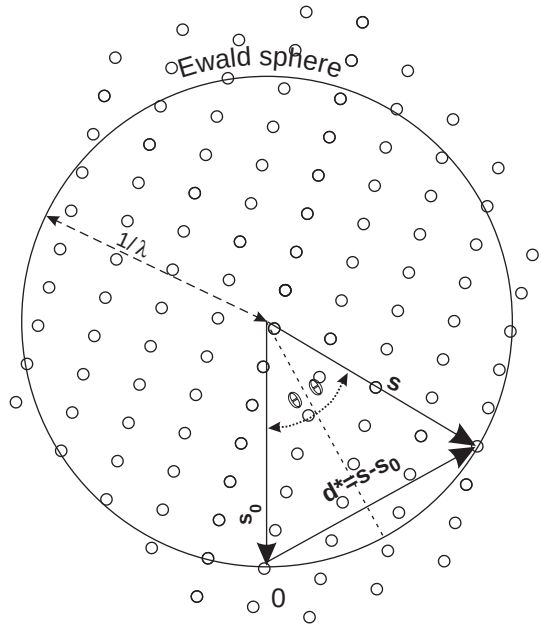



**Figure 1.8** Geometrical construction of the Ewald circle. The "0" marks the origin of reciprocal space. The vectors are defined in the text.

from the sample in the directions where the thin circles from the smeared reciprocal lattice intersect the thick circle of the Ewald sphere. A few representative reflected beams are indicated by the broken lines.

The lowest *d*-spacing reflections accessible in the experiment are determined by the diameter of the Ewald sphere $2/\lambda$. To increase the number of detectable reflections one must decrease the incident wavelength. In the case of an energy dispersive experiment such as time-of-flight neutron powder diffraction, which makes use of a continuous distribution of wavelengths from $\lambda_{min}$ to $\lambda_{max}$ at fixed angle, all smeared out cones between the two limiting Ewald spheres can be detected.

In three dimensions, the circular intersection of the smeared reciprocal lattice with the Ewald sphere results in the diffracted X-rays of the reflection *hkl* forming coaxial cones, the so-called Debye–Scherrer cones (Figure 1.11).

The smearing of reciprocal space in a powder experiment makes the measurement easier but results in a loss of information. Reflections overlap from lattice planes whose vectors lie in different directions but which have the same *d*-spacing. These cannot be resolved in the measurement. Some of these overlaps are dictated by symmetry (systematic overlaps) and others are accidental. Systematic overlaps are less serious for equivalent reflections [*e.g.*, the six Bragg peaks (100), (−100), (010), . . . from the faces of a cube] since the multiplicity is known from the symmetry. For highly crystalline samples, accidental overlaps can be reduced by making measurements

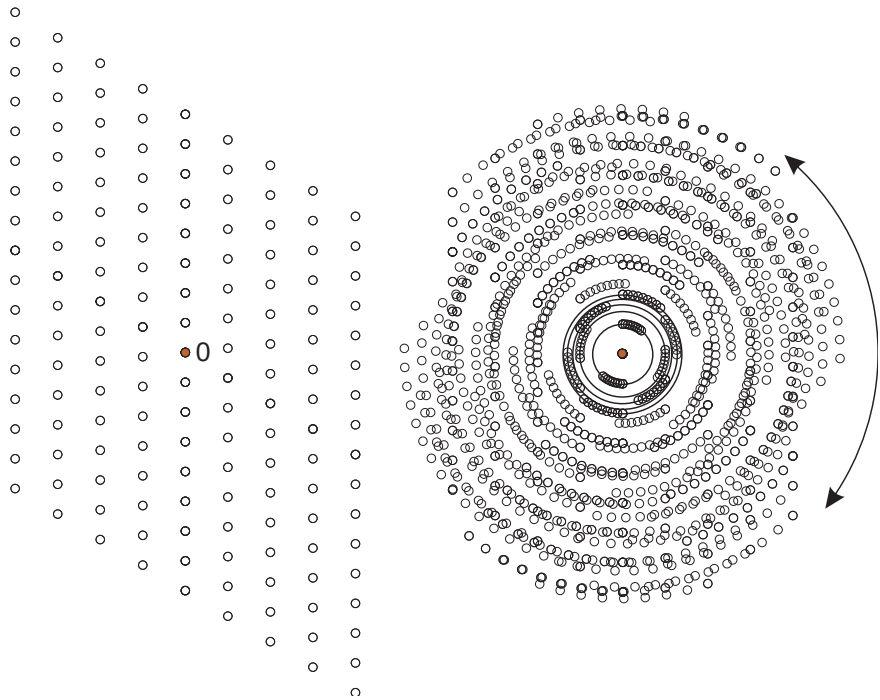



**Figure 1.9** Illustration of the reciprocal lattice associated with a single crystal lattice (left) and a large number of randomly oriented crystallites (right). A real powder consists of so many grains that the dots of the reciprocal lattice form into continuous lines.

with higher resolution, or by taking data at different temperatures in an attempt to remove the overlap by differential thermal expansion of different cell parameters.

To obtain the maximum amount of information, a spherical shell detector would be desirable, though currently impractical. Often, a flat two-dimensional detector, either film, image plate, or CCD is placed perpendicular to the direct beam. In this case, the Debye–Scherrer cones appear as circles as shown in Figure 1.12a.

For an ideal powder, the intensity around the rings is isotropic. Conventional powder diffraction measurements, *e.g.*, Bragg–Brentano geometry, take one-dimensional cuts through the rings, either horizontally or vertically depending on the geometry of the diffractometer. If the full rings, or fractions of them, are detected with two-dimensional detectors the counting statistics can be improved by integrating around the rings. If the powder is non-ideal, the ring intensity is no longer uniform, as illustrated in Figure 1.12b, giving arbitrary intensities for the reflections in a one-dimensional scan. To improve powder statistics, powder samples are generally rotated during measurement. However, the intensity variation around the rings can give important

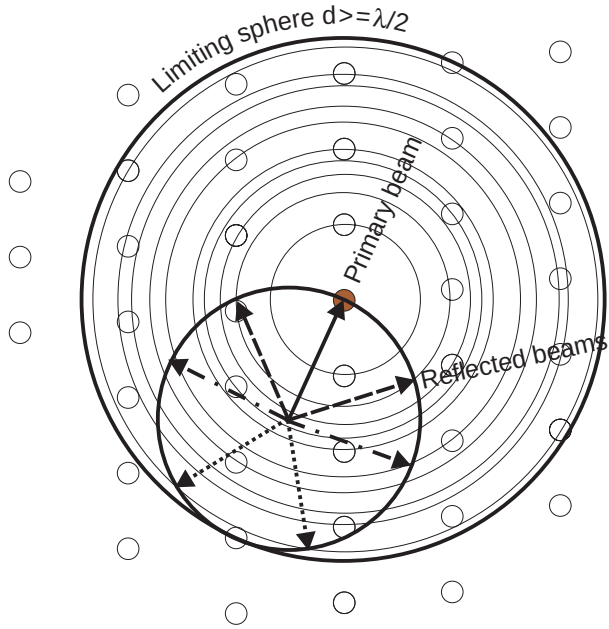



**Figure 1.10** Illustration of the region of reciprocal space that is accessible in a powder measurement. The smaller circle represents the Ewald sphere. As shown in Figure 1.9, in a powder the reciprocal lattice is rotated to sample all orientations. An equivalent operation is to rotate the Ewald sphere in all possible orientations around the origin of reciprocal space. The volume swept out (area in the figure) is the region of reciprocal space accessible in the experiment.

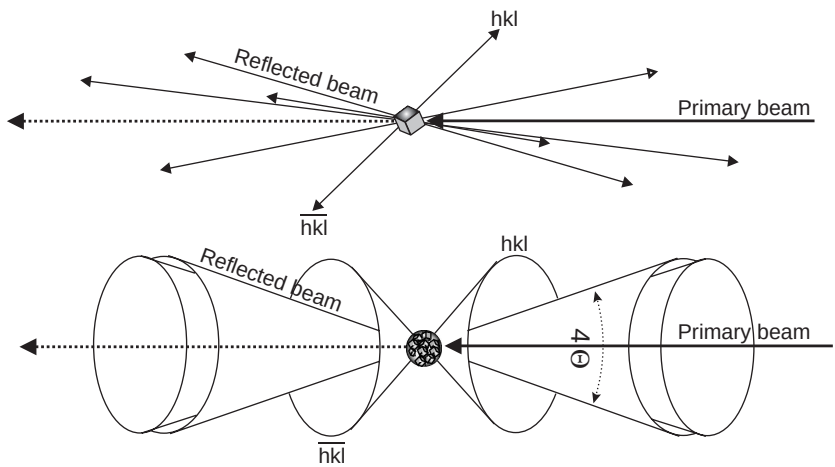



**Figure 1.11** Comparison between the scattered beams originating from a single crystal (top) and a powder (bottom). For the latter, some Debye Scherrer cones are drawn.

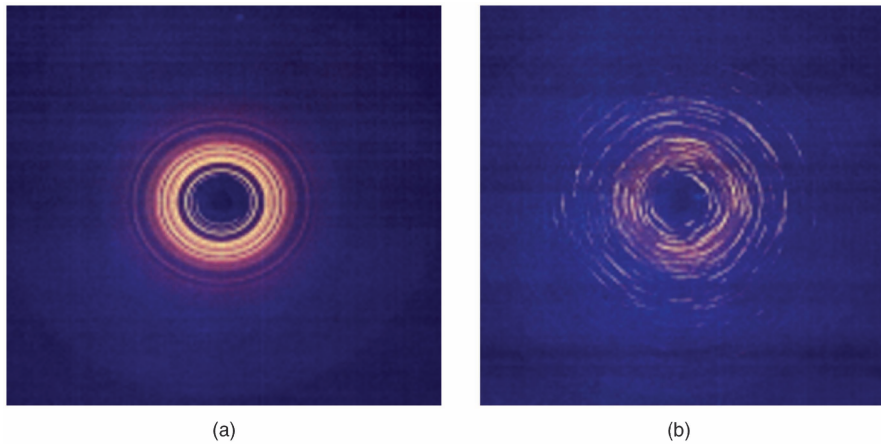



**Figure 1.12** Debye Scherrer rings from an ideal fine grained (a, left) and a grainy (b, right) powder sample.

information about the sample such as preferred orientation of the crystallites or texture.

## 1.6 TAKING DERIVATIVES OF THE BRAGG EQUATION

Several important relationships in crystallography directly follow from a derivative of the Bragg equation [Equation (5)]. First we rewrite Bragg's law making the $d$-spacing the subject of the equation:

$$d = \frac{n\lambda}{2\sin\theta} \tag{37}$$

The uncertainty of the measured lattice spacing is given by the total derivative $\mathrm{d}d$, which can be written according to the chain rule as:

$$\mathrm{d}d = \frac{\partial d}{\partial \theta}\mathrm{d}\theta + \frac{\partial d}{\partial \lambda}\mathrm{d}\lambda \tag{38}$$

leading to:

$$\mathrm{d}d = \frac{n\lambda}{2\sin\theta}\frac{\cos\theta}{\sin\theta}\mathrm{d}\theta + \frac{n}{2\sin\theta}\mathrm{d}\lambda \tag{39}$$

and finally:

$$\frac{\mathrm{d}d}{d} = -\frac{\mathrm{d}\theta}{\tan\theta} + \frac{\mathrm{d}\lambda}{\lambda} \tag{40}$$

This equation allows us to discuss several physically important phenomena.

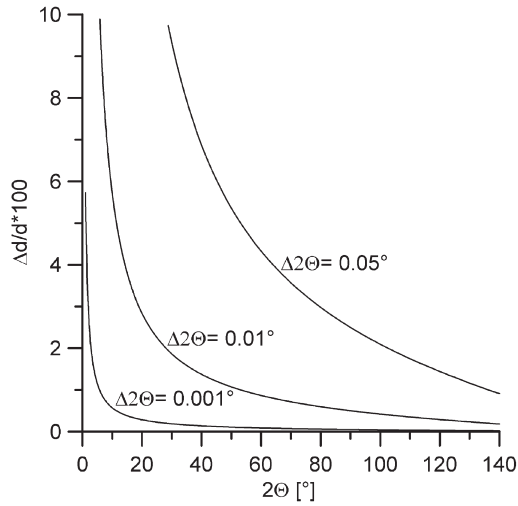



**Figure 1.13** Percentage error in measured $d$ spacing as a function of scattering angle arising from a constant angular misalignment of $\Delta\Theta$ for a well aligned (0.001°), a typically aligned, (0.01°) and a poorly aligned (0.05°) diffractometer.

When a crystal is strained, the $d$-spacings vary. A macroscopic strain changes the interplanar spacing by $\Delta d_{hkl}$, giving rise to a shift in the average position of the diffraction peak of $\Delta\theta$, while microscopic strains give a distribution of $d$-spacings $\Delta d_{hkl}$ which broaden the peak by $\delta\theta$. This is discussed in detail in Chapters 12 and 13.

A constant angular offset due to misalignment of the diffractometer gives rise to a nonlinear error in our determination of $d_{hkl}$, disproportionately affecting low angle reflections (Figure 1.13). Similarly, our ability to resolve two partially overlapping reflections separated by $\Delta d_{hkl}$ is limited by the finite angular resolution $\Delta\theta$ of the diffractometer.

There are many geometrical contributions to the angular resolution (*e.g.*, angular width of the receiving slit in front of the detector). Another contribution comes from finite wavelength spread of the incident beam $\Delta\lambda$. From Equation (40) we get the angular dispersion to be:

$$\frac{\mathrm{d}\theta}{\mathrm{d}\lambda} = \frac{\tan\theta}{\lambda} \tag{41}$$

This is plotted in Figure 1.14, which shows that the resolution due to a finite spread in $\lambda$ is decreasing at higher angles. In a real experiment the angle dependence of the resolution function can be complicated. In traditional modeling programs the Bragg-peak line shapes are modeled using empirical line-shape functions. More recently, approaches have been developed that explicitly account for the different physical processes that result in the line

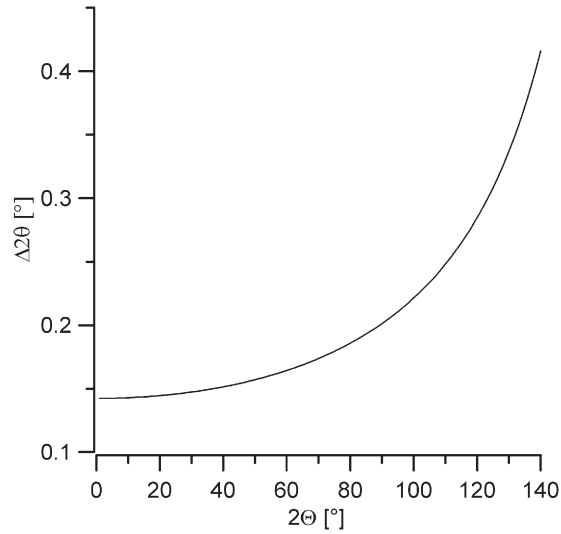



**Figure 1.14** Angular dependence of the intrinsic peak width (resolution function) of the diffractometer due to the wavelength spread between Cu K$\alpha_1$ and Cu K$\alpha_2$ (about 12 eV).

shapes. This is called the fundamental parameters approach and is described in Chapters 5, 6 and 13.

## 1.7 BRAGG'S LAW FOR FINITE SIZE CRYSTALLITES

Assuming an infinite stack of lattice planes, Bragg's equation gives the position of delta-function Bragg peaks. Finite size crystallites give rise to Bragg peaks of finite width. This size broadening is described by the Scherrer equation. We now reproduce the simple derivation following Klug and Alexander (1974; see Bibliography).

Figure 1.15 shows the path length difference *versus* the depth of the lattice plane. When the angle between the incoming beam and the lattice plane $\Theta$ is different by an amount $\varepsilon$ from the Bragg condition, it is always possible to find a lattice plane inside the crystal where the extra path is $\Delta = \lambda/2$ producing destructive interference. For a thick crystal this is true for arbitrarily small $\varepsilon$, which explains the sharp Bragg reflections. For a crystal with finite dimensions, for small $\varepsilon$ the plane for which $\Delta = (n + \frac{1}{2})\lambda$ holds will not be reached. In this case there is not perfect cancellation of the intensity away from the Bragg condition, thus leading to an intensity distribution over some small angular range. We can use this idea to estimate the broadening of a Bragg reflection due to size effects.

The thickness of a crystallite in the direction perpendicular to $p$ ($hkl$) planes of separation $d_{hkl}$ (Figure 1.15) is:

$$L_{hkl} = pd_{hkl} \tag{42}$$

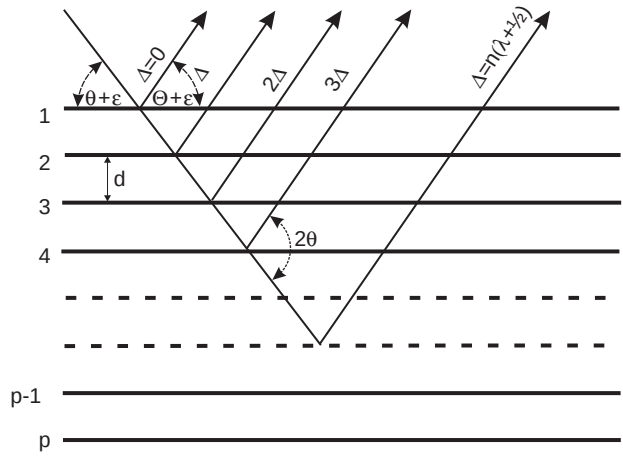



**Figure 1.15** Path length difference of the scattered ray *versus* the depth of the lattice plane in the crystal.

The additional beam path between consecutive lattice planes at the angle $\theta + \varepsilon$ is:

$$\begin{aligned}\Delta &= 2d\sin(\theta+\varepsilon)\\ &= 2d(\sin\theta\cos\varepsilon+\cos\theta\sin\varepsilon)\\ &= n\lambda\cos\varepsilon+\sin\varepsilon 2d\cos\theta\\ &\approx n\lambda+\sin\varepsilon 2d\cos\theta\end{aligned} \tag{43}$$

The corresponding phase difference is then:

$$\delta\varphi = 2\pi\frac{\Delta}{\lambda} = 2\pi n + \frac{4\pi}{\lambda}\varepsilon d\cos\theta = \frac{4\pi\varepsilon d\cos\theta}{\lambda} \tag{44}$$

The phase difference between the top and the bottom layer, $p$ is then:

$$\delta\varphi = p\frac{4\pi\varepsilon d\cos\theta}{\lambda} = \frac{4\pi L_{hkl}\varepsilon\cos\theta}{\lambda} \tag{45}$$

Rearranging Equation (45) leads to:

$$\varepsilon = \frac{\lambda\delta\varphi}{4\pi L_{hkl}\cos\theta} \tag{46}$$

which gives an expression for the misalignment angle in terms of the crystallite size $L_{hkl}$ and the phase difference $\delta\varphi$ between the reflections between the top and the bottom plane. Clearly, the scattered intensity is at a maximum for $\delta\varphi = 0$ ($\varepsilon = 0$). With increasing $\varepsilon$ the intensity decreases giving rise to a peak of finite width. Perfect cancellation of the top and bottom waves occurs a phase difference of $\delta\varphi = \pm\pi$ at which point $\varepsilon = \pm\lambda/(4L_{hkl}\cos\theta)$. On a measured $2\theta$-scale the

measured angular width between these points is:

$$\beta_{hkl} = 4\varepsilon = \frac{\lambda}{L_{hkl}\cos\theta} \tag{47}$$

giving us some measure of the peak width in radians due to the finite particle size. A full treatment taking into account the correct form for the intensity distribution gives:

$$\beta_{hkl} = \frac{K\lambda}{L_{hkl}\cos\theta} \tag{48}$$

with a scale factor of $K = 0.89$ for perfect spheres. In general $K$ depends on the shape of the grains (*e.g.*, $K$ is 0.94 for cubic shaped grains) but is always close to unity. This equation is not valid for crystallites[¶] that are too large or too small. With large crystallites the peak width is governed by the coherence of the incident beam and not by particle size. For nano-scale crystallites, Bragg's law fails and needs to be replaced by the Debye equation (see Chapter 16).

## BIBLIOGRAPHY

1. V. K. Pecharsky and P. Y. Zavalij, *Fundamentals of Powder Diffraction and Structural Characterization of Materials*, Kluwer Academic Publishers, Boston, 2003.
2. D. L. Bish, J. E. Post (Eds.), *Modern Powder Diffraction*, Reviews in Mineralogy Volume 20, Mineralogical Society of America, Chantilly VA, 1989.
3. H. P. Klug and L. E. Alexander, *X-ray Diffraction Procedures*, 2nd edn., John Wiley & Sons, New York, 1974.

[¶] Strictly speaking, the term crystallite size here refers to the dimension of a coherently scattering domain. Only in a perfect crystal, is this the grain size.

CHAPTER 2

# Experimental Setups

JEREMY KARL COCKCROFT[a] AND ANDREW N. FITCH[b]

[a] Department of Chemistry, UCL, Christopher Ingold Laboratories, 20 Gordon Street, London WC1H 0AJ, United Kingdom; [b] European Synchrotron Radiation Facility, BP220, F-38043 Grenoble Cedex, France

## 2.1 INTRODUCTION

In this chapter we describe commonly used experimental setups that are currently used for powder diffraction. We concentrate on modern designs. Excellent descriptions of older setups can be found in books such as Klug and Alexander (H. P. Klug and L. E. Alexander, *X-Ray Diffraction Procedures*, John Wiley & Sons, New York, 2nd edn, 1974).

Great diversity is employed in designing and carrying out powder diffraction experiments, exploiting X-rays from a laboratory generator or from a high-energy storage ring optimised for the generation of synchrotron radiation, or neutrons produced in a reactor or spallation source. A typical wavelength used for a powder diffraction experiment lies in the range 0.1–5 Å, comparable with the spacings between lattice planes in crystals. The spectrum of the X-rays or neutrons employed can range from a tightly defined monochromatic envelope to a wide polychromatic distribution. The object of the experiment being undertaken dictates the radiation to use. The sample can be a self-supporting polycrystalline slab or rod, or a fine powder, mounted in a flat-plate sample holder or contained in a thin-walled glass capillary tube, or are made of platinum for measurements at very high temperatures. Data can be collected in transmission or reflection modes, depending on how strongly the sample absorbs the radiation employed. Sample environments play an important role in many powder experiments, allowing measurements under a wide range of conditions of temperature, pressure, applied stress, or chemical environment (see Chapter 15).

The detector system is a crucial part of any powder diffraction experiment. A standard laboratory instrument may have a single point counter, or may

employ a multichannel, one-dimensional position-sensitive detector (PSD), where the diffracted intensities at many diffraction angles are recorded simultaneously. Diffractometers using monochromatic neutrons or synchrotron X-rays often have several point detectors operating in parallel to increase the efficiency of use of the valuable beam time. One-dimensional PSDs or two-dimensional area detectors are also employed, such as those based on charge-coupled device (CCD) chips or image plates, as these greatly improve the rate of data acquisition, registering complete (or large fractions of) the individual Debye–Scherrer cones. Detectors for experiments using polychromatic X-rays need to be able to distinguish the wavelength of each incoming photon, and therefore need good energy resolution. Similarly, for neutrons from a pulsed source, the time of arrival of each neutron needs to be recorded, so that its time of flight from the source to the detector is known and its speed, and hence wavelength, can be calculated. With multichannel detector systems equipped with fast read-out electronics, diffraction patterns can be measured repeatedly in just a few milliseconds, allowing the investigation of systems that are evolving rapidly during the measurements.

In the following sections we describe in more detail the basic experimental procedures that are used for powder diffraction measurements, and consider important factors that control the performance of the instruments available for laboratory-based experiments, or found at neutron and synchrotron radiation facilities.

## 2.2 SOURCES OF X-RAY RADIATION

### 2.2.1 Laboratory X-ray Sources

X-Rays used for diffraction experiments are electromagnetic radiation with wavelengths in the approximate range $0.1-5$ Å (equivalent to an energy range of about 125 keV$-$2.5 keV). X-Rays were discovered in 1895 by W. C. Röntgen whilst investigating the effects of high tension electrical discharges in evacuated glass tubes. In a standard laboratory instrument, the X-rays are still produced in a sealed-tube source (Figure 2.1), where electrons accelerated by a potential difference of up to 60 kV bombard a metal anode inside a vacuum tube. The electrons induce a cascade of electronic transitions in the atoms of the target material, which emit electromagnetic radiation as they return to the ground state. Divergent X-rays exit the tube *via* beryllium windows in the casing. A typical tube has a power rating of up to 3 kW. Higher power generators exploit spinning anodes to distribute the higher heat load over the target. Such sources differ only in the intensity of the radiation produced. Anode materials must be good conductors of both electricity and heat, and have a suitably high melting point. The most common target elements are Cu and Mo, with Cr, Fe, Co, Ag, and W for specialist applications.

Figure 2.2 illustrates a typical X-ray emission spectrum from a Cu anode. The loss of energy of the electrons by collision with the atoms usually takes place *via* multiple events. The result is the production of a continuous spectrum

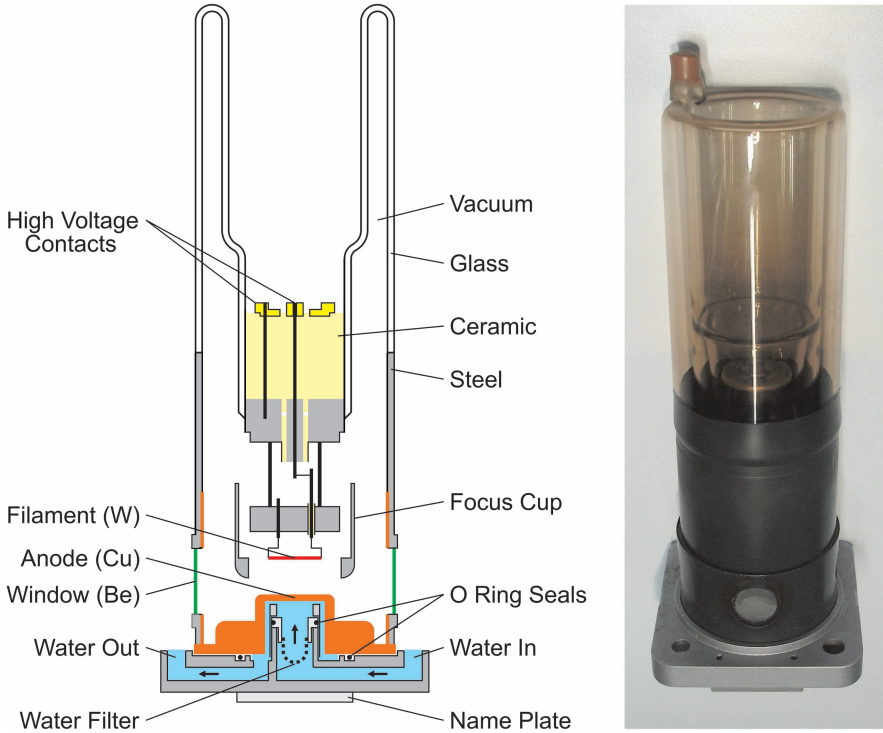



**Figure 2.1** Schematic diagram of a sealed laboratory X ray tube with key components indicated (left), and a photograph of a tube (right). In modern tubes the clear glass vacuum housing has been substituted by ceramic. Manufacturers provide various dimensions for the W filament, leading to "broad", "normal", "fine" and "long fine" focus tubes. The X rays emerge from the four circular Be windows in the base, two of which are parallel to the filament, providing a "line source" of X rays, and two of which are perpendicular, providing a "point source". A line source from a fine or long fine focus tube is preferred for a modern powder diffractometer. Historically, point sources were used for Debye Scherrer cameras.

of X-rays known as *white* radiation. The maximum energy lost, $E(\text{max})$, determines the shortest wavelength, $\lambda(\text{min})$, that can be obtained according to the equation $E = eV = hc/\lambda$, where $e$ is the charge on the electron, $V$ is the accelerating voltage, $h$ is Planck's constant, and $c$ is the speed of light. A more practical form of this equation is given by:

$$\lambda = \frac{12.398}{V}$$

where $V$ is in kV and $\lambda$ is in Å. Thus, the higher the accelerating voltage of the X-ray generator, the shorter the minimum wavelength that can be obtained. The maximum in the intensity of the white radiation occurs at a wavelength

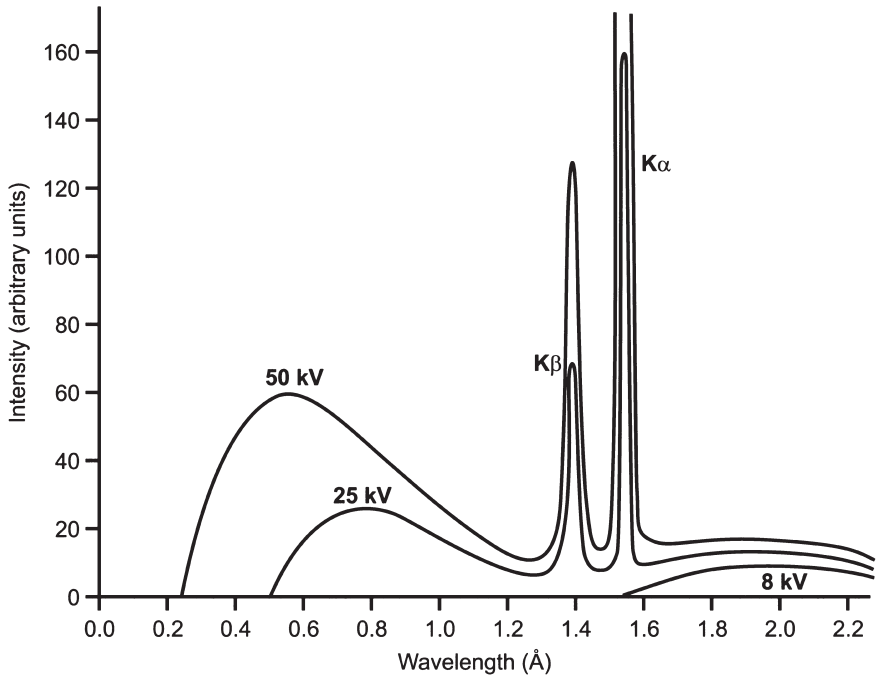



**Figure 2.2** Typical X ray spectra produced by different accelerating voltages from a Cu anode. No characteristic radiation is produced until the voltage level reaches a critical value (about 8.5 kV for Cu). Typical operating voltage is at about 4× the critical voltage: higher voltage levels simply result in an increase in the intensity of the "white" high energy X ray radiation with a relatively small increase in the intensity of the characteristic lines.

that is roughly $1.5 \times \lambda(\text{min})$. Longer wavelengths are obtained by multiple-collision processes. The total intensity, $I(\text{w})$, of the white radiation is approximately proportional to the filament current, $i$, the atomic number of the anode target, $Z$, and the square of the accelerating voltage, $V$.

When the energy of the accelerated electrons is higher than a certain threshold value (which depends on the metal anode), a second type of spectrum is obtained superimposed on top of the white radiation. It is called the *characteristic radiation* and is composed of discrete peaks. The energy (and wavelength) of the peaks depends solely on the metal used for the target and is due to the ejection of an electron from one of the inner electron shells of the metal atom. This results in an electron from a higher atomic level dropping to the vacant level with the emission of an X-ray photon characterised by the difference in energy between the two levels. Figure 2.3 shows the electronic energy levels for a copper atom. In the copper X-ray spectrum, only two characteristic lines are seen at low energy resolution. However, at higher resolution the Kα line is seen to be a doublet, whose components are labelled as $K\alpha_1$ and $K\alpha_2$. The splitting of the 2p orbitals in Cu is very small (0.020 keV)

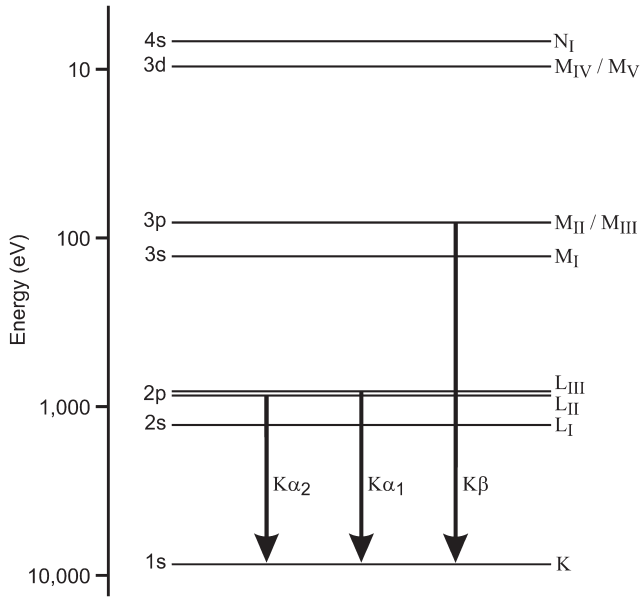



**Figure 2.3** Energy level diagram for a neutral Cu atom. The characteristic peaks illustrated in Figure 2.2 arise from the electronic transitions shown.

**Table 2.1** Approximate principle emission lines for various anode targets.

| *Anode* | *Cu* | *Mo* | *Cr* | *Fe* | *Co* | *Ag* | *W* |
|---|---|---|---|---|---|---|---|
| $\lambda(K\alpha)$ (Å) | 1.54 | 0.71 | 2.29 | 1.94 | 1.79 | 0.56 | 0.21 |

and so the two wavelengths $K\alpha_1$ (1.54056 Å) and $K\alpha_2$ (1.54439 Å) are very similar.

The above description is actually a simplified version of reality since a high-resolution analysis of the spectral lines of Cu K$\alpha$ shows that both the $\alpha_1$ and $\alpha_2$ peaks are distinctly asymmetric. An understanding of the origin of this asymmetry is important in implementing the so-called fundamental *parameters approach* to the profile fitting of powder diffraction data peaks, described in Chapters 5, 6, 9 and 13, in which the detailed spectrum of the incident X-rays must be known. A combination of five Lorentzian functions is commonly used to model the peak shape of Cu $K_\alpha$ radiation,[1,2] though detailed investigations to characterize the X-ray spectrum continue.[3]

Table 2.1 lists the approximate wavelengths of the principle emission lines for various anode targets.

For routine powder diffraction work, a Cu tube is the most common choice, giving the shortest wavelength above 1 Å and the good thermal conductivity of copper, allowing a relatively high power to be applied to the target. The heavier elements give wavelengths too short for most practical use in the laboratory, though they become important for total scattering and PDF

studies (Chapter 16). The longer-wavelength sources are exploited to avoid fluorescence from samples containing elements excited by Cu radiation, *e.g.* to study materials such as steels, Fe and Co tubes are preferred. The disadvantages of such sources are higher absorption by the sample, increased air scatter and fewer accessible Bragg reflections.

### 2.2.2 Synchrotron X-ray Sources

The use of synchrotron X-ray radiation has several advantages over laboratory sources for carrying out high quality powder diffraction measurements. Synchrotron radiation is extremely intense, and is highly collimated in the vertical sense, permitting the design of instruments with much higher $2\theta$ resolution. The wavelength can be chosen to be optimum for a particular measurement, *e.g.* working at short wavelengths to penetrate through absorbing samples, or tuning to the absorption edge of an element in the sample to exploit anomalous scattering phenomena. Beam lines at synchrotron radiation sources have a range of sample environments routinely available. They are staffed by professionals who often are able to provide extensive experimental help. For openly published research, beam-time is typically provided for free to external users following a peer-review of the proposed experiments. Information about gaining access to these facilities can be found at the web-sites of the respective facilities.

Synchrotron radiation is emitted when charged particles travelling at relativistic speeds change velocity, such as when they are made to follow a curved trajectory by a magnetic field. The rapidly spinning neutron star at the centre of the Crab Nebula, the remnants of a supernova that appeared in July 1054, is a celestial source of synchrotron radiation. Early particle accelerators also exhibited synchrotron radiation, which was considered to be a nuisance, as the energy radiating away from the circulating particles needed to be replaced. Modern synchrotron radiation sources are dedicated machines, where electrons or positrons are accelerated to speeds close to that of light and circulate in ultrahigh vacuum tubes, guided by arrays of magnets. The energy of an electron moving with speed $v$ is $E = m_e c^2/\sqrt{1 - v^2/c^2}$ where $m_e$ is the rest mass of the electron [$9.1093826(16) \times 10^{-31}$ kg] and $c$ is the speed of light ($299792458\,\mathrm{m\,s^{-1}}$). The term $1/\sqrt{1 - v^2/c^2}$ is referred to as $\gamma$ and is the factor by which the mass of the electron increases from its rest mass due to its relativistic speed. The energy of the electrons in a storage ring is usually quoted in eV, where 1 eV is $1.60217653(14) \times 10^{-19}$ J. Thus, in the 6 GeV storage ring of the ESRF in Grenoble, the electrons are travelling with a speed of $0.9999999964c$ and have an apparent mass of $11742m_e$, equivalent to 6.44 atomic mass units, 7% more than that of the $^6$Li atom. The circumference of the ESRF ring is 844.4 m so each electron makes a circuit in 2.82 μs, or 355036 circuits per second, corresponding to a current of $5.688 \times 10^{-14}$ A. With $3.516 \times 10^{12}$ electrons stored in the ESRF ring the normal operating current of 200 mA is attained.

The electrons are guided in a storage ring by magnetic fields. Storage rings are made up of several segments, comprising a straight section followed by a curved section where the electrons are steered *via* a bending magnet into the next straight section (Figure 2.4). Synchrotron radiation is emitted in these curved sections, which can therefore serve as the source of X-rays for experiments. In the straight sections arrays of magnets, generally referred to as insertion devices, can be positioned to produce alternating magnetic fields that cause the path of the electrons to oscillate. Each oscillation leads to the emission of synchrotron radiation and by choosing the number, amplitude, frequency and direction of the oscillations, radiation can be tailored for many different applications.

The synchrotron X-ray sources of interest for powder diffraction are the bending magnets, and the insertion devices known as wigglers and undulators. These have their magnetic field in the vertical direction causing deflection of the electrons in the horizontal plane. The radiation is therefore linearly polarised with the electric component lying in the plane of the synchrotron orbit. The radiation emitted by a single electron forms a narrow cone of angular

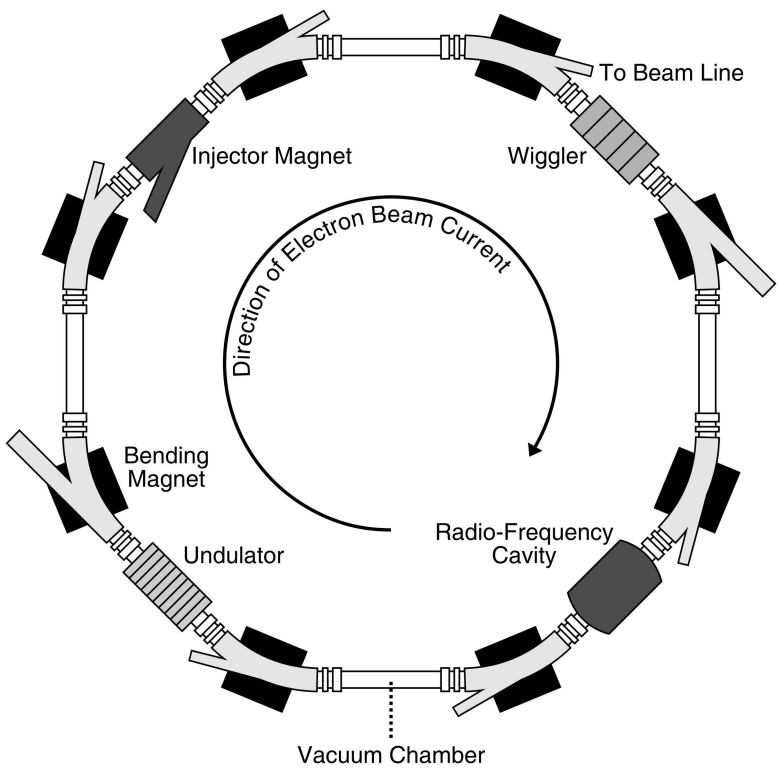



**Figure 2.4** Schematic illustration of a synchrotron storage ring. Third generation machines have many straight sections and are optimised for the exploi tation of wiggler and undulator insertion devices as X ray sources.

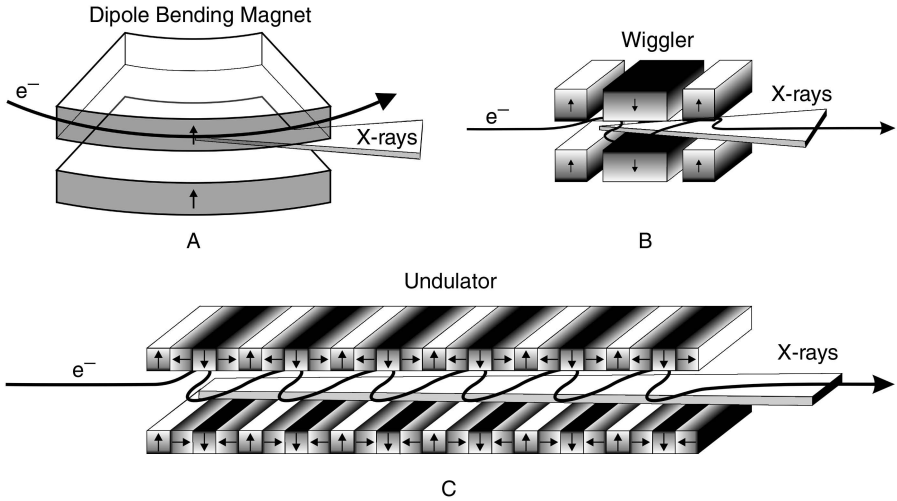



**Figure 2.5** (a) Tangential fan of radiation emitted from a bending magnet. (b) Fan of radiation emitted by a wiggler. (c) Collimated beam emitted by an undulator.

width $\approx 1/\gamma$ radians, leading to the very high vertical collimation of the X-ray beam. For bending magnets, radiation is emitted tangentially throughout the whole curved section, resulting in the emission of a broad tangential fan of X-rays (Figure 2.5a). For insertion devices the magnetic field varies sinusoidally and each oscillation of the electrons produces tangential bursts of synchrotron radiation. For wigglers, the oscillations are of relatively large amplitude, and these add together incoherently, increasing the flux proportional to the number of magnetic periods (Figure 2.5b). For undulators, deflection of the electrons is relatively small and comparable to the natural opening angle of the emitted radiation $1/\gamma$. Radiation from different oscillations interferes, and the beam becomes collimated in the horizontal plane. Thus rather than being spread out in a horizontal fan, as for a bending magnet or a wiggler, the radiation is concentrated into a central on-axis cone surrounded by additional weaker rings (Figure 2.5c). The flux density arriving on a small sample from this central cone is therefore very high.

The spectrum of synchrotron radiation depends on the energy of the electrons in the storage ring, the curvature of their path, and, for an undulator, the interference effects. As a general rule, the greater the electron energy in the storage ring the higher the energy of the emitted X-rays. For bending magnets and wigglers, the tighter the curvature (*i.e.* the higher the magnetic field) the higher the energy of the emitted X-rays. Bending magnets and wigglers have continuous spectra (Figure 2.6) whereas undulators have a series of peaks at integer multiples of a fundamental energy with wavelength $\lambda_1$, which depends on the strength of the magnetic field. The energy of the fundamental and its harmonics can be tuned by varying the vertical gap between the array of

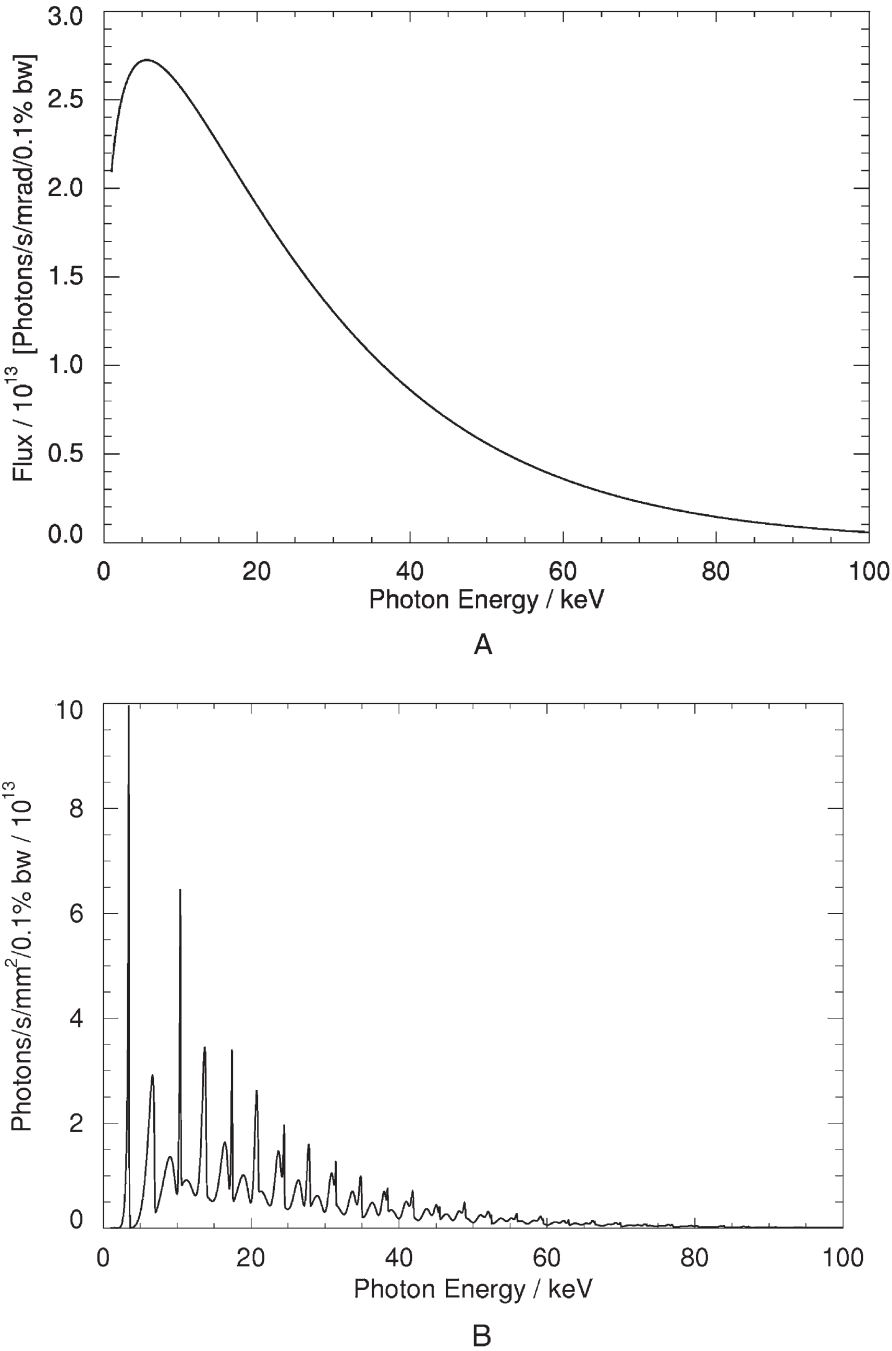



**Figure 2.6** (a) Photon flux *vs.* energy emitted per horizontal milliradian from an ESRF bending magnet with a 0.1% bandwidth (*i.e.* for $\Delta\lambda/\lambda = 0.001$). (b) Photon flux *vs.* energy through a 1 mm$^2$ aperture 30 m from the source, 0.1% bandwidth, for an ESRF U35 undulator (magnetic periodicity 35 mm, 1.6 m long).

magnets. To produce a high flux at a particular wavelength there may be a choice of more than one combination of gap and harmonic. Various considerations (such as the relative flux and the total power-handling capabilities of the beam line) dictate the optimum configuration.

## 2.3 X-RAY OPTICS

Various optical elements can be placed in the beam path to tailor the characteristics of the X-ray beam. These can work by diffraction (*e.g.* a monochromator crystal), reflection (*e.g.* a mirror), or absorption (*e.g.* a filter or slits). A monochromator is used to select a particular wavelength, a mirror can focus the beam or suppress higher harmonics, and filters can be used to remove unwanted radiation.

### 2.3.1 Filters

For powder diffraction experiments using a laboratory source diffraction of the Cu K$\beta$ radiation contaminates the powder pattern from Cu K$\alpha$. Its intensity can be greatly attenuated by placing a Ni filter, a uniform thin sheet of nickel, in the beam path. The energy of the Cu K$\beta$ X-rays ($\lambda = 1.392$ Å) is slightly above the threshold energy of the Ni K absorption edge ($\lambda = 1.488$ Å) which thus absorbs this wavelength strongly, whereas K$\alpha$ X-rays ($\lambda = 1.542$ Å) have insufficient energy to excite this particular transition and are only modestly absorbed. The optimum thickness has to be a compromise between reducing the intensity of the unwanted Cu K$\beta$ and reducing the intensity of the desired Cu K$\alpha$. Most laboratory setups employing a nickel filter for Cu radiation choose 15–20 μm thick foils so as to attenuate K$\beta$ by a factor of 25–50$\times$ more than K$\alpha$, and the overall K$\alpha$ intensity by a factor of about 2.

At synchrotron sources, attenuators such as graphite, aluminium or synthetic-diamond foils can be inserted into the primary beam path to reduce the heat load on an optical element, to prevent saturation of the X-ray detector, or to reduce the rate of radiation damage to the sample.

### 2.3.2 Monochromators

A monochromator is a large flat single crystal set to a particular orientation, $\theta_m$, in the beam that reflects by diffraction only those wavelengths that satisfy the Bragg condition $\lambda = 2d \sin\theta_m$, where $d$ is the spacing between the chosen lattice planes. Typical crystals used include silicon, germanium, quartz, diamond and graphite. For any material used as an X-ray monochromator the following properties are desirable: forms large good quality crystal with an appropriate interplanar distance; mechanically strong and reasonably easy to cut; stable in the beam; large structure factor for the chosen Bragg reflection; small coefficient of thermal expansion; low absorption for X-rays. The actual choice of material also depends on the application, and may take into account

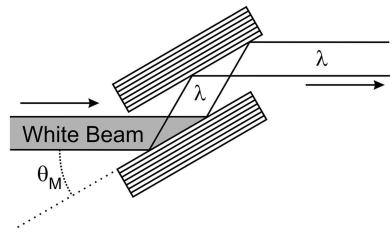



**Figure 2.7** Schematic of a double bounce monochromator as used at synchrotrons. The first crystal selects a wavelength from the polychromatic source, which is reflected along the initial direction by the second crystal. The lattice planes of the latter must be perfectly aligned with the first crystal for efficient transmission of the beam.

the thermal conductivity, degree of crystalline perfection, intrinsic breadth of the Bragg reflection (Darwin width), *etc.*

In the laboratory, a monochromator may be placed in the incident or the diffracted beam. Pre-sample monochromators such as quartz or Si 111 are highly discriminating and can separate Cu $K\alpha_1$ radiation from $K\alpha_2$ (and $K\beta$), though at the expense of overall intensity. Curving the crystal, which therefore must be thin, to focus the beam on the sample or detector helps counteract this loss of intensity. Post sample monochromators, because of the motion of the detector arm, are mechanically less stable, so a less-discriminating crystal such as graphite is used. This can only remove $K\beta$, but has the additional advantage of reducing any fluorescence from the sample.

Monochromators for synchrotron-based diffractometers are used to select the chosen wavelength from the polychromatic source. To preserve the direction of the incident beam, a double-crystal ("double-bounce") arrangement is used (Figure 2.7). This may be either a channel-cut crystal, or two independently-aligned crystals. A common choice of crystal is Si because of its very high degree of crystalline perfection, and its excellent thermal properties in the intense synchrotron beam. The 111 reflection is a frequent choice, though 220 and 311 are also used when higher energy resolution is desired. Cooling is essential to maintain a stable temperature for the crystal(s) under the heat load from the source.

### 2.3.3 Mirrors

Curved mirrors can be used to collimate or focus a divergent X-ray beam. Still rather rare on laboratory instruments, graded-multilayer mirrors may be used to produce a near-parallel incident beam, which may be advantageous when working with non-flat or irregular samples or with samples under non-ambient conditions.

At synchrotrons, mirrors can be used to enhance further the collimation of the already highly collimated beam. This can improve the angular and energy

resolution of the instrument. Alternatively, the beam can be focused onto the sample if desired. A highly polished silicon substrate with a thin metal coating, such as Pt or Rh, set at grazing incidence also provides a means to suppress the high-energy X-rays in the beam. Thus a Rh-coated mirror set at an angle of $0.09^\circ$ to the incident beam will not transmit photons with a wavelength less than about 0.3 Å. Mirrors can sometimes have several stripes of different metal coatings to allow adjustment of the upper-energy cut-off.

## 2.4 X-RAY DETECTORS

X-Ray detectors may be classified as point, linear or area, depending on whether they record the diffraction pattern in zero, one or two spatial dimensions. Point detectors must be scanned to measure the diffraction pattern, whereas linear or area detectors can be fixed. Point detectors are easily compatible with post-sample optical elements. Linear and area detectors allow the data to be acquired much faster, but as more open systems they are prone to detecting parasitic scatter from the air or sample environment. Both linear and area detectors are types of position sensitive detector (PSD).

### 2.4.1 Point Detectors

The most common type of detector in the laboratory is a scintillation counter, which exploits a two-stage process. X-Ray photons collide with a phosphor screen (or scintillator) such as a thallium-doped sodium iodide crystal. This emits photons in the blue region of the visible spectrum, which are subsequently converted to voltage pulses by means of a photomultiplier tube attached directly behind the scintillator. The number of electrons ejected by the photocathode is proportional to the number of visible photons that strike it, which in turn is proportional to the energy of the original X-ray photon. Owing to numerous losses, the energy resolution of the detector is poor, and as such it cannot be used to resolve $K\alpha$ and $K\beta$ X-ray photons. However, it has high quantum efficiency and a low dead time, making it the ideal detector for the point intensity measurements required for step-scanning diffractometers. For synchrotron applications, faster scintillators are often needed, and materials such as doped YAP (yttrium aluminium perovskite) or $LaCl_3$ are used as scintillators, though their light output per incident photon is less. Solid-state detectors based on Si or Ge are used where better energy discrimination is required, and avalanche-photodiodes can work at very high count rates but have poor efficiency at high X-ray energies because Si does not absorb such photons strongly.

### 2.4.2 Linear Detectors

Linear detectors may be straight or curved and record the $2\theta$ position of arrival of each X-ray photon. Linear PSDs may be broadly classified into single anode or multi-anode devices. Single anode devices have a wire or a blade in a

gas-filled chamber and work on the principle that X-ray photons can ionize inert gas atoms such as argon or xenon into an electron ($e^-$) and ion (*e.g.* $Ar^+$) pair. The ionization energy required to eject an outer electron is low (10–20 eV) compared to the energy of the X-ray photon (8 keV for a Cu X-ray tube) so that one X-ray photon can produce several hundred ion pairs. The anode, which is a relatively poor conductor, is set to a potential of about 1000 V. The electrons of the ion pair accelerate towards the anode causing further ionization and an enhanced signal by gas amplification. The burst of electrons on the wire is converted into a charge pulse which travels to both ends of the anode. By comparing the relative arrival time of the pulse at *both* ends of the wire or blade, the position of the detected X-ray photon is obtained. Such "delay-line" detectors can measure only a single X-ray photon at a time and so are relatively slow and lose their linearity at modest count rates. To minimise the dead time of the system, a quenching gas such as methane ($CH_4$) is mixed with the inert gas (*e.g.* 90% Ar : 10% $CH_4$). For higher count rates, multi-wire or micro-strip anodes have been developed in which each individual anode element is an independent detector with a $2\theta$ position fixed relative to the other elements. Such a detector can process many events concurrently.

PSDs record data over a whole range of scattering angles, which can be useful where speed of acquisition is crucial, *e.g.* in time-resolved powder diffraction or thermodiffractometry. PSDs come in various shapes and sizes: small PSDs can only collect data over a limited range, say, 5–10° $2\theta$; large PSDs are usually curved and collect over a much wider range. Both types tend to have a similar number of channels of detection ($2^n$, $n = 9$–12) so that the $2\theta$ channel width for the larger PSDs is relatively coarse. PSDs can be used at a fixed scattering angle or may be scanned to collect data over a wider angular range.

### 2.4.3 Area Detectors

Historically, area detectors in the form of photographic X-ray film were the principle method for recording powder diffraction patterns, *e.g.* using Debye–Scherrer and Guinier cameras. Modern area detectors for X-rays exploit image plate and charge-coupled device (CCD) technology. These detectors accumulate an image of the diffraction pattern, which then has to be read out and stored as a subsequent step. Typical read out times vary from 30 s or more for image plates to 1 s or less for CCDs. Image plates are large area detectors and record the diffracted X-rays directly, whereas CCD chips are small (*e.g.* $1'' \times 1''$ or $2'' \times 2''$) and are coupled to a phosphor screen with a bundle of optical fibres. Area detectors record part or even whole Debye–Scherrer powder diffraction rings, enabling effects such as texture, granularity, and preferred orientation to be observed directly in contrast to linear and point detectors. In addition, the large solid angle greatly increases the counting efficiency, enabling data to be more easily recorded from weakly scattering samples. Data corrections to obtain quantitative intensities from 2D detectors requires special handling, and this is discussed in detail in Chapter 14.

### 2.4.4 Detector Calibration

In contrast to detectors used for point intensity measurements, position sensitive detectors require careful calibration for both $2\theta$ position and efficiency so that scattering angles and intensities can be accurately determined. For each channel an exact $2\theta$ position is required together with an efficiency coefficient. The efficiency can be determined using a sample such as an amorphous foil that fluoresces in the X-ray beam (*e.g.* Fe in a beam of Cu K$\alpha$ radiation), producing a very high flat background and no Bragg peaks. The $2\theta$ calibration is achieved by scanning the different parts of the detector through the Bragg reflection of a strong peak (or peaks), *e.g.* the Si 111 peak. For very large curved detectors, the $2\theta$ calibration has to be made using many diffraction peaks. The calibration can be checked by measuring the complete pattern of a reference material. Sealed gas-filled PSDs should be recalibrated whenever the gas is replenished, in contrast to detectors with a continuous flow of gas that need checking regularly.

## 2.5 LABORATORY INSTRUMENTAL CONFIGURATIONS

There are two principal types of instrument geometry for laboratory powder diffractometers: reflection and transmission. In reflection geometry, the sample is in the form of a flat plate, while in transmission geometry a glass capillary or thin foil is used.

### 2.5.1 Reflection Geometry

The modern flat-plate powder diffractometer is the most common configuration used in industrial and academic laboratories. It achieves a high diffracted intensity without sacrificing good resolution by exploiting parafocussing of the diffracted beam. The divergent incident beam is reflected from the surface of the sample and converges at a fixed radius from the sample position. This geometry is commonly referred to as ''Bragg–Brentano'' (Figure 2.8). The tube is aligned so that the beam divergent on the sample is at angle $\xi$ to the anode surface (which is typically about $6^\circ$) and the divergence of the beam is controlled by one or more slits after the source (Figure 2.9). The footprint of the beam on the sample is proportional to $\cos\theta$ and may overflow the sample at very low scattering angles. Axial divergence, which is a cause of low-angle peak asymmetry, is reduced by inserting Söller collimators. To get a good powder average, the sample is usually spun about an axis normal to the flat plate. An appropriate filter should be inserted after the X-ray source as shown.

Figure 2.10 shows the X-ray optics when a post-sample graphite monochromator is employed. This is perhaps the most common arrangement. The X-ray filter is no longer necessary. Again slits are used to control the divergence of the incident and diffracted beam. With this setup, the source is normally fixed and the monochromator moved around the $2\theta$ circle with the detector arm.

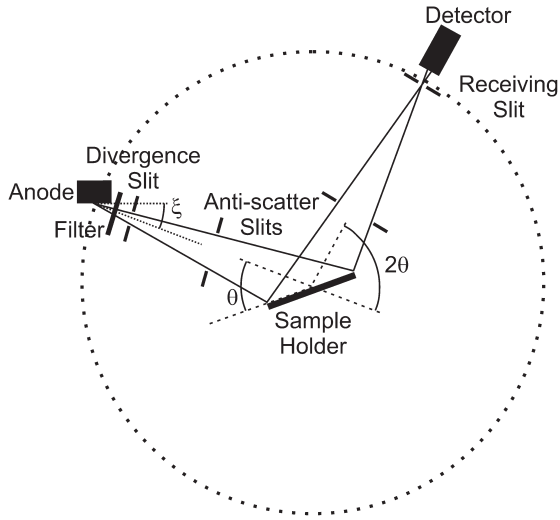



**Figure 2.8** Basic Bragg Brentano geometry. The dotted circle centred on the sample position represents the goniometer circle on which the image of the divergent source of X rays is focussed by diffraction from the flat plate sample. Strictly speaking, true focussing only occurs when the sample plate has a curved surface. However, given that the footprint of the beam on the sample plate is considerably smaller than the radius of the focussing circle, the flat plate approximation works well in practice. The source is usually fixed and to collect the diffraction pattern the sample and detector are rotated by $\theta$ and $2\theta$, respectively. An alternative is to fix the sample (usually in the horizontal position, *e.g.* useful for a liquid sample) and to move both the source and the detector by $\theta$ and $\theta$, respectively.

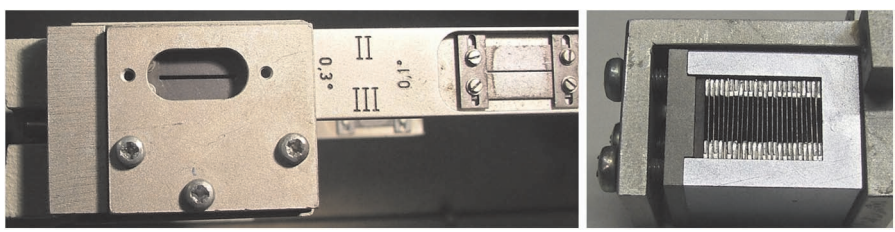



**Figure 2.9** A typical X ray slit is shown in the photograph on the left. The size of the slit is indicated in degrees here (0.3°), though sometimes it is given in mm. Söller collimators are shown on the right. These consist of a set of fine parallel foils that prevent angular divergence of the beam out of the $\theta/2\theta$ plane.

The Bragg angle for the monochromator, $2\theta_M$, is set to satisfy Bragg's law for the diffracting planes of the monochromator crystal.

A higher-resolution setup exploits a perfect-crystal pre-sample monochromator (Figure 2.11) to remove the $K\alpha_2$ radiation. To achieve this and maintain a reasonable X-ray intensity, the monochromator crystal is curved so as to satisfy

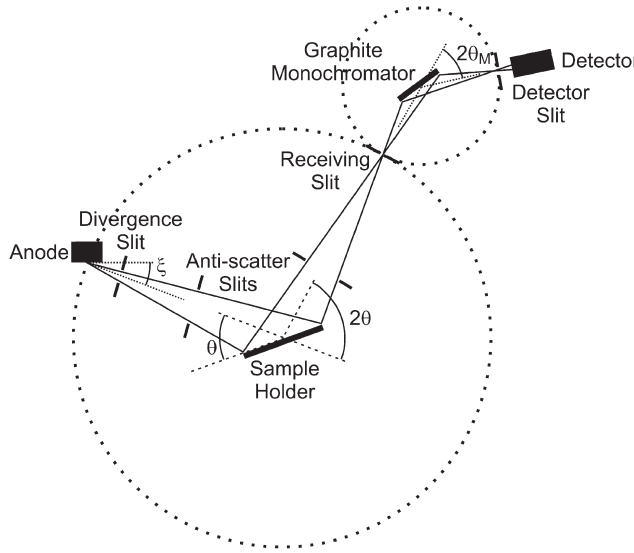



**Figure 2.10** Bragg Brentano geometry with a diffracted beam monochromator. The crystal is usually graphite, which has a low degree of crystalline perfection, and hence a large acceptance angle (tenths of a degree). Thus a flat crystal is adequate.

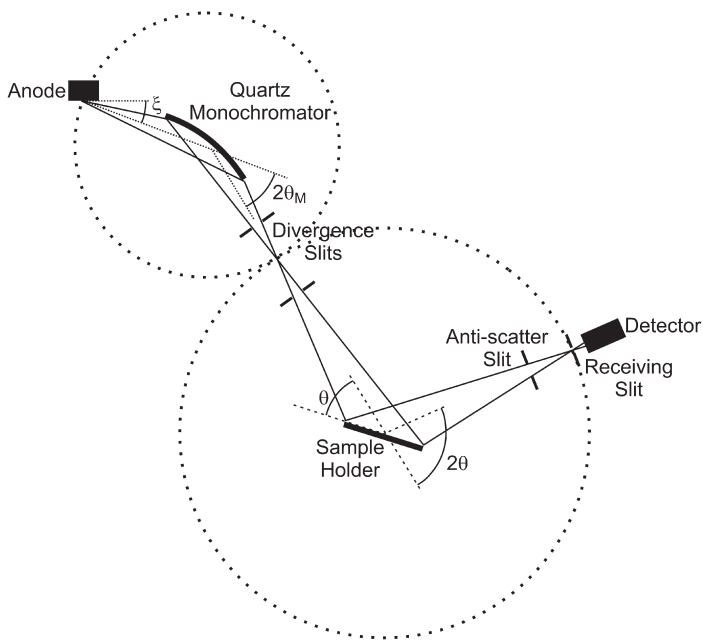



**Figure 2.11** Bragg Brentano geometry with a pre sample monochromator. A near perfect crystal, *e.g.* quartz or germanium, is required to separate $K\alpha_1$ and $K\alpha_2$.

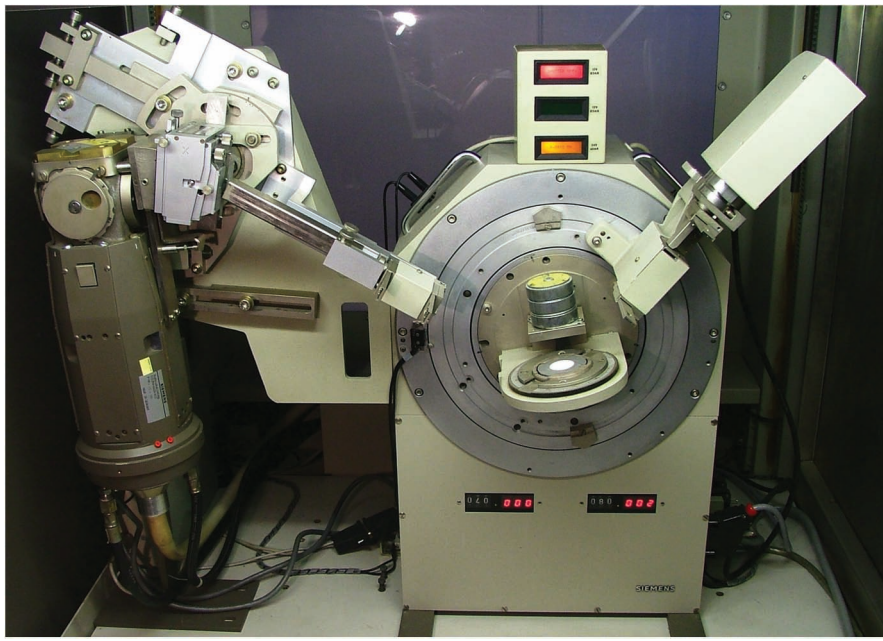


**Figure 2.12** Photograph of a Bragg Brentano diffractometer equipped with a pre sample monochromator (on left) and scintillation detector (on right). Sample stage and detector move in the vertical plane about a horizontal axis in the ratio 1 : 2. The sample is spun about an axis normal to the flat plate. Although this instrument dates from the early 1990s, the latest generation of laboratory Bragg Brentano diffractome ters still function in a similar manner to the one shown here.

the Bragg condition for a divergent source. The path of the $K\alpha_2$ radiation after the monochromator deviates slightly from that of the $K\alpha_1$, and is removed by the slits before the sample position. Accurate alignment of the optical elements in such an instrument is therefore crucial (Figure 2.12). Peak widths of around 0.07° (or better) can be obtained using Cu radiation.

### 2.5.2 Transmission Geometry

The workhorse Debye–Scherrer camera of old has evolved significantly into the modern transmission powder diffractometer, exploiting a curved perfect-crystal monochromator (Figure 2.13). The divergent beam from the X-ray source is focussed not onto the sample but beyond onto the $2\theta$ measuring circle of the detector, which is ideally a curved PSD for efficient data collection. If a straight PSD is employed, it is positioned significantly beyond the focussing circle. This avoids having the central part of the detector on the focussing circle and so in focus with the ends out of focus, which would produce a marked variation in peak width along the PSD. To obtain a good powder average with this

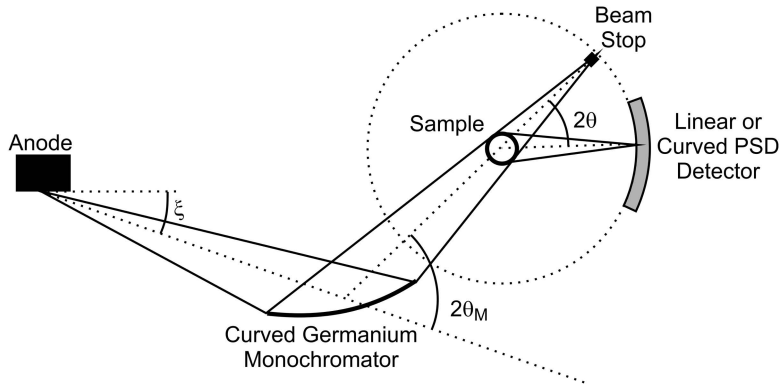



**Figure 2.13** Parafocussing Debye Scherrer diffractometer with curved monochromator crystal and capillary sample. Given the intrinsically worse peak to back ground ratios compared to Bragg Brentano geometry, linear or curved position sensitive detectors (PSDs) are employed to improve counting statistics. As with the equivalent Bragg Brentano geometry, the angle $\xi$ is optimised at about 6°.

geometry, the sample is spun about its axis. Diffraction peak widths of 0.1° (or better) are readily obtained. Foil samples must be correctly orientated to allow maximum transmission and to simplify any corrections for absorption made to the intensities.

## 2.6 SYNCHROTRON INSTRUMENTAL CONFIGURATIONS

### 2.6.1 Pre-sample Optics

Whereas laboratory instruments exploit divergent beams of X-rays, synchrotron-based instruments rely on the highly collimated nature of the radiation. At a synchrotron beam line the presample optics are designed to deliver to the sample a highly collimated and monochromatic beam of the desired wavelength. The optics, which must include at least a double-crystal monochromator, exploit the high degree of vertical collimation (typically in the range 0.003–0.01° at ESRF) of the white beam. Since the vertical divergence of the beam incident on the sample translates directly into peak width in the diffraction pattern, very high-resolution angle-dispersive instruments operate in the vertical plane. In addition, peak widths are affected by the wavelength band pass, $\Delta\lambda/\lambda$, of the monochromatic radiation. The low vertical divergence of the white radiation, coupled with the perfection of the monochromator's diffracting planes, leads to highly monochromatic radiation with a very narrow band pass, of the order $10^{-4}$ for the Si 111 reflection. Although synchrotron radiation already has a very small natural divergence, the latter may be improved even further by the use of a collimating mirror in the optical path. For example, on the high-resolution powder diffraction beam line BM16 at ESRF,[4] the residual

vertical divergence after the collimating mirror was nominally $\approx 0.001^\circ$. In the absence of a mirror, the divergence of the monochromatic beam incident on the sample is limited by the sample size or beam-defining slits, *e.g.* a 1 mm high slit at 40 m from the source defines an angle of $\approx 0.0015^\circ$.

### 2.6.2 Parallel-beam Instruments

High-resolution powder diffractometers at synchrotrons exploit the parallel nature of the incident radiation and are heavy-duty and designed to have excellent angular accuracy, working with substantial loads. A high degree of mechanical accuracy is required to match the high optical accuracy inherent in the parallel-beam concept. Figure 2.14 shows a photograph of the powder diffractometer on beam line ID31 at ESRF. Spinning capillary samples are preferred because they suffer much less from the preferred-orientation problems that bedevil flat-plate samples. In contrast to laboratory instruments, the wavelength can usually be tuned to minimise problems of absorption. If strong absorption cannot be avoided, the sample can be stuck to the outside of the capillary with grease. When flat plate samples are unavoidable, the parallel-beam technique can be used without major change in instrumental configuration, since there are no parafocussing requirements with synchrotron radiation.

The highest resolution instruments, typically used for powder crystallographic studies (*e.g.* structure solution and refinement) are equipped with an analyser crystal between the sample and the detector. The analyser crystal (*e.g.* a perfect Si or Ge 111 crystal) reflects the scattered radiation into the detector, only when the scattered radiation falls on the crystal with precisely the correct incidence angle to fulfil Bragg's law. Since the crystal has a very narrow acceptance angle for diffraction, the crystal defines stringently the direction from which the diffracted radiation must travel to reach the detector. By scanning the $2\theta$ circle on which the analyser crystal and detector are mounted, a complete range of $2\theta$ angles is measured, and a high-resolution powder diffraction pattern may be obtained. The analyser crystal is extremely selective in the photons it transmits. Therefore, a large fraction of the diffracted radiation is rejected at a given $2\theta$ position. Even with the high flux of a synchrotron, the measurements may become slow. Hence to increase the rate of data acquisition, multiple analyser stages can be employed, using several channels of detection simultaneously, separated by small angular offsets of 1 or $2^\circ$. The different channels must be calibrated with respect to each other, in terms of counting efficiency and exact angular offset, by comparing regions of the diffraction pattern scanned by several detectors. The calibration of the incident wavelength and any $2\theta$ zero-point error is best done with a standard sample such as NIST Si 640c, which has a certified lattice parameter.

Because an analyser crystal defines the diffractometer scattering angle $2\theta$ by its own true *orientation* with respect to the incident beam, several aberrations, which can affect diffractometers equipped with a simple receiving slit before the detector or a PSD, do not occur. (In reality for the latter diffractometers, the $2\theta$ scale is inferred from the *position* of the slit or the element of the PSD.) Thus, $2\theta$

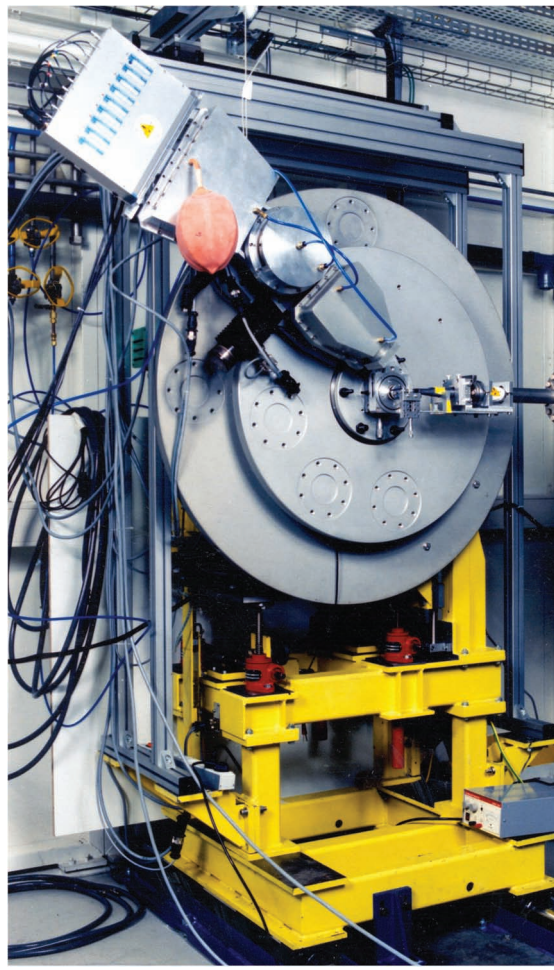


**Figure 2.14** High resolution powder diffractometer on beam line ID31 at ESRF. Note the nine channel multianalyser stage on the detector arm. The balloon contains He gas to reduce background scatter by air in the X ray flight path.

resolution is independent of the capillary diameter, so large capillaries can be used to optimise diffracted intensity, and any modest misalignment of the sample from the diffractometer axis (or the effects of specimen transparency for flat-plate samples) does not lead to shifts in the positions of the Bragg peaks. Neither do movements of the sample with temperature changes in furnaces, *etc.* result in peak shift aberrations. Peak positions from these instruments are therefore highly accurate, and are ideal for indexing the diffraction patterns of materials of unknown unit cell. Moreover, the $\theta/2\theta$ parafocussing condition does not need to be satisfied to have high-resolution data from flat-plate

samples. The peak width does not, therefore, depend on sample orientation, which is useful for measurements of residual strain by the $\sin^2\psi$ technique.

Similar optical robustness can be obtained by using long, fine Söller collimators instead of an analyser crystal. These give lower $2\theta$ resolution than an analyser crystal, because their acceptance angle is necessarily much larger, but afford a significant increase in the measured intensity. They are not particularly suitable for fine capillary specimens, as the separation between foils may be similar to the capillary diameter, resulting in problems of transmission of the diffracted beam. They are achromatic, and so do not need to be carefully reoriented at each change of wavelength, which may have advantages when performing anomalous scattering studies around an element's absorption edge.

### 2.6.3 Debye–Scherrer Geometry Instruments

The simplest optical arrangement is simply to have a fine receiving slit, matched to the capillary diameter, in front of a point detector. An antiscatter slit near the sample should also be employed to reduce parasitic background scatter. The detector arm is scanned and a powder diffraction pattern recorded. This arrangement can be used for narrow capillary samples on relatively low-flux sources, thus avoiding the severe loss of intensity that using an analyser crystal entails. The resolution is largely determined by the angle defined by the capillary diameter, the slit height, and the distance between them. Despite its apparent simplicity, high quality high-resolution data can be obtained with care.

Although methods involving scanning the detector arm produce high quality high-resolution data, they are nevertheless relatively slow, making them less suitable for time-resolved studies where the sample is evolving *in situ*. Much faster data acquisition can be achieved by using a linear PSD or area detector.

Owing to the high intensities scattered from the sample at the synchrotron, linear delay-line detectors are unsuitable as they saturate instantly. Currently, much effort is being devoted to the development of appropriate curved multiwire and mutistrip devices. Perhaps the most successful at the time of writing is the device built at the Swiss Light Source.[5] This consists of 12 modules based on Si-chip technology, each having 1280 independent channels, giving a total of 15 360 channels over about $60^\circ$ $2\theta$. The signal is accumulated in the individual channels of the modules, then read out in around 250 μs. Another approach has been adopted at the Australian National Beamline Facility[6] located at the Photon Factory in Japan. Here several image plates are curved around the inside of an enormous Debye–Scherrer camera (the "Big Diff"). The image is accumulated then read out off-line. For time-resolved studies, the image plates are translated axially behind a mask defining a vertical strip.

Although image plates have been used as area detectors for powder diffraction, their long readout times (many seconds) mean that CCD based detectors are increasingly being preferred, a trend throughout X-ray crystallography. Coupled with the use of a short wavelength, a significant $d$-spacing range can be recorded on the detector, especially if it is positioned off-centre, so that the

main beam would hit the detector close to its edge. In such a case partial rather than full Debye–Scherrer rings are recorded. Specific CCD chips can be read out very quickly, such as the Frelon camera developed at ESRF. An acquisition rate of 20 images per second is possible, which, coupled with the efficiency of the large solid angle subtended, means the device can be used to follow very rapid solid-state reactions, *etc*.

## 2.7 MEASUREMENTS

### 2.7.1 Sample Holders

The choice of sample holder is governed by the choice of instrument geometry used for the powder diffraction experiment, *i.e*. reflection or transmission. Figure 2.15 shows various sample holders for the flat-plate Bragg–Brentano reflection geometry described earlier. Flat plate sample holders have one very big advantage over other sample holders: they are easy to fill. Their biggest disadvantage is that the surface-flattening process induces a preferred orientation in most samples. Other problems include: the sample can sometimes fall out especially if spinning, with horizontal diffractometers when the sample is vertical, or for vertical diffractometers at high $\theta$ angles; it is difficult to work with air-sensitive samples; the holder is quite bulky and so less appropriate for work under non-ambient conditions; peak positions from low-absorbing samples can suffer from aberrations owing to significant penetration of the beam below the surface. For very tiny amounts of sample, *e.g*. for a forensic sample, flat-plate geometry is in fact probably the method of choice, for the sample can be dusted over the surface of a Si crystal, cut to avoid Bragg diffraction, and this gives near-zero background. Block samples can also be mounted in a suitable, deep flat-plate holder.

For transmission geometry, either a cylindrical or thin flat foil sample holder is required. The most common cylindrical sample holders are glass capillaries (Figure 2.16). These come in various nominal sizes: 0.2, 0.3, 0.5, 0.7, 1.0, 1.5, and 2.0 mm are common internal diameter values, but other sizes are available. In the laboratory, the larger diameters are less useful for most powder diffraction work because of sample absorption and decreased resolution, but are very practical for use at synchrotrons given the parallel beam optics and the availability of hard X-rays. Glass capillary sample holders should be flame, grease, or glue sealed to prevent sample loss. They are ideal for low-temperature powder diffraction studies as they are easy to cool with liquid-$N_2$ cold stream devices and are readily rotated in liquid-He cryostats. Given their relatively low melting points, soda- or borosilicate-glass capillaries are usually substituted by quartz-glass ones for high-temperature work.

Capillaries are unpopular for several reasons: firstly, diffuse X-ray scattering from the glass walls, which are approximately 10 μm thick, adds significantly to the background count. Secondly, they take considerably longer to fill than the equivalent flat-plate sample holder. Thirdly, capillaries may require careful alignment on the diffractometer to ensure that the axis of the capillary is

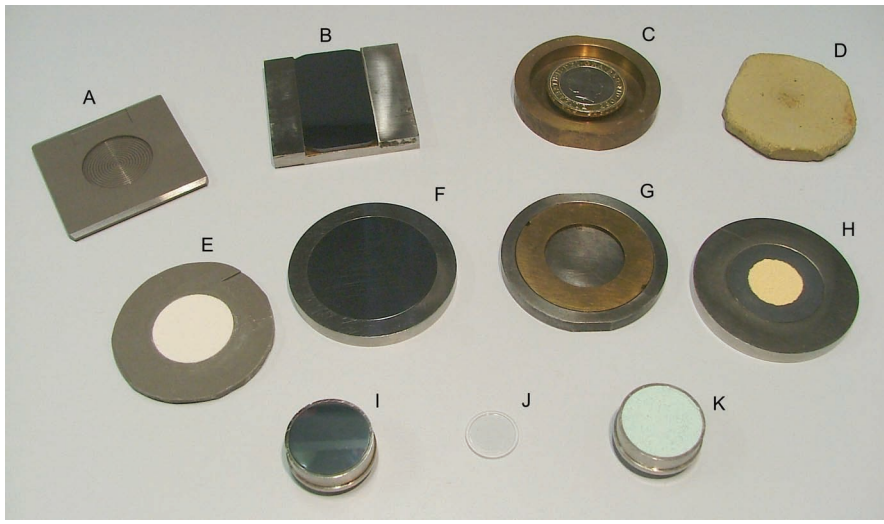



**Figure 2.15** Sample holders for flat plate Bragg Brentano geometry. All of the large (50 mm Ø) sample holders (**A H**) are for room temperature work, whilst the three smaller sample holders (**I K**) are for high temperature furnace use. **A** and **B** are for stationary samples, **A**, **F**, and **I** are for a light dusting of a powder on a low background silicon wafer, whereas **H** is for small quantities of sample in a shallow well silicon crystal. **D** is an example of a solid block sample (*e.g.* solid quartz as used for diffractometer alignment work), while **C** is a deep well sample holder, again for mounting solid objects (though the £2 coin shown would have too rough a surface for practical data collection). **G** is specially designed for back packing, though even for front packing it is preferable to the plastic holders **A** and **E**. Sample holder **J** is made of sapphire.

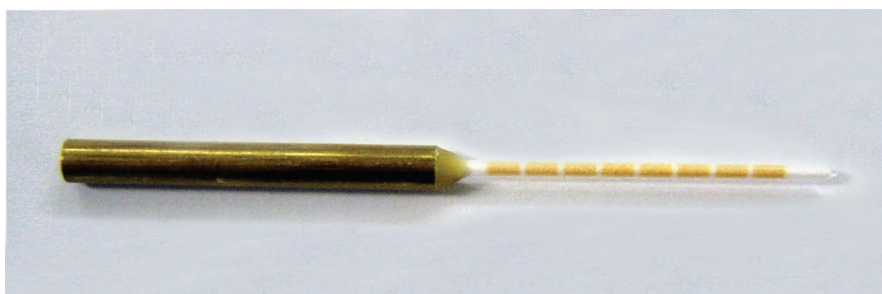


**Figure 2.16** Photograph of a 1 mm diameter thin walled (10 μm thick) borosilicate glass capillary, glued with melted wax into a brass holder for clamping to a spinner. The sample is a white organic compound, but exposure to an intense X ray beam turns it yellow. This sample was translated between successive data collection scans to avoid radiation damage, resulting in the striped appearance.

co-linear with that of the diffractometer. Fourthly, for highly-absorbing samples either fine capillaries have to be used or the sample has to be diluted, and, additionally, an absorption correction should be employed when the data are used for crystal structure refinement.

After all these disadvantages, you might wonder why capillaries are used at all. The huge advantage of capillary geometry is that preferred orientation is much less of a problem, although it may still occur, *e.g.* needle-shaped crystallites may align horizontally-rotated capillaries. Capillaries are also a convenient way of mounting very air-sensitive samples since they are easily sealed against exposure to the air. An alternative to the capillary is the use of a thin glass fibre, or even an empty capillary, thinly coated in silicone grease and then covered by a fine coating of powder. This latter may be better for highly absorbing samples.

An alternative method for measuring powder samples in transmission geometry is to use a very thin and flat sample. This can be achieved by sprinkling the powder onto an adhesive tape, or by trapping the sample between two layers of a thin (say 3 μm or thinner) polymer film. Various polymers including Mylar and Kapton have been used, some of which are better than others: the choice of material is a compromise between obtaining a low background count and a peak-free background count.

### 2.7.2 Standard Samples

It is essential to know that the diffractometer produces data that are reliable and are not affected by systematic and or other, undiscovered errors. Data reliability can be considerably enhanced by pre-checking the diffractometer with a known standard sample. It is good laboratory practice to do this regularly, and essential when the instrument has been realigned or reconfigured. A standard sample can usually be measured relatively quickly and will provide information on instrument calibration, alignment, resolution, background count, source flux, spurious scattering from sample environment equipment (if any) and so on. Even when assured by the person responsible for the instrument that everything is well, a few minutes with a standard sample can avoid many months of wasted effort later.

A good calibrant for a powder diffractometer should be a material of high symmetry because the intensity of the diffraction planes is concentrated into relatively few diffraction peaks. The unit-cell volume, $V$, should be small since the intensity of the diffraction peaks is inversely proportional to $V$. Ideally, the unit cell should contain only 1 or perhaps 2 crystallographic atoms with large scattering factors. The thermal vibrations of the atom (or atoms) characterised by its $B$ value should be as small as possible so that the high-angle peaks have maximum intensity. For capillary geometry the sample absorption should not be too high since this can affect, in extreme cases, the position of the powder lines in addition to reducing their intensity. It must also be possible to obtain large quantities of the material in high purity and crystallinity together with

reproducible crystallite size. Obviously, the materials must be air stable and preferably non-toxic.

Typical standards are powdered Si, $LaB_6$, Ni, ZnO, $TiO_2$, $CeO_2$, $Al_2O_3$, $Cr_2O_3$, and $Y_2O_3$. These samples can be used as calibrants for both X-ray and neutron powder diffraction. All the materials listed above as standards have rigid-lattice structures due to strong chemical bonding with highly charged cations and anions. Note that a simple material such as NaCl does not make a good standard because it is hygroscopic and the $Na^+$ and Cl ions have large thermal parameters due to their single charge. The National Institute of Standards and Technology (NIST) supplies standard calibrating materials for many applications.

A standard may be excellent for one purpose (*e.g.* wavelength calibration) and less useful for another (*e.g.* determination of instrumental resolution) so choose a standard appropriate for the task in-hand. The best samples to check the performance of the diffractometer at low angles are layer-like: mica is one such material supplied by NIST, or silver behenate, which has a layer spacing of 58.38 Å.[11]

### 2.7.3 Data Acquisition

Before collecting a powder pattern, it is a good idea to know what information you hope to get out of it, for this will influence the data collection strategy. Parameters to be considered include angular range, step size, counting time, statistical quality, wavelength, *etc*. For example, phase identification generally requires only a range of $2\theta$ containing the strongest reflections from the sample, whereas meaningful Rietveld refinement of a crystal structure requires high quality data measured to small *d*. Variable count time strategies can improve enormously the statistical quality of the high-angle data, to compensate for the reduction in scattered intensity with geometric and X-ray form factors, thermal motion, *etc*. Studies of a material's microstructure need precise measurement of the shape of the diffraction peaks, so a fine step size is desirable, along with measurement of an appropriate standard, and possibly higher-order reflections. Absorption or the presence of absorption edges will influence the choice of wavelength. There are many factors to be considered for optimum data, and some forethought and planning will make the difference between a successful investigation, and a waste of effort, as it is not usually worth struggling to analyse data that is not fit for the purpose.

Despite one's best efforts, carefully collected data may still suffer from systematic sample errors, such as preferred orientation, granularity, texture, inhomogeneity, impurity phases, radiation damage (especially at the synchrotron) unexpected sensitivity to air or moisture. Measuring the very-same sample again can detect sample evolution during the measurement. Measuring with a different instrumental geometry can reveal some of the other effects. A critical assessment of the data quality and the data-collection strategy after the experiment is to be encouraged. In some cases, a new experiment with a revised strategy may be the optimum course.

## 2.8 ENERGY DISPERSIVE POWDER X-RAY DIFFRACTION

Rather than measuring the *d*-spacings and intensities of a powder X-ray diffraction pattern by varying the scattering angle, $2\theta$, at a fixed wavelength, $\lambda$, according to the Bragg equation $\lambda = 2d\sin\theta$ a diffraction pattern can be obtained by varying the wavelength at a fixed scattering angle. In practice a sample is illuminated with white radiation (usually from a synchrotron source) and an energy-dispersive (ED) detector is used to detect the wavelength of the scattered X-rays (Figure 2.17). The ED detector usually consists of a liquid-$N_2$-cooled Ge crystal, which is a semiconductor. The energy of an absorbed X-ray photon promotes electrons to the conduction band in proportion to its energy. By analysing the magnitude of the charge pulses arriving from the crystal, the energy of the absorbed photon is determined, and the powder diffraction spectrum is thus recorded as a function of energy (typically within the range 10–150 keV, depending on the source) with a multi-channel analyser. The ED detector is in many ways analogous to a linear PSD used in angle-dispersive experiments. Although recorded as a function of energy, *E* (keV), the spectrum is frequently converted into reciprocal *d*-spacing (Å $^{-1}$) *via* $1/d = 2E\sin\theta/12.398$.

Energy-dispersive detectors require calibration for both energy scale and the detector's fixed scattering angle, $2\theta$. Spectra are collected using a multichannel analyser with typically 4096 channels, the channel number, *n*, being approximately proportional to the energy of the measured X-ray photon, *E*. At very high energies, nonlinear behaviour is observed so that in practice a quadratic expression ($E = a + bn + cn^2$) is used for the relationship between *n* and *E*. The coefficients, *a*, *b*, *c*, are obtained by measuring the channel number for certain well-defined detected photon energies. For higher energies, $\gamma$-emitting radioactive sources, such as $^{241}$Am (59.5412 keV) or $^{57}$Co (122.0607 and 136.4736 keV), may be used. The $^{241}$Am source can also be used to stimulate K$\alpha$ and K$\beta$ fluorescence lines from foils of lighter elements (*e.g.* Mo, Ag, Ba, and Tb)

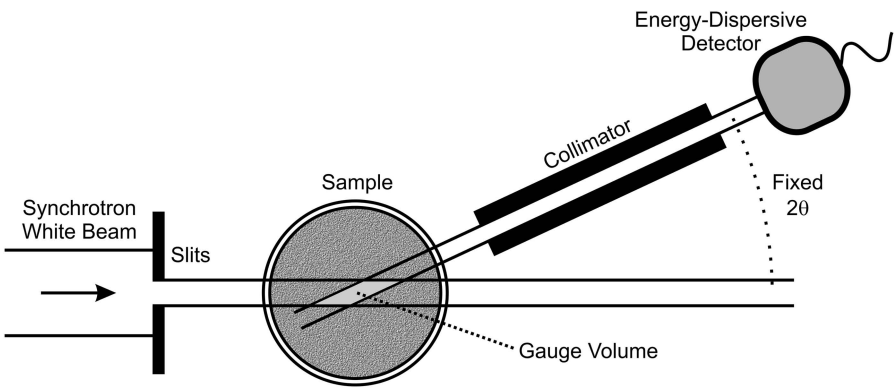



**Figure 2.17** Schematic representation of the energy dispersive diffraction (EDD) technique. The energy discriminating detector at fixed scattering angle determines the wavelength of each detected photon and hence the *d* spacing of the diffracting lattice planes.

whose wavelengths are known precisely. A table of values of these fluorescence lines is available in the *International Tables for Crystallography* and other sources.

The choice of detector angle influences the range of *d*-spacings accessible. As the detector angle is decreased, so the range of *d*-spacings measured by the detector is also decreased, *i.e.* fewer reflections are measured. Thus, decreasing the detector angle in an ED diffraction experiment is analogous to increasing the wavelength in an angle-dispersive experiment. The *d*-spacing range of most interest should be matched to the incident spectrum, taking account also of sample absorption and fluorescence, to produce optimally resolved peaks with high intensity. This depends heavily on the choice of detector angle, which is typically chosen in the range 2–6° $2\theta$. Precise calibration of the detector angle is best done using a standard sample with a large cubic cell parameter, *e.g.* yttria ($a = 10.6039$ Å). It is good practice to use many peaks from the data set and to employ a least-squares fitting procedure to obtain a precise value of $2\theta$ *via* $\sin\theta = 12.398/2Ed$.

For energy-dispersive powder diffraction, the peak widths in energy depend on the energy resolution of the detector ($\approx 2\%$) and the dispersion in the fixed $2\theta$ angle, $\Delta 2\theta$, which is determined by the post sample collimation. It is therefore a low-resolution technique that has it uses where a fixed geometry with penetrating X-rays is required, *e.g.* for *in situ* studies of chemical reactions under hydrothermal conditions or measurements of residual strain. Owing to the need to take into account several energy-dependent effects, *e.g.* absorption and scattering factors, the shape of the incident X-ray spectrum, and the detector response, accurate modelling of the intensities of the powder diffraction pattern is difficult.

## 2.9 POWDER NEUTRON DIFFRACTION

### 2.9.1 Properties of the Neutron

Neutrons were discovered by Sir James Chadwick in 1932, though their existence had been predicted 12 years previously by Ernest Rutherford. The neutron has a mass $m_n$ of $1.67492728(29) \times 10^{-27}$ kg, a charge of zero within experimental uncertainty, a spin of $\frac{1}{2}$ and a resulting magnetic moment of $-1.04187563(25) \times 10^{-3}\,\mu_B$. From the De Broglie relationship, $\lambda = h/m_n v$, where $h$ is Planck's constant and $v$ is the velocity of the particle, a neutron travelling at 2200 m s$^{-1}$ has a wavelength of 1.8 Å and, therefore, is suitable for structural studies. Neutron properties are often quoted at this wavelength. The kinetic energy of a neutron with this speed is 25.3 meV and roughly comparable to thermal energies.

The use of neutrons has several advantages for carrying out high quality powder diffraction measurements. Neutrons scatter predominantly from the nuclei of atoms *via* the strong force. For nuclei with spin, there is also an electromagnetic interaction between the neutron and the nucleus, whose magnitude depends on the spin state of the nucleus. In $^1$H (hydrogen) the large

difference in scattering length between the spin-up and spin-down states of the proton leads to a very large incoherent scattering cross section, resulting in a very high background in a powder neutron diffraction pattern from hydrogen-containing materials. Deuterated materials, if available, are usually used in preference to protonated samples for this reason. The coherent scattering power of an atom is characterised by a scattering length, $b$. The range of the nuclear scattering potential is of the order 1 fm, very much smaller than the wavelength of the neutron, so that there is no variation of $b$ with scattering angle, in contrast to the form factor $f$ of X-rays.

The scattering power of an atom varies with nuclear structure, and can vary significantly between isotopes of an element. Thus light atoms may scatter neutrons as strongly as the heavy atoms, which would dominate an X-ray diffraction pattern, Figure 2.18. Neutrons are uncharged and so highly penetrating into most materials. Notable exceptions are samples containing elements such as Gd, Sm, and isotopes such as $^{6}$Li and $^{10}$B, which absorb neutrons into the nucleus with emission of $\gamma$. Consequently, powder neutron diffraction works well for large amounts of sample and with complex sample environments. Sample containers for neutron diffraction can be made from any appropriate non-absorbing material, so X-ray-standard borosilicate glass is not a good option, whereas silica glass ("quartz" glass, $SiO_2$) is used for construction of *in situ* chemical cells. For routine experiments, sample cans made from vanadium foil are frequently employed, as vanadium gives very little diffraction signal itself because its coherent scattering cross section is very small.

Neutrons also have spin and a magnetic moment that interacts with unpaired electrons in a sample allowing studies of magnetic order. Because the

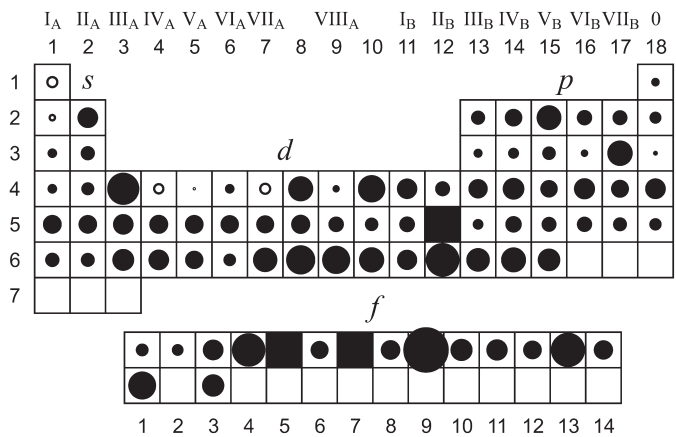



**Figure 2.18** Neutron coherent scattering lengths $b$ and coherent cross sections $\sigma$ shown in the form of a Periodic Table of the elements in which the radius of the circle is proportional to $b$ and the area is proportional to $\sigma$. For a few elements (*e.g.* H) the value of $b$ is negative: this is indicated by the use of open circles. Black squares indicate elements with large absorption cross sections due to the occurrence of nuclear absorption edges.

wavelength of the neutron and the distribution of the spin density are on comparable length scales, neutron magnetic scattering, just like X-ray scattering, has a form-factor fall off. As with synchrotron X-rays, free access to neutron diffraction instruments is generally through a peer reviewed user system that is open to everyone. Beam lines at neutron sources are equipped with extensive special environments and extensive experimental and data analysis help is often available from professional beam-line staff.

### 2.9.2 Sources of Neutrons

Intense neutron beams cannot be produced in the laboratory. Currently, there are two methods for producing neutron beams of sufficient intensity for powder diffraction, namely, a nuclear reactor and a spallation source. The two methods are quite different and result in neutron beams with different characteristics. Both methods involve fission, though with a spallation source it is not necessary to use a naturally fissile material. The consequences of the two methods in terms of the design and function of neutron powder diffractometers are discussed below.

Much of the description that follows is specific to the nuclear reactor at the Institut Laue Langevin (ILL) in Grenoble, France, which produces the world's highest continuous neutron flux for research use. However, the underlying principles behind the design and operation of the reactor and associated neutron instruments are quite general. The nuclear reactor uses the fission reaction of several kilograms of highly enriched $^{235}U$ to produce an intense flux of neutrons at the heart of the reactor. One of the by-products of the nuclear reaction is a lot of heat (57 MW at ILL). The primary coolant uses heavy water ($D_2O$) at about 35 °C, which also acts as a reflector, concentrating the neutrons in a small space, and a moderator, slowing the neutrons and equilibrating them at the ambient temperature. By interacting with the heavy-water the neutrons attain a Maxwellian distribution of wavelengths, corresponding to the temperature of the $D_2O$. This results in "thermal" neutrons whose wavelengths are typically in the range 1–2 Å. For some applications, neutrons may be required where the maximum in the Maxwellian distribution is either at a shorter or longer wavelength. A cold or hot moderator contained within the heavy water vessel can be used to produce "cold" and "hot" neutrons, respectively. Most powder neutron diffractometers at reactor sources use thermal neutrons, though instruments have been built on cold and hot sources.

At a spallation source a heavy-metal target, such as Pb, W, Ta or Hg, is bombarded with energetic particles, usually protons accelerated to energies of up to 1 GeV. Neutrons freshly released from an atomic nucleus have high energies, referred to as "epithermal neutrons", and must be slowed down to be useful for powder diffraction experiments. This occurs by collisions between the neutrons and the moderator – such as liquid methane or water – placed in the path of the neutron beam, which cause the exchange of energy and a trend towards (partial) thermal equilibrium.

With both types of source, neutrons are led to the experimental instruments from the reactor core or spallation target station by means of evacuated guide tubes, rectangular in cross section, that convey the neutrons by means of total external reflection from the walls, often made of highly smooth nickel-coated plate glass. The guides often curve gently to remove the diffractometer from the direct line of sight of the γ-rays that are emitted in the nuclear reactions producing the neutrons.

### 2.9.3 Detection of Neutrons

The most common neutron detectors are of the proportional gas type. Since neutrons themselves have no charge and are non-ionizing, they are harder to detect than X-rays. Detection relies on the absorption of the neutron by an atomic nucleus with the simultaneous emission of a γ-ray photon, often referred to as an (n,γ) reaction. Since the absorbing material must absorb neutrons and be capable of existing in gaseous form, the choice of substances is limited. The most common is $^3$He gas, which relies on the reaction:

$$^3\mathrm{He} + {}^1\mathrm{n} \rightarrow {}^4\mathrm{He} + \gamma$$

Another suitable gas is $BF_3$, which uses the absorption properties of the isotope $^{10}$B, releasing an energetic α particle and $^7$Li:

$$^{10}\mathrm{B} + {}^1\mathrm{n} \rightarrow {}^7\mathrm{Li} + \alpha.$$

$BF_3$ is usually isotopically enriched as normal boron consists of only 20% of the strongly absorbing isotope. For thermal neutrons the $^3$He gas detector is considered superior, but for long-wavelength neutrons $BF_3$ is preferred, but is rarely used nowadays because of the corrosive and toxic nature of the gas. Since the capture cross-section of gases is small, $^3$He detectors are usually operated above atmospheric pressure, 5–10 bar. They are typically 10–15 cm long and 2–5 cm in diameter.

Recent developments have led to the production of single-tube $^3$He detectors with position sensitivity. This is achieved by measuring the charge developed at both ends of a resistive anode wire, a larger charge being related to a shorter distance travelled by the electronic pulse along the wire. Exploited for high-resolution angle-dispersive powder diffractometers such as D2B (described later), they allow a greater solid angle to be measured without compromising instrumental resolution. Furthermore, the low-angle asymmetry due to the curvature of the Debye–Scherrer diffraction cones can be removed *via* software, since the axial position of each detected neutron is known.

Neutron PSDs are also $^3$He based, though they are also filled with a quenching gas such as a mixture of xenon (Xe) and methane ($CH_4$). The original PSDs consisted of an array of vertical wires at fixed intervals chosen to correspond to a convenient angle, *e.g.* 0.1°. They are very large, can be both one- and two-dimensional, and can cover a very large solid angle. A recent

development to improve the spatial resolution has been the development of microstrips which replace the conventional anode wires.

Scintillation detectors have been developed using, for example, $^{6}$Li or Gd as the absorbing atoms. The latter may be used in the mixed oxide-sulfide $Gd_2O_3.Gd_2S_3$, which is able to convert the primary $\gamma$-ray photons directly into a UV-visible photon. The latter is counted using a conventional photomultiplier tube. With scintillation detectors, the neutron is detected in a smaller volume of physical space compared to a gas detector because of the higher density of the absorbing material. This has advantages for some applications. A potential disadvantage is that they may detect sample fluorescence due to (n,$\gamma$) reactions within the sample itself.

One of the problems in detecting neutrons is the background from rogue $\gamma$-rays from the source, plus those produced by interaction of neutrons with the monochromator or the sample. The electronics controlling the detector must therefore be capable of discriminating the energy of the $\gamma$-ray so that only those produced in the detector are counted. In addition, the detector must be shielded from the general cloud of neutrons that surrounds the diffractometer. The shielding is very thick: many centimetres of polythene are used to slow down any fast neutrons, the background neutrons then being absorbed by $B_4C$-doped plastic or rubber.

### 2.9.4 Monochromatic Techniques

Neutron powder diffractometers that exploit a monochromatic beam are normally situated at reactors, which have a steady-state output of neutrons, though the SINQ at the Paul Scherrer Institute in Switzerland is a continuous spallation source. As with synchrotron X-rays, neutrons of a particular wavelength are selected from the polychromatic beam using a single-crystal monochromator, and the diffraction pattern is measured as a function of angle.

Because of the size of neutron beams, very large single crystals are required for neutron monochromators, *e.g.* $10^5$ mm$^3$. Typical materials used are Cu, Be, C (as pyrolytic graphite) Ge, and Si. However, since the neutron beams are of relatively low intensity, perfect Ge and Si crystals have too small a band-pass ($\Delta\lambda/\lambda$) to be of practical use. To improve the transmitted intensity it is necessary to increase the mosaic spread so that a wider range of neutron wavelengths is reflected. One method for doing this is to squash the crystals to broaden the mosaicity. However, in practice this can result in inhomogeneous or broken crystals and, consequently, poorly monochromated neutron beams. A more recent development is to produce fine slices of germanium crystal, and to glue them together with near-perfect alignment, thus simulating the effect of mosaic blocks.

Since there is no issue of polarisation to consider (unlike synchrotron X-rays), and given the massive construction of neutron facilities, neutron diffractometers operate in the horizontal plane, and only a single-bounce monochromator is necessary. The position of the diffractometer on the floor is usually fixed, thus defining the monochromator take-off angle $2\theta_M$. A wavelength is selected by rotating the monochromator crystal about its vertical axis

until a chosen set of lattice planes is aligned correctly to divert neutrons of a specific wavelength towards the axis of the diffractometer. Since the spacings between lattice planes in a crystal have specific values, only certain wavelengths are available, despite the white radiation from the source. In a few instruments, the whole diffractometer can be rotated on air pads about the monochromator axis, thus providing a greater choice of $2\theta_M$ and hence incident wavelengths (and resolution). On the high-resolution instruments D1A and D2B[7] at the ILL, the Ge monochromator crystals are cut so that the normals to the 110 planes lie along the vertical rotation axis of the monochromator. Thus planes of the type *hhl* are available to monochromate the incident neutron radiation. Owing to the crystal symmetry and structure, the reflections *hhl* with non-zero structure factors are those that have $h$ and $l$ either both odd or both even, with $2h + l = 4n$ if both are even. Typical planes used therefore are 111, 113, 115, 335, *etc*., since reflections with odd $h$ values do not diffract the unwanted harmonic wavelength $\lambda/2$ (since $4h + 2l \neq 4n$ for reflection $2h\ 2h\ 2l$).

Monochromator crystals may be cut asymmetrically so that focussing of the beam occurs in the horizontal plane, providing a modest increase in flux at the sample. Vertical focussing is possible by curving the whole monochromator. Typically, several crystals are required to achieve this (Figure 2.19). One disadvantage of vertical focussing is increased axial divergence leading to increased asymmetry in the shape of peaks at low $2\theta$ angles. However, the significant increase in intensity is certainly worthwhile. Neutron fluxes are low and experiments are typically flux limited.

Filters may be used in conjunction with a monochromator. If the monochromator is designed to select a particular wavelength, $\lambda$, then it may also diffract shorter harmonics at the same monochromator angle such as $\lambda/2$, $\lambda/3$, *etc*. If the incident flux of neutrons is intense for the shorter wavelengths, then relatively large amounts of the unwanted wavelengths will be present. The shorter wavelengths can often be eliminated by the use of a neutron filter made

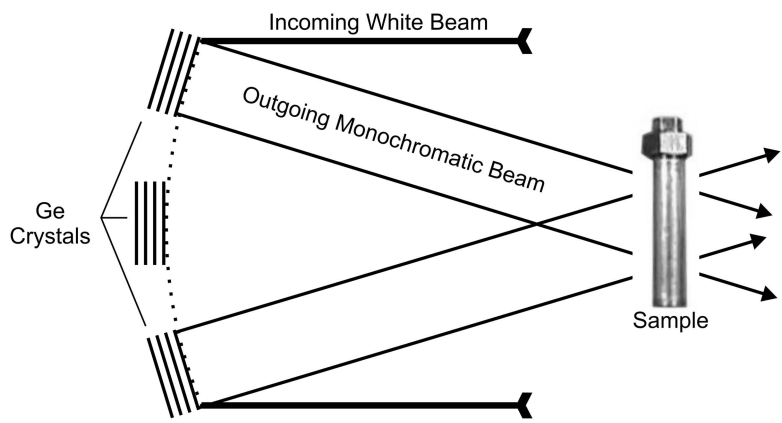



**Figure 2.19** Schematic showing vertical focusing with a curved array of monoch romator crystals.

of a material such as pyrolytic graphite or beryllium cooled in liquid nitrogen. Filters work by diffracting the shorter wavelengths out of the main beam into a neutron absorbing material. The *d*-spacing of the filter is chosen such that the ratio $\lambda/2d_{\text{filter}} > 1$ so that the desired wavelength passes straight through the filter without being affected by Bragg diffraction.

Figure 2.20 shows the layout of the high-resolution powder neutron diffractometer D2B at the ILL. "High-resolution" refers to the fact that the instrumental resolution function results in narrow peaks at high scattering angles. This is achieved by having a large monochromator take-off angle, which for this instrument is 135°. When $2\theta \approx 2\theta_M$, so that the incident, monochromated, and diffracted beams are in a "Z-shaped" configuration, a focussing effect occurs that produces a minimum in the resolution function (Figure 2.21).

The large value of the monochromator angle is also required so that the wavelength dispersion, $\Delta\lambda$, of the incident beam is kept small, which is necessary for narrow diffraction peak widths. To obtain high resolution, the instrument must also be able to detect neutrons with a well-defined Bragg angle. This is achieved by the use of Söller collimators placed in front of each detector, to select the trajectory of the detected neutrons. Finally, given the relatively low flux available at neutron sources, instrument efficiency is greatly improved by using many detectors in parallel, *e.g.* D2B has 64 detectors separated by 2.5°, so scanning by 2.5° records a diffraction pattern over 160°.

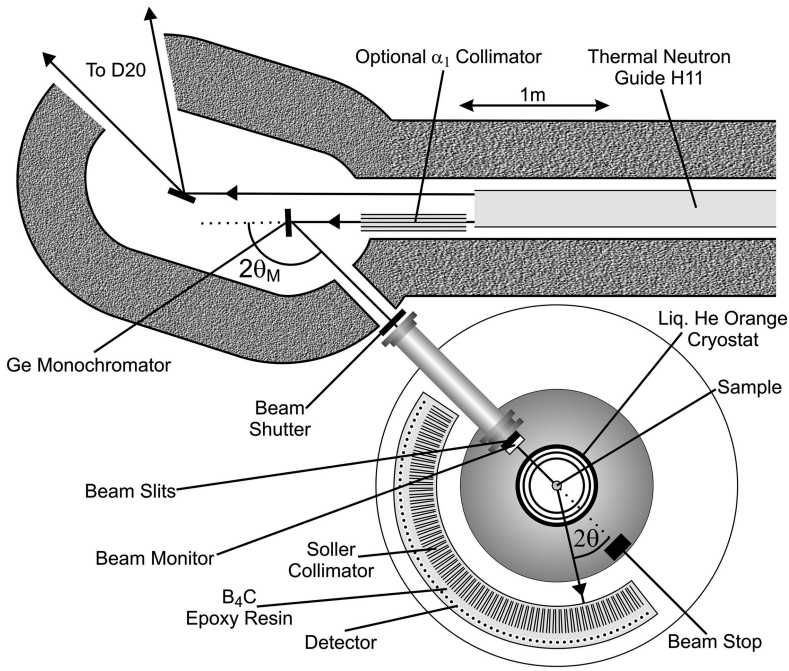



**Figure 2.20** Schematic of the high resolution powder diffractometer D2B (ref. 7) at ILL, Grenoble.

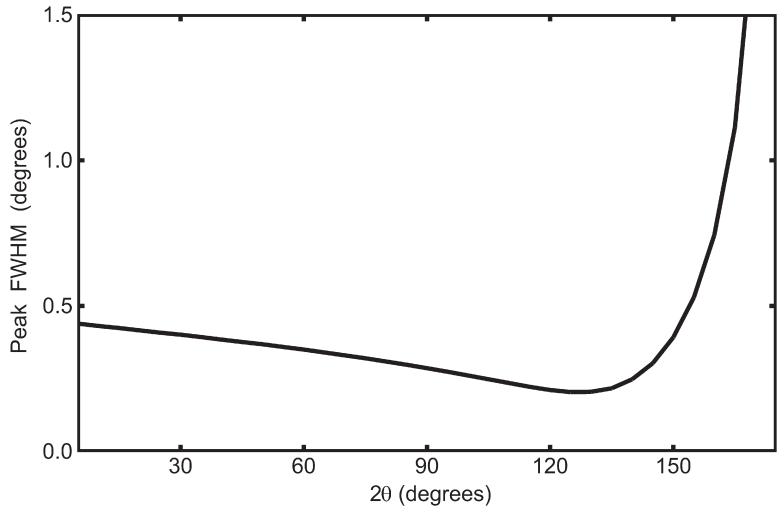



**Figure 2.21** Typical resolution function of a high resolution powder diffractometer.

Where rapid count times are desired it is necessary to replace a scanning detector system with a PSD that covers a wide range of scattering angle, such as on the D20[8,9] instrument at ILL. This has a microstrip detector consisting of 1536 channels each of width 0.1°. To obtain optimum neutron flux at the sample, the instrument has a choice of monochromator crystals, including pyrolytic graphite with a large mosaic spread, and a low take-off angle of 42° to increase $\Delta\lambda/\lambda$. The 002 graphite reflection yields a wavelength of 2.4 Å. In contrast to the X-ray case, where the absorption of long-wavelength X-rays would be a severe problem, the long wavelengths are ideal with neutrons since neutrons are not easily absorbed and the peak-to-background signal is drastically improved as detected intensity increases as a function of $\lambda^3$. The contaminating $\lambda/2$ harmonic, *via* the 004 reflection of the monochromator, is eliminated by the use of a graphite filter between the monochromator and the sample.

### 2.9.5 Time-of-Flight Techniques

Time of flight (TOF) techniques use a polychromatic beam and a pulsed source of neutrons, and exploit the fact that a neutron's wavelength is inversely proportional to its velocity, as indicated by the De Broglie relationship. Thus long-wavelength neutrons are slower than short-wavelength neutrons and take more time to travel from the source to the detector. By recording the arrival time of each neutron of a particular pulse in the detector, its wavelength and the corresponding *d*-spacing of the diffracting planes can be calculated since:

$$\lambda = h/m_n v = ht/m_n L = 2d\sin\theta$$

where $t$ is the time of flight and $L$ is the length of the flight path. TOF machines have no moving detectors, which can be an advantage with complex sample

environments, such as high-pressure cells, where fixed entrance and exit windows can be designed into the apparatus. Banks of detectors covering a large proportion of the volume around the sample are also common.

The pulsed source is usually a spallation source (*e.g.* ISIS in the UK; KENS in Japan; IPNS, LANCE, and SNS in the USA), where accelerated protons are concentrated into tight bunches and are fired at the target with a repetition rate of up to 60 Hz. Note, however, that a 5 Hz pulsed reactor exists at Dubna in Russia, and it is possible to produce pulsed beams from a steady-state source using choppers.

As with angle-dispersive neutron diffractometers, the design of TOF powder diffractometers can be optimised for either high resolution or high intensity or some compromise of both. An understanding of the factors that affect the resolution is therefore important. The relative uncertainty in $d$-spacing, $\delta d/d$, may be determined from the equation:

$$(\delta d/d)^2 = (\delta t/t)^2 + (\delta L/L)^2 + (\cot\theta\,\delta\theta)^2$$

where $\delta t$, $\delta L$, and $\delta\theta$ are the uncertainties in time of flight, path length, and scattering angle, respectively.

From the above equation it may be deduced that high $d$-spacing resolution may be achieved by (a) using a long flight path, $L$, which also increases the TOF, $t$, and (b) by positioning the detectors at a high scattering angle, $2\theta$. The uncertainty in scattering angle depends on the size of the sample and the detector aperture, and can be reduced by increasing the length of the secondary flight path, *i.e.* the sample-to-detector distance. However, an increase in the length of the secondary flight path decreases the solid angle seen by the detectors (for a fixed number of detectors), so that in practice the length of the secondary flight path is of the order of 1–2 m and the primary flight path, from the pulsed source to the sample, is considerably longer. One factor that leads to an uncertainty in the path length is the thickness of neutron detectors: for very high-resolution instruments, thin scintillation counters are generally preferable to the fatter gas-filled detectors. The uncertainty in TOF is largely due to the duration of the initial pulse, which is broadened by the passage of the beam through the moderator: thus the thickness of the moderator is a compromise between moderating the wavelength spectrum of the neutron pulse and maintaining its time structure.

The high-resolution powder diffractometer HRPD[10] at ISIS has a very long flight path of about 100 m with detectors at low angle, 90°, and at back scattering (Figure 2.22). The instrument has two sample positions, but in practice the shorter sample-to-detector distance is preferred given the greater solid angle for the high-angle detectors. The back-scattering detectors provide data with the highest resolution since $\cot\theta$ in the resolution function is then close to zero. The repetition rate of the ISIS source, 50 Hz, and choppers in the primary flight path prevent the occurrence of ''frame overlap'', whereby fast neutrons overtake slower neutrons from a previous pulse before they arrive in the detector.

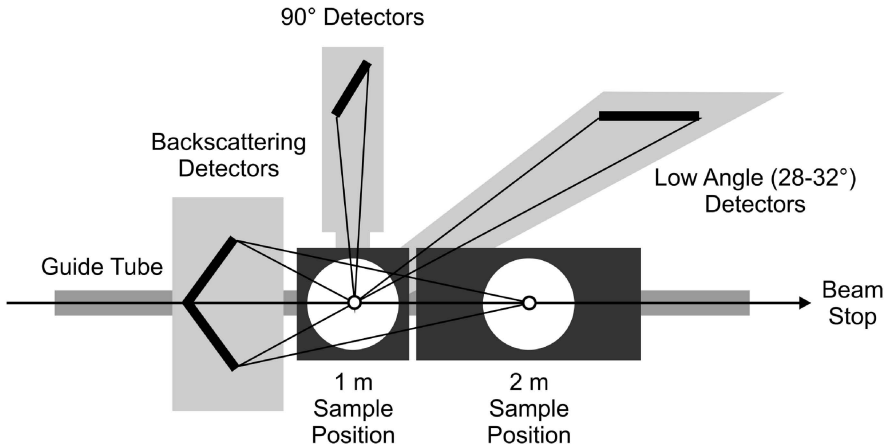



**Figure 2.22** Schematic of the HRPD TOF diffractometer[10] at ISIS. The detector banks at $160^\circ < 2\theta < 176^\circ$ (backscattering) and $80^\circ$ $100^\circ$ are based on ZnS scintillators. The low angle detector bank $28^\circ$ $32^\circ$ uses 12 mm diameter $^3$He gas tubes at a pressure of 10 bar. The three banks have approximate resolutions $\Delta d/d$ of $4 \times 10^{-4}$, $2 \times 10^{-3}$, and $2 \times 10^{-2}$, respectively.

The different detector banks see different ranges of *d*-spacing. Thus if the range of useful wavelengths is, say, 0.5–4 Å, then the *d*-spacings measured by a detector at $160^\circ$ are 0.254–2.031 Å. However, the detectors at $90^\circ$ will simultaneously measure peaks with *d*-spacings up to 2.83 Å, while those at $30^\circ$ will measure *d*-spacings up to 7.7 Å. Thus, the low-angle detectors can be used to measure the larger *d*-spacings, where peak resolution is not so critical given the lower density of peaks in this region.

Data from TOF machines are conveniently displayed as counts against TOF (or *d*-spacing) (Figure 2.23), which is comparable to the X-ray energy-dispersive case of counts against energy. With monochromatic radiation one usually displays counts against angle. Comparison between monochromatic and TOF powder neutron diffraction techniques shows that each has its advantages. With TOF, a large proportion of the neutrons of the polychromatic source is exploited, and, for a high-resolution pattern, all channels are collected simultaneously, rather than scanning a detector bank. Peak shapes are, however, more complicated to model (reflecting the time structure of each neutron pulse, which is affected by the time spent by neutrons coming to partial thermal equilibrium in passing through the monochromator) and there are various energy-dependent factors to be taken into consideration, such as the detailed intensity distribution of the source, and the effects of absorption by the sample. With monochromatic techniques, reflections from large *d*-spacings are usually easier to measure, and modelling the peak shapes and diffracted intensities is more straightforward.

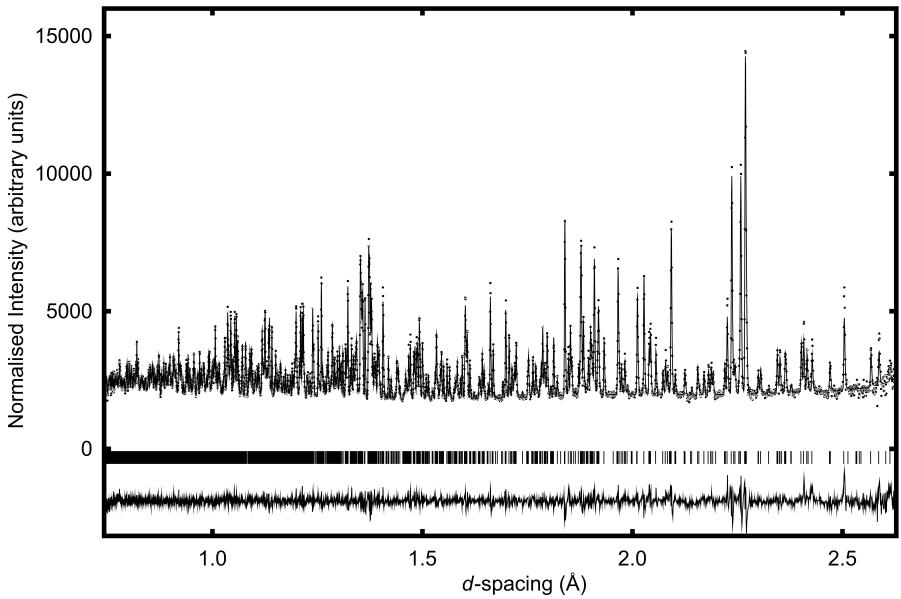



**Figure 2.23** High resolution TOF powder diffraction pattern. Note (a) the range and resolution of the smaller *d* spacings is impressive, but (b) the largest *d* spacings are not present. The consequences of this are that excellent structural parameters can be derived from such data sets, especially for anisotropic displacement parameters, which require a wide range of *d* spacing for their precise determination, but that unit cell indexing may be a problem unless the poorer resolution data from low angle detector banks is exploited.

## REFERENCES

1. R. W. Cheary and A. Coelho, *J. Appl. Cryst.*, 1992, **25**, 109.
2. R. W. Cheary, A. A. Coelho and J. P. Cline, *J. Res. Natl. Inst. Stand. Technol.*, 2004, **109**, 1.
3. M. Deutsch, E. Förster, G. Hölzer, J. Härtwig, K. Hämäläinen, C.-C. Kao, D. Huotari and R. Diamant, *J. Res. Natl. Inst. Stand. Technol.*, 2004, **109**, 75.
4. A. N. Fitch, *J. Res. Natl. Inst. Stand. Technol.*, 2004, **109**, 133.
5. F. Gozzo, B. Schmitt, Th. Bortolamedi, C. Giannini, A. Guagliardi, M. Lange, D. Meister, D. Madena, P. Willmott and B. D. Patterson, *J. Alloys Compd.*, 2004, **362**, 206.
6. R. F. Garrett, D. J. Cookson, G. J. Foran, T. M. Sabine, B. J. Kennedy and S. W. Wilkins, *Rev. Sci. Instrum.*, 1995, **66**, 1351.
7. E. Suard and A. W. Hewat, *Neutron News*, 2001, **12**, 30.
8. P. Convert, T. Hansen, A. Oed and J. Torregrossa, *Physica B (Amsterdam)*, 1998, **241–243**, 195.

9. P. Convert, T. Hansen and J. Torregrossa, *Mater. Sci. Forum*, 2000 **321–324**, 314.
10. R. M. Ibberson, W. I. F. David and K. S. Knight, 1992, report RAL-92-031, http://www.isis.rl.ac.uk/Crystallography/HRPD/index.htm
11. T. C. Huang, H. Toraya, T. N. Blanton and Y. Wu, *J. Appl. Cryst.*, 1993, **26**, 180.

CHAPTER 3

# The Intensity of a Bragg Reflection

R. B. VON DREELE[a] AND J. RODRIGUEZ-CARVAJAL[b]

[a] Intense Pulsed Neutron Source/Advanced Photon Source, Argonne National Laboratory, Argonne, IL, USA; [b] Institut Laue-Langevin, Grenoble, France

## 3.1 INTRODUCTION

Visually, the graph of a powder pattern consists of a sequence of peaks (Bragg reflections) resting on a slowly varying background or as a pattern of rings arranged around a common center (Figure 3.1) on a two-dimensional area detector. To create this pattern, either light in the form of X-rays, or neutrons, is scattered from a polycrystalline sample containing many small crystallites and the scattered intensity is recorded.

In this chapter we discuss the intensities of these peaks; other aspects of this pattern and the experimental procedures for its measurement are considered elsewhere in this volume.

## 3.2 SINGLE ATOM SCATTERING THEORY

### 3.2.1 X-ray Scattering

The scattering of X-rays or neutrons by any material occurs by interaction with the atoms that make up the substance. In the case of X-rays, the scattering process occurs between the photon and the electrons surrounding the atomic nuclei. The classical description[1,2] of scattering of the electric wave component of the photon by an electron gives complete scattering of the perpendicular component and an angular dependence for the parallel component. Consequently, the scattered intensity at some distance, $R$, becomes partially polarized, with the intensity given by:

$$\frac{I}{I_0} = \left(\frac{\mu_0}{4\pi}\right)^2 \frac{e^4}{m_e^2}\left(\frac{1+\cos^2 2\Theta}{2}\right)\frac{1}{R^2} = \sigma_e\left(\frac{1+\cos^2 2\Theta}{2}\right)\frac{1}{R^2} \qquad (1)$$

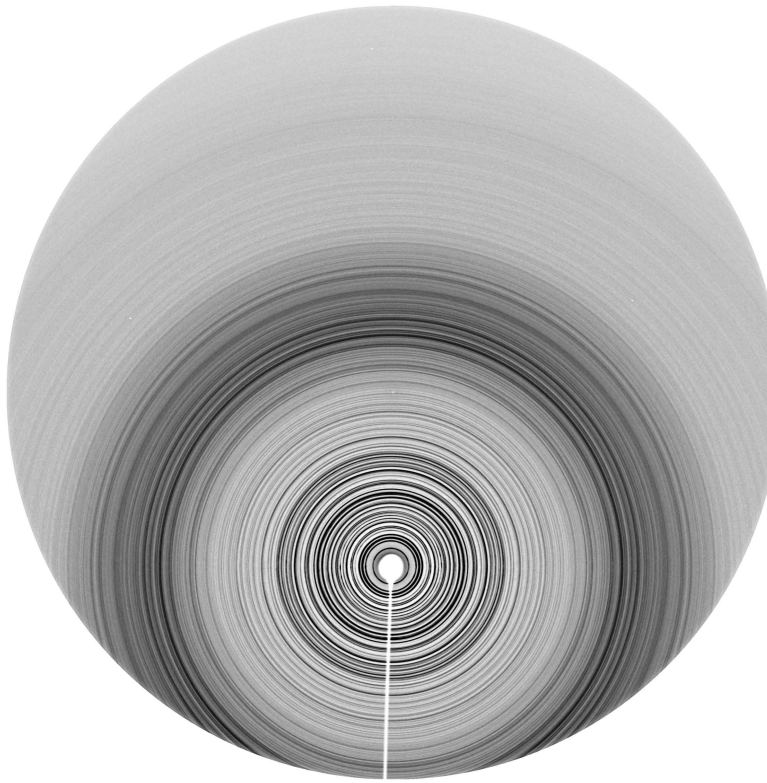


**Figure 3.1** Two dimensional X ray powder pattern from hen egg white lysozyme (HEWL) crystallized from 1.25 M NaCl, pH 4.0, 0.05 M phthalate buffer; taken at 20 keV as a 30 s image plate exposure on beamline 1 BM at the Advanced Photon Source, Argonne National Laboratory.

This is known as the Thompson scattering formula. The value of the factors containing the constants $\mu_0$, $e$, and $m_e$ is $\sigma_e = 7.94 \times 10^{-26}\,\mathrm{cm}^2$ and is the classical electron scattering *cross section*. As there is no change in the energy of the scattered wave, it retains its phase relationship to the incident wave and this scattering is thus *coherent*. At a scattering angle of $2\Theta = 90^\circ$ the polarization is complete with only the electric component perpendicular to the scattering plane retained.

This classical treatment ignores the requirement that both energy and momentum must be conserved in a collision between the X-ray photon and the electron. Application of these rules requires that the X-ray photon loses energy in the collision that depends on the scattering angle. This is known as Compton scattering,[2] and because the incident and scattered X-rays have different energies and their phase relations are lost, this is an *incoherent* scattering process, and only Compton scattering is possible from an isolated electron. However, electrons are bound to atoms that are gathered together in, usually,

solid materials of interest and so they are not free. Consequently, both coherent and incoherent scattering of X-rays from these electrons are possible. When the electron remains bound, there is no change in X-ray energy and so the scattering is coherent. Alternatively, if the electron is ejected from the atom there is a gain in its energy and a corresponding loss in the X-ray energy and this is an incoherent process. The total scattering (coherent + incoherent) is given by the Thompson formula; the coherent part gives rise to Bragg scattering and the incoherent part contributes to the background of a powder measurement.

The quantum mechanical treatment of the electron distribution about an isolated atom nucleus gives an electron density, $\rho(\mathbf{r})$, which is peaked at the nuclear position and falls off smoothly as a function of the distance from the nucleus.[2] Each unit of volume, $dv$, around this center can scatter X-rays and those that are scattered coherently will interfere with those scattered from other unit volumes near this atom, depending on the scattering angle. From Chapter 1 we know that the interference occurs as a phase shift, $\phi$, between the scattered waves parallel to the vector, $\mathbf{S}$, from two unit volumes separated by $\boldsymbol{r}$ by:

$$\varphi = \frac{2\pi}{\lambda}\mathbf{r}\cdot(\mathbf{S}-\mathbf{S_0}) = 2\pi(\mathbf{r}\cdot\mathbf{s}) \tag{2}$$

where the incident wave is parallel to $\mathbf{S_0}$. Since $\mathbf{r}$ is a vector defined in a real space coordinate system, dimensionally $\mathbf{s}$ must be described in a *reciprocal space* coordinate system. Consequently, by integrating the interference from all possible real space vectors around the atom center, the scattering from the electrons around an atom can be described as:

$$f(\mathbf{s}) = \int_{\infty}^{\infty} \rho(\mathbf{r})\ \mathrm{e}^{2\pi\,\mathrm{i}(\mathbf{r}\cdot\mathbf{s})}\mathrm{d}\,\mathbf{r} = f(s) \tag{3}$$

which is the *Fourier transform* of $\rho(\mathbf{r})$ and is known as the atomic *scattering factor* or *form factor*. The electron distribution in an isolated atom can be assumed to be spherically symmetric, thus $f(\mathbf{s})$ only depends on the magnitude of $\mathbf{s}$ ($s = sin\Theta/\lambda$). These are tabulated[3] and may be efficiently represented by a sum of four exponential terms:

$$f(s) = c_0 + \sum_{i=1}^{4} a_i \mathrm{e}^{(\ b_i s^2)} \tag{4}$$

to sufficient precision for crystallographic calculations. Since $\rho(\mathbf{r})$ is peaked at the atomic nucleus and falls off smoothly and monotonically to zero at large distances then the Fourier transform, $f(s)$, also is peaked at $s = 0$ (forward scattering angles) and falls off smoothly and monotonically at large $s$ (back scattering angles). Thus, the maximum at $f(0)$ is just the atomic number, $Z$, corrected for valence charge:

$$f(0) = c_0 + \sum_{i=1}^{4} a_i = Z(\pm\text{valence}) \tag{5}$$

The falloff of $f(s)$ with $s$ is mainly responsible for the general appearance of an X-ray powder pattern where the highest intensity peaks occur at small scattering angles (*i.e.* small $s$) and the pattern quickly falls off in peak intensity with increasing scattering angle (*i.e.* increasing $s$).

Because the valence electron distributions are found in the outer atomic orbitals, they are generally smeared out over a larger volume of space around the atomic nucleus than the inner or core electrons. Consequently, their contribution to the atomic scattering factor is largely confined to the small region of $s$ near $s = 0$ and the choice of neutral atom or valence charged scattering factor only affects the lowest angle part of the scattering. Similarly, the nonspherical electron distributions arising from atomic orbital hybridization (*e.g.* $sp^3$ in carbon or silicon) occur over a large volume and the resulting nonspherical deformation of the atomic scattering factor is also evident only at small $s$.

When the X-ray energy is nearly coincident with the binding energy of any of the electrons in an atom, the scattering process is affected by the possible absorption of the photon and subsequent ejection of the electron. There is a sharp rise in the X-ray absorption with increasing photon energy at each of the electron binding energies (hence the term *absorption edge*). The principal effect to the coherent scattering is a shift in the phase between the incident wave and the scattered wave *via* a resonance effect. This phase shift creates an imaginary component to the atomic scattering factor as well as a modification of the real part:

$$f(s) = f_0(s) + f' + \mathrm{i}f'' \tag{6}$$

where $f_0(s)$ is the atomic scattering factor described in Equation (3). As the effect is largely of concern for absorption *via* inner shell (K for light elements and L for heavier ones) electrons that have distributions confined close to the atomic nucleus, these *anomalous* or *resonance* scattering factors are independent of $s$, but are strongly dependent on $\lambda$. Values of $f'$ and $f''$ are tabulated[3] for the commonly used characteristic X-ray wavelengths obtained from laboratory sources and software[4] is available to compute values over the range usually used in synchrotron sources. These values are reasonably accurate for X-ray energies more than a few eV from an absorption edge but can be seriously in error very close to an edge due to valence and chemical bonding effects that both shift the edge and modify its shape.

The incoherent scattering is then found by difference *via* the Thompson formula as:

$$\frac{I_{\mathrm{incoh}}}{I_0} = \sigma_e \left( \frac{1 + \cos^2 2\Theta}{2} \right) \frac{1}{R^2} \left[ 1 - f^2(s) \right] \tag{7}$$

where, by the product of the atom scattering factor and its complex conjugate:

$$f^2(s) = f(s) f^*(s) = [f_0(s) + f']^2 + f''^2 \tag{8}$$

and is both polarized and increases with scattering angle, thus making an increased contribution to background scattering with angle. Moreover, when

the photon energy is greater than the appropriate K- or L-electron binding energy, the empty orbital left after the electron is ejected is immediately refilled, giving rise to the emission of a new photon. This X-ray *fluorescence* is isotropic and can also contribute to the background scattering.

### 3.2.2 Neutron Scattering

The wave mechanical description[5] of a moving neutron implies an associated wavelength as given by the de Broglie relation:

$$\lambda = \frac{h}{m_n v} \tag{9}$$

Given the values of the constants ($h$ = Planck constant, $m_n$ = neutron mass), the wavelength of a neutron moving at 2200 m s$^{-1}$ is $\lambda = 1.798$ Å, which is coincident with the range of interatomic distances as well as the commonly used X-ray wavelengths used in crystal structure analysis. At this velocity the neutron has a kinetic energy ($E = 25.3$ meV) comparable to typical molecular and lattice vibrational energy transitions. The set of relations between the wavelength, *wavevector*, velocity, energy and temperature of a neutron are then:

$$\begin{aligned} \lambda(\text{Å}) &= 2\pi\frac{1}{\text{k(Å}^{-1})} = 3.956\frac{1}{v(\text{kms}^{-1})} = 9.045\frac{1}{\sqrt{E(\text{meV})}} = \frac{1}{\sqrt{T(\text{K})}} \\ E &= 0.08617T = 5.227v^2 = 81.81\frac{1}{\lambda^2} = 2.072k^2 \end{aligned} \tag{10}$$

A neutron is uncharged but has a magnetic moment (*spin* of $\pm 1/2$) so it can closely approach the atomic nucleus and be scattered by nuclear forces or *via* spin–spin interactions with both nuclear magnetic moments and unpaired electrons in magnetic atoms or ions. There is no polarization comparable to that of X-rays although neutron beams can be produced where the magnetic moments are aligned or *spin polarized*. Because the dimensions over which the nuclear forces operate are about $10^4$–$10^5\times$ smaller than the neutron wavelength, nuclear scattering is just point scattering and the observed neutron scattering factor or *scattering length*, $b$, for a given element is independent of $s$. A total neutron scattering cross section, $\sigma_{\text{Tot}}$, is then given by:

$$\sigma_{\text{Tot}} = 4\pi\,\overline{b^2} \tag{11}$$

The actual values of the atom scattering length depend on the nature of the neutron–nucleus interaction, which cannot be calculated with sufficient precision given our current knowledge of nuclear theory. Moreover, they also depend on the nuclear spin state of the individual atomic nuclei as well as the different scattering powers of the isotopes and their abundance within the sample (usually the "natural" abundance). This distribution of scattering lengths over the individual atoms of a given element gives rise to both coherent

and incoherent scattering, depending on how the phase relation between the incident and scattered neutrons is changed. As with the X-ray case:

$$\sigma_{\text{Tot}} = \sigma_{\text{coh}} + \sigma_{\text{incoh}} \tag{12}$$

where:

$$\sigma_{\text{coh}} = 4\pi\, b^2 \tag{13}$$

and:

$$\sigma_{\text{incoh}} = 4\pi\, (\overline{b^2} - b^2) \tag{14}$$

Note that one term is the average of the squares and the other is the square of the average. Because of the complexities that determine the observed values of neutron cross sections and scattering lengths, these must be determined experimentally, and values are tabulated. These change from time-to-time as the measurements improve; as of writing the most recent values are in ref. 6. The unit used for these cross sections is the "barn" ($10^{-24}\,\text{cm}^2$) and scattering lengths are usually given in units of $10^{-12}$ cm or $10^{-15}$ m (fm). Unlike X-ray scattering factors which monotonically increase with atomic number, neutron scattering lengths vary erratically with atomic number and show considerable variation by isotope. Thus, adjacent elements in the Periodic Table may have very different neutron scattering lengths, which can facilitate their discrimination. The values for $b$ are from about $-3.7$ fm to about $+12.1$ fm and give scattering cross sections that are roughly the same order of magnitude as the corresponding X-ray scattering cross sections. However, for high atomic number elements the large number of electrons will give X-ray scattering cross sections that are much larger than the corresponding neutron scattering cross sections, particularly at low $s$.

## 3.3 SCATTERING FROM A CRYSTAL LATTICE

The arrangement of atoms in a crystal is best described as an infinitely repeating motif or *unit cell* of atoms in a three-dimensional lattice. The arrangement of atoms within the unit cell may exhibit its own repetition properties as a collection or group of *symmetry operations*; these must conform to one of the 230 possible *space groups*.[7] The usual dimensions of the unit cell ($2-100^{+}$ Å on a side) are sufficiently small that the infinite lattice approximation is valid for crystals about 1 μm on a side or larger. Consequently, the scattering density (electrons for X-ray scattering or neutron scattering lengths) can be represented by the Fourier series:

$$\rho(\mathbf{r}) = \frac{1}{V_c} \sum_{\mathbf{h}} F_{\mathbf{h}} \mathrm{e}^{-2\pi \mathrm{i}(\mathbf{h}\cdot\mathbf{r})} \tag{15}$$

where $V_c$ is the unit cell volume. The Fourier coefficients, $F_{\mathbf{h}}$, are known as *structure factors* and in general are complex quantities. Just as the vectors **r**

cover the real space outlined by the crystal unit cell, the vectors **h** cover a *reciprocal space* coordinate system dimensioned in $\text{Å}^{-1}$ which is filled with the values of $F_{\mathbf{h}}$. The infinite lattice approximation ensures that the $F_{\mathbf{h}}$ are δ-functions in this reciprocal space and are located as a *reciprocal lattice* array with the dimensions of reciprocal lattice parameters. As discussed in Chapter 1, if the translation vectors of the crystal lattice are denoted as **a**, **b**, **c**, then the reciprocal lattice translation vectors are **a***, **b***, **c***, where **a*** is perpendicular to the **b–c** plane, **b*** is perpendicular to the **a–c** plane and **c*** is perpendicular to the **a–b** plane. Moreover, their magnitudes are such that:

$$\mathbf{a}^* \cdot \mathbf{a} = \mathbf{b}^* \cdot \mathbf{b} = \mathbf{c}^* \cdot \mathbf{c} = 1 \tag{16}$$

From this one can see that the perpendicular distance between the **b–c** planes on adjacent unit cells along **a** is the reciprocal of $|\mathbf{a}^*|$. We can denote the stack of these **b–c** planes by their respective intercepts on the **abc** triplet of real space axes as (**a**/1, **b**/0, **c**/0), or simply (100). Similarly, another stack of planes can be constructed by selection of reciprocal integer intercepts (**a**/*h*, **b**/*k*, **c**/*l*) and denote them with just the denominators (*hkl*). These are the Miller indices for this stack of planes; they correspond to a lattice point in reciprocal space coincident with the vector **h** which has an associated structure factor $F_{\mathbf{h}}$ as defined in Equation (15). Because of the connection between the real and reciprocal lattices, the vector **h** is perpendicular to its respective stack of planes and the interplanar spacing is the reciprocal of the magnitude of **h**; this is the *d*-spacing for these planes.

The Fourier transform of Equation (15) is:

$$F(\mathbf{h}) = \int_V \rho(\mathbf{r}) \mathrm{e}^{2\pi \mathrm{i}(\mathbf{h}\cdot\mathbf{r})} \mathrm{d}\mathbf{r} \tag{17}$$

and gives the structure factor from the scattering density. The integral is over the real space volume and if confined to the unit cell gives structure factors that are an "absolute scale". Alternatively, one can postulate that the scattering density is localized on the atom centers and assign a scattering factor, $f(s)$, to each one. The integral then becomes a sum over the $N$ atom positions in the unit cell and if the vector **h** is the dimensionless indices (*hkl*) and the vector **r** becomes the fractional coordinates, $\mathbf{x}_i$, for each of the atoms:

$$\begin{aligned}
F(\mathbf{h}) &= \sum_{i=1}^{N} f_i(s_h) \mathrm{e}^{2\pi \mathrm{i}(\mathbf{h}\cdot\mathbf{x}_i)} \\
F(\mathbf{h}) &= \sum_{i=1}^{N} f_i(s_h) \{\cos[2\pi(\mathbf{h}\cdot\mathbf{x}_i)] + \mathrm{i}\sin[2\pi(\mathbf{h}\cdot\mathbf{x}_i)]\} \\
F(\mathbf{h}) &= A(\mathbf{h}) + iB(\mathbf{h}) \\
A(\mathbf{h}) &= \sum_{i=1}^{N} f_i(s_h)\cos[2\pi(\mathbf{h}\cdot\mathbf{x}_i)] \quad B(\mathbf{h}) = \sum_{i=1}^{N} f_i(s_h)\sin[2\pi(\mathbf{h}\cdot\mathbf{x}_i)] \\
F(\mathbf{h}) &= |F(\mathbf{h})| \mathrm{e}^{i\phi(\mathbf{h})}
\end{aligned} \tag{18}$$

The second form of Equation (18) is the expansion of the complex exponential into its trigonometric form showing the real and imaginary parts of the structure factor. The last form shows that the structure factor can be expressed as a magnitude and a phase angle, $\phi(\mathbf{h})$. A possible simplification of Equation (18) can occur if the atoms are in positions that are related by an inversion center. If the unit cell origin is chosen to coincide with the inversion center then for pairs of atoms related by that inversion the sine terms in Equation (18) are of opposite sign and cancel to give:

$$F(\mathbf{h}) = \sum_{i=1}^{N} f_i(s_h) \cos[2\pi(\mathbf{h} \cdot \mathbf{x}_i)] \tag{19}$$

Thus the structure factor for a *centrosymmetric* arrangement of atoms, with appropriate origin choice, can consist of just the cosine terms. Most computer programs that are used for crystallographic structure factor calculations will use this time saving simplification. Since $f(s)$ can be complex, $F(\mathbf{h})$ may also be complex even for a centrosymmetric structure. Also, if the unit cell origin is chosen so that it does not coincide with an inversion center then Equation (19) is not valid. Atom arrangements that lack an inversion center are *noncentrosymmetric* and their structure factor is given by Equation (18).

The scattered intensity (*Bragg scattering*) from a small single crystal is determined by the interference between the individual scattering centers that make up the crystal structure:

$$\begin{aligned} I(\mathbf{h}) &= \iint_{\mathbf{r}_i \mathbf{r}_j} \rho(\mathbf{r}_i)\rho(\mathbf{r}_j)\mathbf{e}^{2\pi\,\mathrm{i}(\mathbf{h}\cdot\mathbf{r}_i)}\mathbf{e}^{\;\;2\pi\,\mathrm{i}(\mathbf{h}\cdot\mathbf{r}_j)}\mathrm{d}\mathbf{r}_i\mathrm{d}\mathbf{r}_j \\ I(\mathbf{h}) &= F(\mathbf{h})F^*(\mathbf{h}) \\ I(\mathbf{h}) &= A^2(\mathbf{h}) + B^2(\mathbf{h}) \end{aligned} \tag{20}$$

or the self convolution of the structure factors (the * means *complex conjugate*). Thus, only the magnitude of the structure factor can be inferred from a measurement of the scattered intensity and the phase, $\phi(\mathbf{h})$, is lost. Consequently, one can not directly recover the scattering density *via* Equation (15); this is known as the *phase problem* in crystallography.

As one can see from the forgoing, there is a strong connection between the Bragg intensities observed in X-ray or neutron scattering and stacks of planes having reciprocal integral intercepts with the crystal lattice; this is embodied in the frequent use of the term *Bragg reflections* for this type of scattering.

### 3.3.1 Thermal Motion Effects

In the forgoing we have assumed that the atoms are in fixed positions within the crystal lattice. However, in reality the atoms are not fixed but are in at least an oscillation about their equilibrium positions that depends on temperature. An X-ray or neutron diffraction experiment records a time average of the possible instantaneous atom positions; this smears the scattering density about the

average position to an extent that depends on this thermal displacement. As a result Equation (18) becomes:

$$F(\mathbf{h}) = \sum_{i=1}^{N} f_i(s)\mathbf{e}^{2\pi\,\mathrm{i}(\mathbf{h}\cdot\mathbf{x}_i)}\mathbf{e}^{\ 8\pi^2 s^2 < u_i^2 >} \tag{21}$$

where $< u_i^2 >$ is the mean square displacement of the *i*th-atom from its equilibrium position, $\mathbf{x}_i$. In many cases these factors are not the same in all directions (*e.g. isotropic*) but describe an ellipsoidal distribution. These *anisotropic* thermal displacement factors modify Equation (18) as:

$$F(\mathbf{h}) = \sum_{i=1}^{N} f_i(s)\mathbf{e}^{2\pi\,\mathrm{i}(\mathbf{h}\cdot\mathbf{x}_i)}\mathbf{e}^{\ 2\pi^2[u_{11}h^2a^{*2}+u_{22}k^2b^{*2}+u_{33}l^2c^{*2}+2u_{12}hka^*b^*+2u_{13}hla^*c^*+2u_{23}klb^*c^*]} \tag{22}$$

In terms of the Debye–Waller factor, *B*, which is used in some crystallographic computing codes, Equation (21) is:

$$F(\mathbf{h}) = \sum_{i=1}^{N} f_i(s)\mathbf{e}^{2\pi\,\mathrm{i}(\mathbf{h}\cdot\mathbf{x}_i)}\mathbf{e}^{\ Bs^2} \tag{23}$$

Notably, the anisotropic thermal displacement factors form the elements of a $3 \times 3$ symmetric matrix. The physically meaningful form of this matrix when it is positive-definite is that of an ellipsoidal probability surface centered at the equilibrium atom position. An alternative form for Equation (22) frequently used in crystallography:

$$F(\mathbf{h}) = \sum_{i=1}^{N} f_i(s)\mathbf{e}^{2\pi\,\mathrm{i}(\mathbf{h}\cdot\mathbf{x}_i)}\mathbf{e}^{\ \mathbf{h}^T\boldsymbol{\beta}\mathbf{h}} \tag{24}$$

uses the 2nd-rank symmetric tensor form of the thermal displacement, $\boldsymbol{\beta}$, containing the unique elements $\beta_{11}$, $\beta_{22}$, $\beta_{33}$, $\beta_{12}$, $\beta_{13}$ and $\beta_{23}$.

### 3.3.2 The Lorentz Factor

In an experiment to measure the scattered intensity, $I_{\mathbf{h}}$, from a small single crystal the scattering power is spread over a small and non-zero volume of reciprocal space arising from a combination of slight incident beam angular and energy divergence, and a mosaic spread within the crystal. To sample this intensity accurately, a diffraction experiment is devised to scan over this reciprocal space volume and record the *integrated intensity*, which can be directly related to the square of the structure factors given in Equations (18–24) and be proportional to the illuminated sample volume. The usual means of scanning over the requisite region of reciprocal space is to rotate the crystal so that the selected vector $\mathbf{h}$ passes through the reflection condition of $\mathbf{s} = \mathbf{h}$; the

corresponding integral yields:

$$Q_{\mathbf{h}} = \sigma_e \left( \frac{1 + \cos^2 2\Theta}{2 \sin 2\Theta} \right) \frac{\lambda^3}{V_c^2} F_{\mathbf{h}}^2 \tag{25}$$

for the crystalline X-ray reflecting power,[1,2] where the term in $\lambda^3/\sin 2\Theta$ is known as the *Lorentz factor*. From the Thompson Equation (1), the remaining part in parentheses is the polarization factor for an unpolarized incident X-ray beam. Together they are referred as the *Lorentz-polarization* factor.

Most X-ray diffraction experiments are done with an incident beam that is partially polarized either by use of monochromators or from the nature of the source itself (*e.g.* synchrotron radiation). The degree of polarization, $P$, defined as:

$$P = \frac{I_\perp}{I_\perp + I_{||}} \tag{26}$$

can be 95% or greater for synchrotron radiation. The two terms of the Thompson formula are then modified by the effect of this incident beam polarization. Assuming that the perpendicular component of the incident beam is perpendicular to the diffraction scattering plane then the two terms are modified as:

$$Q_{\mathbf{h}} = \sigma_e \left( \frac{P + (1 - P) \cos^2 2\Theta}{2 \sin 2\Theta} \right) \frac{\lambda^3}{V_c^2} F_{\mathbf{h}}^2 \tag{27}$$

In the case of neutron diffraction there is no polarization effect, but the Lorentz factor applies so that the neutron reflecting power is:

$$Q_{\mathbf{h}} = \left( \frac{1}{\sin 2\Theta} \right) \frac{\lambda^3}{V_c^2} F_{\mathbf{h}}^2 \tag{28}$$

### 3.3.3 Scattering from a Modulated Crystal Lattice

In some crystalline materials a phase transition on lowering the temperature may produce a modulated structure. This is characterized by the appearance of "satellite" or "superstructure" reflections that are adjacent reflections (called *fundamental* reflections) already observed for the high temperature phase. The superstructure reflections, usually much weaker than fundamental reflections, can in some cases be indexed by a unit cell that is a multiple of the high temperature cell. In such a case the term "commensurate" modulated structure is commonly used. However, the most general case arises when the additional reflections appear in incommensurate positions in reciprocal space. This diffraction effect is due to a distortion of the high temperature phase normally due to cooperative displacements of atoms, ordering of mixed occupied sites, or both. Let us consider the case of a displacive distortion.

The positions of the atoms of the high temperature phase in the whole crystal can be written as: $\mathbf{R}_{lj} = \mathbf{R}_l + \mathbf{x}_j$, where $\mathbf{R}_l = l_1\mathbf{a} + l_2\mathbf{b} + l_3\mathbf{c}$ is the position vector

of the origin of the unit cell labeled $l=(l_1, l_2, l_3)$ and $\mathbf{x}_j = x_j\,\mathbf{a} + y_j\,\mathbf{b} + z_j\,\mathbf{c}$ (with $j=1, 2, \ldots N$) are the position vectors of the atoms within a unit cell. The fact that the vector positions $\mathbf{x}_j$ do not depend on the cell index $l$ is at the origin of the simplified form of the Bragg intensity [Equation (18–20)] involving only the content of a single unit cell. In the low temperature structure a modulation appears as a displacement field $\mathbf{u}_{lj}$, so the positions of the atoms become $\mathbf{R}_{lj} = \mathbf{R}_l + \mathbf{x}_j + \mathbf{u}_{lj}$ with all vectors referred to the unit cell obtained from the fundamental reflections (''average structure''). The scattered intensity of a crystal with this kind of structure cannot be simplified for arbitrary $\mathbf{u}_{lj}$ but, in the situation we are interested in here, a generalized harmonic model, the displacements can be written as a finite Fourier series:

$$\begin{aligned}\mathbf{u}_{lj} &= \sum_{n=1}^{2d} \mathbf{U}_{j\mathbf{q}_n} \exp\{-2\pi\mathrm{i}\,\mathbf{q}_n(\mathbf{R}_l + \mathbf{f}_j)\} \\ &= \sum_{n=1}^{d} [\mathbf{c}_{jn}\,\cos\{2\pi\,\mathbf{q}_n(\mathbf{R}_l + \mathbf{f}_j)\} + \mathbf{s}_{jn}\,\sin\{2\pi\,\mathbf{q}_n(\mathbf{R}_l + \mathbf{f}_j)\}]\end{aligned} \tag{29}$$

where the vectors $\mathbf{q}_n$ are called ''modulation vectors'' and can be referred to the reciprocal lattice of the high temperature phase. The vectors $\mathbf{f}_j$ are the phase reference points and are usually taken as $\mathbf{f}_j = \mathbf{x}_j$ in the literature of incommensurate crystal structures but they can be taken all equal to zero or to a common vector for a group of atoms.[8] In the following we take $\mathbf{f}_j = 0$ to simplify the formulas. The Fourier coefficients $\mathbf{U}_{j\mathbf{q}_n}$ are complex vectors, verifying $\mathbf{U}_{j(\ \mathbf{q}_n)} = \mathbf{U}^*_{j\mathbf{q}_n}$, which can be reduced to two real vectors as written in the second part of the expression. The cosine, $\mathbf{c}_{jn}$, and sine, $\mathbf{s}_{jn}$, vector coefficients usually have absolute values lower than a fraction of 0.1 Å. Of course the particular values of their components depend on the choice of the vectors $\mathbf{f}_j$. Notice that the second sum is reduced to half the number of terms because in the first there exist the terms for $\mathbf{q}$ and $-\mathbf{q}$.

More general anharmonic modulations can be considered by extending the sum in Equation (29) to a higher number of waves, say $D$; in such a case the $D$ $\mathbf{q}$ vectors are linear combinations of the basic (rationally independent) $d$ $\mathbf{q}$ vectors ($d < D$). In the following we considered only the harmonic model of dimension $d$.

The scattered amplitude, neglecting thermal vibrations and eventual chemical disorder for simplicity, by the whole crystal is:

$$\begin{aligned}A(\mathbf{s}) &= \sum_{lj} f_{lj}(s)\mathrm{e}^{2\pi\mathrm{i}\,\mathbf{s}\cdot\mathbf{R}_{lj}} = \sum_{lj} f_j(s)\mathrm{e}^{2\pi\mathrm{i}\,\mathbf{s}\cdot\mathbf{R}_l}\mathrm{e}^{2\pi\mathrm{i}\,\mathbf{s}\cdot\mathbf{x}_j}\mathrm{e}^{2\pi\mathrm{i}\,\mathbf{s}\cdot\mathbf{u}_{lj}} \\ &= \sum_j f_j(s)\ \mathrm{e}^{2\pi\mathrm{i}\ \mathbf{s}\cdot\mathbf{x}_j} \sum_l e^{2\pi i\ \mathbf{s}\cdot\mathbf{R}_l}\mathrm{e}^{2\pi\mathrm{i}\ \mathbf{s}\cdot\mathbf{u}_{lj}}\end{aligned} \tag{30}$$

Taking into account the well known Jacobi–Anger expressions:

$$\mathrm{e}^{\mathrm{i}z\sin\phi} = \sum_{r=\ -\infty}^{+\infty} \mathrm{e}^{\ \mathrm{i}r\phi} J_{\ r}(z), \quad \mathrm{e}^{\mathrm{i}z\cos\phi} = \sum_{r=\ -\infty}^{+\infty} \mathrm{e}^{\ \mathrm{i}r(\phi+\pi/2)} J_{\ r}(z) \tag{31}$$

where $J_r$ is the Bessel function of order $r$. An important property of the Bessel functions is:

$$J_{-r}(z) = (-1)^r J_r(z).$$

Importantly, for small values of the arguments the Bessel functions behave as:

$$J_r(z) = \frac{z^r}{2^r r!} + \ldots, \quad J_0(z) = 1 - \frac{z^2}{4} + \ldots \tag{32}$$

Developing Equation (30) one arrives at the scattered amplitude written in a more specific form:

$$\begin{aligned} A(\mathbf{s}) \approx & \sum_j f_j e^{2\pi i\, \mathbf{s}\cdot\mathbf{x}_j} \sum_{\substack{r_{c1}..r_{cd},\\ r_{s1}..r_{sd}=}}^{+\infty} \prod_{n=1}^{d} \{J_{-r_{cn}}(2\pi\mathbf{s}\cdot\mathbf{c}_{jn}) J_{r_{sn}}(2\pi\mathbf{s}\cdot\mathbf{s}_{jn}) e^{-i\pi r_{cn}/2}\} \\ & \times \sum_{\mathbf{H}} \delta(\mathbf{s} - \sum_n (r_{cn} + r_{sn})\mathbf{q}_n - \mathbf{H}) \end{aligned} \tag{33}$$

The corresponding intensity is obtained by multiplying Equation (33) by its complex conjugate. The last sum over reciprocal lattice vectors **H** of the average structure and the delta function, coming from the lattice sum over $l$, shows that the intensity in reciprocal space is nearly zero everywhere except for discrete scattering vectors, $\mathbf{s} = \mathbf{h}$, given by:

$$\mathbf{h} = \mathbf{H} + \sum_{n=1}^{d} m_n \mathbf{q}_n \tag{34}$$

The above expression gives fundamental reflections ($\mathbf{h} = \mathbf{H}$) when all $m_n = r_{cn} + r_{sn} = 0$. For all other cases the Equation (34) corresponds to "satellite" or "superstructure" reflections.

The structure factor corresponding to a particular reflection **h**, indexed as in Equation (34), is given by:

$$\begin{aligned} F(\mathbf{h}) &= \sum_j f_j(h) e^{2\pi i\, \mathbf{h}\cdot\mathbf{x}_j} \sum_{\substack{r_{c1}..r_{cd},\\ r_{s1}..r_{sd}=}}^{+\infty} \prod_{n=1}^{d} J_{-r_{cn}}(2\pi\mathbf{h}\cdot\mathbf{c}_{jn}) J_{r_{sn}}(2\pi\mathbf{h}\cdot\mathbf{s}_{jn}) e^{-i\pi r_{cn}/2} \\ &= \sum_j f_j(h) e^{2\pi i\, \mathbf{h}\cdot\mathbf{x}_j} g_j(\mathbf{h}) \end{aligned} \tag{35}$$

The structural parameters characterizing the modulated structure correspond to the average positions of the atoms, $\mathbf{x}_j$, in the average unit cell as well as the components of the cosine and sine vector terms $\mathbf{c}_{jn}$ and $\mathbf{s}_{jn}$. Clearly, the structure factor is similar to that of a conventional crystal structure but with an atomic contribution weighted by the rather cumbersome function $g_j(\mathbf{h})$ containing the information about the modulation displacements.

A further simplification is possible by taking into account the fact that only the projections along the scattering vector of the vectors $\mathbf{c}_{jn}$ and $\mathbf{s}_{jn}$ appear in the amplitude expression. Defining the quantities:

$$U_{jn} = \left[(\mathbf{s}\cdot\mathbf{s}_{jn})^2 + (\mathbf{s}\cdot\mathbf{c}_{jn})^2\right]^{1/2}, \quad \sin\chi_{jn} = \frac{\mathbf{s}\cdot\mathbf{c}_{jn}}{U_{jn}}, \quad \cos\chi_{jn} = \frac{\mathbf{s}\cdot\mathbf{s}_{jn}}{U_{jn}} \tag{36}$$

The products $\mathbf{s}\cdot\mathbf{u}_{lj}$ can be written as:

$$\begin{aligned}\mathbf{s}.\mathbf{u}_{lj} &= \sum_{n=1}^{d} U_{jn}\{\sin\chi_{jn}\,\cos(2\pi\,\mathbf{q}_n\mathbf{R}_l) + \cos\chi_{jn}\,\sin(2\pi\,\mathbf{q}_n\mathbf{R}_l)\} \\ &= \sum_{n=1}^{d} U_{jn}\sin(\chi_{jn} + 2\pi\,\mathbf{q}_n\mathbf{R}_l)\end{aligned} \tag{37}$$

so the structure factor of the reflection $\mathbf{h} = \mathbf{H} + \sum_{n=1}^{d} m_n\mathbf{q}_n$ is also given by:

$$\begin{aligned}F(\mathbf{h}) = \sum_j f_j(h)\mathrm{e}^{2\pi\mathrm{i}\,\mathbf{h}\cdot\mathbf{x}_j} g_j(\mathbf{h}) &= \sum_j f_j(h)\mathrm{e}^{2\pi\mathrm{i}\,\mathbf{h}\cdot\mathbf{x}_j} \\ &\times \sum_{m_1,m_2,\ldots m_d=-\infty}^{+\infty} \prod_{n=1}^{d}\{\mathrm{e}^{-\mathrm{i}m_n\chi_{jn}} J_{m_n}(2\pi U_{jn})\}\end{aligned} \tag{38}$$

in which the weighting function $g_j(\mathbf{h})$ adopts a more compact form.

In practice the infinite sums can be reduced to a maximum number of harmonics. From Equation (32) it is easily seen that the Bessel functions diminish rapidly with the order of the satellite. The intensity of a Bragg reflection, proportional to the square of the structure factor Equation (35) or Equation (38), is then reduced due to the presence of the Bessel functions.

Let us consider the simplest case. Suppose that we have a pure sinusoidal ($\mathbf{c}_\mathbf{q} = 0$) wave modulation with a single modulation vector $\mathbf{q}$. The expression of the structure factor for the satellite reflection $\mathbf{h} = \mathbf{H} + m\mathbf{q}$ is reduced to:

$$\begin{aligned}F(\mathbf{h}) &= \sum_j f_j(h)\mathrm{e}^{2\pi\mathrm{i}\,\mathbf{h}\cdot\mathbf{x}_j} J_m(2\pi\mathbf{h}\cdot\mathbf{s}_j) \\ &= \sum_j f_j(h)\mathrm{e}^{2\pi\mathrm{i}\,(\mathbf{H}+m\mathbf{q})\cdot\mathbf{x}_j} J_m(2\pi(\mathbf{H}+m\mathbf{q})\cdot\mathbf{s}_j)\end{aligned} \tag{39}$$

One can see that the structure factor for a fundamental reflection is not the same as that of the non-distorted structure. For the fundamental reflection $\mathbf{H}$ the structure factor is:

$$F(\mathbf{H}) = \sum_j f_j(H)\mathrm{e}^{2\pi\mathrm{i}\,\mathbf{H}\cdot\mathbf{x}_j} J_0(2\pi\mathbf{H}\cdot\mathbf{s}_j). \tag{40}$$

In the case of modulated structures having cosine and sine components the general expressions Equation (35) or Equation (38) should be used and the

calculation of a particular set of integers $\{m_n = r_{cn} + r_{sn}\}_{n\ \ 1,\ldots d}$ should be extended to all integer values $r_{cn}$ and $r_{sn}$, giving rise to the same set of $m_n$. Let us consider now a single modulation vector but a structure with cosine and sine terms in Equation (29), the structure factor Equation (35) for the satellite $\mathbf{h} = \mathbf{H} + m\mathbf{q} = \mathbf{H} + (r_c + r_s)\mathbf{q}$ reduces to:

$$F(\mathbf{h} = \mathbf{H} + m\mathbf{q}) = \sum_j f_j(h) \mathrm{e}^{2\pi \mathrm{i}\,(\mathbf{H}+m\mathbf{q})\cdot\mathbf{x}_j} \times \sum_{\substack{r_c, r_s = \\ r_c + r_s = m}}^{+\infty\ \ \infty} J_{\ r_c}\{2\pi(\mathbf{H} + m\mathbf{q}) \cdot \mathbf{c}_j\} J_{\ r_s}\{2\pi(\mathbf{H} + m\mathbf{q}) \cdot \mathbf{s}_j\} \mathrm{e}^{\ \mathrm{i}\pi r_c/2} \tag{41}$$

The symmetry treatment of incommensurate structures is beyond the scope of this chapter. From Equation (33) it is readily seen that for indexing, whatever the reflection of the diffraction pattern of an incommensurately modulated structure, we need to specify $3 + d$ integers: ($h$, $k$, $l$, $m_1$, $m_2 \ldots m_{\ d}$). It can be demonstrated that the observed 3D structure can be considered as a projection of a periodic structure in $3 + d$ dimensions over the real 3D space, which is a hyper-plane not cutting the points of the $3 + d$ lattice except the origin. The superspace approach of de Wolff, Janssen and Janner[9] is now well established and has become the routine way of treating the symmetry of the displacive incommensurate structures. The same approach has been extended to study general quasiperiodic structures (composite structures and quasicrystals).

We have not considered modulations of the displacement (thermal) parameters and occupation parameters. The explicit consideration of these terms, together with 3 + d-dimensional symmetry operators, in the structure factors gives rise to more complex expressions than those written in this section. The reader interested in a deeper knowledge of this subject is invited to check the specialized articles in the existing literature.[10,11] An excellent review of the different structure factor formalisms is provided by Van Smaalen.[12]

### 3.3.4 Neutron Magnetic Moment Scattering

The intensity of magnetic Bragg peaks from neutron scattering by magnetically ordered systems can be calculated in a similar way. The most important difference is that the scattering amplitude is not a scalar variable. Here we will give a summary of the most important expressions needed to calculate the intensity of a Bragg reflection. For more details consult Rossat-Mignod[13] and references therein.

The interaction of neutrons with the magnetic moments of atoms is of dipolar origin through the magnetic moment of the neutron. The magnetic moment of atoms is due to the existence of unpaired electrons and it contains, in general, an orbital and a spin contribution. For our purposes we assume that there are atoms, in positions $\mathbf{R}$, with magnetic moments that are usually disordered in the paramagnetic state ($\forall \mathbf{R}, \langle \mathbf{m}_{\mathbf{R}} \rangle_t = 0$, where $\langle\rangle_t$ means time

average) and become frozen ($\langle \mathbf{m}_{\mathbf{R}} \rangle_t \neq 0$), and eventually ordered, below a certain temperature. A magnetic structure corresponds to a particular, nearly static, spatial arrangement of magnetic moments that sets up below the ordering temperature. Above the ordering temperature the system is in the paramagnetic state.

The magnetic structures are commonly represented as a set of arrows associated with the magnetic moments, with magnitudes and orientations characteristic of the particular structure.

The magnetic scattering amplitude vector, for a single atom with atomic moment $\mathbf{m}$, is given by:

$$\begin{aligned} \mathbf{a}(\mathbf{Q}) &= pf(Q)\mathbf{m}_{\perp} = \frac{1}{2} r_e \gamma f(Q) \left( \mathbf{m} - \frac{\mathbf{Q}(\mathbf{m} \cdot \mathbf{Q})}{Q^2} \right) \\ &= \frac{1}{2Q^2} r_e \gamma f(Q)(\mathbf{Q} \times \mathbf{m} \times \mathbf{Q}) \end{aligned} \tag{42}$$

where $r_e = e^2/mc^2 = 2.81776 \times 10^{-13}$ cm is the classical radius of the electron, $\gamma$ ($= 1.9132$) is the gyromagnetic factor, $f(Q)$ is the atomic magnetic form-factor [Fourier transform of the unpaired electron density, normalized as $f(0) = 1$, assumed to be spherical], and $\mathbf{m}_{\perp}$ is the component of the atomic moment perpendicular to the scattering vector $\mathbf{Q} = 2\pi\mathbf{s}$. Only the perpendicular component of $\mathbf{m}$ contributes to the magnetic scattering of neutrons by matter. The vectorial character of the interaction allows the determination of the magnetic moment direction with respect to the crystal lattice.

For unpolarized neutrons the nuclear and magnetic intensities are simply additive and are, in general, of the same order of magnitude. An important difference between nuclear and magnetic scattering is that the latter is strongly reduced at high $Q$. The absence of a "form factor" in the case of nuclear scattering gives rise to a decrease with $Q$ due only to thermal vibrations, whereas the magnetic form factor $f(Q)$ in Equation (42) is the Fourier transform of the unpaired electron density having a spatial extension of the order of magnitude of the neutron wavelength.

The elastically scattered intensity from a crystal, as a function of $\mathbf{Q}$ or $\mathbf{s}$, is proportional to the square of the total amplitude (also called "magnetic interaction vector"):

$$\begin{aligned} \mathbf{M}_{\perp}^{T}(\mathbf{s}) &= \sum_{lj} p f_j(s) \mathbf{m}_{\perp lj} \mathrm{e}^{2\pi \mathrm{i} \mathbf{s} \cdot \mathbf{R}_{lj}} \\ &= \frac{p}{s^2} \mathbf{s} \times \sum_{lj} f_j(s) \mathbf{m}_{lj} \mathrm{e}^{2\pi \mathrm{i} \mathbf{s} \cdot \mathbf{R}_{lj}} \times \mathbf{s} = \frac{1}{s^2} \mathbf{s} \times \mathbf{M}^{T}(\mathbf{s}) \times \mathbf{s} \end{aligned} \tag{43}$$

The vector $\mathbf{M}^T$ is the magnetic structure of the whole crystal. The scattered intensity is calculated by multiplying Equation (43) by its complex conjugate as usual.

Contrary to most crystal structures, many magnetic structures are incommensurate: the periodicity of the orientation of the magnetic moments is not commensurate with the underlying crystal structure. This is a consequence of

the existence of competing exchange interactions giving rise to a kind of frustration in many compounds. We shall develop the Equation (43) using the formalism of propagation vectors, similar to that of the previous paragraph on incommensurate crystal structures. This approach has the advantage of treating commensurate and incommensurate magnetic structures in the same way. Using this formalism we do not need to use the concept of the magnetic unit cell even in the case of commensurate structures.

*3.3.4.1 Formalism of Propagation Vectors for Describing Magnetic Structures. Examples of Common Magnetic Structures.* If we disregard for the moment the symmetry properties of the magnetic moment configuration, whatever class of magnetic structure can be represented by the Fourier series:

$$\mathbf{m}_{lj} = \sum_{\{\mathbf{k}\}} \mathbf{S}_{\mathbf{k}j} \exp(-2\pi \mathrm{i}\, \mathbf{k}\, \mathbf{R}_l) \tag{44}$$

This defines the magnetic moment of the atom numbered $j$ in the unit cell having as origin the lattice vector $\mathbf{R}_l$ (the atom at $\mathbf{R}_{lj} = \mathbf{R}_l + \mathbf{x}_j$). The $\mathbf{k}$ vectors are defined in reciprocal space and are called propagation vectors of the magnetic structure. For the description of magnetic structures they can be restricted to the first Brillouin zone (BZ). The Fourier coefficients $\mathbf{S}_{\mathbf{k}j}$ are, in general, complex vectors and must verify the equality $\mathrm{S}_{\mathbf{k}j} = \mathrm{S}^*_{\mathbf{k}j}$ to make the sum result in a real vector. Even disordered magnetic structures, like that of a *spin glass*, may eventually be described with an expression like Equation (44) if a nearly continuous distribution of $\mathbf{k}$ vectors inside the BZ is considered. In practice, most of the magnetic structures can be described by a small number (1 to 3) of propagation vectors.

We may have defined Equation (44) in a slightly different manner as is usual in the literature. Instead of writing $\mathbf{R}_l$ in the argument of the exponential function, one can write $\mathbf{R}_{lj} = \mathbf{R}_l + \mathbf{x}_j$ [similarly to $\mathbf{f}_j = \mathbf{x}_j$ vectors in Equation (29) for atom displacements]. In such a case the Fourier coefficients, $\mathbf{T}_{\mathbf{k}j}$, of the new expression are related to those of Equation (44) by a phase factor, $\mathbf{S}_{\mathbf{k}j} = \mathbf{T}_{\mathbf{k}j} \exp(-2\pi \mathrm{i}\, \mathbf{k}\mathbf{x}_j)$, that depends on the atom positions inside the unit cell. We shall see that the convention we have adopted is more convenient for a unified description of commensurate and incommensurate magnetic structures.

The formulas above are written in vector form, so they are independent of the particular frame for describing the magnetic moments, propagation vectors, atom positions and so on. Atom positions inside the unit cell are normally referred to on the conventional basis $A = (\mathbf{a}, \mathbf{b}, \mathbf{c})$, so that fractional coordinates are dimensionless. The Fourier coefficients, $\mathbf{S}_{\mathbf{k}j}$, have the same units as magnetic moments, usually Bohr magnetons, and their components are given with respect to the unitary frame of the conventional unit cell $U = (\mathbf{a}/\mathrm{a},\ \mathbf{b}/\mathrm{b},\ \mathbf{c}/\mathrm{c}) = (\mathbf{e}_1,\ \mathbf{e}_2,\ \mathbf{e}_3)$. The components of reciprocal lattice vectors of the nuclear structure, $\mathbf{H}$, and those of the propagation vectors, $\mathbf{k}$, are given with respect to the reciprocal basis of the conventional unit cell and are also dimensionless. This is a very important point because in many of the available tables of

irreducible representations of space groups the **k** vectors are given with respect to a *primitive basis* of the reciprocal lattice $b = (\mathbf{b}_1, \mathbf{b}_2, \mathbf{b}_3)$ which coincides with $a^* = (\mathbf{a}_1^*, \mathbf{a}_2^*, \mathbf{a}_3^*)$ only for primitive direct lattices. When the Bravais lattice of the crystal is centered, the set $b$ is obtained from a primitive basis of the direct cell and not from the Bravais (or conventional) unit cell. Izyumov and collaborators[14] have introduced a set of vectors $B = (\mathbf{B}_1, \mathbf{B}_2, \mathbf{B}_3)$ as a reference frame for the reciprocal lattice. The set $B$ correspond to the "Bravais cell" of the reciprocal lattice. This is a frame that is not used by crystallographers and giving the components of the reciprocal vectors with respect to it is confusing. We do not recommend the use of this frame for studies of magnetic structures.

The lattice vectors $\mathbf{R}_l$ appearing in the argument of the exponential function are integer linear combinations of the basis vectors of frame $A$ only for primitive lattices. For centered lattices two formal types of lattice vectors exist: $\mathbf{R}_l = \mathbf{R}_n = n_1\mathbf{a} + n_2\mathbf{b} + n_3\mathbf{c}$ with $n_i \in Z$ and $\mathbf{R}_l = \mathbf{R}_n + \mathbf{t}_c$, where $\mathbf{t}_c$ is one of the centering vectors of the lattice with components $t_i \in Q$. There is nothing special about these two types of lattice vectors, the different type of components is just a matter of convention. The minimum set of magnetic atoms to be considered for describing a magnetic structure, without considering at this stage the symmetry, should not be related to lattice centering translations. Equation (44) assures the knowledge of the magnetic moments in the whole crystal when we know the Fourier coefficients of the elemental set of atoms in the reference zero-cell $\mathbf{R}_0 = (0, 0, 0)$.

Let us describe general types of magnetic structures of increasing degrees of complexity, using the formalism of propagation vectors through Equation (44).

a. The simplest types of magnetic structures existing in complex crystals have a single null propagation vector at the centre of the BZ: $\mathbf{k} = (0,0,0) = \mathbf{0}$. The Fourier coefficients should be real and can be identified by the magnetic moments directly:

$$\mathbf{m}_{lj} = \mathbf{S}_{\mathbf{0}j}\exp(-2\pi i\, \mathbf{0}\, \mathbf{R}_l) = \mathbf{S}_{\mathbf{0}j} = \mathbf{m}_{\mathbf{0}j}. \tag{45}$$

This expression tells us that the orientation and magnitudes of the magnetic moments in all cells of the crystal are identical to those of the zero-cell. The translational symmetry of the magnetic structure is identical to that of the crystal structure: the magnetic unit cell is the same as the chemical cell. This class of magnetic structures may be ferromagnetic, ferrimagnetic or antiferromagnetic, collinear or non-collinear. The propagation vector at the centre of the BZ does not mean that the magnetic structure is ferromagnetic. This is only true for Bravais lattices (a single atom per primitive cell).

Notice that if we had taken the convention for the Fourier series Equation (44) that puts the global vector position of the atom, $\mathbf{R}_{lj} = \mathbf{R}_l + \mathbf{x}_j$, in the exponential term the Fourier coefficients $\mathbf{T}_{\boldsymbol{k}j}$ could not be identified with magnetic moments because of the phase factor containing the atom positions.

An example of this kind of structure is that of $LaMnO_3$ (Figure 3.2).

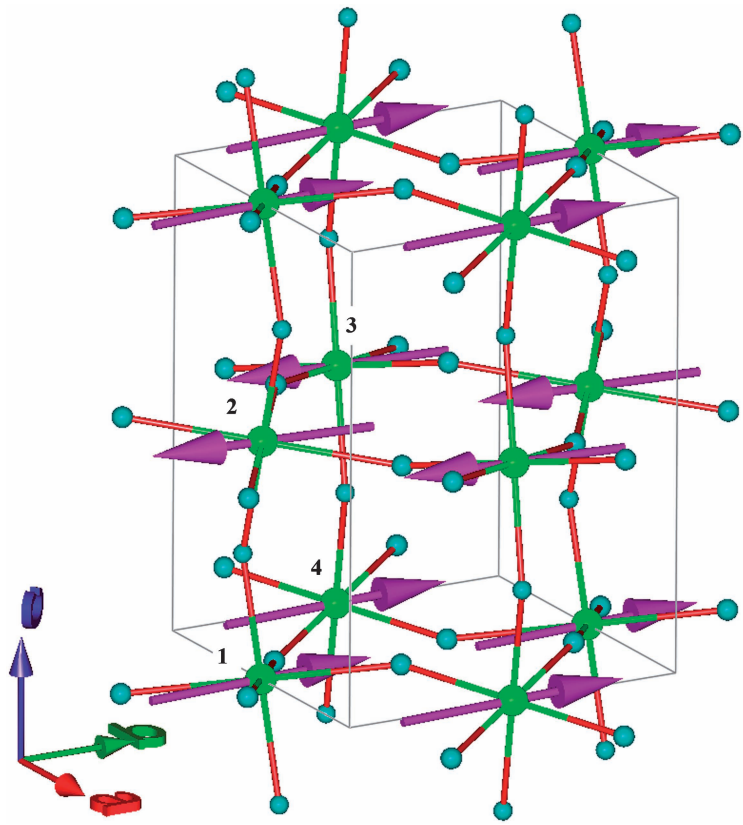



**Figure 3.2** Magnetic structure of $LaMnO_3$, space group P*bnm*. Mn atoms in position 4b: 1(1/2,0,0), 2(1/2,0,1/2), 3(0,1/2,1/2) and 4(0,1/2,0). Propagation vector $\mathbf{k} = (0, 0, 0)$. The magnetic unit cell is identical to the nuclear cell. The magnetic moments of the four atoms are: 1($u$, $v$, $w$), 2($\bar{u}$, $\bar{v}$, $w$), 3($u$, $\bar{v}$, $w$), 4($\bar{u}$, $v$, $w$), with $u \approx 0$, $v = 3.8\,\mu_B$ and $w \approx 0$. The structure is antiferromagnetic with a weak ferromagnetic component along c and formed by ferromagnetic planes stacked antiferromagnetically along c. This is the so called A type AF structure in the perovskite literature.[15]

b. The next class of magnetic structures corresponds also to a single propagation vector, in this case of the form: $\mathbf{k} = 1/2\mathbf{H}$, where $\mathbf{H}$ is a reciprocal lattice vector. The propagation vectors of this kind correspond to high symmetry points of the surface of the BZ (Liftchitz points). In this case we have:

$$\begin{aligned} \mathbf{m}_{lj} &= \mathbf{S}_{\mathbf{k}j} exp(-2\pi i\, \mathbf{k} \cdot \mathbf{R}_l) = \mathbf{S}_{\mathbf{k}j} \exp(-\pi \mathrm{i} \mathbf{H} \cdot \mathbf{R}_l) \\ &= \mathbf{S}_{\mathbf{k}j}(-1)^{\mathbf{H}\cdot\mathbf{R}_l} = \mathbf{S}_{\mathbf{k}j}(-1)^{n_l} = \mathbf{m}_{0j}(-1)^{n_l} \end{aligned} \tag{46}$$

This expression tells us that the orientation and magnitudes of the magnetic moments in all cells of the crystal are either identical or opposite to those of the zero-cell. The translational symmetry is lower than that of the chemical cell. The magnetic cell can easily be deduced from the

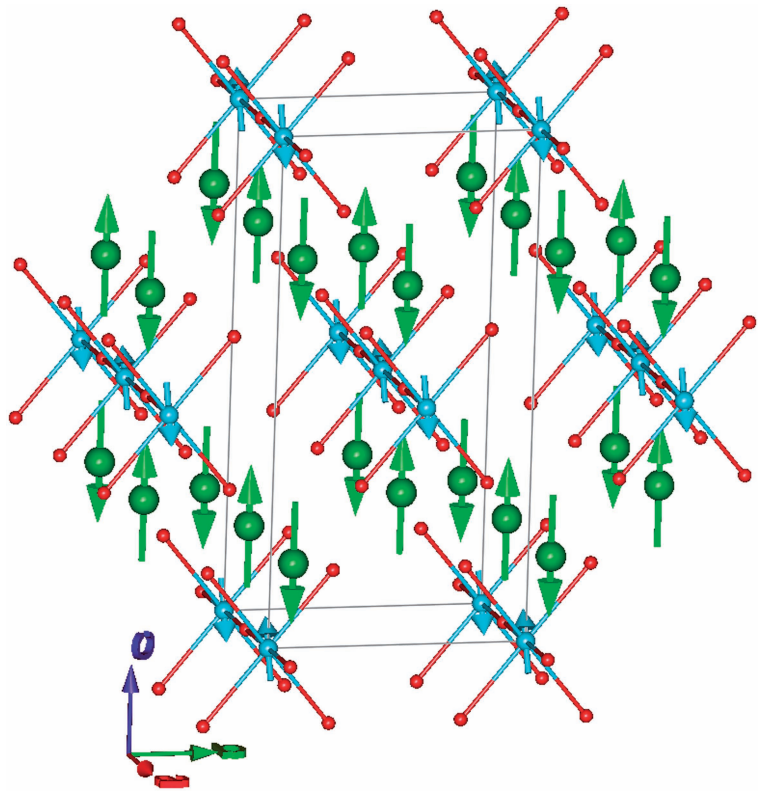



**Figure 3.3** Magnetic structure of $Ho_2BaNiO_5$, space group I*mmm*. There are only three magnetic atoms per primitive unit cell. Ni at (0, 0, 0) and Ho at positions 1(1/2, 0, *z*), 2( 1/2, 0, *z*) with $z = 0.2025$. The propagation vector is $\mathbf{k} = (1/2,0,1/2)$. The magnetic moments are not in scale, the amplitude of those of Ho atoms have been arbitrarily multiplied by 0.3 for representation purposes. The magnetic unit cell doubled along **a** and **c**. The magnetic moments of the three atoms are: Ni(*u*, 0, *w*), with $u \approx 0.59\,\mu_B$, $w \approx 1.3\,\mu_B$ , Ho1(*p*, 0, *q*), Ho2(*p*, 0, *q*), with $p \approx 0.1\,\mu_B$ and $q \approx 9\,\mu_B$ (ref. 17).

particular values of the propagation vector (see Izyumov, et al.[16] for a classification of magnetic lattices in terms of propagation vectors). The magnetic structures of this kind are necessarily antiferromagnetic. An example of this kind of structure is that of $Ho_2BaNiO_5$ (Figure 3.3).

The general expression for the Fourier coefficient for the atom *j* is explicitly given by:

$$\begin{aligned}\mathbf{S}_{\mathbf{k}j} &= \frac{1}{2}\left\{\vec{R}_{\mathbf{k}j} + \mathrm{i}\,\vec{I}_{\mathbf{k}j}\right\}\exp(-2\pi\mathrm{i}\phi_{\mathbf{k}j}) \\ &= \frac{1}{2}\left\{R^x_{\mathbf{k}j}\mathbf{e}_1 + R^y_{\mathbf{k}j}\mathbf{e}_2 + R^z_{\mathbf{k}j}\mathbf{e}_3 + \mathrm{i}(I^x_{\mathbf{k}j}\mathbf{e}_1 + I^y_{\mathbf{k}j}\mathbf{e}_2 + I^z_{\mathbf{k}j}\mathbf{e}_3)\right\}\exp(-2\pi\mathrm{i}\phi_{\mathbf{k}j})\end{aligned}$$

Only six real parameters define the $\mathbf{S}_{\mathbf{k}j}$ vectors, so the phase factor $\phi_{\mathbf{k}j}$ is not generally needed, but it is convenient to use it when particular relations or constraints between real and imaginary vectors ($\vec{R}_{\mathbf{k}j}$, $\vec{I}_{\mathbf{k}j}$) are given. The magnetic moment of the atom $j$ in the unit cell of index $l$, should be calculated by using Equation (44), which may be also written in this case as:

$$\mathbf{m}_{lj} = \sum_{\langle \mathbf{k} \rangle} \left\{ \vec{R}_{\mathbf{k}j} \cos 2\pi \left[ \mathbf{k}\,\mathbf{R}_l + \phi_{\mathbf{k}j} \right] + \vec{I}_{\mathbf{k}j} \sin 2\pi \left[ \mathbf{k}\,\mathbf{R}_l + \phi_{\mathbf{k}j} \right] \right\} \tag{47}$$

where the sum is now extended to half the number of propagation vectors, *i.e.* over the total number of pairs $(\mathbf{k},-\mathbf{k})$.

If the magnetic structure represents a helical order the Fourier coefficients are of the form:

$$\mathbf{S}_{\mathbf{k}j} = \frac{1}{2} \left\{ m_{1j}\mathbf{u}_j + \mathrm{i}\, m_{2j}\mathbf{v}_j \right\} \exp(-2\pi \mathrm{i} \phi_{\mathbf{k}j}), \quad \text{with} \quad \begin{array}{l} |\mathbf{u}_j| = |\mathbf{v}_j| = 1, \\ \mathbf{u}_j \cdot \mathbf{v}_j = 0 \end{array} \tag{48}$$

where $\mathbf{u}_j$ and $\mathbf{v}_j$ are orthogonal unit vectors. If $m_{1j} = m_{2j}$ the magnetic structure for the sublattice $j$ corresponds to a classical helix (or spiral) of cylindrical envelope, if the propagation vector is perpendicular to the plane formed by the vectors $\mathbf{u}_j$ and $\mathbf{v}_j$. If the propagation vector is within the $(\mathbf{u}, \mathbf{v})$ plane, the structure is called a cycloid. All $j$ atoms have equal magnetic moments. If $m_{1j} \neq m_{2j}$ the helix (or cycloid) has an elliptical envelope and the moments have values between $\min(m_{1j}, m_{2j})$ and $\max(m_{1j}, m_{2j})$.

If $m_{2j} = 0$ the magnetic structure corresponds to a modulated sinusoid of amplitude $\mathrm{A} = m_{1j}$.

Simple artificial examples of sinusoidal, helical and cycloid magnetic structures are given in Figure 3.4. In Figure 3.5 there is a real example of the incommensurate conical structure of $DyMn_6Ge_6$: propagation vector $\mathbf{k}_1 = (0,0,0)$ and $\mathbf{k}_2 = (0,0,\delta)$ at the interior of Brillouin Zone.

*3.3.4.2 Magnetic Structure Factor.* From Equation (43) we can develop in a compact form the magnetic structure factor of the crystal defined as:

$$\begin{aligned} \mathbf{M}^T(\mathbf{s}) &= p \sum_{lj} f_j(s) \mathbf{m}_{lj} \mathrm{e}^{2\pi \mathrm{i} \mathbf{s}\cdot\mathbf{R}_{lj}} = p \sum_{lj} f_j(s) \mathrm{e}^{2\pi \mathrm{i} \mathbf{s}\cdot\mathbf{R}_{lj}} \sum_{\mathrm{k}} \mathbf{S}_{\mathbf{k}j} \mathrm{e}^{\ 2\pi \mathrm{i} \mathbf{k}\cdot\mathrm{R}_l} \\ &= p \sum_{j} f_j(s) \mathrm{e}^{2\pi \mathrm{i} \mathbf{s}\cdot\mathbf{x}_j} \sum_{\mathrm{k}} \mathbf{S}_{\mathrm{k}j} \sum_{l} \mathrm{e}^{2\pi \mathrm{i}(\mathbf{s}\ \ \mathbf{k})\cdot\mathbf{R}_l} \approx p \sum_{j} f_j(s) \mathrm{e}^{2\pi \mathrm{i} \mathbf{s}\cdot\mathbf{x}_j} \\ &\quad \times \sum_{\mathrm{k}} \mathbf{S}_{\mathbf{k}j} \sum_{\mathrm{H}} \delta(\mathbf{s} - \mathbf{k} - \mathbf{H}) \end{aligned} \tag{49}$$

This indicates that the magnetic intensity in reciprocal space occurs at positions given by:

$$\mathbf{s} = \mathbf{h} = \mathbf{H} + \mathbf{k} \tag{50}$$

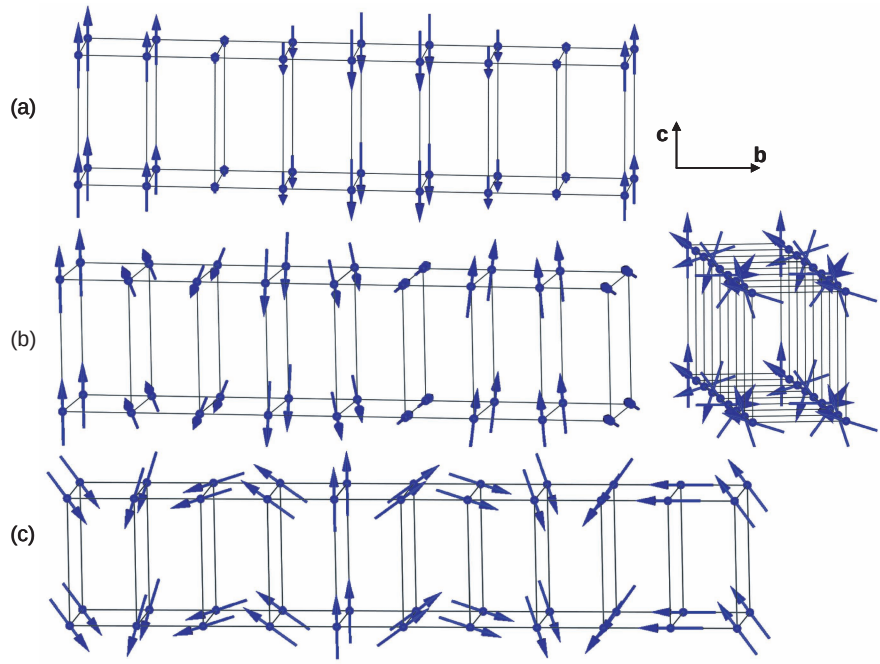



**Figure 3.4** Examples of magnetic structures. In all cases the orientation of the lattice is similar, except in the second view of (b), where the point of view is nearly along **a**. (a) Sinusoidal structure with propagation vector $\mathbf{k} = (0,\delta,0)$ and $\mathbf{S}_\mathbf{k} = (0,0,w)$. (b) Helical, or spiral, structure with propagation vector $\mathbf{k} = (0,\delta,0)$ and $\mathbf{S}_\mathbf{k} = (ui,0,u)$. (c) Cycloidal structure with propagation vector $\mathbf{k} = (0,\delta,0)$ and $\mathbf{S}_\mathbf{k} = (0,u,ui)$.

Notice that, contrary to the modulated crystal structures, there is no multiple of the propagation vector **k** and no sum within the delta function appearing in Equation (49) because the absence of the Fourier series included in the exponential argument. Magnetic diffraction appears like a filter. Each satellite is decoupled from the rest of the satellites, so if there are different propagation vectors **k** there is no interference between them; there is always a phase factor between the Fourier coefficients $\mathbf{S}_\mathbf{k}$ corresponding to different propagation vectors that is not accessible by diffraction methods. Notice also that the concept of "fundamental reflections" does not apply here because $\mathbf{h} = \mathbf{H}$ corresponds to nuclear reflections. Only when $\mathbf{k} = 0$ is there a magnetic contribution on top of the nuclear reflections.

For a particular magnetic reflection indexed as in Equation (50) the magnetic structure factor of the unit cell is:

$$\mathbf{M}(\mathbf{h}) = \mathbf{M}_\mathbf{h} = p\sum_j f_j(h)\mathbf{S}_{\mathbf{k}j}e^{2\pi i\mathbf{h}\cdot\mathbf{x}_j} = p\sum_j f_j(|\mathbf{H}+\mathbf{k}|)\mathbf{S}_{\mathbf{k}j}e^{2\pi i(\mathbf{H}+\mathbf{k})\cdot\mathbf{x}_j} \qquad (51)$$

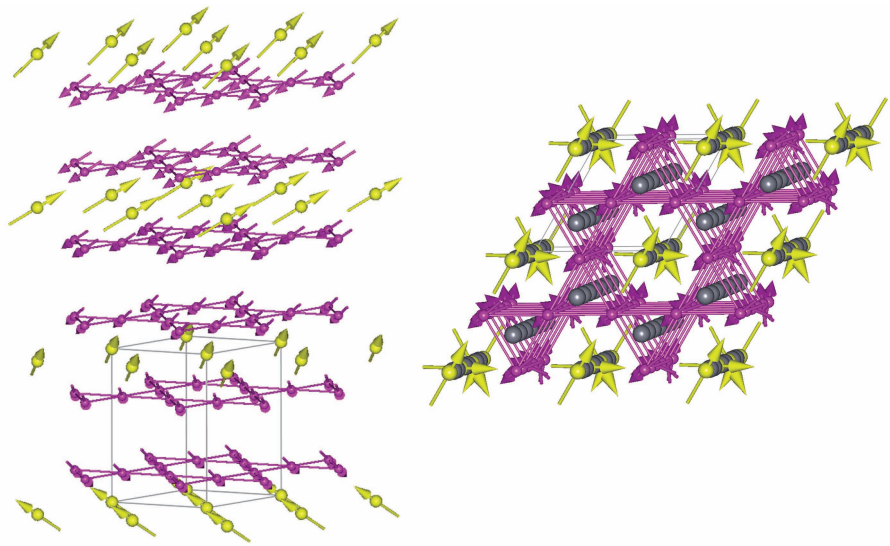


**Figure 3.5** Magnetic structure of $DyMn_6Ge_6$, space group P6/*mmm*, $a \approx 5.21$ Å, $c \approx 8.15$ Å, propagation vectors $\mathbf{k}_1 = (0,0,0)$ and $\mathbf{k}_2 = (0,0,\delta)$ with $\delta = 0.1651$. This is a conical structure with a net magnetization along **c**. Details can be found in ref. 18.

The constant $p = r_e\gamma/2 = 0.2695$ allows the conversion of the Fourier components of magnetic moments given in Bohr magnetons into scattering length units of $10^{-12}$ cm.

The intensity of a magnetic Bragg reflection is proportional to the square of the magnetic interaction vector:

$$\mathbf{M}_{\perp\mathbf{h}} = \frac{1}{h^2}\mathbf{h} \times \mathbf{M}_\mathbf{h} \times \mathbf{h} = \mathbf{e} \times \mathbf{M}_\mathbf{h} \times \mathbf{e} = \mathbf{M}_\mathbf{h} - (\mathbf{e} \cdot \mathbf{M}_\mathbf{h})\mathbf{e} \tag{52}$$

where **e** is the unit vector along the scattering vector $\mathbf{h} = \mathbf{H} + \mathbf{k}$. For a propagation vector $\mathbf{k} = 0$ the intensity of a Bragg reflection for non polarized neutrons is given by:

$$I_\mathbf{h} = N_\mathbf{h} N_\mathbf{h}^* + \mathbf{M}_{\perp\mathbf{h}} \cdot \mathbf{M}_{\perp\mathbf{h}}^*, \tag{53}$$

where $N_\mathbf{h} = F(\mathbf{h})$ is the nuclear structure factor, otherwise only the second term (pure magnetic scattering) of the sum contributes to the intensity of reflection **h**.

*3.3.4.3 Magnetic Structure Factor when Symmetry is Considered.* The symmetry properties of the magnetic structures are currently described using two different approaches: the magnetic Shubnikov groups[19,20] and the group representation analysis.[14,16,21] In the general framework for describing magnetic structures that we have presented above both approaches can be used. We stress that the concept of propagation vector(s) of a magnetic structure for describing their translational symmetry and group representation analysis are

more general. The Shubnikov groups can only be strictly used in the special case of commensurate magnetic structures.

Let us consider that the magnetic atom site $j$ has equivalent atoms labeled as $js$ ($j1$, $j2, \ldots j\mathrm{p}$) under the application of symmetry operators of the crystal space group G belonging to the wave vector group $\mathrm{G_k}$. The group $\mathrm{G_k}$ is formed by the set of symmetry operators that leave invariant the propagation vector: $\mathrm{G_k} = \{g \in \mathrm{G} \mid g\mathbf{k} = \mathbf{k}' \in \mathrm{L}^*\}$, where L* is the crystallographic reciprocal lattice.

The important result of the representation analysis of magnetic structures is that the Fourier coefficients $\mathbf{S_k}$ corresponding to a complete orbit of the site $j$ are linear combinations of the so-called atomic basis functions of the relevant active representation.[21] The expression of the Fourier coefficients is given by:

$$\mathbf{S}_{\mathbf{k}js} = \sum_{n\lambda} C^{\nu}_{n\lambda} \mathbf{S}^{\mathbf{k}\nu}_{n\lambda}(js) \tag{54}$$

where $v$ labels the active irreducible representation, $\Gamma_v$, of the of the propagation vector group, $\lambda$ labels the component corresponding to the dimension of the representation $\Gamma_v$, $n$ is an index running between one and the number of times the representation $\Gamma_v$ is contained in the global magnetic representation $\Gamma_M$. Finally the quantities $\mathbf{S}^{\mathbf{k}\,\nu}_{n\lambda}$ $(js)$ are constant vectors, in general complex, obtained by the application of the projection operator formula to axial unit vectors along the directions of the unit cell axes attached to the site $j$. These vectors are similar to the normal modes in lattice dynamics except that they are axial vectors. An additional sum over $v$ is sometimes necessary when more than one irreducible representation is involved in the magnetic phase transition. See ref. 16 for examples and details. In the case where the representation analysis is fully used the coefficients $\mathrm{C}^{\nu}_{n\lambda}$ are the free parameters of the magnetic structure (they correspond to the *order parameters* in the Landau theory of phase transitions) and usually their total number is much lower than the number of Fourier components of each magnetic atom in the unit cell.

Alternatively, an approach closer to traditional crystallography can be considered in some cases. The Fourier component $\mathbf{k}$ of the magnetic moment of atom $j1$, which transforms to the atom $js$ when the symmetry operator $g_s$ of $\mathrm{G_k}$ is applied ($\mathbf{x}_{js} = g_s\mathbf{x}_{j1} = \mathrm{S}_s\ \mathbf{x}_{j1} + \mathbf{t}_s$), is transformed as:

$$\mathbf{S}_{\mathbf{k}js} = M_{js}\mathbf{S}_{\mathbf{k}j1}\exp\{-2\pi\mathrm{i}\phi_{\mathbf{k}js}\} \tag{55}$$

The matrices $M_{js}$ and phases $\phi_{\mathbf{k}js}$ can be deduced from the relations between the Fourier coefficients and atomic basis functions [Equation (54)]. The matrices $M_{js}$ correspond, in the case of commensurate magnetic structures, to the rotational parts of the magnetic Shubnikov group acting on magnetic moments.

If isotropic thermal motion is considered and if symmetry relations are established for coupling the different Fourier components, we obtain the

general expression of the magnetic structure factor:

$$\mathbf{M}(\mathbf{h}) = p\sum_{j=1}^{n_a} O_j f_j(\mathbf{h}) \mathrm{e}^{\ B_j|h/2|^2} \sum_{s=1,\ldots p} M_{js}\mathbf{S}_{\mathbf{k}j1}\exp\{2\pi\mathrm{i}[(\mathbf{H}+\mathbf{k})\{S|\mathbf{t}\}_s\mathbf{x}_{j1} - \psi_{\mathbf{k}js}]\} \tag{56}$$

The sum over $j$ concerns the atoms of the magnetic asymmetric unit for the wave vector $\mathbf{k}$. So that $j$ labels different sites. The sum over $s$ concerns the symmetry operators of the wave vector group $\mathrm{G}_{\mathbf{k}}$. The phase factor $\psi_{\mathbf{k}js}$ has two components:

$$\psi_{\mathbf{k}js} = \Phi_{\mathbf{k}j} + \phi_{\mathbf{k}js} \tag{57}$$

$\Phi_{\mathbf{k}j}$ is a phase factor that is not determined by symmetry. It is a free parameter and it is significant only for an independent set of magnetic atoms (one orbit) with respect to another one. The component $\phi_{\mathbf{k}js}$ is a phase factor determined by symmetry as shown in Equation (55). The sign of $\phi_{\mathbf{k}js}$ changes for $-\mathbf{k}$. In the general case $\mathbf{S}_{\mathbf{k}j}$ is a complex vector with six components. These six components per magnetic orbit constitute the parameters that have to be refined from the diffraction data. Symmetry reduces the number of free parameters per orbit to be refined. Notice that we have adopted a different phase convention than that used in ref. 22.

For a commensurate magnetic structure one can calculate the magnetic structure factor in the magnetic unit cell. In such a case $\mathbf{S}_{\mathbf{k}j}$ are real vectors corresponding to the magnetic moment of the atom $j$, the matrices $M_{js}$ are real and all phases verify $\phi_{\mathbf{k}js} = 0$. The crystallographic magnetic group theory can be fully applied in such a case.[19,20]

In the case when the general decomposition in terms of atomic basis functions [Equation (54)] is used, the magnetic structure factor is written as:

$$\mathbf{M}(\mathbf{h}) = p\sum_{j=1}^{n} O_j f_j(\mathbf{h}) \mathrm{e}^{\ B_j|h/2|^2} \sum_{n\lambda} C^{\nu}_{n\lambda} \sum_{s} \mathbf{S}^{\mathbf{k}\nu}_{n\lambda}(js)\exp\{2\pi\mathrm{i}\,(\mathbf{h}_s\cdot\mathbf{x}_j + \mathbf{h}\cdot\mathbf{t}_s)\} \tag{58}$$

where we have written $\mathbf{h}_s = S_s^T\mathbf{h}$ (superscript $T$ stands here for transpose).

*3.3.4.4 Limitations of Neutron Scattering for Determining Magnetic Structures.* If the magnetic structure has several propagation vectors $\mathbf{k}$, it is not possible to determine unambiguously the spin configuration, because the phase between the different Fourier components cannot be determined by diffraction methods. One can see easily what the origin of this problem is; let us rewrite Equation (44) as:

$$\mathbf{m}_{lj} = \sum_{\{\mathbf{k}\}} \mathbf{S}_{\mathbf{k}j}\exp\{-2\pi\mathrm{i}(\,\mathbf{k}\cdot\mathbf{R}_l + \Phi_{\mathbf{k}})\} = \sum_{\{\mathbf{k}\}} \mathbf{S}^m_{\mathbf{k}j}\exp\{-2\pi\mathrm{i}\,\mathbf{k}\cdot\mathbf{R}_l\} \tag{59}$$

in which we have added an arbitrary phase factor $\Phi_{\mathbf{k}}$ depending only on $\mathbf{k}$. We can understand easily that the modified Fourier coefficients, $\mathbf{S}^m_{\mathbf{k}j}$, give rise, in

general, to another kind of magnetic structure. However, the diffraction pattern obtained with a Fourier series like Equation (59) is identical to that obtained with Equation (44). This is readily demonstrated because the new magnetic structure factor [Equation (51)] and the intensity corresponding to the reflection $\mathbf{h} = \mathbf{H} + \mathbf{k}$ are given by:

$$\begin{aligned}\mathbf{M}^m(\mathbf{h}) &= p\sum_j f_j(h)\mathbf{S}^m_{\mathbf{k}j}\mathrm{e}^{2\pi\mathrm{i}(\mathbf{H}+\mathbf{k})\cdot\mathbf{x}_j} = p\mathrm{e}^{\ 2\pi\mathrm{i}\Phi_\mathbf{k}}\sum_j f_j(h)\mathbf{S}_{\mathbf{k}j}\mathrm{e}^{2\pi\mathrm{i}(\mathbf{H}+\mathbf{k})\cdot\mathbf{x}_j} \\ &= \mathrm{e}^{\ 2\pi\mathrm{i}\Phi_\mathbf{k}}\mathbf{M}(\mathbf{h})\,\mathbf{I}_{\mathrm{mag}}(\mathbf{h}) = \mathbf{M}^m_\perp(\mathbf{h})\cdot\mathbf{M}^{*m}_\perp(\mathbf{h}) \\ &= \mathrm{e}^{\ 2\pi\mathrm{i}\Phi_\mathbf{k}}\mathrm{e}^{+2\pi\mathrm{i}\Phi_\mathbf{k}}\mathbf{M}_\perp(\mathbf{h})\cdot\mathbf{M}^*_\perp(\mathbf{h}) = \mathbf{M}_\perp(\mathbf{h})\cdot\mathbf{M}^*_\perp\end{aligned} \tag{60}$$

The arbitrary phase factor disappears on calculating the intensity. So, if several propagation vectors exist in a diffraction pattern, infinitely many structures are able to explain the observed pattern and diffraction alone is unable to provide a unique solution. Symmetry constraints and, more importantly, restrictions on the amplitude of the magnetic moments can reduce the number of solutions. A study of the different kinds of propagation vectors that can be combined to provide constant moment structures, among the study of the physical properties, was performed a long time ago by Nagamiya[23] Fortunately, nature often selects simple solutions and many magnetic structures have a single propagation vector, or display some symmetry constraints that reduce the complexity of the periodic magnetic structure given by Equation (44).

Special consideration requires that the sinusoidal structures in which the single pair $(\mathbf{k},-\mathbf{k})$ of propagation vectors at the interior of the Brillouin Zone has commensurate components. Here the change of the global phase $\Phi_\mathbf{k}$ modifies the physical properties of the magnetic arrangement. If $\mathbf{k}$ is incommensurate the change of phase means only a change of global origin in the crystal and all the amplitudes of the magnetic moments between extreme values are realized somewhere in the crystal. If $\mathbf{k}$ is commensurate some particular values of the phases give a picture of the magnetic ordering that is really different to a conventional sinusoid. Let us consider the simplest case of a single atom per primitive unit cell and a propagation vector $\mathbf{k} = 1/4\mathbf{H}$. To be specific, consider the case described in Figure 3.4(a). The magnetic moment, Equation (59), in the lattice position $\mathbf{R}_l = (l_1, l_2, l_3)$ is given by:

$$\begin{aligned}\mathbf{m}_l &= \sum_{\mathbf{k},\ \mathbf{k}} \mathbf{S}_\mathbf{k}\exp\{-2\pi\mathrm{i}(\,\mathbf{k}\,\mathbf{R}_l + \Phi_\mathbf{k})\} = (0,0,w)\cos 2\pi(\,1/4\mathbf{H}\,\mathbf{R}_l + \Phi_\mathbf{k}) \\ &= (0,0,w)\cos 2\pi\left(\frac{l_2}{4} + \Phi_\mathbf{k}\right)\end{aligned} \tag{61}$$

with $l_2$ integer. It is easy to see that when $\Phi_\mathbf{k} = 0$ the sequence of magnetic moment components along $\mathbf{c}$ for the lattice points $l_2 = (0, 1, 2, 3, 4, 5\ldots)$ are: $(w, 0, -w, 0, w, 0\ldots)$. If $\Phi_\mathbf{k} = 1/8$ the sequence is: $(w', w', -w', -w', w', w', -w', -w'\ldots)$, with $w' = w/\sqrt{2}$. Both sequences give exactly the same diffraction pattern up to the constant factor $1/\sqrt{2}$, so they are indistinguishable. In the first case there are paramagnetic atoms and in the second we have a constant moment magnetic structure. Other experimental techniques (Mössbauer

spectroscopy, μ-SR, NMR *etc.*) can help in getting the best choice among a set of indistinguishable solutions.

For powder diffraction, all the expressions in the following paragraphs can be applied to magnetic powder diffraction by replacing the expression of the square of the structure factor by the square of the magnetic interaction vector.

The problem of the degeneracy of solutions (different magnetic structures giving rise to the same diffraction pattern) is exacerbated in the case of powder diffraction. To a particular observed peak there is the contribution of different Bragg reflections so that the magnetic structure of compounds with symmetry higher than orthorhombic cannot be determined unambiguously. A paper by G. Shirane[24] examines the case of "uniaxial" (collinear) magnetic structures and concludes that for cubic symmetry the direction of the magnetic moments cannot be determined by powder diffraction. In the case of tetragonal, rhombohedral and hexagonal systems, only the assumed "common" angle of the magnetic moments with the **c**-axis can be determined. The diffraction pattern is not sensitive to the orientation angle in the **a**–**b** plane.

## 3.4 SCATTERING FROM A POLYCRYSTALLINE POWDER

As mentioned at the beginning of this chapter, an ideal polycrystalline powder sample consists of a very large number (*e.g.* $\approx 10^9$ mm $^3$) of very small crystals (ideally $\approx 1$ μm) that are randomly oriented with respect to each other. Inevitably, the orientation of some of these crystallites will satisfy the condition that the scattering vector ($\mathbf{s} = \mathbf{S}$–$\mathbf{S_o}$) will coincide with some reciprocal lattice vector **h** and Bragg scattering will occur per Equation (20) irrespective of the azimuthal angle of the scattered beam about the incident beam. Thus, the scattering pattern from a powder sample will consist of rings (*cf.* Figure 3.1) centered about the incident beam direction. This is in contrast with diffraction from a single crystal which requires a specific orientation of the reciprocal lattice matching **h** with **s**. The corresponding construction of reciprocal space for an ideally random powder is a set of nested spherical shells of uniform density centered at the reciprocal space origin. Each shell arises from one of the reciprocal lattice points, **h**, of the crystal structure and its density is given by the magnitude of $F_{\mathbf{h}}$. Consequently, the vector character of **h** is lost in a powder pattern and only its magnitude can be determined directly.

Every nonzero structure factor, $F_{\mathbf{h}}$, where $|\mathbf{h}| = |\mathbf{s}|$ will make a contribution to the observed intensity in a powder pattern, *e.g.* when Bragg's Law is satisfied. Consequently, scattering from structure factors having identical values of $|\mathbf{h}| = 1/d_{\mathbf{h}}$ will occur simultaneously so that their respective diffraction rings will exactly superimpose. Some of these overlaps are coincidental, *i.e.* they occur at particular combinations of **h** and the unit cell dimensions and the values of the overlapping $F_{\mathbf{h}}$ are not identical. In other cases the overlaps arise from the symmetry of the unit cell; these cases will be discussed in turn below.

### 3.4.1 Friedel Pair Overlap

The pair of Bragg reflections $F_{\mathbf{h}}$ and $F_{\ \mathbf{h}}$ arise from the same stack of planes but they are the scattering from the opposite sides; these are a *Friedel pair* of reflections. They always exactly overlap in a powder pattern since $|\mathbf{h}| = |-\mathbf{h}|$, but they may not have the same value of $|F|$ if the structure is noncentrosymmetric and there is significant resonant scattering from some of the atoms. Their average intensity is given by:

$$F^2 = (A_0 + A')^2 + B''^2 + (B_0 + B')^2 + A''^2 \tag{62}$$

where:

$$\begin{aligned} A_0 &= \sum_{i=1}^{N} f_i(s_h)\cos[2\pi(\mathbf{h}\cdot\mathbf{x}_i)] & B_0 &= \sum_{i=1}^{N} f_i(s_h)\sin[2\pi(\mathbf{h}\cdot\mathbf{x}_i)] \\ A' &= \sum_{i=1}^{N} f_i'\cos[2\pi(\mathbf{h}\cdot\mathbf{x}_i)] & B' &= \sum_{i=1}^{N} f_i'\sin[2\pi(\mathbf{h}\cdot\mathbf{x}_i)] \\ A'' &= \sum_{i=1}^{N} f_i''\cos[2\pi(\mathbf{h}\cdot\mathbf{x}_i)] & B'' &= \sum_{i=1}^{N} f_i''\sin[2\pi(\mathbf{h}\cdot\mathbf{x}_i)] \end{aligned} \tag{63}$$

### 3.4.2 Reflection Multiplicity

The overlap of Friedel pairs of reflections discussed in the previous section is an example of symmetry controlled overlap where, in that case, the observed intensity of a Bragg reflection in a powder pattern is double what would be obtained from Equations (62) and (63), *i.e.* the reflection *multiplicity* is 2 and is true for all reflections from a triclinic crystal structure. For crystal symmetries other than triclinic, additional reflections may form exact overlaps of identical structure factors, depending on how the symmetry is displayed in the reciprocal lattice. For example, all tetragonal space groups that only have symmetry operators associated with the **c**-axis (*e.g.* $P4_1$ or P4/n) will have identical structure factors for $F_{hkl}$, $F_{\ khl}$, $F_{\ h\ kl}$, $F_{k\ hl}$, $F_{hk\ l}$, $F_{\ kh\ l}$, $F_{\ h\ k\ l}$ and $F_{k\ h\ l}$ in the absence of resonant scattering and for nonzero *hkl*. Since $|\mathbf{h}|$ is identical for all eight *equivalent reflections*, they will all exactly overlap in a powder pattern, giving an intensity eight times what would be obtained from $F_{hkl}$ alone; in other words the reflection multiplicity is 8. If the *l* Miller index is zero (*i.e.* for *hk0* reflections) then the set of equivalent reflections is $F_{hk0}$, $F_{\ kh0}$, $F_{\ h\ k0}$ and $F_{k\ h0}$, and the reflection multiplicity is 4. From this one can see that Equations (62) and (63) need only be used for just a subset of all possible reciprocal lattice points; these are the *unique reflections*. Use of their respective reflection multiplicities will give the observed result of the reflection overlaps from the remaining equivalent reflections.

### 3.4.3 Texture Effects

In the foregoing it is assumed that the powder sample is ideally random, *i.e.* all crystallite orientations are equally probable so that the diffraction rings are of

uniform density and independent of the sample orientation (aside from bulk absorption effects). While this can be experimentally achieved in many cases, some samples will have some preference for the orientation of the crystallites with respect to some external sample direction. For example, the flat samples used in Bragg–Brentano X-ray powder diffraction may have a *preferred orientation* to either flat platy shaped or needle shaped crystallites in the part of the sample exposed to the X-ray beam. Both platy crystals and needles would tend to lie flat on the surface, enhancing the intensities of some reflections while suppressing the intensities of others. Samples that consist of a polycrystalline mass and not a loose powder may also have been subject to a process that may have deformed the material and induced a *texture* to the crystallite orientations that will change the Bragg reflection intensities. For example, a metal plate that was manufactured in a rolling mill frequently displays the effects of rolling texture on the diffraction intensities.

A complete description of the texture (or preferred orientation) is formulated as a probability for finding a particular crystallite orientation within the sample; this is the *orientation distribution function* (ODF). For an ideally random powder the ODF is the same everywhere (ODF$\equiv$1) while for a textured sample the ODF will have positive values both less and greater than unity. This ODF can be used to formulate a correction to the Bragg intensities *via* a four-dimensional surface (*general axis* equation) that depends on both the direction in reciprocal space and the direction in sample coordinates:

$$O(\phi,\beta,\psi,\gamma) = 1 + \sum_{L=2}^{N_L} \frac{4\pi}{2L+1} \sum_{m=\ L}^{L} \sum_{n=\ L}^{L} C_L^{mn} k_L^m(\phi,\beta) k_L^n(\psi,\gamma) \qquad (64)$$

In a diffraction experiment the crystal reflection coordinates ($\phi$, $\beta$) are determined by the reflection index (**h**) while the sample coordinates ($\psi$, $\gamma$) are determined by the orientation of the sample on the diffractometer. This formulation assumes that the probability surface is smooth and can be described by a sum of $N_L$ spherical harmonic terms, ${k_L}^m$ and ${k_L}^n$, that depend on **h** and sample orientation, respectively, to some maximum harmonic order, $L$ (ref. 25). The coefficients ${C_L}^{mn}$ then determine the strength and details of the texture. Notably, only the even order, $L = 2n$, terms in these harmonic sums affect the intensity of Bragg reflections; the odd order terms in the ODF are invisible to diffraction.

While the general axis equation in Equation (64) can be used to describe the effect of texture on diffraction intensities in the most general case, most powder diffraction experiments are performed to simplify the problem. Rotation of the sample about an axis (normal to the surface in a Bragg–Brentano experiment or about the capillary axis for a Debye–Scherrer experiment) will simplify Equation (64) *via* symmetry to:

$$O(\phi,\beta,\gamma) = 1 + \sum_{L=2}^{N_L} \frac{4\pi}{2L+1} \sum_{m=\ L}^{L} C_L^{m0}\ k_L^m(\phi,\beta) k_L^0(\gamma) \qquad (65)$$

with substantially fewer coefficients than the more general case Equation (64). Notably, spinning the sample does not remove the effect of preferred orientation; it only simplifies the form of the correction.

A further simplification of the texture correction can be made if the form of the ODF is assumed to be cylindrically symmetric (*e.g.* from spinning the sample) and ellipsoidal.[26] If the unique ellipsoid axis is parallel to the diffraction vector (**s**) and perpendicular to a flat sample surface as it is in a Bragg–Brentano experiment, the general axis equation (commonly referred to as the March–Dollase equation) is:

$$O(\phi) = \frac{1}{M}\sum_{j=1}^{M}\left(R_0^2\cos^2\phi_j + \frac{\sin^2\phi_j}{R_0}\right)^{3/2} \tag{66}$$

where the sum is over the set of $M$ equivalent reflections, each at some angle $\phi_j$ to a particular lattice direction (usually the unique axis, if present, for the space group). The coefficient $R_0$ is the ellipse axis ratio and determines the amount of texture; if $R_0 = 1.0$ the distribution is spherical and there is no texture effect. For platy crystals tending to lie flat on the sample surface the plate normal would be coincident with the diffraction vector and would enhance the intensity of basal reflections (*e.g.* 00*l* for hexagonal, trigonal or tetragonal crystal systems) and $R_0$ would be greater than 1.0. However, needle crystals lying flat on the sample surface would have the basal planes perpendicular to the sample surface, thus suppressing the intensity of the basal reflections and $R_0$ is less than 1.0. For relatively large diameter ($>1$ mm) cylindrical samples (*e.g.* those used in neutron powder diffraction) where the data is collected in a Debye–Scherrer experiment, platy crystals may lie preferentially with their plate normal parallel to the cylinder axis. In this case the basal reflection intensities will be suppressed and $R_0$ is less than 1.0. Similarly, needle crystals would tend to lie with their long axis perpendicular to the sample cylinder axis, enhancing the basal reflection intensities and $R_0$ would be greater than 1.0. However, it has commonly been observed that there is little or no texture effect for very small ($<1$ mm) diameter Debye–Scherrer samples used for X-ray powder diffraction.

### 3.4.4 Absorption Effects

In a well-designed Bragg–Brentano X-ray powder diffraction experiment the sample is of uniform density throughout and is thick enough so that there is no transmission of the radiation through the sample at all scattering angles. Additionally the divergence slit is chosen so that the beam foot print covers only the sample surface (*i.e.* there is no "spillover" at low scattering angles). Under these conditions, the absorption is independent of scattering angle and therefore has no effect on the relative intensities of the Bragg reflections. However, very highly absorbing samples may have sufficient nonuniform density at the surface to affect the intensities of Bragg reflections. Usually, the surface density is lower than the bulk so that at low angles there is

effectively less material in the beam than at high angles. Consequently, the low angle (large *d*-spacing) reflection intensities are suppressed relative to the higher angle ones. This *surface roughness* effect will usually reveal itself by systematically depressing the apparent atom thermal motion parameters. Empirical correction factors[27] have been employed in various Rietveld refinement programs to describe this systematic Bragg intensity effect.

Absorption in the cylindrical samples used for Debye–Scherrer experiments with either X-ray or neutron radiation will cause an angle dependent change in the measured Bragg intensity. In general, the lower angle intensities will be suppressed more than the higher angle ones and if not corrected can lead to a systematic downward shift of the apparent atom thermal motion parameters. Values of the absorption correction for cylinders when the plane containing the incident and diffracted beams is normal to the cylinder axis (typical Debye–Scherrer geometry) are tabulated[28] and empirical fits to these values are available for use in computer programs. Generally, these corrections are only valid for small values of the absorption ($\mu r < 10$); when the absorption is higher one can not assume that the entire sample volume is contributing to the scattering.

## ACKNOWLEDGEMENTS

Support for this work is obtained from the Institut Laue-Langevin and from the U.S. Department of Energy, Office of Science, Office of Basic Energy Sciences, under Contract No. DE-AC-02-06CH11357.

## REFERENCES

1. B. E. Warren, *X-Ray Diffraction*, Dover, New York, 1990.
2. A. Guinier, *X-Ray Diffraction in Crystals, Imperfect Crystals and Amorphous Bodies*, Dover, New York, 1994.
3. *International Tables for Crystallography, Vol. C, Mathematical, Physical and Chemical Tables*, ed. A. J. C. Wilson, Kluwer, Dordrecht, 1992.
4. D. T. Cromer and D. A. Liberman, *J. Chem. Phys.*, 1970, **53**, 1891–1898; R. B. Von Dreele, FPrime for Windows, 1994, http://www.ccp14.ac.uk/ccp/ccp14/ftp-mirror/gsas/public/gsas/windows/fprime.zip.
5. G. L. Squires, *Introduction to the Theory of Thermal Neutron Scattering*, Dover, New York, 1996.
6. *Neutron Data Booklet*, 2nd edn, ed. A.-J. Dianoux and G. Lander, Institut Laue Langevin, Grenoble, 2003.
7. *International Tables for Crystallography, Vol. A*, Space Group Symmetry, ed. T. Hahn, Reidel, Dordrecht, 1983.
8. V. Petricek and P. Coppens, *Acta Crystallogr., Sect. A*, 1985, **41**, 478.
9. P. M. de Wolff, T. Janssen and A. Janner, *Acta Crystallogr., Sect. A*, 1981, **37**, 625.
10. V. Petricek and P. Coppens, *Acta Crystallogr., Sect. A*, 1988, **44**, 235, and references therein.

11. W. A. Paciorek and G. Chapuis, *Acta Crystallogr., Sect. A*, 1994, **50**, 235, and references therein.
12. S. Van Smaalen, *Cryst. Rev.*, 1995, **4**, 79–202.
13. J. Rossat-Mignod, Neutron Scattering (Magnetic Structures), in: *Methods of Experimental Physics*, ed. K. Sköld, D. L. Price, Academic Press, New York, 1987, Vol. 23, Part C, p. 69.
14. (a) Y. A. Izyumov and V. E. Naish, *J. Magn. Magn. Mater.*, 1979, **12**, 239; (b) Y. A. Izyumov, V. E. Naish and V. N. Syromiatnikov, *J. Magn. Magn. Mater.*, 1979, **12**, 249; (c) Y. A. Izyumov, V. E. Naish and S. B. Petrov, *J. Magn. Magn. Mater.* 1979, **13**, 267; **13**, 275; (d) Y. A. Izyumov, *J. Magn. Magn. Mater.*, 1980, **21**, 33.
15. F. Moussa, M. Hennion, J. Rodríguez-Carvajal, L. Pinsard and A. Revcolevschi, *Phys. Rev. B: Solid State*, 1996, **54**, 15149.
16. Y. A. Izyumov, V. E. Naish and R. P. Ozerov, *Neutron Diffraction of Magnetic Materials*, Consultants Bureau, New York, 1991.
17. (a) E. García-Matres, J. Rodríguez-Carvajal, J. L. Martínez, A. Salinas-Sánchez and R. Sáez-Puche, *Solid State Commun.*, 1993, **85**, 553; (b) E. García-Matres, J. L. Martínez and J. Rodríguez-Carvajal, *Eur. Phys. J. B*, 2001, **24**, 59–70.
18. (a) P. Schobinger-Papamantellos, F. B. Altorfer, J. H. V. J. Brabers, F. R. de Boer and K. H. J. Buschow, *J. Alloys Compd.*, 1994, **203**, 243; (b) P. Schobinger-Papamantellos, J. Rodríguez-Carvajal, G. André and K. H. J. Buschow, *J. Magn. Magn. Mater.*, 1995, **150**, 311.
19. W. Opechowski and R. Guccione, Magnetic Symmetry, in *Magnetism*, ed. G. T. Rado and H. Shull, Academic Press, New York, 1965, Vol. II A, ch. 3, p. 105.
20. W. Opechowski, *Crystallographic and Metacrystallographic Groups*, Elsevier Science Publishers B.V., Amsterdam, 1986.
21. Y. A. Izyumov, V. E. Naish and R. P. Ozerov, *Neutron Diffraction of Magnetic Materials*, Consultants Bureau, New York, 1991.
22. J. Rodríguez-Carvajal, *Physica B (Amsterdam)*, 1993, **192**, 55.
23. T. Nagamiya, *Solid State Phys.*, 1967, **20**, 305–411.
24. G. Shirane, *Acta Crystallogr.*, 1959, **12**, 282.
25. (a) H.-J. Bunge, *Texture Analysis in Materials Science*, Cuviller Verlag, Göttingen, 1982; (b) R. B. Von Dreele, *J. Appl. Crystallogr.*, 1997, **30**, 517–525.
26. (a) W. A. Dollase, *J. Appl. Crystallogr.*, 1986, **19**, 267–272; (b) A. March, *Z. Kristallogr.*, 1932, **81**, 285–297.
27. (a) P. Suortti, *J. Appl. Crystallogr.*, 1972, **5**, 325–331; (b) W. Pitschke, H. Hermann and N. Mattern, *Powder Diffr.*, 1993, **8**, 74–83; (c) C. J. Sparks, K. Kumar, E. D. Specht, E. D. Zschack and G. E. Ice, *Adv. X-Ray Anal.*, 1991, **35**, 57–83.
28. *International Tables for X-Ray Crystallography*, vol. II, *Mathematical Tables*, ed. J. S. Kasper and K. Lonsdale, Kynoch, Birmingham, 1967; *International Tables for Crystallography, Vol. C., Mathematical, Physical and Chemical Tables*, ed. A. J. C. Wilson, Kluwer, Dordrecht, 1992.

CHAPTER 4

# General Data Reduction

RUDOLF ALLMANN

Im Grund 5, D-35043, Marburg, Germany

## 4.1 INTRODUCTION

In modern powder diffraction the measurement delivers a raw-file of some thousand step-scan data of counted X-ray photons per step. This raw file contains all the needed information to carry out a crystallographic analysis, but in a way that requires follow up. More informative is a list of distinguishable reflections that includes the position (mostly in the form of *d*-values) and intensity of each reflection. This dif-file (d-values and intensities) contains some tens to hundreds of reflections. The number of reflections depends on the complexity of the structure and the crystal symmetry: the more atoms per cell and the lower the symmetry the more reflections can be identified. But the number of detectible reflections also depends on the resolving power of the equipment, best documented by the half-width of the reflections (more accurately: half-width at half-maximum, FWHM). Reflections nearer together than this half-width (or even two half-widths) cannot be resolved. In a second step, very often the Miller indices of the originating lattice planes are added to the dif-file. For this the knowledge of the unit cell is necessary (though not of the crystal structure itself). The powder diffraction file PDF of the International Centre for Diffraction Data (ICDD) contains over 100 000 such dif-files for the identification and discrimination of solid state samples.

The way from the raw-file to the dif-file is called data reduction and consists of several steps, not all of them may be necessary:

1. Elimination of fake reflections (outliers)
2. Fitting and subtraction of the background
3. Data smoothing (Savitzky–Golay method)
4. K$\alpha_2$-stripping
5. Peak-searching

6. Profile-fitting
7. Detection of systematic errors

All steps of these numerical methods use the given advantages of raw-files:

Equal step widths (very often 0.02° in $2\theta$) for the complete pattern and about equal half-widths of all peaks (for routine measurements 0.1–0.2°). A very powerful method is the application of sliding polynomial fitting procedures, which rely on a constant step-width and an approximately constant peak form, and can by used for steps 1, 3, and 5.

## 4.2 ELIMINATION OF FAKE REFLECTIONS (OUTLIERS)

If the counting electronics for the X-ray pulses are insufficiently screened, jamming sources like the starter of a neon lamp may contribute to the counting rate. Also an oscillating circuit of the electronics can be excited to resonance. This results in excessive counting rates, which may last for one or several seconds and will simulate a non-existing reflection. Such fake reflections, however, exhibit smaller half-widths than regular reflections and thus can be recognized and eliminated. Very often only one step is affected. Because the count rates of adjacent steps are not independent of each other – all reflections more or less have the same shape – the count rate of one step can be estimated from the measured count rates of the adjacent steps by a kind of interpolation. If this estimated value $\hat{y}_k$ differs significantly (*e.g.* more than 4–5$\sigma$ with $\sigma = \sqrt{\hat{y}_k}$) from the measured value $y_k$, the measured value probably is a fake one and should be replaced by the estimation (possibly increased by approx. 2$\sigma$).

The value $\hat{y}_k$ is best estimated by sliding polynomials (similar to smoothing, see below), for which the innermost weight or weights are set to 0, *e.g.* $\hat{y}_k = 1/6(-y_{k\ 2} + 4y_{k\ 1} + 4y_{k+1} - y_{k+2})$. Table 4.1 tabulates the coefficients of polynomials of 2nd order (and, at the same time, for 3rd order) for up to 12 neighbors. On the left only the weight of the central value is set to 0 (for isolated fake counting rates), on the right the 3 central weights (for 2 or 3 adjacent fake

**Table 4.1** Coefficients for the determination of fake reflections. On the left for isolated fake counting rates, on the right for groups of up to 3 fake rates $\hat{y}_k = (\Sigma_i\, c_i \ldots y_{k+i})/\text{norm}$ (for $i = -n \ldots, n-1, n$).

| *Number of used neighbors* | *4* | *6* | *8* | *10* | *12* | *4* | *6* | *8* | *10* |
|---|---|---|---|---|---|---|---|---|---|
| **Norm** | 6 | 14 | 172 | 340 | 118 | 10 | 436 | 332 | 1090 |
| *i* | | | | | $c_i$ | | | | |
| 0 | 0 | 0 | 0 | 0 | 0 | 0 | 0 | 0 | 0 |
| ±1 | 4 | 6 | 54 | 84 | 24 | 0 | 0 | 0 | 0 |
| ±2 | 1 | 3 | 39 | 69 | 21 | 9 | 237 | 127 | 319 |
| ±3 | | 2 | 14 | 44 | 16 | 4 | 92 | 82 | 244 |
| ±4 | | | 21 | 9 | 9 | | 111 | 19 | 139 |
| ±5 | | | | 36 | 0 | | | 62 | 4 |
| ±6 | | | | | 11 | | | | 161 |

rates). The sum of the individual weights $c_i$ yields the norm or denominator, for the example above: $6 = -1 + 4 + 4 - 1$, by which the weighted sum must be divided ($i$ is the distance from the central step).

Isolated fake counting rates should be corrected for deviations of approx. $4\sigma$ and more (*i.e.* if $y_k - \hat{y}_k > 4\sqrt{\hat{y}_k}$, then $y_{k\text{cor}} = \hat{y}_k + 2.\sqrt{\hat{y}_k}$), accumulated fake rates for $5\sigma$ and more. To better fix the background it is reasonable to correct in a second run those values that have accidentally been measured too low. They should be increased if $\hat{y}_k - y_k > (4 - 5)\sigma$. Before such corrections are accepted definitively, the proposals calculated by the computer should be manually examined for their plausibility. A copy of the original raw file should be kept in any case, which holds for the following steps as well.

## 4.3 FITTING AND SUBTRACTION OF BACKGROUND

Powder patterns always contain statistical noise, which has several sources: elastic scattering from the sample holder (Figure 4.1), an amorphous part of the sample, or from air in the beam-path (Figure 4.2); inelastic scattering (*i.e.* with

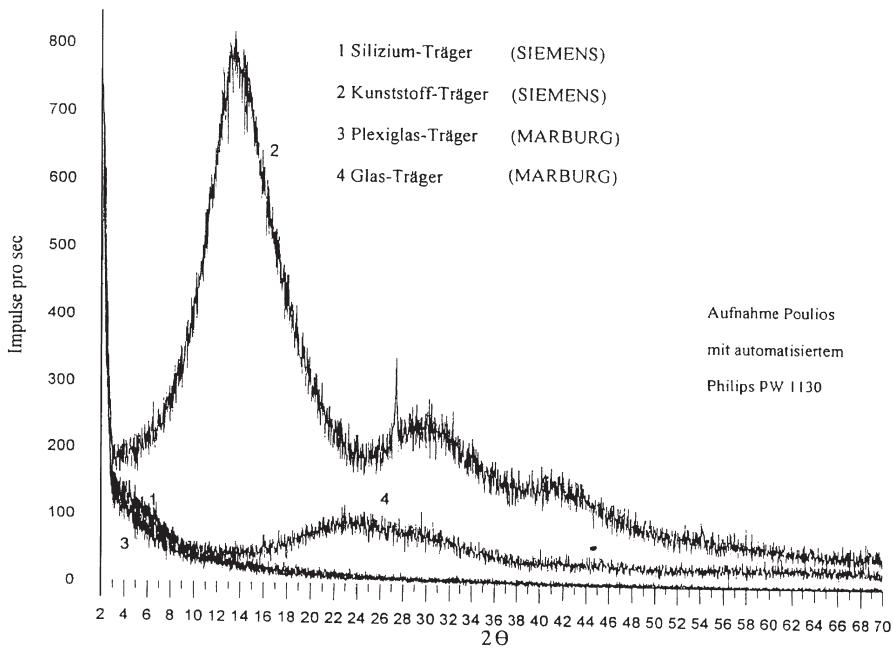



**Figure 4.1** Diffraction patterns of usual sample holders (0.5° div. slit). For thin samples, or with a too wide divergence slit, these patterns may be superimposed on the sample pattern. For a plastic framed "background free" Si single crystal holder a plastic hump appears in the lower angle area (for 1° div. slit this starts already at 18°). The sharp reflections in 2 originate from the inorganic filler (feldspar?). Normal white Perspex resembles the given plastic curve (4). A blue Perspex of unknown origin was found to be almost free of background (3).

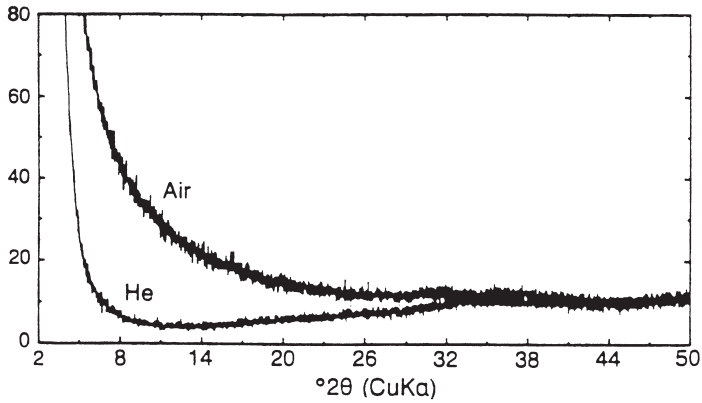



**Figure 4.2** Influence of the atmosphere in the beam path on the background, measured with a quartz single crystal sample holder (above: in air, below: in helium).[25]

alteration of wavelength) and fluorescence radiation, and extraneous radiation (*e.g.* the inevitable cosmic rays). According to the construction of the divergence slit in front of the X-ray tube (fixed or variable to ensure illumination of a constant sample area) the background decreases more or less with increasing $2\theta$. With amorphous sample holders (*e.g.* silica glass), wide "amorphous" humps can be found in certain regions of the background if the sample is not thick enough or too small so that the sample holder itself is illuminated, especially at small angles. In the upper angular region, especially for sample material of low crystal symmetry, the numerous individual reflections may overlap so strongly that the background itself will no longer be reached. In such a case the background is easily estimated as too high, resulting in the intensities of these overlapping reflections being determined to be too low.

Sonneveld and Visser (1975) [1] report a method for digitally processed X-ray films that is easily programmed and which delivers background curves very much resembling, visually, estimated ones. A similar procedure can be found at Goehner (1978).[2] For this procedure it will be sufficient to take every tenth or twentieth point of the raw file (possibly also the minimum of some adjacent points) as base for the background to be evaluated. These points represent the zero approximation of the background. Because some of the points belong to a reflection and therefore are too high, they must be pulled down by an iterative procedure. To do so, for every point (except for the edge points) the average of both adjacent points is calculated as a new estimation. If this is lower than the old background in the middle, the old background value is to be replaced by the calculated average. This "pulling down" must be repeated about 30 times.

In the area of expected amorphous humps (also for very great $2\theta > 120^\circ$ the background may increase again) one can admit a minor increase of the background above that of adjacent points by about $1–2\sigma$, *i.e.* omit the substitution by the estimated value (or substitution only if the original

value > average $+1$–$2\sigma$). At the end, the total background is linearly interpolated between the corrected base points and subtracted from the raw data point by point. If the starting values were not the measured ones themselves but the minima of 3 or 5 adjacent points, the so-determined background line is positioned in the lower part of the background noise and may be enhanced by 1–$2\sigma$ to avoid too many spurious weak reflections in the following peak search. A manual correction of the preliminary calculated background may be meaningful in some cases. The base points for the background may be set manually too. Some authors use cubic splines to connect these points.

Another method for fitting the background is used by the program EVA of Bruker AXS. Here parabolas with a variable curvature (set by the user) are shifted upwards from below the pattern until they touch the background. The envelope of all these parabolas is then taken as background curve.

The original background also represents a good estimation of the white noise of the measurement. Only counting rates that significantly [*i.e.* with. (2–3)σ, $\sigma = \sqrt{\text{original background}}$] supersede the background can be taken as belonging to a peak region. Regions below this level can be completely neglected in the following peak search procedure.

## 4.4 DATA SMOOTHING

To improve the signal/noise ratio, noisy measurements often are submitted to a smoothing procedure, which filters out the wanted information (in our case the X-ray reflections). Practically, two approaches can be used for smoothing powder patterns: (1) the *sliding polynomial smoothing*, which presupposes an approximately known signal (peak) form, and which was used successfully for the first time by Savitzky and Golay (1964)[3] for processing infrared spectra; (2) originating from communication technology, the *low pass filters*, which in signal processing are used to separate low-frequency signals from high-frequency noise (*e.g.* DOLBY to suppress the noise of tape recorders).

### 4.4.1 Smoothing by Sliding Polynomials (Savitzky–Golay Method)

This method was successfully introduced into spectroscopy and popularized by Savitzky and Golay.[3] Therefore, the best sources for papers on this topic are not mathematical journals and textbooks, but the chemical journal *Analytical Chemistry*. However, the method of sliding polynomials itself has long been known. As an example, formulas for calculating the necessary coefficients (see Table 4.2) can already be found in the textbook of Whittaker and Robinson (1924).[4] Only because of the missing computational possibilities at this time were these formulas not used in practice.

A prerequisite for the application of this method is a set of equally separated base points, as they are obtained in step scan measurements with a constant step width, and a signal shape that can be approximated by a polynomial of *n*th order. This way, X-ray reflections in the region of their half-width can be

**Table 4.2** Coefficients for a sliding polynomial fit after Savitzky and Golay (1964, corrected).[3] The weighted sum (weights $c_i$) must be divided by the norm.

| | *Smoothing (2nd and 3rd order)* | | | | | | *2nd Derivative (2nd and 3rd order)* | | | | | |
|---|---|---|---|---|---|---|---|---|---|---|---|---|
| *m* | 5 | 7 | 9 | 11 | 13 | 15 | 5 | 7 | 9 | 11 | 13 | 15 |
| *n* | 2 | 3 | 4 | 5 | 6 | 7 | 2 | 3 | 4 | 5 | 6 | 7 |
| Norm | 35 | 21 | 231 | 429 | 143 | 1105 | 7 | 42 | 462 | 429 | 1001 | 6188 |
| *i* | | | | | | | $c_i$ | | | | | |
| 0 | 17 | 7 | 59 | 89 | 25 | 167 | 2 | 4 | 20 | 10 | 14 | 56 |
| ±1 | 12 | 6 | 54 | 84 | 24 | 162 | 1 | 3 | 17 | 9 | 13 | 53 |
| ±2 | 3 | 3 | 39 | 69 | 21 | 147 | 2 | 0 | 8 | 6 | 10 | 44 |
| ±3 | | 2 | 14 | 44 | 16 | 122 | | 5 | 7 | 1 | 5 | 29 |
| ±4 | | | 21 | 9 | 9 | 87 | | | 28 | 6 | 2 | 8 |
| ±5 | | | | 36 | 0 | 42 | | | | 15 | 11 | 19 |
| ±6 | | | | | 11 | 13 | | | | | 22 | 52 |
| ±7 | | | | | | 78 | | | | | | 91 |

| | *1st Derivative (1st and 2nd order)* | | | | | | *1st Derivative (3rd and 4th order)* | | | | | |
|---|---|---|---|---|---|---|---|---|---|---|---|---|
| *m* | 5 | 7 | 9 | 11 | 13 | 15 | 5 | 7 | 9 | 11 | 13 | 15 |
| *n* | 2 | 3 | 4 | 5 | 6 | 7 | 2 | 3 | 4 | 5 | 6 | 7 |
| Norm | 10 | 28 | 60 | 110 | 182 | 280 | 12 | 252 | 1188 | 5148 | 24024 | 334152 |
| *i* | | | | | | | $c_i$ | | | | | |
| 7 | | | | | | 7 | | | | | | 12922 |
| 6 | | | | | 6 | 6 | | | | | 1133 | 4121 |
| 5 | | | | 5 | 5 | 5 | | | | 300 | 660 | 14150 |
| 4 | | | 4 | 4 | 4 | 4 | | | 86 | 294 | 1578 | 18334 |
| 3 | | 3 | 3 | 3 | 3 | 3 | | 22 | 142 | 532 | 1796 | 17842 |
| 2 | 2 | 2 | 2 | 2 | 2 | 2 | 1 | 67 | 193 | 503 | 1489 | 13843 |
| 1 | 1 | 1 | 1 | 1 | 1 | 1 | 8 | 58 | 126 | 296 | 832 | 7506 |
| 0 | 0 | 0 | 0 | 0 | 0 | 0 | 0 | 0 | 0 | 0 | 0 | 0 |
| 1 | 1 | 1 | 1 | 1 | 1 | 1 | 8 | 58 | 126 | 296 | 832 | 7506 |
| 2 | 2 | 2 | 2 | 2 | 2 | 2 | 1 | 67 | 193 | 503 | 1489 | 13843 |
| 3 | | 3 | 3 | 3 | 3 | 3 | | 22 | 142 | 532 | 1796 | 17842 |
| 4 | | | 4 | 4 | 4 | 4 | | | 86 | 294 | 1578 | 18334 |
| 5 | | | | 5 | 5 | 5 | | | | 300 | 660 | 14150 |
| 6 | | | | | 6 | 6 | | | | | 1133 | 4121 |
| 7 | | | | | | 7 | | | | | | 12922 |

approximated quite well by a parabola (polynomial of 2nd order) and shoulders (*e.g.* a weak peak at the slope of a strong one) by a polynomial of 3rd order.

In $m = 2n + 1$ adjacent base points $x_{k\ n}, x_{k\ n+1}, \ldots, x_{k\ 1}, x_k, x_{k+1}, \ldots, x_{k+n}$ one tries to approximate the measured values $y_{k\ n} \ldots y_{k+n}$ by a polynomial of *n*th order (*e.g.* $y = a + bx + cx^2$) by means of the method of least squares. Because the wanted parameters a, b, c appear as linear factors, one deals with a linear system, which immediately (in one step) delivers the correct solution, which will be independent of the used step width and of any starting values (assumed to be 0). The solution for a parabola through $m = 5$ points ($n = 2$)

reads as:

$$a = 1/35\,(-3y_{k\ \ 2} + 12y_{k\ \ 1} + 17y_k + 12y_{k+1} - 3y_{k+2}),$$

$$b = 1/10(-2y_{k\ \ 2} - y_{k\ \ 1} + y_{k+1} + 2y_{k+2}) \text{ and}$$

$$c = 1/14(y_{k\ \ 2} - y_{k\ \ 1} - 2y_k - y_{k+1} + 2y_{k+2}).$$

For the central point with $i = 0$ it holds $y(0) = a$, $y'(0) = b$ and $y''(0) = 2c$, *i.e.* as smoothed value $y_k$ of the central point one just takes the value "a" of the absolute term: $y_k = 1/35(-3y_{k\ \ 2} + 12y_{k\ \ 1} + 17y_k + 12y_{k+1} - 3y_{k+2})$. With b and 2c one furthermore gets approximations of the 1st and 2nd derivative at the position $k$, *i.e.* the derivatives of a complete pattern can easily be calculated without knowing any peak-shape functions. For the next point the polynomial is just shifted by one step width and exactly the same formulas are applied. Only those $n$ points both at the beginning and the end of the raw file cannot be smoothed by these formulas. The easiest way is to leave these few points unsmoothed or to use a narrower smoothing interval at both ends of the file. The general expression for (explicit) digital filters reads:

$$y_k = (\Sigma c_i \,.\, y_{k+i})/\text{norm}, \ (i = -n, \ldots, -1, 0, 1, \ldots, n)$$

As during the least-squares refinement, every other coefficient of the normal equations sums up to 0, the values for the 0th (=smoothing) and 2nd derivative hold for polynomials of 2nd and of 3rd order as well. The coefficients for 1st derivatives are different for 2nd and 3rd order (but equal for 1st and 2nd order, and for 3rd and 4th order, respectively).

The coefficients of a sliding polynomial fit can be summarized in a simple formula.[5] For smoothing (2nd and 3rd order) one gets for $m = 2n + 1$ points:

$$\text{norm} = (4n^2 - 1)(2n + 3)/3, \ldots c_i = 3n(n + 1) - 1 - 5i^2.$$

Since the X-ray reflections within one pattern mostly are rather uniform, the Savitzky–Golay smoothing can be optimized for each pattern, namely by adapting the width of the smoothing interval to the average half-width of the reflections (at most 20% wider than the half-width) (Figure 4.3). This means the number $m$ of base points for smoothing should be about the number of measuring steps per half-width (possibly + 20%). If fewer points are used too much noise will remain. If too many points are used the shape of the reflection will be affected: the peak becomes wider and less high, *i.e.* the resolution gets worse (oversmoothed). As the norm in all cases is equal to the sum of the weights $c_i$, the integrated intensity (=peak area) remains unchanged after any smoothing (cf. ref. 6).

For the 1st and higher derivatives the step width $\Delta x$ must be taken into account (but not for smoothing): The exact expression is $y' = b/\Delta x$, $y'' = 2c/(\Delta x)^2$. This must be considered, if one wants to compare two patterns measured with different step widths. For patterns with varying half-widths the minima of the 2nd derivative (=peak position) decrease with the squares of the

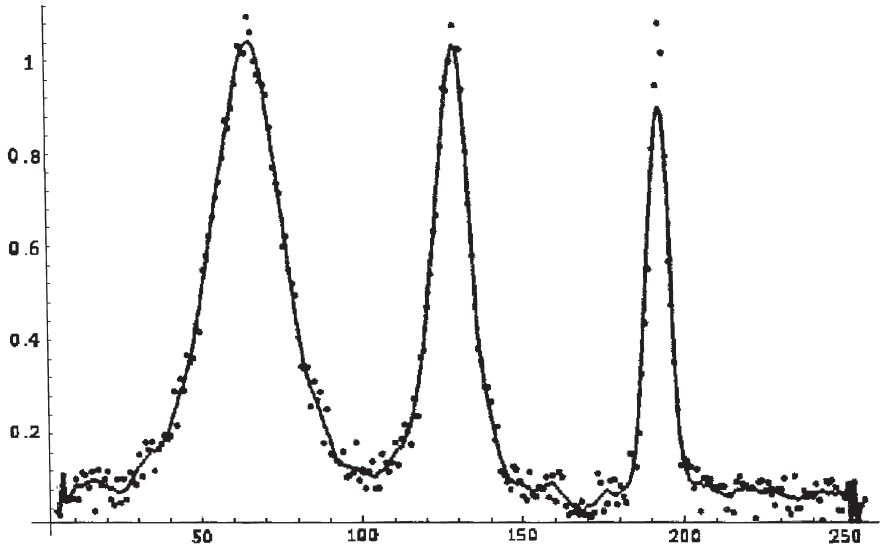



**Figure 4.3** Effect of sliding polynomial smoothing. Presented are three noisy, modified Lorentz peaks of equal height and different half widths of 27, 13, and 7 (points). For smoothing (lines), 13 points were used. The narrow reflection (right) is somewhat oversmoothened, yielding a light widening and lowering of the peak. For the central peak the smoothing is well adjusted and the left reflection could have been smoothed more aggressively.

half-widths, *i.e.* broad reflections are recognized less well if the peak search uses the method of 2nd derivatives (Figure 4.4). Also for this reason the number of measuring points should not be increased above 10 per half-width.

The low pass characteristics of the Savitzky–Golay method are not extremely good, because in the frequency domain strong negative regions occur (cf. Figure 4.4). However, since after the twofold application of a filter (also the Savitzky–Golay smoothing can be understood as a digital filter) the frequency domain simply is squared and the negative regions vanish (Figure 4.5). Thus, the low pass characteristics of the Savitzky–Golay smoothing can be greatly enhanced by twofold application and, therefore, this method always should be used twice with the same coefficients (smoothing of smoothed data). For very noisy signals, possibly a 100-fold repeated smoothing with sliding polynomials may enhance a weak signal above the noise level (example in ref. 5).

### 4.4.2 Digital Low Pass Filters

A test series (*e.g.* a raw file) can be viewed as a superposition of signals plus noise. Since a Fourier transform is additive, the frequency spectrum of a measurement is the sum (superposition) of the signal frequency spectrum and the noise frequency spectrum. If a reflection can be fitted by a Pearson VII profile (Chap. 4.7) and if the maximum of this even function is put in $x = 0$,

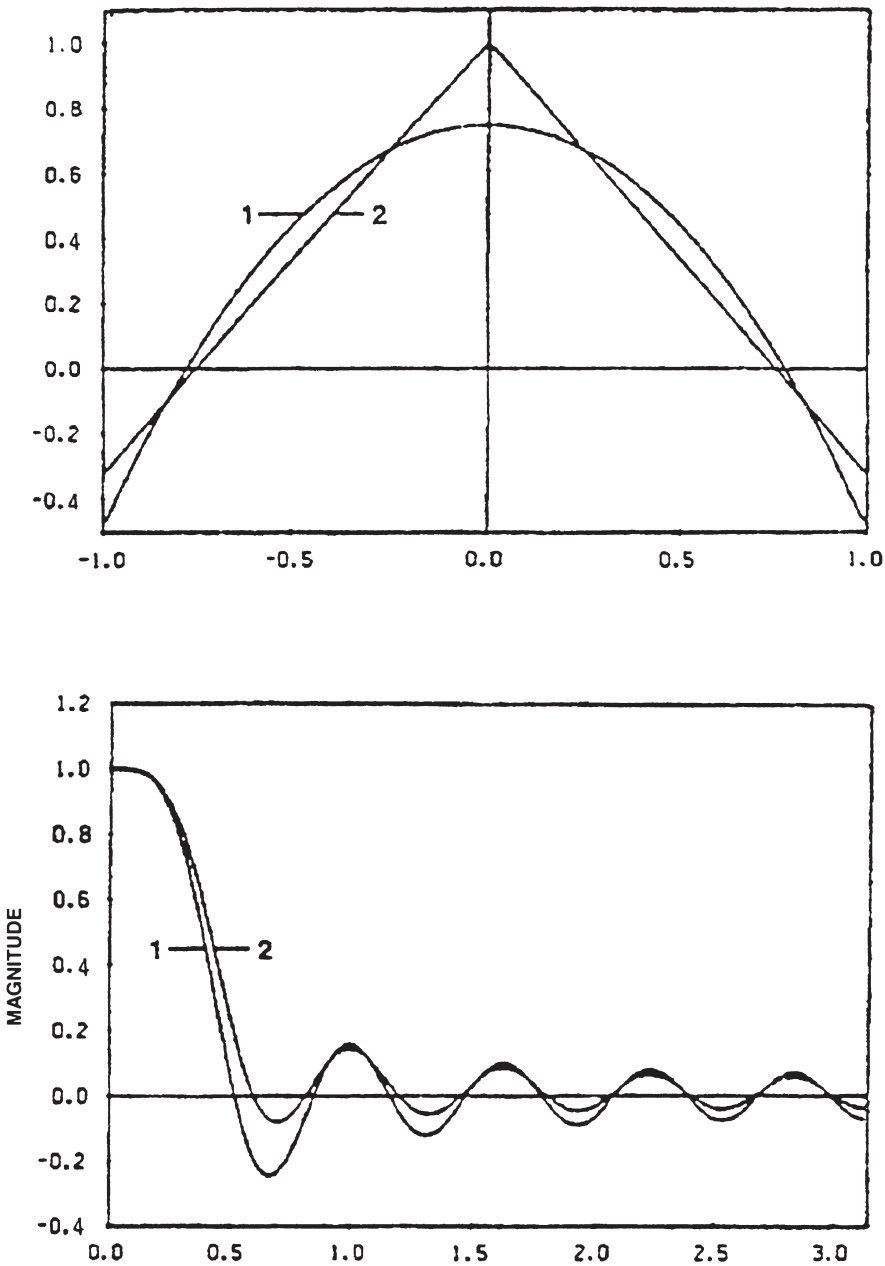



**Figure 4.4** Similar to the sliding polynomial smoothing (Savitzky Golay filter, the coefficients for 2nd order fit to a parabola) is the effect of Bromba Ziegler filters [Bromba and Ziegler, (1983c),[7] coefficients fit to a triangle: upper figure]. Both have bad low pass filter characteristics, as shown in the lower figure with the Fourier transforms of filters through 21 points each.

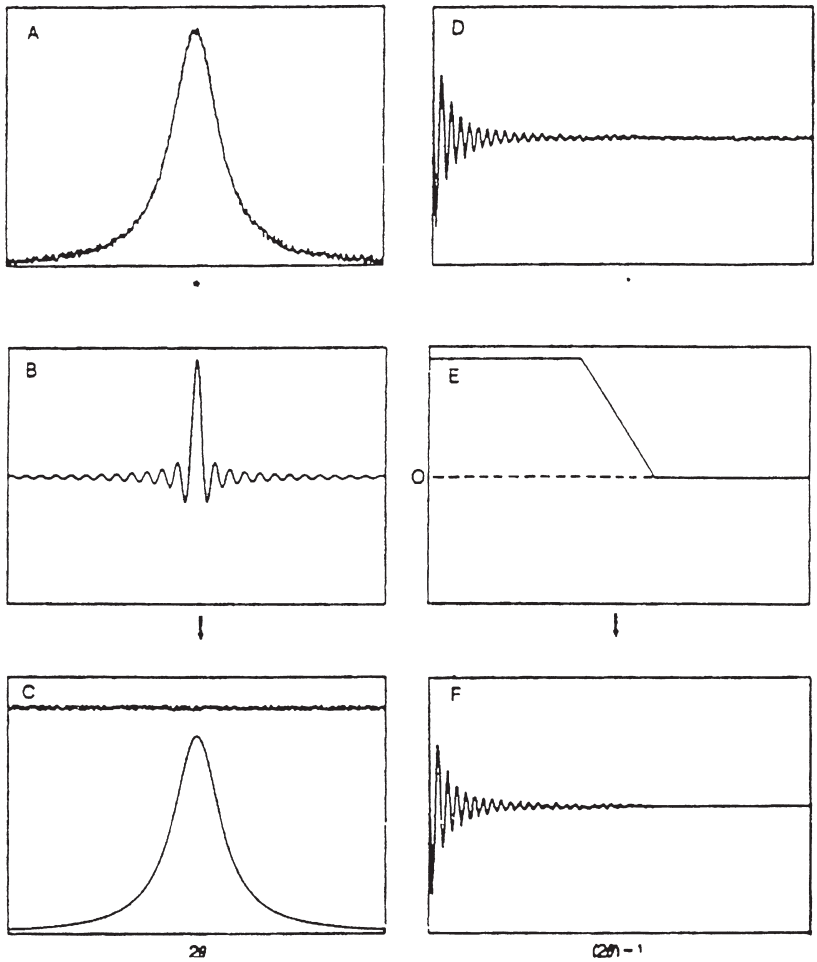



**Figure 4.5** Effect of a low pass filter in the amplitude (left) domain and in the frequency (right) domain. (A) A noisy Lorentz peak. The left part of its frequency spectrum D (low frequencies) is mainly determined by the frequency spectrum of the noiseless reflection. To the right, only the spectrum of the (white) noise contributes. If D is multiplied point by point with the low pass filter E (in the front part = 1, in the back part = 0 with a transition zone), one gets F, a spectrum without noise in the upper frequency range. C, the reverse transform of F, is the desired smoothed curve. In the upper part of C the difference to A is given, *i.e.* the eliminated high frequency part of noise. Instead of the detour through the frequency domain with two time consuming Fourier transforms one also can convolute the original curve A with the Fourier transform B of the low pass filters E. For discontinuous measurements (such as any step scan method) a convolution is a sliding, weighted mean. The coefficients of this filter are discrete points at the curve B. For a pure rectangle function (without a transition zone between 1 and 0 as in E) the Fourier transform is shaped like $(\sin x)/x$. (After Cameron and Armstrong, 1988.[8])

so the Fourier transform is a real function, which steadily approximates 0. The exact solution for the Fourier transform of:

$$f(x) = (1 + (x/b)^2)^{\ m}$$

reads:

$$g(w) = ((\sqrt{2\pi} \cdot |\mathrm{b}|^{m+1/2})/(2^{m\ 1} \cdot \Gamma(m)) \cdot |\mathrm{w}|^{m\ 1/2} \cdot \mathrm{Bessel\,K}(m - 1/2,\ |b \cdot w|)$$

especially for

$$m = 1 :\ g(w) = \pi \cdot \mathrm{b}/[\exp(\mathrm{b} \cdot |w|)]$$

and for

$$m = 2 :\ g(w) = \pi \cdot \mathrm{b}^2\,(|w| + 1/b)/[2\exp(\mathrm{b} \cdot |w|)].$$

That is, for a steady signal the share of higher frequencies approximates zero whereas the frequency response of the noise stays more or less constant. Therefore, above a certain frequency only the noise will contribute. If one suppresses this high-frequency part by multiplication with 0, after the reverse transform into the amplitude domain the signal is kept unchanged, only slightly disturbed by the low-frequency part of the noise.

Instead of the application of a low pass filter in the frequency domain itself (multiplication with 1 in the low-frequency range and above that with 0, *i.e.* multiplication of the frequency response with a rectangle function), one can use in the amplitude domain (*i.e.* for the measurement itself) the mathematically fully equivalent convolution with the Fourier transform of that rectangle function.

Numerically the convolution of a step scan is merely the application of a sliding weighted mean (*e.g.* like the Savitzky–Golay method). The Fourier transform of the rectangular function has the shape of $\sin(\mathrm{n}x)/(\mathrm{n}x)$ (whereby n is inversely proportional to the width of the rectangle) and unfortunately approaches 0 only very slowly. To make do with a small number of points for a convolution, one must tolerate a compromise and renounce the ideal rectangular shape of the low pass filter (in the frequency domain).

According to an algorithm of Hamming (1983)[9] for the construction of monotonous low pass filters a set of coefficients was calculated that can be used like the Savitzky–Golay coefficients for the smoothing of powder patterns. For greater ranges, the demand of monotony was renounced, because otherwise the norm increases very rapidly with $4^n$. However, the following conditions were observed: $\Sigma c_i = \mathrm{norm}$, $\Sigma c_i(-1)^i = 0$, $\Sigma c_i \cdot i^2 = 0$ (*i.e.* a parabola will be reproduced exactly). The number of points should be about 1/4 larger than the number of points per half-width. However, one run will suffice. Both end ranges should be smoothed with 5 points, so only 2 points each at every end remain unsmoothened. Table 4.3 tabulates these new coefficients, together with two low pass filters of Spencer (1904),[10] who used these for smoothing life expectance tables.

**Table 4.3** Coefficients for digital low pass filters.

| | *Digital low pass filter for smoothing* | | | | | | | | | | | *Spencer (1904)*[10] | |
|---|---|---|---|---|---|---|---|---|---|---|---|---|---|
| *m* | 5 | 7 | 9 | 11 | 13 | 15 | 17 | 19 | 21 | 23 | 25 | 15 | 21 |
| *n* | 2 | 3 | 4 | 5 | 6 | 7 | 8 | 9 | 10 | 11 | 12 | 7 | 10 |
| Norm | 16 | 32 | 64 | 512 | 512 | 512 | 512 | 512 | 512 | 512 | 1024 | 320 | 350 |
| *i* | | | | | | | | $c_i$ | | | | | |
| 0 | 10 | 16 | 26 | 186 | 154 | 128 | 104 | 96 | 90 | 80 | 152 | 67 | 57 |
| ±1 | 4 | 9 | 18 | 139 | 127 | 111 | 96 | 89 | 83 | 75 | 145 | 67 | 57 |
| ±2 | 1 | 0 | 4 | 46 | 64 | 72 | 73 | 70 | 68 | 65 | 125 | 46 | 47 |
| ±3 | | 1 | 2 | 8 | 10 | 29 | 42 | 46 | 47 | 49 | 98 | 21 | 33 |
| ±4 | | | 1 | 11 | 11 | 0 | 16 | 22 | 26 | 32 | 66 | 3 | 18 |
| ±5 | | | | 3 | 9 | 9 | 2 | 4 | 9 | 16 | 36 | 5 | 8 |
| ±6 | | | | | 2 | 8 | 9 | 6 | 2 | 3 | 12 | 6 | 2 |
| ±7 | | | | | | 3 | 8 | 8 | 6 | 4 | 4 | 3 | 5 |
| ±8 | | | | | | | 4 | 6 | 7 | 8 | 11 | | 5 |
| ±9 | | | | | | | | 5 | 5 | 7 | 13 | | 3 |
| ±10 | | | | | | | | | 2 | 4 | 10 | | 1 |
| ±11 | | | | | | | | | | 1 | 6 | | |
| ±12 | | | | | | | | | | | 2 | | |

In Table 4.4 some smoothing functions are applied on a modified Lorentz curve with a half-width of HW = 4. At each slope the data run until 5HW (=20 steps). The results of smoothing a, b, c are insufficient, since the reflection shapes are deformed too much (as c furthermore changes the position of the maximum, both slopes are reported; c simulates an old rate meter recording). Both d and e are single Savitzky–Golay smoothings, whereby d is adjusted to the half-width whereas e uses too many points (oversmoothing); f and g are the corresponding results with low pass filters (Figure 4.6).

## 4.5 $K\alpha_2$-STRIPPING

Since the Kα-radiation from a conventional source consists of two very narrow peaks with rather similar wavelengths (for CuK: $\lambda\alpha_2/\lambda\alpha_1 = 1.00248$), which can be separated only with great effort, each Kα-spectrum is a superposition of two slightly shifted spectra. At lower angles this splitting is not resolved. At larger angles the $K\alpha_2$-peak appears at somewhat higher angles than, and is about half the intensity of, the $K\alpha_1$-peak. The beginning of the visible splitting depends on the half-width HW of the reflections. For CuKα-radiation and for HW = 0.1° the splitting starts at $2\theta = 39°$, for HW = 0.2° at 70° and for HW = 0.3° at 93° (see Table 4.5). For various reasons the $\alpha_2$-Peaks have about a 20% greater half-width than the $\alpha_1$-peaks.

The splitting $\Delta 2\theta = 2\theta(\alpha_2) - 2\theta(\alpha_1)$ increases with increasing $2\theta$, as can be seen in Table 4.5 [for CuKα with $\lambda(\alpha_2)/\lambda(\alpha_1) = 1.00248$]. Up to $2\theta = 140$–150° the splitting is quite well approximated by the formula:

$$\Delta 2\theta\,[1 - \lambda(\alpha_1)/\lambda(\alpha_2)] \cdot \tan\theta(\alpha_2) \cdot 360°/\pi$$

**Table 4.4** Standard curves with equal height and half-width and the results of several smoothings, applied to the modified Lorentz curve ML (3rd column).[a]

| *k* | *L* | *ML* | *a* | *b* | $c_-$ | $c_+$ | *d* | *e* | *f* | *g* |
|---|---|---|---|---|---|---|---|---|---|---|
| 0 | 10000 | 10000 | 7285 | 8094 | | 7907 | 9631 | 8149 | 9731 | 9095 |
| ±1 | 8000 | 8212 | 6820 | 7280 | 5814 | 8060 | 8198 | 7517 | 8201 | 7981 |
| ±2 | 5000 | 5000 | 5461 | 5355 | 3416 | 6530 | 5184 | 5800 | 5134 | 5444 |
| ±3 | 3076 | 2679 | 3617 | 3318 | 1831 | 4605 | 2731 | 3564 | 2717 | 2996 |
| ±4 | 2000 | 1417 | 2064 | 1845 | 983 | 3011 | 1406 | 1679 | 1409 | 1464 |
| ±5 | 1379 | 776 | 1118 | 1001 | 550 | 1893 | 763 | 689 | 767 | 732 |
| ±6 | 1000 | 447 | 617 | 558 | 324 | 1170 | 440 | 335 | 442 | 409 |
| ±7 | 755 | 271 | 356 | 327 | 200 | 720 | 268 | 206 | 269 | 250 |
| ±8 | 588 | 172 | 216 | 201 | 129 | 446 | 170 | 140 | 171 | 162 |
| ±9 | 471 | 113 | 138 | 129 | 86 | 280 | 113 | 99 | 113 | 109 |
| ±10 | 385 | 78 | 91 | 87 | 60 | 179 | 77 | 70 | 77 | 75 |
| ±11 | 320 | 55 | 63 | 60 | 43 | 117 | 54 | 51 | 54 | 53 |
| ±12 | 270 | 39 | 45 | 43 | 31 | 78 | 39 | 38 | 39 | 39 |
| ±13 | 231 | 29 | 32 | 31 | 23 | 54 | 29 | 28 | 29 | 29 |
| ±14 | 200 | 22 | 24 | 23 | 18 | 34 | 22 | 21 | 22 | 22 |
| ±15 | 175 | 17 | 18 | 18 | 14 | 27 | 17 | 17 | 17 | 17 |
| ±16 | 154 | 13 | 14 | 14 | 11 | 20 | 13 | 13 | 13 | 13 |
| ±17 | 137 | 10 | 11 | 11 | 9 | 15 | 10 | 10 | 10 | 10 |
| ±18 | 122 | 8 | 9 | 9 | 7 | 11 | 8 | 8 | 8 | 8 |
| ±19 | 110 | 7 | 7 | 7 | 6 | 9 | 7 | 7 | 7 | 7 |
| ±20 | 99 | 6 | 6 | 6 | 5 | 8 | 6 | 6 | 6 | 6 |
| HW | 4 | 4 | 5.9 | 5.3 | | 5.0 | 4.3 | 5.5 | 4.2 | 4.7 |

[a] Columns a g are calculated with the following coefficients from the modified Lorentz curve ML (HW are the half widths of the current profiles):
a Sliding average over 5 points: (1 1 1 1 1)/5.
b Triangular average over 5 points ( twice sliding average over 3 p.): (1 2 3 2 1)/9.
c Rate meter simulation: implicit:$y_n$ $(y_n + y_{n-1})/2$ explicit.: $(1/2^{n+1}$. 1/8 1/4 1/2 0 0.0).
d Savitzky Golay filter with 5 points: ( 3 12 17 12 3)/35.
e Savitzky Golay filter with 9 points: ( 21 14 39 54 59 54 39 14 21)/231.
f Low pass filter, 5 points: ( 1 4 10 4 1)/16.
g Low pass filter, 9 points: ( 1 2 4 18 26 18 4 2 1)/64.

For even greater angles, which are measured only rarely, the exact formula: $2\theta(K\alpha_1) = 2\arcsin\{\sin[\theta(K\alpha_2)].\lambda(K\alpha_1)/\lambda(K\alpha_2)\}$ must be used (exact and approximated values in Table 4.5).

Ladell *et al.* (1975)[11] have calculated for the 234-reflection of quartz (at $2\theta = 153^\circ$) the convolution function, which must be applied to the measured $K\alpha_1$-peak to obtain the $K\alpha_2$-peak (Figure 4.7). Because of the somewhat greater half-width of the $K\alpha_2$-peak this convolution is not a simple δ-function at $\lambda\alpha_2/\lambda\alpha_1$, but besides a rather sharp convolution peak at 1.0024536 (experimental value negligibly smaller than the value calculated from tabulated wavelengths) less sharp satellites appear to the left and to the right, which

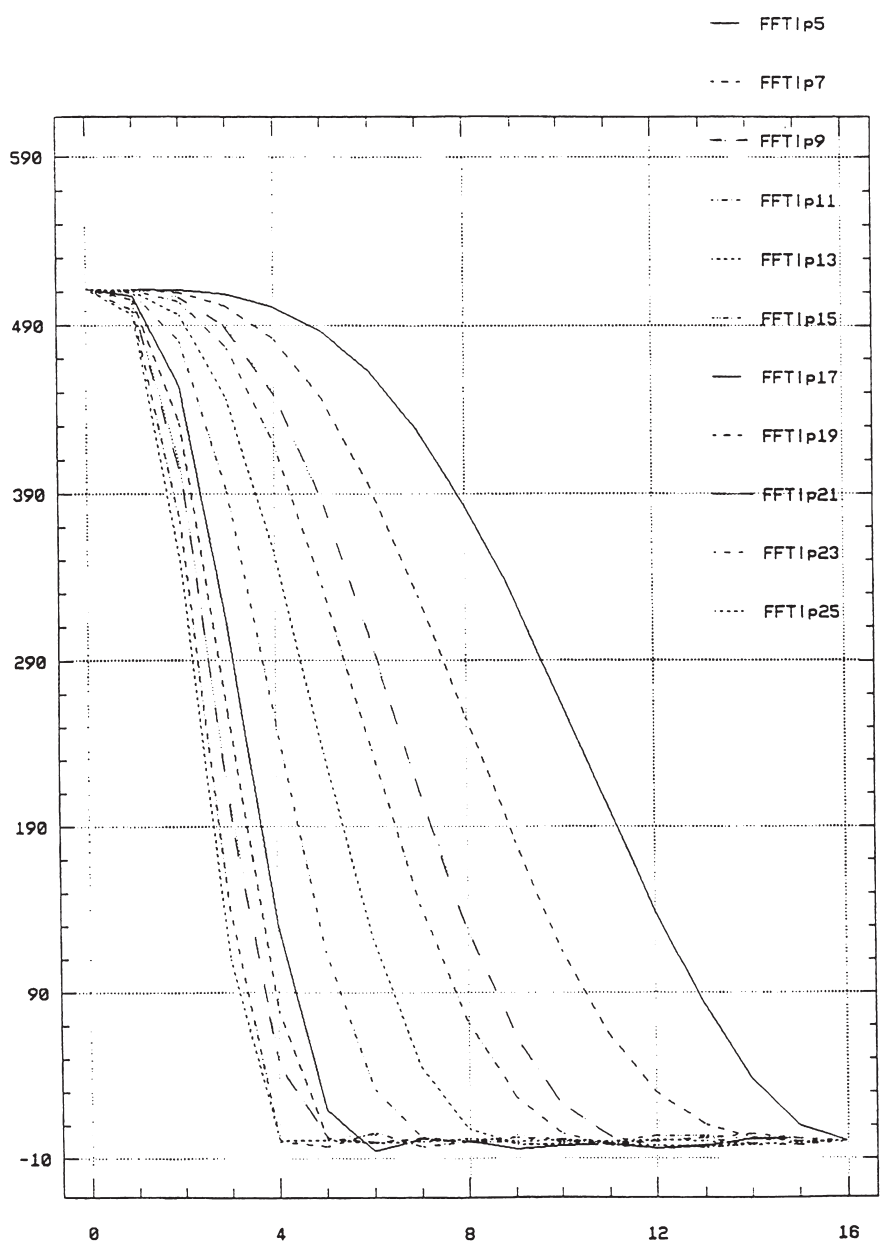



**Figure 4.6** Fourier transforms of the cited low pass filters through 5 25 points. For 5 and 7 points the filters are monotonous (no oscillation below 0). For such filters the original curve can be recalculated out of the smoothed one.

**Table 4.5** $K\alpha_1/K\alpha_2$-Splitting for CuK$\alpha$-radiation.

| *2θ (Kα₂) (°)* | *Δ2θ (°)* | *Approx. (°)* | *2θ(Kα₂) (°)* | *Δ2θ (°)* | *Approx. (°)* |
|---|---|---|---|---|---|
| 20 | 0.050 | 0.050 | 120 | 0.489 | 0.491 |
| 40 | 0.103 | 0.103 | 140 | 0.772 | 0.779 |
| 60 | 0.164 | 0.164 | 160 | 1.548 | 1.608 |
| 80 | 0.238 | 0.238 | 170 | 2.839 | 3.240 |
| 100 | 0.337 | 0.338 | 180 | 8.062 | $\infty$ |

together possess about the same area as the central peak. Therefore, within the amplitude domain the real $\alpha_2$-wavelength must be supplemented by three pseudo-wavelengths (or even more). The approximation with three wavelengths, however, is sufficient in practice. Table 4.6 lists the corresponding wavelengths-ratios and weights. Beside the original data the sum of the weights was standardized also to 0.5 (other authors use even smaller values of 0.49 or 0.48).

R. Kužel,[12] Prague, uses in his profile fitting program DIFPATAN corresponding values for Co- und Cr-radiation [given as $\lambda\alpha_2/\lambda\alpha_1$ (weight)]:

Co : 1.0020914 (0.18162568), 1.0021705 (0.20707717), 1.0022506 (0.1974514)

Cr : 1.0014772 (0.15847990), 1.0017061 (0.23304335), 1.0018215 (0.21635673)

As an approximation these values are used to interpolate values for Fe:

Fe : 1.0019560 (0.17724375), 1.0020351 (0.21573256), 1.0021152 (0.20061567).

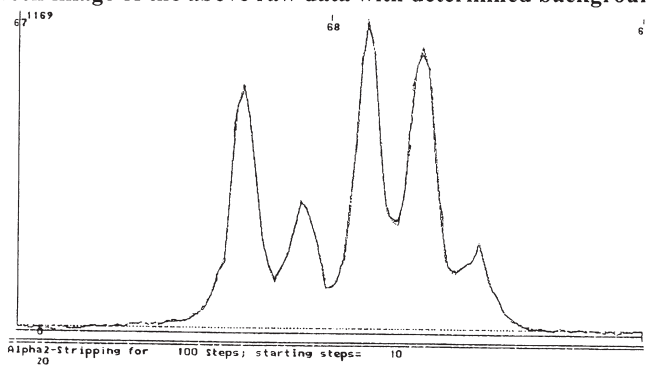
In practice, $\alpha_2$-stripping runs like opening a zipper. One starts at the low end and assumes for the first few base points within the splitting range (minor at small $2\theta$), that 2/3 of the corresponding count numbers belong to $\alpha_1$ and 1/3 to $\alpha_2$ [possibly slightly modified, if $I(\alpha_1)/I(\alpha_2)$ differs from 2.0]. For all following points the $\alpha_2$-part at the first non-stripped position $2\theta(\alpha_2)$ can be calculated from the already $\alpha_2$-stripped pure $\alpha_1$-values of the preceding points. The correct positions $2\theta(\alpha_1)$ can be obtained by the above formulas (exactly or approximated) for all three wavelengths.

These $\alpha_1$-positions fall into the already stripped range, mostly between two base points, and the corresponding $\alpha_1$-intensities must be (linearly) interpolated and multiplied with the above weights. So for each of the three wavelengths one gets the $\alpha_2$-part to be subtracted from the original count number at the position $2\theta(\alpha_2)$. Then the next unstripped point is to be cleaned and so on until the very last measured point is stripped too. Because for every raw data point one has to calculate one sinus [of $\theta(\alpha_2)$] and three arcsine-values [of $\theta(\alpha_1)$], this stripping procedure takes some time and a floating-point coprocessor is highly recommended. If the given approximation is used, only one trigonometric function must be calculated per step [the error at $2\theta = 150^\circ$ amounts to $0.018^\circ$ for the calculated $\theta(\alpha_1)$].

**Printout of raw data file quartz2.raw**

```
test quint
   100    67.000    69.000      2.00     1
 67.00 16 16 14 18 18 13 6 20 14 15
 67.20 13 19 23 19 24 22 29 20 31 31
 67.40 36 29 34 31 44 48 45 48 70 69
 67.60 114 148 234 283 583 835 930 790 557 348
 67.80 252 194 236 290 383 493 456 387 288 173
 68.00 173 205 262 468 684 987 1169 1043 678 455
 68.20 415 404 514 778 985 1071 976 650 410 250
 68.40 225 250 263 274 345 262 183 140 87 57
 68.60 49 30 31 25 29 22 17 28 21 17
 68.80 25 17 19 16 13 21 12 18 17 20
 69.00 19
```

**Screen image of the above raw data with determined background**




**Printout of the worked pattern with 2nd derivative and peak positions**

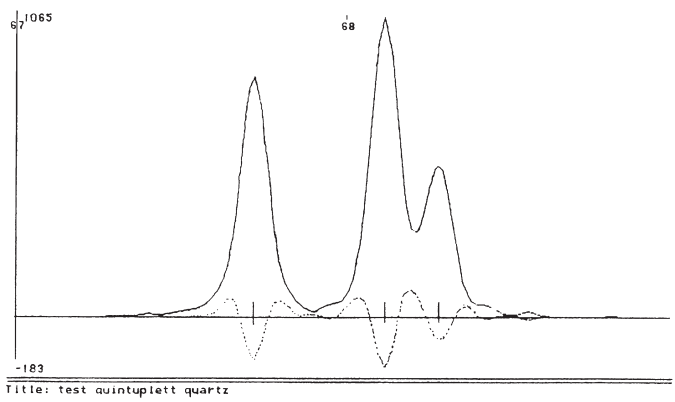



**Figure 4.7** Example of the $K\alpha_2$ stripping for the quartz quintuplet (3 $\alpha_1/\alpha_2$ doublets) at $2\theta = 68°$. Top: list of raw data (count numbers for 0.02° step width). Middle: unsmoothened pattern with constructed background. Bottom: result of $K\alpha_2$ stripping, background subtraction and 5 point smoothing. Also drawn is the 2nd derivative, which was used for the peak search (found positions indicated).

**Table 4.6** Wavelength-ratios and weights for convolution functions $\alpha_1 \rightarrow \alpha_2$ after Ladell *et al.* (1975)[11] for CuK$\alpha$-radiation. Beside the original weights, also weights with a sum of 0.5 are reported.

| $\lambda\alpha_2/\lambda\alpha_1$ | *Weight (orig.)* | *Weight (sum 0.5)* |
|---|---|---|
| 1.00235350 | 0.15276646 | 0.1436781 |
| 1.00245360 | 0.2686876 | 0.2527031 |
| 1.00257883 | 0.1101731 | 0.1036188 |
| $\Sigma$ | 0.53162716 | 0.5000000 |

If the weights are somewhat too large, overcompensation effects will occur. At the $\alpha_2$-position too much will be subtracted and just beyond the remaining $\alpha_1$-peaks negative values will give results that, physically, are nonsense. Such negative values should be raised by the evaluation program to a reasonable background value, at least to 0. For isolated reflections this, usually, causes no problems. For superimposed groups of reflections the overcompensation may be amplified from peak to peak. Mostly, a small reduction of the weight sum will help (*e.g.* from 0.50 to 0.48 or, if weak peaks remain at the $\alpha_2$-positions, to 0.52). Figure 4.7 shows the well-known quartz quintuplet at $2\theta = 68^\circ$ before and after $\alpha_2$-stripping (the three $\alpha_1/\alpha_2$-doublets 212, 203 und 301).

## 4.6 PEAK SEARCH ALGORITHMS

By eye, it is rather easy to identify even weak peaks that scarcely stand out from the background, because our brain processes a wider range simultaneously. For digitally stored powder patterns only individual measurements exist, which are to be compared with the counting rates of adjacent points. First, one needs the decision as to whether a measured point belongs to the background or to a reflection range. If a step rate and its direct neighbors lie significantly above the background curve it belongs to a reflection range. Differences to the background are to be considered as "significant" if they surpass 2–3$\sigma$ (background) with $\sigma(\text{background}) = \sqrt{(\text{uncorrected background})}$. Only if 3 and more adjacent points surpass this threshold is it reasonable to begin with one of the following peak search procedures for that range. Another possible threshold is a certain fraction (*e.g.* 0.5%) of the absolute maximum of the entire data file (neglecting outliers).

### 4.6.1 Trend-oriented Peak Search

In this method one scans the data file (mostly in direction of increasing $2\theta$) until three adjacent points lie 2–3 $\sigma$ above the background, *i.e.* until one reaches the beginning slope of a reflection (*e.g.* for a mean background of about 25 pulses per step the counting rates must surpass 35–40 pulses). The following 2–3 points should have even greater rates (4–5 $\sigma$, ascent of slope). If this is true, one scans the following points until a local maximum is reached, *i.e.* until

a counting rate is greater than the average of the two following as well as that of the two preceding points. This local maximum can be taken as a first approximation of a reflection. Furthermore, this value should exceed a certain minimum (*e.g.* 0.5% of the global maximum of all points) to exclude accidental background ripples from the list of reflections.

The refinement of a preliminary peak position can easily be obtained by fitting a parabola $a + bx + cx^2$ into 5 (or more) points around the local maximum, using the solutions for a, b, and c after Savitzky and Golay.[3] The maximum of this parabola is the wanted refinement of the peak position and is calculated as the root of the 1st derivative: $y'(x_{max}) = 0 = b + 2c.x_{max}$. So far the 5-point appoximation one gets:

$$x_{max} = -b/2c = (2y_{2} + y_{1} - y_1 - 2y_2)/(2y_{2} - y_{1} - 2y_0 - y_1 + 2y_2) \cdot 7/10$$

(referred to the local maximum in $x_o$, $y_o$). Also the height of the maximum (in first approximation $y_o$) can be calculated by this approach: $y_{max} = a + b.x_{max} + c.x^2_{max}$. If one assumes a Lorentzian shape for a peak, the formulas from Chapter 4.6.3 can be applied.

As additional criterion for the acceptance of an X-ray reflection a certain minimal size of the 2nd derivative can be used (denominator in the above-mentioned equation $< 0$, *e.g.* $2c < -1$ or $-2$). This is certainly necessary to avoid a possible division by 0. The points following a maximum must be discarded as further peaks as long as the 1st derivative stays negative, *i.e.* as one remains in the decreasing slope.

After peak recognition both flanks are searched for the half height (above background, possibly by interpolation) and the difference of the corresponding $x$-values is taken as full width at half maximum of this peak (FWHM, short: half-width). This difference should surpass a certain threshold (*e.g.* 0.06° in $2\theta$) to accept a found elevation above background as a true reflection. Thus, one has a further possibility at this point to eliminate possible outliers because they cause much narrower ''peaks'' than real reflections.

The right and left half-widths of a peak should not differ too greatly. If one half-width is greater than 1.5 or 2-times the other, there probably exists a shoulder, *i.e.* a superimposition with a weaker reflection without an individual local maximum. In such a case the half-width estimated by the half-heights on both flanks systematically becomes too large and should be corrected using the smaller of both half-widths only (which hopefully is not affected by a shoulder).

Shoulders cannot be recognized as separate reflections by this method, but only peaks with individual local maxima in the pattern (roots of the 1st derivative).

In the case of a missing $K\alpha_2$-elimination the list of reflections must be checked for the possibility of $\alpha_1/\alpha_2$-split peaks before the list can be stored or printed. If a $d$-value, which at first was calculated with $\lambda(K\alpha_1)$, is smaller by about the factor $\lambda(K\alpha_2)/\lambda(K\alpha_1)$ ($=1.00248 \pm$ tolerance $\approx 0.0004$ for CuK$\alpha$) and its intensity amounts to about the half (*e.g.* 25–75%) of that of the preceding peak, so it is very probably the $K\alpha_2$-twin of that stronger $K\alpha_1$-peak, the $d$-value

should be recalculated with $\lambda(K\alpha_2)$. Both *d*-values for $K\alpha_1$ and $K\alpha_2$ of the same reflection should be equal in the range of the statistical uncertainty.

### 4.6.2 Peak Search by Second Derivatives

The roots (zeroes) of the 2nd derivative correspond to the points of inflection and for the central part of a peak between these points the 2nd derivative is negative with a sharp minimum at the position of the peak maximum (for asymmetric peaks the minimum is shifted into the direction of the steeper slope). For Gaussian as well as for Lorentzian shaped peaks (see Section E.2.6) as limiting shapes of a X-ray peak the half-widths of the minima of the 2nd derivative are about half as wide as the half-widths of the peaks themselves (theoretically 53% for Gaussian and 33% for Lorentzian peaks), *i.e.* the resolution of the 2nd derivative is twice as good (and better) as that of the original pattern itself (Figure 4.8). Shoulders in the original pattern possess their own minima in the second derivative and so can get their own and

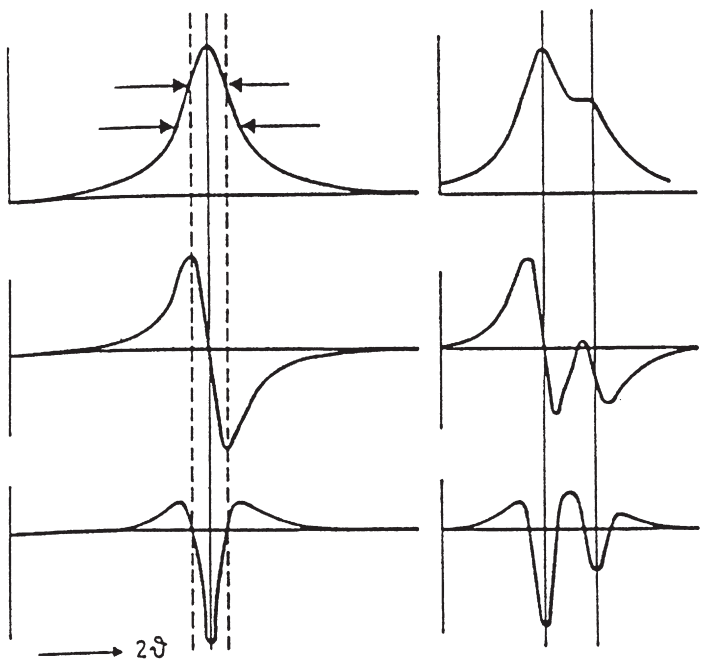



**Figure 4.8** Left: A simple Lorentz peak with its 1st (middle) and 2nd derivative (bottom). Dotted lines indicate the positions of the points of inflection, whose distance is narrower than that of the half heights (lower arrows). Right: A double peak with the weaker one only showing up as shoulder. In the 2nd derivative both reflections are clearly separated (after Schreiner and Jenkins, 1980).

unambiguous reflection position. The numerical calculation of the 2nd derivative occurs by sliding polynomials (see Section E.4.1).

A disadvantage of the 2nd derivative is the considerable enhancement of noise. Numerical derivatives are calculated *via* differences and every difference has a greater relative error than its both constituents since $\sigma^2(\text{A–B}) = \sigma^2(\text{A}) + \sigma^2(\text{B})$. Therefore, the applicability of this method asks for certain minimal counting numbers for the individual reflections (Figure 4.9). According to an estimation of Naidu and Houska (1982)[13] these counting numbers should surpass $10^4$ per reflection (if smoothed, otherwise even more), but in practice total counting numbers of $10^3$ above background (and even less per reflection) turned out to be sufficient. Very weak reflections ($< 1\%$ of the strongest) are poorly recognized by this method and after the end of an automatic peak search the weak reflections should be checked visually.

Because of the deterioration of the signal/noise ratio the reproducibility of the minimum positions within the 2nd derivative are somewhat worse than those of the roots of the 1st derivative. For asymmetric peaks the minimum of a 2nd derivative is shifted in the direction of the narrow flank (Figure 4.7). Therefore, for isolated reflections the root of the 1st derivative (maximum of peak) should be calculated and preferred, after a preliminary position has been obtained from the minima of the 2nd derivative. For shoulders without a local

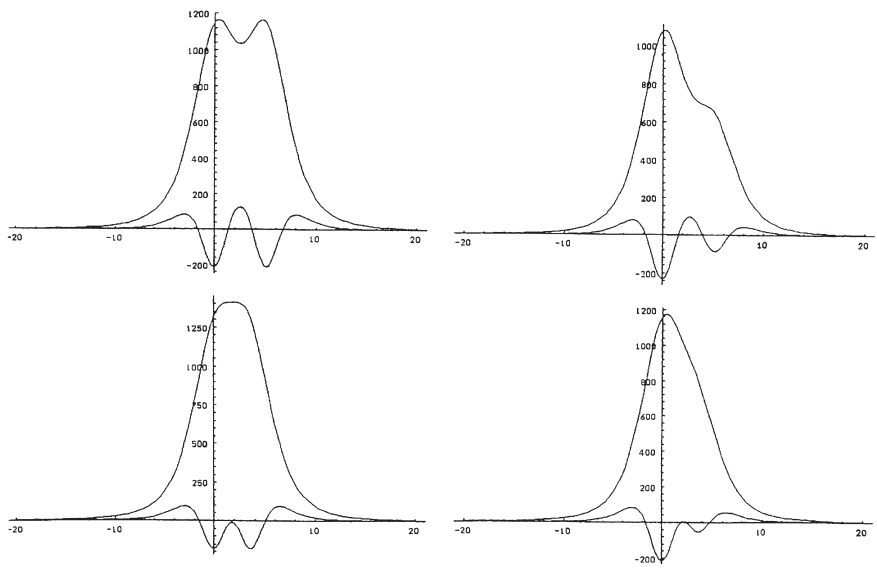



**Figure 4.9** Superimpositions of two modified Lorentz peaks (ML) of equal FWHM ($\approx 5$). Left: Both peaks of equal height (1000). Right: Second peak only half as high as the first (1000, resp. 500). Top: Distance of both peak positions = 5 (=1 FWHM). Bottom: Distance = 3.5 (0.7 FWHM). In every case the minima of the 2nd derivatives are clearly separated and lie at the correct positions.

maximum (*i.e.* without a zero of the 1st derivative) the preliminary position from the 2nd derivative has to be taken as the final result.

An advantage of the peak search by 2nd derivatives is its insensitivity to a linearly decreasing or increasing background, which will not shift the minimum position (Figure 4.10). Because the slope of a stronger peak can be taken in first approximation as a linear background for an adjacent weak reflection, the minimum corresponding to a shoulder represents rather accurately the position of a weak peak, whereas the peaks themselves are shifted in a direction towards the strong adjacent peak. In theory, the maxima of the 4th derivative exhibit even better resolution, but, practically, the noise is enhanced so strongly that nothing can be seen with normal counting rates.

The peak search by 2nd derivatives represents a kind of sharpening (deconvolution), *i.e.* a division by the Fourier transform of a certain peak shape in the frequency domain. This is possible only if this Fourier transform has no zeroes, *i.e.* if it monotonically approaches zero. Bromba and Ziegler (1984)[7d] report such an algorithm, but its usability for X-ray patterns was not proved until now.

The 2nd derivative can also be used for the estimation of half-widths by looking for its zeroes at both sides of a minimum. These correspond to the points of inflexion. As they are placed somewhat higher than the points of half heights (in 61% of the height of Gaussian peaks and in 75% of Lorentzian peaks) the distances between both zeroes are smaller than the half widths (for Gaussian peaks 85% of FWHM, and for Lorentzian peaks 58%). In practice,

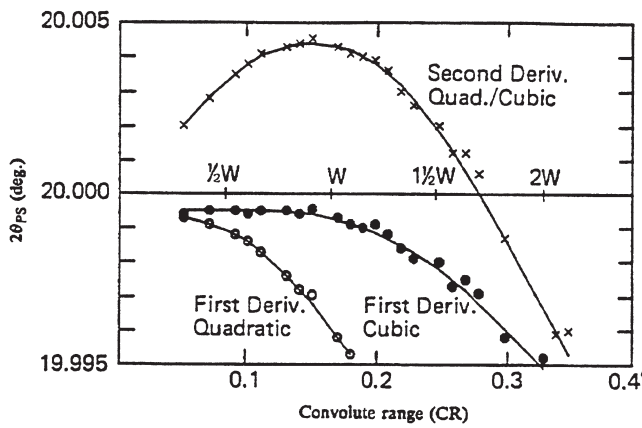



**Figure 4.10** Error in the determination of the position of a simulated, asymmetrical reflection (without noise) at $2\theta = 20°$ and with 0.17° half width (W). Top: With minimum of 2nd derivative calculated with a polynomial of 2nd/3rd order. Middle: With zero of the 1st derivative calculated with a polynomial of 3rd/4th. order (best result as long as the filter width does not appreciably surpass the half width) Bottom: With zero of 1st derivative with a polynomial of 1st/2nd order. (After Huang, 1988,[28] or Huang and Parrish, 1984.[29])

adding 25% to the distance between both zeroes of a 2nd derivative gives a good estimation of FWHM undisturbed by shoulders.

### 4.6.3 Peak Search with a Predefined Peak Shape

The advantage of X-ray powder patterns over other spectra is the roughly common shape of the individual reflections (equal half width and equal shape of the flanks). Therefore, one can use peak search methods that presume a special peak shape. Sánchez (1991)[14] reports a peak search algorithm for Gaussian peaks with an average half width 2D. This method can be easily adapted for Lorentzian peaks ($y = A/[1 + ((x-\mu)/b)^2]$ with FWHM $= 2b$) or Pearson-VII peaks ($y = A/[1 + ((x-\mu)/b)^2]^m$ with FWHM $= 2b \cdot \sqrt{(\sqrt[m]{2}-1)}$). X-ray peaks very often exhibit a peak shape with $m$ between 1.5 and 2.

To scan the pattern for peaks one uses three equally spaced points $x_i$,$y_i$ ($i = 1,2,3$) with distances $x_2 - x_1 = x_3 - x_2 = D$, with D about equal to half the FWHM. The width D should include several steps (at least $n = 3$). That means that a step width of $0.02^\circ$ in $2\theta$, which is sufficient for most other methods, possibly must be reduced to $0.01^\circ$. The $y_i$ are heights above background, *i.e.* before the application of this method the background should be subtracted and the remaining pattern smoothed.

These three points $x_i$, $y_i$ are shifted like a sensor along the pattern. If all three points are placed significantly above the background ($\approx 2\sigma$) and if the central value is greater than the edge values $y_1$ and $y_3$, than this sensor is probably placed within a reflection range. This condition, $y_2 > y_1$, $y_3$, must hold for about $n$ adjacent points and the middle of this range corresponds approximately to the wanted peak position. For a more exact estimation of the peak position $\mu$, the peak height A and the half width 2b, the following formulae are used, into which the intermediate parameters $\alpha_{ik} = (y_i/y_k) - 1$ are introduced (resp. $\alpha_{ik} = \sqrt[m]{(y_i/y_k)} - 1$ for Pearson VII). In the central range of a reflection the parameters $\alpha_{21}$ and $\alpha_{23}$ are positive. As a first approximation of the peak position, $x_2$ and $y_2$ shall be placed at the local maximum of the smoothed pattern. For the exact peak parameters then the following formulas are to be used:

$$\mu = x_2 + D/2 \cdot (\alpha_{21} - \alpha_{23})/(\alpha_{21} + \alpha_{23}),\ b^2 = 2D^2/(\alpha_{21} + \alpha_{23}) - (x_2 - \mu)^2$$

$$\begin{aligned} A &= y_2 + y_2 \cdot [(x_2 - \mu)/b]^2, \text{ resp. (for Pearson VII) } A \\ &= y_2 \cdot [1 + ((x_2 - \mu)/b)^2]^m. \end{aligned}$$

Also, this method does not allow the recognition of shoulders, but of real local maxima only. If, especially for large step widths, a maximum is placed just between two grid points, the measured counting rates at both points will be smaller by several percent than the (unmeasured) maximum itself. Using the above formula for A permits a rather accurate estimation of the unknown peak height.

Reich (1987)[15] used the KNN (*k*-nearest-neighbors) algorithm to recognize similar ranges (*i.e.* peaks) by sliding a presumed peak shape along a measured pattern. As a measure for the distance in a *k*-dimensional space (corresponding to the *k* pairs of values to be compared) for instance, the correlation coefficient between the *k* values of the presumed standard peak and *k* adjacent counting rates of the pattern can be used. The regions with the greatest correlation coefficients ($>0.95$) correspond to the wanted peak positions.

## 4.7 PROFILE FITTING AND PROFILE SHAPE FUNCTIONS

A completely different approach represents the method of profile fitting in which mathematically simple functions are declared for the individual reflections (profile shape functions = PSF, see Howard and Preston, 1989) (Figure 4.11).[16] In this method the reflections are no longer defined by only 2 or 3 parameters (peak position, height and half width), but all approximately 20–40 grid points within one reflection are to be fitted by the model shape using the method of least squares (or more robust variations of it like the Marquardt method, 1963[31]). Therefore, a prior smoothing is not necessary and may even be contradictory. A preceding background subtraction is harmless, provided not too many reflections overlap so that the proper background is not reached

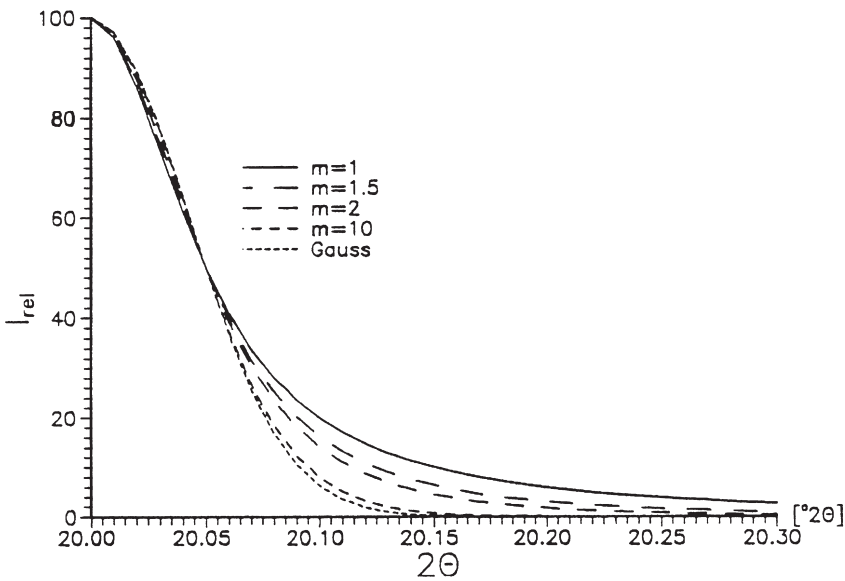



**Figure 4.11** A series of Pearson VII profiles with equal peak position, peak height, and half width, but with different slope shapes (given by the exponent *m*), and area. For $m=1$: Lorentzian (L), $m=1.5$: intermediate Lorentzian (IL), $m=2$: modified Lorentzian (ML). Already with $m=10$ a Gaussian is approximated (exact at $m=\infty$). X ray peaks mostly exhibit *m* values between 1.5 and 2. (After Howard and Preston, 1989.[16])

at all for wide ranges. An $\alpha_2$-stripping is superfluous, as it needs rather no extra effort to construct a profile shape function for a doublet $K\alpha_1 + K\alpha_2$ instead of a pure $\kappa\alpha_1$-function. The parameters for the $K\alpha_2$-peak are derived from those of the corresponding $K\alpha_1$-peak and no additional parameters are necessary to construct the doublet.

The PSF itself is defined by 3–4 parameters: the peak position $2\theta_k$ or $\mu_k$, the peak height $y_{ok}$ (above background) or the integral intensity $I_k$, and the half width $FWHM = HW_k$. Important are the widths of the flanks, which for X-ray peaks are appreciably wider than for a Gaussian peak (normal distribution), and whose size changes slightly with $2\theta$. Moreover, without a preceding background subtraction the background must be estimated, which for a small angular range (under one reflection) can be taken as constant. For wider ranges the background is fitted by a polynomial of 1st to 3rd order.

The particular strength of profile fitting turns out to be for regions with overlapping reflections (Figure 4.12). Presuming a certain peak shape, which must be derived from the non-overlapping reflections of the same pattern, the background can be estimated when the background is not accessed at any point. Certainly there exists a strong correlation between background and peak shape, and by that both entities cannot be refined simultaneously. A too high background inevitably cuts wide slopes. By that the peaks seem to be not only less high but narrower too (greater $m$) and the integral intensities are estimated too low.

Mainly Gaussian and Lorentzian profile shape functions, and intermediates between these two shapes, are used. The following functions are all

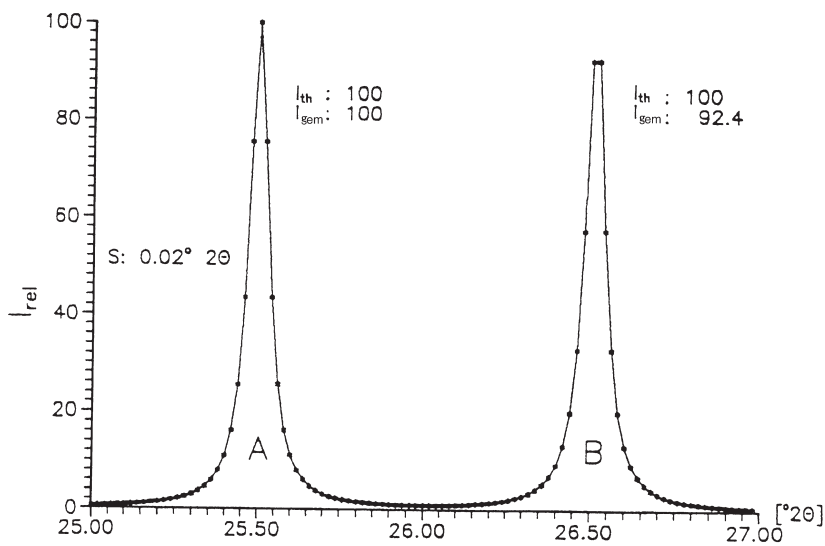



**Figure 4.12** Without profile fitting the peaks A and B would get different heights. Thereby both peaks are equal, but for A the maximum falls onto a grid point, whereas for B just between two grid points. Using the formulas in 4.6.3 the height can be interpolated exactly. (After Kern, 1992.[17])

standardized to the same integral intensity (area) $I_k$. With the same half width $HW_k$ and same area a Lorentzian reaches only 68% of the peak height of a Gaussian because of its wider slopes. The peak position of the $k$th reflection is $2\theta_k$, $i$ is the running number of the grid point and $\delta_{ik} = (2\theta_i - 2\theta_k) \cdot 2/HW_k$ is used as an auxiliary parameter. With three parameters ($2\theta_k$, $HW_k$ and $I_k$) the following expressions are obtained for $y_{ik}$ (elevation above background for the $k$th reflection at grid point $i$, peak maximum at position $2\theta_k = I_{max},k$):

Gaussian (G):

$$y_{ik} = I_k/HW_k \cdot 2\sqrt{(\ln 2)}/\sqrt{\pi} \cdot \exp[-\ln 2 \cdot \delta_{ik}^2], \ldots 2\sqrt{(\ln 2)}/\sqrt{\pi} = 0.939$$

Lorentzian (L):

$$y_{ik} = I_k/HW_k \cdot 2/\pi \cdot [1 + \delta_{ik}^2]^{\ 1}, \ldots 2/\pi = 0.637$$

Intermediate Lorentzian (IL):

$$y_{ik} = I_k/HW_k \cdot \sqrt{(2^{2/3} - 1)} \cdot [1 + (2^{2/3} - 1)\delta_{ik}^2]^{\ 1.5}, \ldots \sqrt{(2^{2/3} - 1)} = 0.766$$

Modified Lorentzian (ML):

$$y_{ik} = I_k/HW_k \cdot 4\sqrt{(\sqrt{2} - 1)}/\pi \cdot [1 + (\sqrt{2} - 1)\delta_{ik}^2]^{\ 2}, \ldots 4\sqrt{(\sqrt{2} - 1)}/\pi = 0.819.$$

The area $I_k$ of a reflection (integral intensity) is obtained by $I_k = I_{max,k} \cdot HW_k/\text{norm}$ (the norm values are given with the above formulas and range from 0.637 to 0.939). Within one pattern with similar peak shapes relative integral intensities can approximately be calculated by the simple product $I_{max,k} \cdot HW_k$.

IL and ML represent already hybrid functions between G and L and simulate rather well the shape of a symmetrical X-ray reflection. If a variable slope width is introduced as a 4th parameter one gets the two following, widely used peak shape functions:

Pseudo-Voigt (PV) (Table 4.7b): With mixing parameter $w$ (or individual $w_k$):

$$y_{ik} = w \cdot L_{ik} + (1 - w) \cdot G_{ik}$$

Pearson VII (P7) (Table 4.7a): With shape exponent m (or individual $m_k$):

$$y_{ik} = I_k/HW_k \cdot 2\sqrt{(2^{1/m} - 1)}/\sqrt{\pi} \cdot \Gamma(m)/\Gamma(m - 1/2) \cdot [1 + (2^{1/m} - 1)\delta_{ik}^2]^{\ m}.$$

The pseudo-Voigt function is the weighted mean between a Lorentzian and a Gaussian. For this function the common factor $I_k/HW_k$ of L and G can be factored out, *i.e.* neither the area $I_k$ nor the halfwidth $HW_k$ will change with a change of the mixing factor $w_k$. L, IL, ML and G are special cases of the Pearson-VII function with $m = 1$, 1.5, 2 and $\infty$ (but with $m = 20$ a Gaussian is approximated already rather accurately). For equal area and half width the maximum of a Gaussian is 48% higher than that of a Lorentzian. The complicated and computationally time-consuming Voigt-function is the convolution of a Gaussian with a Lorentzian.

**Table 4.7** (a) Shape of flanks of a Pearson-VII-peak in relation to the slope parameter (shape exponent) $m$. Peak height = 1. By definition the elevation at $\pm HW_k/2$ away from the maximum drops to 0.5. (b) Shape of flanks of a pseudo-Voigt-peak in relation to the mixing parameter $w$ ($w = 1$: pure Lorentzian, $w = 0$: pure Gaussian).

| *(a)* | | | | *Distance* $\lvert 2\theta_i \quad 2\theta_k \rvert$ *as multiple of* $HW_k$ | | |
|---|---|---|---|---|---|---|
| $m$ | 0.5 | 1 | 1.5 | 2 | 2.5 | 3 |
| 1 | 0.5 | 0.2000 | 0.1000 | 0.0588 | 0.0385 | 0.0270 |
| 1.5 | 0.5 | 0.1631 | 0.0634 | 0.0298 | 0.0161 | 0.0096 |
| 2 | 0.5 | 0.1417 | 0.0447 | 0.0172 | 0.0078 | 0.0039 |
| 3 | 0.5 | 0.1178 | 0.0269 | 0.0073 | 0.0024 | 0.0009 |
| 6 | 0.5 | 0.0914 | 0.0116 | 0.0015 | 0.0002 | 0.0000 |
| $\infty$ | 0.5 | 0.0625 | 0.0027 | 0.0000 | | |
| *(b)* | | | | *Distance* $\lvert 2\theta_i \quad 2\theta_k \rvert$ *as multiple of* $HW_k$ | | |
| $w$ | 0.5 | 1 | 1.5 | 2 | 2.5 | 3 |
| 1.0 | 0.5 | 0.2000 | 0.1000 | 0.0588 | 0.0385 | 0.0270 |
| 0.7 | 0.5 | 0.1467 | 0.0620 | 0.0360 | 0.0236 | 0.0165 |
| 0.4 | 0.5 | 0.1053 | 0.0325 | 0.0183 | 0.0120 | 0.0084 |
| 0.1 | 0.5 | 0.0722 | 0.0088 | 0.0041 | 0.0027 | 0.0019 |
| 0.0 | 0.5 | 0.0625 | 0.0027 | 0.0000 | | |

Of the functions with three parameters IL is best suited for X-ray reflections. For Rietveld analyses mostly the four-parameter pseudo-Voigt function is used, for pure profile fitting (without structure refinement) often the Pearson-VII function is also used.

It follows from the tables that for the usual X-ray reflections with $m \approx 1.5$ at least three half widths each at the right and left of a peak position must be taken into account before the slopes drop below 1% of the peak maximum, *i.e.* for a half width of 0.1–0.2° in $2\theta$ the slopes reach at least 0.3–0.6° to each side and for peak distances smaller than 0.6–1.2° the background line will not be reached at all between such reflections. For low-symmetry crystals such a dense peak sequence occurs rather soon after a few isolated reflections at low angles, and therefore a correct background fixation and subtraction becomes a problem (Figure 4.13).

Not all parameters must be refined for every reflection, but only the peak position and the peak height. The half widths $HW_k$ in the 0th approximation can be considered as constant. For laboratory X-ray sources, a certain tendency on $2\theta_k$ mostly is simulated after Cagliotti *et al.* (1958)[34] by the expression:

$$HW_k^2 = U \cdot \tan^2\theta_k + V \cdot \tan\theta_k + W$$

A similar approach can be applied to the shape parameter, *e.g.*: $m_k = a \cdot \theta_k^2 + b \cdot \theta_k + c$.

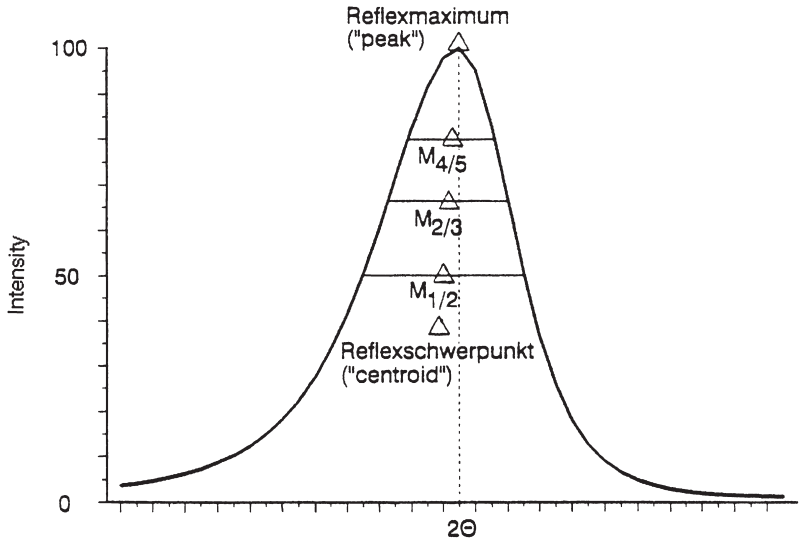



**Figure 4.13** For asymmetrical reflections the peak position depends on its definition. Mostly the position of the maximum (= zero of 1st derivative) is reported. The centers of the secants in 4/5, 2/3 and 1/2 peak height are shifted in direction of the wide flank, as does the centre of gravity (centroid). In contrast, the minimum of the 2nd derivative [not given, but see figure 4.17 (middle)] is shifted to the narrow flank. (After Kern, 1992.[17])

By doing so, instead of $k$ parameters for $HW_k$ (*i.e.* for each of $k$ reflections) only three parameters are to be refined. The same is true for the $m_k$. (See Figure 4.14 with a curve of the parameters of a split-Pearson-VII function *vs.* $2\theta$.)

The agreement between the observed values $y_{oi}$ and the calculated values $y_{ci}$ is described by the *residual* R resp. $R_w$, *i.e.* by the mean deviation, which mostly is reported in % (by multiplication with 100):

$$R = \Sigma_i |y_{oi} - y_{ci}| / \Sigma_i y_{oi}$$

$$R_w = \left[ \Sigma_i w_i (y_{oi} - y_{ci})^2 / \Sigma_i w_i (y_{oi})^2 \right]^{1/2}$$

The $R_w$ are the quantities that become minimized by the method of least squares. As weights $w_i$, at best, the reciprocal variances $1/\sigma^2$ of the measured values $y_{oi}$ are used. By the statistics of the counting process one obtains $wi = 1/\sigma^2(y_{oi}) = 1/y_{oi}$. By this weighting scheme the slope regions (and the background) become more important than the peaks themselves (with their high counting rates). Mostly the $R$-values after a successful fitting reach 10–20%, for good fittings even 2–10%. As expectation value for $R$ one can calculate:

$$R_{exp} = [(N - P)\Sigma_i (y_{oi})]^{1/2}$$

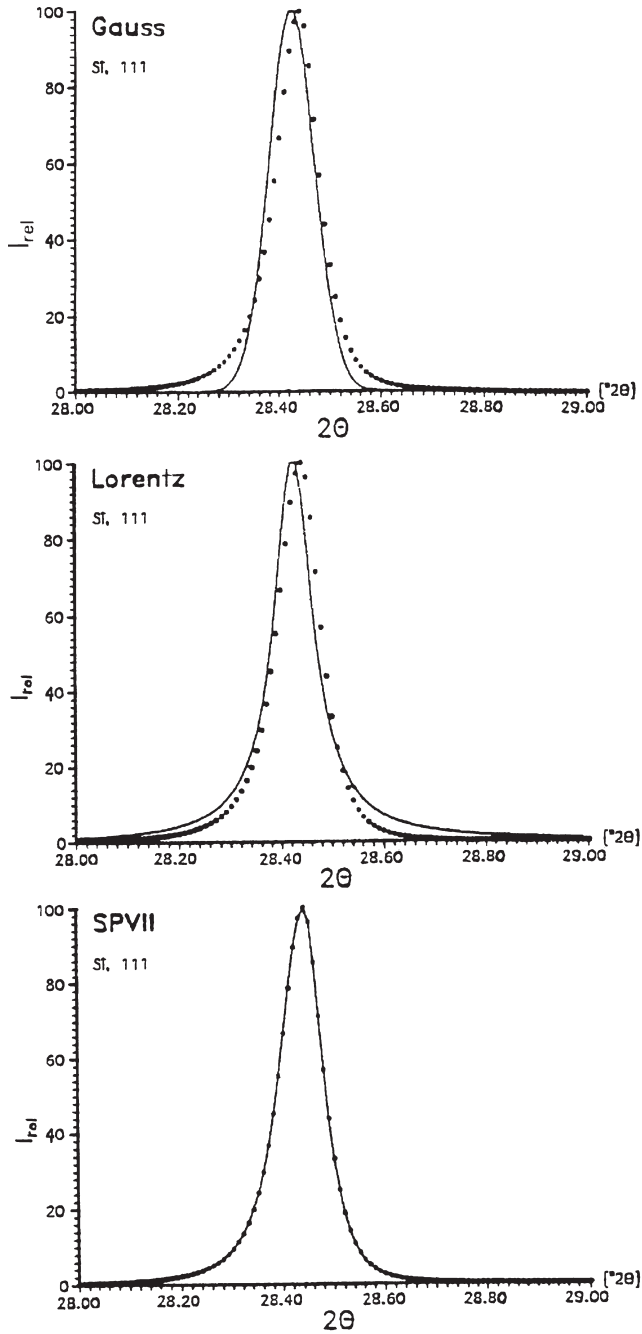



**Figure 4.14** Fitting of a measured, asymmetrical Si(111) reflection (points) by a Gaussian, a Lorentzian, and a split Pearson VII profile (full lines). Besides the not considered asymmetry (above and middle) the flanks above are too narrow (Gaussian) and in the middle too wide (Lorentzian. See also figure 4.17. (After Kern, 1992.[17])

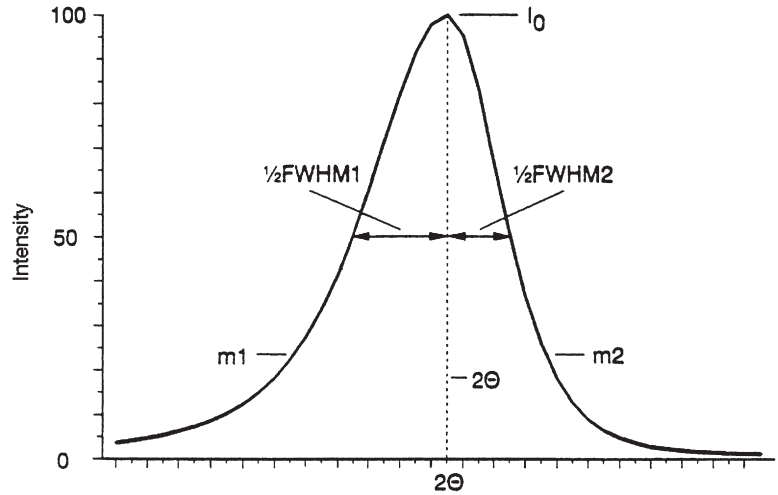



**Figure 4.15** Schematic representation of the split Pearson VII profile (SP7) with six parameters: common peak position $2\theta$ and peak height $I_o$, but separate half widths FWHM and slope parameters $m$ for the left and right peak moieties. (After Kern, 1992.[17])

with $N =$ number of grid points and $P =$ number of parameters to be varied. $R_{exp}$ approximately corresponds to (mean counting rate per step) $^{1/2}$, $\Sigma_i(y_{oi})$ is the total number of measured pulses. For a good refinement $R_w$ should not supersede $R_{exp}$ by a factor greater than 2 (Figure 4.15).

A complication is represented by the *asymmetry* of X-ray peaks, which mainly is caused by the axial divergence of the X-ray beam. By the installation of parallel Mo-sheets into the path of rays (Söller-slits) one tries to limit this divergence. Especially at low angles the flanks at the low side are distinctly wider than at the high side. Until about $2\theta = 90^\circ$ this asymmetry vanishes and at even greater angles a reverse asymmetry shows up. In this central $2\theta$-range the half width is least and increases to higher and lower angles (Figure 4.16).

A widely used method is the separate handling of the left and the right peak moieties (split-Pearson VII or SP7). The peak heights and positions are taken as identical for both halves, but for half widths and slope parameters separate parameter sets are used (*i.e.* two additional parameters per reflection, respectively parameter sets U,V,W and a,b,c for the left and right moieties each).

It was also attempted to use asymmetry parameters in closed, mathematical expressions. *e.g.* an asymmetrical pseudo-Voigt function with:

$$y_{ik} = w \cdot \mathrm{L_{ik}}(x - \delta) + (1 - w) \cdot \mathrm{G_{ik}}(x + \delta)$$

*i.e.* both curves L and G are slightly shifted against each other.

Rietveld (1969)[19] reported an asymmetry correction for neutron powder patterns (with Gaussians):

$$y_{ik,\mathrm{corr}} = y_{ik} \cdot [1 - P(2\theta_i - 2\theta_k)^2 \cdot \mathrm{sign}/\tan\theta_k]$$

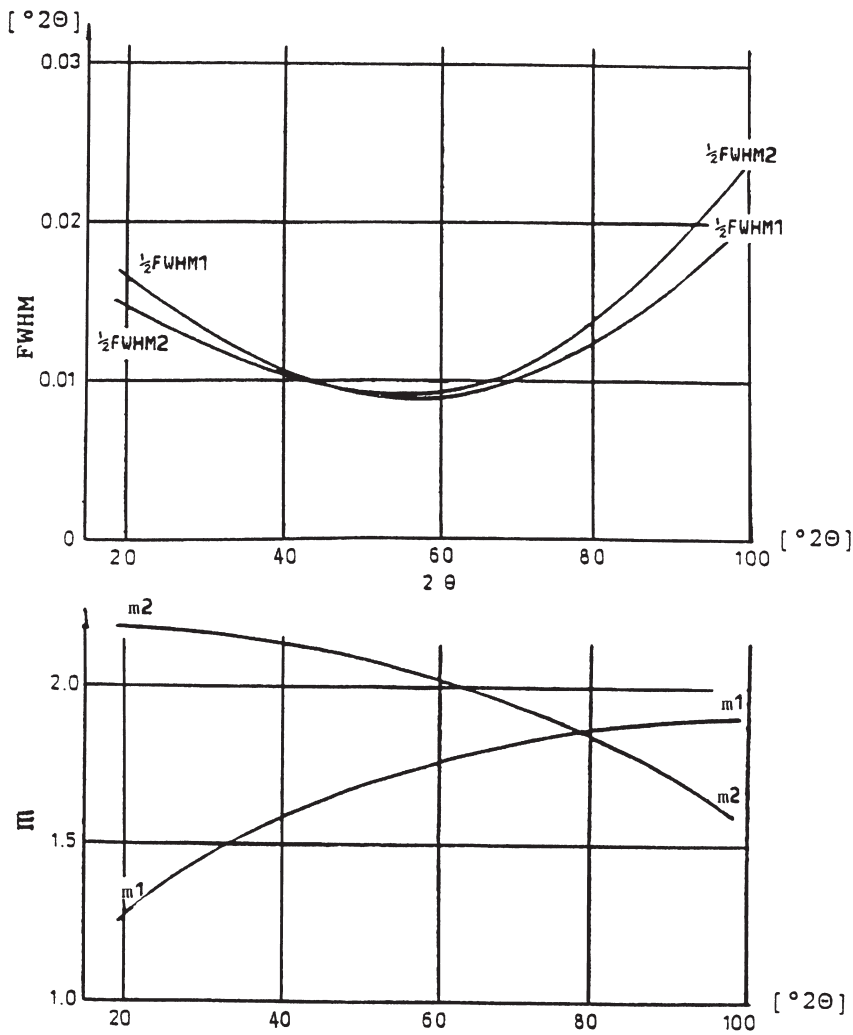



**Figure 4.16** Patterns of the changes of half widths (top) and of slope parameters $m$ (bottom) for split Pearson VII profiles (SP7), which were taken with a Guinier camera for a $PbNO_3$ sample. By such curves the number of profile parameters to be refined can appreciably be reduced (After Brown and Edmonds, 1980.[18])

with sign $= 1,0,-1$ depending on $(2\theta_i - 2\theta_k)$ being positive, 0 or negative. P is the asymmetry parameter to be fitted. The expression $P(2\theta_i - 2\theta_k)^2$ increases with the distance from $2\theta_k$. However, because a Gaussian approaches zero faster than any power goes to infinity, the given function will converge if $y_{ik}$ follows a Gaussian (which can be assumed for neutron patterns but not so for X-ray patterns). However, on the narrow slope this convergence to zero happens from the negative (physically wrong) side.

With an odd power of $(2\theta_i - 2\theta_k)$ one can avoid the unsteady expression sign$(2\theta_i - 2\theta_k)$. If by an asymmetry correction the maximum (*i.e.* the peak position) must not be shifted, the 1st derivative of the correction curve to be added must equal zero at the place of the maximum. The following correction fulfils these prerequisites (see Figure 4.17):

$$y_{ik,\mathrm{corr}} = y_{ik} \cdot [1 - \mathrm{P_k} \cdot (2\theta_i - 2\theta_k)^3 / [(\mathrm{HW_k}/2)^2 + (2\theta_i - 2\theta_k)^2]^{1.5}]$$

for

$$y_{ik} = I_{\max,k} / \{1 + [(2\theta_i - 2\theta_k)/(\mathrm{HW_k}/2)]^2\}^m$$

For not too asymmetrical reflections this one-parameter correction is sufficient and as good as the two-parameter correction of SP7. The amount added and the wide slope is subtracted on the narrow side, *i.e.* the integral intensity itself remains unchanged. The corrected curve remains positive, as long as $|\mathrm{P_k}| \leq 1$. Up to $|\mathrm{P_k}| = 2$, however, a slight sag of the narrow flank into negative values is tolerable.

Peak fitting is best done in two steps: at first symmetrical curves are fitted. Only after that does one try to determine the asymmetry parameters $\mathrm{P_k}$, if possible as a $2\theta_k$-dependent function (as for the $\mathrm{HW_k}$ and $\mathrm{m_k}$ or $\mathrm{w_k}$).

Lauterjung *et al.* (1985)[20] described a peak search program based on the profile fitting of groups of reflections (originally for Gaussians only), which in a modified form was used with success for the interpretation of the numerous samples from the German continental deep-drilling program (KTB).

## 4.8 DETECTION AND CORRECTION OF SYSTEMATIC ERRORS

As it is rather difficult to mathematically describe all possible errors that lead to shifts of peak positions during the measurement of a pattern, one tries to evaluate empirically the total error by measuring substances with known and very accurate lattice constants (standards) (Table 4.8). The measured $2\theta$-values $2\theta_{\mathrm{obs}}$ of these standards are compared with the known (tabulated or calculated) values $2\theta_{\mathrm{calc}}$. For that purpose the differences $\Delta 2\theta = 2\theta_{\mathrm{obs}} - 2\theta_{\mathrm{calc}}$ are plotted *versus* $2\theta_{\mathrm{obs}}$ and these points are to be approximated by a smooth curve, the *calibration curve*. As approximation functions, mostly polynomials of 0th–4th order are used. Equally well suited are cubic splines. Mathematically, polynomials can be extrapolated but in practice such extrapolations mostly render themselves as nonsense. This is especially true for higher orders (see Figure 4.19), and therefore the complete measuring range should be covered by reflections of the standard. Especially at low angles ($2\theta < 10^\circ$), the systematic errors pile up and the mathematical models are rather inadequate (see Figure 4.20). For the calculation of lattice constants the use of reflections below $10^\circ$ should be avoided (but for indexing they are very important).

The *calibration curve* is used to correct $2\theta$-values of a sample that was measured under the same conditions as the standard (external standard). Some errors, especially the sample position and the transparency error, differ from

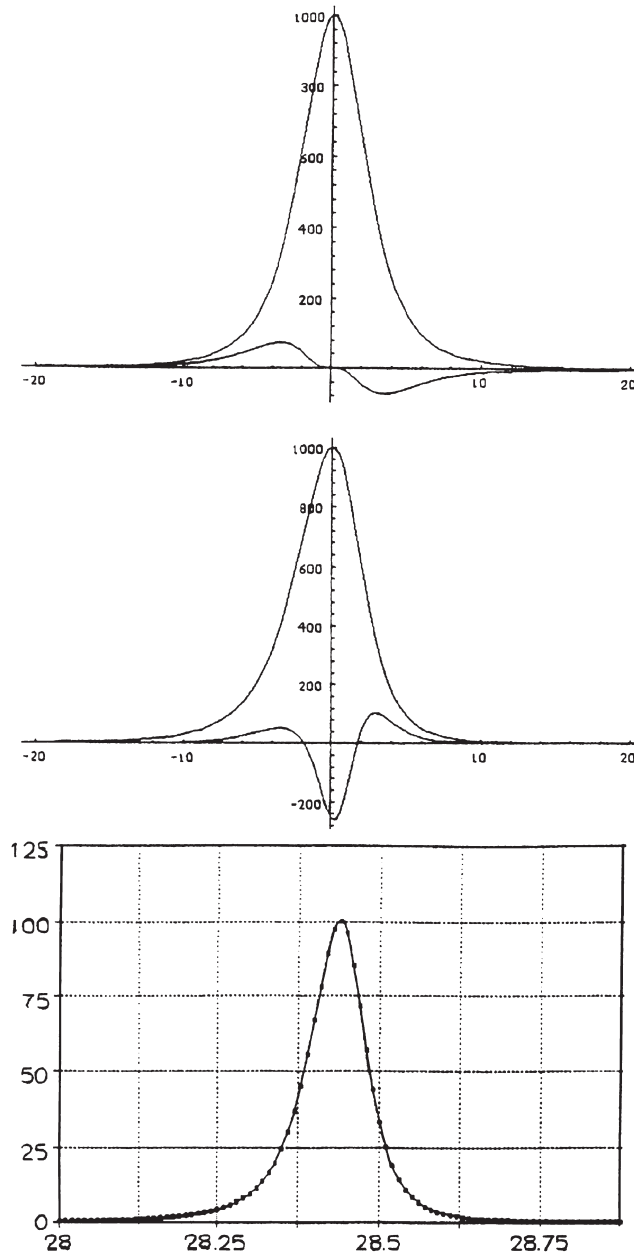



**Figure 4.17** Example for the one parameter asymmetry correction. Top: a symmetrical ML curve with the correction function added ($k = 0.8$). This is an odd function that does not change either the integral intensity or the peak height. Moreover the 1st derivate of the correction is zero at the central part. Thereby, also the peak position is kept unchanged. Middle: The sum of both curves yields an asymmetrical peak. The minimum of the 2nd derivative is slightly shifted to the narrow slope. Bottom: Application of the asymmetrical profile (in total five parameters) on the Si(111) reflection from Figure 4.14.

**Table 4.8** 2$\theta$-Values of the Si-standards at 25 °C measured with CuK$\alpha_1$-radiation ($\lambda = 1.5405981$ Å). $I_{rel,a}$: Sample stuffed from the side, $I_{rel,b}$: Sample firmly pressed from the front side into the sample holder. The 2θ-values for SRM 640 were calculated from the *d*-values of PDF 27-1402 (these and the very last value from the lattice constant). $2\theta_{obs}$ after Hubbard (1983)[21] for one of the 12 averaged samples.

| | *SRM640a* | *SRM640b* | | | *SRM 640* |
|---|---|---|---|---|---|
| *hkl* | $2\theta_{obs}$ | $2\theta_{calc}$ | $I_{rel,a}$ | $I_{rel,b}$ | $2\theta_{calc}$ |
| 111 | 28.425 | 28.442 | 100 | 100 | 28.443 |
| 220 | 47.299 | 47.303 | 55 | 64 | 47.303 |
| 311 | 56.124 | 56.122 | 30 | 34 | 56.123 |
| 400 | 69.128 | 69.130 | 6 | 8 | 69.131 |
| 331 | 76.382 | 76.376 | 11 | 12 | 76.377 |
| 422 | 88.030 | 88.030 | 12 | 16 | 88.032 |
| 511 | 94.951 | 94.953 | 6 | 8 | 94.954 |
| 440 | 106.710 | 106.709 | 3 | 5 | 106.710 |
| 531 | 114.098 | 114.092 | 7 | 9 | 114.094 |
| 620 | 127.551 | 127.545 | 8 | 7 | 127.547 |
| 533 | 136.904 | 136.893 | 3 | 3 | 136.897 |
| 444 | | 158.632 | * | 3 | 156.638 |

sample to sample. For the detection of such errors the standard must be mixed into the sample itself (internal standard). Sometimes, even two different standards are advisable simultaneously, because standards with simple structures (elements and simple oxides) have strong reflections in the upper 2θ-range, but their foremost reflections only start above 20°. Conversely, compounds with complicated structures and therefore greater lattice constants show useful reflections in the lower angular region, but they rather rapidly lose intensity with increasing angles.

Periodical errors originating from the gears for the angle setting cannot be detected by standards. Often the gears include one cog wheel turning just one revolution per degree in $2\theta$ and which is connected by an axis to a scale for reading the parts of a degree. Every revolution changes the registration for the integer angles by $\pm 1$. For driving the detector and the sample these revolutions must be reduced by 1 : 360 and 1 : 180 respectively. The mechanical error of these gears may well reach up to 20–30 seconds of an arc (0.005–0.008°) and it is rather difficult to measure and correct. The mechanical quality of the gears so influences essentially the possible accuracy of the measurements. This accuracy should not be mistaken as the reproducibility. The reproducibility of a measurement (including the reproducibility of mechanical errors) amounts to only about 0.0005° (for horizontal measuring circles a little bit better than for vertical ones), as long as all measurements are done in the same direction (Jenkins and Schreiner, 1986[32]). The mechanical play between increasing and decreasing measurement amounts to some 1/1000° and can be easily determined by measuring a test sample in both directions. For an older, analogously registering equipment with a rate meter this mechanical play is superimposed

by the systematic shift stemming from analogously averaging the pulse rates. This shift strongly depends on the chosen half-life time of the rate meter.

For several years the National Institute of Standards and Technology in Gaithersburg, MD (NIST) has offered standard reference materials (SRM) in portions of 10 g, which were measured very accurately. Best known for $2\theta$-calibration is a Si-powder (99.9999% pure) named NBS SRM 640 with a mean grain size of 10 µm and a lattice constant of 5.43088(4) Å at 25 °C (PDF 27-1402). After selling out this standard in 1983 the next smaller grain fraction of the same ground Si-powder with a mean grain size of 5 µm was offered as SRM 640a with a newly refined lattice constant of 5.430825(11) Å at 25 °C. The Si-standard itself was calibrated against a mixture of Ag [$a_o = 4.08651(2)$ Å] and W-powder [$a_o = 3.16524(4)$ Å]. By doing so the 111-Si-reflection was about 10° below the first Ag-reflection and therefore could not be corrected sufficiently and was not used for the refinement of the lattice constant. Since 1987 the standard SRM 640b is delivered with $a_o = 5.43094(4)$ Å (average of 25 measurements).

For such precise specifications many disturbing influences must be considered, which for routine measurements may be neglected. First of all the temperature during the measurement must be recorded, and the measured *d*-values must be corrected for expansion with the temperature coefficient to a standard temperature (mostly 25 °C = 293 K). For pure Si (99.9999%) the temperature coefficient amounts to $\alpha = 2.56 \times 10^{-6}$, *i.e.* 0.000014 Å change in $a_o$ per °C. For less pure Si $\alpha$ is somewhat greater. Table 4.8 shows that reflections with great $2\theta$ are rather sensitive to small changes of the lattice constants. For silicon another effect causes disturbance, which for most other powders can be neglected: the surface tension of the oxide-skin.

Deslattes and Henins (1973)[22] determined, with a large single-crystal, for which the influence of the oxide-skin can be neglected, the lattice constant of Si as $a_o = 5.4310628(9)$ Å at 25 °C. The same measurement was also used for a refinement of $\lambda(CuK\alpha_1) = 1.5405981$ Å, which value was used for all measurements on SRM 640. Taking these results, $a_o$ of the single-crystal is greater than that of the Si-powder by 0.000183 Å. Theoretically, this corresponds to a temperature difference of 13 °C. The real reason is a difference in pressure caused by the surface tension of the oxide-skin. For a constant surface tension the induced pressure increases with decreasing grain size. With a module of compressibility of $1.023.10^{-6}$ bar$^{-1}$ for Si (*i.e.* a relative linear change of $0.341 \times 10^{-6}$ bar$^{-1}$ and an absolute change of $1.852 \times 10^{-6}$ Å bar$^{-1}$ for $a_o$) the above difference of 0.000183 Å means an induced pressure of about 100 bar within the grains of SRM 640. An accurate long-time measurement with narrow divergence slits of an older Si-powder (> 5 years after grinding) with a mean grain size of 2 µm revealed in the front-slope of the 111-Si reflection at 28.47° (integral intensity 520 930 pulses) a very weak reflection at 26.64° (5072 pulses, only 15% above background), which corresponds to the strongest quartz reflection, *i.e.* after some time the at-first amorphous oxide-skin becomes crystallized.

For smaller angles a synthetic fluorphlogopite, $KMg_3[Si_3AlO_{10}/F_2]$, is available as SRM 675 with $d_{001} = 9.98104(7)$ Å at 25 °C (Table 4.9). This mica material should possibly be oriented parallel to the sample surface (strong

**Table 4.9** 00$\ell$-reflections of the standard SRM 675, fluorphlogopite. CuK$\alpha_1$-radiation, $d_{001} = 9.98104(7)$ Å at 25 °C.

| $2\theta$ (°) | $\ell$ | $I_{rel}$ | $2\theta$ (°) | $\ell$ | $I_{rel}$ |
|---|---|---|---|---|---|
| 8.853 | 1 | 81 | 65.399 | 7 | 2 |
| 17.759 | 2 | 4.8 | 76.255 | 8 | 2 |
| 26.774 | 3 | 100 | [a] | | |
| 35.962 | 4 | 6.8 | 101.025 | 10 | 0.5 |
| 45.397 | 5 | 28 | 116.193 | 11 | 0.5 |
| 55.169 | 6 | 1.6[b] | 135.674 | 12 | 0.1 |

[a] Reflection 009 is too weak.
[b] $2\theta_{006}$ inaccurate, because of a superposition with 135.

texture). One can obtain this preferred orientation by the sedimentation of a suspension of some standard in acetone onto a single-crystal sample holder. For a good calibration only the first reflections of SRM 675 should be used. If K$\alpha_1$ + K$\alpha_2$-radiation is used, for the front reflections both wavelengths cannot be separated and the reported $2\theta$-values (for K$\alpha_1$) must be transformed into the averaged wavelength (for CuK$\alpha$ approximately a multiplication with 1.00083). If for older PDF-cards $2\theta$-values are to be recalculated from the listed $d$-values then the reported (at that time valid) wavelength is to be used.

For powders of rock samples quartz offers itself as a natural standard, especially because quartz is a rather pure compound with approximately constant lattice constants (Table 4.10). Natural calcite often contains Mg in solid solution with decreased lattice constants and is less suited as standard. Furthermore, calcite exhibits a negative temperature coefficient in the $a$-direction.

As secondary standards for the calibration of $d$-values the following compounds are used:

W (cub. I, $a = 3.16524(4)$ Å, $\Delta a/°C = 0.000015$ Å, PDF 4-806)
Ag (cub. F, $a = 4.08651(2)$ Å, $\Delta a/°C = 0.000078$ Å, PDF 4-783)
$\alpha$-$Al_2O_3$ (rhombohedr., $a = 4.75893(10)$, $c = 12.9917(7)$ Å, SRM 674)
Quartz (trig., $a = 4.9133(2)$, $c = 5.4053(4)$ Å at 25 °C) ($\Delta a/°C = 0.000070$, $\Delta c/°C = 0.000047$ Å, PDF 33-1161)
$MgAl_2O_4$ (cub. F, $a = 8.0831$ Å, PDF 21-1152)
Al (cub. F, $a = 4.04934$ Å at 21 °C, $\Delta a/°C = 0.000093$Å, PDF 4-787)
Calcite (rhombohedr.; $a = 4.990$, $c$: 17.002 Å, PDF 24-27) ($\Delta a/°C = -0.000030$ Å, $\Delta c/°C = 0.00044$ Å)
Diamond (cub. F, $a = 3.5667$ Å (26 °C), $\Delta a/°C = 0.00000424$, PDF 6-675).

For very small angles the salt of a long-chained carboxylic acid lead myristate, $Pb(C_{14}H_{27}O_2)_2$, with a layer distance of $d = 40.20$ Å (refined 40.26 Å) was proposed. With CuK$\alpha$-radiation ($\lambda = 1.5419$ Å) the reflections up to the 13th order could be observed. The measured $2\theta$-values were: 2.28, 4.47, 6.66, 8.86, 11.06, 13.27, 15.48, 17.69, 19.93, 22.15, 24.40, 26.65, and 28.91° (Schreiner, 1986, see Figure 4.18).

**Table 4.10** Quartz reflections after PDF 46-1041 ($2\theta_{obs}$). $2\theta_{calc}$ was calculated with the above lattice constants and $\lambda = 1.5405981$ Å (both values at 25 °C). Only the stronger reflections with $I_{rel} > 1$ are reported.

| *hkl* | $2\theta_{obs}$ | $2\theta_{calc}$ | $I_{rel}$ | *hkl* | $2\theta_{obs}$ | $2\theta_{calc}$ | $I_{rel}$ |
|---|---|---|---|---|---|---|---|
| 100 | 20.860 | 20.859 | 16 | 113 | 64.036 | 64.036 | 2 |
| 101 | 26.640 | 26.640 | 100 | 212 | 67.744 | 67.744 | 6 |
| 110 | 36.544 | 36.546 | 9 | 203 | 68.144 | 68.144 | 7 |
| 102 | 39.465 | 39.467 | 8 | 301 | 68.318 | 68.315 | 5 |
| 111 | 40.300 | 40.292 | 4 | 104 | 73.468 | 73.467 | 2 |
| 200 | 42.450 | 42.453 | 6 | 302 | 75.660 | 75.661 | 3 |
| 201 | 45.793 | 45.796 | 4 | 220 | 77.675 | 77.672 | 1 |
| 112 | 50.139 | 50.141 | 13 | 213 | 79.884 | 79.884 | 2 |
| 202 | 54.875 | 54.875 | 4 | 114 | 81.173 | 81.171 | 2 |
| 103 | 55.325 | 55.327 | 2 | 310 | 81.491 | 81.491 | 2 |
| 211 | 59.960 | 59.961 | 9 | 312 | 90.831 | 90.831 | 2 |

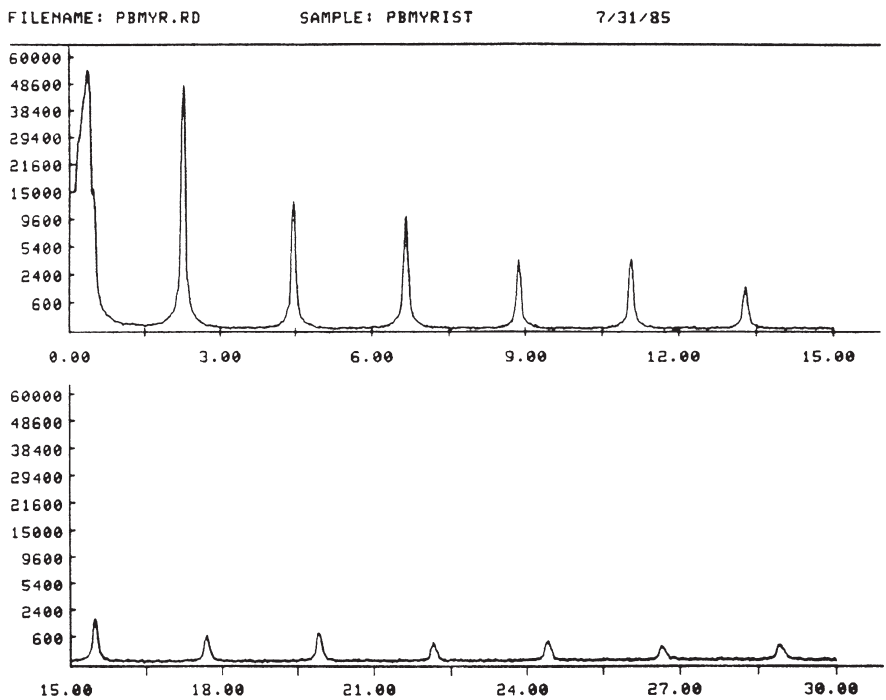



**Figure 4.18** Powder pattern of Pb myristate, $Pb(C_{14}H_{27}O_2)_2$, taken with CuK$\alpha$ radiation and variable divergence slit. The closing of the divergence slit produces a false peak at $2\theta$ 0.5° (Schreiner, 1986.[23])

Also, for *intensity calibration* standards are available. The NIST offers under SRM 674 a set of five materials with a mean grain size of 2 µm:

$\alpha$-$Al_2O_3$ (rhombohedr., $a = 4.75893(10)$, $c = 12.9917(7)$ Å), ZnO (hexag., $a = 3.24981(12)$, $c = 5.20653(13)$ Å), $TiO_2$ (rutile, tetrag., $a = 4.59365(10)$,

$c = 2.95874(8)$ Å), $Cr_2O_3$ (rhombohedr., $a = 4.95916(12)$, $c = 13.5972(6)$ Å) and $CeO_2$ (cub., $a = 5.41129(8)$ Å).

For a quantitative analysis of phase mixtures the relative intensities of the PDF do not suffice, and therefore recently a scaling factor I/Ic from relative to absolute intensities is reported (RIR = relative intensity reference).

In recent releases of the ICDD powder diffraction file the reported value I/Ic refers to the intensity ratio of the strongest (100%) reflection of the substance in relation to the strongest reflection of corundum, $Al_2O_3$ (113 at 43.35°), if both materials were mixed and measured using an 1 : 1 weight ratio. The I/Ic-values of the four standards in SRM 674 (besides $Al_2O_3$ itself) are: for ZnO, 5.17(13) (101 at 36.25°); for $TiO_2$, 3.39(12) (110 at 27.42°); for $Cr_2O_3$, 2.10(5) (104 at 33.59°); and for $CeO_2$, 7.5(2) (111 at 28.55°). For completeness, the I/Ic-value for quartz = 4.3 is given here too. If the strongest reflection of corundum coincides with a reflection of the material to be calibrated, one may use another reflection of corundum. Therefore, the corundum intensities of SRM 674 were measured very accurately and are certified (Figure 4.19).

If one intends to determine the I/Ic-value for a new material the integral intensities must be used, especially if sample and corundum exhibit great differences in their half widths. For rock samples, quartz can be used as an intensity reference.

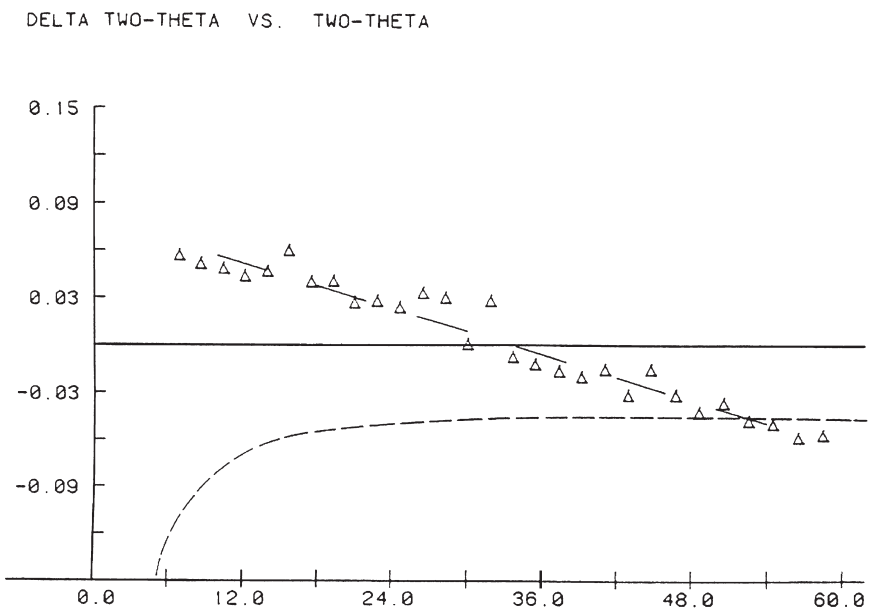



**Figure 4.19** Mathematical models for systematic errors (dotted curve) often fail at small angles. The measured values for lead stearate (triangle s = differences to calculated 2θ values) exhibit a completely different behavior. (Schreiner and Surdowski, 1983 [24]).

**Table 4.11** 2θ-values ($CuK\alpha_1$) and intensities of a sintered corundum-plate (SRM 1976, at 25 °C, with texture). The $2\theta_{calc}$ were calculated from $a = 4.74885(11)$, $c = 12.9931(24)$ Å, and $\lambda = 1.540629$ Å (total error for $I_{int} = 6.12\%$, for the peak height $I_{max} = 7.85\%$).

| *hkl* | $2\theta_{calc}$ | $I_{int}$ | $I_{max}$ | *Hkl* | $2\theta_{calc}$ | $I_{int}$ | $I_{max}$ |
|---|---|---|---|---|---|---|---|
| 012 | 25.577 | 32.34 | 33.31 | 02.10 | 88.995 | 11.76 | 8.99 |
| 104 | 35.150 | 100.00 | 100.00 | 226 | 95.252 | 10.14 | 7.25 |
| 113 | 43.355 | 51.06 | 49.87 | 21.10 | 101.074 | 16.13 | 10.94 |
| 024 | 52.552 | 26.69 | 25.17 | 324 | 116.107<br>116.597 | 20.86 | 10.09 |
| 116 | 57.499 | 92.13 | 83.6 | 01.14 | | | |
| 300 | 68.213 | 19.13 | 16.89 | 13.10 | 127.684 | 15.58 | 7.56 |
| 10.10 | 76.871<br>77.234 | 55.57 | 34.61 | 146 | 136.085 | 15.47 | 6.55 |
| 119 | | | 40.10 | 145.177 | 11.29 | 4.06 | |

**Table 4.12** 2θ-values ($CuK\alpha_1$) and intensities of corundum (SRM 674) at 25 °C.

| *hkl* | $2\theta(^\circ)$ | $I_{rel}(674)$ | *hkl* | $2\theta(^\circ)$ | $I_{rel}(674)$ |
|---|---|---|---|---|---|
| 012 | 25.576 | 55.4(24) | 024 | 52.552 | 45.5(13) |
| 104 | 35.151 | 87.4(19) | 116 | 57.501 | 92.5(26) |
| 110 | 37.777 | 36.5(14) | 214 | 66.519 | 34.7(10) |
| 113 | 43.354 | 100.0 | 300 | 68.210 | 55.5(22) |

Since 1991 a ground sintered plate of corundum is available as SRM 1976, intended for the calibration of the whole $2\theta$-range of an individual equipment (Table 4.11). The individual grains are plates along (001) with a diameter of 5–7 μm and thickness of 1–2 μm. This plates are oriented more or less parallel to the surface. Therefore, the intensities (measured with a fixed divergence slit) with a large $\ell$ are enhanced with respect to the intensities of SRM 674 (Table 4.12). The standard was measured at 25 °C. For $\lambda$ a slightly greater value than usual is given (1.540629 Å). The textures of both corundum standards are different because of different grain shapes.

For the calibration of half widths an $LaB_6$-standard was described (SRM 660).

### 4.8.1 External Standards

Errors in the alignment of the goniometer that change rather slowly with time can be controlled by external standards. The calibration specimen should mechanically be rather sturdy and not change its surface structure during the life-time of the goniometer. Pressings with tiny amounts of binder only or ground sintered plates, for instance from Si, corundum, or quartz are suitable. Consequently, Bruker AXS delivers with its goniometers (*e.g.* D5000) a section of a fine-grained, natural quartzite without any sample holder. This specimen should be measured every other month under identical measuring conditions

(high voltage, tube current, slits, counting electronics *etc*.) and all records kept in a safe place. A slow decrease of the intensities with time may not indicate an unquestionable misalignment, but can be caused by a decreasing yield of the X-ray tube due to the deposition of tungsten vapor on the tube windows and the burning-in of the focal spot roughening the anode. If this loss of intensity exceeds about 30%, a new tube should be installed.

Of great importance is the calibration specimen for the determination of the mechanical zero-point of the goniometer, which seldom fits the real zero-point exactly but deviates by some $1/100^\circ$. Even if this zero-point error amounts to $0.1^\circ$, the lattice constants calculated from the shifted $2\theta$-values will differ significantly from the true ones (*i.e*. by over $3\sigma$). Provided that the reflections are indexed correctly, a zero-point error can be recognized by about an equal difference (positive or negative) between the measured and the expected $2\theta$-values. After a least-squares refinement of the lattice constants using zero-point shifted data the final differences of the $2\theta$-values are not randomly distributed but exhibit a systematic trend from $-$ve to $+$ve or *vice versa*. Non-periodical mechanical failures of the gears, which only slowly change with $2\theta$, can also be detected and corrected using an external standard.

Not detectable by an external standard are systematic errors that differ from specimen to specimen, such as a variable packing density of the sample (leading to variable transparency errors) or – most frequent and most severe – the sample displacement error. Even if the same person puts the same specimen repeatedly into the same equipment the sample displacement error will vary. During a test at our Siemens-diffractometer D500 about every third sample was placed too deep by about 30 μm (away from the wanted tangential plane at the focusing circle) despite a very careful procedure on the part of the operator. For other equipment displacement errors of up to 100 μm are reported. Especially if the sample holder is pressed plane to plane against the goniometer axis, a single powder grain between both planes suffices to displace the specimen from the correct position. Visually such a small error cannot be detected in a pattern, but it will show up during the refinement of lattice constants and will change these by $4$–$5\sigma$. These sample offset errors are removed in synchrotron setups with analyzer crystals after the sample.

### 4.8.2 Internal Standards

For accurate measurements of diffraction angles internal standards should be used, which are to be mixed with the sample itself. Unfortunately, after that the sample is contaminated by the standard and further investigations, as would be possible with the pure sample alone, are rendered difficult or impossible. Tests to use magnetite as a standard were rather promising, as the magnetite standard can be removed after the measurement completely with a simple magnet. Also, a Rietveld-refinement becomes more complicated with an internal standard, as the parameters of the standard must be refined too. A great advantage of the internal standard is the common mass absorption $(\mu/\rho)$m of the mixture, *i.e*. for

sample and for standard the same transparency (depth of penetration) is to be applied, which facilitates a quantitative analysis.

A $2\theta$-calibration takes place in four steps:

1. Selection of one or several standards,
2. preparation and measuring of the mixture,
3. exclusion of unsuitable standard reflections,
4. construction of a calibration curve and correction of $2\theta$-values.

When selecting a standard one must pay attention to finding a standard peak, which is placed before the first peak of the sample, or that at least the first standard peak is only some few degrees behind, as the extrapolation of a calibration curve is rather liable to faults. Also the peaks of the standard and the sample should not overlap. If in the front range no standard peaks are available, auxiliary points can be constructed if higher orders of the front peaks can be measured. In this case the higher order is calibrated first and the position of the first order peak is calculated from that of the higher order one using Bragg's law. This auxiliary point is in any case more reliable than an extrapolation. The calculated positions can be used to extend the calibration curve to smaller angles.

The admixture of the standard should be dimensioned so that the strongest lines of sample and standard become about equal. The right ratio can be calculated if the $I/I_c$-values of standard ($I_s/I_c$) and sample ($I_p/I_c$) are known (see above at intensity calibration). The weight ratio $X_p$ ( sample) : $X_s$ (standard) can be estimated by:

$$X_p{:}X_s = I_s/I_c : I_p/I_c$$

(If both mass absorptions differ strongly this must be taken into account in a correction term.)

If the I/Ic-values are not known, one can admix the standard in small portions until the strongest reflections show about equal intensity.

If fluorphlogopite is used as an internal standard, an alignment of the mica flakes parallel to the sample surface is preferred. This can be obtained if a small amount of the mixture sample/standard is suspended in acetone or isopropanol and is sedimented to a single crystal sample holder.

For the Guinier-camera a compromise between external and internal standard is possible, as the camera allows the simultaneous recording of several samples onto the same film by dividing the camera by the installation of separating disks. Mostly three individual patterns are taken simultaneously: pure sample, mixture sample/standard, and pure standard. If one wants to dispense with the mixture, it will be sufficient to put the sample pattern in the centre and a standard pattern at each side of the Guinier-film.

Only those standard reflections are suited for a calibration that do not overlap with sample reflections. If unavoidable, one may try to separate standard and sample reflections by profile fitting. But in the plot for the calibration curve the $\Delta 2\theta$-values of these standard reflections should follow

the trend of the non-overlapping reflections, otherwise they must be abandoned (Figure 4.20).

Similar to what is done for the external standard, for the construction of the *calibration curve* the $\Delta 2\theta$-values are plotted *versus* $2\theta_{obs}$ and then approximated by a smooth curve. For polynomials $a + bx + cx^2 + \ldots$ one can calculate all approximations from 0th order (zero point error only) up to 4th order (if at least six calibration points are available) and compare the corresponding sums of the squared differences ($\chi^2$). As an optimal polynomial one can take that one

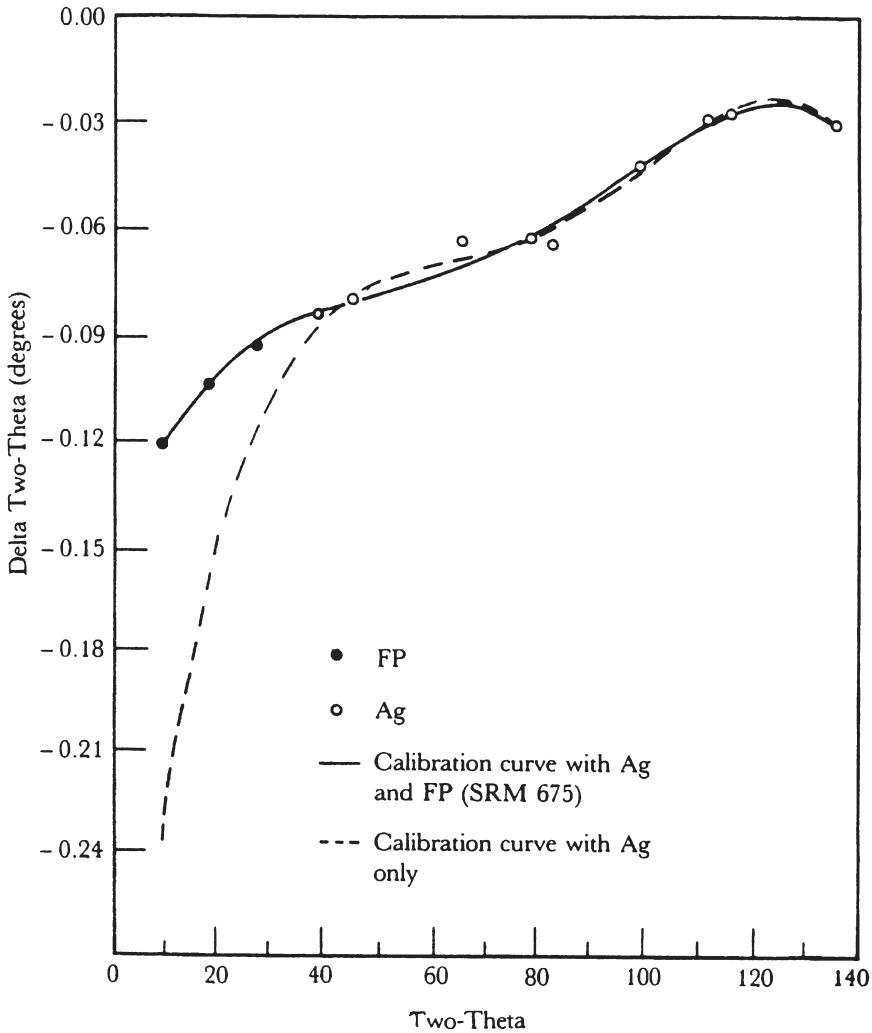



**Figure 4.20** Calibration curve of 4th order. Dashed line: Calculated only with Ag reflections. It results an erroneous extrapolation to smaller angles. Full line: Same procedure but with the inclusion of additional fluor phlogopite reflections. (Wong Ng & Hubbard (1987)[30]).

which exhibits the last large drop in $\chi^2$. Often this is a polynomial of 2nd order. The higher the order the more risky becomes an extrapolation of the calibration curve to greater or smaller angles.

For Rietveld structure refinements it is possible to apply a $2\theta$-correction on the complete raw data set. But as after such a correction the step widths between the individual data are no longer constant, the complete data set must be rectified to a new grid with constant step width. As the new grid points do not coincide with those of the original measurement, the counting rates at the new grid points must be estimated by an interpolation of the old values. As the maximum possible shift is only a half step width long, a linear interpolation between the two adjacent original counting rates will suffice. Better will be an interpolation by using a polynomial of 2nd or 3rd order, especially to reproduce correctly the reflection maxima. In the program GUFI such a *angle rectification* is provided (Dinnebier & Eysel, 1990[33]). Other corrections, such as smoothing or $K\alpha_2$-stripping, should be abandoned for a Rietveld analysis but are handled in the refinement itself by corresponding parameters. A background curve may be constructed before and subtracted, though this too can be parameterized and fit in the Rietveld refinements. Peak intensity extraction using full-profile refinement methods when the unit cell is known, but without a full knowledge of the structure, are also possible.

### 4.8.3 Correction Together with the Refinement of Lattice Constants

If only a restricted quantity of material is available, which after taking the powder pattern shall be used for other experiments, the admixture of an internal standard is prohibited, and errors are to be corrected without a standard. If a systematic error can be described by a mathematical model, the parameters of this model can be refined together with the lattice constants. In practice one should restrict this refinement to one additional error only, as rather strong correlations may exist between different errors. For example, the zero-point error, $\Delta 2\theta$, and the sample-displacement error, $\Delta 2\theta \cdot \cos\theta$, differ only by the slowly changing factor $\cos\theta$. For a measurement up to $2\theta = 90^\circ$ this factor changes by only 29%, and a simultaneous refinement of both errors can yield rather meaningless values.

In Table 4.13 an example is worked out for the determination of the sample-displacement error without an internal standard. Other errors should be excluded before if possible. For example, the zero-point error should be corrected by using an external standard. If the reflections can be indexed unequivocally (uncertain reflections must be omitted), the sample-displacement error – the most important error changing from sample to sample – can be easily refined with the lattice constants. The author's program, LATCO, refines the lattice constants twice, with and without sample-displacement error, and one has to decide oneself which of the two refinements is to be preferred. The main criterion for accepting the refinement *with* sample-position error is the size of the error in comparison with its standard deviation: it must amount to at least twice the standard deviation. Furthermore $\chi^2$ should be significantly

**Table 4.13** Refinement of brucite.

*(a) Refinement without sample displacement error*

| *h* | *k* | *l* | *d(obs)* | *d(calc)* | $\Delta d$ | $2\theta(obs)$ | $2\theta(calc)$ | $\Delta 2\theta$ |
|---|---|---|---|---|---|---|---|---|
| 0 | 0 | 1 | 4.7672 | 4.7627 | 0.0045 | 18.598 | 18.615 | 0.018 |
| 1 | 0 | 0 | 2.7306 | 2.7295 | 0.0011 | 32.771 | 32.785 | 0.014 |
| 1 | 0 | 1 | 2.3686 | 2.3681 | 0.0005 | 37.957 | 37.965 | 0.008 |
| 1 | 0 | 2 | 1.7944 | 1.7944 | 0.0000 | 50.844 | 50.844 | 0.000 |
| 1 | 1 | 0 | 1.5758 | 1.5759 | 0.0001 | 58.527 | 58.525 | 0.002 |
| 1 | 1 | 1 | 1.4961 | 1.4961 | 0.0000 | 61.978 | 61.978 | 0.001 |
| 1 | 0 | 3 | 1.3723 | 1.3723 | 0.0000 | 68.294 | 68.293 | 0.001 |
| 2 | 0 | 1 | 1.3119 | 1.3119 | 0.0000 | 71.912 | 71.910 | 0.002 |

LQ sum $= 2.61\ (10^{-8})$; $a = 3.15171 \pm 0.00013$ Å; mean deviation in $Q = 0.57\ (10^{-4})$; $c = 4.76271 \pm 0.00038$ Å.

*(b) Refinement together with sample displacement error*

| *h* | *k* | *l* | *d.cor* | *d(cal)* | $\Delta d$ | $2\theta(obs)$ | $2\theta(cor)$ | $2\theta(cal)$ | $\Delta 2\theta$ |
|---|---|---|---|---|---|---|---|---|---|
| 0 | 0 | 1 | 4.7630 | 4.7617 | 0.0013 | 18.598 | 18.614 | 18.619 | 0.005 |
| 1 | 0 | 0 | 2.7293 | 2.7289 | 0.0004 | 32.771 | 32.787 | 32.792 | 0.005 |
| 1 | 0 | 1 | 2.3677 | 2.3676 | 0.0000 | 37.957 | 37.973 | 37.973 | 0.000 |
| 1 | 0 | 2 | 1.7939 | 1.7940 | 0.0001 | 50.844 | 50.859 | 50.855 | 0.004 |
| 1 | 1 | 0 | 1.5754 | 1.5755 | 0.0001 | 58.527 | 58.542 | 58.539 | 0.003 |
| 1 | 1 | 1 | 1.4958 | 1.4958 | 0.0000 | 61.978 | 61.992 | 61.993 | 0.001 |
| 1 | 0 | 3 | 1.3721 | 1.3720 | 0.0000 | 68.294 | 68.308 | 68.309 | 0.001 |
| 2 | 0 | 1 | 1.3117 | 1.3117 | 0.0000 | 71.912 | 71.925 | 71.927 | 0.002 |

LQ sum $= 0.70\ (10^{-8})$; $a = 3.15105 \pm 0.00019$ Å; mean deviation in $Q = 0.30\ (10^{-4})$; $c = 4.76174 \pm 0.00034$ Å; applied displacement $= \quad 0.02909\,\text{mm} \pm 0.00788\,\text{mm}$; correction in $2\theta = (0.0167 \pm 0.0045)^{\circ}\ \cos\theta$; $R = 20\,\text{cm}$.

smaller for the refinement with error correction and the standard deviations of the lattice constants should decrease too. More precisely, a $\chi^2$-test of statistics may decide whether the additional parameter is meaningful.

## REFERENCES


1. E. J. Sonneveld and J. W. Visser, Automatic collection of powder data from photographs, *J. Appl. Crystallogr.*, 1975, **8**, 1–7.
2. R. P. Goehner, Background subtract subroutine for spectral data, *Anal. Chem.*, 1978, **50**, 1223–1225.
3. A. Savitzky and M. J. E. Golay, Smoothing and differentiation of data by simplified least squares procedures, *Anal. Chem.*, 1964, **36**, 1627–1639. Tables corrected by: Steinier, Termonia and Deltour in *Anal. Chem.* 1972, **44**, 1906–1909.
4. E. T. Whittaker and G. Robinson, *The Calculus of Observations* (1924), Blackie, London, 4th edn 1965, 397 S.
5. A. Proctor and P. M. A. Sherwood, Smoothing of digital X–ray photoelectron spectra by an extended sliding least-squares approach, *Anal. Chem.*, 1980, **52**, 2315–2321.

6. W. H. Press and S. A. Teukolsky, Savitzky–Golay smoothing filters, *Comput. Phys.*, 1990, **4**, 689–692.
7. (a) M. A. U. Bromba and H. Ziegler, Application hints for Savitzky–Golay digital smoothing filters, *Anal. Chem.*, 1981, **53**, 1583–1586; (b) M. A. U. Bromba and H. Ziegler, Digital smoothing of noisy spectra, *Anal. Chem.*, 1983, **55**, 648–653; (c) M. A. U. Bromba and H. Ziegler, Digital filter for computationally efficient smoothing of noisy spectra, *Anal. Chem.*, 1983, **55**, 1299–1302; (d) M. A. U. Bromba and H. Ziegler, Varible filter for digital smoothing and resolution enhancement of noisy spectra, *Anal. Chem.*, 1984, **56**, 2052–2058.
8. D. G. Cameron and E. E. Armstrong, Optimization of stepsize in X–ray powder diffractogram collection, *Powder Diff.*, 1988, **3**, 32–37 (also: ICDD, Methods & Practices).
9. R. W. Hamming, *Digital Filters* (2nd edn.). Prentice Hall Inc., 1983.
10. Spencer (1904) cited in ref. 4.
11. J. Ladell, A. Zagofsky and S. Pearlman, Cu $K\alpha_2$ elimination algorithm, *J. Appl. Crystallogr.*, 1975, **8**, 499–506.
12. *DIFPATAN, Ver. 1.3*, 1992, R. Radomír Kužel, Faculty of Mathematics and Physics, Charles University, Ke Karlovu 5, CZ 12116 Prague 2, Czechia.
13. S. V. N. Naidu, C. R. Houska; Profile separation in complex powder patterns, *J. Appl. Crystallogr.*, 1982, **15**, 190–198.
14. H. J. Sánchez, A new peak search routine for fast evaluation on small computers, *Comput. Phys.*, 1991, **5**, 407–413.
15. G. Reich, Recognizing chromatographic peaks with pattern recognition methods, *Anal. Chim. Acta*, 1987, **201**, 153–170 and 171–183.
16. S. A. Howard and K. D. Preston, Profile fitting of powder diffraction patterns, *Rev. Mineral.*, 1989, **20**, 217–275.
17. A. Kern, Präzisionspulverdiffraktometrie: Ein Vergleich verschiedener Methoden, Diploma Thesis, Heidelberg, 1992, 175 S.
18. A. Brown and J. W. Edmonds, The fitting of powder diffraction profiles to an analytical expression and the influence of line broadening factors, *Adv. X-Ray Anal.*, 1980, **23**, 361–374.
19. H. M. Rietveld, A profile refinement method for nuclear and magnetic structures, *J. Appl. Crystallogr.*, 1969, **2**, 65–71.
20. J. Lauterjung, G. Will and E. Hinze, A fully automatic peak-search program for the evaluation of Gauss-shaped diffraction patterns, *Nucl. Instrum. Methods Phys. Res., Sect. A*, 1985, **239**, 281–287.
21. C. R. Hubbard, Certification of Si powder diffraction standard reference material 640a, *J. Appl. Crystallogr.*, 1983, **16**, 285–288.
22. R. D. Deslattes and A. Henins, X-ray to visible wavelength ratios, *Phys. Rev. Lett.*, 1973, **31**, 972–975 (see also *ibid.* 1974, **33**, 463–466 and 1976, **36**, 898–890).
23. W. N. Schreiner, Towards improved alignment of powder diffractometrs, *Powder Diff.*, 1986, **1**, 26–33.

24. W. N. Schreiner and C. Surdowski, Systematic and random powder diffractometer errors relevant to phase identification, *Norelco Rep*., 1983, **30** 1X, 40–44.
25. D. L. Bish and R. C. Reynolds, Jr., Sample preparation for X-ray diffraction, *Rev. Min*, 1989, **20**, 73–99.
26. W. N. Schreiner and R. Jenkins, A second derivative algorithm for identification of peaks in powder diffraction patterns, *Adv. X-Ray Anal*., 1980, **23**, 287–293.
27. W. N. Schreiner and R. Jenkins, A second derivative algorithm for identification of peaks in powder diffraction patterns, *Adv. X-Ray Anal*., 1980, **23**, 287–293.
28. T. C. Huang, Precision peak determination in X-ray powder diffraction, *Aust. J. Phys*., 1988, **41**, 201–212.
29. T. C. Huang and W. Parrish, A combined derivative method for peak search analysis, *Adv. X-Ray Anal*., 1984, **27**, 45–52.
30. W. Wong-Ng, and C. R. Hubbard (1987), Standard reference materials for X-ray powder diffraction. Part II. Calibration using d-spacing standards, in: Methods and Practices in X-ray powder diffraction, published by the International Centre of Powder Diffraction, Newton Square, Pennsylvania, USA, (1987 ff.).
31. D. W. Marquardt, An algorithm for least–squares estimation of nonlinear parameters, *J. Soc. Indust. Appl. Math*., 1963, **11**, 431–441.
32. R. Jenkins and W. N. Schreiner, Considerations in the design of goniometers for use in X-ray powder diffractometers, *Powder Diff*., 1986, **1**, 305–319.
33. GUFI (Guinier–film–evaluation), Ver. 3.01 (1992), Dinnebier, R.E. and Eysel, W. (1990) Powder diffraction satellite meeting of the XVth congress of the International Union of crytallography, Toulouse (France), abstract PS-07.03.15 (also as supplement to Acta Cryst. A46).
34. G. Cagliotti, A. Paoletti and F. P. Ricci, Choice of collimators for a crystal spectrometer for neutron diffraction, *Nucl. Instr*., 1958, **3**, 223–228.

CHAPTER 5

# The Profile of a Bragg Reflection for Extracting Intensities

ARMEL LE BAIL

Laboratoire des Fluorures-UMR 6010, Université du Maine, Faculté des Sciences, Avenue Olivier Messiaen, 72085 LE MANS Cedex 9, France

## 5.1 INTRODUCTION

A Bragg reflection from a perfect crystalline material, measured on a perfect diffractometer, would have a simple Dirac peak profile (the δ function) exactly located at the diffracting angle position $2\theta$ expected from the Bragg law ($2d\sin\theta = \lambda$). Unfortunately, there is no such thing as a perfect diffractometer: an instrumental effect is observed on the profile in the form of peak broadening and asymmetry. This is also discussed Chapters 4 and 6. Moreover, the detection of a Bragg reflection is possible only if there is a crystalline phase in the sample, characterized by a high degree of three-dimensional order extending over a large number of unit cells. Otherwise there is a sample effect as well, and the profiles are broadened inversely proportional to the crystal size (size effect), and if the periodicity is not well respected, due to various cell imperfections in dimensions and content. It is not always easy to distinguish between the powder pattern of a poorly crystallized or very defective compound, or of a nanocrystalline material, and that of a glassy or amorphous material for which no Bragg reflections occur, but only diffuse scattering. As an alternative, the method of atomic pair-distribution function (PDF) analysis may be applied to any powder pattern without the need for considering Bragg reflections, as discussed in Chapter 16. The present chapter discusses the various approaches of tackling the profiles of Bragg reflections in a powder diffraction pattern, either individually or as a whole.

Almost everything possible today was already dreamed of 30 or 40 years ago. The realizations of these dreams occurred slowly and progressively, thanks to the increase in computer power, the improvements in graphical user interfaces,

diffractometer data digitalization and the availability of synchrotron and neutron radiation. Some important innovations were not instantly accepted (*e.g.*, the whole powder pattern fitting methods such as the Rietveld and decomposition methods) or could not be applied to every radiation type or diffractometer before adaptations made by that essential category of crystallographers: the conceivers and developers of the software.

## 5.2 OVERVIEW OF CONTRIBUTIONS TO THE PEAK PROFILE FUNCTION

There is no reason for an experimental Bragg peak to be exactly described by a simple analytical function. Bragg peaks are generally very complicated objects. In the early usual simplified formalism, still in use, the experimental function $h(x)$ describing a broadened Bragg peak profile observed on a powder diffraction pattern is due[1] to the convolution of the instrumental aberration function $g(x)$ with the sample function $f(x)$:

$$h(x) = \int_{\infty}^{+\infty} f(y)g(x-y)dy = f \otimes g \tag{1}$$

The reality is that the aberration function $g(x)$ itself is the convolution of many contributions depending first on the radiation source and then on the diffractometer geometry and various experimental imperfections. Usually, the sample function $f(x)$ is considered to depend only on size and distortion effects, but other sample-dependent contributions can play an important role on the final peak profile, especially depending on the sample absorption (and related to the thickness, compaction, roughness), and depending on the diffractometer geometry and sample holder shape (flat specimen, capillary); these effects being more or less important, depending on the incoming beam quality (parallel or not). These additional sample effects are reported as well in the above global instrumental aberration function $g(x)$. It would be appropriate to rename it as the "instrumental and sample aberration function", as opposed to the "sample size and distortion function" $f(x)$. As discussed in Chapter 4, it is considered implicit that $g(x)$ would be determined experimentally from a well crystallized sample with the same chemical formulation (or by using a standard reference sample, sufficiently similar to the defective sample, so as to present an analogous absorption coefficient), and prepared in the same condition (thickness, compaction, *etc.*) as the sample showing additional line broadening by size and distortion effects to be characterized. Forgetting this, and using inappropriate standard reference samples, could lead to wrong size and distortion parameter estimations. Thus, a more complete description of the $h$ profile would be:

$$h = f_s \otimes f_d \otimes g_1 \otimes g_2 \otimes .. \otimes g_n \tag{2}$$

where $f_s$ and $f_d$ are the size and distortion sample contributions ($f = f_s \otimes f_d$), respectively, and $g_1$ to $g_n$ would be all the instrumental and sample aberration

effects, including the imperfections due to the primary beam radiation (wavelength distribution), focusing, collimator and slit dimensions, sample size, detector slit and monochromator dimensions, misalignment, *etc*. Experimentally, Equation (2) is incomplete: the background is removed, and some multiplicative factors are not included (scale, Lorentz-polarization effect, see Chapter 3), some of them depending on the diffraction angle. When the sample is perfectly crystallized and if the homogeneous grain size is, say, larger than 3–5 μm, the $f(x)$ contribution is close enough to a δ function and then $h(x) \approx g(x)$. However, interestingly, the instrumental resolution on the best instruments using synchrotron radiation has increased so incredibly that extremely fine $f_s$ and $f_d$ contributions can now be disclosed. The largest size ever detected[2] (producing a measurable broadening of the Bragg reflections) by powder diffraction is about 3.6 μm, obtained from a NAC[3] reference sample ($Na_2Ca_3Al_2F_{14}$), showing negligible microstrain (distortion), which can be compared to 1.2 μm obtained from SRM 660 $LaB_6$ (the standard reference material from NIST proposed for the characterization of the instrumental contribution to observed line profile shapes from X-ray diffraction equipment) plus some amount of microstrain. Of course, such small broadening effects due to large sample size are almost completely negligible on Bragg peaks observed with a laboratory instrument, affected by a dominant larger $g(x)$ contribution; nevertheless, a new SRM 660a $LaB_6$ is now proposed by the NIST. It can also be concluded that the necessary recommendation that a powder should contain a sufficiently large number of randomly disoriented crystallites (recommendation fulfilled if sizes are as small as 5 μm) would lead finally to the observation of a non-negligible line broadening with the highest resolution instruments at synchrotron radiation facilities. Let us now examine in more detail the $g(x)$ part.

## 5.3 INSTRUMENTAL ABERRATIONS

Most early studies of powder diffractometer aberrations are due to Wilson[4–6] and Alexander.[7,8] The approach, now called "Fundamental Parameters Approach" (FPA),[9] pushes the concept of a convolution approach to powder line profile fitting by taking account of every $g_n$ contribution in $h$ instead of fitting globally the $h$ profile by selected empirical profile shapes. Fitting $h$ globally is easy when the lineshapes are simple Gaussians, as is the case when considering low resolution, constant wavelength, neutron powder diffraction data. This was behind the original success of the Rietveld method[10] (Chapter 9). However, the resolution of neutron instruments has also improved considerably since the first applications of the Rietveld method. Spallation sources are increasingly used in neutron ToF (time-of-flight) mode (Chapter 2), resulting in complicated line-shapes that are much more difficult to fit, not to mention X-ray data (conventional or synchrotron sources). Of all the single-function profile models currently in use[11–14] for X-ray powder data, none of them gives an accurate description over the whole $2\theta$ range. Learned profiles, by using experimental peak shapes on the pattern of interest, are by definition (either by parametrization[15,16] or Fourier representation[17]) able to fit exactly, but one has

to introduce an angular variation, and extrapolation to the regions of the diagram where isolated peaks are not available. Profiles can look more Gaussian at low angles and more Lorentzian at large angles and peak asymmetry vanishing generally quickly from low to large angles. The importance of the various aberrations depends on the instrument geometry.

### 5.3.1 Largest Size Effect Ever Detected

It is quite interesting to see how the instrument line profile from synchrotron radiation was recently illustrated[2] in the case of the BM16 (now ID31) beamline[18] at ESRF, for capillary samples. The synchrotron parallel beam makes the instrument free of displacement-type aberrations.[19] The resolution of this instrument is such that it revealed non-negligible microstructural effects (size and microstrain broadening) for $LaB_6$ NIST SRM (standard reference material). The study was performed on the NAC, with a wavelength close to 0.5 Å, using a 1 mm capillary sample (a small decrease of the line width was noticed by using smaller capillaries, arising from a change of the effective equatorial divergence of the incident beam), with a step size of about $0.0004^\circ$ $2\theta$. In this geometry, the instrument line profile can be described as the convolution of the axial and equatorial profiles. Modeling the axial divergence has been the subject of many studies[20–24] and is considered to be perfectly modeled by the Finger et al. asymmetry correction.[21] For a non-parallel beam, as in the case of conventional laboratory diffractometers in Bragg–Brentano geometry, the low absorption coefficient of NAC induces extra broadening, sufficient for obtaining larger FWHM than from $LaB_6$. To correct for this, the path of a ray through the different parts of the diffractometer (monochromator, collimator, entry slit, sample, output slit, analyzer) should be completely modeled and the angle relationships established. The probability of a ray passing through the system and reaching the counter is proportional to the product of the reflection curves of the different components of the system. Concerning the BM16 instrument, the equatorial instrumental profile is shown[2] to be the convolution of three independent contributions: the equatorial angular divergence of the incident beam, and the reflection profiles of the monochromator and the analyzer [Equations (1) to (4b) in Masson et al.[2]]. In the case where an equatorial slit is inserted in the incident beam to limit the equatorial divergence, then the function characterizing the incident beam source becomes the product of a Gaussian function and a square-top function. This would also be the case if a collimating mirror was inserted. For non-perfect optical elements, some additional effects would have to be included. The characteristics of the shape of each aberration profile do not change with $2\theta$ – only the width changes. The analyzer gives a constant contribution over the whole scattering angle. For synchrotron instruments, there is no satisfactory analytical expression for any of the aberration functions. It is necessary to determine the individual components under working conditions (rocking-curve measurements). The instrument profiles were modeled for the 12 most intense lines of the NAC sample in three analyzer settings (Ge 333, Ge 111 and Si 111), revealing a small extra line broadening interpreted

as due to microstructural effects and fitted by a Voigt function. Figure 5.1 shows the fitting results for two of the NAC lines (lower and higher angle region of the 12 lines) for the Ge(111) analyzer used routinely on BM16.

In contrast to a conventional laboratory diffractometer, the axial divergence of the primary beam is generally very small compared with the axial divergence of the diffracted rays for synchrotron instruments. For the Ge(111) crystal, the profile shape is completely dominated by the analyzer reflection shape and is largely super-Lorentzian. At large angle, the contribution of the monochromator gives a non-negligible Gaussian contribution. The full widths at half maximum (FWHM) are of the order of $0.003^\circ$ $2\theta$. The NAC, as seen with a laboratory instrument (Bruker D8 Advance), for the same two lines, gives FWHM 0.044 and $0.071^\circ$ $2\theta$, respectively (Figure 5.2), this being 15 to 24 times larger (in fact "only" 5 to 8 times taking account of the fact that the wavelength is three times larger) than the synchrotron data.

Another contribution to the peak width from conventional sources is that the incident beam source profile shows a double contribution in this Bragg–Brentano geometry, selected here without any monochromator in the incident beam (showing the Cu K$\alpha$ doublet $\lambda_{\alpha 1} = 1.54056$ Å, $\lambda_{\alpha 2} = 1.54433$ Å – though the wavelength distribution has to be considered as being much more complex;[25,26] see also, Chapter 4). These partial fits are extracted from a whole powder pattern decomposition. The main, but not only, part of this additional broadening comes from the instrument. Indeed, a $LaB_6$ SRM measurement on the same laboratory instrument now provides slightly narrower FWHM than from the NAC. This is due to a very reduced X-ray penetration depth in the $LaB_6$ sample as compared to NAC, because of the much higher absorption coefficient of the former. So, using $LaB_6$ as a standard for obtaining a global $g(x)$ would here lead to a strong error on the size and distortion estimations from a low-Z sample such as the NAC. In principle, all $g_n$ contributions can be modeled by the FPA, but for methods using a reference sample for modeling $g(x)$, this poses the question of which reference to use. In a recent size strain round robin,[27] a $CeO_2$ microstructured sample was proposed for characterization to the experts on an international scale, and the selected reference material was preferred to be the annealed $CeO_2$ instead of the $LaB_6$ SRM. It was suggested[28] by FPA that this reference $CeO_2$ sample presented a significant intrinsic broadening. Perhaps it is too early to consider now that the FPA is an exact science allowing one to calculate perfectly any $g(x)$ contribution, for any diffractometer, including sample effects in some reflection geometry, though progress in this area has been rapid and is, clearly, highly valuable.

### 5.3.2 Monte Carlo Ray-tracing

The instrument design of neutron or X-ray diffractometers is realized nowadays with the help of Monte Carlo ray-tracing simulations[29 33] to obtain optimal results (for instance best resolution and peak shapes for powder diffractometers). The program GEOMET inside the BGMN[34,35] FPA package simulates device profiles by Monte Carlo ray-tracing, depending on many geometric

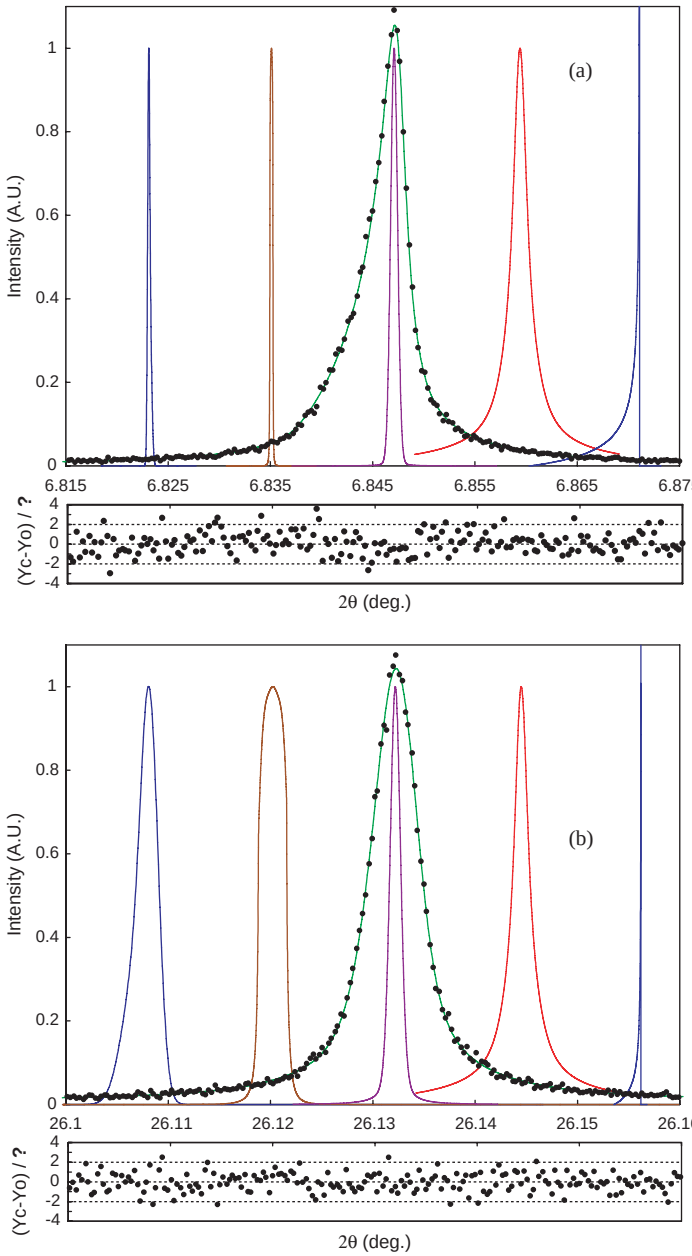



**Figure 5.1** Least squares fit of the NAC reference sample synchrotron powder profiles obtained with the Ge(111) analyzer crystal. (a) NAC (211) Bragg reflection; (b) NAC (921) Bragg reflection. The five other curves are, from left to right, the incident beam source profile, the transfer function of the monochromator, the pure sample profile, the reflection profile of the analyzer, and the axial divergence asymmetry function, respectively. (From Masson, Doryhée, Fitch, by courtesy of *J. Appl. Crystallogr.*)[2]

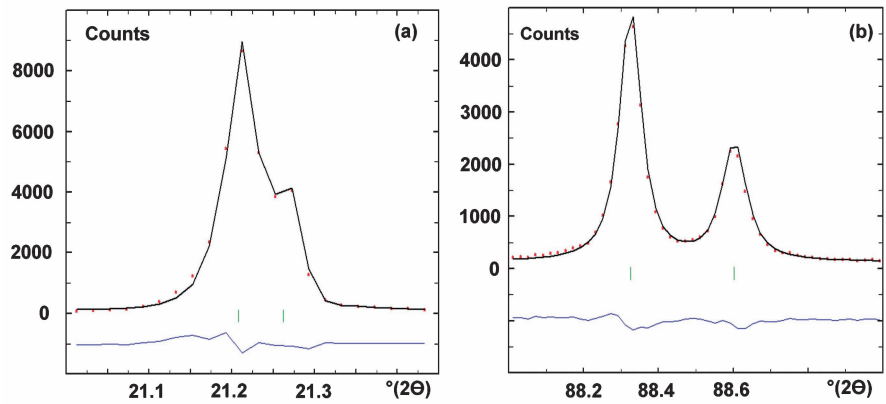



**Figure 5.2** Part of a whole powder pattern fit of the NAC reference sample. Same reflections (211) (a) and (921) (b) as on Figure 5.1, measured with a conventional laboratory diffractometer (Bruker D8 Advance), in Bragg Brentano geometry, using Cu $K_\alpha$ radiation, without a primary beam monochromator.

input parameters such as sample dimensions (for irradiating and penetrating the sample), linear attenuation coefficient of the sample, formula describing the ADS divergence, a misfit angle between line focus and slit edge, the focus dimensions and all the known (since Wilson[6 8]) divergence influences from the slits and collimators. Besides Bragg–Brentano one can also choose flat sample transmission and capillary geometries. Thus, the instrumental profile is predefined and not to refine within Rietveld calculations. Raytracing does millions of simple geometric calculations of possible X-ray paths and calculates true $\theta$ values for a fixed $\theta_0$ (which is the diffractometer's angle). All events are stored in a narrow grid, each channel for a narrow range of difference $\theta - \theta_0$. The result is a point by point description of the geometry function. In a second step, this description is fitted by a sufficient number of squared Lorentzians (Figure 5.3).

The choice of Lorentzians rather than Fourier series (or something else) for the fit is because they can be convoluted easily, and need only some dozens of parameters (instead of much more if Fourier series were used) for a good expansion (error below 0.7%) of a given geometry function. However, the developers do not believe that a further refinement of some of these parameters (once the profile shape is deduced from ray-tracing) can be done together with real structure parameters without correlation problems. All the models used contain a simplification, *e.g.* a box shape for the intensity distribution inside the focus and so on, and the input of initial geometric parameters is somewhat problematic. For example, it is difficult to know precisely the actual divergence of the collimators, including any missetting by the manufacturer or the operator, or the angle between the line focus and the slit edges (always 0°?), or the effective width of the line focus and the intensity distribution emitted (exact box shape versus double peak and feet), or the effective penetration depth/linear attenuation of a packed powder sample in reflection geometry, or

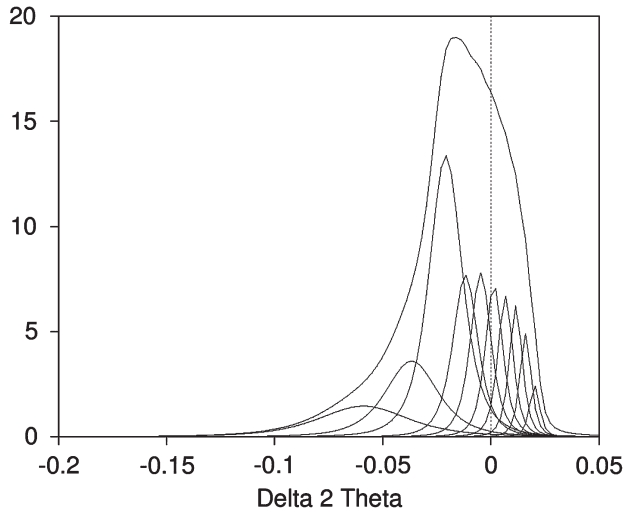



**Figure 5.3** Ray traced data for a given diffractometer set up, fitted by a sum of 10 squared Lorentzians in BGMN. (Courtesy of J. Bergmann.)

the thickness of the prepared sample in transmission geometry, or the effective sample roughness, and so on. We obviously need much more work before claiming the absolute power of the FPA.

Besides ray-tracing, the other way to conduct FPA calculations is by refining parameters related to focus width, primary and secondary axial divergence angles, detection slit width, sample penetration depth, equatorial divergence angle, *etc*., all these aberrations being modeled and numerically convoluted.[9,28] Given the FPA tendency for modeling *h*, we expect to see a decrease in the number of new propositions of algorithms for $K\alpha_2$ elimination (Chapter 4) or an improved deconvolution process, though these methods may be useful when trying to extract the *f* part by deconvolution, in studying sample broadening effects.

## 5.4 SAMPLE BROADENING

Contributions to the line broadening from the sample is dealt with in detail in Chapter 13. One equation can be applied to powder diffraction data of any kind (with or without three-dimensional ordering: liquids, amorphous or crystalline solids, and any intermediate stage) the Debye scattering equation:[36]

$$f(s) = \sum_m \sum_n f_m f_n (\sin 2\pi s r_{mn})/2\pi s r_{mn} \tag{3}$$

where $s = (2\sin\theta)/\lambda$, and $r_{mn}$ is the magnitude of the distances of each atom from every other atom with $f_m$ and $f_n$ scattering factor. This equation gives the average intensity, provided the sample can be considered as a rigid body, taking with equal probability all orientations in space. For samples that

have a one-, two- or three-dimensional ordering, other expressions can be derived from Equation (3) by successive approximations. For instance, for a perfect three-dimensional ordering, such as in perfect crystal, the double sums that run over every atom in the sample can be approximated by only a few of the shortest terms that are factored by using the so-called structure factor amplitude relative to the repetitive cell content. It is difficult to define a limit of applicability of such approximate equations. They are said to be applicable in the case of "homogeneous" systems, and if there are "not too many" imperfections, but people continue to apply them for samples showing large concentration variations or enormous disorder induced by extensive defects. Let us look at the most usual equations retained for describing size and distortion effects.

### 5.4.1 Crystallite Size

A treatment of the analysis of line-shapes to extract particle size, shape and strain information is discussed in detail in Chapter 13. Here we present an overview.

In 1918, Scherrer established[37] his famous relation giving a mean crystallite size from the X-ray line profile width (see Chapters 1 and 13). In that sense, "crystallite" is equivalent to "homogeneous domain giving rise to coherent diffraction", so that it is supposed that there is no complete break in the three-dimensional order inside of it, though there could be some limited distortion. Bertaut demonstrated,[38,39] in 1949, the important result that the size distribution can be estimated by Fourier analysis of the diffraction line profile. The Bragg law[40] ($2d\sin\theta = \lambda$) (Chapter 1) expresses the ideal geometrical conditions of diffraction; it implies that the crystal dimensions can be considered as infinite compared to the distance between two diffraction centers, otherwise a size effect broadens the Bragg peaks. To characterize the peak broadening, several parameters are useful:

- The half width, ω, introduced by Scherrer,[37] corresponding to the angular range in which the intensity is larger or equal to half the maximal intensity (now designed as the FWHM, full width at half maximum). A size parameter $\varepsilon_\omega$ is defined from ω by:

$$\varepsilon_\omega = K_\omega \lambda / \omega \cos\theta \tag{4}$$

  where $K_\omega$ is the Scherrer constant.[41]
- The integral breadth, $\beta$, introduced by Laue,[42] is the ratio of the integrated intensity to the intensity at the maximum $f_m$:

$$\beta = \left[\int f(2\theta)\,\mathrm{d}\,(2\theta)\right] \Big/ f_m \tag{5}$$

  is related to the crystallite size by the equation:

$$\varepsilon_\beta = \lambda / \beta \cos\theta \tag{6}$$

- The variance $W$, introduced by Tournarie[43] and Wilson:[44]

$$W_{2\theta} = \left[\int (2\theta - <2\theta>)^2 f(2\theta)\,\mathrm{d}(2\theta)\right] \Big/ \int f(2\theta)\,\mathrm{d}(2\theta) \qquad (7)$$

where $<2\theta>$ is the peak centroid, first rank order moment of the intensity distribution $f(2\theta)$, $W_{2\theta}$ being the second rank order moment. Langford and Wilson have shown[45] that, instead of the above relation, it was preferable to calculate a "true" variance, using the integrated intensity as a function of the truncation range $\Delta(2\theta)$ centered on the peak centroid. The tails of a $f(s)$ profile, broadened only by a size effects, are expected to vary approximately according to $s^{-2}$, and in that case the variance $W$, expressed as a function of the truncation range $\Delta(2\theta)$, is a straight line close to the curve tails:

$$W = W_0 + k\,\Delta(2\theta) \qquad (8)$$

The slope $k$ of that line leads[44] to an "apparent" mean size according to:

$$\varepsilon_k = \lambda/2\pi^2 k \cos\theta \qquad (9)$$

This $\varepsilon_k$ has the same signification as the $\varepsilon_F$ defined below from the Fourier analysis. In both cases, the "true" mean size is the product of the "apparent" dimension by the Scherrer constant relative to the variance, $K_v$. Tournarie and Wilson have tabulated $K_v$ for different crystallite shapes as a function of the Miller indices $hkl$.

- Finally, Bertaut imagined[38,39] the homogeneous domains of coherent diffraction as constituted by columns of elementary cells juxtaposed orthogonally to the diffracting planes, and he defined a size distribution $P(n)$ as the numerical fraction of columns of length $n$ cells. From that size distribution function, the size-only Fourier coefficients $A_n^S$ can be defined:[46]

$$A_n^S = \frac{1}{<N>} \sum_{i=|n|}^{m} (i - |n|)\, P(i) \qquad (10)$$

where $<N>$ is the mean number of cells per column. The sum extends from $i = |n|$ to $m$; $m$ being the finite maximum size of the columns. The size-only $f_s$ profile shape is the Fourier transform of $A_n^S$ according to:

$$f_s(x) = A_0^S + 2\sum_{n=1}^{m} A_n^S \cos 2\pi \mathrm{n}x \qquad (11)$$

where $x$ is the reciprocal variable and $n$ is the harmonic number. The first coefficient for $n = 0$ is normalized to 1 and the summation is made two times from $n = 1$ to $m$, since $A_{(+n)} = A_{(-n)}$. Usually $x$ takes the form of $(s–s_0)/\Delta s$ where $s = (2\sin\theta)/\lambda$, $s_0 = (2\sin\theta_0)/\lambda$, $\Delta s = 2(\sin\theta_2 - \sin\theta_1)/\lambda$, and $[\theta_1,\theta_2]$ is the angular range in which is defined the profile shape. The origin $\theta_0$ corresponds to the angular position of the peak maximum $f_m$, the function $f$ being symmetrical, and $m$ is the maximum number of significant

Fourier coefficients. Note that it is preferred here to use summations instead of integrals, since the problem is discontinuous (number of cells). To the harmonic number $n$ is associated a distance $M$, expressed in angstroms, in the direction orthogonal to the diffracting planes:

$$M = n/\Delta s\,(\text{Å}) \tag{12}$$

A size distribution $P(M)$, expressed along the variable $M$ in angstrom units can replace $P(n)$, and the average size is defined by the equation:

$$< M > = \sum_{M=0}^{L} MP(M) \Big/ \sum_{M=0}^{L} P(M) \tag{13}$$

where $L$ is the maximal length (Å) of the columns. $< M >$ is the so-called area-weighted average size. From $P(M)$ can be defined a size distribution in volume, $G(M) = M\,P(M)/< M >$, verified if $G(M)$ and $P(M)$ are normalized, *i.e.* $\Sigma G(M) = \Sigma P(M) = 1$.

The average of the $G(M)$ function is the so-called volume-weighted mean size:

$$< \mathrm{M}_1 > = \sum_{M=0}^{L} MG(M) \Big/ \sum_{M=0}^{L} G(M) \tag{14}$$

Another way to obtain the area-weighted size $< M >$, also called sometimes the Fourier size $\varepsilon_{\mathrm{F}}$, is from the slope at the origin of the $A_n$ function:

$$-1/\varepsilon_{\mathrm{F}} = |\mathrm{d}A_{\mathrm{n}}/\mathrm{d}M|_{M\to 0} = (A_1 - A_0)/(M_1 - M_0) \tag{15}$$

$P(n)$ can be expressed from $A_n$ as being proportional to its second derivative (which instability explains why spurious oscillations are generally obscuring the size distribution):

$$P(n)/< N > = \mathrm{d}^2 A_n/\mathrm{d}n^2 \tag{16}$$

which can be replaced by:

$$P(n) = (A_{n+1} - 2A_n + A_{n\ 1})/(A_0 - A_1) \tag{17}$$

Substitution of Equation (10) in Equation (11) gives directly $f$ as a function of the size distribution $P$:

$$f_s(x) = 1/< N > \sum_{n=1}^{m} P(n) \sin^2 \pi nx/\sin^2 \pi x \tag{18}$$

This expression was used for the $P(n)$ extraction directly from $f(x)$, but as this did not remove spurious oscillations, a smoothing procedure was applied, and the method was tested on composite specimens prepared by mixing known quantities of samples of nickel hydroxide, whose crystallite size distributions were previously determined.[47] The Fourier method is in principle an exact

approach, though not always easy to apply because of peak overlap problems, difficulties to locate the background, and in deconvoluting and separating the size effect from the distortion effect. We are supposed to have the exact relations $<M> = \varepsilon_F$ and $<M_1> = \varepsilon_{\beta F} = \varepsilon_\beta$, whereas the variance $\varepsilon_k$ and Scherrer $\varepsilon_\omega$ dimensions are obtained from approximations. Expecting that all samples presenting the same average crystallite size but different size distribution functions would lead to the same peak width (Scherrer formula) or to the same peak tail behavior in $s^{-2}$ (variance method) is a strong simplification. It is interesting to see if there is any systematic difference between these parameters (those approximated, and those in principle exact) by a study of theoretical profiles built up from some hypothetical size distributions. The relations $<M> = \varepsilon_F$ and $<M_1> = \varepsilon_\beta$ were exactly verified,[48] though it was recently shown that the diffraction profile is not strongly sensitive to the fine details of the size distribution.[49] The variance $\varepsilon_k$ showed a systematic difference that was always smaller than $<M>$ by up to 34%, the best agreement being obtained for an exponential size distribution $P(n)$ leading to a Lorentzian $f$ profile. This systematic discrepancy is confirmed in many papers where both $\varepsilon_F$ and $\varepsilon_k$ were determined. The Scherrer size $\varepsilon_\omega$ showed a systematic error as well, being always larger than $<M_1>$, up to 40%, the best agreement being obtained for a Gaussian size distribution $P(n)$ (Table 5.1).

The attraction of using the Scherrer equation is the simplicity of its use. However, given the rough approximations that underlie it,[50] and the existence of superior approaches to determining particle size, it should be time to abandon its use. Expecting that the FWHM will provide a precise crystallite size is not realistic, a page must be turned. We should also stop expecting that all crystallites are of the same shape and size, along with other considerations that are behind many approximations in that domain: generalizing special cases that are rarely, if ever, encountered. For a simple approach not requiring the size distribution extraction, it seems more appropriate to rely on calculating the integral breadth, which provides the correct $<M_1>$ estimation. All these developments suppose one to have obtained the true sample profile $f$. Ways of obtaining size estimations if $f$ or $g$ or both are either Gaussian or Lorentzian or Voigtian are based on approximations[51,52] and will not be developed here.

**Table 5.1** Comparison of crystallite sizes calculated from the variance ($\varepsilon_k$) and Scherrer ($\varepsilon_\omega$) formula, with the area-weighted $<M>$ and volume-weighted $<M_1>$ average sizes corresponding to different cases of simulated size distribution functions $P(n)$.

| *P(n) type* | $<M>$ | $\varepsilon_k$ | $<M_1>$ | $\varepsilon_\omega$ |
|---|---|---|---|---|
| Window | 100.00 | 86.13 | 123.88 | 140.62 |
| Gaussian | 100.00 | 88.94 | 104.00 | 109.75 |
| Half Lorentzian | 105.08 | 98.40 | 200.08 | 281.25 |
| Bimodal | 100.00 | 65.90 | 198.28 | 225.00 |
| Real case | 104.55 | 75.79 | 151.41 | 199.82 |

Such peak shapes correspond to special cases of $P(n)$ size distributions, sometimes showing unphysical negative proportions of crystallites at some $n$ values. Clearly, the maximum of information (the size distribution and the area-weighted and volume-weighted average sizes) will be obtained by using the Fourier analysis with a stabilization scheme,[47] or Monte Carlo/Bayesian/maximum entropy methods.[53 58]

The presence of lattice strain seriously complicates the problem, and even raises some doubts about the validity of the definition for the size effect in the presence of distortions.

### 5.4.2 Lattice Strain

The effects of lattice strain on powder line profiles are also developed in detail in Chapters 12 and 13. Again, here we give an introduction and overview.

The most convincing lattice strain description is again provided by the Fourier analysis approach. A profile $f_d$ that would be affected by only distortion effects can be asymmetrical and has to be represented by sine as well as cosine terms:

$$f_d(x) = \sum_{n=\ m}^{+m} A_n^D \cos 2\pi nx + B_n^D \sin 2\pi nx \tag{19}$$

The demonstration is usually made for an *00l* reflection from a crystal having orthorhombic axes (Warren,[59] Chapter 13.4), leading one to obtain the following definitions for $A_n^D$ and $B_n^D$, which are dependent on the harmonic number $l$ of the reflection family considered:

$$A_n^D = <\cos 2\pi l Z_n>;\ B_n^D = <\sin 2\pi l Z_n> \tag{20}$$

where $Z_n$ is the distortion variable expressing the possible differences in cell positions for cells separated by $n$ cells (in fact the component of the displacement perpendicular to the diffracting plane, neglecting the $X$ and $Y$ components). It is seen here that the broadening due to microstrain increases with the $l$ order, whereas the size broadening is independent of the order of a reflection. If we define a distribution function $D_{n,Z}$ as representing the probability for the distortion to have the value $Z_n$ between one cell and its $n$th neighbor in the whole sample, then we have:

$$A_n^D = \int_{1/2}^{+1/2} D_{n,Z} \cos(2\pi l Z)\, \mathrm{d}Z;\ B_n^D = \int_{1/2}^{+1/2} D_{n,Z} \sin(2\pi l Z)\, \mathrm{d}Z \tag{21}$$

This time, the problem is continuous in $Z$; however, the integral is not supposed to extend from $-\infty$ to $+\infty$, since $Z_n$ is expected to vary between $-1:2$ and $+1:2$ times the cell parameter (if it would be more, then we would have to consider $Z_{n+1}$, *etc.*). We could obtain a generalization for the whole *00l* family ($l = 1, 2$, *etc.*) that would enable us to calculate the profile shapes,

extending along the whole powder pattern, including the possible size effect, according to:

$$f(x,l) = \sum_{n=\ -m}^{+m} \int_{1/2}^{+1/2} A_n^S \, D_{n,Z} \cos\left[2\pi(nx + lZ)\right] \mathrm{d}Z \tag{22}$$

A generalization to any *hkl* direction would build the complete powder pattern, provided the structure factor is integrated. A $f(x,l)$ reflection is not supposed to extend outside of the range $x = l - 1:2$ to $x = l + 1:2$.

For a large distortion, the question arises as to what extent the use of the above equation will provide erroneous results, and does the size effect become the consequence of the distortion effect. It is not conceivable that the average size of a "homogeneous" domain of coherent diffraction could be larger than the average distance (to an arbitrary origin) for which the disorder is complete, or the periodicity definitely broken. In metals, it was found[60] that the values of size corresponded to the average distance between dislocations. We have to note that the above equations for microstrain effects are approximate ones. In the case of large distortions, the $f(x,l)$ values for $x$ close to $l - 1:2$ or $l + 1:2$ would not be zero, so that, if the observed powder pattern would show continuous changes in intensity, the pattern calculated according to Equation (22) would present large staircase steps, when scaled by the structure factor $F^2_{(hkl)}$. This is a logical effect when using an average representation of the cell content instead of using the real cell content, using the approximate expression Equation (22) instead of the Debye scattering Equation (3). Even more approximations are in use. The equations about the strain effect above already are the result of approximations that are admissible only if there is little distortion. The following scalar product (using the Warren[59] notation) is reduced to its more simple expression:

$$(\boldsymbol{s} - \boldsymbol{s}_0)/\lambda \cdot \delta_m = (h_1\boldsymbol{b}_1 + h_2\boldsymbol{b}_2 + h_3\boldsymbol{b}_3) \cdot (X_m\boldsymbol{a}_1 + Y_m\boldsymbol{a}_2 + Z_m\boldsymbol{a}_3) \approx lZ_m \tag{23}$$

Any distortion within the unit cell is neglected, allowing one to use the same structure factor for all cells. This is valid if the description of distortions by fluctuations of cell parameters is a reasonable view. This is far from being demonstrated for many kinds of defect such as different sorts of dislocations and faults, twin boundaries, concentration variations, *etc*. It should work better for simple defects like the substitution of one element by another without changing the local order, but only displacing a bit its environment due to different radii. For distortions associated with large faults, the size-strain Fourier analysis view is obviously an oversimplification already in its more perfect definitions above. Moreover, generally the approximations do not stop here. The $B_n^D$ sine terms are usually neglected, considering only symmetric profile shapes. After that, in the so-called Warren and Averbach method,[46] it is admitted that, for small values of $l$ and $n$, the cosine can be expanded:

$$<\cos 2\pi Z_n> \approx 1 - 2\pi^2 l^2 <Z_n^2> \tag{24}$$

providing the possibility to separate the size and strain effects in the product $A_n = A_n^S A_n^D$ from the disposal of two harmonic reflections (for $l = 1$ and $l = 2$ for instance). Further approximations may come from this hypothesis. For instance, if the strain distribution is Gaussian, then:

$$<\cos 2\pi l Z_n> = \exp(-2\pi^2 l^2 <Z_n^2>) \tag{25}$$

If this model is correct and if the root mean squared strain varies as the square of the distance ($<Z_n^2> = n^2 <Z_1^2>$), then the profile would have a Gaussian peak shape whereas if the variation was linear ($<Z_n^2> = n <Z_1^2>$) the profile would be Lorentzian. Using an expression like $<Z_n^2> = n^k <Z_1>$ allows the modeling of the profile by refining only two parameters, $k$ and $<Z_1^2>$ (for $n = 1$). This model was used in an approach[17] for introducing the Fourier method inside of the Rietveld method. Trying to establish the limits of validity of these above approximations could be done by the study of very large models affected by more or fewer defects, of which the corresponding powder pattern could be calculated exactly by the Debye scattering, Equation (3). Applying then the above approximate equations to separate the size and distortion effects would certainly be quite instructive about the errors made. Anyway, one cannot expect that reducing the complexity of disordered condensed matter by a few parameters will provide anything more than a vague characterization.

Going in the reverse sense, modeling patterns (WPPM:[61 63] Whole Powder Pattern Modeling, Chapter 13) by using the above equations or even more simplified (but without using arbitrary profile functions) would have the same limitations. Nevertheless, the fit of glass powder patterns gave not such bad results in some cases[64,65] (including glassy $SiO_2$ or fluoride glasses), and by using an extreme isotropic distortion of the average structure models being used then in RMC[66] (Reverse Monte Carlo) modeling was even more successful.[67,68] The ideal modeling would be that of real defects, respecting real distances between atoms at any place in the model, and only then applying the Debye scattering equation. This was done for Ni-Mo-S compounds,[69,70] for modeling nanocrystalline solids,[71,72] or two-dimensional materials,[73] including turbostratically stacked layer systems.[74] Another modeling approach for calculating diffracted intensities from crystals containing planar faults is implemented in the DIFFaX program.[75]

### 5.4.3 Anisotropic Sample Broadening: Faulting

Unless all crystallites are spheres, in the general case there will be a directional *hkl*-dependency of the broadening. Of course, distortions may occur in preferred directions and generate both anisotropic size and microstrain effects. Some kinds of fault can produce a break of the long-range order for only a part of the cell content. A relatively simple case[76] is that of antiphase domains in $KAlF_4$, where perovskite layers of corner-sharing [$AlF_6$], disconnected along the $c$ axis by the intercalation of $K^+$ ions, can undergo a change in the tilting angle. The effect is that of an ordering of K, Al and axial F atoms, whereas the

equatorial F atoms generate a size effect according to the distance between antiphase domains. The F atoms, being on more general positions than the others, are the only atoms that contribute to some *hkl* combinations which, as a consequence, are especially broadened. This is more apparent in neutron rather than the X-ray data. Such a special anisotropic broadening effect causes difficulties in whole pattern decomposition process or Rietveld refinements. A simple slight hand-crushing causes the disappearance of some reflections, while annealing makes them appear again, but with residual broadening (Figure 5.4)

By using a crushing machine for 20 min, a huge broadening appears, and asymmetric lines appear, probably associated with misorientations of the perovskite layers. Such asymmetric bands, rather than reflections, are common in layered silicates. An example is shown in Figure 5.5 for a commercial talc sample. Obtaining an excellent fit for such a powder pattern, showing narrow lines together with large asymmetrical bands, is extremely difficult.

Another interesting case of faulting is observed for $HNbO_3$, which adopts a cubic double perovskite structure.[77] It is probably due to a three-dimensional generalization of the phenomenon corresponding to the previous $KAlF_4$ example. The anisotropic effect due to faulting is especially obvious on the neutron powder pattern (Figure 5.6). Anisotropic line broadening is especially hard to model in whole powder pattern fitting. For those wanting to test by themselves, the patterns shown in the Figures 5.4, 5.5 and 5.6 are available at

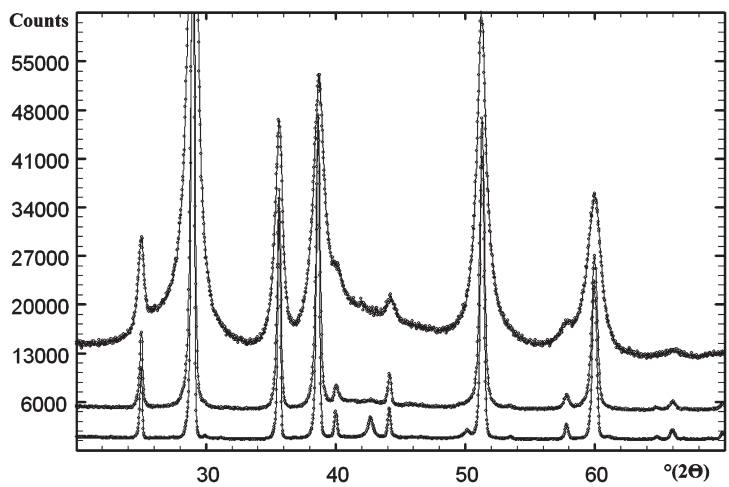



**Figure 5.4** Three $KAlF_4$ conventional X ray powder patterns (Cu $K_\alpha$). Bottom: sample slightly ground by hand, then annealed (see the small peak close to 42.5°2θ, still broader than others, related to antiphase domains). Middle: sample slightly ground by hand (some peaks vanish, there is already a complete disorder in the octahedral tilting angle along the ***c*** direction). Top: sample ground to 20 mn with a crusher, the perovskite layers are now partly disoriented, generating peak asymmetry.

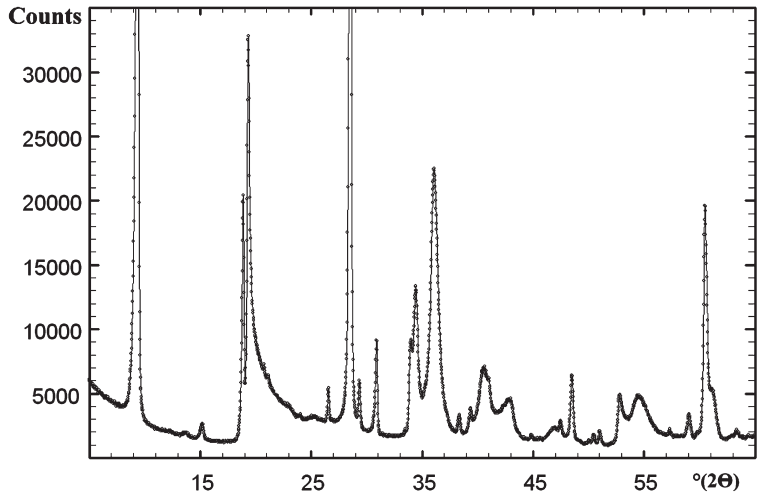



**Figure 5.5** X ray powder pattern (Cu $K_\alpha$) of a commercial talc sample showing the complex coexistence of narrow peaks, broad ones, and very broad asymmetrical bands related to turbostratic effects (strongly disoriented layers). An excellent fitting of such a pattern with a complete physical description of the distortions is far beyond our current capabilities.

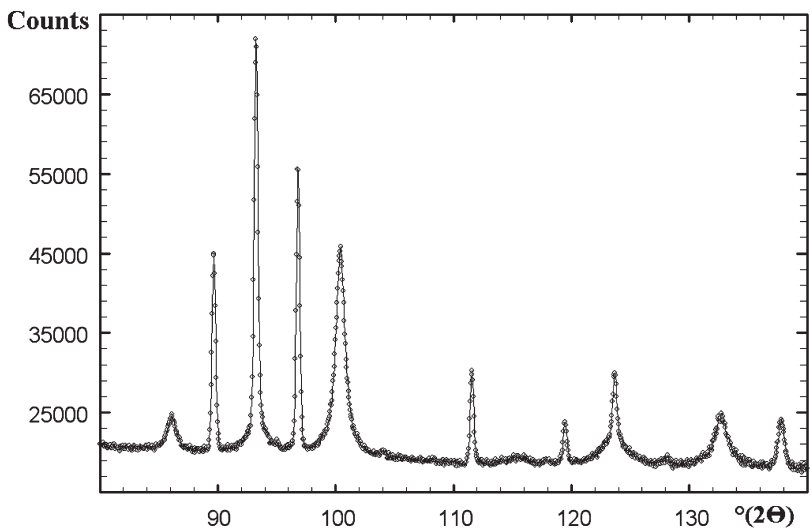



**Figure 5.6** Part of the neutron powder pattern ($\lambda = 1.909$ Å) of cubic double perovskite $HNbO_3$, showing very different profile shapes and widths. No excellent fit of that pattern has ever been produced from a realistic model, though the most probable faulting inside of the sample is a simple three dimensional antiphase effect due to $[NbO_6]$ octahedra inversion of the tilting angles of connection.

the PowBase[78] Internet Web site. The recent size strain round robin[27] was limited to the study of an isotropic size effect for a cubic sample with a short cell parameter. We still wait for a comparative study of different methods, for a reasonably complex problem, say an orthorhombic sample, with both size and strain effects, anisotropy, and a relatively large cell resulting in significant peak overlap. This limitation of the round robin to a very simple cubic structure suggests how much disagreement exists in the international community about the correct way to tackle such effects, as may be seen in review papers[79 83] about including microstructure characterization inside of the Rietveld method.

Attempts to consider a *hkl* dependence of the broadening in the Rietveld method were made by using different approaches involving ellipsoid,[17,84 87] quartic and quadratic forms,[88 90] either representing the modulation of the average sizes $<M>_{hkl}$ and $<M_1>_{hkl}$ and microstrain $<Z^2>_{hkl}$, or used for a purely phenomenological qualitative fit without trying to extract any physical parameters.

## 5.5 INDIVIDUAL PEAK FITTING AND LINE PROFILE ANALYSIS

Analyzing or fitting individual Bragg peaks can be done for very different purposes, at different steps of a sample characterization: extraction of peak positions for indexing purposes, stress characterization (Chapter 12), extraction of microstructural parameters by line profile analysis (LPA) according to different methods (Chapter 13), *etc*. From Equation (1), LPA would require deconvolution, *i.e*. extracting $f$ knowing $h$ and $g$. This operation is more delicate than convoluting $f$ from a model with $g$ and obtaining a calculated $h$ to be compared to the observed one. Moreover, deconvolution requires that there is not any peak overlap, so that only simple cases are manageable (high symmetry, small unit cell). Working in Fourier space facilitates the deconvolution process since it is replaced by a simple product. Designating $H$, $F$ and $G$ as the Fourier transform respectively of $h$, $f$ and $g$, then the deconvolution is replaced by a division in the Fourier space, so that $F(n) = H(n)/G(n)$. That process has long been used[91] in LPA techniques, *e.g*., the Stokes method, but leads to some oscillations on $F(n)$ and possibly to negative values for large harmonic $n$ numbers. Many methods[92] were proposed to avoid such spurious effects. Early use of direct convolution product to model powder diffraction profiles described[93 97] the instrument contribution as a convolution of two functions, one representing the diffractometer's optics, and a second representing the wavelength distribution of the X-rays (incomplete FPA). In model-based peak-shape and semi-empirical approaches, the double-Voigt[98 102] is the more elaborated line shape since size as well as microstrain is described by Voigt or pseudo-Voigt functions. Besides the Gaussian peak shape used early on (for instance in the Rietveld method[10]) for the fit of constant-wavelength neutron data, many other analytical profiles were selected for enabling individual peak fitting or the global fit of $h$ or $g$. Most of these analytical peak shapes are listed by Young and Wiles,[103] such as Lorentzian,[104] squared

Lorentzian, Voigt,[105] Pseudo-Voigt,[106] Pearson-VII,[107] Split Pearson-VII,[108] the latter allowing the modeling of peak asymmetry, *e.g.*, when introducing an asymmetry parameter for Gaussians in the original Rietveld method, or using modified a Lorentzian,[109] *etc.* For time of flight (ToF) data, the profile shapes are harder to model.[110] Using either of these peak shapes approaches, the fit can be attempted without any cell knowledge, or trying to find peaks where they should be, according to the cell and space group knowledge, on one peak, one group of peaks or on the whole pattern; this is the subject of the following sections.

### 5.5.1 Peak Fitting for Intensity/Position Extraction – With or without Cell Knowledge

There is an incredibly large number of interactive computer programs for fitting analytical models to powder diffraction patterns. The problem with individual peak fitting without cell knowledge is that there is a limit to the number of overlapping peaks that can be seriously undertaken whereas knowing the cell parameters adds a restraint on the peak position. The fit can be done either by using analytical profile shapes chosen empirically (frequently a pseudo-Voigt) with the purpose of obtaining the best fit, or by applying the FPA. Some defenders of the FPA consider that the refining of "fundamental parameters" is nonsense, unless one is not familiar with his diffractometer or want/must "absorb" any unknown effects or weaknesses of his model. However, other FPA programmers consider it legitimate to allow the possibility of adjusting a few parameters (source, sample and slit lengths; receiving slit and source widths; horizontal divergence; primary and secondary Söller slits angles) during the fit.[9,111,112] The same considerations extend to the fitting of the complete pattern, this being treated in Section 5.5 about whole profile fitting.

### 5.5.2 Using Individual Peaks for Size/Distortion Extraction

Here, there are three possibilities: full analysis (Fourier methods), partial treatment (integral breadth, variance,...), or peak fitting using models (with FPA or not). A huge literature exists on this subject,[92] including the outdated "single line methods" that assume that the size or strain constituent profiles are either Lorentzian or Gaussian. The Williamson–Hall Plot,[113] based on integral breadth, is still in use despite the approximation that profiles due to size and strain are Lorentzian – it is applicable only if one analyzes a series of individual peaks.

### 5.5.3 Further Approximations

Usually not taken into account is the variation of the structure factor due to the variation of the diffusion factor (X-ray), or of the Lorentz-polarization factor.

When a peak is large, this may become quite significant,[114,115] including in the case of whole powder pattern decomposition detailed in the next section.

## 5.6 WHOLE POWDER PATTERN DECOMPOSITION (WPPD) – NO STRUCTURE

If the structure is used for the calculation of the intensities, then this is the whole powder pattern fitting (WPPF) Rietveld method for structure refinement (Chapter 13). In this section, it is considered that the structure is not used, but the indexing and the cell parameters are used. So, this is still WPPF but is the second variant, generally designated by WPPD (Whole Powder Pattern Decomposition). Clearly, any WPPF approach should be able to model the peak shape and width variation according to the diffraction angle. Again, this can be done either by fitting some analytical profile parameters in a semi-empirical approach, and the angular variation of these parameters is generally controlled by refining the U, W and W terms in the Cagliotti law[116] $(\mathrm{FWHM})^2 = U\tan^2\theta + V\tan\theta + W$, or using the FPA by ray-tracing.

### 5.6.1 No Cell Restraint

Obtaining all the peak positions, areas, breadths and shape parameters for a whole powder pattern without using the unit cell information is obviously limited to simple cases where there is not too much peak overlap. With such an approach one has to provide the number of peaks to be fitted so that the fit of an intricate group of peaks does not lead to large uncertainties if the cell is unknown. However, knowing the cell and space group and still using the peak position as a refinable parameter provides at least the correct number of peaks and an estimation of their starting position. Such calculations were made as an alternative to the Rietveld method, during the first stage of the so-called two-stage method for refinement of crystal structures.[117] In the case of X-ray data, early WPPF programs used profile shapes being a sum of Lorentzian curves,[118] or double-Gaussian.[119] The computer program PROFIT, deriving from a software for individual profile fitting[94] and extended to the whole pattern, was applied to the study of crystallite size and strain in zinc oxide[120] and for the characterization of line broadening in copper oxide.[121] Studying a whole pattern can also be done in simple cases by using software designed for the characterization of single or small groups of peaks, an example is a ZnO study[122] by using the computer program FIT (Socabim/Bruker). However, WPPD is mostly realized nowadays by using peak positions controlled by the cell parameters, even if the loss of that degree of freedom leads to slightly worst fits, increasing the profile *R* factors.

### 5.6.2 Cell-restrained Whole Powder Pattern Decomposition

Imposition of the peak positions calculated from a cell knowledge marked a great step in the quest for *ab initio* structure determination by powder

diffractometry (SDPD). Arguably, leaving free the peak positions will allow for taking account of subtle effects in position displacement (in stressed samples for example, Chapter 12). But variation with regard to the theoretical position as expected from cell parameters can be modeled as well in WPPD or the Rietveld method. Nowadays, two generic names are retained for such cell-constrained WPPD methods which can produce a set of extracted intensities suitable for attempting a structure solution; the Pawley and Le Bail methods. Both were derived from the Rietveld method.

*5.6.2.1 The Pawley Method.* Removing the crystal structure refinement in a Rietveld software, and adding the possibility to refine an individual intensity for every expected Bragg peak produced a new software (named ALLHKL) allowing the refinement of the cell parameters very precisely and the extraction of a set of structure factor amplitudes. The process was later called the Pawley method.[123] The least-squares ill-conditioning due to peak overlap was overcome by using slack constraints. The usefulness of that procedure for the confirmation of the cell indexing of a powder pattern of an unknown was completely obvious in this original paper. Nevertheless, no SDPD was realized by using the Pawley method before several years, probably because of the limitations in computer power. During these pioneering years, the version of ALLHKL could not extract the intensities for more than 300 peaks, so that for more complex cases it was necessary to divide the pattern into several parts. Moreover, it was a little difficult to avoid completely the under constrained nature of the problem due to peak overlap. Being successful provides equipartitioned intensities (*i.e.*, equal structure factors for those *hkl* Bragg peaks with exact overlap), but being unsuccessful could well produce negative intensities. Also, the first version applying Gaussian peak shapes could not produce any SDPD due to the relatively poor resolution of constant wavelength neutron data, and so it needed to be adapted to X-ray data, with the implementation of more complex peak shapes. A series of programs were proposed next, based on the same principles as the original Pawley method. Some programs were used to produce intensities to apply the so-called two-step-method for structure refinement, instead of using the Rietveld method (Cooper controversy[117]). Toraya introduced two narrow band matrices instead of a large triangular matrix, saving both computation time and memory space in his program WPPF.[124] Other program names are PROFIT,[125] PROFIN[126] (no slack constraints, but equal division of the intensity between expected peaks when the overlap is too close), FULFIT,[127] LSQPROF[128] and POLISH[129] (see also Chapter 17 for a snapshot of computer programs available at the time of printing). Improving the estimation of intensities of overlapping reflections in LSQPROF by applying relations between structure factor amplitudes derived from direct methods and the Patterson function was considered in a satellite program DOREES.[130] The question of how to determine the intensities of completely (or largely) overlapping reflections (systematic due to symmetry or fortuitous) in powder diffraction patterns cannot have a definite simple answer but continues to be much discussed since it is essential for improving our ability

to solve structures. An early view with a probabilistic approach was given by David,[131] introducing later[132] Bayesian statistics inside the Pawley method. Early findings of preferred orientation on the basis of an analysis of *E*-value distributions was another way[133] to improve the structure factor amplitude estimate.

*5.6.2.2 The Le Bail Method.* To be able to estimate *R* factors related to integrated intensities, Rietveld[10,134] stated "a fair approximation to the observed integrated intensity can be made by separating the peaks according to the calculated values of the integrated intensities, *i.e.*":

$$I_K(\text{obs}) = \sum_j \{w_{j,K} \cdot S_K^2(\text{calc}) \cdot y_j(\text{obs})/y_j(\text{calc})\} \tag{26}$$

where $w_{j,K}$ is a measure of the contribution of the Bragg peak at position $2\theta_K$ to the diffraction profile $y_j$ at position $2\theta_j$. The sum is over all $y_j$(obs) that can theoretically contribute to the integrated intensity $I_K$(obs). There is a bias introduced here by the apportioning according to the calculated intensities, which is why the observed intensities are in fact said to be "observed", in quotes, in Rietveld's work. These "observed" intensities are used in the $R_B$ and $R_F$ calculations (reliabilities on intensities and structure factor amplitudes). They are also required for Fourier map estimations, which, as a consequence, are less efficient than from single crystal data. The process of using iteratively the Rietveld decomposition formula Equation (26) for WPPD purposes is now called the Le Bail method.[135] In the original computer program (ARITB) that first applied this method, arbitrarily all equal $S^2{}_K$(calc) values are first injected into Equation (26), instead of using structure factors calculated from the atomic coordinates. This results in "$I_k$(obs)" which are then reinjected as new $S^2{}_K$(calc) values at the next iteration, while the usual profile and cell parameters (but not the scale) are refined by least-squares. Equipartitioning of exactly overlapping reflections comes from the strictly equal result from the Equation (26) for Bragg peaks at the same angles that would have starting equal calculated intensities. Starting from a set of $S^2{}_K$(calc) values that are not all equal would produce $I_K$(obs) values keeping the same original ratio for the exactly overlapping reflections. Understandably, such an iterative process requires as good a starting cell and profile parameters as the Rietveld method itself. The process is easier to incorporate inside an existing Rietveld code than the Pawley method, so that most Rietveld codes propose now the structure factor amplitudes extraction as an option (generally multiphase, with the possibility to combine a Rietveld refinement together with a Le Bail fit). A list of earlier programs (1990–1995) applying the Le Bail method (the name coming later) includes MPROF,[136] FULLPROF,[137] EXTRACT,[138] EXTRA[139] (EXPO[140] is the integration of EXTRA and SIRPOW92 for the solution and refinement of crystal structures), followed now by most well-known Rietveld codes (BGMN, GSAS, MAUD, TOPAS, *etc.*) or standalone programs (AJUST[141]). Many improvements were incorporated in the pattern decomposition Le Bail method by the Giacovazzo group: by obtaining information about the possible presence

of preferred orientation by the statistical analysis of the normalized structure factor moduli;[142] by using the positivity of the Patterson function inside of the decomposition process[143] (this having been considered previously[131,144 146]); by the characterization of pseudotranslational symmetry used as prior information in the pattern decomposition process;[147] by multiple Le Bail fits with random attribution of intensity to the overlapping reflections, instead of equipartition, followed by application of direct methods to large numbers of such datasets;[148 150] by the use of a located structure fragment for improving the pattern decomposition process;[151] and by the use of probability (triplet-invariant distribution functions) integrated[152] with the Le Bail algorithm.

*5.6.2.3 Comparisons of the Pawley and Le Bail Methods.* The Giacovazzo group considered[153] that pattern-decomposition programs based on the Le Bail algorithm are able to exploit the prior information in a more effective way than Pawley-method-based decomposition programs. Other comparisons of both methods are given by Giacovazzo,[154] and David and Sivia,[155] finding that the Le Bail method could lead to negative intensities in ranges of the pattern where the background is overestimated. Another approach for solving the overlapping problem was proposed by using maximum-entropy coupled with likelihood evaluation.[156] The fact is that both the Pawley and Le Bail methods are able to estimate structure factor amplitudes that can lead to solved structures from powder diffraction data in a more efficient way than was previously possible.

### 5.6.3 Main Applications of WPPD

The list of the possible WPPD applications is impressive (see for instance review papers by Toraya[157] or Le Bail[158]), by either the Pawley or Le Bail methods. In the SDPD maze,[159] there is no other path than to use at least one of them. With both methods, the fit quality is checked from agreement factors that are the same as with the Rietveld method: $R_P$, $R_{WP}$, $R_{EXP}$ (moreover, a careful visual check is recommended). The reliabilities relative to the structure ($R_B$ and $R_F$), which can still be calculated, are meaningless (both programs tending to obtain zero for them). It is recommended[160] to have confidence preferably in the original Rietveld estimated profile R factors (calculated after background subtraction, and removing ''non-peak'' regions). WPPD provides help in cell parameter refinement, determination of space group. The main target is the extraction of intensities (Figure 5.7) for *ab initio* structure solution purposes (it was not until 1987 that the first SDPD was realized by using the Pawley method, for solving a really unknown structure[162]), or at least for the establishment of the profile parameters to be used in a direct-space solution program exploiting a raw powder pattern. These WPPD methods will provide the smallest profile R factors attainable, smaller than those obtained at the Rietveld method final step. With neutron data, besides solving the nuclear structure, the FULLPROF program allows for solving magnetic structures as well.[163] Reusing extracted intensities for structure solution by direct space

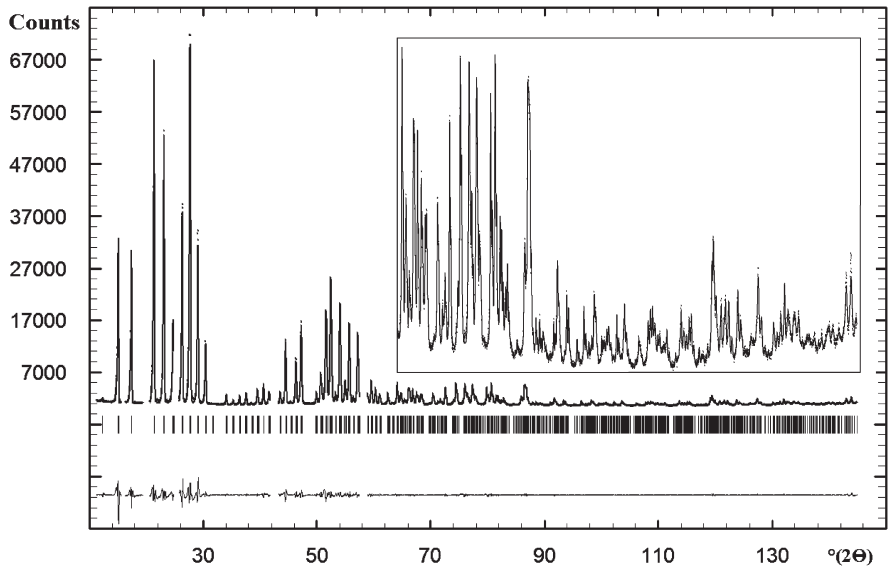



**Figure 5.7** An old example (1992) of Le Bail fit for structure factor amplitude extraction, prior to structure determination by powder diffractometry of the τ $AlF_3$ polymorph[161] (conventional Cu $K_\alpha$ X ray data). No isostructural phase is known for that metastable compound based on [$AlF_6$] octahedra exclusively connected by corners in a completely new 3D framework, synthesized only in fine powder form, either from organometallic or hydrated amorphous precursors. The structure was solved by applying the direct methods (no heavy atom), revealing totally the 11 independent atom sites.

methods can be made in a way that is not sensitive to the equipartitioning problems. This was done in the ESPOIR program[164] by regenerating a powder pattern from the extracted "|Fobs|", using a simple Gaussian peak shape whose width follows the Cagliotti law established from the raw pattern. With such a pseudo powder pattern, without profile asymmetry, background, *etc.*, the calculations are much faster than if the raw pattern was used. In another direct-space structure solution program, PSSP,[165] based on the Le Bail method as well, an agreement factor allowing one to define the best model takes account of the overlap significant for nearby peaks. In DASH, a similar method[166] is applied to the intensities extracted by the Pawley method through the use of the correlation matrix.

When using direct methods instead of the direct-space methods, the approaches are different. The direct methods necessitate the more complete possible dataset (up to $d = 1$ Å) of accurate "|Fobs|". However, removing up to half of them (those with too much overlapping, *i.e.* being too nearby than 0.5 FWHM, for instance) is possible while obtaining some success with the direct methods (one can even remove up to 70–80% if the Patterson method is applied and if only a small number of heavy atoms are to be located). David

provided a demonstration[167] recently of the equivalence of the Rietveld method and the correlated intensities method in powder diffraction (it is unlikely that this demonstration, related to the old two-stage controversy, could lead to abandonment of the Rietveld method; however, research is made on the question[168]). Another application of WPPD is for data generation used for Fourier map calculations for structure completion. The "|Fobs|" are estimated at the end of a Rietveld refinement by the Rietveld decomposition formula, so that the exactly overlapping reflections are given intensities in the same ratio as they are calculated from the structural model. The Le Bail method could be applied here, performing more than one iteration of the decomposition formula, which would be insufficient for attaining the minimum if there is a large discrepancy between the observed and calculated patterns.

Calculations of electron density distributions from powder data also benefit from the WPPD methods. Finally, it may be interesting to realize size-strain analysis together with WPPD, if the structure model cannot provide a very good fit, or when systematic errors distort the observed intensities. However, the structure constraint will at least impose an almost correct intensity to overlapping peaks, which is not the case in either the Pawley or Le Bail methods. The structure constraints may preclude errors in attributing a wrong broadening to some peaks with exact overlapping. Prudence is thus recommended. Including size-strain analysis in WPPD requires the use of special formula for taking account of the angular variation of the FWHM or of the integral breadth, the same formula as those used with the Rietveld method: either the so-called TCH[169] formula (with different angular dependence for the Gaussian and Lorentzian components of a pseudo-Voigt) or the Young and Desai[79] formula recommending the use of both G and L components for both size and microstrain effects. A different approach would be by whole Powder Pattern Modeling (WPPM[61 63]), consisting of the introduction of a physical model, including deformations, twin fault, dislocations and crystallite size distributions, with the expectation of obtaining realistic quantities to define microstructures, as discussed in Chapter 13. However, if this is done through the microstrain approximations implicit in Equations (19) to (25) above, then the distortions should not be too large.

## 5.7 CONCLUSIONS

The profile of a Bragg reflection, if seen through a high-resolution diffractometer, may reveal very fine details of the microstructure. The present chapter provides an overview and reviews the limitations of our possibilities of analysis of such microstructures by using only diffraction profiles and global distortion parameters supposed to represent an averaging of all kind of imperfections. Using Bragg peak shape analysis for microstructure characterization, we should restrain ourselves to consider small deviations from regularity, otherwise the very few extracted parameters will not have much sense owing to the complexity and diversity of imperfections that could be at the origin of the line

broadening. It appears logical that a large part of the distortion effects due to large imperfections lead to diffracted X-rays that are not included inside of the Bragg peaks, unless these defects have the same periodicity as the cell, or would lead only to a size effect (some kinds of stacking faults). If the size-only effect appears more manageable with confidence, it has still to be established that there is not any distortion effect.

The view about line profile analysis given in this chapter is pessimistic, it is the consequence of the complexity of the Bragg peak shapes as they occur from poorly-crystallized material. More optimistic is the future of the main whole powder pattern fitting applications (decomposition or Rietveld methods) that have moved beyond the initial stages, enabling structure determinations (almost routinely) and refinements (routinely) of moderately complex structures to even complex crystal structures such as proteins (sometimes).

## REFERENCES


1. F. W. Jones, *Proc. R. Soc. London, Ser. A*, 1938, **2**, 98.
2. O. Masson, E. Dooryhée and A. N. Fitch, *J. Appl. Crystallogr.*, 2003, **36**, 286.
3. G. Courbion and G. Férey, *J. Solid State Chem.*, 1988, **76**, 426.
4. A. J. C. Wilson, *X-Ray Optics*, Methuen, London, 1962.
5. A. J. C Wilson, *Mathematical Theory of X-ray Powder Diffractometry*, Gordon & Breach, New York, 1963.
6. A. J. C. Wilson, *Elements of X-ray Crystallography*, Addison-Wesley, Reading, Massachusetts, 1970.
7. L. E. Alexander, *J. Appl. Phys.*, 1954, **25**, 155.
8. H. P. Klug and L. E Alexander, *X-ray Diffraction Procedures*, Wiley, New York, 1954; 2nd edn., 1974.
9. R. W. Cheary and A. Coelho, *J. Appl. Crystallogr.*, 1992, **25**, 109.
10. H. M. Rietveld, *J. Appl. Crystallogr.*, 1969, **2**, 65.
11. G. Malmros and J. O. Thomas, *J. Appl. Crystallogr.*, 1977, **10**, 7.
12. R. A. Young, P. E. Mackie and R. B. von Dreele, *J. Appl. Crystallogr.*, 1977, **10**, 262.
13. D. B. Wiles and R. A. Young, *J. Appl. Crystallogr.*, 1981, **14**, 149.
14. S. A. Howard and K. D. Preston, *Rev. Mineral.*, 1989, **20**, 217.
15. A. Hepp and C. Baerlocher, *Aust. J. Phys.*, 1988, **41**, 229.
16. H. Toraya, *J. Appl. Crystallogr.*, 1990, **23**, 485.
17. C. Lartigue, A. Le Bail and A. Percheron-Guégan, *J. Less-Common Met.*, 1987, **129**, 65.
18. A. N. Fitch, *Mater. Sci. Forum*, 1996, **228–231**, 219.
19. J. B. Hastings, W. Thomlinson and D. E. Cox, *J. Appl. Crystallogr.*, 1984, **17**, 85.
20. B. Van Laar and W. B. Yellon, *J. Appl. Crystallogr.*, 1984, **17**, 47.
21. L. W. Finger, D. E. Cox and A. P. Jephcoat, *J. Appl. Crystallogr.*, 1994, **27**, 892.

22. R. W. Cheary and A. Coelho, *J. Appl. Crystallogr.*, 1998, **31**, 851.
23. V. Honkimäki, *J. Appl. Crystallogr.*, 1996, **29**, 617.
24. O. Masson, R. Guinebretière and A. Dauger, *J. Appl. Crystallogr.*, 2001, **34**, 436.
25. H. Berger, *X-Ray Spectrom.*, 1986, **15**, 241.
26. G. Hölzer, M. Fritsch, M. Deutsch, J. Härtwig and E. Förster, *Phys. Rev.*, 1997, **56**, 4554.
27. D. Balzar, N. Audebrand, M. R. Daymond, A. Fitch, A. Hewat, J. I. Langford, A. Le Bail, D. Louër, O. Masson, C. N. McCowan, N. C. Popa, P. W. Stephens and B. H. Toby, *J. Appl. Crystallogr.*, 2004, **37**, 911.
28. A. Kern, A. A. Coelho and R. W. cheary, in *Diffraction Analysis of the Microstructure of Materials*, Springer, Berlin, 2004, p. 17.
29. G. Zsigmond, K. Lieutenant and F. Mezei, *Neutron News*, 2002, **13**(4), 11.
30. J. Šaroun and J. Kulda, *Neutron News*, 2002, **13**(4), 15.
31. P. A. Seeger, L. L. Daemen, T. G. Thelliez and R. P. Hjelm, *Neutron News*, 2002, **13**(4), 20.
32. P. A. Seeger, L. L. Daemen, E. Farhi, W.-T. Lee, X.-L. Wang, L. Passel, J. Šaroun and G. Zsigmond, *Neutron News*, 2002, **13**(4), 24.
33. W.-T. Lee and X.-L. Wang, *Neutron News*, 2002, **13**(4), 30.
34. J. Bergmann, P. Friedel and R. Kleeberg, *IUCr CPD Newsletter*, 1998, **20**, 5.
35. J. Bergmann, R. Kleeberg, A. Haase and B. Breidenstein, *Mater. Sci. Forum*, 2000, **347–349**, 303.
36. P. Debye, *Ann Physik*, 1915, **46**, 809.
37. P. Scherrer, *Nachr. Ges. Wiss. Göttingen*, 1918, 26 Sept., 98.
38. F. Bertaut, *C. R. Acad. Sci. Paris*, 1949, **228**, 492.
39. E. F. Bertaut, *Acta Crystallogr.*, 1950, **3**, 14.
40. W. L. Bragg, *Proc. Cambridge Phil. Soc.*, 1913, **17**, 43.
41. C. C. Murdock, *Phys. Rev.*, 1930, **35**, 8.
42. M. Laue, *Z. Kristallogr.*, 1926, **64**, 115.
43. M. Tournarie, *C. R. Acad. Sci. Paris*, 1956, **242**, 2016.
44. A. J. C. Wilson, *Proc. Phys. Soc. London*, 1962, **80**, 286.
45. J. I. Langford and A. J. C. Wilson, *Crystallography and Crystal Perfection*, ed. G. N. R. Ramachandran, Academic Press, London, 1963, p. 207.
46. B. E. Warren and B. L. Averbach, *J. Appl. Phys.*, 1950, **21**, 585; 1952, **23**, 497.
47. A. Le Bail and D. Louër, *J. Appl. Crystallogr.*, 1978, **11**, 50.
48. A. Le Bail, 3ème Cycle Thesis, Rennes, 1976. http://tel.ccsd.cnrs.fr/documents/archives0/00/00/70/41/.
49. S. Rao and C. R. Houska, *Acta Crystallogr. Sect. A*, 1986, **42**, 6.
50. J. I. Langford and A. J. C. Wilson, *J. Appl. Crystallogr.*, 1978, **11**, 102.
51. R. Delhez, Th. H. de Keijser and E. J. Mittemeijer, *Fresenius Z. Anal. Chem.*, 1982, **312**, 1.

52. Th. H. de Keijser, E. J. Mittemeijer and H. C. F Rozendaal, *J. Appl. Crystallogr.*, 1983, **16**, 309.
53. P.-Y. Chen and C.-Y. Mou, *J. Chin. Chem. Soc.*, 1994, **41**, 65.
54. P. E. Di Nunzio, S. Martelli and R. Ricci Bitti, *J. Appl. Crystallogr.*, 1995, **28**, 146.
55. P. E. Di Nunzio and S. Martelli, *J. Appl. Crystallogr.*, 1999, **32**, 546.
56. N. Armstrong and W. Kalceff, *J. Appl. Crystallogr.*, 1999, **32**, 600.
57. N. Armstrong, W. Kalceff, J. P. Cline and J. Bonevich, *Res. Natl. Inst. Stand. Technol.*, 2004, **109**, 155.
58. N. Armstrong, W. Kalceff, J. P. Cline and J. Bonevich, in *Diffraction Analysis of the Microstructure of Materials*, ed. E. J. Mittemeijer and P. Scardi, Springer, Berlin, 2004, ch. 8, p. 187.
59. B. E. Warren, *X-Ray Diffraction*, Addison-Wesley, Reading, Massachusetts, 1969.
60. W. H. Hall, *Proc. Phys. Soc. London, Ser. A*, 1949, **62**, 741.
61. P. Scardi, M. Leoni and Y. H. Dong, *Mater. Sci. Forum*, 2001, **376–381**, 132.
62. P. Scardi and M. Leoni, *Acta Crystallogr., Sect. A*, 2002, **58**, 190.
63. P. Scardi and M. Leoni, *Diffraction Analysis of the Microstructure of Materials*, ed. E. J. Mittemeijer and P. Scardi, Springer, Berlin, 2004, ch. 3, p. 51.
64. A. Le Bail, *J. Non-Cryst. Solids*, 1995, **183**, 39.
65. A. Le Bail, *J. Non-Cryst. Solids*, 2000, **271**, 249.
66. R. L. McGreevy and L. Pusztai, *Mol. Simulation*, 1998, **1**, 359.
67. A. Le Bail, Chemistry Preprint Server, 2000: http://preprint.chemweb.com/inorgchem/0008001.
68. A. Le Bail, Chemistry Preprint Server, 2003: http://preprint.chemweb.com/inorgchem/0310001.
69. D. Espinat, E. Godart and F. Thevenot, *Analusis*, 1987, **15**, 337.
70. D. Espinat, F. Thevenot, J. Grimoud and K. El Malki, *J. Appl. Crystallogr.*, 1993, **26**, 368.
71. B. Bondars, S. Gierlotka, B. Palosz and S. Smekhnov, *Mater. Sci. Forum.*, 1994, **166–169**, 737.
72. J.-W. Hwang, J. P. Campbell, J. Kozubowski, S. A. Hanson, J. F. Evans and W. L. Gladfelter, *Chem. Mater.*, 1995, **7**, 517.
73. D. Yang and R. F. Frindt, *J. Appl. Phys.*, 1996, **79**, 2376.
74. D. Yang and R. F. Frindt, *J. Mater. Res.*, 1996, **11**, 1733.
75. M. M. Treacy, J. M. Newsam and M. W. Deem, *Proc. R. Soc. London, Ser. A*, 1991, **433**, 499.
76. A. Gibaud, A. Le Bail and A. Bulou, *J. Phys. C: Solid State Phys.*, 1986, **19**, 4623.
77. J. L. Fourquet, M. F. Renou, R. De Pape, H. Theveneau, P. P. Man, O. Lucas and J. Pannetier, *Solid State Ionics*, 1983, **9–10**, 1011.
78. Powbase, Powder Pattern Database, 1999: http://sdpd. univ-lemans. fr/PowBase/.

79. R. A. Young and P. Desai, *Arkiwum Nauli Mater*., 1989, **10**, 71.
80. A. Le Bail, *NIST Special Publication*, 1992, **846**, 142.
81. R. Delhez, T. H. de Keijser, J. I. Langford, D. Louër, E. J. Mittemeijer and E. J. Sonneveld, in *The Rietveld Method*, ed. R. A. Young, Oxford University Press, New York, 1993, ch. 8, p. 132.
82. A. Le Bail, in *Defect and Microstructure Analysis by Diffraction*, ed. R. Snyder, J. Fiala and H. Bunge, Oxford Science Publications, 1999, ch. 22, p. 535.
83. A. Le Bail, *Adv. X-ray Anal*., 2000, **42**, 191.
84. L. Lutterotti and P. Scardi, *J. Appl. Crystallogr*., 1990, **23**, 246.
85. W. I. F. David and J. D. Jorgensen, in *The Rietveld Method*, ed. R. A. Young, Oxford University Press, New York, 1993, ch. 11, p. 197.
86. T. B. Žunic and J. Dohrup, *Powder Diffr*., 1999, **14**, 203.
87. A. Le Bail and A. Jouanneaux, *J. Appl. Crystallogr*., 1997, **30**, 265.
88. P. Thompson, J. J. Reilly and J. M. Hastings, *J. Less Common Met*., 1987, **129**, 105.
89. N. C. Popa, *J. Appl. Crystallogr*., 1998, **31**, 176.
90. P. W. Stephens, *J. Appl. Crystallogr*., 1999, **32**, 281.
91. A. R. Stokes, *Proc. Phys. Soc. London*, 1948, **61**, 382.
92. J. I. Langford and D. Louër, *Rep. Prog. Phys*., 1996, **59**, 131.
93. D. Taupin, *J. Appl. Crystallogr*., 1973, **6**, 266.
94. E. J. Sonneveld and J. W. Visser, *J. Appl. Crystallogr*., 1975, **8**, 1.
95. T. C. Huang and W. Parrish, *Appl. Phys. Lett*., 1975, **27**, 123.
96. H. Toraya, *J. Appl. Crystallogr*., 1986, **19**, 440.
97. W. Parrish, T. C. Huang and G. L. Ayers, *Am. Crystallogr. Assoc. Monogr*., 1976, **12**, 65.
98. D. Balzar, *J. Appl. Crystallogr*., 1992, **25**, 559.
99. D. Balzar and H. Ledbetter, *J. Appl. Crystallogr*., 1993, **26**, 97.
100. D. Balzar, *J. Appl. Crystallogr*., 1995, **28**, 244.
101. D. Balzar and H. Ledbetter, *Adv. X-ray Anal*., 1995, **38**, 397.
102. D. Balzar and S. Popovic, *J. Appl. Crystallogr*., 1996, **29**, 16.
103. R. A. Young and D. B. Wiles, *J. Appl. Crystallogr*., 1982, **15**, 430.
104. C. P. Khattak and D. E. Cox, *J. Appl. Crystallogr*., 1977, **10**, 405.
105. J. I. Langford, *J. Appl. Crystallogr*., 1978, **11**, 10.
106. G. K. Wertheim, M. A. Butler, K. W. West and D. N. E. Buchanan, *Rev. Sci. Instrum*., 1974, **11**, 1269.
107. M. M. Hall, V. G. Veeraraghavan, H. Rubin and P. G. Winchell, *J. Appl. Crystallogr*., 1977, **10**, 66.
108. H. Toraya, M. Yoshimura and S. Sõmiya, *J. Appl. Crystallogr*., 1983, **16**, 653.
109. A. Brown and J. W. Edmonds, *Adv. X-ray Anal*., 1980, **23**, 361.
110. S. Ikeda and J. M. Carpenter, *Nucl. Instrum. Methods, Phys. Res., Sect. A*, 1985, **239**, 536.
111. R. W. Cheary and A. A. Coelho, *J. Appl. Crystallogr*., 1994, **27**, 673.
112. R. W. Cheary, A. A. Coelho and J. P. Cline, *J. Res. Natl. Stand. Technol*., 2004, **109**, 1.

113. G. K. Williamson and W. H. Hall, *Acta Metall.*, 1953, **1**, 22.
114. F. Bley and M. Fayard, *J. Appl. Crystallogr.*, 1976, **9**, 126.
115. R. Delhez, E. J. Mittemeijer, Th. H. de Keijser and H. C. F Rozendaal, *J. Phys. E*, 1977, **10**, 784.
116. G. Cagliotti, A. Paoletti and F. P. Ricci, *Nucl. Instrum.*, 1958, **3**, 223.
117. M. J. Cooper, K. D. Rouse and M. Sakata, *Z. Kristallogr.*, 1981, **157**, 101.
118. G. Will, W. Parrish and T. C. Huang, *J. Appl. Crystallogr.*, 1983, **16**, 611.
119. G. Will, N. Masciocchi, W. Parrish and M. Hart, *J. Appl. Crystallogr.*, 1987, **20**, 394.
120. J. I. Langford, D. Louër, E. J. Sonneveld and J. W. Wisser, *Powder Diffr.*, 1986, **1**, 211.
121. J. I. Langford and D. Louër, *J. Appl. Crystallogr.*, 1991, **24**, 149.
122. J. I. Langford, A. Boultif, J. P. Auffredic and D. Louër, *J. Appl. Crystallogr.*, 1993, **26**, 22.
123. G. S. Pawley, *J. Appl. Crystallogr.*, 1981, **14**, 357.
124. H. Toraya, *J. Appl. Crystallogr.*, 1986, **19**, 440.
125. H. G. Scott, PROFIT-a peak-fitting program for powder diffraction profiles, 1987.
126. G. Will, *Z. Kristallogr.*, 1989, **188**, 169; *Aust. J. Phys.*, 1988, **41**, 283.
127. E. Jansen, W. Schäfer and G. Will, *J. Appl. Crystallogr.*, 1988, **21**, 228.
128. J. Jansen, R. Peschar and H. Schenk, *J. Appl. Crystallogr.*, 1992, **25**, 231.
129. P. G. Byrom and B. W. Lucas, *J. Appl. Crystallogr.*, 1993, **26**, 137.
130. J. Jansen, R. Peschar and H. Schenk, *J. Appl. Crystallogr.*, 1992, **25**, 237.
131. W. I. F. David, *J. Appl. Crystallogr.*, 1987, **20**, 316.
132. D. S. Sivia and W. I. F. David, *Acta Crystallogr., Sect. A*, 1994, **50**, 703.
133. R. Peschar, H. Schenk and P. Capkova, *J. Appl. Crystallogr.*, 1995, **28**, 127.
134. *The Rietveld Method*, ed. R. A. Young, Oxford University Press, New York, 1993.
135. A. Le Bail, H. Duroy and J. L. Fourquet, *Mater. Res. Bull.*, 1988, **23**, 447.
136. A. Jouanneaux, A. D. Murray and A. N. Fitch, Program MPROF, 1990.
137. J. Rodriguez-Carvajal, "FULLPROF: A Program for Rietveld Refinement and Pattern Matching Analysis", Abstracts of the Satellite Meeting on Powder Diffraction of the XVth IUCr Congress, Toulouse, France, 1990, p. 127.
138. Ch. Baerlocher, "EXTRACT, A Fortran Program for the Extraction of Integrated Intensities from a Powder Pattern." Institut für Kristallograpie, ETH, Zürich, Switzerland, 1990.
139. A. Altomare, M. C. Burla, G. Cascarano, C. Giacovazzo, A. Guagliardi, A. G. G. Moliterni and G. Polidori, *J. Appl. Crystallogr.*, 1995, **28**, 842.
140. A. Altomare, M. C. Burla, M. Camalli, B. Carrozzini, G. L. Cascarano, C. Giacovazzo, A. Guagliardi, A. G. G. Moliterni, G. Polidori and R. Rizzi, *J. Appl. Crystallogr.*, 1999, **32**, 339.

141. J. Rius, J. Sane, C. Miravitlles, J. M. Amigo, J. M. M. M. Reventos and D. Louër, *Anal. Quim.*, 1996, **92**, 223.
142. A. Altomare, G. Cascarano, C. Giacovazzo and A. Guagliardi, *J. Appl. Crystallogr.*, 1994, **27**, 1045.
143. A. Altomare, J. Foadi, C. Giacovazzo, A. G. G. Moliterni, M. C. Burla and G. Polidori, *J. Appl. Crystallogr.*, 1998, **31**, 74.
144. M. A. Eastermann, L. B. McCusker and Ch. Baerlocher, *J. Appl. Crystallogr.*, 1992, **25**, 539.
145. M. A. Eastermann and V. Gramlich, *J. Appl. Crystallogr.*, 1993, **26**, 396.
146. M. A. Estermann and W. I. F. David, in *Structure Determination from Powder Diffraction Data*, ed. W. I. F. David, K. Shankland, L. B. McCusker and Ch. Baerlocher, Oxford Science Publications, 2002, ch. 12, p. 202.
147. A. Altomare, J. Foadi, C. Giacovazzo, A. Guagliardi and A. G. G. Moliterni, *J. Appl. Crystallogr.*, 1996, **29**, 674.
148. A. Altomare, C. Giacovazzo, A. G. G. Moliterni and R. Rizzi, *J. Appl. Crystallogr.*, 2001, **34**, 704.
149. A. Altomare, R. Caliandro, C. Cuocci, C. Giacovazzo, A. G. G. Moliterni and R. Rizzi, *J. Appl. Crystallogr.*, 2003, **36**, 906.
150. A. Altomare, R. Caliandro, C. Cuocci, I. da Silva, C. Giacovazzo, A. G. G. Moliterni and R. Rizzi, *J. Appl. Crystallogr.*, 2004, **37**, 204.
151. A. Altomare, C. Giacovazzo, A. Guagliardi, A. G. G. Moliterni and R. Rizzi, *J. Appl. Crystallogr.*, 1999, **32**, 963.
152. B. Carrozzini, C. Giacovazzo, A. Guagliardi, R. Rizzi, M. C. Burla and G. Polidori, *J. Appl. Crystallogr.*, 1997, **30**, 92.
153. A. Altomare, B. Carrozzini, C. Giacovazzo, A. Guagliardi, A. G. G. Moliterni and R. Rizzi, *J. Appl. Crystallogr.*, 1996, **29**, 667.
154. C. Giacovazzo, *Acta Crystallogr., Sect. A*, 1996, **52**, 331.
155. W. I. F. David and D. S. Sivia, in *Structure Determination from Powder Diffraction Data*, ed. W. I. F. David, K. Shankland, L. B. McCusker and Ch. Baerlocher, Oxford Science Publications, 2002, ch. 8, p. 136.
156. W. Dong and C. J. Gilmore, *Acta Crystallogr., Sect. A*, 1998, **54**, 438.
157. H. Toraya, *Adv. X-Ray Anal.*, 1994, **37**, 37.
158. A. Le Bail, *Powder Diffr.*, 2005, **20**, 316.
159. W. I. F. David, K. Shankland, L. B. McCusker and Ch. Baerlocher, in *Structure Determination from Powder Diffraction Data*, eds. W. I. F. David, K. Shankland, L. B. McCusker and Ch. Baerlocher, Oxford Science Publications, 2002, ch. 1, p. 1.
160. R. J. Hill and R. X. Fisher, *J. Appl. Crystallogr.*, 1990, **23**, 462.
161. A. Le Bail, J. L. Fourquet and U. Bentrup, *J. Solid State Chem.*, 1992, **100**, 151.
162. M. S. Lehmann, A. Norlund Christensen, H. Fjellvag, R. Feidenhans and M. Nielsen, *J. Appl. Crystallogr.*, 1987, **20**, 123.
163. J. Rodriguez-Carvajal, *Phys. B*, 1993, **192**, 55.
164. A. Le Bail, *Mater. Sci. Forum*, 2001, **378–381**, 65.

165. S. Pagola, P. W. Stephens, D. S. Bohle, A. D. Kowar and S. K. Madsen, *Nature*, 2000, **404**, 307.
166. W. I. F. David, K. Shankland and N. Shankland, *Chem. Commun.*, 1998, 931.
167. W. I. F. David, *J. Appl. Crystallogr.*, 2004, **37**, 621.
168. J. P. Wright, *Z. Kristallogr.*, 2004, **219**, 791.
169. P. Thompson, D. E. Cox and J. B. Hastings, *J. Appl. Crystallogr.*, 1987, **20**, 79.

CHAPTER 6

# Instrumental Contributions to the Line Profile in X-Ray Powder Diffraction. Example of the Diffractometer with Bragg–Brentano Geometry

ALEXANDER ZUEV

Max Planck Institute for Solid State Research, Stuttgart, Germany

## 6.1 INTRODUCTION

X-Ray powder diffractograms contain in encrypted form information about the structure of the sample material. The positions and intensities of diffraction peaks reveal the information about an ideal crystal structure. The form of the peaks reflects the information about defects in the structure.[1] Instrumental aberrations affect the apparent peak positions (especially at low and high scattering angles) and intensities of the diffraction peaks as well as the form of the peaks.[2,3] Hence, properly taking into account the instrumental contributions is essential both for studies aimed at obtaining information about the ideal crystal structure of the material and information about deviations from this ideal structure.

Two important fields of interest in powder diffraction research today are *ab initio* structure determination from powder diffraction data (SDPD) and line profile analysis (LPA).

The prerequisites for structure solution are to find the correct peak position and intensity. For the last step of SDPD, refinement of the structure (Rietveld refinement[4,5]), it is also important to know the form of the diffraction peak, taking into account the instrumental contributions. Notably, in modern SDPD there is the ability to obtain information about deviation from the ideal structure. Crystallite size and microstrain broadening should be considered primarily as the contributors to the physical profile. All main Rietveld programs take into account these deviations from the ideal structure.

In addition to these deviations from the ideal structure, other crystal structure defects (*e.g.*, stacking faults) are the subject of line profile analyses.[1,6] Correction by taking into account instrumental contributions is of even greater importance in the study of defects and microstructure (LPA), as discussed in Chapter 13.

The problem of the instrumental function has been under intensive study for over 50 years.[7 52] However, despite repeated attempts there is no generally recognized method today for calculation of the instrumental function in powder diffraction. Standard Rietveld refinement is dominated by the phenomenological description of the profile.

The main difficulties encountered in numerical calculations of the instrumental function are associated with the wide range of instrumental parameters [diffractometer radius, sizes of X-ray source, sample, receiving slit, using (or not using) Soller slits in incident and/or diffracted beam, using (or not using) monochromator], the contributions of some of which differ by three orders of magnitude.

There are two different approaches for calculation of the instrumental function. The first is the convolution approach. Proposed more than 50 years ago, initially to describe the observed profile as a convolution of the instrumental and physical profiles,[7 9] it was extended for the description of the instrumental profile by itself.[2,11] According to this approach the total instrumental profile is assumed to be the convolution of the specific instrumental functions. Representation of the total instrumental function as a convolution is based on the supposition that specific instrumental functions are completely independent. The specific instrumental functions for equatorial aberrations (caused by finite width of the source, sample, deviation of the sample surface from the focusing circle, deviation of the sample surface from its ideal position), axial aberration (finite length of the source, sample, receiving slit, and restriction on the axial divergence due to the Soller slits), and absorption were introduced. For the main contributors to the asymmetry – axial aberration and effect of the sample transparency – the derived (half)-analytical functions for corresponding specific functions are based on approximations. These aberrations are being studied intensively (see reviews refs. 46 and 47).

The convolution approach is realized in the fundamental parameter approach (FPA) developed by Cheary and Coelho.[27] Special attention was given to calculating a specific instrumental function caused by axial divergence.[34] Additionally, axial divergence was studied in detail experimentally.[35] The convolution approach provides much more reliable results (for peak position, intensity, and form) than methods that used analytical functions to fit the experimental profile. To achieve the best fit for experimental data it is also necessary to tune the fundamental parameters.[51] Masson *et al.*[50] used the convolution approach to determine the instrumental function for high-resolution synchrotron powder diffraction, and showed that it can be represented as a convolution of four specific instrumental functions describing the equatorial intensity distribution, the monochromator and analyzer transfer function, and the axial aberration function. The specific instrumental functions for the conventional diffractometer with Bragg–Brentano geometry, as well as in the case of synchrotron radiation, have been studied by Ida and coworkers.[39 45]

The second method for calculating the total instrumental function is ray-tracing simulations, in which the contribution of all possible incident and diffracted rays to the total intensity are treated numerically.[25,26,36 38] Like any pure numerical treatment it is limited in the analysis. In addition, the Monte-Carlo ray-tracing simulations are time-consuming. Nevertheless, ray-tracing simulations provide a reliable calculation of the instrumental function.

In Rietveld refinement, it is standard practice to use a phenomenological description of the diffraction profile. Several analytical functions are in use. The variation of the full width at half-maximum (FWHM) with diffraction angle $2\theta$ associated with the instrumental aberrations can be described using simple analytical formulas.[14,22] The apparent shift of peak positions was considered in detail by Wilson.[3] Asymmetry of the profile at low and high diffraction angles due to axial divergence can be taken into account by the correction proposed by Finger, Cox, and Jephcoat.[31] Distinguishing sample from instrumental contributions to the line profile is possible by a preliminary measurement with a so called line profile standard (*e.g.,* NIST SRM 660a $La_{B6}$).

In the field of powder diffraction related to the retrieval of the defects and microstructural information the requirements for using physically meaningful instrumental profile are greater than in the field related to the crystal structural analysis. Thus the following main methods are used. (1) The use of a special high-resolution diffractometer. (2) Experimental determination of the instrumental function for the same material but without defects. (3) Numerical calculations of the instrumental function with ray-tracing simulations.

Recently, a new comprehensive approach to calculate the total instrumental function has been proposed,[53,54] in which all aberration effects are treated simultaneously in the same manner. The method is based on an exact analytical solution, derived from diffraction optics, for the contribution of each incident ray to the intensity registered by a detector of finite size.

The main difference between the proposed method and the convolution approach (in which the line profile is synthesized by convolving the specific instrumental functions) lies in the fact that the former provides an exact solution for the total instrumental function (exact solutions for specific instrumental functions can be obtained as special cases), whereas the latter is based on the approximations for the specific instrumental functions, and their coupling effects after the convolution are unknown. Unlike the ray-tracing method, in the proposed method the diffracted rays contributing to the registered intensity are considered as combined (part of the diffracted cone) and, correspondingly, the contribution to the instrumental line profile is obtained analytically for this part of the diffracted cone and not for a diffracted unit ray as in ray-tracing simulations.

There are no limitations on the size of the source, sample or receiving slit, and correspondingly on the axial or equatorial divergence. The proposed method, valid over a full range of $2\theta$ from 0 to 180°, can be applied to different diffractometer geometries. We shall restrict our consideration here to the common Bragg–Brentano geometry.

## 6.2 CONTRIBUTIONS TO THE OBSERVED PROFILE

The line profile in X-ray powder diffraction for a monochromatic beam is determined by sample broadening and instrumental aberration. Figure 6.1 shows schematically contributions to the observed profile $h(\varphi)$ from instrumental aberration $g(\varphi)$ and physical profile $f(\varphi)$ for monochromatic X-rays. Measurements of a sample of the material without physical broadening ("ideal sample") with the diffractometer without instrumental aberration would give the profile as a Dirac $\delta$-function.

For the ideal sample only the instrumental aberrations cause the line profile to be distributed over the angular region. The instrumental function can be conceived of as a response function of the diffractometer to the input signal in the form of a $\delta$-function. In contrast, measurements with the ideal diffractometer would give the physical profile of the real structure. The physical profile can be represented as a sum of the $\delta$-functions. The observed peak profile of the non-ideal structure obtained from the measurements with non-ideal diffractometer can then be considered as a linear superposition of profiles corresponding to the responses of the diffractometer to the given set of the $\delta$-functions. In this case we can write for the observed intensity at the scanning angle $\varphi$:

$$h(\varphi) = \int_{\infty}^{\infty} f(\eta)g(\varphi, \eta)\mathrm{d}\eta \tag{1}$$

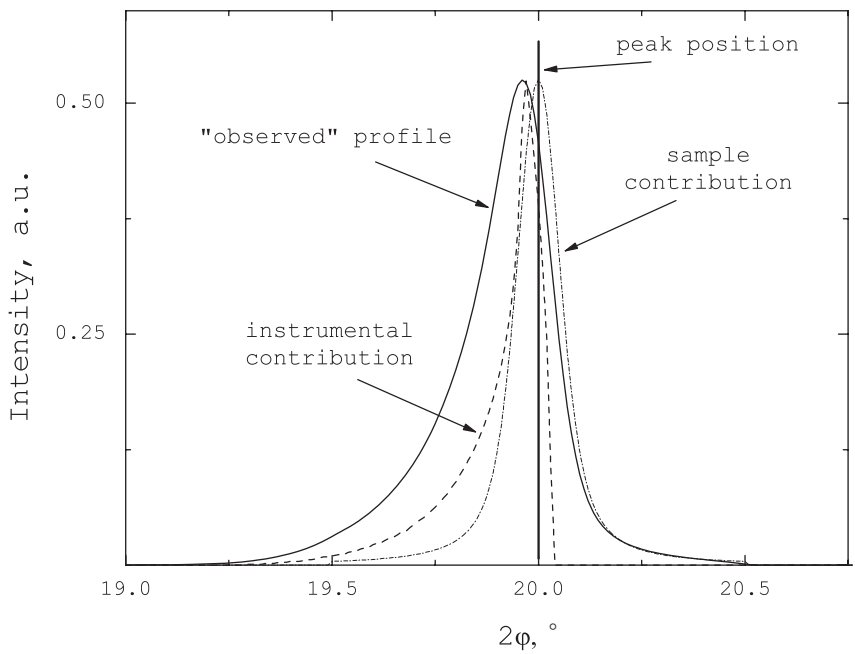



**Figure 6.1** Contributions to the observed profile for monochromatic X ray radiation.

Let us consider two ideal diffraction peaks $\delta_1(\theta)$ and $\delta_2(\theta-\eta)$ with equal intensity, but shifted relative to each other by an angle $\eta$. The response functions of the diffractometer to these $\delta$-functions are $g_1(\varphi,\theta)$ and $g_2(\varphi,\theta-\eta)$ which, strictly speaking, have different forms and intensities, and, consequently cannot be considered as shifted by the angle $\eta$ relative to each other. If the shift angle $\eta$ is small, there is reason to believe that, firstly, the response functions have the same form and intensity and, secondly, the shift between the response functions is $\eta$. This led us to the convolution integral:[2]

$$h(\varphi) = \int_{\infty}^{\infty} f(\eta)g(\varphi - \eta)\mathrm{d}\eta \tag{2}$$

The convolution of the two functions $f(\eta)$, $g(\eta)$ is denoted by the symbol $f \otimes g$:

$$\int_{\infty}^{\infty} f(\eta)g(\varphi - \eta)\mathrm{d}\eta = f \otimes g \tag{3}$$

The characteristic emission of X-rays from an X-ray tube, in the strict sense, is not monochromatic (Figure 6.2). The energy distribution of a single characteristic emission line can be described by the Lorentz function:[51]

$$W(E) = \frac{\Gamma/2\pi}{(E - E_0)^2 + (\Gamma/2)^2}$$

Here $E_0$ is the characteristic energy, and $\Gamma$ determines the width of the distribution. In the case of using copper radiation, which is widely used in powder diffraction experiments, the $K\alpha$ radiation can be represented as a sum of four Lorentz functions.[51,55] Table 6.1 gives the parameters for this function.

Using such radiation means that the profile of the ideal structure recorded on the ideal diffractometer without aberration is no more a $\delta$-function (Figure 6.2b).

Analogously to the above discussion, the total observed profile can be represented as a convolution of the three functions $h = f \otimes g \otimes w$, where

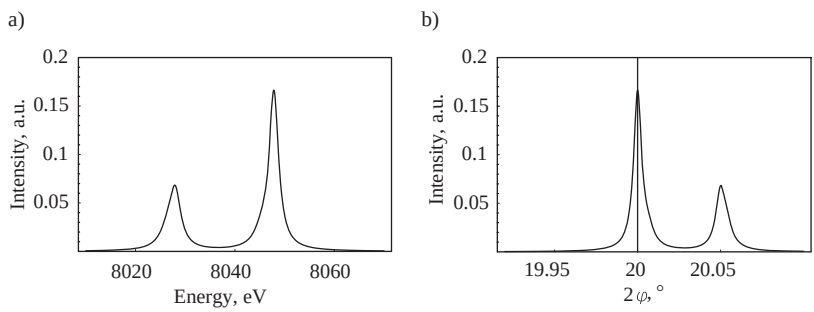



**Figure 6.2** Energy distribution for copper $K\alpha$ radiation (a), and corresponding line profile (ideal sample, ideal diffractometer) (b).

**Table 6.1** Parameters for the Lorentz function for energy distribution of the X-ray tube.

| *Component* | *Energy (eV)* | $\Gamma$ | $I_{integr}$ |
|---|---|---|---|
| $\alpha_{11}$ | 8047.84 | 2.285 | 0.579 |
| $\alpha_{12}$ | 8045.37 | 3.358 | 0.08 |
| $\alpha_{21}$ | 8027.99 | 2.666 | 0.236 |
| $\alpha_{22}$ | 8026.5 | 3.571 | 0.105 |

function $w$ is peak profile function related to the wavelength distribution of the X-ray tube.

## 6.3 GENERAL DESCRIPTION OF THE METHOD

Suppose an X-ray coming from surface element $dS_1$ is scattered by a powder sample at surface element $dS_2$. The sizes of the elements $dS_1$ and $dS_2$ are small enough to be considered as points $A_1$ and $A_2$ respectively (Figure 6.3).

The scattered photons form a cone with vertex at point $A_2$ and half angle $2\theta$. The total scattered intensity $I_0(\theta)$ at the Bragg angle $\theta$ is proportional to the intensity $I(A_1,A_2)$ incident on the element $dS_2$. If the registration of the scattered X-rays is performed by a detector of limited size which intersects a part of the diffraction cone the registered intensity is proportional to the curvilinear integral over the line $l$ of intersection of the diffraction cone and detector:

$$I(P_{c1}, P_{c2}) = \int_{P_{c1}}^{P_{c2}} I(P)\mathrm{d}l \tag{4}$$

Here $I(P)$ is the unit line intensity at point $P$ lying on $l$. $P_{c1}$ and $P_{c2}$ are the points of intersection of the line $l$ and the detector boundaries. If absorption between the scattering point $A_2$ and the detector is neglected, the integral can easily be calculated, because the number of photons between rays $R_1$ and $R_2$ of the cone remains unchanged. Then we can write for the registered intensity:

$$I(P_{c1}, P_{c2}) = I(R_1, R_2) = (2\pi)\ {}^1I_0\psi \sim I(A_1, A_2)\psi \tag{5}$$

Here $\psi$ is the dihedral angle between two planes. Both share a common line – the incident ray $A_1A_2$. The first plane passes through point $P_{c1}$ and the second one passes through the point $P_{c2}$.

As a consequence the efforts of calculating the registered intensity are directed toward calculating the intersection points of the line $l$ and the boundary of the receiving slit. The intersection of the receiving slit plane and diffraction cone is a conical section. It can be an ellipse, parabola, or hyperbola, depending (for a given diffraction cone) on the angle between the receiving-slit plane and the incident ray.

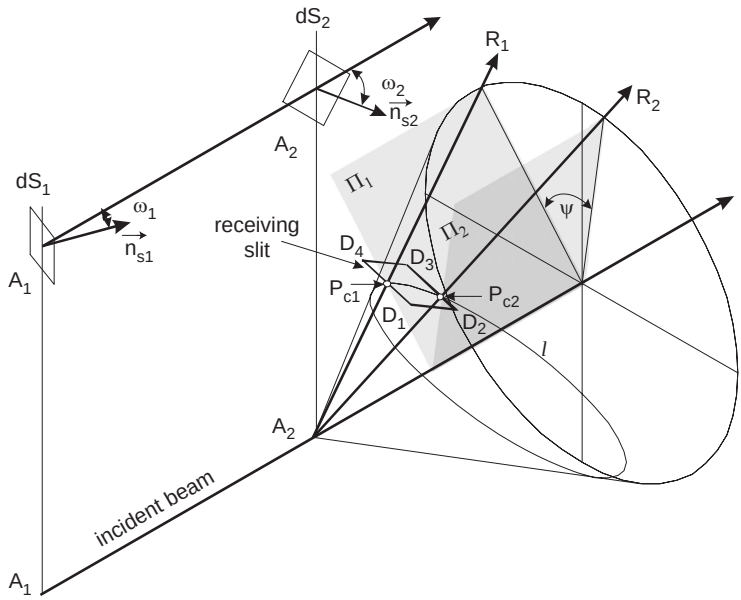



**Figure 6.3** The positions of the incident beam, the diffraction cone and the receiving slit. $dS_1$ is an element of the source surface and $dS_2$ is an element of the sample surface. These elements are shown on an enlarged scale above points $A_1$ and $A_2$. (Reprinted from Ref. 50. Permission of the International Union of Crystallography.)

Finding the intersection points $P_{c1}$ and $P_{c2}$ can be realized in various ways. In the previous work of the author,[53] the equation of the conic in polar coordinates was used:

$$\rho = \frac{p}{1 + e\cos\varphi} \tag{6}$$

A prerequisite for using this equation is finding for each incident ray the corresponding coordinate system, coordinates of the focus and parameters $p, e$ of the conic. To find the coordinates of the focus and parameters $p, e$ of the conic the Dandelin sphere was used.[53]

Another possibility of applying this method is using a general equation of a conic.[54] The general equation of a conic can be mathematically expressed by a second degree polynomial:[56]

$$ax^2 + 2bxy + 2cy^2 + 2dx + 2fy + g = 0 \tag{7}$$

The coefficients of Equation (7) have to be found as functions of the diffractometer radius, scanning angle, diffraction cone angle, and coordinates of points on the source and sample, which determine the incident ray.

## 6.4 BASIC EQUATIONS

In this section a common equation of a cone in an arbitrary coordinate system is used. A common equation of a conic can be obtained from the common equation of the cone in the coordinate system related to the cutting plane by setting $z = 0$, where $z$ is the coordinate normal to the cutting plane.

### 6.4.1 Vector Equation of a Cone

The position of the diffraction cone is defined by the position of its vertex described by the position vector **V**, the direction vector **U** that is parallel to the axis of the cone, and a half-angle $2\theta$ (Figure 6.4).

The equation of the cone can be given in vector form as:[57]

$$\frac{\mathbf{X}-\mathbf{V}}{|\mathbf{X}-\mathbf{V}|}\cdot\frac{\mathbf{U}}{|\mathbf{U}|}=\cos 2\theta \tag{8}$$

Here **X** is the position vector of any point $X$ on the cone. After squaring both sides and regrouping the terms:

$$(\mathbf{U}\cdot\mathbf{X}-\mathbf{U}\cdot\mathbf{V})^2-\cos^2 2\theta U^2(\mathbf{X}-\mathbf{V})^2=0 \tag{9}$$

Opening the parentheses and regrouping the terms accordingly to their order in the components of the vector $\mathbf{X}=\{x, y, z\}$ we get:

$$\begin{aligned}(\mathbf{U}\cdot\mathbf{X})^2-\cos^2 2\theta\mathbf{X}^2-2((\mathbf{U}\cdot\mathbf{V})\mathbf{U}-\cos^2 2\theta\mathbf{V})\cdot\mathbf{X}\\ +(\mathbf{U}\cdot\mathbf{V})^2-\cos^2 2\theta\mathbf{V}^2=0\end{aligned} \tag{10}$$

### 6.4.2 Equation of a Conic

A conic is the intersection of a cone with a plane. Introducing a system coordinate related to the plane in a such way that the $z$-axis is perpendicular

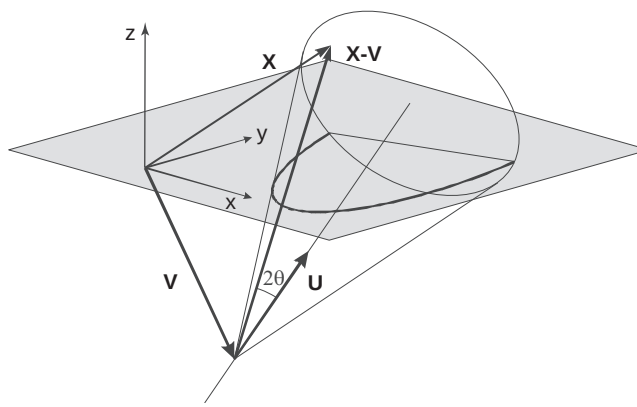



**Figure 6.4** Cone, cutting plane, and vectors **U**,**V**.

to the plane, we can obtain the equation of a conic in this coordinate system by setting $z = 0$ in the equation for a cone. For the points of the cone in the $XY$-plane we have $\mathbf{X} = \{x, y, 0\}$.

Substituting in Equation (10) gives for the second order terms:

$$\begin{aligned}(\mathbf{U}\cdot\mathbf{X})^2 - \cos^2 2\theta \mathbf{U}^2\mathbf{X}^2|_{z=0} \\ = x^2U_x^2 + 2xyU_xU_y + y^2U_y^2 - \cos^2 2\theta U^2x^2 - \cos^2 2\theta U^2y^2 \\ = (U_x^2 - \cos^2 2\theta U^2)x^2 + 2U_xU_yxy + (U_y^2 - \cos^2 2\theta U^2)y^2\end{aligned} \tag{11}$$

and consequently:

$$a = U_x^2 - \cos^2 2\theta U^2 \tag{12a}$$

$$b = U_xU_y \tag{12b}$$

$$c = U_y^2 - \cos^2 2\theta U^2 \tag{12c}$$

First order terms are:

$$\begin{aligned}-(2(\mathbf{U}\cdot\mathbf{V})\mathbf{U} - 2\cos^2 2\theta U^2\mathbf{V})\mathbf{X}|_{z=0} = &-(2(\mathbf{U}\cdot\mathbf{V})U_x - 2\cos^2 2\theta U^2V_x)x \\ &-(2(\mathbf{U}\cdot\mathbf{V})U_y - 2\cos^2 2\theta U^2V_y)y\end{aligned}$$

and consequently:

$$d = -(\mathbf{U}\cdot\mathbf{V})U_x - \cos^2 2\theta U^2V_x \tag{12d}$$

$$f = -(\mathbf{U}\cdot\mathbf{V})U_y - \cos^2 2\theta U^2V_y \tag{12e}$$

and for the free term $g$ we have;

$$g = (\mathbf{U}\cdot\mathbf{V})^2 - \cos^2 2\theta U^2V^2 \tag{12f}$$

The scalar products $\mathbf{U}\cdot\mathbf{V}$, $\mathbf{U}\cdot\mathbf{U}$, and $\mathbf{V}\cdot\mathbf{V}$ can be expressed in terms of their components as:

$$\mathbf{U}\cdot\mathbf{V} = U_xV_x + U_yV_y + U_zV_z \tag{13a}$$

$$\mathbf{U}\cdot\mathbf{U} = U_xU_x + U_yU_y + U_zU_z \tag{13b}$$

$$\mathbf{V}\cdot\mathbf{V} = V_xV_x + V_yV_y + V_zV_z \tag{13c}$$

Hence, for the given diffraction angle $\theta$ the coefficients of Equation (7) are a function of the values $U_x$,$U_y$,$V_x$, $V_y$ and $V_z$.

The position vector $\mathbf{V}$ is determined by the point $A_2$ (on the sample), and vector $\mathbf{U}$ is a vector from point $A_1$ (on the source) to point $A_2$. Equations (12a–12f) together with Equations (13a–13c) can be used in an arbitrary coordinate system to obtained the equation of the conic in form Equation (7). In the next section

these equations are applied to obtain the equations of the conic for two important cases – in the plane related to the receiving slit, and in the plane related to the sample.

## 6.5 DIFFRACTOMETER WITH BRAGG–BRENTANO GEOMETRY

### 6.5.1 Coordinate Systems for Bragg–Brentano Geometry

For the diffractometer with Bragg–Brentano geometry the following right-hand coordinate systems related to the source, sample and receiving slit are used (Figure 6.5).

The coordinate system $CS_s$ is associated with the well-aligned sample. The $x_s$-axis coincides with the rotation axis of the diffractometer. The $y_s$-axis is an intersection of the sample surface with the equatorial plane. The origin of the coordinate system is the center of the sample.

The coordinate system $CS_f$ is associated with the source. Without source misalignment $y_f\, z_f$ -plane lies in the equatorial plane of the diffractometer and the $y_f$ -axis has angle $\pi/2-\varphi$ with the $y_s$-axis of the coordinate system $CS_s$. The origin of the coordinate system $CS_f$ lies in the middle of the source.

The coordinate system $CS_r$ is associated with the receiving slit. Without misalignment the $y_r\, z_r$ -plane lies in the equatorial plane of the diffractometer

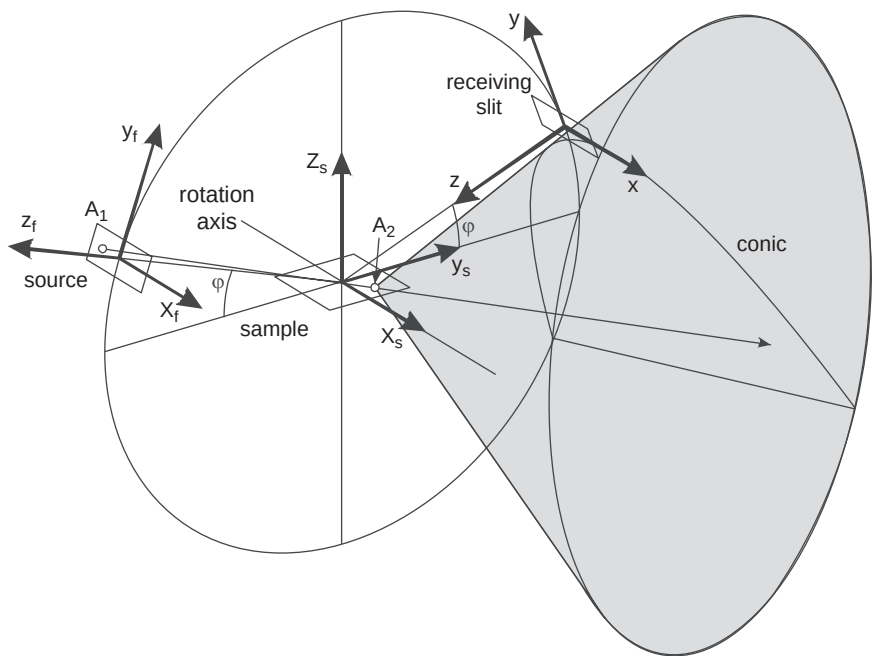



**Figure 6.5** Coordinate systems related to the source, sample, and receiving slit. (Reprinted from Ref. 54. Permission of the International Union of Crystallography.)

and the $y_r$ -axis makes an angle $\pi/2+\varphi$ with the $y$ -axis of the coordinate system $CS_s$.

### 6.5.2 Equation of a Conic in the Receiving Slit Plane (Coordinate System *CS*)

Table 6.2 gives the coordinates of the points $A_1$ and $A_2$ in the coordinate systems used.

Consequently, the components of the vectors **U** and **V** in the coordinate system $CS_r$ are given as:

$$\begin{aligned} U_x &= x_s - x_f \\ U_y &= z_s\cos\varphi - y_f\cos 2\varphi - (y_s + 2R\cos\varphi)\sin\varphi \\ U_z &= -y_s\cos\varphi - R\cos 2\varphi - z_s\sin\varphi + y_f\sin 2\varphi \end{aligned} \tag{14}$$

and:

$$\begin{aligned} V_x &= x_s \\ V_y &= z_s\cos\varphi - y_s\sin\varphi \\ V_z &= R - y_s\cos\varphi - z_s\sin\varphi \end{aligned} \tag{15}$$

Substituting this in Equation (10) and simplifying we obtain the equation of a conic in the receiving slit plane in implicit form:

$$\begin{aligned} &\cos^2 2\theta(R^2 - 2\cos\varphi y_s R + y^2 + (x - x_s)^2 + y_s^2 + 2yy_s\sin\varphi) \\ &\quad\times(R^2 + 2y_s R\cos\varphi + (x_f - x_s)^2 + y_f^2 + y_s^2 - 2y_f y_s\sin\varphi) \\ &\quad= (y_s^2 + y_s(y - y_f)\sin\varphi + (x - x_s)(x_f - x_s) \\ &\quad+(y + y_f)R\sin 2\varphi + (yy_f - R^2)\cos 2\varphi)^2 \end{aligned} \tag{16}$$

This equation (representing the polynomial of second degree in two variables $x$ and $y$) describes the line of an intersection of the diffraction cone produced by an arbitrary incident X-ray with the receiving slit plane of the diffractometer in Bragg–Brentano geometry. The parameters of the equation are the diffractometer radius $R$, scanning angle $\varphi$, diffraction angle $\theta$, and coordinates of points on the source and the sample in the source or sample related coordinate systems. Notably, point $A_2$ related to the sample can have three coordinates. The coordinate $z_s$ corresponds to the deviation of the sample surface from its ideal position. The graph of Equation (16) for given parameters can be easily

**Table 6.2** Coordinates of the points $A_1$ and $A_2$.

| *Point/vector* | *Coordinate system* | *Coordinates* |
|---|---|---|
| $A_1$ | $CS_f$ | $\{x_f,\ y_f,\ 0\}$ |
| | $CS_s$ | $\{x_f,\quad R\cos\varphi + y_f\sin\varphi, R\sin\varphi + y_f\cos\varphi\}$ |
| | $CS_r$ | $\{x_f,\ y_f\cos 2\varphi + R\sin 2\varphi,\ 2\cos\varphi(R\cos\varphi \quad y_f\sin\varphi\}$ |
| $A_2/\mathbf{V}$ | $CS_s$ | $\{x_s,\ y_s,\ z_s\}$ |
| | $CS_r$ | $\{x_s,\ z_s\cos\varphi \quad y_s\sin\varphi,\ R \quad y_s\cos\varphi \quad z_s\sin\varphi\}$ |

drawn using *Mathematica*.[58] For the most part, the figures in this paragraph were prepared with *Mathematica*.[58]

### 6.5.3 Equation of a Conic in the Sample Surface Plane (Coordinate System *CS*)

In the coordinate system related to the sample we have for the component of the direction vector **U** and **V**:

$$\begin{aligned} U_x &= x_s - x_f \\ U_y &= y_s + R\cos\varphi - y_f \sin\varphi \\ U_z &= z_s - y_f \cos\varphi - R\sin\varphi \end{aligned} \tag{17}$$

$$\begin{aligned} V_x &= x_s \\ V_y &= y_s \\ V_z &= z_s \end{aligned} \tag{18}$$

In the same way as in the case of the coordinate system related to the receiving slit, the equation of the conic in the sample plane in implicit form can be obtained:

$$\begin{aligned} &(y_s^2 - y_s y + z_s^2 + (x - x_s)(x_f - x_s) + \sin\varphi y_f (y - y_s) - R z_s \sin\varphi \\ &\quad - \cos\varphi (R(y - y_s) + y_f z_s))^2 = \cos^2 2\theta ((x - x_s)^2 + (y - y_s)^2 + z_s) \\ &\quad \times ((x_f - x_s)^2 + (R\cos\varphi - \sin\varphi y_f + y_s)^2 + (R\sin\varphi + \cos\varphi y_f - z_s)^2) \end{aligned} \tag{19}$$

This equation is important for the study of the effect of absorption because it can be used for estimations of the length of the scattered X-rays in the sample from the diffraction cone vertex to the sample surface.

### 6.5.4 Case of the Degenerated Cone ($2\theta = 90^\circ$)

For the diffraction angle $2\theta = 90^\circ$ the diffraction cone degenerates to the plane $P_{90}$ passing through the point $A_2$ and perpendicular to the incident ray $\mathbf{U} = A_1A_2$. The equation of this plane in vector form is:

$$\mathbf{U} \cdot (\mathbf{X} - \mathbf{V}) = 0 \tag{20}$$

The plane $P_{90}$ determines, together with the equation of the receiving slit plane, the line of the intersection of these planes. In the coordinate system $CS_r$ the line of the intersection can be obtained easily from Equation (20) by setting the component $z$ of the vector **X** to 0. Substituting coordinates of vector **V** and vector **U** in the coordinate system $CS_r$ we obtain the equation of a straight line in the receiving slit plane:

$$U_x x + U_y y - \mathbf{U} \cdot \mathbf{V} = 0 \tag{21}$$

or:

$$y = \frac{\mathbf{U} \cdot \mathbf{V} - U_x x}{U_y} \tag{22}$$

An example of the intersection of the degenerated diffraction cone is given in Section 6.6.

### 6.5.5 Intersections of the Conic and Receiving Slit Boundary

There are three common cases related to the intersections of the conics with the receiving slit. (1) No intersection with the receiving slit; (2) the conic intersects the receiving slit in two points; (3) the conic intersects the receiving slit in four points. The case of the conic touching the receiving slit boundary can be reduced to the first two cases. Finding the points of the intersection of the conic with the receiving slit boundaries reduces, in most cases, to the solution of quadratic equations. For the horizontal sides of the receiving slit (axial direction) $y = \pm d_w/2$ the quadratic equation $a_x x^2 + b_x x + c_x = 0$ has the coefficients:

$$\begin{aligned} a_x &= a \\ b_x &= 2d \pm bd_w \\ c_x &= \frac{cd_w}{4} \pm fd_w + g \end{aligned}$$

For the sides $x = \pm l_w/2$ that lie parallel to the equatorial plane the quadratic equation $a_y x^2 + b_y x + c_y = 0$ has the coefficients:

$$\begin{aligned} a_y &= c \\ b_y &= 2f \pm bl_w \\ c_y &= \frac{cl_w}{4} \pm dl_w + g \end{aligned}$$

In a special case there is only one intersection of the line and the conics. This can occur if the line is parallel to the main axis of the conic (in the case of a parabola), or the line is parallel to the asymptote of the hyperbola. Only the intersection points $\{x_i, y_i\}$ lying on the receiving slit boundary are of interest.

The conditions $-l_w/2 < x_i < l_w/2$ and $-d_w/2 < y_i < d_w/2$ should be met. Care should be taken at the Bragg and scanning angles near 90° to ensure the intersection points lie on the proper branch of the hyperbola.

### 6.5.6 Angle Between Two Planes

Suppose points $X_1 = \{x_1, y_1, 0\}$ and $X_2 = \{x_2, y_2, 0\}$ represent the intersections of the conic and receiving slit boundary. The registered intensity is proportional to the dihedral angle $\phi$ between two planes containing points $A_1$, $A_2$, $X_1$ and $A_1$, $A_2$, $X_2$.[53] This angle is the angle between the two normals $\mathbf{N_1}$ and $\mathbf{N_2}$ to the plane in question:

$$\begin{aligned} \mathbf{N}_1 &= (\mathbf{X}_1 - \mathbf{V}) \times \mathbf{U} \\ \mathbf{N}_2 &= (\mathbf{X}_2 - \mathbf{V}) \times \mathbf{U} \end{aligned} \tag{23}$$

Here $\mathbf{X_i}$ are the position vectors to points $X_i$. Introducing the unit vectors $\mathbf{n_1} = \mathbf{N_1}/|\mathbf{N_1}|$ and $\mathbf{n_2} = \mathbf{N_2}/|\mathbf{N_2}|$ and taking into account $|\mathbf{N_i}| = |\mathbf{X_i} - \mathbf{V}| \cdot |\mathbf{U}|$

$\sin 2\theta (i = \{1, 2\})$ we have:

$$\cos\phi = \mathbf{n_1} \cdot \mathbf{n_2} = \frac{((\mathbf{X_1} - \mathbf{V}) \times \mathbf{U}) \cdot ((\mathbf{X_2} - \mathbf{V}) \times \mathbf{U})}{|\mathbf{X_1} - \mathbf{V}| \cdot |\mathbf{X_2} - \mathbf{V}| U^2 \sin^2 2\theta} \tag{24}$$

Components of the vector $\mathbf{N_i} = (\mathbf{X_i} - \mathbf{V}) \times \mathbf{U}$ can be expressed through the components of the vectors **U**, **V**, and $\mathbf{X_i}$:

$$\begin{aligned} N_{ix} &= -U_z V_y + U_y V_z + U_z y_i \\ N_{iy} &= U_z V_x - U_x V_z - U_z x_i \\ N_{iz} &= -U_y V_x + U_x V_y + U_y x_i - U_x y_i \end{aligned}$$

## 6.6 APPLICATION OF THE METHOD

The equation of the conic (16) can be used for very illustrative demonstrations of the influence of different parameters on the relative positions of the conic and the receiving slit, and correspondingly to the registered intensity. The different behavior of the conics due to axial and equatorial aberrations is given in subsequent subsections to demonstrate their different contributions to the registered intensity.

The proposed method for calculating the total instrumental function can be used to calculate specific instrumental functions. The principal point in the calculations is the finite width of the receiving slit, *i.e.* the special instrumental function will be calculated coupled with the finite width of the receiving slit. Notably, in the proposed method the convolution is not used to synthesize the total instrumental function from the specific instrumental functions. In fact, there is no need to calculate specific instrumental functions,[†] but it may be useful for comparison with methods based on the convolution approach or for testing approximations. In the following sections, comparisons are made between the profiles of some specific instrumental functions suggested previously by Klug and Alexander[2] and later by others[41,42,51] and the profiles calculated by the proposed method. For the purpose of comparison with the proposed method, the specific instrumental function used in the convolution approach was convolved with the instrumental function representing the receiving slit. In Section 6.6.3 the total instrumental profile calculated by the proposed method is compared with the profile obtained using a Monte Carlo ray-tracing simulation (by using the program BGMN[36–38]).

### 6.6.1 Some Illustrative Examples of the Conic in the Receiving Slit Plane

*6.6.1.1 Relative Positions of the Conics and Receiving Slit.* The relative positions of the conic and receiving slit can be characterized by the number $N_c$

[†] Furthermore, in experiment it is difficult to make comparisons with functions (*e.g.*, specific function for flat specimen or axial aberration) having singularity.

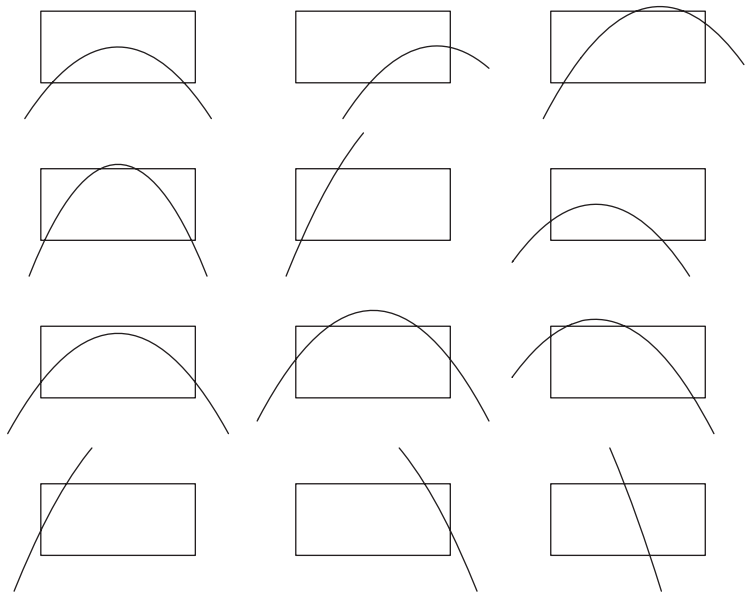


**Figure 6.6** Possible intersections of the conics and receiving slit ($2\theta < 90^\circ$).

and position of the intersection points of the conic and receiving slit. Figure 6.6 gives the positions of the conics and receiving slit for all cases. The cases are related to the Bragg angle $\theta = 10^\circ$ (with one exception: second row, left, $\theta = 6^\circ$) and to the receiving slit with the size $10 \times 0.25\,\text{mm}^2$.

To illustrate more clearly the intersection details the $y$-axis range was scaled out by a factor of about 20. Generally, the conic section can intersect the receiving slit boundary in two or four points. The two intersections with the side boundary are related to the high registered intensity. The two intersections with bottom and top of the receiving slit can be related to a low registered intensity (*e.g.* small Bragg angle, scanning angle far from Bragg angle) as well as to the high registered intensity.

*6.6.1.2 Different Bragg Angles.* Figure 6.7 shows the set of conics in the receiving slit plane for different diffraction angles $\theta_i$ (10°, 40°, 50°, and 80°). The scanning angle $\varphi_i$ is set to the diffraction angle $\theta_i$. The receiving slit is $10 \times 0.25\,\text{mm}^2$.

All conics were calculated for the incident rays with the fixed point $A_1 = \{0, 0\}$ from the source center and for points $A_2 = \{x_s, 0, 0\}$ having only axial components. The set of the conics from the other point $A_1 = \{x_f, 0\}$ can be obtained easily from that shown on the picture by the shift of the conics by $x_f$.

As can be seen from the figure the conics produced by the diffraction cone with the different Bragg angles fill the receiving slit plane differently, being responsible for the asymmetry, apparent shift, and width of the diffraction peak (see also the Section 6.6.1.4).

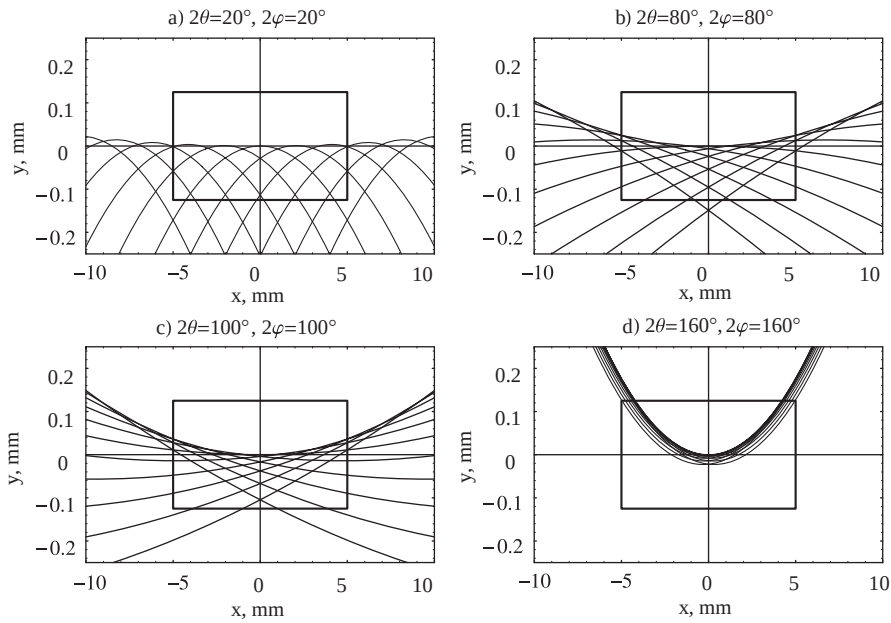



**Figure 6.7** Set of conics near the receiving slit for different Bragg angles. Diffraction cones are produced by the incident ray from fixed point $A_1 = \{0, 0\}$ to points on the sample $A_2$ having only axial component. (Reprinted from Ref. 54. Permission of the International Union of Crystallography.)

*6.6.1.3 Degenerated Cone.* In the special case of the degenerated diffraction cone ($2\theta = 90^\circ$) the conic sections represent straight lines (Figure 6.8). Asymmetry and shift do not disappear for this case.

The next section illustrates the effects of the asymmetry, shift and width.

*6.6.1.4 Asymmetry, Shift, and Width of the Diffraction Peaks.* For a given Bragg and scanning angle the points of intersections of scattered X-rays and the receiving slit plane fill a certain region $R(\theta_B,\varphi)$ in the latter. Figure 6.9 shows examples of these regions for different diffraction angles $\theta_B$ and scanning angles.

In all cases the scanning angles are equal to the Bragg angles. Strictly speaking, the density of these points, for a given Bragg angle, depends on the scanning angle. However, for qualitative purposes only, we can assume that for other scanning angles the corresponding region can be obtained by moving the region $R(\theta_B,\varphi_B)$ by the value $2R(\theta_B-\varphi)$. By such a consideration it is easy to see the origin of the asymmetry, apparent shift of the peak position and changing the width of the peak.

*6.6.1.5 Non-convolution Calculation of the Observed Profile.* The proposed method can be applied to the calculation of the total registered intensity in the case where the physical profile $f(\theta)$ is no longer a $\delta$-function. In this case the scattered X-rays for a given incident ray and point $A_2$ are no longer distributed

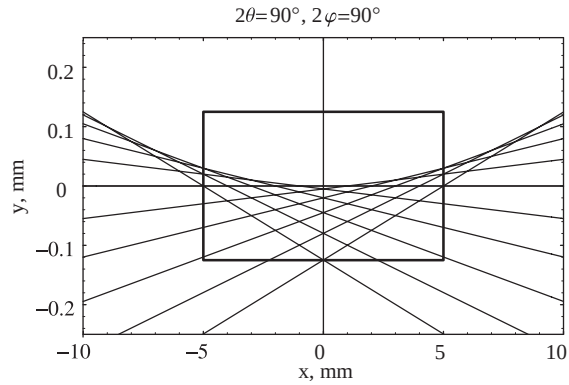



**Figure 6.8** Intersections of the degenerated diffraction cone ($2\theta = 90^\circ$) and receiving slit plane. Diffraction cones are produced by the incident ray from fixed point $A_1 = \{0, 0\}$ to points on the sample $A_2$ having only an axial compo nent. The black rectangle represents the receiving slit. (Reprinted from Ref. 54. Permission of the International Union of Crystallography.)

on a conical surface with half angle $2\theta$, but have a spatial distribution. Now we can consider a set of diffraction cones with the common vertex and axes but with different scattering angles $\theta_i$. Full scattered intensity for each cone is described by the physical diffraction profile. For each diffraction cone the corresponding conic can be easily calculated.

Figure 6.10a shows as an example one physical profile, and Figure 6.10b shows the corresponding conic sections. For a given incident ray we can write for the registered intensity at the scanning angle $\varphi_0$:

$$I_{reg}(\varphi_0) \approx \sum_i g(\varphi_0, \theta_i) f(\theta_i)$$

or as an integral:

$$I_{reg}(\varphi_0) = \int g(\varphi_0, \theta) f(\theta) \mathrm{d}\theta$$

Hence, for a given physical profile point on the observed profile there can be calculated by an additional integration.

### 6.6.2 Specific Instrumental Function

*6.6.2.1 Equatorial Aberrations*. For a well-aligned diffractometer the following factors affect equatorial aberration: finite width of the source and receiving slit, and flat specimen effect (we also assume that angular distribution in the equatorial plane is uniform). The first two factors produce rectangular profiles without shifts. The convolution of these two instrumental functions provides an exact solution as a triangular or trapezoidal profile where the receiving slit width equals or does not equal the width of the source,

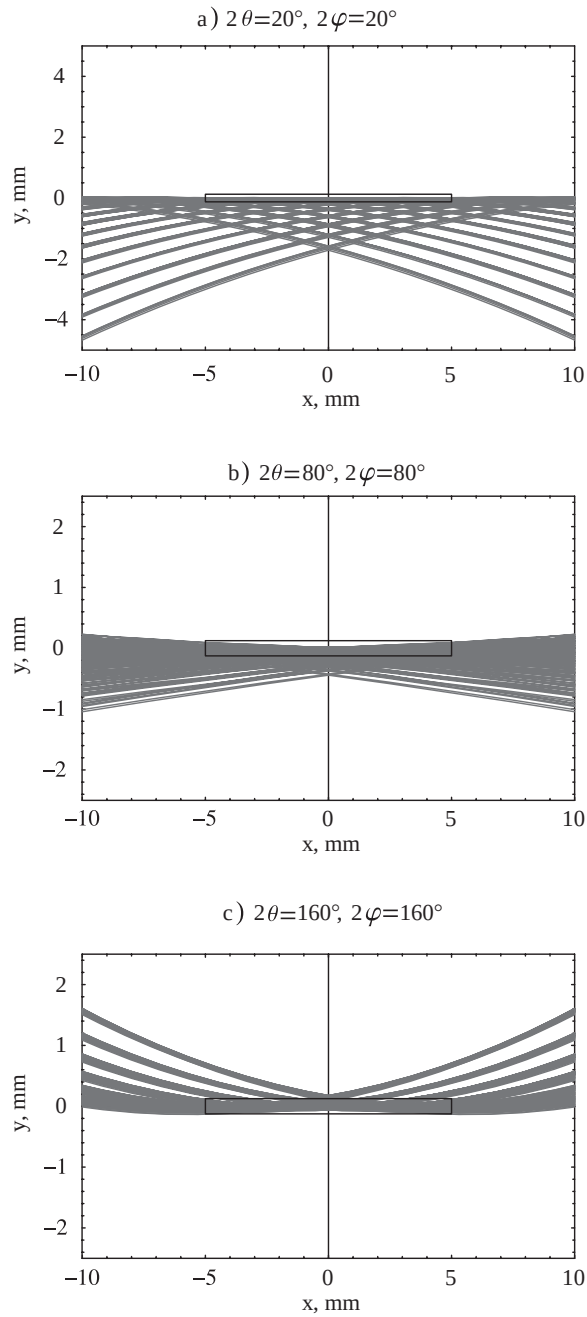



**Figure 6.9** Filling the receiving slit plane with the conics. Diffraction cones are produced by the incident ray from set of points $A_1 = \{x_f, 0\}$ to the set of points on the sample $A_2 = \{x_s, y_s\}$. The black rectangle represents the receiving slit.

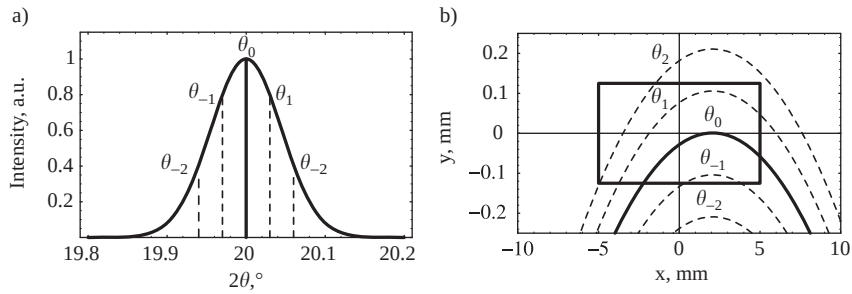



**Figure 6.10** Calculation of the combined contribution due to the physical broadening and due to geometrical aberrations in the observed profile. a) Physical profile; b) set of the conics corresponding to the the diffraction cones at the angles $\theta_i \cdot A_1 = \{0, 0\}$, $A_2 = \{1, 0, 0\}$, $\theta_0 = 10^\circ$, $\varphi = 10^\circ$.

respectively. This is a simple situation to calculate. The flat specimen aberration causes a shift and asymmetry of the diffraction line profile. For a point source and point receiving slit the exact solution for flat specimen aberration can be obtained.[2,41,51] Our interest is the consideration of the flat specimen aberration together with the aberration caused by the finite width of the receiving slit because (1) the first is responsible for asymmetry (for equatorial aberrations) and (2) the measurement are always carried out with a finite receiving slit.

First, we compare these instrumental profiles calculated with the proposed method and with the convolution approach. Secondly, a fine difference between an exact solution and a solution based on the convolution approach is demonstrated.

The approximation for the specific instrumental function for the flat specimen aberration as given by Cheary *et al.*[51] and Ida and Kimura[41] is:

$$J_{FS}(\varepsilon) = 1/\left[2(\varepsilon\varepsilon_M)^{1/2}\right], \qquad \varepsilon_M \le \varepsilon \le 0$$

where $\varepsilon = 2\varphi - 2\theta$, $\varepsilon_M = -[L_x/(2R)]^2 \sin 2\theta$ and $L_x$ is the specimen length along the equatorial direction.

Calculation of this type of aberration is simple when using the proposed method. For the profile on Figure 6.11 the grid used for calculating the flat specimen aberration coupled with the receiving slit function is $1 \times 1$ for the source and $1 \times 20$ for the sample; the length of the receiving slit was set to be much smaller than $R \sin 2\theta$. One can see quite clearly that the results agree very well.

Of some interest is to consider the coupling effects by the example of the flat specimen aberration and finite width of the receiving slit. Assuming the size of the receiving slit in the axial direction is negligibly small (that means $x = 0$), and taking into account $x_f = 0$, $y_f = 0$, $x_s = 0$, we obtain from Equation (16) the following equation:

$$\begin{aligned}(-R^2 \cos 2\varphi + yR \sin 2\varphi + yy_s \sin \varphi + y_s^2)^2 \\ = (y_s^2 + R^2 + 2y_s R \cos \varphi) \times ((y_s \cos \varphi - R)^2 + (y + y_s \sin \varphi)^2) \cos^2 2\theta\end{aligned}$$

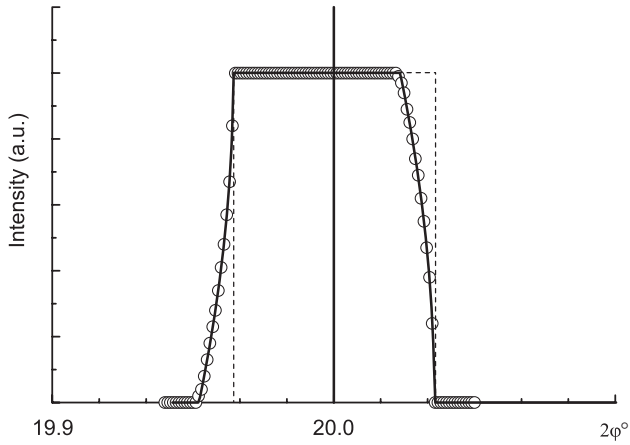



**Figure 6.11** Equatorial aberration coupled with the receiving slit width calculated by the proposed method (solid line) and as a convolution (open circles) of JFS with the rectangle function (dashed line) representing the receiving slit. The vertical line at 20° represents the Bragg angle to which the aberration function is related. (Reprinted from Ref. 53. Permission of the International Union of Crystallography.)

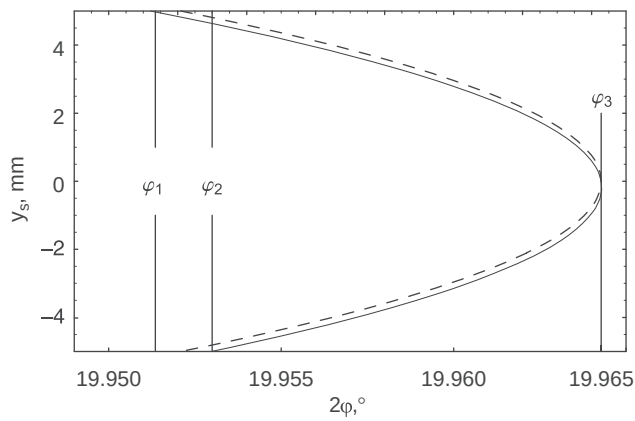



**Figure 6.12** Asymmetrical contribution from equatorial peripheral points of the sample: coupling effect of flat specimen aberration with finite width of the receiving slit. For the scanning angle $\varphi_1 < \varphi < \varphi_2$ there is only contribution from one side of the sample. The dashed line corresponds to the symmetrical contribution from the sample. (Reprinted from Ref. 54. Permission of the International Union of Crystallography.)

Setting $y = \pm d_w$ we obtain the equation linking angle $\varphi$ and equatorial positions $y_s$ on the sample from which the diffracted rays hit exactly on the boundary of the receiving slit.

Figure 6.12 shows the solution of the equation for the top side of the receiving slit. The four scanning angle regions related to the signal front can be

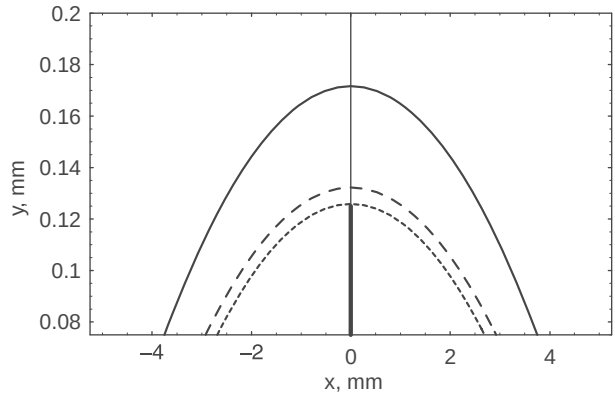



**Figure 6.13** Conic sections near top side of the receiving slit. The conics are produced with the following incident rays: point $A_1$ is the center of the source, points $A_2$ have coordinates: {0, 5} (short dashed line), {0, 0} (continuous line), {0, −5} (dashed line). The vertical thick line represents part of the receiving slit (infinitesimally small in the axial direction). (Reprinted from Ref. 54. Permission of the International Union of Crystallography.)

distinguished. (1) For angles $\varphi < \varphi_1$ diffracted rays from the sample do not fall into the receiving slit. (2) For angles $\varphi_1 < \varphi < \varphi_2$ diffracted rays from the region on the top of the sample contribute to the registered intensity (see Figure 6.13). (3) For angles $\varphi_2 < \varphi < \varphi_3$ diffracted rays from the regions on the top and bottom of the sample contribute to the registered intensity. The region in the middle of the sample does not contribute to the registered intensity. (4) For angles $\varphi > \varphi_3$ diffracted rays from the all-illuminated surface of the sample contribute to the registered intensity. Notably, this case cannot be realized for a very narrow receiving slit (for the conditions of Figure 6.12 $d_w \leq 0.0025$ mm), because a region of the illuminated sample always exists from which the diffracted rays miss the receiving slit. The asymmetry of the contribution of the diffracted points from the periphery of the sample causes the slight break in the profile at the angle $\varphi_2$. Since the break is slight, the front of the instrumental function for this case can be calculated on the assumption that symmetrical points $\pm y_s$ on the sample contribute symmetrically to the registered signal. We will come to the convolution approach;[2] however, for best fit we may need to fine tune the "fundamental" parameters[51] (here a width of the receiving slit). Although this break is small, it makes sense to provide tools to enable the quantitative estimation of the effect.

*6.6.2.2 Axial Aberration.* The equation of the conic for the case that points $A_1$ and $A_2$ have only axial components can be obtained from the general Equation (16) by setting their equatorial components $y_f$, $y_s$ to 0.

For this case the equation of the conic can be expressed in the form:

$$(R^2 + y^2 + (x - x_s)^2)(R^2 + (x_f - x_s)^2)\cos^2 2\theta = (-R^2 \cos 2\varphi + yR \sin 2\varphi + (x - x_s)(x_f - x_s)^2)$$

Figure 6.7 gives a set of the conics produced by the diffraction cone with the incident rays from the source center $A_1 = \{0, 0\}$ (in coordinate system $CS_f$) to the points along the rotation axis of the diffractometer $A_2 = \{x_s, 0, 0\}$ (in coordinate system $CS_s$).

The specific instrumental function $J_{AX}$ for the axial aberration can be analytically calculated for the special case in which there is no divergence of the incident rays:[51]

$$J_{AX}(\varepsilon) = \begin{cases} |\varepsilon_1 - \varepsilon_2|^{-1}\left[(\varepsilon_2/\varepsilon)^{1/2}\right], & \varepsilon_1 < \varepsilon < 0 \\ |\varepsilon_1 - \varepsilon_2|^{-1}\left[(\varepsilon_2/\varepsilon)^{1/2} - 1\right], & \varepsilon_2 \le \varepsilon \le \varepsilon_1 \end{cases}$$

where:

$$\varepsilon_1 = -\frac{\cot 2\theta}{2}\left(\frac{L_r - L_s}{2R}\right)^2, \quad \varepsilon_2 = -\frac{\cot 2\theta}{2}\left(\frac{L_r + L_s}{2R}\right)^2$$

and $L_s$ and $L_r$ are axial sample and receiving slit lengths.

Function $J_{AX}(\varepsilon)$ was convolved with the receiving slit function representing the rectangular function. Figure 6.14 shows axial instrumental functions. The results are consistent with our model.

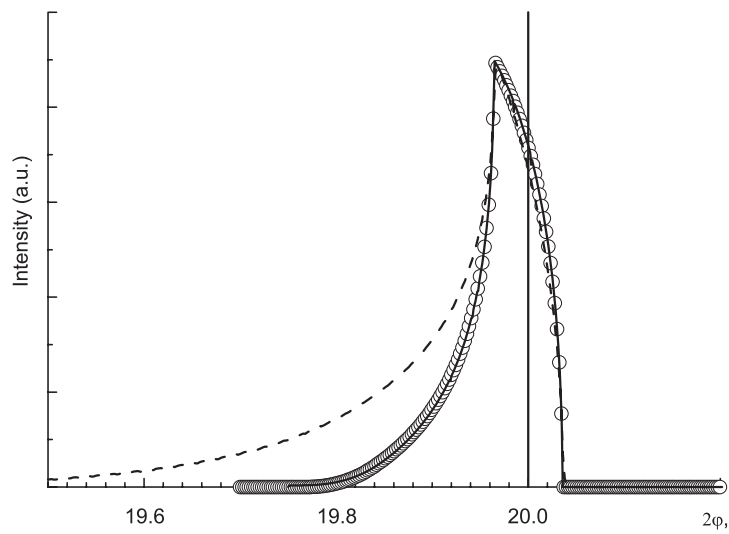



**Figure 6.14** Axial aberration. Source and sample: axial length 10 mm; receiving slit: length 10 mm, width 0.25 mm. Solid and dashed lines: calculation by the proposed method without and with divergence in the incident beam, respectively. Open circles: calculation as a convolution of $J_{AX}$ with the rectangle function representing the receiving slit. The vertical line at $\varphi = 20^\circ$ represents the Bragg angle to which the aberration function is related. (Reprinted from Ref. 53. Permission of the International Union of Crystallography.)

The analytical approximation for the axial aberration in the convolution approach is possible only for the case in which the divergence of incident X-rays is sufficiently small [$<1^\circ$ (ref. 51)]. Axial aberration for the general case can be calculated by using the semi-analytical approach developed by Cheary and Coelho.[34]

In the proposed method the axial aberration function (coupled with the finite sizes of the receiving slit) for the general case of a non-parallel incident X-ray beam can be calculated without difficulty by taking grid points along the lines passing through the center of the source or sample in the axial direction. The results are given in Figure 6.14. As can be seen from Figures 6.11 and 6.14, the axial aberration has a greater impact on the profile shape than does the equatorial aberration.

Figure 6.15 shows the instrumental profile caused by axial shift of the points $A_1$ and $A_2$ (*i.e.* arbitrary axial divergence).

Some characteristic angle regions can be distinguished. The incident rays with maximal axial divergence are responsible for the first signals at the scanning angle $\varphi_1$. For the small scanning angles far below the peak position only the incident rays having axial components contribute to the registered intensity. The incident rays that are parallel to the equatorial plane (without axial divergence) do not contribute to the registered intensity until the scanning angle of the diffractometer reaches the angle $\varphi_2$. Angle $\varphi_2$ refers to the angle at which the incident ray with maximal axial shift (without axial divergence) starts with the contribution to the registered intensity. From angle $\varphi_2$ to $\varphi_3$ only incident rays having an axial shift contribute to the registered intensity. In other words, there is no contribution to the registered intensity from the incident ray determined by the source and sample center. Starting from the angle $\varphi_3$ the incident rays from the center of the source to the center of the sample contribute to the registered intensity.

The next region (scanning angles $\varphi_4 < \varphi < \varphi_5$) corresponds to that with maximal registered intensity. In this region the vertex of the conic produced by

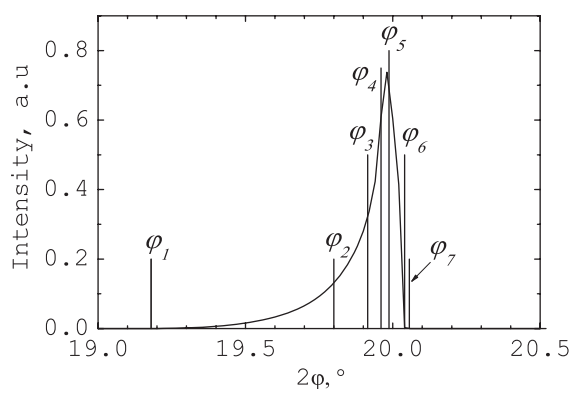



**Figure 6.15** Instrumental profile caused by an axial aberration (see explanations for angles $\varphi_1$ in the text). (Reprinted from Ref. 54. Permission of the International Union of Crystallography.)

the incident ray without any axial shifts (incident ray from the source center to the sample center – central incident ray) (i) falls into the receiving slit and (ii) the conic intersects both vertical sides of the receiving slit. From the angles near $\varphi = \varphi_5$ the registered intensity takes a sharp downward turn. Angle $\varphi_5$ is characterized by the fact the conic produced by the central incident ray intersects the bottom side of the receiving slit.

The angle $\varphi_6$ corresponds to the angle at which the vertex of the conic produced by the central incident ray meets the bottom side of the receiving slit. However, after the exit of this vertex from the receiving slit, the arcs of the conics produced by the incident rays having axial divergence contribute to the registered intensity. The end of the registration refers to the scanning angle $\varphi_7$, which differs somewhat from the angle $\varphi_6$.

*6.6.2.3 Absorption.* An absorption correction is important for thick specimens with small absorption coefficient for X-rays. Consideration of absorption means that point $A_2$ has a non-zero $y$ component. As a consequence of this there is another conic that is important for considering the absorption. This conic is the intersection of the diffraction cone and the surface plane of the sample. Figure 6.16 shows schematically a part of the diffraction cone and a cross-section of the latter with the sample surface plane (plane $X_sY_s$ in coordinate system $CS_s$). Points $D_{ip}$ ($i = 1$–4) are point projections of the receiving slit from point $A_2$. Points $P_{cip}$ are projections of the intersection points $P_{ci}$ of the receiving slit and conic in the receiving slit plane.

The contribution to the recorded intensity should be corrected for each incident and scattered ray by the factor $\exp(-\mu l)$, where $\mu$ is the linear absorption coefficient and $l$ is the length of the ray in the sample, which consists of two components; the first is the length $l_1$ passed by the incident ray in the sample to point $A_2$ from the sample surface, and the second is the distance $l_2$ traversed by the diffracted rays from point $A_2$ to the sample surface. The distance $l_2$ can be considered as a function of dihedral angle $\psi$ between planes $\Pi(A_1, A_2, P_{c1})$ and $\Pi(A_1, A_2, P)$, where $P$ is a point on the conic in the sample plane. Because the scattered rays have different lengths in the sample the corrections, strictly speaking, should be introduced for each scattered ray:

$$I(P_{c1}, P_{c2}) \sim \exp(-\mu l_1) \int_0^{\psi_2} \exp[-\mu l_2(\psi)] \mathrm{d}\psi$$

where $\psi$ is the dihedral angle between planes $\Pi(A_1, A_2, P_{c1})$ and $\Pi(A_1, A_2, P)$, where $P$ is the current point on the conic within the receiving slit. Preliminary estimations show that the length $l_2$ can be taken as constant for a given incident ray. However, for specific conditions the corresponding estimations should be made to be sure the length changes are negligible.

Figure 6.17 shows one example of the conic in the receiving slit plane (a) and corresponding conic in the sample surface plane (b). The conic in the sample plane can be considered also as a point projection (point $A_2$) of the conic in the

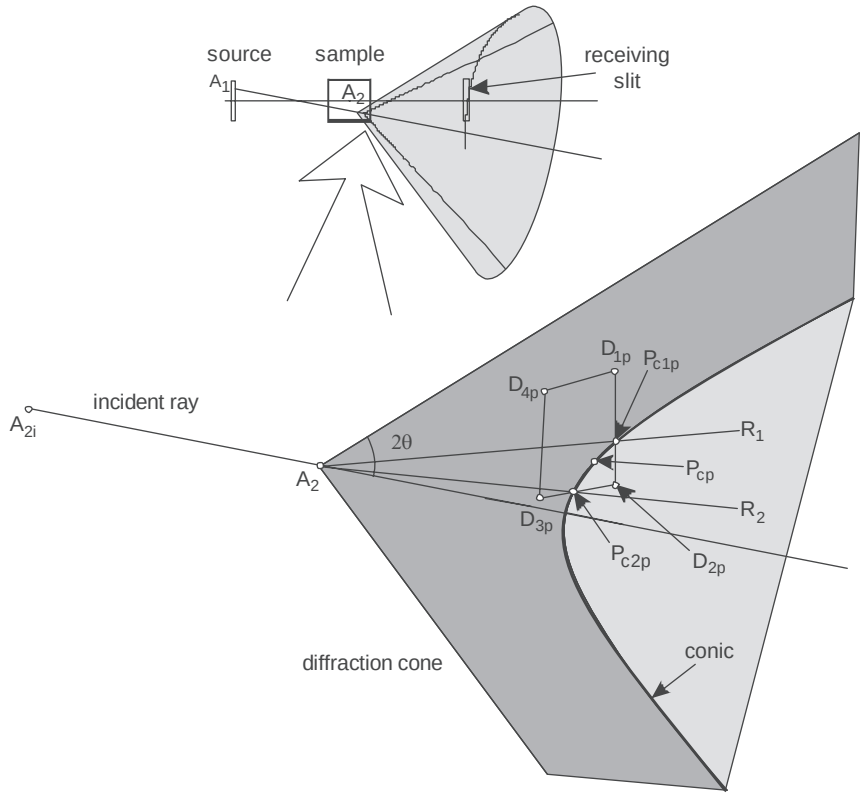



**Figure 6.16** An intersection of the diffraction cone and sample surface. Point $A_2$ is located under the sample surface. Points $D_{ip}$ are point projections of the receiving slit on the sample surface.

receiving slit plane into the sample plane. In this specific case, as can be easily seen from Figure 6.17b, the change of the coordinate of the point $P$ between points $P_{c1p}$ and $P_{c2p}$ causes an insignificant change in the length $l_2$.

A simplified consideration is given by Ida and Kimura[42] and Cheary, Coelho and Cline.[51] The specific instrumental function for the sample with a thickness of $T$ is given as:

$$J_\mu(\varepsilon) = \frac{\exp(\varepsilon/\delta)}{\delta[1 - \exp(\varepsilon_{\min}/\delta)]}, \qquad \varepsilon_{\min} \le \varepsilon \le 0$$

where:

$$\varepsilon_{\min} = -(2T/R)\cos\theta, \qquad \delta = \sin\theta/(2\mu R)$$

Figure 6.18 shows the convolution of the aberration function $J_\mu(\varepsilon)$ with the receiving-slit instrumental function. Here the profile calculated according to the proposed method is also represented. The calculation was carried out with a fixed point $A_1$ at the center of the source; points $A_2$ lie on the $y$-axis from the

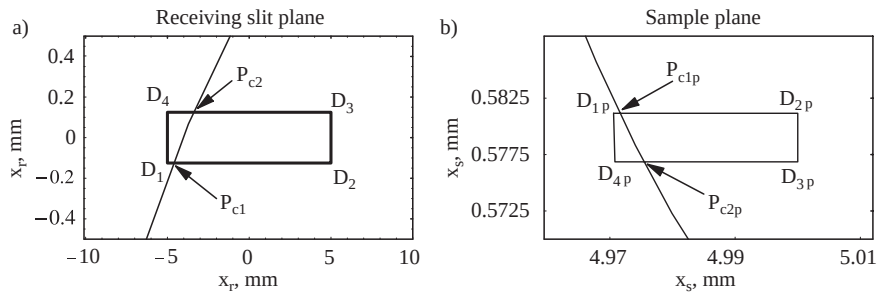



**Figure 6.17** Intersection of the diffraction cone with a) the receiving slit plane, and b) the sample plane. Case of absorption (the vertex of the diffraction cone is under the sample plane). $D_1D_2D_3D_4$ receiving slit. $D_{1p}D_{2p}D_{3p}D_{4p}$ projection of the receiving slit from vertex of the diffraction cone into the sample plane.

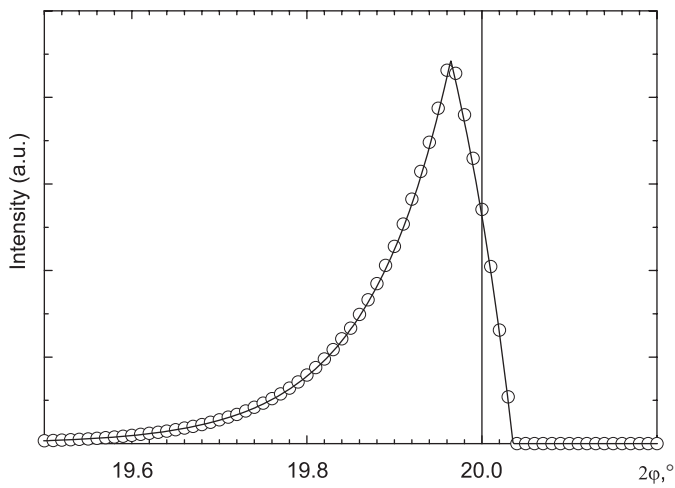



**Figure 6.18** The effect of absorption in the specimen. The absorption coefficient $\mu$ corresponds to that of graphite. Sizes of the receiving slit: length 0.1 mm, width 0.25 mm. The calculation according to the proposed method and the convolution approach are shown as a solid line and open circles, respectively. The vertical line at $2\varphi = 20^\circ$ represents the Bragg angle to which the aberration function is related. (Reprinted from Ref. 53. Permission of the International Union of Crystallography.)

center into the specimen. To eliminate the axial aberration, here due to the length of the receiving slit, the length of the receiving slit was reduced to 0.1 mm. Comparison of the axial aberration (Figure 6.14) and the absorption effect (Figure 6.18) shows that for samples with a low absorption the influence of absorption on the line profile may be comparable with the influence of the axial aberration.

Figure 6.18 shows that there is good agreement between these two approaches in this case as well.

### 6.6.3 Total Instrumental Profile

The instrumental function calculated by the proposed method for two angles was compared with the instrumental function obtained using the BGMN program (Figure 6.19).[36 38]

In the program *geomet* of the BGMN package Monte Carlo ray-tracing is used to calculate the instrumental function. The advantage of using the ray-tracing simulation is that it provides a correct instrumental profile for a given instrument geometry. As shown in Figure 6.19, the agreement between these two methods is very good. However, precise calculations using the ray-tracing method are time-consuming.

*6.6.3.1 Precision and Calculation Time.* To calculate one point on the instrumental profile we need to calculate a multidimensional integral. For the case where absorption can be neglected this integral reduces to a four-dimensional integral. To estimate how the number of points on the calculation grid affects the precision and calculation time, the calculations of the total instrumental profile were performed for four cases. They are given in Table 6.3.

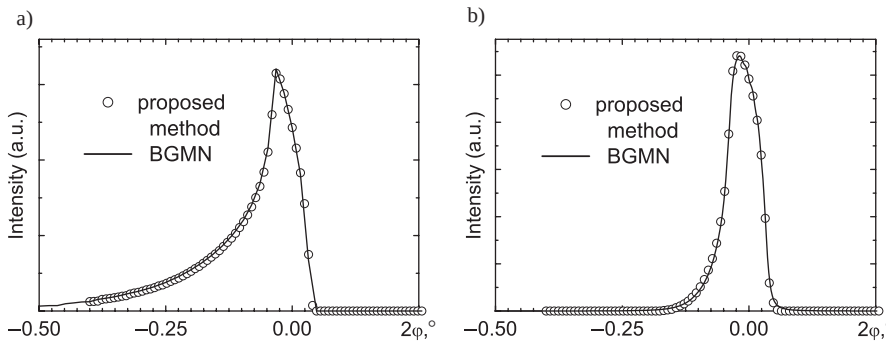



**Figure 6.19** Comparison of the calculated instrumental function with the instrumental function obtained using the BGMN program. Sample sizes: $5 \times 10\,mm^2$; receiving slit sizes: $0.25 \times 10\,mm^2$. Bragg angle: (a) $2\theta = 20^\circ$, (b) $2\theta = 80^\circ$. (Reprinted from Ref. 53. Permission of the International Union of Crystallography.)

**Table 6.3** Effect of the number of points on the calculation grid on the precision and calculation time.

| *Number of points* | *R(50,n) (%)* | *Time (s)* |
|---|---|---|
| 50 | | 260 |
| 20 | 0.06 | 6.5 |
| 10 | 0.25 | 0.45 |
| 5 | 1 | 0.046 |

The precision of the calculations with $n \times n \times n \times n$-calculation points was referred to the grid with $50 \times 50 \times 50 \times 50$ points as:

$$R(50, n) = \frac{\sum_i |y_i(50) - y_i(n)|}{\sum_i y_i(50)}$$

The number of calculation points on the instrumental profile for the given cases is 100.

Figure 6.20 compares two total instrumental profiles calculated with $50 \times 50 \times 50 \times 50$ and $5 \times 5 \times 5 \times 5$ points. As is easy to see, it is enough to take only 5 calculation points in each direction to reach a precision of $\sim 1\%$. The calculation time for this case is about 0.05 s. The calculation time can be decreased still further by taking an unequal number of calculation points in each direction from the line position.

Taking into account absorption leads, generally, to a six-dimensional integral. However, within certain limits it can be reduce to the five-dimensional integral because the length of scattered X-rays in the sample changes insignificantly.

For realizing the algorithm for calculation of the integral, the following factors reducing the calculation time can be taken into account. (1) Symmetry relative to the equatorial plane (time reducing by a factor 2). (2) Parallel shift of the incident X-ray in the axial direction causes the same parallel shift of the conic in the receiving slit plane. Thus, the intersection with the horizontal lines can be easily calculated by adding the value of the shift. The coefficients of the

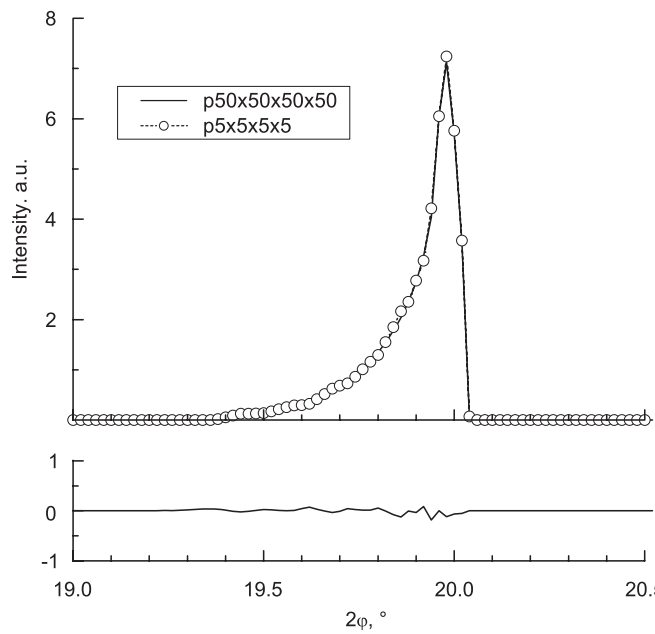



**Figure 6.20** Instrumental functions calculated on different grids.

quadratic form can be re-calculated and used for finding the intersections with vertical lines. For the shift by $\Delta$ in the axial direction the quadratic form Equation (7) changes to:

$$ax^2 + bxy + cy^2 + (d + 2a\Delta)x + (f + b\Delta)y + (g + d\Delta + a\Delta^2) = 0$$

The four-dimensional integral (case without absorption) can be reduced to a three-dimensional integral.

## 6.7 ABOUT MISALIGNMENT, SOLLER SLITS, MONOCHROMATOR

The effects of misalignment and Soller slits can also be included in the calculation as well as a different diffractometer geometry. For the case of the diffractometer equipped with a crystal monochromator it is also possible to provide a solution in the context of the proposed method. For reasons of space, we outline here the possible treatment of these effects without going into details.

### 6.7.1 Misalignment

The most interesting case of the misalignment is referred to the deviation of the sample from its ideal position. This misalignment can be described by the translation vector $V_{mis}$ and rotation matrix $M_{mis}$.

Knowing the coordinates of the point $A_{2,mis}$ in the coordinate system related to the sample we can calculate the coordinate of the point $A_2$ in the coordinate system $CS_s$. The relationship between coordinates of point $A_{2,mis} = \{x_{mis}, y_{mis}, z_{mis}\}$ in the coordinate system $CS_{mis}$ and coordinates of this point $A_2 = \{x, y, z\}$ in the coordinate system $CS_s$ is $A_2 = M_{mis}^T \cdot A_{2,mis} + V_{mis}$. The further treatment is the same as for the case without misalignment. Figure 6.21 shows two total instrumental functions calculated for well-aligned and mis-aligned samples. The mis-aligned position was obtained from a well-aligned one by a shift of the sample by 0.05 mm along the $z$-axis.

It is easy to see that the position of the instrumental function is very sensitive to the position of the sample.

### 6.7.2 Soller Slits

For the case of Soller slits in the incident beam, the condition of rays passing through the slits is given by the inequality:

$$\arctan\left[\frac{|x_s - x_f|}{R + y_s \cos\varphi}\right] < \alpha_{slits}$$

For Soller slits in the diffracted beam each point $A_2$ on the sample "sees" only parts of the receiving slit (Figure 6.22).

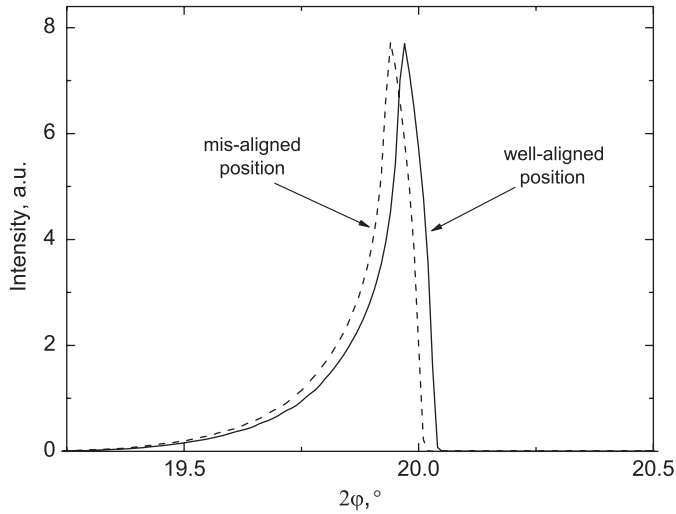



**Figure 6.21** Influence of the position of the sample on the instrumental function.

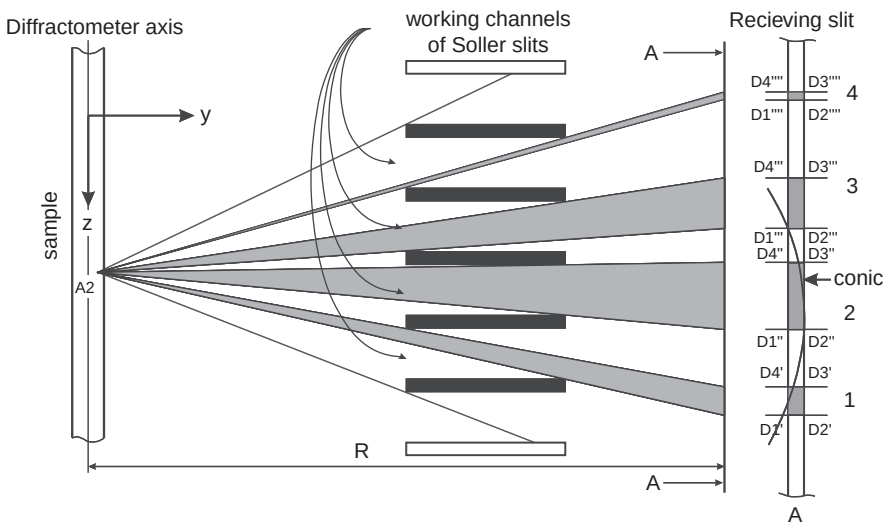



**Figure 6.22** Soller slits in the diffracted cone. A drawing plane passes through the rotation axis of the diffractometer and the center of the receiving slit. The $z$ axis is shown on an exaggerated scale. The lamellae of the working channels of the Soller slits are highlighted in black. Corresponding 'new' receiving slits (gray) and the conic section are shown on the right. (Reprinted from Ref. 53. Permission of the International Union of Crystallography.)

Therefore, instead of one full receiving slit, several (the number depends on the positions and geometrical parameters of the Soller slits) smaller receiving slits should be considered. The corner points of these new sub-receiving slits for given Soller slits depend on the position of point $A_2$ and angle $\varphi$ and can be

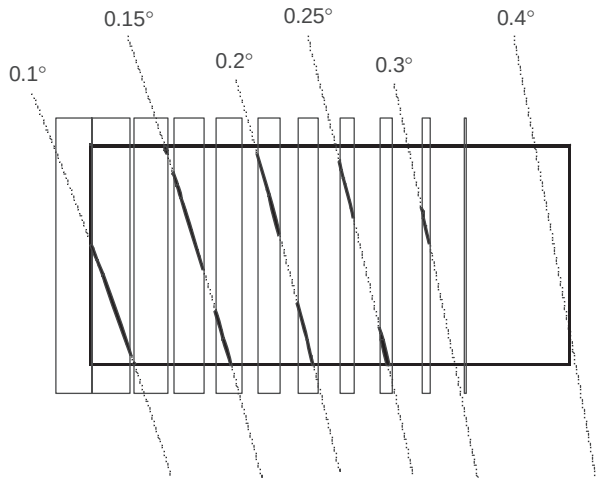



**Figure 6.23** Parts of the conics passing through the Soller slits. Dot lines conics corresponding different scanning angles (shown on figure as $\varepsilon = \theta \quad \varphi$ ) in the receiving slit plane. $\theta = 10^{\circ}$. $A_1 = \{5, 0\}$, $A_2 = \{ \quad 5, 0, 0\}$. Set of the rectangles with the vertical long sides represent parts of the receiving slit plane as they are seen from point $A_2$. Thick lines part of the conics passing through the Soller slits.

easily calculated. Further calculations of points $P_{ci}$ should be carried out for each sub-receiving slit. Such a consideration provides an exact solution for the instrumental function for the diffractometer with the Soller slits in the same way as in the case without the Soller slits. Figure 6.23 shows conics at different scanning angles produced by the incident rays from point $A_1 = \{5, 0\}$ on the source to the point $A_2 = \{-5, 0, 0\}$ on the sample (points with maximal axial divergence) and parts of the conics passed through the Soller slits. It is easy to see that Soller slits restrict the contribution to the registered intensity at low scanning angles.

Calculations in this case can take more time (test calculation with four sub-receiving slits gave a factor of about 2 in comparison with the case without Soller slits). Obviously, related approximations can be devised and tested using the exact solution.

### 6.7.3 Monochromator

Notably, there is no satisfactory solution, based on a physically meaningful model, for incorporating a monochromator during the calculation of the instrumental function in X-ray powder diffraction.[51] In the context of the proposed method, the case of the diffractometer with a monochromator can be considered as follows.

*Monochromator in the incident beam*. Figure 6.24 shows beam paths in the diffractometer with an incident-beam focusing monochromator. The rays from

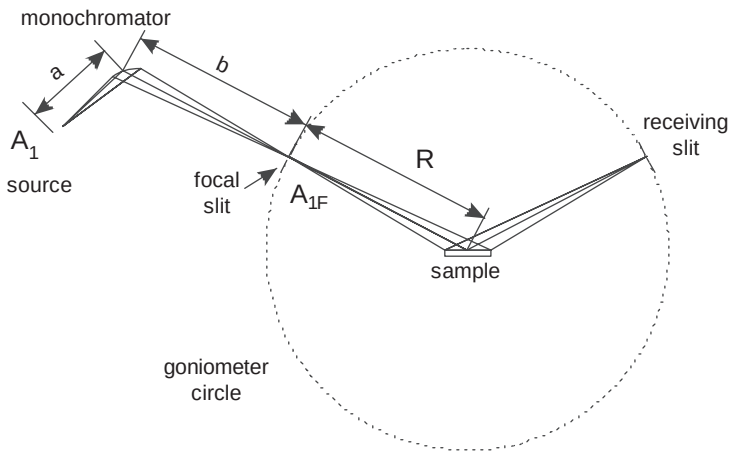



**Figure 6.24** Bragg Brentano diffractometer with incident beam monochromator.

the X-ray source are focused at the focal slit plane. The focal slit is placed at the goniometer radius. Now the image of the source in the focal slit can be considered as the source of the X-rays.

The corrections should be made to take into account the change, first of all, in the axial divergence and, perhaps, in the equatorial divergence. It is easy to see from Figure 6.24 that the maximal axial divergence can be estimated as $\gamma_{AX} = l_{AX}/(R + a + b)$. Substituting the values $l_{AX} = 10\text{mm}$, $R = 217.5\,\text{mm}$, $a = 120\,\text{mm}$, and $b = 360\,\text{mm}$, gives $\gamma_{AX} = 0.014$, which corresponds to about $0.8^\circ$. Without a monochromator the axial divergence would be about $2.6^\circ$. The intensity distribution in the equatorial and axial directions perhaps will be slightly charged from uniform. The corresponding correction should be made.

For a non-monochromatic X-ray beam an additional integration over the wavelength distribution is required.

*Plane crystal monochromator in the diffracted beam*. This case is considered in the next two sections.

## 6.8 PLANE CRYSTAL MONOCHROMATOR IN THE DIFFRACTED BEAM

The influence of the plane crystal monochromator in the diffracted beam can also be considered in the context of using the conic section. The plane crystal monochromator is located after the receiving slit at the radius $R_m$.

### 6.8.1 Setting of the Monochromator

The diffracted ray coming from the center of the sample and passing through the center of the receiving slit strikes the center of the monochromator crystal. The angle between this ray and the crystal plane is equal to $\pm\theta_m$. Signs $+$, $-$ corresponds to the respective clockwise and counter-clockwise rotations of the

crystal. We consider the case of counter-clockwise rotation. The rotation axis of the monochromator crystal is parallel to the rotation axis of the diffractometer and has the same direction.

### 6.8.2 Reflection Cones

We can consider point $A_2$ as a source of the monochromatic radiation. The reflection region can be represented as a ring limited by the two circles. The center of the circles is the projection $A_2^p$ of point $A_2$ on the monochromator plane, and the radii are $d\cot\theta_1$, $(\theta_1 = \theta_B + \delta_1)$ and $d\cot\theta_2$, $(\theta_2 = \theta_B + \delta_2)$, where $\theta_B$ is the Bragg angle of the crystal, $\delta_1$ and $\delta_2$ determine the width and the shift of Bragg angle according to the dynamical theory of X-rays scattering,[59] and $d$ is a distance between points $A_2$ and $A_2^p$. We suppose now that the crystal is set up in such way that the ray from the center of sample and passing through the center of the receiving slit comes in the middle of the reflection ring. Then:

$$\theta_m = \theta_B + (\delta_1 + \delta_2)/2,\ \theta_1 = \theta_m - \delta,\ \text{and}\ \theta_2 = \theta_m + \delta$$

For a well-aligned monochromator crystal the normal to the crystal plane lies in the equatorial plane. In this case the registered intensity will be maximal for the narrow receiving slit at the angles corresponding to the peak positions. We can introduce the reflection cones as the cones whose axes are parallel to the normal of the monochromator plane vertex with point $A_2$ and directrices as the circles bounding the reflection region. The common equation of the cone Equation (8) can be used to obtain the conic equation corresponding to intersection of the receiving slit plane and reflection cones. For this case the direction vector is constant in the coordinate system related to the receiving slit and equal to the unit vector normal to the monochromator plane. The vector parallel to the axis of the reflection cone is the normal $n$ to the crystal plane:

$$\begin{aligned} n_x &= 0 \\ n_y &= -\cos\theta_m \\ n_z &= -\sin\theta \end{aligned}$$

The half-angles of the reflection cones are $\pi/2 - (\theta_m \pm \delta)$. The common equation of the cone Equation (8) takes the form for the reflection cone:

$$\frac{\mathbf{X} - \mathbf{V}}{|\mathbf{X} - \mathbf{V}|} \cdot \mathbf{n} = \sin(\theta_m \pm \delta) \tag{25}$$

The coefficients of the reflection conic in the receiving slit plane are:

$$\begin{aligned} a &= -\sin^2(\theta_m \pm \delta) \\ b &= 0 \\ c &= \cos\delta\cos(2\theta_m + \delta) \\ d &= x_s \sin^2(\theta_m + \delta) \\ f &= -\big(y_s \sin\varphi \sin^2(\theta_m + \delta) + \cos\theta_m (R\sin\theta_m - y_s \sin(\varphi + \theta_m))\big) \\ g &= -R^2 \sin\delta \sin(2\theta_m + \delta) + 2y_s R\big(\cos\varphi \sin^2(\theta_m + \delta) - \sin\theta_m \sin(\varphi + \theta_m)\big) \\ &\quad + y_s^2 \sin(\varphi - \delta)\sin(\varphi + 2\theta_m + \delta) - x_s^2 \sin^2(\theta_m + \delta) \end{aligned}$$

as functions of the coordinates of point $A_2$, the diffractometer radius $R$ and angle $\varphi$, the Bragg angle $\theta_m$ of the monochromator crystal, and $\delta$ which is the half width of the reflection ring.

### 6.8.3 Intersection of the Diffraction and Reflection Conics in the Receiving Slit Plane

There are four solutions in the general case of an intersection of two conics. In our case there are not more than two possible solutions. This occurs because the diffraction and reflection cones have the same vertex-point $A_2$. Let us denote by $\theta_{un}$ the angle between the axes of the diffraction and reflection cones. These cones will intersect with one another

$$|2\theta - (\pi/2 - \theta_m - \delta)| < \theta_{un} < 2\theta + \pi/2 - \theta_m - \delta$$

Using Equations (8) and (24) we can obtain:

$$(\mathbf{X} - \mathbf{V}) \cdot \mathbf{A} = 0$$

where $\mathbf{A} = \mathbf{u} \sin\theta_m - \mathbf{n} \cos 2\theta$

Taking into account that for points on the receiving slit plane $\mathbf{X} = \{x, y, 0\}$ and expressing the scalar product by the sum of the component products we can obtain the relation between $x$ and $y$:

$$A_x x + A_y y = \mathbf{V} \cdot \mathbf{A}$$

or:

$$y = \frac{\mathbf{V} \cdot \mathbf{A} - A_x x}{A_y} \tag{26}$$

Substituting the last expression for $y$ in the equation of the reflection (or diffraction) conic we obtain the quadratic equation $a_m x^2 + b_m x + c_m = 0$ for $x$. The coefficients of this equation are:

$$a_m = \frac{A_x^2}{A_y^2} c - \frac{A_x}{A_y} b + a$$

$$b_m = \left( \frac{b}{A_y} - 2\frac{A_x}{A_y^2} c \right) \mathbf{A} \cdot \mathbf{V} + d - \frac{A_x}{A_y} f$$

$$c_m = \left( \frac{c}{A_y^2} \mathbf{A} \cdot \mathbf{V} + \frac{f}{A_y} \right) \mathbf{A} \cdot \mathbf{V} + g$$

Solving the quadratic equation and using Equation (26) we obtain the coordinates of intersection points $P_{cmi}$ of the diffraction and reflection cones. The registered intensity is proportional to the dihedral angle and can be found using Equation (25). There is one special case that requires special consideration. This is where the diffraction conic lies completely in the reflection region. The registered intensity for this case is determined by the part of the diffraction conic lying in the receiving slit.

The other way to calculate the registered intensity after the plane monochromator can be described as follows. To calculate angle between two planes we need only know the unit direction vector $\mathbf{m} = \{m_1, m_2, m_3\}$ to the points $P_{cmi}$. These direction vectors are determined by the line of the intersection of the diffraction and reflection cones. To find this direction we use the following equations:

$$\mathbf{m} \cdot \mathbf{u} = \cos 2\theta$$
$$\mathbf{m} \cdot \mathbf{u} = \sin \theta_m$$
$$\mathbf{m} \cdot \mathbf{u} = 1$$

However, it should be tested whether the ray comes into the receiving slit.

## 6.9 EFFECT OF THE PLANE MONOCHROMATOR ON INSTRUMENTAL FUNCTION

### 6.9.1 Equatorial Aberration in the Presence of the Monochromator

With the shift $y_s$ of the point $A_2$ in the equatorial direction, the point $A_r$ in the receiving slit corresponding to the middle point of the ring on the crystal plane moves by the value $\delta y = -y_s \sin \varphi$. The maximal shift of point $A_r$ in the equatorial plane can be taken as the width of the receiving slit. As a consequence the only rays of the reflection cone from the points of the sample with a shift smaller than $d_w/(2 \sin \varphi)$ go through the receiving slit. As an example $y_s = -0.125/\sin 10^\circ \approx -0.72\,\text{mm}$ and $y_s = -0.125/\sin 40^\circ \approx -0.19\,\text{mm}$. Hence only the points near the rotation axis of the diffractometer contribute to the registered intensity. Contrary to the case without the monochromator, only points from one side of the sample contribute to the registered intensity. For scanning angles smaller than the Bragg angle only points on the sample with positive coordinates contribute to the registered intensity. For scanning angles larger than the Bragg angle only points on the sample with negative coordinates contribute to the registered intensity. Changing the distance from the points on the sample causes a slight change in intensity in the instrumental line profile. As an example, for $\theta_B = 10^\circ$ and $R = 200$ the change of intensity is equal $\approx 0.7\%$. The front and back of the equatorial instrumental function is smeared by the length corresponding to the width of the reflection region, and is considerably smaller than the length of the front/back of the instrumental function without the monochromator.

Figure 6.25 shows the equatorial instrumental functions with and without taking into account the monochromator.

The reflection region was represented by the rectangular function:

$$R(\psi) = \begin{cases} 1, & |\psi - \theta_m| \le \delta \\ 0, & |\psi - \theta_m| > \delta \end{cases}$$

The form of the reflection function $R(\psi)$ influences only the very narrow front and back of the profile.

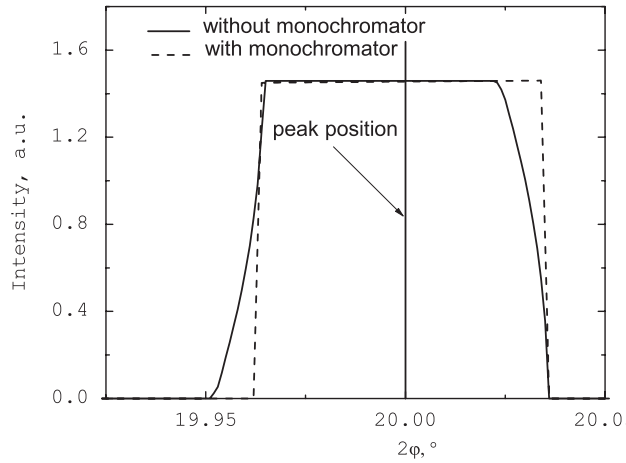



**Figure 6.25** Equatorial aberration with and without monochromator. (Reprinted from Ref. 54. Permission of the International Union of Crystallography.)

### 6.9.2 Axial Aberration in the Presence of the Monochromator

The shift of point $A_2$ in the axial direction causes an equal axial shift of the middle point of the reflection conic in the receiving slit plane. In this sense the axial aberration is equivalent to using a narrow receiving slit with the width equal to that of the reflection region in the receiving slit plane.

Because of this, we will compare two instrumental profiles. Both are the profiles caused by the axial aberrations with the difference that the first is registered by the narrow receiving slit in the absence of a monochromator and the second is the profile taking into account the monochromator. In the latter case the width of the receiving slit is selected so that the reflection regions intersect only the vertical boundaries of the receiving slit. If this condition is fulfilled the registered intensity depends only on the length of the receiving slit and not on its width.

Figure 6.26 shows the axial instrumental functions for these two cases.

### 6.9.3 Total Instrumental Function in the Presence of the Monochromator

Figure 6.27 shows the total instrumental functions with and without a monochromator. (Reprinted from Ref. 54. Permission of the International Union of Crystallography.)

The profile with the monochromator was scaled by a factor of about 250. The difference between the profiles calculated with and without the monochromator is explained by the differences in the equatorial and axial aberration profile (Figures 6.25 and 6.26).

## 6.10 CONCLUSIONS

The general form of a conic was used to calculate the instrumental function of a diffractometer in Bragg-Brentano geometry. The coefficients of the quadratic

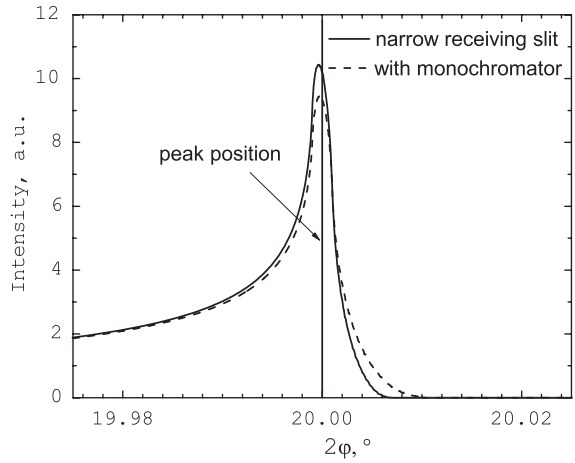



**Figure 6.26** Axial instrumental functions with and without monochromator. (Reprinted from Ref. 54. Permission of the International Union of Crystallography.)

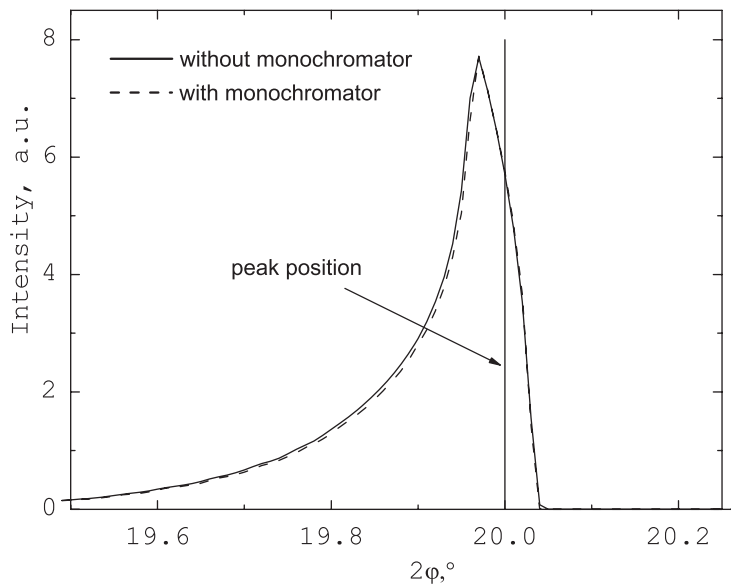



**Figure 6.27** Total instrumental functions with and without monochromator. (Reprinted from Ref. 54. Permission of the International Union of Crystallography).

form representing the intersection of the diffraction cone and the receiving slit plane are given in a general form as functions of the coordinates of the points $A_1$ (at the source), $A_2$ (at the sample), the scattering angle $\theta$, and the diffractometer angle $\varphi$. The equation of the conic for a diffractometer in Bragg-Brentano geometry is also given in implicit form.

Calculation of the instrumental contribution to the line profile at the diffractometer angle $\varphi$ is reduced to the calculation of the integral over two well defined regions – the source and the sample. The calculation of the integrand is reduced, in turn, to solving quadratic equations. All aberrations and coupling effects are taken into account. The specific instrumental functions can be easily deduced from the common consideration. This mathematical formalization enables a straightforward calculation (also strengthened by the illustrative basis) of the instrumental function and the analysis of contribution different instrumental factors to the line profile in X-ray powder diffraction.

## ACKNOWLEDGEMENTS

The author is very thankful to Dr. R. Dinnebier for his interest in this work and for stimulating discussions.

## REFERENCES

1. R. L. Snyder, J. Fiala and H. J. Bunge (eds.), *Defect and Microstructure Analysis by Diffraction*, International Union of Crystallography/Oxford University Press, Oxford, 1999.
2. H. P. Klug and L. E. Alexander, *X-ray Diffraction Procedure for Polycrystalline and Amorphous Materials*, John Wiley, New York, 1974.
3. A. E. C. Wilson, *Mathematical Theory of X-Ray Powder Diffractometry*, Philips technical library, 1963.
4. H. M. Rietveld, *J. Appl. Crystallogr.*, 1969, **2**, 65–71.
5. R. A. Young (ed.), *The Rietveld Method, IUCr Monographs on Crystallography*, International Union of Crystallography/Oxford University Press, Oxford, 1995.
6. *Commission on Powder Diffraction IUCr Newsletter*, No. 28, December 2002.
7. R. C. Spencer, *J. Appl. Phys.*, 1949, **20**, 413–414.
8. R. C. Spencer, *Phys. Rev.*, 1939, **55**, 239.
9. F. W. Jones, *Proc. Roy. Soc. A*, 1938, **166**, 16–43.
10. J. N. Eastabrook, *Br. J. Appl. Phys.*, 1952, **3**, 349–352.
11. L. Alexander, *J. Appl. Phys.*, 1954, **25**(2), 155–161.
12. E. R. Pike, *J. Sci. Instrum.*, 1957, **34**, 355–363.
13. E. R. Pike, *J. Sci. Instrum.*, 1959, **36**, 52–53.
14. G. Caglioti, A. Paoletti and F. P. Ricci, *Nucl. Instrum. Methods*, 1958, **3**, 223–228.
15. J. I. Langford, *J. Sci. Instrum.*, 1962, **39**, 515–516.
16. R. A. Young and D. B. Wiles, *J. Appl. Crystallogr.*, 1982, **15**, 430–438.
17. C. J. Howard, *J. Appl. Crystallogr.*, 1982, **15**, 615–620.
18. E. Prince, *J. Appl. Crystallogr.*, 1983, **16**, 508–511.
19. B. van Laar and W. B. Yelon, *J. Appl. Crystallogr.*, 1984, **17**, 47–54.
20. J. B. Hastings, W. Thomlinson and D. E. Cox, *J. Appl. Crystallogr.*, 1984, **17**, 85–95.

21. I. C. Madsen and R. J. Hill, *J. Appl. Crystallogr.*, 1988, **21**, 398–405.
22. D. Louer and J. I. Langford, Peak shape and resolution in conventional diffractometry with monochromatic X-rays, *J. Appl. Crystallogr.*, 1988, **21**, 430–437.
23. J. I. Langford, R. J. Cernik and D. Louer, *J. Appl. Crystallogr.*, 1991, **24**, 913–919.
24. J. I. Langford, D. Louer and P. Scardi, *J. Appl. Crystallogr.*, 2000, **33**, 964–974.
25. J. Timmers, R. Delhez, F. Tuinstra and F. Peerdeman, *Accuracy in Powder Diffraction II*, ed. E. Prince and J. K. Stalick (U.S. Government Printing Office, Washington), 1992, NIST Special Publication 846, p. 217.
26. V. A. Kogan and M. F. Kupriyanov, *J. Appl. Crystallogr.*, 1992, **25**, 16–25.
27. R. W. Cheary and A. Coelho, *J. Appl. Crystallogr.*, 1992, **25**, 109–121.
28. C. E. Matulis and J. C. Taylor, *J. Appl. Crystallogr.*, 1993, **26**, 351–356.
29. R. L. Snyder, Analytical profile fitting of X-ray powder diffraction profiles in Rietveld analysis, in Ref. 1, 111–132.
30. P. Suortti, Bragg reflection profile shape in X-ray powder diffraction pattern, in Ref. 1, 167–185.
31. L. W. Finger, D. E. Cox and A. P. Jephcoat, *J. Appl. Crystallogr.*, 1994, **27**, 892–900.
32. D. Reefman, *Powder Diffr.*, 1996, **11**(2), 107–113.
33. V. Honkimäki, *J. Appl. Crystallogr.*, 1996, **29**, 617–624.
34. R. W. Cheary and A. Coelho, *J. Appl. Crystallogr.*, 1998, **31**, 851–861.
35. R. W. Cheary and A. Coelho, *Powder Diffr.*, 1998, **13**, 100–106.
36. J. Bergmann and R. Kleeberg, *Mater. Sci. Forum*, 1998, **278–281**, 300–305.
37. J. Bergmann, P. Friedel and R. Kleeberg, 1998, www.bgmn.de.
38. J. Bergmann, P. Friedel and R. Kleeberg, *CPD Newsletter*, 1998, **20**, 5–8.
39. T. Ida, *The Rigaku J.*, 2002. **19**, 1, 47–56 (Rigaku Corp., Japan).
40. T. Ida, *Rev. Sci. Instrum.*, 1998, **69**, 2268–2272.
41. T. Ida and K. Kimura, *J. Appl. Crystallogr.*, 1999, **32**, 634–640.
42. T. Ida and K. Kimura, *J. Appl. Crystallogr.*, 1999, **32**, 982–991.
43. T. Ida and H. Hibino, *J. Appl. Crystallogr.*, 2006, **39**, 90–100.
44. T. Ida, H. Hibino and H. Toraya, *J. Appl. Crystallogr.*, 2003, **36**, 181–187.
45. T. Ida and H. Toraya, *J. Appl. Crystallogr.*, 2002, **35**, 58–68.
46. M. Čerňanský, Restoration and Preprocessing of Physical Profiles from Measured Data, in Ref. 1, 613–651.
47. D. Reefman Towards Higher Resolution: A Mathematical Approach, in Ref. 1, 652–670.
48. A. D. Stoica, M. Popovici and W. B. Yelon, *J. Appl. Crystallogr.*, 2000, **33**, 137–146.
49. O. Masson, R. Guinebretiere and A. Dauger, *J. Appl. Crystallogr.*, 2001, **34**, 436–441.
50. O. Masson, E. Dooryhee and A. N. Fitch, *J. Appl. Crystallogr.*, 2003, **36**, 286–294.
51. R. W. Cheary, A. A. Coelho and J. Cline, *J. Res. Natl Inst. Stand. Technol.*, 2004, **109**, 1–25.

52. E. Prince and B. H. Toby, *J. Appl. Crystallogr.*, 2005, **38**, 804–807.
53. A. Zuev, *J. Appl. Crystallogr.*, 2006, **39**, 304–314.
54. A. Zuev, *J. Appl. Crystallogr.*, submitted.
55. M. Deutsch, E. Förster, G. Hölzer, J. Härtwig, K. Hämäläinen, C.-C. Kao, S. Huotari and R. Diamant, *J. Res. Natl. Inst. Stand. Technol.*, 2004, **109**, 75–98.
56. I. N. Bronstein, K. A. Semendjajew, G. Musiol and H. Mühlig. *Taschenbuch der Mathematik*, Thun, Frankfurt am Main, 1997.
57. C.-K. Shene, in *GRAPHICS GEMS IV*, ed. P. Heckbert, Academic Press, New York, 1994.
58. *Mathematica*, Version 5.2, Wolfram Research, Inc., Champaign, IL, 2005.
59. A. Authier, *Dynamical Theory of X-ray Diffraction*, Oxford University Press, Oxford, 2001.

CHAPTER 7

# Indexing and Space Group Determination

ANGELA ALTOMARE,[a] CARMELO GIACOVAZZO[a,b] AND ANNA MOLITERNI[a]

[a] Istituto di Cristallografia (IC), C.N.R., Sede di Bari. Via G. Amendola 122/o, 70126 Bari, Italy; [b] Dipartimento Geomineralogico, Università degli Studi di Bari, Campus Universitario, via Orabona 4, 70125 Bari, Italy

## 7.1 THE CRYSTALLINE LATTICE IN POWDER DIFFRACTION

Solving a crystal structure *via* a diffraction experiment is a many-step process, which requires the previous identification of the unit cell parameters and the determination of the space group. If these items are incorrectly defined the process inevitably fails.

A single-crystal diffraction experiment generates thousands of diffracted beams whose intensities may be measured in correspondence to the reciprocal lattice points:

$$\mathbf{r}^*_{hkl} = h\mathbf{a}^* + k\mathbf{b}^* + l\mathbf{c}^*$$

As was shown in Equation (34) of Chapter 1, Bragg's law dictates that the scattering vectors for a Bragg peak, **h**, correspond to these reciprocal lattice vectors. The three-dimensionality of the diffraction pattern makes the identification of the three vectors **a***, **b***, **c***, straightforward, from which the direct space unit cell vectors:

$$\mathbf{a} = \frac{\mathbf{b}^* \wedge \mathbf{c}^*}{V}, \quad \mathbf{b} = \frac{\mathbf{c}^* \wedge \mathbf{a}^*}{V}, \quad \mathbf{c} = \frac{\mathbf{a}^* \wedge \mathbf{b}^*}{V}$$

may be derived (see Chapter 1). The unit cell parameters suggest (and only suggest) the *crystal system*, which has to be confirmed *via* identification of the *Laue group*. This group may be singled out as follows. Let us suppose that the set of symmetry operators:

$$\mathbf{C}_s \equiv (\mathbf{R}_s, \mathbf{T}_s), \quad s = 1, \ldots, m \tag{1}$$

is present ($\mathbf{R}_s$ is the rotation matrix, $\mathbf{T}_s$ the translation component). Then:

$$\mathbf{r}_{js} = \mathbf{R}_s\mathbf{r}_j + \mathbf{T}_s, \quad s = 1, \ldots m$$

are *symmetry equivalent positions* in direct space ($\mathbf{r}_j$ is a generic positional vector in the unit cell). If the space group is centrosymmetric, in the reciprocal space we will observe, for the reflections with indices:

$$\mathbf{hR}_s, \quad s = 1, \ldots m \tag{2}$$

the intensity condition:

$$I_{\mathbf{hR}_s} = I_{\mathbf{h}}, \quad s = 1, \ldots m \tag{3}$$

The reflections (2) are called *symmetry equivalent reflections*: the set contains both the Friedel opposites (Chapter 3). If the space group is non-centrosymmetric, the reflections (2) and their Friedel opposites, say:

$$\mathbf{hR}_s, s = 1, \ldots m, -\mathbf{hR}_s, s = 1, \ldots m$$

constitute the set of *symmetry equivalent reflections*, for which the condition:

$$I_{\mathbf{hR}_s} = I_{\ \mathbf{hR}_s} = I_{\mathbf{h}}, \quad s = 1, \ldots m \tag{4}$$

is true. From Equations (3) or (4) the Laue group may be identified. For example, the relation:

$$I_{hkl} = I_{hkl} = I_{hkl} = I_{hkl} = I_{hkl} = I_{hkl} = I_{hkl} = I_{hkl}$$

identifies the Laue group $2/m\ 2/m\ 2/m$. These relationships are tabulated in the *International Tables for Crystallography*.[1]

To single out the correct space group among those showing the same Laue symmetry the *systematically absent reflections* have to be studied. Since the structure factor:

$$F_{\mathbf{hR}} = F_{\mathbf{h}}\exp(-2\pi i\mathbf{hT}) \tag{5}$$

we have:

$$|F_{\mathbf{hR}}| = |F_{\mathbf{h}}|, \quad \phi_{\mathbf{hR}} = \phi_{\mathbf{h}} - 2\pi i\mathbf{hT}$$

If $\mathbf{hR} = \mathbf{h}$ but $\mathbf{hT} \neq n$, with $n$ a generic integral number, Equation (5) is violated unless the **h**-reflection is a systematically absent reflection. The use of Equation (5) therefore leads to the conditions for the systematically absent reflections, *e.g.* in the space group $P2_1$ or $P2_1/m$, $I_{0k0} = 0$ for $k$ odd. In the space group $P2_1/c$, $I_{0k0} = 0$ for $k$ odd and $I_{h0l} = 0$ for $l$ odd. These conditions also are tabulated in the *International Tables for Crystallography*.[1]

The combination of the information on the Laue group with the analysis of the systematically absent reflections allows the determination of the so-called *Extinction symbol* (*ES*). In the *International Tables for Crystallography*[1] the list of extinction symbols is given *per* crystal system. There are 14 *ES* for the

**Table 7.1** Some *extinction symbols* and the corresponding compatible space groups.

| *Cryst. system* | *Ext. symb.* | *Space groups* |
|---|---|---|
| *Mon.* | *P 1 1* | *P2, Pm, P2/m* |
| *Orth.* | *P* | *P222, Pm2m, P2mm, Pmm2, Pmmm* |
| *Orth.* | *P a* | *Pm2a, P2$_1$ma, P mma* |
| *Tetr.* | *P* | *P4, P4, P4/m, P422, P4mm, P42m, P4m2 P4/mmm* |
| *Hex* | *P6$_1$* | *P6$_1$, P6$_5$ P6$_1$22, P6$_5$22* |
| *Cub.* | *P n* | *P43n, Pm3n* |

monoclinic, 111 for the orthorhombic, 31 for the tetragonal, 12 for the trigonal-hexagonal, and 18 for the cubic system. In the first position of the *ES* the centric type of the cell is shown, then the reflection conditions for the successive symmetry directions are given. Symmetry directions without conditions are represented by a dash. A symmetry direction with reflection conditions is represented by the symbol of the corresponding screw axis or glide plane.

The *ES* does not unambiguously define the space group. Table 7.1 shows some *extinction symbols* and the corresponding compatible space groups.

The above practice is rather straightforward for a single-crystal experiment, but often provides doubtful results when only powder diffraction data are available. The basic reason is that the powder diffraction pattern is one-dimensional, owing to the collapse of the reciprocal lattice of the individual crystallites onto the $2\theta$ axis. Consequently, reflections with the same $|\mathbf{r}^*_{hkl}|$ modulus (*i.e.* with the same interplanar spacing $d_{hkl}$: indeed $d_{hkl} = 1/|\mathbf{r}^*_{hkl}|$) will overlap on the $2\vartheta$ axis. For convenience, we quote in Table 7.2 the algebraic expressions of $d_{hkl}$ for the various crystal systems.

As an example, in Figure 7.1 we show the reciprocal plane $hk0$ for an orthorhombic lattice defined by the unit cell parameters $a = 10.00$ Å, $b = 5.77$ Å, $c = 14.32$ Å.

Because of the orthorhombic symmetry the reflections $(hk0)$, $(-h,-k,0)$, $(-h,k,0)$, $(h,-k,0)$ will precisely overlap on the $d$-axis (the one-dimensional axis of interatomic spacing, $d$) since, in Table 7.2, the expressions of $1/d^2_{hkl}$ depend on the squares of $h$, $k$, $l$. The number of overlapping symmetry equivalent reflections is given by the *reflection multiplicity* $m_{\mathbf{h}}$. The value of $m_{\mathbf{h}}$ is reflection dependent: for example $m_{\mathbf{h}} = 2$ for the reflection $(h00)$, $m_{\mathbf{h}} = 4$ for the reflection (110), $m_{\mathbf{h}} = 8$ for a generic $(hkl)$ reflection.

The value of $m_{\mathbf{h}}$ may be calculated for each space group and for each reflection by the following algorithm. Let $\mathbf{C}_s = (\mathbf{R}_s, \mathbf{T}_s)$, $s = 1, \ldots m$ be the set of symmetry operators of the space group: the number of distinct vectors $\mathbf{h}_s = \mathbf{h}\mathbf{R}_s$ obtained by varying $s$ from 1 to $m$, added to the Friedel opposites $-\mathbf{h}_s = -\mathbf{h}\mathbf{R}_s$ if the space group is non-centric, corresponds to the multiplicity of the reflection $\mathbf{h}$.

The multiplicity is not a problem for the correct estimation of the integrated intensity (say $\mathbf{I}_{\mathbf{h}}$) to associate with a given unique reflection $\mathbf{h}$. If, at a given $2\vartheta$ value, only $m_{\mathbf{h}}$ equivalent reflections overlap, the value of $I_{\mathbf{h}}$ will be equal to the

**Table 7.2** Algebraic expressions of $d_{hkl}$ for the various crystal systems.

| *System* | $1/d_{hkl}^2$ |
|---|---|
| Cubic | $(h^2 + k^2 + l^2)/a^2$ |
| Tetragonal | $\dfrac{h^2 + k^2}{a^2} + \dfrac{l^2}{c^2}$ |
| Orthorhombic | $\dfrac{h^2}{a^2} + \dfrac{k^2}{b^2} + \dfrac{l^2}{c^2}$ |
| Hexagonal and Trigonal (P) | $\dfrac{4}{3a^2}(h^2 + k^2 + hk) + \dfrac{l^2}{c^2}$ |
| Trigonal (R) | $\dfrac{1}{a^2}\left(\dfrac{(h^2 + k^2 + l^2)\sin^2\alpha + 2(hk + hl + kl)(\cos^2\alpha \quad \cos\alpha)}{1 + 2\cos^3\alpha \quad 3\cos^2\alpha}\right)$ |
| Monoclinic | $\dfrac{h^2}{a^2\sin^2\beta} + \dfrac{k^2}{b^2} + \dfrac{l^2}{c^2\sin^2\beta} \quad \dfrac{2hl\cos\beta}{ac\sin^2\beta}$ $(1 \quad \cos^2\alpha \quad \cos^2\beta \quad \cos^2\gamma + 2\cos\alpha\cos\beta\cos\gamma)^{-1}$ |
| Triclinic | $\left(\dfrac{h^2}{a^2}\sin^2\alpha + \dfrac{k^2}{b^2}\sin^2\beta + \dfrac{l^2}{c^2}\sin^2\gamma + \dfrac{2kl}{bc}(\cos\beta\cos\gamma \quad \cos\alpha)\right.$ $\left. + \dfrac{2lh}{ca}(\cos\gamma\cos\alpha \quad \cos\beta) + \dfrac{2hk}{ab}(\cos\alpha\cos\beta \quad \cos\gamma)\right)$ |

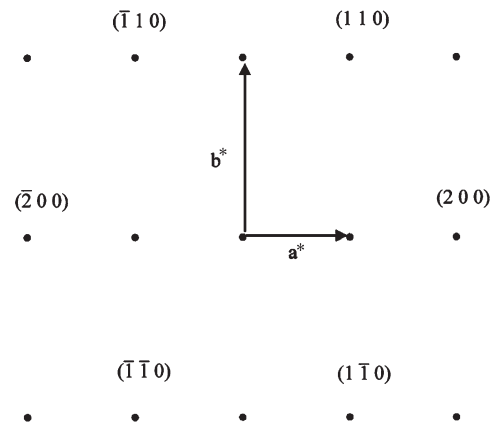



**Figure 7.1** The plane $hk0$ of a reciprocal orthorhombic lattice.

overall measured integrated intensity divided by $m_{\mathbf{h}}$. However, from Figure 7.1 we see that reflections that are not symmetry equivalent, can occasionally overlap on the $2\vartheta$-axis because of the special relationship between the $a$ and $b$ values (*i.e.* $b \approx a/\sqrt{3}$). In our case the reflections (200) and (110) will nearly

overlap, as well as the reflections (400) and (220), *etc*. Of course, according to the $c$ values, reflections of ($hkl$) type can occasionally overlap with ($hk0$) reflections. This type of overlapping (total or partial according to the $2\vartheta$ misfit) is called *occasional* because it does not depend on the symmetry, but on some particular relationships among the lattice parameters. This kind of occasional overlap can sometimes be resolved by collecting datasets at different temperatures, if the thermal expansivity is different along the different axes.

A further type of overlapping, called *systematic overlapping*, may occur for high symmetry crystal systems (*i.e*., in tetragonal, hexagonal and cubic systems), where the lattice symmetry may be higher than the Laue symmetry. For example, for any space group belonging to the Laue class $4/m$ the symmetry equivalent reflections are:

$$(hkl), (\bar{h}\bar{k}l), (khl), (\bar{k}\bar{h}l), (\bar{h}\bar{k}\bar{l}), (hk\bar{l}), (\bar{k}\bar{h}\bar{l}), (kh\bar{l})$$

Owing to the lattice symmetry ($4/mmm$ in the tetragonal system), $1/d^2_{hkl}$ depends on the value of $(h^2 + k^2)$ and the following reflections will systematically overlap:

$$(hkl), (\bar{h}\bar{k}l), (khl), (\bar{k}\bar{h}l), (\bar{h}\bar{k}\bar{l}), (hk\bar{l}), (\bar{k}\bar{h}\bar{l}), (kh\bar{l})$$

$$(\bar{h}kl), (h\bar{k}l), (\bar{k}hl), (k\bar{h}l), (h\bar{k}\bar{l}), (\bar{h}k\bar{l}), (k\bar{h}\bar{l}), (\bar{k}h\bar{l})$$

The first eight reflections are symmetry equivalent to ($hkl$) and the second eight to the reflection ($khl$). Since there is no symmetry relation between $I_{hkl}$ and $I_{khl}$, the two intensities are expected to be uncorrelated. Then the measured overall intensity (summing the contributions of the 16 reflections) cannot be reliably partitioned into $I_{hkl}$ and $I_{khl}$.

Let us now refer to the cubic system. For all the space groups belonging to the Laue class $m3$ the 24 equivalent reflections are:

$$\begin{aligned}&(hkl), (\bar{h}\bar{k}l), (h\bar{k}\bar{l}), (\bar{h}k\bar{l}), (lhk), (\bar{l}\bar{h}k), (l\bar{h}\bar{k}), (\bar{l}h\bar{k}), (klh), (\bar{k}\bar{l}h), (k\bar{l}\bar{h}), (\bar{k}lh)\\ &\quad + \textit{Friedel opposites}\end{aligned} \tag{6}$$

Owing to the lattice symmetry (*i.e*. $m3m$) there are 48 reflections that have the same value of $d^2_{hkl}$. In particular, besides the reflections (6), also the following ones overlap:

$$\begin{aligned}&(khl), (\bar{k}\bar{h}l), (kh\bar{l}), (\bar{k}\bar{h}\bar{l}), (lkh), (\bar{l}\bar{k}h), (lk\bar{h}), (\bar{l}\bar{k}\bar{h}), (hlk), (\bar{h}\bar{l}k), (h\bar{l}\bar{k}), (\bar{h}lk)\\ &\quad + \textit{Friedel opposites}\end{aligned} \tag{7}$$

Since there is no symmetry relation between $I_{hkl}$ and $I_{khl}$, the two intensities are expected to be uncorrelated. Then the measured overall intensity (summing the contributions of the 48 reflections) cannot reliably be partitioned into $I_{hkl}$ and $I_{khl}$.

From the above considerations two consequences arise:

a. The problem of identifying the unit cell parameters is a classical inversion problem. That is, the $d$-values of all the reflections may be easily

calculated if the unit cell parameters are known, the reverse is not a simple process owing to the one-dimensionality of the diffraction pattern.

b. Owing to the reflection overlap, the estimate of the reflection intensities is difficult. The presence of *preferred orientation* (see Chapter 3, Section 3.4.3, and Chapter 12) may make such an estimate even more difficult. Then it may be rather difficult to verify the extinction rules (the reflections that are expected to be systematically absent may overlap with non-absent reflections), and complex mathematical methods of a probabilistic type should be applied to obtain the correct answer.

The special algorithms necessary to derive, from a typical powder diffraction pattern, the unit cell parameters and the correct space group are described in Sections 7.2 and 7.3, respectively. They are present in numerous computer programs for this purpose (Chapter 17).

## 7.2 INDEXING OF A POWDER PATTERN

### 7.2.1 Introduction

The main goal of the powder-pattern indexing process is the geometrical rebuilding of the three-dimensional reciprocal space from the one-dimensional distribution of the observed $d$ values. The name ''indexing'' is related to the fact that the unit cell determination step is equivalent to assigning the appropriate triple of Miller indices to each observed inter-planar distance.[2]

Powder-pattern indexing is the first necessary step in the *ab initio* structure determination process. The first important indexing tentative was proposed by Runge.[3] Despite its long history and the great recent advances in experimental devices, mathematical methods and computing speed, powder pattern indexation can still be a challenge. The basic indexing equation relating reciprocal cell parameters and indices consists of the following quadratic form:

$$Q_{hkl} = h^2 A_{11} + k^2 A_{22} + l^2 A_{33} + hk A_{12} + hl A_{13} + kl A_{23} \tag{8}$$

where

$$Q_{hkl} = \frac{10^4}{d_{hkl}^2}, d_{hkl} = \frac{\lambda}{2 \sin \theta_{hkl}}$$

$$A_{11} = 10^4 a^{*2}, A_{22} = 10^4 b^{*2}, A_{33} = 10^4 c^{*2}, A_{12} = 10^4 \cdot 2a^* b^* \cos \gamma^*,$$
$$A_{13} = 10^4 \cdot 2a^* c^* \cos \beta^*, A_{23} = 10^4 \cdot 2b^* c^* \cos \alpha^*$$

The correct unit cell may be identified by associating indices to $n$ inter-planar distances, where $n$ depends on the lattice symmetry. In accordance with Table 7.3, the minimum values of $n$ are: $n = 1$ for the cubic system, $n = 2$ for tetragonal and hexagonal crystals, $n = 3, 4, 6$ for orthorhombic, monoclinic and triclinic systems, respectively.

**Table 7.3** $Q_{hkl}$ as a function of the lattice symmetry.

| *Lattice symmetry* | $Q_{hkl}$ |
|---|---|
| Cubic | $Q_{hkl}=(h^2+k^2+l^2)\ A_{11}$ |
| Tetragonal | $Q_{hkl}=(h^2+k^2)\ A_{11}+l^2\ A_{33}$ |
| Hexagonal | $Q_{hkl}=(h^2+hk+k^2)\ A_{11}+l^2\ A_{33}$ |
| Orthorhombic | $Q_{hkl}=h^2\ A_{11}+k^2\ A_{22}+l^2\ A_{33}$ |
| Monoclinic | $Q_{hkl}=h^2\ A_{11}+k^2\ A_{22}+l^2\ A_{33}+hl\ A_{13}$ |
| Triclinic | $Q_{hkl}=h^2\ A_{11}+k^2\ A_{22}+l^2\ A_{33}+hk\ A_{12}+hl\ A_{13}+kl\ A_{23}$ |

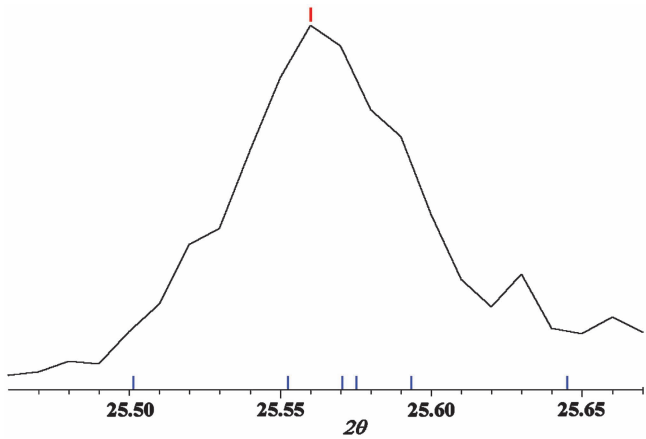



**Figure 7.2** Zoom of the powder diffraction pattern of VNI. The upper vertical bar (in red) indicates the result of a peak search procedure, the lower verticals bars (in blue; on the *x* axis) the reflection positions calculated by the published refined cell parameters.

Once the reciprocal cell parameters have been calculated, the direct cell is easily derived. The goodness of indexing results depends on the quality of $\{Q_{hkl}\}$, and therefore on the accuracy of the peak positions. The importance of data accuracy has been emphasized by de Wolff:[4]

> The "indexing problem" is essentially a puzzle ( . . . ). It would be quite an easy puzzle if errors of measurement did not exist.

Many years later Shirley[5] stated:

> Powder indexing is not like structure analysis, which works well on good data and will usually get by on poor data given a little more time and attention. Powder indexing works beautifully on good data, but with poor data it will usually not work at all.

Despite their age, the previous two sentences are still valid. The errors in peak location may be (see Section 7.1 and Chapter 4): (a) *Accidental*. In Figure 7.2 we

**Table 7.4** Indexing results for $LaB_6$.

| $d_{hkl}$ | $h\ k\ l$ | $d_{hkl}$ | $h\ k\ l$ | $d_{hkl}$ | $h\ k\ l$ |
|---|---|---|---|---|---|
| 4.1605 | 1 0 0 | 1.3873 | 3 0 0 | 1.0090 | 4 1 0 |
| 2.9418 | 1 1 0 | 1.3158 | 3 1 0 | 0.9806 | 3 3 0 |
| 2.4023 | 1 1 1 | 1.2546 | 3 1 1 | 0.9544 | 3 3 1 |
| 2.0815 | 2 0 0 | 1.2012 | 2 2 2 | 0.9302 | 4 2 0 |
| 1.8611 | 2 1 0 | 1.1540 | 3 2 0 | 0.9078 | 4 2 1 |
| 1.6991 | 2 1 1 | 1.1120 | 3 2 1 | 0.8868 | 3 3 2 |
| 1.4712 | 2 2 0 | 1.0401 | 4 0 0 | | |

show a zoom of the VNI[6] pattern, where, due to the overlap, the peak is located between the positions of the two reflections. (b) *Systematic*, owing to sample effects (*i.e.*, transparency) or shift of the $2\theta_0$ position.

Special attention and care are required when numerical relationships between cell axes exist (geometrical ambiguities, see Section 7.2.3). In addition, the presence of impurities makes the indexing process more difficult. Errors in $Q_{hkl}$ modify the problem to one of finding $\{A_{ij}\}$ satisfying the following relation:

$$Q_{hkl} - \Delta < h^2A_{11} + k^2A_{22} + l^2A_{33} + hkA_{12} + hlA_{13} + klA_{23} < Q_{hkl} + \Delta \qquad (9)$$

where $\Delta$ is a suitable tolerance parameter.

A simple indexing exercise is the case of the crystal structure $LaB_6$ (NIST Reference St'andard Material 660A),[7] certified cell $a = 4.1569162$ Å, whose observed (by a conventional diffractometer) $d_{hkl}$ values in Å are given in Table 7.4. If a cubic lattice is supposed and the Miller indices (100) are tentatively assigned to the first observed line ($d_{hkl} = 4.1605$ Å), then $A_{11}$, as defined in Table 7.3, leads to the direct cell parameter, by means of which all the remaining lines can be indexed.

### 7.2.2 Figures of Merit

Whatever the indexing method, many plausible cells are usually suggested. It is then useful to apply a figure of merit (*FOM*) for discriminating the most probable ones and for assessing their reliability. The most adopted FOMs are $M_{20}$ and $F_N$, proposed by de Wolff[8] and by Smith and Snyder,[9] respectively. $M_{20}$ is defined as:

$$M_{20} = \frac{Q_{20}}{2 < \varepsilon > N_{20}}$$

where $Q_{20}$ is the $Q$ value in case of the 20th observed peak, $<\varepsilon>$ is the average discrepancy between the observed and calculated $Q$ values for the 20 indexed peaks, $N_{20}$ is the number of calculated reflections up to the $d$ value corresponding to $Q_{20}$.

$M_{20}$ depends on: (a) the fit between calculated and observed lines (*via* $<\varepsilon>$); (b) the volume of the unit cell (*via* $N_{20}$). The smaller the average difference $<\varepsilon>$ and the cell size, the larger $M_{20}$, the greater the confidence in the proposed unit

cell. There is not a threshold value of $M_{20}$ ensuring the correctness of the cell. De Wolff suggested that if the number of unindexed peaks among the first 20 lines is not larger than 2 and if $M_{20} >$ than 10, the indexing results should be substantially correct.[8] In addition, if better solutions are not found, due to the possible presence of impurities, a check of cells having some unindexed lines and higher de Wolff figure of merit is advised.[10]

The $F_N$ figure of merit is defined as follows:

$$F_N = \frac{1}{<|\Delta 2\theta|>} \cdot \frac{N}{N_{poss}}$$

where $<|\Delta 2\theta|>$ is the average absolute discrepancy between the observed and calculated $2\theta$ values and $N_{poss}$ is the number of possible diffraction lines up to the $N$th observed line. Usually the $F_N$ value is joined with the couple $(<|\Delta 2\theta|>, N_{poss})$.

Smith and Snyder[9] compared $F_N$ and $M_{20}$ performances, analyzing a set of compounds belonging to triclinic, orthorhombic and cubic systems. They emphasized the superiority of $F_N$ with respect to $M_{20}$ because the latter is (a) defined for exactly 20 lines, (b) strongly dependent on the crystal class and the space group. But Werner[10] noted that the increasing value of $M_{20}$ with symmetry is not a disadvantage, since a cubic indexing of a powder pattern is more probable than a triclinic one.

### 7.2.3 Geometrical Ambiguities

A powder pattern can be indexed by different lattices.[8,11,12] Systematic ambiguities may occur when "two or more different lattices, characterized by different reduced forms, may give calculated powder patterns with identical $2\theta$ positions".[13] Table 7.5 supplies some examples of lattices giving geometrical ambiguities, and the related matrix transformation.[13] If geometrical ambiguities occur, additional prior information (*e.g.*, a single-crystal study) is required to choose between one of the two possible lattices.

### 7.2.4 Historical Indexing Programs

The most common and widely used indexing programs are ITO,[12] TREOR[14] and DICVOL91.[15] All three classic programs are present in the indexing Crysfire suite.[16] Their approach to the indexing problem is different and will be briefly described.

• ***ITO*** is based on a method originally suggested by Runge[3] and enriched by Ito[17,18] and by de Wolff.[4,19] A crystallographic zone in the reciprocal space (*i.e.*, a plane trough the origin) can be defined *via* the origin itself and any two lattice points. If $Q'$ and $Q''$ are the squared distances of the two points from the origin, the $Q$ value of any lattice point belonging to the zone can be defined by:

$$Q_{m,n} = m^2 Q' + n^2 Q'' + mnR \qquad (10)$$

**Table 7.5** Examples of lattices leading to geometrical ambiguities in the indexing results.[13] $\boldsymbol{P} = \{P_{ij}\}$ is the matrix transformation from lattice I into lattice II, described by the $\{\mathbf{a}_i\}$ and $\{\mathbf{b}_i\}$ translations, respectively with $\mathbf{b}_i = \Sigma_j \, \mathrm{P}_{ij}\mathbf{a}_j$.

| *Lattice I* | *Lattice II* | *P* |
|---|---|---|
| Cubic *P* | Tetragonal *P* | $0\frac{1}{2}\frac{1}{2}/0\frac{1}{2}\frac{1}{2}/100$ |
| Cubic *I* | Tetragonal *P* | $0\frac{1}{2}\frac{1}{2}/0\frac{1}{2}\frac{1}{2}/\frac{1}{2}00$ |
| | Orthorhombic *F* | $\frac{1}{3}\frac{1}{3}0/001/110$ |
| | Orthorhombic *P* | $\frac{1}{4}\frac{1}{4}0/00\frac{1}{2}/\frac{1}{2}\frac{1}{2}0$ |
| Cubic *F* | Orthorhombic *C* | $\frac{1}{2}0\frac{1}{2}/010/\frac{1}{4}0\frac{1}{4}$ |
| | Orthorhombic *I* | $\frac{1}{6}0\frac{1}{6}/\frac{1}{2}0\frac{1}{2}/010$ |
| Hexagonal | Orthorhombic *P* | $\frac{1}{2}\frac{1}{2}0/\frac{1}{2}\frac{1}{2}0/001$ |
| Rhombohedral | Monoclinic *P* | $\frac{1}{2}0\frac{1}{2}/\frac{1}{2}0\frac{1}{2}/010$ |

where $m$ and $n$ are integers, $R = 2\sqrt{Q'Q''}\cos\varphi$ and $\varphi$ is the angle between the positional vectors of the two points. Then:

$$R = (Q_{m,n} - m^2Q' - n^2Q'')/mn \tag{11}$$

According to the algorithm, all the observed $Q_{hkl}$ values and a few positive $m$ and $n$ integers are inserted into Equation (11): a great number of $R$ values is obtained and stored, some of them are equal within suitable limits of error. From them the angle between the zone base vectors is easily determined. The procedure is repeated for different zones (*i.e.*, for different pairs $Q'$ and $Q''$). The most important zones will be those for which the $R$ value is found many times. Once the search of zones has been performed, the next steps of ITO are: (a) to find pairs of zones having a common row, (b) to determine the angle between two zones to describe the lattice. The method has been generalized by Visser,[12] who explicitly takes into account the reciprocal space symmetry. The program ITO is very efficient for indexing low-symmetry patterns.

• ***TREOR*** starts with the cubic symmetry analysis and step-by-step performs tests for lower symmetry crystal systems. For each investigated system TREOR selects the ''basis lines'', a term used for diffraction lines (usually belonging to the low $2\theta$ region) to which tentative (by trial and error techniques) indices are associated to find the unit cell. Five sets of basis-lines are generally sufficient for orthorhombic tests, while seven sets of basis-lines may not be enough for monoclinic tests owing to the presence of a dominant zone (in this case more than five basis lines can be indexed with a common zero index). To detect the presence of dominant zones a special short-axis test aiming at finding two-dimensional lattices parameters is performed for monoclinic symmetry.[14]

If **M** is the square matrix of Miller indices, **A** is the vector of the unknown $\{A_{ij}\}$ and **L** is the vector of $\{Q_{hkl}\}$ for the basis lines, each trial set of $\{A_{ij}\}$ in Equation (8) is obtained by solving the system of linear equations $\mathbf{MA} = \mathbf{L}$. The correctness of the trial parameters $\{A_{ij}\}$ is related to the accuracy of low-order lines. Testing several different combinations of the basis lines can enable one to find a correct solution even in the case of error in one or more of the basis lines. A plausible solution is found if the indexed pattern is characterized by $M_{20} > 10$ with no more than one unindexed line among the first 20.

The success of TREOR is related to the standard set of parameters suggested by the accumulated experience of the authors:[14] in case of failure these parameters can be easily changed by the user *via* suitable keywords in the input file. The method has been classified by Shirley[5] as semi-exhaustive because judicious deductions are made ''to limit the size of the solutions field in order to gain speed''.

• ***DICVOL91*** has an indexing approach based on the *dichotomy method*, introduced by Louër and Louër.[20] Shirley[5] defined this method as ''probably the optimal exhaustive strategy in parameter-space''. The original version of the program was written for orthorhombic and higher symmetry. Later, the method was extended to monoclinic[21] and to triclinic symmetry.[15]

The dichotomy method is based on the variation in direct space, by finite increments, of the lengths of cell edges and of the interaxial angles (an *m*-dimensional search, where *m* is the number of unknown unit cell parameters): the variations are reduced when they contain a possible solution. The following example for a cubic system can help to understand how DICVOL91 works. The $a$ $(= b = c)$ parameter is varied from a minimum value $a_0$ up to a maximum value $a_M$ by using a step of $p = 0.5$ Å. The search space can be explored *via* the interval $[a_0 + np,\ a_0 + (n+1)p]$ where $n$ is a variable integer. Let:

$$Q\ \ (hkl) = \frac{h^2 + k^2 + l^2}{[a_0 + (n+1)p]^2}, Q_+(hkl) = \frac{h^2 + k^2 + l^2}{[a_0 + np]^2}$$

If, for the given $n$ value, all the observed $Q_i$ lines satisfy the relation:

$$Q\ \ (hkl) - \Delta Q_i \leq Q_i \leq Q_+(hkl) + \Delta Q_i,$$

where $\Delta Q_i$ is a suitable tolerance value, then the domain $[a_0 + np,\ a_0 + (n+1)p]$ is halved and the procedure is repeated for six times $(n = 6)$ up to a final step length of $p/2^6 = 78 \times 10^{-4}$ Å.

The search is performed from high to low symmetry crystal systems by using partitions of the volume space and by analyzing shells of 400 Å$^3$ of volume, except for triclinic symmetry for which the volume variation is related to the value suggested by Smith:[22]

$$V_{\text{est}} = \frac{0.6\, d^3}{\frac{1}{N} - 0.0052}$$

This author proposed a method for estimating the unit-cell volume ($V_{est}$) directly from the powder diffraction data, *via* $d$ and $N$, where $d$ is the value of the $N$th observed line (*i.e.* if $N = 20$ and $d_{20}$ is the value of the 20th observed line, $V_{est} \approx 13.39 d_{20}^3$). In the triclinic system $Q(hkl)$ is a complicated function of the direct cell parameters (see Table 7.2): then the algorithm is applied in $Q$ space by using Equation (8). DICVOL91 is highly sensitive to the quality of the data.

### 7.2.5 Evolved Indexing Programs

In more recent years the indexing problem has been revisited.[23] Some of the classic indexing packages, TREOR and DICVOL91, have evolved toward more powerful and effective versions: N-TREOR[24] and DICVOL04,[25] respectively. In addition, completely new packages have been developed, encouraged by the availability of increased computing speed. Among them we quote: a genetic-algorithm based program by Kariuki *et al.*,[26] SVD-Index,[27] X-Cell,[28] and McMaille.[29] All the above programs are here briefly described: for more details the reader is referred to the exhaustive papers of Shirley[2] and Bergmann *et al.*[23]

- ***N-TREOR*** is the evolved version of TREOR. Even though this new package retains the main strategy of TREOR, new changes have been introduced to make it more exhaustive and powerful. Several automatic decisions are taken by N-TREOR, among which we quote:

1. If N-TREOR does not find satisfactory results in the default run, it will repeat the unit cell search with wider tolerance limits. If still no solution is found, the maximum ($h$,$k$,$l$) Miller indices of the orthorhombic and monoclinic base lines are increased, and correspondingly the tolerance limits are narrowed to 50% of the default value to avoid the generation of a large number of wrong large unit cells.
2. If the maximum observed $d$ value is greater than 10 Å, the largest cell volume and axis length investigated by N-TREOR are set to 4000 Å$^3$ and 35 Å, respectively (the default values in TREOR are 2000 Å$^3$ and 25 Å, respectively).
3. A wavelength dependence of the error tolerance:

$$\Delta = |\sin^2(\theta_{obs}) - \sin^2(\theta_{calc})| < \varepsilon$$

has been introduced, where $\varepsilon$ is a threshold value, $\theta_{obs}$ and $\theta_{calc}$ are the observed and calculated (*via* the trial cell) Bragg $\theta$ values, respectively. In TREOR the default value of $\varepsilon$ was optimized only for the case of $CuK_\alpha$ radiation ($\varepsilon_{Cu}$), in N-TREOR the $\varepsilon$ value depends on the wavelength according to $\varepsilon = (\lambda/\lambda_{Cu})^2 \varepsilon_{Cu}$, where $\lambda$ is the experimental neutron or X-ray wavelength and $\lambda_{Cu}$ is the $CuK_\alpha$ wavelength.
4. Monoclinic solutions are checked for possible rhombohedral symmetry. If the symmetry is likely to be rhombohedral N-TREOR calculates the possible hexagonal axes.

5. A modified de Wolff[8] figure of merit $M'_{20}$ has been introduced:

$$M'_{20} = (7 - N_{\text{par}}) \cdot M_{20}$$

where $N_{\text{par}}$ is the number of cell parameters to be determined. $M'_{20}$ enables one to select from among the candidate cells the one with the highest symmetry.
6. If the selected cell has $M'_{20}$ $(= M_{20}) \geq 20$ for triclinic crystal systems, or $M'_{20} \geq 30$ (*i.e.*, $M_{20} \geq 10$) for monoclinic or higher symmetry crystal systems, it will be automatically refined by *PIRUM*, originally an interactive program, suitably modified to perform the automatic refinement of the unit-cell parameters. If more than 25 observed lines are available, the first 25 lines will be used for finding the cell, while all the lines will be involved in the refinement step. At the end of the PIRUM refinement a statistical study of the index parity of the assigned reflections is performed to detect the presence of doubled axes or of additional lattice points (A-, B-, C-, I-, R- or F-centred cell). If one of the index parity conditions is verified, an additional refinement is performed taking into account this information.
7. An automatic correction of the $2\theta_0$-shift is made. As soon as the standard run (the first run) is finished, whatever the results are, the indexing process is repeated after the application of origin shifts $\Delta_{2\theta}$ in both directions of the $2\theta$ axis, being:

$$\Delta_{2\theta} = \pm(n - 1) \cdot \Delta_{2\theta\text{step}}$$

where $n$ is a sequential number indicating the current N-TREOR run ($n = 1$ for the first run, $n = 2$ for the second run...) and $\Delta_{2\theta\text{step}}$ is two times the experimental $2\theta$ step. For each $n$th run N-TREOR stores the $M'_{20}$ value and the corresponding unit cell. The origin shift for which $M'_{20}$ is a maximum [*i.e.*, $(M'_{20})_{\max}$] is assumed to be the best shift leading to the set of correct $2\theta$ values. The automatic $2\theta$ correction procedure stops as soon as a cell with $M'_{20} < (M'_{20})_{\max}$ is found.

N-TREOR has been implemented in the package EXPO2004[30] and it is also available as a stand-alone program.

• ***DICVOL04***. Among the new facilities we quote:

1. Refinement of the "zero-point" of powder data. Two approaches are proposed: (a) in case of small shift ($< 0.03^\circ$) a refinement option for the $2\theta$ zero offset and for the cell parameters may be applied; (b) when the shift is not negligible ($\approx 0.10^\circ$) the reflection-pair method[31] is applied to estimate the zero origin *via* the angular separation between two orders of reflections.
2. A tolerance for unindexed lines. DICVOL04 can tolerate a limited number (fixed by the user) of unindexed lines. This option must be carefully used since it can generate erroneous cells.

3. The use of a systematic reduced-cell analysis in monoclinic and triclinic systems to choose among equivalent (having the same reduced cell) solutions.

• ***Direct space methods: Indexing* via *a Genetic Algorithm* (*GA*)**. GA is an optimization technique exploiting the idea of Darwinian evolution: the fittest member of a population survives and procreates to lead to improved generations, with random mutations allowing the system to evolve.[32,33] Methods for indexing powder diffraction data were proposed by Tam and Compton[34] and Paszkowicz.[35] Their approaches, like the traditional indexing methods, exploit the diffraction geometry. Kariuki *et al.*[26] apply GA techniques by using also whole-profile fitting. The aim is to find the lattice parameters $\{a,b,c,\alpha,\beta,\gamma\}$ having the best agreement with the experimental powder diffraction pattern. *i.e.*, the agreement in correspondence with the global minimum of the hypersurface $R_{\mathrm{wp}}$ $\{a,b,c,\alpha,\beta,\gamma\}$, where:

$$R_{\mathrm{wp}} = \sum_{\mathrm{regions}} \left[ \frac{\sum_i w_i (y_i - y_{ci})^2}{\sum_i w_i y_i^2} \right]^{\frac{1}{2}}$$

$\Sigma_{\mathrm{regions}}$ indicates the sum on the $2\theta$ regions in which the pattern has been split by the user, $i$ runs over the points in each region, $y_i$ and $y_{ci}$ are the observed and calculated diffraction patterns at the $i$th experimental step. The intensities are estimated *via* the Le Bail algorithm.[36] The procedure is more time consuming but it may be less sensible to the presence of a minority impurity (the global minimum in $R_{\mathrm{wp}}$ will be reached when the majority phase is correctly indexed).

• ***Direct space methods: Indexing* via *a Monte Carlo approach – McMaille***. This is an indexing program that exploits the information of the whole powder profile, as already proposed by Kariuki *et al.*,[26] and uses Monte Carlo methods to randomly generate cell parameters. Once the parameters have been generated the Miller indices and the peak positions are calculated, the goodness of the cell is assessed by a suitable figure of merit. The use of the intensities makes the program relatively insensitive to impurities provided the sum of their intensities is less than 10–15% of the total intensity. The allowed tolerance of zero-point errors is $|0.05^\circ|$.

The indexing problem is usually solved in a few minutes if: (a) the symmetry is not lower than monoclinic; (b) the cell volume is less than 2000 $\mathrm{\AA}^3$; (c) the cell parameters are less than 20 Å. More computing time is required for triclinic symmetry: indeed the main drawback of the McMaille approach is the high request of computing time in the case of low crystal symmetry.

• ***SVD-Index***. This is a commercial indexing program[27] belonging to the TOPAS[37] suite from Bruker AXS. The reciprocal-lattice relationship defined in Equation (8) is solved *via* the iterative use of the Singular Value Decomposition (SVD) approach.[38] This method is recommended for cases in which there are more equations than variables.[38]

Unlike N-TREOR and TREOR, *SVD-Index* involves the indexing procedure not only for a few lines (the basis lines in TREOR or N-TREOR) but for all the observed lines. The new approach is claimed to be insensitive to $2\theta_0$ errors, to the presence of impurities and to a lack of low-angle diffraction peaks.

• ***X-CELL***. This is a commercial program within the Materials Studio suite from Accelrys.[39] It performs an exhaustive search *via* the successive dichotomy approach, like the package DICVOL, combined with: (a) a search for the zero-point shift of the diffraction pattern; (b) impurity tolerance levels (user defined), specifying how many unindexed diffraction peaks are tolerated.

Some final remarks may be useful. Bergman *et al.*[23] compared the performances of classic and new indexing programs. Even if they observed that some of the recent indexing packages are more robust against zero-shift error, impurity lines, lack of data accuracy, their main conclusion (see also ref. 10) was that the chances of success of the indexing step increases proportionally with the number of different applied indexing programs.

## 7.3 SPACE GROUP DETERMINATION

### 7.3.1 Introduction

As specified in Section 7.1, the analysis of the diffraction intensities provides information on the Laue group and on the systematically absent reflections, from which the extinction symbol and, in favourable cases, the space group may be identified. Unfortunately, in the case of powders, the experimental diffraction pattern cannot be unambiguously interpreted: the peak overlap (systematic or casual), the background contribution, the occasional presence of preferred orientation and/or impurity peaks make uncertain the intensity evaluation. Consequently, the intensity of reflections corresponding to small peaks cannot be accurately estimated. Careful visual inspection of the experimental pattern is the most common practice for identifying the space group: frequently, more space groups are compatible with the experimental peak distribution. When more than one choice is available the correct extinction symbol may be determined by one of the following strategies: (a) by considering the prior information on the molecular properties of the structure under study, which may condition the choice of the space group; (b) by attempting the complete solution process for each probable space group: then the most reliable solution is chosen.

To give a practical example, Figure 7.3 shows a small $2\theta$ interval of the experimental pattern of a $P2_1/n$ crystal structure. The three vertical bars, generated in the Laue group $P2/m$, correspond to the positions of the reflections (20–1), (210) and (201). The reflection (20–1) corresponds to a systematically absent reflection, but its intensity is ambiguous because it is overlapped with (210).

In recent years, several new procedures, strategies and programs have been developed devoted to the *ab initio* automatic solution of powders. These include innovative approaches, avoiding the manual inspection of the diffraction

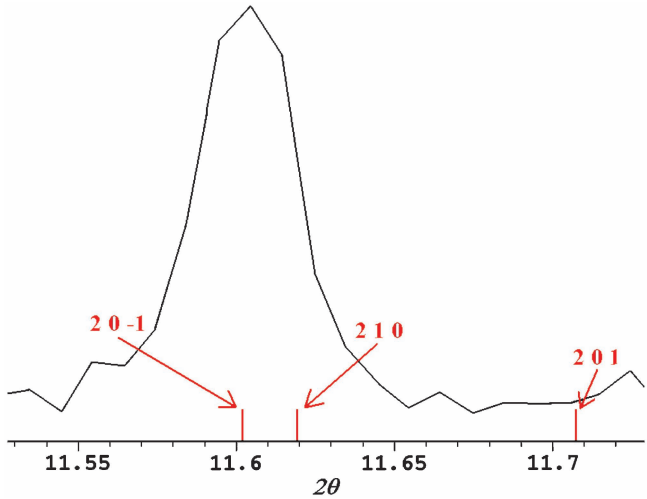



**Figure 7.3** The $2\theta$ interval (11.5° 11.8°) in the diffraction pattern of a $P2_1/n$ crystal structure.

pattern and based on statistical analysis of the reflection integrated intensity, for determining the space group automatically. Two alternative methods have been proposed, the first by Markvardsen *et al.*,[40] implemented into the package DASH,[41] and the second by Altomare *et al.*,[42,43] implemented into EXPO2004.[30] Both of them: (a) are based on the statistical analysis of the reflection integrated intensities, and therefore avoid the manual inspection of the diffraction pattern; (b) provide a quantitative estimate of the relative probabilities of all the different extinction groups compatible with the crystal system (as determined by the indexing process). The extinction group with the largest probability is preferred: the space groups compatible with it are the best candidates.

### 7.3.2 The DASH Procedure

This is based on the evaluation of the joint probability $p(\mathrm{E_{gr}}|\mathbf{I^p})$, where $\mathrm{E_{gr}}$ denotes the extinction symbol, and $\mathbf{I^p} = (I_1, I_2 \ldots I_N)$ are the correlated reflection intensities obtained from the linear least-squares Pawley refinement, when the most general extinction group of the crystal system under consideration is adopted. From Bayes's theorem:

$$p(\mathrm{E_{gr}}|\mathbf{I^p}) = p(\mathrm{E_{gr}})p(\mathbf{I^p}|\mathrm{E_{gr}})/p(\mathbf{I^p}).$$

The prior probability distribution $p(\mathrm{E_{gr}})$ is constant because all the extinction symbols are assumed to be equally probable; $p(\mathbf{I^p})$ is also constant because data do not change by varying the extinction group. Accordingly:

$$p(\mathrm{E_{gr}}|\mathbf{I^p}) \propto p(\mathbf{I^p}|\mathrm{E_{gr}})$$

where $p(\mathbf{I^p}|E_{gr})$ provides the relative probability of each extinction group $E_{gr}$. It may be shown that:

$$p(\mathbf{I^p}|E_{gr}) = \int p(\mathbf{I}|E_{gr})p(\mathbf{I^p}|\mathbf{I})d\mathbf{I}$$

where $p(\mathbf{I^p}|\mathbf{I})$ is the multivariate Gaussian likelihood function:

$$p(\mathbf{I^p}|\mathbf{I}) = (2\pi)^{N/2}|\mathbf{C}|^{1/2}\exp[-1/2(\mathbf{I^P} - \mathbf{I})^{T}\mathbf{C}^{1}(\mathbf{I^P} - \mathbf{I})]$$

and **C** is the Pawley covariance matrix. All the intensities are assumed to be statistically independent and identically distributed; consequently, $p(\mathbf{I}|E_{gr}) = \Pi\, p(I_i|E_{gr})$. If, in agreement with the given $E_{gr}$, the *i*th intensity is expected to be absent, then $p(I_i|E_{gr})$ is a delta function, while in the contrary case it coincides with the Wilson acentric distribution.[44] In the ideal case that the N peaks in the experimental pattern are non-overlapping, then the **C** matrix is diagonal and the $p(\mathbf{I^p}|E_{gr})$ calculation requires the evaluation of N one-dimensional integrals which can be analytically solved. In the more realistic case that the reflections are overlapping, **C** can be approximated by a block diagonal matrix: the corresponding integrals (with dimensions higher than one) may be solved numerically by Monte Carlo techniques.

### 7.3.3 The EXPO2004 Procedure

This may be synthesized into the following steps:

1. The experimental powder diffraction diagram is decomposed *via* the Le Bail algorithm[36] into single diffraction intensities in the space group having the largest Laue symmetry and no extinction conditions (*e.g.*, *P2/m* for monoclinic, *P2/m2/m2/m* for orthorhombic, *P4/mmm* for tetragonal, *P6/mmm* for trigonal-hexagonal systems, and *Pm3m* for the cubic system).
2. The normalized intensities $z_{\mathbf{h}} = |E_{\mathbf{h}}|^2$ are submitted to statistical analysis for the determination of the space group symmetry.
3. The algorithm provides a probability value for each extinction symbol compatible with the lattice symmetry established by the indexing procedure.

Step 2 may be clarified by an example. In the orthorhombic system any space group may be represented by the string:

$$M \quad r_1/s_1 \quad r_2/s_2 \quad r_3/s_3$$

*M* denotes the unit cell type; $r_j$, $j = 1,\ldots,3$ are the symmetry elements along the three axes; $s_j$, $j = 1,\ldots,3$ are the symmetry elements perpendicular to the axes. The occurrence probabilities for the axes are:

$$\begin{aligned} p(2_{1[100]}) &= 1 - <z_{h00}>_{h=2n+1}, p(2_{1[010]}) \\ &= 1 - <z_{0k0}>_{k=2n+1}, p(2_{1[001]}) = 1 - <z_{00l}>_{l=2n+1} \end{aligned}$$

The probabilities are equal to unity if the $z$ averages are equal to zero, they vanish if the averages are equal to (or larger than) unity. Conversely, for the two-fold axes:

$$p(2_{[100]}) = 1 - p(2_{I[100]}), p(2_{[010]}) = 1 - p(2_{I[010]}), p(2_{[001]}) = 1 - p(2_{I[001]})$$

For the glide planes normal to [100] and for the mirror plane:

$$p(b) = 1 - <z_{0kl}>_{k=2n+1}, p(c) = 1 - <z_{0kl}>_{l=2n+1}, p(n) = 1 - <z_{0kl}>_{k+l=2n+1}$$
$$p(d) = 1 - <z_{0kl}>_{k+l\neq 4n}, p(m) = 1 - \max[p(b), p(c), p(n), p(d)]$$

The probabilities for the different types of unit cell are obtained as follows:

$$p(A) = p'(A)[1 - p'(B)][1 - p'(C)], p(B) = p'(B)[1 - p'(A)][1 - p'(C)]$$
$$p(C) = p'(C)[1 - p'(A)][1 - p'(B)], p(I) = p'(I), p(F) = 1 - <z_{hkl}>_{[g]}$$
$$p(P) = 1 - \max[p(A), p(B), p(C), p(I), p(F)]$$

where:

$$p'(A) = 1 - <z_{hkl}>_{k+l=2n+1}, p'(B) = 1 - <z_{hkl}>_{h+l=2n+1},$$
$$p'(C) = 1 - <z_{hkl}>_{h+k=2n+1}, p'(I) = 1 - <z_{hkl}>_{h+k+l=2n+1}$$

and $[g]$ is the subset of reflections with all the indices odd or even. In practice, owing to the low accuracy of the $z_{\mathbf{h}}$ estimates, a suitable weight $w$ is introduced in the statistical averages. Accordingly $< z_w > = (\Sigma w_j\, z_j)/(\Sigma w_j)$, where $w$ takes the overlapping into account.

All the probabilities of the symmetry operators are combined to provide the probability of the extinction group. For example, in the orthorhombic system, the probability of the extinction symbol *P*--- is given by:

$$p(P\text{---}) = p(P)p(2_{[100]})p(m\perp\mathbf{a})p(2_{[010]})p(m\perp\mathbf{b})p(2_{[001]})p(m\perp\mathbf{c})$$

Consider now $p(Bb\text{-}b)$; the string *b*-*b* implies the following symmetry elements:

$$b\perp\mathbf{a}, b\perp\mathbf{c}, 2_{I[010]}$$

The presence of *B* additionally implies:

$$c\perp\mathbf{a}, n\perp\mathbf{b}, a\perp\mathbf{c}, 2_{I[100]}, 2_{I[001]}$$

Then:

$$p(Bb\text{-}b) = p(B)p(2_{I[100]})p(b, c\perp\mathbf{a})p(2_{I[010]})p(n\perp\mathbf{b})p(2_{I[001]})p(a, b\perp\mathbf{c})$$

The procedure is fully automatic and is supported by a graphic interface that provides: (a) a graphic window where the possible extinction groups are ranked according to their probabilities; (b) the list of compatible space groups for each selected extinction symbol; (c) on user request, the list of the reflections that, according to the selected extinction symbol, are expected to be systematically absent. For each of them the following specifications are given: the type of

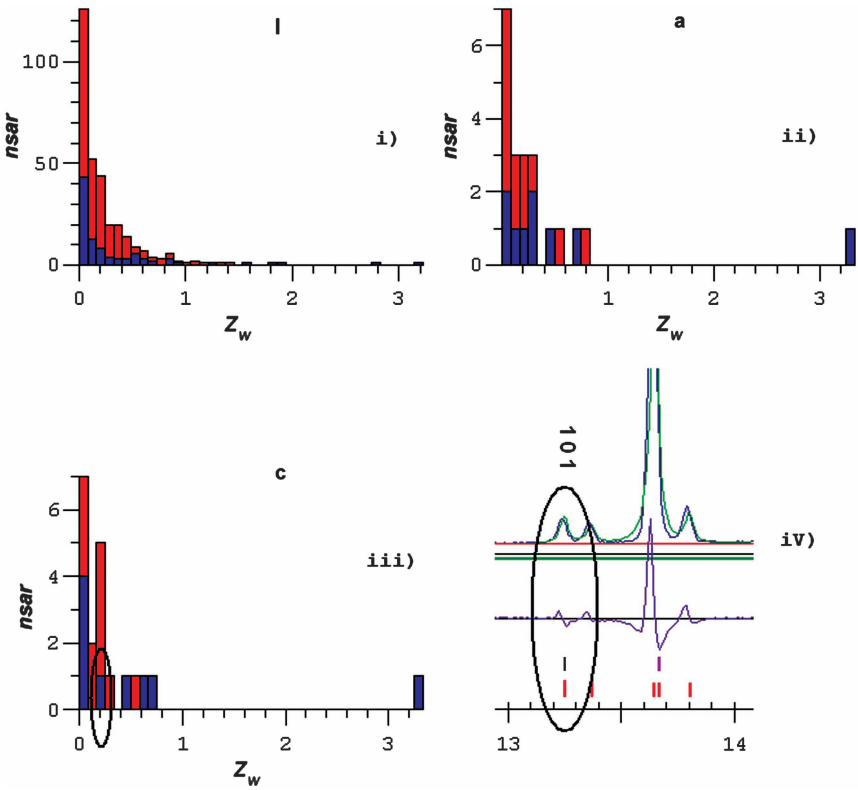



**Figure 7.4** (i iii) Histogram plots of METYL corresponding to the symmetry operators *I*, *a*, and *c*. Part (iv) shows the experimental pattern: the ellipse emphasizes the presence of the reflection (101).

reflection (single or overlapped with other reflections), the corresponding $z_w$ and the symmetry operator(s) responsible for the extinction. Furthermore, a histogram for each symmetry operator is supplied, giving the number of systematically absent reflections (*nsar* in Figure 7.4) *versus* the $z_w$ values. In Figure 7.4 we show the information provided by the graphical interface for METYL, a test structure crystallizing in *I222*.[45] The most probable extinction symbol is *I*–(*ac*)–; the second in the order is *I*---, which is the correct one. For *I*–(*ac*)– the program calculates three histograms (Figures. 7.4i–iii) corresponding to the three symmetry operators *I*, *a*, *c* respectively: in each figure the blue histogram refers to single and the red one to overlapping reflections. In Figure 7.4(iv), in the ellipse, the reflection (101) is emphasized. In the chosen $2\theta$ range two rows of vertical bars are present: the lower, in red, locate the peaks. The higher bars of different colours mark the absent reflections only: black for single or for reflections overlapping with other absent reflections, purple for absent reflections overlapped with reflections not expected to be absent. Clearly, the extinction symbol *I*–(*ac*)– must be eliminated from the list of candidates.

## REFERENCES


1. *International Tables for Crystallography*, ed. Th. Hahn, Kluwer Academic Publishers, Dordrecht, 1992, vol. A, p. 39.
2. R. Shirley, *IUCr Comput. Commission Newsletter*, 2003, **2**, 48.
3. C. Runge, *Phys. Z.*, 1917, **18**, 509.
4. P. M. de Wolff, *Acta Crystallogr.*, 1957, **10**, 590.
5. R. Shirley, *NBS Spec. Publ.*, 1980, **567**, 361.
6. L. B. McCusker, R. W. Grosse-Kunstleve, Ch. Baerlocher, M. Yoshikawa and M. E. Davis, *Microporous Mater.*, 1996, **6**, 295.
7. http://www.nist.gov.
8. P. M. de Wolff, *J. Appl. Crystallogr.*, 1968, **1**, 108.
9. G. S. Smith and R. L. Snyder, *J. Appl. Crystallogr.*, 1979, **12**, 60.
10. P.-E. Werner, in *Structure Determination from Powder Diffraction Data*, ed. W. I. F. David, K. Shankland, L. B. McCusker and Ch. Baerlocher, Oxford University Press, Oxford, 2002.
11. P. M. de Wolff, *Acta Crystallogr.*, 1961, **14**, 579.
12. J. W. Visser, *J. Appl. Crystallogr.*, 1969, **2**, 89.
13. A. D. Mighell and A. Santoro, *J. Appl. Crystallogr.*, 1975, **8**, 372.
14. P.-E. Werner, L. Eriksson and M. Westdahl, *J. Appl. Crystallogr.*, 1985, **18**, 367.
15. A. Boultif and D. Louër, *J. Appl. Crystallogr.*, 1991, **24**, 987.
16. R. Shirley, *The Crysfire 2002 System for Automatic Powder Indexing: User's Manual*, 2002, Lattice Press, Guildford, UK.
17. T. Ito, *Nature*, 1949, **164**, 755.
18. T. Ito, in *X-ray Studies on Polymorphism*, Maruzen, Tokyo, 1950, 187.
19. P. M. de Wolff, *Acta Crystallogr.*, 1958, **11**, 664.
20. D. Louër and M. Louër, *J. Appl. Crystallogr.*, 1972, **5**, 271.
21. D. Louër and R. Vergas, *J. Appl. Crystallogr.*, 1982, **15**, 542.
22. G. S. Smith, *J. Appl. Crystallogr.*, 1977, **10**, 252.
23. J. Bergmann, A. Le Bail, R. Shirley and V. Zlokazov, *Z. Kristall.*, 2004, **219**, 783.
24. A. Altomare, C. Giacovazzo, A. Guagliardi, A. G. G. Moliterni, R. Rizzi and P.-E. Werner, *J. Appl. Crystallogr.*, 2000, **33**, 1180.
25. A. Boultif and D. Louër, *J. Appl. Crystallogr.*, 2004, **37**, 724.
26. B. M. Kariuki, S. A. Belmonte, M. I. McMahon, R. L. Johnston, K. D. M. Harris and R. J. Nelmes, *J. Synchrotron Radiat.*, 1999, **6**, 87.
27. A. A. Coelho, *J. Appl. Crystallogr.*, 2003, **36**, 86.
28. M. Neumann, *J. Appl. Crystallogr.*, 2003, **36**, 356.
29. A. Le Bail, *Powder Diffr.*, 2004, **19**, 249.
30. A. Altomare, R. Caliandro, M. Camalli, C. Cuocci, C. Giacovazzo, A. G. G. Moliterni and R. Rizzi, *J. Appl. Crystallogr.*, 2004, **37**, 1025.
31. C. Dong, F. Wu and H. Chen, *J. Appl. Crystallogr.*, 1999, **32**, 850.
32. D. E. Goldberg, *in Genetic Algorithms in Search, Optimization and Machine Learning*, Addison-Wesley, Reading, MA, 1989.

33. K. D. M. Harris, R. L. Johnston and B. M. Kariuki, *Acta Crystallogr., Sect. A*, 1998, **54**, 632.
34. K. Y. Tam and R. G. Compton, *J. Appl. Crystallogr.*, 1995, **28**, 640.
35. W. Paszkowicz, *Mater. Sci. Forum*, 1996, **228–231**, 19.
36. A. Le Bail, H. Duroy and J. L. Fourquet, *Mater. Res. Bull.*, 1988, **23**, 447.
37. A. A. Coelho, *TOPAS* Version 3.1, 2003, Bruker AXS GmbH, Karlsruhe, Germany.
38. J. C. Nash, in *Compact Numerical Methods for Computers*, ed. Adam Hilger, Bristol, 1990.
39. http://www.accelrys.com.
40. A. J. Markvardsen, W. I. F. David, J. C. Johnson and K. Shankland, *Acta Crystallogr., Sect. A*, 2001, **57**, 47.
41. W. I. F. David, K. Shankland, J. Cole, S. Maginn, W. D. S. Motherwell and R. Taylor, *DASH User Manual*, Cambridge Crystallographic Data Centre, Cambridge, UK, 2001.
42. A. Altomare, R. Caliandro, M. Camalli, C. Cuocci, I. da Silva, C. Giacovazzo, A. G. G. Moliterni and R. Spagna, *J. Appl. Crystallogr.*, 2004, **37**, 957.
43. A. Altomare, M. Camalli, C. Cuocci, I. da Silva, C. Giacovazzo, A. G. G. Moliterni and R. Rizzi, *J. Appl. Crystallogr.*, 2005, **38**, 760.
44. A. J. C. Wilson, *Acta Crystallogr.*, 1949, **2**, 318.
45. E. Weiss, S. Corbelin, J. K. Cockcroft and A. N. Fitch, *Chem. Ber.*, 1990, **123**, 1629.

CHAPTER 8

# Crystal Structure Determination

ROCCO CALIANDRO,[a] CARMELO GIACOVAZZO[a,b] AND ROSANNA RIZZI[a]

[a] Istituto di Cristallografia (IC), C.N.R., Sede di Bari. Via G. Amendola 122/o, 70126 Bari, Italy; [b] Dipartimento Geomineralogico, Università degli Studi di Bari, Campus Universitario, via Orabona 4, 70125 Bari, Italy

## 8.1 INTRODUCTION

Typical X-ray diffraction experiments provide structure factor moduli, while the relative phases are lost. Recovery of the phase information is crucial for crystal structure solution and is referred to in crystallography as the *phase problem*. In single-crystal diffraction this problem is solved by different approaches:

a. By using only the diffraction data of the compound under study when no supplementary information about its molecular geometry is available (*ab initio* methods). *PM* and *DM* belong to this category.
b. By using the diffraction data of the compound under study when supplementary information about its molecular geometry is available (*DST*: a particular case is the *molecular replacement method*).
c. By using the diffraction data of the compound under study and the diffraction data of one or more isomorphous structures (*isomorphous replacement methods*).
d. By making use of anomalous dispersion effects. One or more (at different wavelengths) sets of data are measured that simulate isomorphous structures (*SAD-MAD*, *SIRAS-MIRAS* techniques).
e. By using the experimental measure of the triplet invariant phases (*multiple diffraction effect*). The three-beam diffraction effect can be treated in accordance with dynamical theory and used for the experimental solution of the phase problem.

Crystal structure solution from powder data is not straightforward owing to the following problems: the uncertainty in the determination of the

background, the possible presence of preferred orientation effects and, fundamentally, the collapse of the three-dimensional reciprocal space onto a one-dimensional diffraction pattern, which implies a severe overlapping of the diffraction peaks. As a consequence, the diffraction moduli of the reflections are only approximately estimated (see Chapter 5). The uncertainty about moduli makes some of the above-described approaches unsuitable for powder crystallography. For example, case (e) is today experimentally inapplicable to powder samples and cases (c) and (d) rely on very small differences among structure factor moduli that can hardly be obtained with sufficient accuracy from the powder diffraction pattern [furthermore, $|F_{\mathbf{h}}|$ and $|F_{\mathbf{h}}|$ overlap, and the difference $(|F_{\mathbf{h}}| - |F_{\mathbf{h}}|)$ cannot be appreciated]. Accordingly, in this chapter we will mostly refer to cases (a) and (b); for a complete review of the phasing techniques in crystallography, the reader is referred to a textbook.[1]

However, powder diffractometry plays a central role in research and technology, making possible the analysis of materials that are not available as single crystals of adequate dimensions and quality. For this reason much recent effort has been devoted to the improvement of experimental techniques (*i.e.*, use of synchrotron radiation, optics, generator, detector, *etc.*) as well as to the development of new methods for data analysis. For example, in the last decade alternative structure solution strategies have been suggested (*direct-space approaches*), which directly use the powder diffraction profile rather than the single reflection intensities, thus avoiding the problematic extraction process.

In this chapter *PM* will be described first, then *DM* will be analyzed more extensively and, finally, an overview of the most commonly used global optimization methods in direct space is given.

## 8.2 THE PATTERSON FUNCTION

The Patterson function is the convolution of the electron density $\rho(\mathbf{r})$ with itself inverted with respect to the origin:

$$P(\mathbf{u}) = \rho(\mathbf{r}) * \rho(-\mathbf{r}) = \int_{\mathbf{v}} \rho(\mathbf{r})\rho(\mathbf{r}+\mathbf{u})\mathrm{d}\mathbf{u} \tag{1}$$

where * indicates the convolution operation. It may also be shown that:

$$P(\mathbf{u}) = T^{-1}\left[|F(\mathbf{r}^*)|^2\right] = \int_{S^*} |F(\mathbf{r}^*)|^2 \exp(-2\pi i \mathbf{r}^*\mathbf{u})\mathrm{d}\mathbf{r}^*$$

where the operator $T$ represents the Fourier transform and $S^*$ all of reciprocal space.

Since $|F(\mathbf{r}^*)|$ is sampled only at the nodes of the reciprocal lattice (where $\mathbf{r}^* = \mathbf{h}$), we have:

$$P(\mathbf{u}) = \frac{1}{V}\sum_{\mathbf{h}} |F_{\mathbf{h}}|^2 \exp(-2\pi i \mathbf{h}\mathbf{u}) \tag{2}$$

where $V$ is the volume of the unit cell. From Equation (2) it is possible to deduce the following Patterson features:

a. $P(\mathbf{u}) = P(-\mathbf{u})$, *i.e.* the Patterson map is always centrosymmetric.
b. The maxima of $P(\mathbf{u})$ correspond to the interatomic vectors.
c. Each peak has an intensity proportional to the product of the atomic numbers of the two atoms related by the interatomic vector $\mathbf{u}$. More pairs of atoms can have the same interatomic vector $\mathbf{u}$ and therefore may contribute to the same Patterson peak.
d. A unit cell containing $N$ atoms generates $N^2$ interatomic vectors $\mathbf{r}_i - \mathbf{r}_j$. $N$ of them will be located at the origin, while the remaining $N(N-1)$ are distributed over the cell. This implies that Patterson peaks usually overlap (also owing to the fact that the Patterson peaks are wider than the electron density peaks).
e. Patterson maps calculated by powder data are less informative than those obtained by single-crystal data because of the unavoidable errors in the diffraction moduli provided by full pattern decomposition procedures.

The above features can make it difficult to derive the atomic positions from analysis of the Patterson map. The most traditional approach involves the use of the so-called *Harker sections*: they contain the interatomic vectors between an atom and its symmetry equivalents. For instance, let us consider the space group $P2_1$, with equivalent positions:

$$(x, y, z), (-x, y + 0.5, -z)$$

The Harker vector $(2x, 0.5, 2z)$ lies in the Harker section $(u, 0.5, w)$ and may be used to derive the position of the atom; indeed: $x = u/2$, $y$ undefined (the origin in $P2_1$ floats freely along the $z$-axis), $z = w/2$.

The use of the Harker sections is made easier when a few heavy atoms are present in the unit cell: their Harker maxima can be recognized and used to locate the heavy atoms. If they have a sufficiently high atomic number, they can be used as a good initial model to which one can apply the so-called *Method of Fourier Recycling*, to obtain the light atom positions and then to recover the complete structure.

Some tricks can be useful to simplify the analysis of the Patterson map. The peaks may be sharpened by using $|E_{\mathbf{h}}|^2$ instead of the $|F_{\mathbf{h}}|^2$ coefficients; in addition, considering that the sharpening procedure can produce serious Fourier truncation effects that generate large ripples in the Patterson map, mixed coefficients ($|E_{\mathbf{h}}||F_{\mathbf{h}}|$) or $(|E_{\mathbf{h}}|^3|F_{\mathbf{h}}|)^{1/2}$ may be employed[2 4] to reduce the ripples in the map. It is also very convenient to remove the "origin peak" from the Patterson map: this is obtained by using in the Patterson calculation the coefficients:

$$|F'_{\mathbf{h}}|^2 = |F_{\mathbf{h}}|^2 - \sum_{j=1}^{N} f_j^2$$

or equivalently, the coefficients $(|E_{\mathbf{h}}|^2 - 1)$.

A strategy for the determination of the crystal structure by Patterson search methods by using large known molecular fragments has been described by Rius and Miravitlless.[5] More recently the Patterson information has been used to evaluate diffraction moduli more accurately than the full pattern decomposition procedures.[6 8] The idea lies on the relation ($|F(\mathbf{r}^*)|^2 = T[P(\mathbf{u})]$): the Patterson is first modified by enforcing the positivity of the Patterson map and then it is Fourier transformed. As an example, the automatic procedure[8] implemented in the EXPO program[9] may be described in terms of the following steps:

1. The integrated intensities ($|F|^2$) are extracted from the powder pattern *via* the Le Bail method.[10]
2. A Patterson map $P(\mathbf{u})$ is calculated and modified into a new map $P'(\mathbf{u})$. A truncation criterion is used. All the points of the map having density smaller than a defined threshold are set to zero to take into account only the main peaks in the map.
3. The inversion of $P'(\mathbf{u})$ provides new diffraction intensities. These are used with the default values given by the EXPO program to obtain the new set of $|F|^2$.
4. The procedure returns to step 2 and is repeated for some cycles.

## 8.3 DIRECT METHODS

*DM* are *ab initio* crystal structure solution techniques able to estimate phases directly from structure factor magnitudes. These methods started in 1948.[11] With the advent of modern computers and the use of sophisticated mathematical approaches, they are able to definitively solve, in practice, the phase problem for small molecules. Protein structures, up to say 2000 non-hydrogen atoms in the asymmetric unit, are today solved *ab initio*, provided single-crystal diffraction data with resolution better than 1.2 Å are available.

The application of *DM* to powder data requires the previous application of a full pattern decomposition procedure (see Chapter 5): in the following we will suppose that single diffraction intensities are available for each reflection in the measured $2\theta$ range. Owing to the peak overlap the estimates of the diffraction moduli will be affected by unavoidable errors: this weakens the efficiency of *DM* (naively, wrong moduli will produce wrong phases), and still today makes crystal structure solution from powder data a challenge.

The role of the full pattern decomposition techniques has been recently investigated:[12] two different extraction approaches, Pawley[13] and Le Bail algorithms were applied, and different peak profile functions were used. The results may be summarized as follows:

a. Systematic attempts to improve the profile fitting do not necessarily lead to more accurate extracted intensities. In Figure 8.1 the profile residual $R_p$

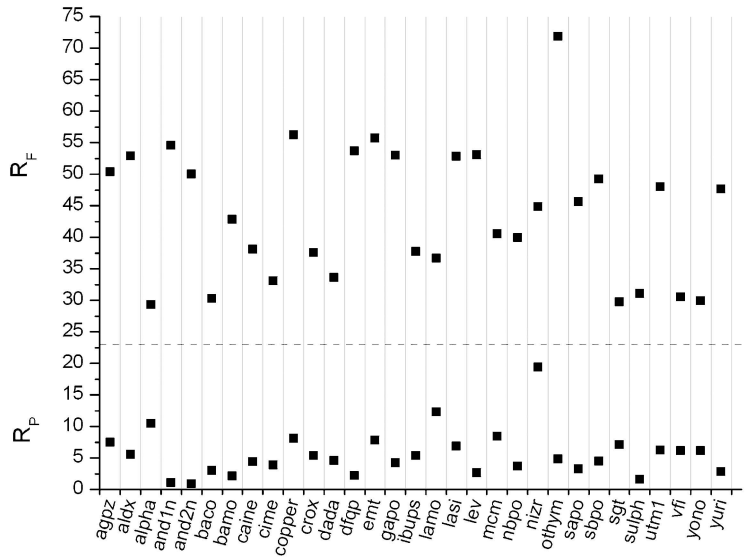



**Figure 8.1** $R_F$ (top part) and $R_p$ (bottom) obtained by EXPO using the Pearson VII profile function for a set of test structures. $R_p$ is the residual (%) between the observed profile and that calculated from the chosen profile function. $R_F$ is the residual (%) between the moduli provided by decomposition techniques and the structure factor moduli calculated from the published structure model.

and the error on the estimated |F| moduli ($R_F$) are given for several test structures: the two quantities are not strictly correlated.

b. A suitable choice of the peak-shape function may improve the profile fitting but not necessarily the decomposition efficiency.

The high values of $R_F$ are mainly due to the limited information contained in a powder pattern. A way to overcome this limitation has been proposed by Altomare *et al.*,[14,15] based on a Monte Carlo approach: several sets of extracted intensities, called decomposition trials, are calculated and submitted one after the other to *DM*. Each decomposition trial is obtained by partitioning in a specific way the overall intensity of one or more clusters of overlapping reflections under the constraint that the intensity of each cluster is constant.

In their basic form *DM* exploit two types of prior information: the positivity of the electron density map (this condition may be relaxed, *e.g.*, for neutron diffraction, see Section 8.4.7), and the atomicity (the electrons are non-dispersed into the unit cell but concentrated around the nuclei). This information, apparently trivial, is very useful to succeed in all the steps of a modern *DM* procedure: (1) scaling of the observed intensities and normalization of the structure factors; (2) estimate of the structure invariants; (3) application of the tangent formula; (4) crystal structure completion and refinement.

### 8.3.1 Scaling of the Observed Intensities and Normalization of the Structure Factors

X-Ray diffraction experiments may provide thousands of diffraction intensities $|F_{\mathbf{h}}|^2_{\text{obs}}$, which are on a relative scale:

$$|F_{\mathbf{h}}|^2_{\text{obs}} = K|F_{\mathbf{h}}|^2 \tag{3}$$

The scale factor $K$ may be determined, together with the average isotropic thermal factor $B$, by the Wilson method.[16] On assuming that $B_j$ is equal to $B$ for all the atoms, Equation (3) may be rewritten as:

$$|F_{\mathbf{h}}|^2_{\text{obs}} = K|F_{\mathbf{h}}|^2 = K\left|F^0_{\mathbf{h}}\right|^2 \exp(-2Bs^2) \tag{4}$$

where $s^2 = \sin^2\vartheta/\lambda^2$ and $|F^0_{\mathbf{h}}|$ is the structure amplitude on an absolute scale when the atoms are at rest. To calculate $K$ and $B$ the observed diffraction data are divided into ranges with constant $s^2$, and average values of the intensities are calculated in each shell. For each shell we can write:

$$\left\langle |F_{\mathbf{h}}|^2_{\text{obs}} \right\rangle = K\left\langle \left|F^o_{\mathbf{h}}\right|^2 \right\rangle \exp(-2Bs^2) = K\sum\nolimits_s^o \exp(-2Bs^2) \tag{5}$$

where, in the absence of any structural information, $\sum_s^o = \varepsilon(\mathbf{h})\sum_{j=1}^N (f_j^o)^2$. $\varepsilon(\mathbf{h})$ is the so-called Wilson statistical coefficient taking into account the space group symmetry. From Equation (5) we get straightforwardly:

$$\ln\left(\frac{\left\langle |F_{\mathbf{h}}|^2_{\text{obs}} \right\rangle}{\sum_s^o}\right) = \ln\ K - 2Bs^2 \tag{6}$$

Equation (6) represents a straight line: the intercept on the vertical axis yields the value of $K$; $2B$ is the slope of the line. In practice, owing to structural regularities (atoms are not randomly located) the experimental values are not rigorously aligned: the best evaluation of $K$ and $B$ is then obtained by calculating a least squares line. Figure 8.2 shows a typical Wilson plot.

Once scale and average thermal factors have been determined, normalized structure factors $|E_{\mathbf{h}}|$ can be calculated as follows:

$$|E_{\mathbf{h}}|^2 = \frac{|F_{\mathbf{h}}|^2_{\text{obs}}}{\left\langle |F_{\mathbf{h}}|^2_{\text{obs}} \right\rangle} = \frac{|F_{\mathbf{h}}|^2_{\text{obs}}}{K\sum_s^o \exp(-2Bs^2)} \tag{7}$$

The $|E_{\mathbf{h}}|$'s are differently distributed for centric and non-centric space groups;[16,17] their probability distribution functions are, respectively:

$$P_1(|E|) = \sqrt{\frac{2}{\pi}}\exp(-|E|^2/2) \quad \text{(centric)}$$

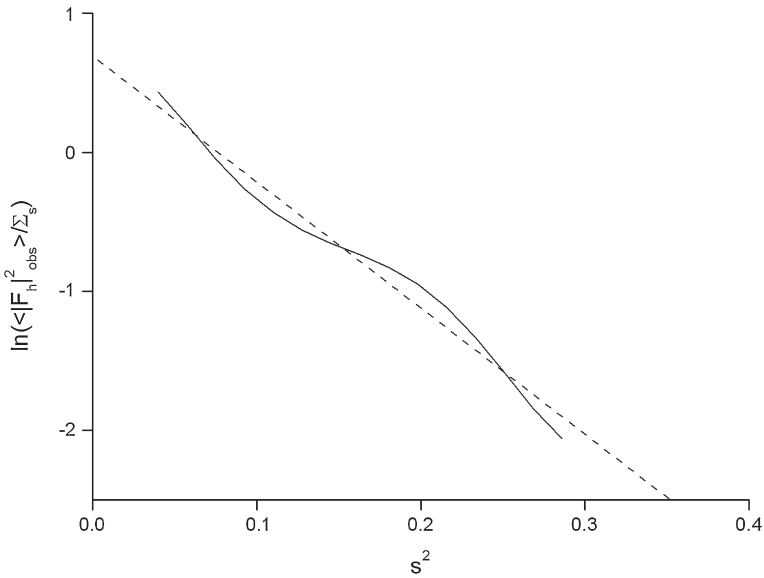



**Figure 8.2** Typical Wilson plot.

$$P_1(|E|) = 2|E|\exp(-|E|^2) \quad \text{(acentric)}$$

which are represented in Figure 8.3.

The above distributions are widely used to identify the correct space group when single-crystal data are available. Unfortunately, they are unusable for powder data owing to the fact that the $|E_{\mathbf{h}}|^2$ distribution is strongly dependent on the algorithm used for the pattern decomposition (Pawley/Le Bail).[18] When two or more reflections heavily overlap, the Pawley technique often provides negative intensities for some of the overlapped reflections. Conversely, the Le Bail algorithm intrinsically tends to equipartition the overall intensity among the severely overlapped reflections. The general statistical consequence is that the distribution of the structure factor amplitudes will be biased towards the centric nature for Pawley based methods, and towards the non-centric for Le Bail based techniques.

Furthermore, the distributions of the normalized structure factors are strongly affected by pseudotranslational symmetry, and for powder data also by preferred orientation effects. The above information can also be used as prior information to perform a better powder pattern decomposition,[19,20] so improving the efficiency of *DM*.

### 8.3.2 Estimate of Structure Invariants

Structure invariants are products of structure factors that remain invariant whatever the origin. They may be written as

$$F_{\mathbf{h}_1}F_{\mathbf{h}_2}\ldots F_{\mathbf{h}_n} = \left|F_{\mathbf{h}_1}F_{\mathbf{h}_2}\ldots F_{\mathbf{h}_n}\right|\exp[i(\phi_{\mathbf{h}_1} + \phi_{\mathbf{h}_2} + \cdots + \phi_{\mathbf{h}_n})] \qquad (8)$$

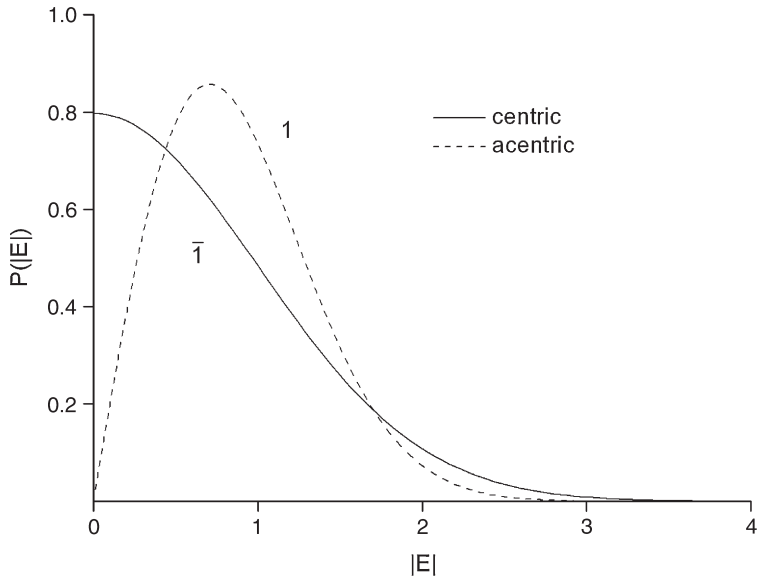



**Figure 8.3** Probability distribution function of normalized structure factor amplitudes for centrosymmetric (centric) and non centrosymmetric (acentric) structures.

with $\mathbf{h}_1 + \mathbf{h}_2 + \cdots + \mathbf{h}_n = \mathbf{0}$. Indeed, owing to the shift of origin $\boldsymbol{x}_0$, the single phase $\phi_{\mathbf{h}}$ changes according to:

$$\phi'_{\mathbf{h}} = \phi_{\mathbf{h}} - 2\pi \mathbf{h}\mathbf{x}_0$$

but Equation (8) does not change:

$$F'_{\mathbf{h}_1} F'_{\mathbf{h}_2} \ldots F'_{\mathbf{h}_n} \equiv F_{\mathbf{h}_1} F_{\mathbf{h}_2} \ldots F_{\mathbf{h}_n}$$

The simplest structure invariants are:

a. for $n = 1$, $F_{000}$;
b. for $n = 2$, the product $F_{\boldsymbol{h}} F_{-\boldsymbol{h}} = |F_{\boldsymbol{h}}|^2$;
c. for $n = 3$, $F_{\boldsymbol{h}} F_{\boldsymbol{k}} F_{-\boldsymbol{h}-\boldsymbol{k}} = |F_{\boldsymbol{h}} F_{\boldsymbol{k}} F_{-\boldsymbol{h}-\boldsymbol{k}}| \exp[i(\phi_{\mathbf{h}} + \phi_{\mathbf{k}} - \phi_{\mathbf{h}+\mathbf{k}})]$;
d. for $n = 4$, $F_{\boldsymbol{h}} F_{\boldsymbol{k}} F_{\boldsymbol{l}} F_{-\boldsymbol{h}-\boldsymbol{k}-\boldsymbol{l}} = |F_{\boldsymbol{h}} F_{\boldsymbol{k}} F_{\boldsymbol{l}} F_{-\boldsymbol{h}-\boldsymbol{k}-\boldsymbol{l}}| \exp[i(\phi_{\mathbf{h}} + \phi_{\mathbf{k}} + \phi_{\mathbf{l}} - \phi_{\mathbf{h}+\mathbf{k}+\mathbf{l}})]$ *etc*.

The first structure invariant containing phase information is the *triplet invariant*, which is the most important one (together with the *quartet invariants*). Since the moduli are known from the experiment, it is usual to refer to structure invariants as to a combination of phases, *e.g*., the sum:

$$\Phi_{\mathbf{h},\mathbf{k}} = \phi_{\mathbf{h}} + \phi_{\mathbf{k}} - \phi_{\mathbf{h}+\mathbf{k}}$$

is denoted as the triplet phase invariant, and the sum:

$$\Phi_{\mathbf{h},\mathbf{k},\mathbf{l}} = \phi_{\mathbf{h}} + \phi_{\mathbf{k}} + \phi_{\mathbf{l}} - \phi_{\mathbf{h}+\mathbf{k}+\mathbf{l}}$$

is called quartet phase invariant.

A probabilistic formula for estimating structure invariants has been given by Cochran:[21]

$$P(\Phi_{\mathbf{h},\mathbf{k}}) = [2\pi I_0(G_{\mathbf{h},\mathbf{k}})]^{\ 1} \exp(G_{\mathbf{h},\mathbf{k}} \cos \Phi_{\mathbf{h},\mathbf{k}}) \tag{9}$$

where $I_0$ is the modified Bessel function of order zero:

$$G_{\mathbf{h},\mathbf{k}} = 2\sigma_3\sigma_2^{\ 1/2}|E_{\mathbf{h}}E_{\mathbf{k}}E_{\mathbf{h}+\mathbf{k}}| \tag{10}$$

and $\sigma_n = \sum_{j=1}^{N} Z_j^n$. For equal atom structures Equation (10) reduces to:

$$G_{\mathbf{h},\mathbf{k}} = \frac{2}{\sqrt{N}}|E_{\mathbf{h}}E_{\mathbf{k}}E_{\mathbf{h}+\mathbf{k}}|$$

Equation (9) is a von-Mises type function:[22] it is shown in Figure 8.4 for different values of $G_{\mathbf{h},\mathbf{k}}$. We note: (a) $P(\Phi_{\mathbf{h},\mathbf{k}})$ always attains the maximum when $\Phi_{\mathbf{h},\mathbf{k}} = 0$; (b) the curves become more and more sharp with increasing values of $G_{\mathbf{h},\mathbf{k}}$. Accordingly, only for large values of $G_{\mathbf{h},\mathbf{k}}$ is the estimate $\Phi_{\mathbf{h},\mathbf{k}} = 0$ reliable; (c) the number of reliable triplets is small for large structures (those with large $N$ values).

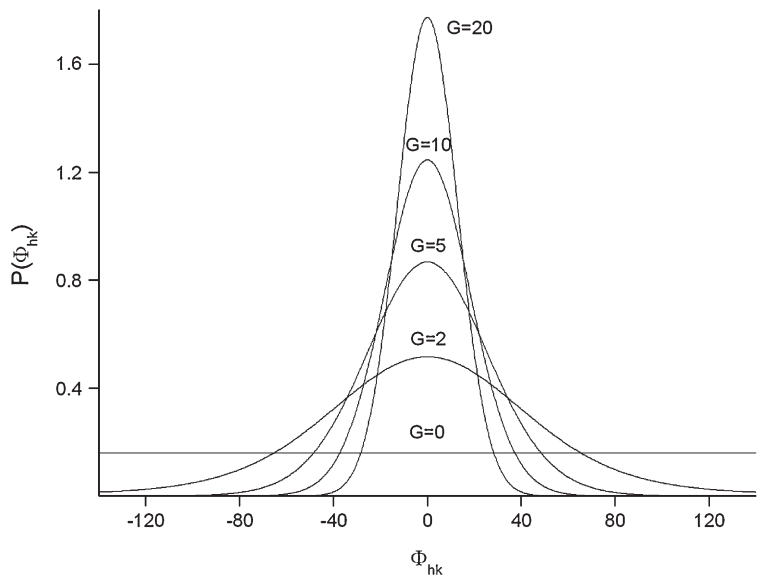



**Figure 8.4** Probability distributions (Equation 9) for different values of the parameter $G_{h,k}$ given by (Equation 10).

The Cochran formula, Equation (9), estimates the triplet phase $\Phi_{\mathbf{h,k}}$ only exploiting the information contained in the three moduli $|E_{\mathbf{h}}|,|E_{\mathbf{k}}|,|E_{\mathbf{h+k}}|$. The representation theory proposed by Giacovazzo[23,24] indicates how the information contained in all reciprocal space could be used to improve the Cochran's estimate of $\Phi_{\mathbf{h,k}}$. The conclusive conditional probability distribution[25] has again a von Mises expression:

$$P_{10}(\Phi_{\mathbf{h}_1,\mathbf{h}_2}) = [2\pi I_0(G)]^{\ 1} \exp(G\cos\Phi_{\mathbf{h}_1,\mathbf{h}_2})$$

with $G = C(1+Q)$,

$C = 2\left|E_{\mathbf{h}_1}E_{\mathbf{h}_2}E_{\mathbf{h}_3}\right|/\sqrt{N}$ is the Cochran reliability parameter:

$$Q = \sum_{\mathbf{k}} \left( \frac{\sum_{i=1}^{m} A_{\mathbf{k},i}/N}{1 + \left(\varepsilon_{\mathbf{h_1}}\varepsilon_{\mathbf{h_2}}\varepsilon_{\mathbf{h_3}} + \sum_{i=1}^{m} B_{\mathbf{k},i}\right)/2N} \right),$$

$$\begin{aligned} A_{\mathbf{k},i} = \varepsilon_{\mathbf{k}}\big[&\varepsilon_{\mathbf{h}_1+\mathbf{kR_i}}\left(\varepsilon_{\mathbf{h}_2\ \ \mathbf{kR_i}} + \varepsilon_{\mathbf{h}_3\ \ \mathbf{kR_i}}\right) + \varepsilon_{\mathbf{h}_2+\mathbf{kR_i}}\left(\varepsilon_{\mathbf{h}_1\ \ \mathbf{kR_i}} + \varepsilon_{\mathbf{h}_3\ \ \mathbf{kR}_i}\right) \\ &+ \varepsilon_{\mathbf{h}_3+\mathbf{kR_i}}\left(\varepsilon_{\mathbf{h}_1\ \ \mathbf{kR_i}} + \varepsilon_{\mathbf{h}_2\ \ \mathbf{kR}_i}\right)\big], \end{aligned}$$

$$\begin{aligned} B_{\mathbf{k},i} = &\varepsilon_{\mathbf{h}_1}\left[\varepsilon_{\mathbf{k}}\left(\varepsilon_{\mathbf{h}_1+\mathbf{kR_i}} + \varepsilon_{\mathbf{h}_1\ \ \mathbf{kR_i}}\right) + \varepsilon_{\mathbf{h}_2+\mathbf{kR_i}}\varepsilon_{\mathbf{h}_3\ \ \mathbf{kR_i}} + \varepsilon_{\mathbf{h}_2\ \ \mathbf{kR_i}}\varepsilon_{\mathbf{h}_3+\mathbf{kR_i}}\right] \\ &+ \varepsilon_{\mathbf{h_2}}\left[\varepsilon_{\mathbf{k}}\left(\varepsilon_{\mathbf{h}_2+\mathbf{kR_i}} + \varepsilon_{\mathbf{h}_2\ \ \mathbf{kR_i}}\right) + \varepsilon_{\mathbf{h}_1+\mathbf{kR_i}}\varepsilon_{\mathbf{h}_3\ \ \mathbf{kR_i}} + \varepsilon_{\mathbf{h}_1\ \ \mathbf{kR_i}}\varepsilon_{\mathbf{h}_3+\mathbf{kR_i}}\right] \\ &+ \varepsilon_{\mathbf{h}_3}\left[\varepsilon_{\mathbf{k}}\left(\varepsilon_{\mathbf{h}_3+\mathbf{kR_i}} + \varepsilon_{\mathbf{h}_3\ \ \mathbf{kR_i}}\right) + \varepsilon_{\mathbf{h}_1+\mathbf{kR_i}}\varepsilon_{\mathbf{h}_2\ \ \mathbf{kR_i}} + \varepsilon_{\mathbf{h}_1\ \ \mathbf{kR_i}}\varepsilon_{\mathbf{h}_2+\mathbf{kR_i}}\right]; \end{aligned}$$

$$\varepsilon = |E|^2 - 1$$

and $\mathbf{R}_i$ is the rotational matrix of the $i$th symmetry operator. The summation goes over the free $\mathbf{k}$ vectors and on the $m$ symmetry operators.

We will denote such a probability by $P_{10}(\Phi_{\mathbf{h}_1,\mathbf{h}_2})$ to emphasize the fact that the formula explores the reciprocal space by means of a ten-node figure.

An appropriate probability distribution of von Mises type has been provided to estimate the quartet invariants:[26,27]

$$P(\Phi_{\mathbf{h,k,l}}|R_1, R_2, ....., R_7) = [2\pi I_0(G)]^{\ 1} \exp(G\cos\Phi_{\mathbf{h,k,l}}) \tag{11}$$

where:

$$G = \frac{2R_1R_2R_3R_4(1+\varepsilon_5+\varepsilon_6+\varepsilon_7)}{1+Q},$$

$$Q = [(\varepsilon_1\varepsilon_2+\varepsilon_3\varepsilon_4)\varepsilon_5 + (\varepsilon_1\varepsilon_3+\varepsilon_2\varepsilon_4)\varepsilon_6 + (\varepsilon_1\varepsilon_4+\varepsilon_2\varepsilon_3)\varepsilon_7]/2N$$

and $\varepsilon_i = R_i^2 - 1$

For simplicity we used the following notation:

$$\varepsilon_1 = \varepsilon_{\mathbf{h}}; \quad \varepsilon_2 = \varepsilon_{\mathbf{k}}; \quad \varepsilon_3 = \varepsilon_{\mathbf{l}}; \quad \varepsilon_4 = \varepsilon_{\mathbf{h+k+l}}; \quad \varepsilon_5 = \varepsilon_{\mathbf{h+k}}; \quad \varepsilon_6 = \varepsilon_{\mathbf{h+l}}; \quad \varepsilon_7 = \varepsilon_{\mathbf{k+l}}$$

The reflections with indices $\mathbf{h}$, $\mathbf{k}$, $\mathbf{l}$, $\mathbf{h+k+l}$ are called *basis reflections*, those with indices $\mathbf{h+k}$, $\mathbf{h+l}$, $\mathbf{k+l}$ are called *cross reflections*. Equation (11) suggests

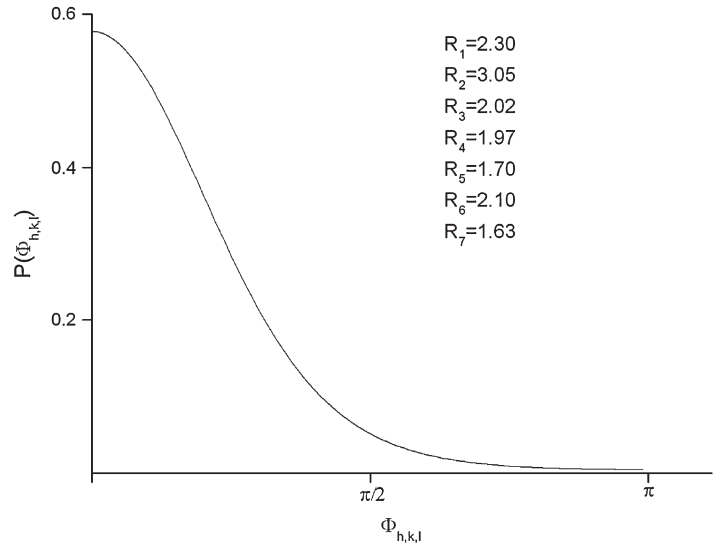



**Figure 8.5** Typical probability distribution for quartet phases characterized by large cross magnitudes.

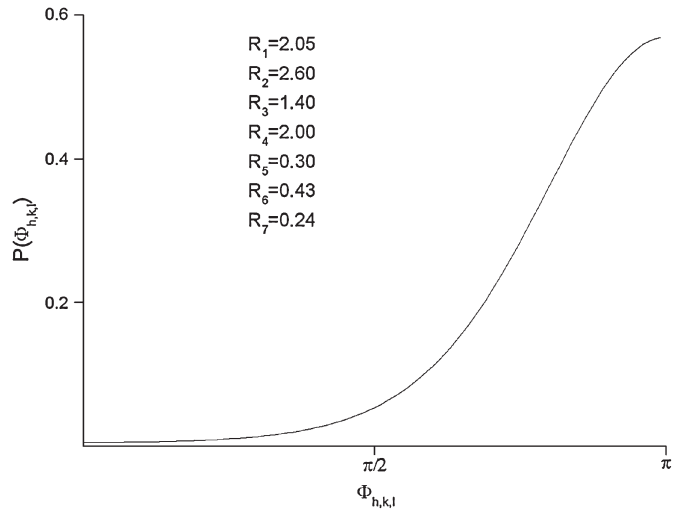



**Figure 8.6** Typical probability distribution for quartet phases characterized by small cross magnitudes.

that: (a) quartets are phase relationships of order $N^{-1}$: their average reliability is therefore not very high, at least for large structures; (b) the reliability increases for large values of $|E_{\mathbf{h}}E_{\mathbf{k}}E_{\mathbf{l}}E_{\mathbf{h}+\mathbf{k}+\mathbf{l}}|$; (c) if the cross moduli are large, $\Phi_{\mathbf{h},\mathbf{k},\mathbf{l}}$ is expected to be close to zero (see Figure 8.5); (d) if the cross moduli are all small, $\Phi_{\mathbf{h},\mathbf{k},\mathbf{l}}$ is expected to be close to $\pi$ (see Figure 8.6).

These last quartets are the most important ones because they add supplementary information to that provided by triplets.

### 8.3.3 Tangent Formula

By just changing **k** into $-\mathbf{k}$ the generic triplet invariant may be rewritten as: $\Phi_{\mathbf{h},\ \mathbf{k}} = \phi_{\mathbf{h}} - \phi_{\mathbf{k}} - \phi_{\mathbf{h}\ \mathbf{k}}$. For this invariant the Cochran formula states that $\phi_{\mathbf{h}} - \phi_{\mathbf{k}} - \phi_{\mathbf{h}\ \mathbf{k}} \approx 0$, with reliability given by $G_{\mathbf{h},\ \mathbf{k}} = 2\sigma_3\sigma_2^{\ 1/2}|E_{\mathbf{h}}E_{\ \mathbf{k}}E_{\mathbf{h}\ \mathbf{k}}|$. Equivalently, one can say that $\phi_{\mathbf{h}}$ is distributed about $\phi_{\mathbf{k}} + \phi_{\mathbf{h}\ \mathbf{k}}$ according to the von Mises formula:

$$P(\phi_{\mathbf{h}}) = [2\pi I_0(G_{\mathbf{h},\ \mathbf{k}})]^{\ 1} \exp[G_{\mathbf{h},\ \mathbf{k}} \cos(\phi_{\mathbf{h}} - \vartheta_{\mathbf{h}})]$$

where $\vartheta_{\mathbf{h}} = \phi_{\mathbf{k}} + \phi_{\mathbf{h}\ \mathbf{k}}$

Generally, each **h** reflection takes part in **r** triplets, for each of which the expectation:

$$\phi_{\mathbf{h}} \approx \vartheta_j = \phi_{\mathbf{k_j}} + \phi_{\mathbf{h}\ \mathbf{k_j}}$$

may be established. By combining the corresponding probabilities, one obtains:

$$P(\phi_{\mathbf{h}}) = \prod_{j=1}^{r} P_j(\varphi_{\mathbf{h}}) = A \exp\left(\sum_{j=1}^{r} G_{\mathbf{h},\ \mathbf{k_j}} \cos(\varphi_{\mathbf{h}} - \vartheta_j)\right) \tag{12}$$

where $A$ is a normalizing structure factor. Since the exponential can be rewritten as:

$$\begin{aligned}&\cos\varphi_{\mathbf{h}} \sum_{j=1}^{r} G_{\mathbf{hk}_j} \cos(\varphi_{\mathbf{k}_j} + \varphi_{\mathbf{h}\ \mathbf{k}_j}) + \sin\varphi_{\mathbf{h}} \sum_{j=1}^{r} G_{\mathbf{hk}_j} \sin(\varphi_{\mathbf{k}_j} + \varphi_{\mathbf{h}\ \mathbf{k}_j}) \\ &\quad = \alpha_{\mathbf{h}} \cos(\varphi_{\mathbf{h}} - \beta_{\mathbf{h}})\end{aligned}$$

Equation (12) becomes:

$$P(\phi_{\mathbf{h}}) = [2\pi I_0(\alpha_{\mathbf{h}})]^{\ 1} \exp[\alpha_{\mathbf{h}} \cos(\phi_{\mathbf{h}} - \beta_{\mathbf{h}})]$$

where:

$$\alpha_{\mathbf{h}} = \left[\left(\sum_{j=1}^{r} G_j \cos\vartheta_j\right)^2 + \left(\sum_{j=1}^{r} G_j \sin\vartheta_j\right)^2\right]^{1/2}$$

and:

$$\tan \beta_{\mathbf{h}} = \frac{\sum_{j=1}^{r} G_j \sin \vartheta_j}{\sum_{j=1}^{r} \cos \theta_j} \tag{13}$$

with $G_j = G_{\mathbf{h},\ \mathbf{k}_j}$. Equation (13) is known as the *tangent formula*;[28] it gives the most probable value of $\phi_{\mathbf{h}}$ , say $\beta_{\mathbf{h}}$, when a certain number of pair of phases $(\phi_{\mathbf{k}_j}, \phi_{\mathbf{h}\ \mathbf{k}_j})$ are known. The term $\alpha_{\mathbf{h}}$ is the reliability parameter of the phase indication: $\beta_{\mathbf{h}}$ has to be considered a good estimate of $\phi_{\mathbf{h}}$ only for large $\alpha_{\mathbf{h}}$.

### 8.3.4 A Typical Direct Methods Procedure

A modern direct phasing procedure may be described schematically as follows:

a. The structure factors are normalized according to Section 8.4.1.
b. The largest normalized structure factors (*e.g.*, those with $|E| > 1.3$) are selected. We will denote this set by $N_{LARGE}$. Triplet and negative quartet invariants are found among the $N_{LARGE}$ reflections.
c. Random phases are given to each of the $N_{LARGE}$ reflections. Cycles of tangent formula are then applied until the phases are stable (until *convergence*). This set of phases constitutes a *trial* and an eventual figure of merit (*FOM*) is calculated evaluating the quality of the trial (see Section 8.4.5).
d. Since it is unlikely that the tangent formula drives any random set of phases to the correct values, a new trial is attempted starting from the point (c).
e. After a sufficient number of trials have been obtained, the most reliable one (that with the highest value of *FOM*) is explored. An E-map is calculated according to:

$$\rho(\mathbf{r}) = V^{-1} \sum_{\mathbf{h}} w_{\mathbf{h}} |E_{\mathbf{h}}| \exp(i\varphi_{\mathbf{h}}) \exp(-2\pi i\, \mathbf{hr})$$

where $w_{\mathbf{h}}$ takes into account the reliability of the phase $\phi_{\mathbf{h}}$. The locations of the highest peaks are automatically found: to them stereochemical criteria of acceptable bond lengths and angles are applied to identify possible molecular fragments. If the molecular model has no chemical sense, a new trial is explored.

### 8.3.5 Figure of Merit

As mentioned, the phasing process usually leads to more than one trial solution and the most promising ones are detected by application of some *FOM*s. Several functions have been proposed, which are expected to be minima or

maxima for the correct solution. The most usual for small molecules are:[29,30]

$$Z = \sum_{\mathbf{h}} \alpha_{\mathbf{h}} = \max$$

$$MABS = \frac{\sum_{\mathbf{h}} \alpha_{\mathbf{h}}}{\sum_{\mathbf{h}} \langle \alpha_{\mathbf{h}} \rangle} - 1 = \min$$

$$R_{Karle} = \sum_{\mathbf{h}} \left| |E_{\mathbf{h}}| - |E_{\mathbf{h}}|_{calc} \right| / \sum_{\mathbf{h}} |E_{\mathbf{h}}| = \min$$

the so-called $\psi_0$ FOM,[31] their combinations and evolutions.

When powder data are available and a molecular model has been obtained, the so-called $\chi^2$ figure of merit may be used. Its expression is:

$$\chi^2 = \frac{\sum_i |y_i(\text{obs}) - y_i(\text{calc})|}{N} \cdot 100$$

where $y_i$(obs) and $y_i$(calc) are the observed and the calculated profile intensity at the angular step $i$, respectively. $N$ is the number of counting steps in the powder diagram (the summation is over $N$). This *FOM* considers the entire intensity profile, count-by-count, rather than the integrated intensities of individual diffraction peaks.

### 8.3.6 Completion of the Crystal Structure and Preliminary Refinement

The structural models generally obtained by *PM* or *DM* are often incomplete and distorted fragments, which are only rough approximations of the real structures: therefore methods for completing the model and for its refinement have to be used. When single-crystal data are available such methods can be summarized as in the flow diagram shown in Figure 8.7 (method of *Fourier Recycling*). Starting from the partial model {**X**,B} obtained by Patterson or *DM* procedures, cycles of least-squares refinement, in which atomic coordinates and isotropic thermal parameters are refined, are combined with observed Fourier syntheses. The process should be repeated until the structure is complete.

Often the least-squares refinement is combined with an *EDM* (electron density modification) procedure:[32,33] the advantage is that it is not necessary to interpret electron density peaks in terms of atomic species. In practice the map is modified by a suitable function "*g*" to obtain a better representation $\rho'$ of the structure:

$$\rho' = g(\rho) \tag{14}$$

The function $g$ is designed for exploiting positivity and atomicity of the electron density (the same information exploited in reciprocal space by the probabilistic formulae estimating structure invariants). Therefore the inversion of $\rho'$ is expected to produce better phase values than those used for calculating the map $\rho$.

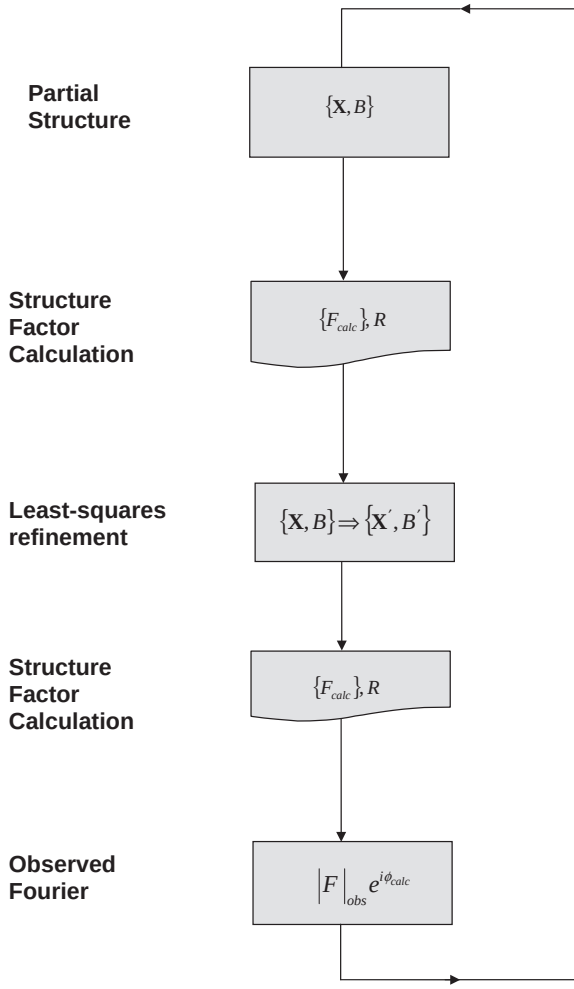



**Figure 8.7** Flow diagram of the Method of Fourier Recycling for single crystal data. $\{\mathbf{X},B\}$ represent the set of atomic positions and vibrational parameters, respectively. $F_{\text{obs}}$ and $F_{\text{calc}}$ are respectively the observed and calculated structure factor amplitudes. $R$ is the crystallographic residual between $F_{\text{obs}}$ and $F_{\text{calc}}$.

The above techniques have to be optimized for application to powder diffraction data.[34] In particular:

a. With reference to Figure 8.7, the observed Fourier synthesis may be replaced by a difference ($F_{\text{obs}} - F_{\text{calc}}$) or by a ($2F_{\text{obs}} - F_{\text{calc}}$) Fourier synthesis.
b. When powder data are available the $F_{\text{obs}}$ are replaced by the moduli provided by full pattern decomposition techniques. As shown in

Figure 8.1 such moduli are generally far from the true $F_{obs}$. The least-squares procedures are then rather unstable and Fourier syntheses are less effective.

### 8.3.7 Solving Crystal Structures from Powder Neutron Data

Neutrons do not interact with electrons but with atomic nuclei. The neutron–nucleus interaction is governed by very short-range nuclear forces ($\sim 10^{-13}$ cm); since the nuclear radius is of the order of $10^{-15}$ cm (several orders of magnitude less than the wavelength associated with the incident neutrons) the nucleus behaves like a point scatterer: accordingly its scattering factor $b_o$ will be isotropic and not dependent on $\sin\vartheta/\lambda$. As a result, strong reflections can be observed at both long and short $d$-spacing, so making easier structure solution and refinement. Also, $b_o$ is not proportional to $Z$, as in X-rays and this property allows one to distinguish between atoms having quite close $Z$ values and makes it easy to localize hydrogen atoms (usually these are replaced by deuterium, which has $b_o > 0$ and negligible incoherent scattering).

The neutron–atom interaction involves also the interaction between the magnetic moment associated with the spin of the neutron and the magnetic moment of the atom (this last generated by the presence of unpaired electrons). This allows the investigation of magnetic structures, whose magnetic scattering does decline with $\sin\theta/\lambda$.

Some relevant neutron properties are:

1. The interaction of neutrons with matter is weaker than for X-rays and electrons. Therefore higher neutron fluxes are needed to measure appreciable scattered intensities.
2. For some elements $b_o < 0$.
3. Coherent scattering, giving rise to Bragg scattering, defines the structure factor:

$$F_{\mathbf{h}} = \sum_{j=1}^{N} b_j \exp(2\pi \mathbf{h}\mathbf{r}_\mathbf{j}) \exp\left(-B_j \sin^2\theta/\lambda^2\right)$$

where $b_j$ is a positive or negative value.

We have underlined that positivity and atomicity of the electron density are basic conditions for the validity of traditional *DM*. What then is the effect of the possible violation of the positivity criterion on *DM* procedures? It has been assessed[35–37] that positivity is not an essential ingredient of *DM*. In particular the triplet phase invariants can again be evaluated *via* a von Mises distribution, but now the value of $N$ has to be replaced by $N_{eq}$, where:

a. $N_{eq}$ is calculated as $N$ if all the scatterers have positive $b_0$ values;
b. $N_{eq}$ is equal to $-N$ if all the scatterers have negative $b_0$ values;

c. $N_{eq}$ is equal to $\infty$ if the scattering power of the negative scatterers equals the scattering power of the positive ones. In this case no triplet can be evaluated;
d. if the scattering power of the positive scatterers is predominant the triplets are expected to be positive but with a large value of $N_{eq}$.

By collecting both neutron and X-ray data the available experimental information increases. It is common opinion that neutron powder diffraction is a particularly good technique for structure refinement while X-rays should be used for structure determination.

## 8.4 DIRECT-SPACE TECHNIQUES

As stated in the preceding sections, crystal structure solution from powder diffraction data is traditionally achieved by first extracting the intensities of individual reflections from the experimental profile, and then by using *PM* or *DM*. The efficiency of these last techniques is affected by the difficulty of extracting unambiguous values of the individual intensities. If information about the molecular geometry is available, the so-called *Direct-Space Techniques* (*DST*) can be used, which do not require pattern decomposition and directly use as target the experimental diffraction profile. *DST* use *global optimization algorithms* to orient and locate the structural model. These algorithms are able to locate the global minimum from any random starting point, thus being able to escape from local minima (which correspond to incorrectly determined structures). An appropriate figure of merit, called the *cost function* (*CF*), is associated with each generated structural model: the *CF* quantifies the agreement between experimental and calculated powder diffraction patterns. Global optimization techniques are used to find the trial structure associated with the lowest *CF*, which is equivalent to finding the global minimum of the hypersurface defined by the *CF*, by varying the set of variables that defines the generated crystal structure. Grid search, Monte Carlo, simulated annealing and genetic algorithms are the search methods most commonly used for this purpose: they will be described in the following sections.

*DST* are advantageous only when substantial prior information on the molecular geometry, and/or on its crystal chemistry, is available. Such information introduces a dependence on the prior chemical restraints: only wrong solutions can be obtained if the prior information is wrong, but, if it is correct, only chemically feasible structural models are generated. A class of structures particularly suited for direct-space approaches (and particularly resistant to *DM*) are the molecular organic compounds: they generally contain structural units of well-defined geometry and atoms with known connectivity. Model building programs, such as Cerius[2] (ref. 38), Chem3Dultra (ref. 39) and Sybyl (ref. 40), and the Cambridge Structural Database (*CSD*)[41] can be used to construct a chemically feasible structural model. The resulting model is generally described in terms of internal coordinates, *i.e.*, bond lengths, bond angles and torsion angles. Usually the only variables that are determined by search methods are the torsion angles (internal degrees of freedom, or internal *DOF*s)

and the parameters defining position and orientation of the molecular fragment(s) (external *DOF*s).

Among inorganic structures, the extended framework structures constituted by well-defined building units, such as zeolites, are particularly suited for *DST*. In this case the chemical information can be encoded in building units, *e.g.*, polyhedra of atoms with known geometry, in which case the variables are only the positions and the orientations of the scattering objects (only external *DOF*s are present in this case).[42]

The use of the prior chemical information allows a dramatic reduction of the number of *DOF*s necessary to describe the structure, both for organic and inorganic compounds, compared with the description in terms of atomic coordinates. Generally reductions can be obtained of a factor 2 for inorganic structures and by a factor of at least 3 for organic ones.[42] Moreover, the use of internal coordinates greatly reduces the number of generated trial structures, since only the chemically plausible ones are explored.

The most commonly used approach to cope with the generation of flexible models is to express the internal coordinates of the model by the so-called *Z-matrix* (Figure 8.8), where the position of each atom is determined from the bond distance, the bond angle and the torsion angles with respect to three preceding atoms in the matrix. In the first column of the matrix of Figure 8a a number is assigned to all the atoms of Figure 8b, the second column contains the bond lengths to connect the atoms on the left with the atom on the right (third column), the fourth column contains the bond angles formed by atoms in columns 1, 3, 5 of the same row, and the sixth column contains the torsion angles formed by atoms in columns 1, 3, 5, 7 of the same row. During the *DST*

(a)

| | | | | | | |
|---|---|---|---|---|---|---|
| 1 | | | | | | |
| 2 | $d_{12}$ | 1 | | | | |
| 3 | $d_{23}$ | 2 | $\theta_{123}$ | 1 | | |
| 4 | $d_{24}$ | 2 | $\theta_{124}$ | 1 | $\tau_{1234}$ | 3 |

(b)

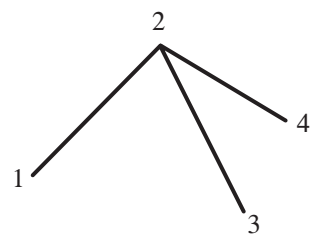



**Figure 8.8** (a) *Z* matrix description for the tetrahedron shown in (b). $d_{ij}$, $\theta_{ijk}$ and $\tau_{ijkl}$ indicate, respectively, the bond length between atoms $i$ and $j$, the bond angle between atoms $i, j$ and $k$ and the torsion angle formed by atoms $i, j, k$ and $l$.

calculations, the crystallographic coordinates for each model are frequently required: the algebra and techniques to convert internal coordinates into atomic coordinates in a Cartesian frame and finally in crystallographic coordinates are well described in ref. 43.

### 8.4.1 Grid Search Methods

The most intuitive approach to tackle the crystal structure solution by *DST* is to define a grid over the parameter space of interest and systematically explore every grid point. This method is simple and easily implemented in a computer code, and guarantees that the global minimum may be found, provided a suitably fine grid is used. However, it can be applied only when the parameter space is relatively small, namely when the number of *DOF*s necessary to describe the model is limited.

The systematic translations and rotations are performed within the corresponding asymmetric regions, while molecular and crystallographic symmetries can be used to further limit the ranges of the positional and orientational parameters.[44] Moreover, the rotational space can be better sampled by a redefinition of the relative parameters: the number of sampling points can be reduced by a factor $2/\pi \approx 0.64$, with equal volumes sampled per each point, if the conventional Euler angles $\vartheta,\phi,\psi$ are replaced by the quasi-orthogonal Euler angles:[45]

$$\vartheta_+ = \vartheta + \psi, \quad \varphi, \quad \vartheta \quad = \vartheta - \psi$$

Grid search procedures have been mainly applied to rigid structural fragments.[46 48] For cases in which internal *DOF*s are necessary to describe the conformational flexibility, the number of grid points to be explored undergoes a combinatorial explosion that prohibits the exhaustive search procedure. Some authors have avoided this difficulty by a two-step procedure: first a rigid model is moved in a six-dimensional grid described by the external *DOF*s, then it is refined in the position corresponding to the minimum *CF*, by allowing conformational modifications subject to bond restraints.[49]

### 8.4.2 Monte Carlo Methods

To approximately locate the global minimum (*i.e.*, to obtain a good quality crystal structure solution) in a reasonable amount of time, grid search methods should be replaced by the stochastic ones, based on a random sampling of the parameter space. This technique, called Monte Carlo (*MC*), has been widely used in other scientific fields to simulate the behavior of complex systems. Its application to crystal structure determination from powder diffraction data has been developed by many authors: the main strategies are outlined below.

*MC* methods require the construction of a Markov chain of structures, *i.e.*, a sequence of structures, each exclusively depending on the previous one. Each structure of the sequence, called a *configuration*, is defined by the set of external

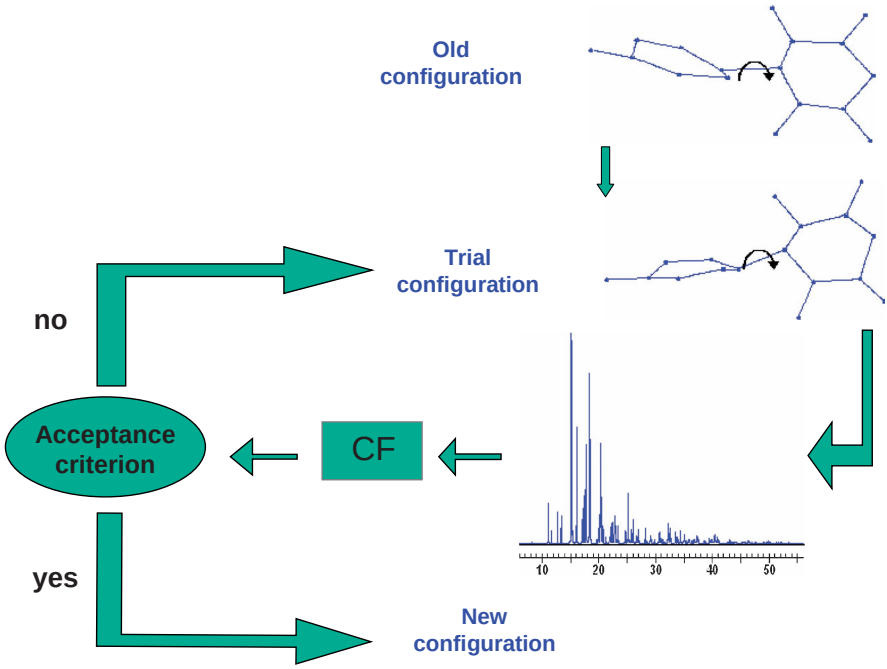



**Figure 8.9** Summary of the steps involved in a single Monte Carlo move for a structural model having a single unknown torsion angle between the two rings.

and internal *DOF*s necessary to fix position, orientation and intramolecular geometry of the predefined structural model. A given configuration is derived from the previous one by random variations of its *DOF*s, and two successive configurations represent a *MC* move. In Figure 8.9 the steps involved in a single *MC* run are sketched for a structural model having a single internal *DOF* (the unknown torsion angle between the two rings). The steps can be summarized as follows:

a. A trial configuration is generated from a given old configuration through small random displacements of the set $\{p_i\} = \{x, y, z, \theta, \varphi, \psi, \tau_1 \tau_2, \ldots, \tau_n\}$, where the first three parameters represent the position of the center of mass of the structural model in an orthonormalized reference frame, the second three parameters (usually coinciding with the Euler angles) fix the orientation of the model and the last $n$ parameters are the variable torsion angles. For each $i$th parameter, the new value $p_i$ is calculated from the old one (say $p_i^{\text{old}}$) according to the relation:

$$p_i = p_i^{\text{old}} + r_i s_i \Delta p \tag{15}$$

where $r_i$ is a random bit that assumes the values $+1$ or $-1$, giving the sense of the displacement, $s_i$ is a random number extracted uniformly in the

range (0, 1) and $\Delta p$ is a predefined maximum step width for the $i$th parameter.

b. A powder diffraction pattern is calculated for the trial structure and it is compared with the experimental profile. The profile weighted index $R_{wp}$ is frequently used as agreement factor:

$$R_{wp} = \sqrt{\frac{\sum_t w_t (y_t^o - K y_t^c)^2}{\sum_t w_t (y_t^o)^2}} \tag{16}$$

where $y_t^o$ and $y_t^c$ are, respectively, the observed (background subtracted) and calculated counts corresponding to the $t$th point in the powder diffraction profile, $K$ is a scale factor and $w_t$ is a weighting factor, usually chosen as Poissonian ($w_t = 1/y_t^o$). $R_{wp}$ is used as the $CF$ to asses the suitability of the trial structure.

c. An acceptance criterion decides whether the trial structure is accepted or rejected. In most of the cases it is based on the importance sampling algorithm developed by Metropolis and coworkers:[50] the trial configuration is accepted if $CF < CF_{\text{old}}$, otherwise it is accepted with probability:

$$\exp[-(CF - CF_{\text{old}})/T] \tag{17}$$

where $T$ is an appropriate scaling factor. This is accomplished by taking a random number $r$ between 0 and 1 and accepting the trial configuration if $\exp[-(CF - CF_{\text{old}})/T] > r$.

d. If the trial configuration is accepted, it is considered as a new configuration in the Markov chain, and becomes the starting point for a subsequent generation. If the trial configuration is rejected, a new one is attempted from the old configuration until the acceptance criterion is fulfilled.

Several *MC* moves are repeated until a sufficiently long chain of structures is obtained, which can be viewed as a random walk through the parameter space. It is guided by the importance sampling algorithm towards the global minimum of the *CF* hypersurface, which should be reached provided a sufficiently wide-region of the parameter space has been explored. In fact, Equation (17) avoids the system being trapped into local minima, since it allows a configuration with higher *CF* to be accepted with finite probability, and hence the random walk to climb over barriers of the *CF* hypersurface. The rate at which this happens is governed by the temperature parameter $T$, which can be varied during the minimization process in a process called *simulated annealing*, as described below.

Among the various *MC* procedures designed to solve the phase problem from powder data, we quote the pioneering work of Harris *et al.*,[51] the paper by Andreev *et al.*,[43] where the mathematical procedures for generating flexible molecular structures has been clearly described, and the contribution by Tremayne *et al.*,[52] implemented in the computer program OCTOPUS,[53] where a local minimization at each *MC* move is introduced to increase the efficiency

of the global optimization algorithm. The two latter works are examples of how one of the major drawbacks of *DST* may be solved: its dependence on the initially guessed structural model. In the paper of Andreev and coworkers the unknown part of the structural geometry is parameterized and actively used during global minimization, but has the effect of widening the parameter space of the search algorithm. In the paper by Tremayne and coworkers it is fixed in the global search algorithm, yielding a smaller parameter space, but relaxed during local minimization. The acceptance probability, Equation (17), is then calculated using the *CF* associated to the locally minimized configurations: if a trial structure is accepted, the new one is generated starting from the structure with standard geometry (not from that with relaxed geometry), to avoid substantial deviations from the standard molecular geometry of the structural fragment during the *MC* calculation.

*MC* methods can benefit by the calculation of the potential energy of the structural model: its use avoids or highly reduces the generation of unrealistic structures, characterized by too short intermolecular contacts or impossible bond length and angles. As the primary aim for introducing the potential energy is to avoid implausible structures, rather than to introduce a fine discrimination among different plausible structures, a simple potential energy function is frequently used, consisting only of repulsive terms. Lanning *et al*.[54] and Brodski *et al*.[55] used the following Leonard-Jones potential:[56]

$$E = \sum_i \sum_{j>i} \frac{B_{ij}}{r_{ij}^{12}} \tag{18}$$

where the summation is carried out over all pairs of atoms (labelled $i$ and $j$) within a cut-off radius and the parameters $B_{ij}$ are estimated by molecular mechanics force field calculations.[57] Coelho[58] used the Born–Mayer potential:[59]

$$E = \sum_i \sum_{j>i} C_{ij} \exp(-Dr_{ij}) \tag{19}$$

For inorganic compounds, Putz *et al*.[60] used the potential:

$$E = \sum_i \sum_{j>i} E_{ij}$$

$$E_{ij} = \begin{cases} 0 & if \quad r_{ij} \geq r_{ij}^{\min} \\ \left( r_{ij}^{\min} / r_{ij} \right)^6 - 1 & if \quad r_{ij} < r_{ij}^{\min} \end{cases} \tag{20}$$

where $r_{ij}^{\min}$ is the parameter indicating the minimum observed distance between the two atom types, which can be obtained from the Inorganic Crystal Structure Database.[61] For ionic atomic models, a Coulomb term:

$$E = A \sum_i \sum_{j>i} \frac{Q_i Q_j}{r_{ij}}$$

can be added to the repulsive term, where $Q_i$ and $Q_j$ are the ionic valences of atoms $i$ and $j$.[60]

Most of the authors used a mixed *CF*, by summing the energy term to that assessing the agreement between calculated and experimental profiles.[54,58,60] More recently, Brodski *et al.*[55] have considered the potential energy function and the weighted profile *R*-factor [see Equation (16)] as two independent *CF*s to be minimized. In their *MC* strategy the Metropolis acceptance criterion is replaced by the following: a trial configuration is accepted if either its energy term or its profile agreement index is lower than the respective term of the old configuration, otherwise it is rejected.

Another promising modification of the Metropolis acceptance criterion has been proposed by Hsu *et al.*,[62] who replaced the difference $CF - CF_{\text{old}}$ in Equation (17) by the term:

$$CF - CF_{\text{old}} + \varepsilon \frac{H(CF,t) - H(CF_{\text{old}},t)}{H(CF,t) + H(CF_{\text{old}},t)}$$

where $\varepsilon$ is a tuning constant and $H(CF,t)$ is the cumulative histogram of configurations with cost function equal to *CF*. It depends on the "time" $t$ since it is updated at each *MC* move: if the configuration is accepted, $H(CF) = H(CF) + 1$, otherwise $H(CF_{\text{old}}) = H(CF_{\text{old}}) + 1$. When a local minimum is reached, the acceptance rate decreases, hence the additional term deforms locally the energy landscape in such a way that the local minimum is no longer favoured. As a result, the process keeps track of the number of prior explorations of a particular energy region and avoids trapping in local minima. This technique, called *energy landscape paving*, enhances the convergence of a *MC* search applied to organic molecules from single-crystal data, but has still to be checked against powder diffraction data.

### 8.4.3 Simulated Annealing Techniques

The fundamental difference between standard *MC* and simulated annealing (*SA*) techniques concerns the way in which the scaling factor $T$ of Equation (17) is used to control the sampling algorithm. In the former method, $T$ is fixed or varied empirically, whereas in the latter $T$ is slowly reduced during the procedure, according to an annealing schedule. To get the rationale underlying this strategy, it is useful to introduce an equivalence between the *DOF*s of the structural model to be varied during the minimization and the particles of an imaginary physical system. We will follow the arguments of Kirkpatrick *et al.*,[63] who first introduced the *SA* technique. The cost function represents the energy of the physical system, hence the global minimum configuration corresponds to its ground state. The probability factor of the Metropolis criterion resembles the Boltzmann factor $\exp(-E/k_{\text{B}}T)$ for the energy level $E$ to be populated, where $k_{\text{B}}$ is the Boltzmann's constant and $T$ is the temperature. In the evolution of the physical system the ground state may be reached by slowly lowering its temperature, through states of thermodynamic equilibrium:

correspondently, the correct crystal structure can be reached provided the $T$ parameter of Equation (17) is continuously reduced, avoiding the system being trapped in local minima, corresponding to false structure solutions. The optimal annealing schedule, suggested by Kirkpatrik,[64] can be deduced by considering the properties of the physical systems consisting of many interacting atoms. To bring the fluid into a low energy state one should first warm the system until it is completely melted, then one should slowly lower the temperature, spending a long time at temperatures near the freezing point, and finally one should cool more rapidly to bring the atoms to rest. The same sequence can be followed in the global optimization algorithm, considering as key parameters the $T$ factor and the fraction of accepted $MC$ moves (acceptance ratio). The system starts at a given $T$ value, $T$ is then increased until the acceptance ratio is high enough (this ensures that the system is melted, *i.e.*, the *DOFs* can vary freely in the parameter space); then $T$ is decreased, keeping the same value until a fixed number of moves has been performed. This is the longest stage, during which the system should reach the global minimum without being trapped in local minima. Finally, the global minimum position is refined by a rapid decrease of $T$ and the iteration is stopped when the acceptance ratio reaches some allotted low value, indicating that no further improvements are observed. It has been shown[65] that convergence to the global minimum can be achieved for a logarithmic annealing schedule, but scarcity of computing time could suggest a choice of faster annealing schedules, for which success is no longer guaranteed.

Several variants of the basic *SA* algorithm have been developed, which differ in the choice of the *CF*, in the design of the annealing schedule or in the procedure for the generation of the trial configurations. For example, Andreev *et al.*[66] reduce $T$ at a preset rate and, for each $T$, perform several moves which increase as the acceptance ratio decreases; David *et al.*[67] introduced the following relevant novelties, included in the computer program DASH:[68]

a. The *CF* is based on the comparison between the calculated structure-factor magnitudes and the integrated intensities extracted to Pawley techniques according to the formula:

$$CF = \sum_h \sum_k [(I_h - c|F_h|^2)(V^{-1})_{hk}(I_k - c|F_k|^2)] \tag{21}$$

where $I_{\boldsymbol{h}}$ and $I_{\boldsymbol{k}}$ are the integrated intensities assigned, respectively, to reflections $\boldsymbol{h}$ and $\boldsymbol{k}$ by a Pawley refinement, $V_{\boldsymbol{hk}}$ is the covariance matrix obtained by the Pawley refinement, $c$ is a scale factor and $|F_{\mathbf{h}}|$ and $|F_{\mathbf{k}}|$ are the structure-factor magnitudes calculated from the trial structure. The calculation of this *CF* is much faster than that of the *R*-profile factor, so leading to a rapid identification of the correct solution. For cases where the structural model being optimized is not a complete description of the asymmetric unit, a *CF* derived by a maximum-likelihood approach has been employed, leading to an improved success rate of the *SA* algorithm.[69]

b. The temperature reduction is related to fluctuations in the cost function, so that the cooling schedule slows down when the *CF* fluctuations are large. This allows a more extensive exploration of the parameter space when the algorithm is sampling both good and bad solutions: it is equivalent to cooling more slowly if the heat capacity of the physical system is large.
c. The parameter generation occurs according to an exponential probability distribution, contrary to the uniform generation implicit in Equation (15). The shift $\Delta p$ of the parameter $p_i$ is extracted according to the probability distribution:

$$P(\Delta p) = \frac{\Delta p}{\Delta p_0} \exp\left(-\frac{\Delta p}{\Delta p_0}\right)$$

where $\Delta p_0$ is the current characteristic distance for the parameter $p_i$. This allows one to efficiently sample the neighboring parameter space, whilst ensuring that there is a finite chance of sampling well away from the current point.[70]
d. The quaternion representation is used for rotations of the model.[71] Three of the four quaternions fix the orientation of a rotation axis, the remaining determines the rotation around the axis. The advantage is that they ensure a uniform sampling of orientations, avoiding the singularities introduced by the description in terms of Euler angles.[70]

The *SA* algorithm implemented in the program *PowderSolve*[72] includes similar techniques, with the addition of a dependence of the step width for parameter changes [$\Delta p$ in Equation (15)], on the acceptance ratio and on the *CF* fluctuations. A local quenching has also been introduced, *i.e.*, a local Rietveld optimization is performed whenever a promising structure solution is obtained during the calculation. This avoids going to very low annealing temperatures during the main SA run, enhancing the efficiency of the method.

The program ENDEAVOUR[60] can find the crystal structure of ionic and intermetallic compounds without using a starting structural model, but generating random distributions of atoms within the unit cell. In each *MC* move a new random atom configuration is generated from the previous one by randomly displacing 95% of the atoms (randomly chosen) and exchanging in pairs the remaining 5%. A local optimization is also performed, whose number of cycles depends on the number of atoms in the unit cell. This dependence is present also in the annealing schedule, so that the whole procedure is strongly influenced by the unit cell content provided by the user. In this program part of the *prior* structural knowledge usually exploited in *DST* is embedded on an energy term included in the *CF*, which for metallic compounds is expressed by Equation (20) and in general depends on the type of compound under study. A similar approach has been followed by Coelho[58] and implemented in the program TOPAS,[73] where several energy terms of the type shown in Equations (18) and (19), representing the atom–atom interaction, are summed to define

the *CF*, and, in addition, the magnitude of the atomic random displacements are related to the expected mean bond length of the considered compound.

The program ESPOIR[74] uses a novel *CF* that combines the rapidity inherent in the handling of extracted intensities (instead of profile counts) with the necessity to take into account the reflection overlapping. The intensities extracted from the observed profiles are used to reconstruct a pseudo-pattern, where background, Lorenz-Polarization, complex profile shapes and reflection multiplicity are not included. A simple Gaussian shape with short tails, sampled by no more than five profile points above the full width at half maximum, is used to grossly mimic the overlapping in the experimental profile. The *CF* states the agreement between observed and calculated pseudo-patterns.

An improved version of the *SA* search algorithm, called *parallel tempering*, has been included in the program FOX.[42] Since a single chain of configurations could be trapped in local minima if the temperature decreases prematurely, a small number of parallel optimizations are performed, each at a different temperature. Exchanges of configurations among parallel optimization processes are allowed, using the same acceptance criterion adopted in the single chain generation, to ensure an optimal exploration of the parameter space. This approach is particularly suited for structural models defined by a high number of *DOF*s (typically more than 10).

### 8.4.4 Genetic Algorithm Techniques

The genetic algorithm (*GA*)[75] is an alternative global optimization technique to *MC* and *SA* approaches. It is based on the principles of the Darwinian theory of evolution and allows a population composed of many individuals to evolve under specified selection rules to a state of best *fitness*. To fit our crystallographic problem into the biological evolution terminology, we should consider the following equivalences: a *DOF* corresponds to a gene; the sequence of *DOF*s necessary to identify the position, orientation and internal conformation of the structural model corresponds to a chromosome; the *CF* corresponds to the fitness associated with each molecule; the search for the structural solution is equivalent to searching for the molecule with the best fitness, which is the result of a series of evolution steps from one initial population of molecules. The operations involved in a single evolution step are:

a. *Natural selection*. It selects the individuals destined to survive or to take part in mating. It implies the calculation of the fitness for all the members of a given population and a selection procedure, somehow analogous to the *SA* acceptance criterion, capable of tagging the members with highest probability of survival (thus containing some random element).
b. *Mating*. It procreates the new offspring by mixing the genetic information of two selected parents.
c. *Mutation*. It generates new individuals (*mutants*) by randomly changing part of the genetic information of individuals randomly chosen from the population.

All these three processes play a fundamental role in the *GA* method: mating is responsible for the preservation and improvement of selected characters in the population, mutation is responsible for genetic diversity and prevents the stagnation of the population, natural selection drives the evolution towards the best fitted populations, enhancing the lifetime of individuals containing the best suited groups of genes (*schemata*). As a general strategy, the number of members from one generation to the next is kept constant, so that a crucial parameter is the size of the populations: too small populations tend to be dominated by few individuals, leading to stagnation and poor sampling of the parameter space, while too large ones could slow down the convergence towards the optimal member.

A relevant feature of *GA* methods is its implicit parallelism, being able to treat at the same time different members of a population, so investigating simultaneously different regions of the parameter space. This makes the *GA*, just like the above-mentioned parallel tempering, particularly advantageous for the solution of problems with many *DOF*s.

Two research groups have independently introduced the *GA* technique for structural solution from powder diffraction data: Kariuki *et al.*[76] and Shankland *et al.*[77] They both use the following strategy:

- The initial population of randomly chosen individuals is constituted by chromosomes of the following kind: $\{x,y,z|\vartheta,\phi,\psi|\tau_1,\tau_2,\ldots,\tau_n\}$, containing the translation, rotation and internal conformation schemata.
- The mating procedure is performed by a single-point crossover, *i.e.*, the chromosomes of the two parents are cut in a single position and the cut segments are swapped.
- The chromosomes are mutated by assigning a new random value to one or more randomly chosen genes.

In detail, the two approaches differ in many other implementation aspects, the most relevant of which is the definition of the fitness function: Shankland and coworkers use the same function based on integrated intensities as that used in DASH [see Equation (21)], while Kariuki and coworkers use the profile agreement factor. In addition they dynamically scale this cost function by the transformation:

$$\rho = \frac{CF - CF_{\min}}{CF_{\max} - CF_{\min}}$$

where $CF_{\min}$ and $CF_{\max}$ are the $CF$ minimum and maximum values within a given population, respectively. $\rho$ is the argument of a tan*h* or an exponential function that is maximum for $\rho = 0$ and minimum for $\rho = 1$.[78] In a more recent implementation of the algorithm[79] the Lamarckian conception of evolution has been introduced, assuming that an individual can improve its fitness during its lifetime. This is accomplished by locally minimizing the agreement factor of each new structure generated during the calculation before the operations of

natural selection, mating or mutation are applied. As for *MC* procedures, the introduction of local minimization produces a significant increase in the convergence rate of the algorithm.

A new evolutionary algorithm, called differential evolution (*DE*)[80] has been successfully applied to powder data crystal structure solution.[81] *DE* is a simpler and more deterministic method with respect to *GA*, and is based on the generation of children from a unique parent. In particular, each member of the population creates a child having the chromosome:

$$parent + K(member_1 - parent) + F(member_2 - member_3) \qquad (22)$$

where *parent* is the chromosome of its parent, $member_i$, $i = 1,3$ refers to the chromosomes of other three randomly selected members of the populations and the parameters $K$ and $F$ tune respectively the level of recombination and mutation present in the algorithm. The operations shown in Equation (22) are applied to individual genes of the chromosomes, taking into account the allowed bounds associated to each of them: if the newly generated value of any gene exceeds its upper or lower bound, it is reset to a median value between the parent and the overstepped boundary. The new population is formed in a deterministic manner, by comparison of the newly created child with its parent: the fitter of the two survive. The *DE* algorithm was shown to be more robust than *GA*, at the price of a slower convergence.

### 8.4.5 Hybrid Approaches

Recent developments of global optimization methods have led to hybrid algorithms that have the merit of combining the best features of two different techniques. An example concerns an algorithm derived from *MC* and molecular dynamics (*MD*) techniques.[82] The orientation and location of a model molecule is here figured as the problem of driving a hypothetical particle into a well of potential energy defined in the parameter space. The coordinates of the particle correspond to the internal and external *DOF*s of the structural model and its momentum components represent the shifts of the corresponding *DOF*s. Molecular dynamics rule the motion of the particle through the parameter space by means of Hamilton's equations, where the initial momentum components are randomly extracted from a Gaussian distribution and the potential energy coincides with the *CF* given by Equation (21). After a fixed number of *MD* steps, the particle describes a trajectory in the parameter space, but its total energy (kinetic + potential) value tends to deviate from the initial one, due to systematic errors introduced by the finite step size of the *MD* simulation. Therefore, a *MC* step is performed to force the conservation of the total energy of the particle, and the trajectory undergoes a Metropolis acceptance criterion, based on the comparison of its initial ($E_{old}$) and final ($E$) total energy. The trajectory is accepted if $E < E_{old}$, otherwise it is accepted with probability given by:

$$\exp[-(E - E_{old})/T]$$

in analogy with Equation (17). If the trajectory is accepted, a new one begins at its endpoint, otherwise it begins at the starting point of the rejected trajectory; in both cases, new momentum components are randomly extracted from the Gaussian distribution. The hybrid Monte Carlo stops either when a predetermined lower bound on the potential energy is reached or when a maximum number of *MD* plus *MC* steps is exceeded. When applied to a single test structure, this approach has increased the success rate of 35% with respect to the *SA* algorithm implemented in DASH.

Another hybrid approach involves the use of the structure envelope. It is generated by using few strong low-resolution reflections, which are less affected by overlap and whose phases need to be estimated, and produces a partition of the unit cell into regions of high and low electron density. This allows the restriction of the parameter space used for global optimization methods. A grid search procedure limited to the grid points falling within the region of the asymmetric unit defined by the structure envelope succeeded in finding the solution of a zeolite[83] and of an organic[84] structure. In a more recent version of the procedure, the envelope information has been embedded in the framework of an *SA* algorithm, specifically in the definition of its *CF*: $CF = wR_{wp} + (1 - w)P$, where $w$ is a weighting factor that can be adjusted depending upon the reliability of the generated envelope and $P$ is a penalty function measuring the fit of the model in the actual configuration with the envelope.[85]

Altomare *et al*. have attempted to combine *DM* with *SM* techniques:[86] the procedure has been implemented in the package EXPO2004.[87] It is justified by the necessity to exploit the prior information on the molecular geometry for cases in which the classical *DM ab initio* approach applied to powder data is not able to reach a fully interpretable electron density map. As a first step, a procedure to complete inorganic crystal structures *via* a *MC* method has been developed. It takes advantage of the prior knowledge on the coordination polyhedra around the heavy atoms located by means of *DM* procedures and, for each polyhedron, of the average cation–anion distance.[86] The expected types of coordination polyhedron about each of the cations in the asymmetric unit are specified by the user *via* directives, together with the expected average bond distances and the tolerance parameters. Then the following steps are performed:

- The positional parameters of the heavy atoms provided by *DM* are submitted to automatic Rietveld refinement to improve their accuracy.
- The distances between the heavy atoms are analyzed to derive (or confirm) the cation connectivity (tetrahedral or octahedral). Let us suppose that two cations, say C1 and C2 (see Figure 8.10), have been located. The bridge anion A1, bonding C1 to C2, is expected to lie on the circle intersection of the two coordination spheres, centred in C1 and C2. A random point on the circle is chosen as a trial location of A1: it is *a feasible atomic position*. The positions of the other anions A2, A3, A4 may be (randomly) fixed by a random rotation of the C1 polyhedron about the

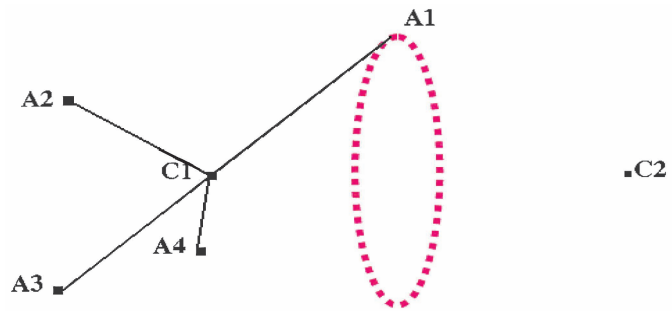



**Figure 8.10** Schematic view of the Monte Carlo procedure to locate a tetrahedron of anions (A) starting from the positions of two cations (C).

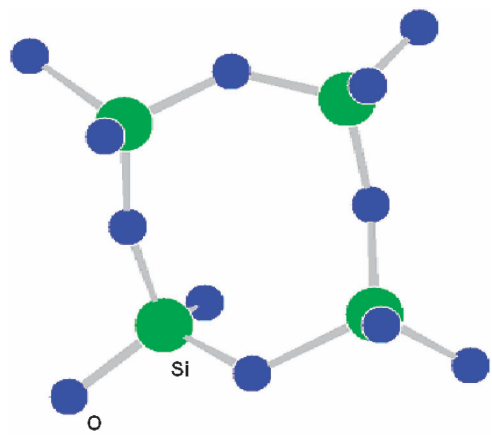



**Figure 8.11** Structural fragment of SAPO.[89] Ten of the 12 O anions are located by the Monte Carlo method starting from a partial map containing the four symmetry independent Si cations and using prior knowledge of their coordination polyhedra.

C1–A1 axis. The site symmetry of the new anions is checked, their symmetry equivalents are generated, and the completeness of the polyhedra is controlled.

- The process is cyclic: the procedure stops when all anions have been positioned. For each feasible model the profile residual is calculated and those corresponding to the best agreement factors are selected for Rietveld refinement.

As an example, when applied to the structural fragment shown in Figure 8.11 the procedure was able to assign 10 of the 12 O anions, starting from the four Si peaks initially located by *DM*.

Subsequently, the procedure has been generalized to cope with cases in which not all the heavy atoms present in the structure are correctly located, allowing

the location of missing cations and surrounding anions when the cation coordination is tetrahedral or octahedral.[88] With this new procedure the complete structure of the fragment shown in Figure 8.11 may be found when starting from only two Si peaks located by *DM*.

The completion of an organic structure is a challenging task, since the electron density maps resulting from the application of *DM* usually contain partial and distorted molecular fragments. Tanahashi *et al.*[90] accomplished it by combining *DM* with a *MC* approach borrowed from the procedure described in Harris *et al.*[51] The positions of three missing atoms were found by varying their coordinates in each *MC* move.

Altomare *et al.*[91] combined *DM* with *SA*. The peaks of the electron density map provided by *DM* are used to reduce the number of *DOF*s of the global optimization algorithm according to three protocols:

a. If triplets or quadruplets of connected peaks are present in the *DM* electron density map, they are in turn associated to all (if any) similar multiplets of the structural model. Each association is followed by an *SA* run with external *DOF*s strictly bounded around their initial values (the position and orientation of the structural model is almost fixed during the *SA* process).
b. Couples of connected peaks are in turn associated to all the couples of bounded atoms of the model. The *SA* run following each association has a parameter space restricted by the requirements that the barycentres of the map and model pairs coincide and that the model preferably rotates around the axis of the pair.
c. Each peak of the map is in turn associated with all the atoms of the model. In this case only the position of the model is fixed, while its orientation and internal conformation has to be found by the *SA* runs.

During the *SA* runs, a combined *CF* is adopted, defined by the product of the usual profile agreement factor (16) by a figure of merit that measures the degree of overlap between the actual configuration and the peaks of the map. After having associated all the multiplets of the model with a corresponding multiplet of the map, according to one of the three protocols, the best solutions resulting from the different *SA* runs are selected and subjected to a local minimization, to improve the location of the assessed model by relaxing the constraints introduced to define the association. It is worth noticing that, with this approach, different *SA* runs can lead to the correct solution, which strongly suggests that the true global minimum has been found.

### 8.4.6 Application to Real Structures

In recent years an increasing number of crystal structures have been solved by application of pure or hybrid global optimization methods applied to powder diffraction data. The most striking applications regard organic structures particularly resistant to traditional methods. The first organic material of

unknown crystal structure to be solved by a direct-space approach was p-$BrC_6H_4CH_2CO_2H$ using the *MC* method.[51] Since then, the algorithmic development of global optimization techniques has lead to the solution of increasingly complex structures, with more non-hydrogen atoms and/or with a larger amount of flexibility. Today most reported structure determinations in the field of organic structures (particularly those of pharmaceutical interest) have employed direct-space techniques for structure solution.

A list of representative organic structures recently solved by the Direct-Space algorithms outlined in this chapter is given in Table 8.1, where the arrows superimposed on the molecular models indicate the unknown torsion angles varied during the minimization procedure. As a general trend, the use of hybrid approaches allows one to undertake more difficult cases, such as structures with a higher number of unknown torsion angles (internal *DOF*s) or non-hydrogen atoms. The solution of the structure in the 7th row of Table 8.1, for example, was originally obtained by a *SA* algorithm[92] by using 18 variable parameters to be optimized: six describing the position and orientation, nine describing torsion angles for the cation and three describing the position of the chloride. With the hybrid approach of Altomare *et al.*[88] the solution was more easily obtained by positioning the isolated chloride ion in correspondence with the highest peak of the *DM* electron density map and by independently minimizing the flexible structural model of the cation using the remaining peaks of the map as pivots. The solution of the Tri-β-peptide shown in the last row of Table 8.1, instead, was reached by using an envelope calculated from the correctly estimated phases of seven low-order reflections.

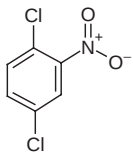
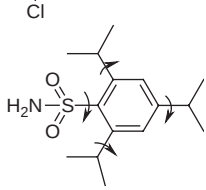
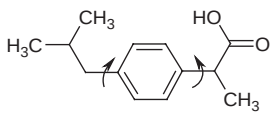
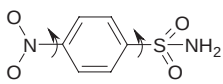
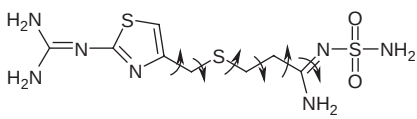
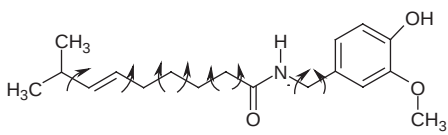
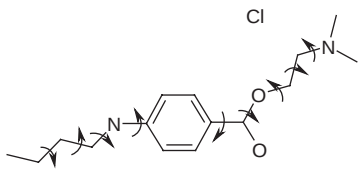
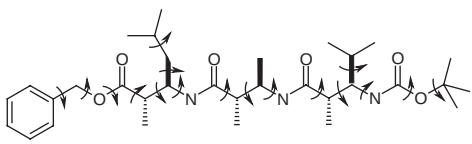
### 8.4.7 Crystal Structure Prediction

A process even more challenging than structure determination is the prediction of a crystal structure without the use of experimental information relevant to that particular structure. This process, called crystal structure prediction (*CSP*), would allow one to announce a crystal structure before any confirmation by chemical synthesis or discovery in nature. The outcome of *CSP* is the prediction of the atomic coordinates of the structural model, together with the space group and cell constant specifications. The relation of *CSP* with powder diffraction relies on the fact that a powder pattern can be calculated using this outcome, which could further be used to identify a real compound not yet characterized.

Current methodologies allow the prediction of some organic molecules with no more than 20 non-H atoms in the asymmetric units, with rigid structure or with a limited amount of flexibility (no more than two torsion angles) and with no more than one molecule per asymmetric unit.[93] All the methods involve three stages:

- Construction of a three-dimensional molecular model either by molecular mechanics methods or by analogy with other *CSD* structures;
- Generation of trial structures with different positions and orientations in asymmetric units of varying dimensions and in various space groups, with eventual modifications of the internal conformation.

**Table 8.1** Recent examples of organic structures solved by global optimization methods applied to powder diffraction data.

| *Molecular structure* | *Internal DOFs* | *Non H atoms* | *Algorithm* | *Ref.* |
|---|---|---|---|---|
|  | 0 | 11 | Grid | *a* |
|  | 4 | 19 | MC | *b* |
|  | 2 | 15 | GA | *c* |
|  | 2 | 13 | DE | 81 |
|  | 6 | 20 | SA | 70 |
|  | 8 | 22 | SA | 67 |
| | | | MC + MD | 82 |
|  | 9 | 20 | SA<br>SA + DM | 92<br>91 |
|  | 17 | 41 | SA + envelope | 85 |

[a] K. Goubitz, E. J. Sonneveld, V. V. Chernyshev, A. V. Yatsenko, S. G. Zhukov, C. A. Reiss and H. Schenk, *Z. Kristallogr.*, 1999, **214**, 469.
[b] M. Tremayne, E. J. MacLean, C. C. Tang and C. Glidewell, *Acta Crystallogr., Sect. B*, 1999, **55**, 1068.
[c] K. Shankland, W. I. F. David, T. Csoka and L. McBride, *Int. J. Pharm.*, 1998, **165**, 117.

- Global optimization through the parameter space using the lattice energy as *CF*. It is generally parameterized according to atom–atom potentials of the type in Equations (18) and (19), but more recent algorithms include more elaborate intermolecular potentials.

Among the currently available methods we quote ZIP-PROMET,[94] which can only handle rigid models and generates the trial structures by a stepwise construction of dimers and layers, UPACK[95] which uses a grid search algorithm, and Polymorph Predictor,[96] which uses a *SA* search.

Among the computer programs producing predictions for inorganic structures we cite GULP,[97] which uses atomic potentials, and GRINSP,[98] which uses a *MC* algorithm whose *CF* depends exclusively on the weighted differences between calculated and ideal interatomic first neighbor distances.

## 8.5 CONCLUSIONS AND OUTLOOK

The last decade has been characterized by the intensive development of new algorithms, which has made easier the crystal structure solution from powder data. Crystal structure determination of compounds with 20–40 atoms in the asymmetric unit is now possible. *DM* advances have been accompanied by the strong evolution of *DST*: their integration may be one of the most promising tools for the near future.

*DM* are particularly suited for the cases in which the molecular geometry is unknown. Their efficiency depends on the number of atoms in the asymmetric unit, on the quality of the diffraction pattern and on the resolution of the data. *DM* will profit from any improvement (deterministic or stochastic) of the full pattern decomposition techniques.

*DST* methods are particularly competitive for organic compounds, which are more resistant to the traditional approaches and whose structural models can be easily guessed. At present, the complexity of crystal structures solved by direct-space methods is essentially limited by the number of *DOF*s that can be handled by the global optimization algorithms within a reasonable amount of time. In prospect, improvement of both search algorithms and computer power may overcome this limitation. The major pitfalls for the use of *DST* are: (a) they are time consuming; (b) they are dependent on the existence of reliable prior structural information. Partially incorrect models may compromise the success of the procedure independent of the computer time spent; (c) they are sensitive to the accuracy of the peak profile parameterization through peak-shape and peak-width functions.[99]

In accordance with the above considerations, hybrid approaches involving *DM* and *DST* seem to have the best prospects in the long run. In this contest, the contribution of *DM* is to reduce the extension of the search space and to allow the optimization of more than one molecule in the asymmetric unit; that of *DST* is to make easier the solution for compounds with only light atoms, even if measured by a home-built diffractometer.

## SYMBOLS AND NOTATION

| | |
|---|---|
| $N$ | number of atoms in the unit cell |
| $f_j$ | scattering factor of the $j$th atom |
| $f_j^o$ | scattering factor of the atom at rest |
| $Z_j$ | atomic number of the $j$th atom |
| $\mathbf{r}_j$ | positional vector of the $j$th atom |
| $B_j$ | isotropic thermal factor of the $j$th atom |
| $F_{\mathbf{h}} = \sum_{j=1}^{N} f_j \exp\left[2\pi i \mathbf{h}\mathbf{r}_j\right]$ | |
| $= \sum_{j=1}^{N} f_j^o \exp\left(-B_j \frac{\sin^2\theta}{\lambda^2}\right) \exp\left(2\pi i \mathbf{h}\mathbf{r}_j\right)$ | structure factor with vectorial index $\mathbf{h} \equiv (h,k,l)$. $\varphi_{\mathbf{h}}$ is its phase. |
| $= \lvert F_{\mathbf{h}} \rvert \exp(i\varphi_{\mathbf{h}})$ | |
| *DM* | Direct Methods |
| *DST* | Direct-Space Techniques |
| *PM* | Patterson Methods |
| *MC* | Monte Carlo |
| *SA* | Simulated Annealing |
| *GA* | Genetic Algorithm |
| *DOF* | Degree of Freedom |
| *CF* | Cost Function |

## REFERENCES


1. C. Giacovazzo, *Direct Phasing in Crystallography: Fundamentals and Applications*, Oxford University Press, Oxford, 1998.
2. D. P. Shoemaker, J. Donohue, V. Schomaker and R. B. Corey, *J. Am. Chem. Soc.*, 1950, **72**, 2328.
3. R. A. Jacobson, J. A. Wunderlich and W. N. Lipscomb, *Acta Crystallogr.*, 1961, **14**, 598.
4. G. M. Sheldrick, in *Crystallographic Computing 5*, ed. D. Moras, A. D. Podjarny and J. C. Thierry, Oxford University Press, Oxford, 1991, p. 145.
5. J. Rius and C. Miravitlless, *J. Appl. Crystallogr.*, 1988, **21**, 224.
6. W. I. F. David, *J. Appl. Crystallogr.*, 1987, **20**, 316.
7. M. A. Estermann, *Nucl. Instrum. Methods Phys. Res. A*, 1995, **354**, 126.
8. A. Altomare, J. Foadi, C. Giacovazzo, A. G. G. Moliterni, M. C. Burla and G. Polidori, *J. Appl. Crystallogr.*, 1998, **31**, 74.
9. A. Altomare, M. C. Burla, M. Camalli, B. Carrozzini, G. Cascarano, C. Giacovazzo, A. Guagliardi, A. G. G. Moliterni, G. Polidori and R. Rizzi, *J. Appl. Crystallogr.*, 1999, **32**, 339.
10. A. Le Bail, H. Duray and J. L. Fourquet, *Math. Res. Bull.*, 1988, **23**, 447.

11. D. Harker and J. S. Kasper, *Acta Crystallogr.*, 1948, **1**, 70.
12. A. Altomare, R. Caliandro, C. Cuocci, I. da Silva, C. Giacovazzo, A. G. G. Moliterni and R. Rizzi, 2004, *Internal Report* Istituto di Cristallografia (C.N.R), sede di Bari, Via Amendola 122/0, 70126 Bari, Italy.
13. G. S. Pawley, *J. Appl. Crystallogr.*, 1981, **14**, 357.
14. A. Altomare, R. Caliandro, C. Cuocci, C. Giacovazzo, A. G. G. Moliterni and R. Rizzi, *J. Appl. Crystallogr.*, 2003, **36**, 906.
15. A. Altomare, R. Caliandro, C. Cuocci, I. da Silva, C. Giacovazzo, A. G. G. Moliterni and R. Rizzi, *J. Appl. Crystallogr.*, 2004, **37**, 204.
16. A. J. C. Wilson, *Nature*, 1942, **150**, 151.
17. A. J. C. Wilson, *Acta Crystallogr.*, 1949, **2**, 318.
18. C. Giacovazzo, *Acta Crystallogr., Sect. A*, 1996, **52**, 331.
19. A. Altomare, J. Foadi, C. Giacovazzo, A. Guagliardi and A. G. G. Moliterni, *J. Appl. Crystallogr.*, 1996, **29**, 674.
20. A. Altomare, M. C. Burla, G. Cascarano, C. Giacovazzo, A. Guagliardi, A. G. G. Moliterni and G. Polidori, *J. Appl. Crystallogr.*, 1996, **29**, 341.
21. W. Cochran, *Acta Crystallogr.*, 1955, **8**, 473.
22. R. von Mises, *Physikalisches Z.*, 1918, **19**, 490.
23. C. Giacovazzo, *Acta Crystallogr., Sect. A*, 1977, **33**, 933.
24. C. Giacovazzo, *Acta Crystallogr., Sect. A*, 1980, **36**, 362.
25. G. Cascarano, C. Giacovazzo, M. Camalli, R. Spagna, M. C. Burla, A. Nunzi and G. Polidori, *Acta Crystallogr., Sect. A*, 1984, **40**, 278.
26. C. Giacovazzo, *Acta Crystallogr., Sect. A*, 1976, **32**, 958.
27. H. A. Hauptman, *Acta Crystallogr., Sect. A*, 1975, **31**, 671.
28. J. Karle and H. Hauptman, *Acta Crystallogr.*, 1956, **9**, 635.
29. G. Germain, P. Main and M. M. Woolfson, *Acta Crystallogr., Sect. B*, 1970, **26**, 274.
30. G. Cascarano, C. Giacovazzo and A. Guagliardi, *Acta Crystallogr., Sect. A*, 1992, **48**, 859.
31. W. Cochran and A. S. Douglas, *Proc. R. Soc. London, Ser. A*, 1957, **243**, 281.
32. A. Altomare, M. C. Burla, M. Camalli, G. L. Cascarano, C. Giacovazzo, A. Guagliardi, A. G. G. Moliterni, G. Polidori and R. Spagna, *J. Appl. Crystallogr.*, 1999, **32**, 115.
33. M. C. Burla, M. Camalli, B. Carrozzini, G. L. Cascarano, C. Giacovazzo, G. Polidori and R. Spagna, *J. Appl. Crystallogr.*, 2003, **36**, 1103.
34. A. Altomare, C. Cuocci, C. Giacovazzo, A. Guagliardi, A. G. G. Moliterni and R. Rizzi, *J. Appl. Crystallogr.*, 2002, **35**, 182.
35. H. A. Hauptman, *Acta Crystallogr., Sect. A*, 1976, **32**, 877.
36. Y. Ferchaux, F. Villani and A. H. Navaza, *Acta Crystallogr., Sect. C*, 1990, **46**, 346.
37. A. Altomare, G. Cascarano, C. Giacovazzo and A. Gagliardi, *J. Appl. Crystallogr.*, 1994, **27**, 1045.
38. http://www.accelrys.com/cerius2/index.html.
39. http://www.cambridgesoft.com/products/.
40. http://www.tripos.com/software/sybyl.html.

41. F. H. Allen and O. Kennard, *Chem. Des. Autom. News*, 1993, **8**, 1.
42. V. Favre-Nicolin and R. Černý, *J. Appl. Crystallogr.*, 2002, **35**, 734.
43. Y. G. Andreev, P. Lightfoot and P. G. Bruce, *J. Appl. Crystallogr.*, 1997, **30**, 294.
44. F. L. Hirshfeld, *Acta Crystallogr., Sect. A*, 1968, **24**, 301.
45. B. E. Lattman, *Acta Crystallogr., Sect. B*, 1972, **28**, 1065.
46. V. V. Chernyshev and H. Schenk, *Z. Kristallogr.*, 1998, **213**, 1.
47. R. B. Hammond, K. J. Roberts, R. Dorcherty, M. Edmondson and R. Gairns, *J. Chem. Soc., Perkin Trans. 2*, 1996, 1527.
48. N. Ma Sciocchi, M. Moret, P. Cairati, A. Sironi, G. Ardizzoia and G. La Monica, *J. Am. Chem. Soc.*, 1994, **116**, 7668.
49. V. V. Chernishev, *Acta Crystallogr., Sect. A*, 2000, **56**, s132.
50. N. Metropolis, A. Rosenbluth, M. Rosenbluth, A. Teller and E. Teller, *J. Chem. Phys.*, 1978, **21**, 1087.
51. K. D. M. Harris, M. Tremayne, P. Lightfoot and P. G. Bruce, *J. Am. Chem. Soc.*, 1994, **116**, 3543.
52. M. Tremayne, B. M. Kariuki, K. D. M. Harris, K. Shankland and K. S. Knight, *J. Appl. Crystallogr.*, 1997, **30**, 968.
53. M. Tremayne, B. M. Kariuki and K. D. M. Harris, *OCTOPUS Monte Carlo Technique for Powder Structure Solution*, 1997, Universities of Birmingham, England, and St Andrews, Scotland.
54. O. J. Lanning, S. Habershon, K. D. M. Harris, R. L. Johnston, B. M. Kariuki, E. Tedesco and G. W. Turner, *Chem. Phys. Lett.*, 2000, **317**, 296.
55. V. Brodski, R. Peshar and H. Schenk, *J. Appl. Crystallogr.*, 2003, **36**, 239.
56. M. Born and A. Lande, *Sitzungsber. Preuss. Akad. Wiss. Berlin*, 1918, **45**, 1048.
57. A. K. Rappé, C. J. Casewit, K. S. Colwell, W. A. Goddard III and W. M. Skiff, *J. Am. Chem. Soc.*, 1992, **114**, 10024.
58. A. A. Coelho, *J. Appl. Crystallogr.*, 2000, **33**, 899.
59. M. Born and J. E. Mayer, *Z. Phys.*, 1932, **75**, 1.
60. H. Putz, J. C. Schon and M. Jansen, *J. Appl. Crystallogr.*, 1999, **32**, 864.
61. G. Bergerhoff, R. Hundt, R. Sievers and I. D. Brown, *J. Chem. Inf. Comput. Sci.*, 1983, **23**, 66.
62. H.-P. Hsu, S. C. Lin and U. H. E. Hansmann, *Acta Crystallogr., Sect. A*, 2002, **58**, 259.
63. S. Kirkpatrick and C. D. Gelatt, Jr. and M. P. Vecchi, *Science*, 1983, **220**, 671.
64. S. Kirkpatrick, *J. Stat. Phys.*, 1984, **34**, 975.
65. S. Geman and D. Geman, *IEEE Trans. Pattern Anal. Mach. Intell.*, 1984, **PAMI–6**, 721.
66. Y. G. Andreev and P. G. Bruce, *J. Chem. Soc., Dalton Trans.*, 1998, 4071.
67. W. I. F. David, K. Shankland and N. Shankland, *Chem. Commun.*, 1998, 931.

68. W. I. F. David, K. Shankland, J. Cole, S. Maginn, W. D. S. Motherwell and R. Taylor, *DASH User Manual*., 2001, Cambridge Crystallographyc Data Centre, Cambridge, UK.
69. A. J. Markvardsen, W. I. F. David and K. Shankland, *Acta Crystallogr., Sect. A*, 2002, **58**, 316.
70. K. Shankland, L. McBride, W. I. F. David, N. Shankland and G. Steele, *J. Appl. Crystallogr*., 2002, **35**, 443.
71. A. Leach, in *Molecular Modelling, Principles and Applications*, Addison Wesley Longman Ltd., London, 1996.
72. G. E. Engel, S. Wilke, O. König, K. D. M. Harris and F. J. J. Leusen, *J. Appl. Crystallogr*., 1999, **32**, 1169.
73. A. A. Coelho, TOPAS Version 3.1, 2003, Bruker AXS GmbH, Karlsruhe, Germany.
74. A. Le Bail, *Mater. Sci. Forum*, 2001, **378–381**, 65.
75. D. E. Goldberg, in *Genetic Algorithms in Search, Optimization, and Machine Learning*, Addison-Wesley, New York, 1989.
76. B. M. Kariuki, H. Serrano-González, R. L. Johnston and K. D. M. Harris, *Chem. Phys. Lett*., 1997, **280**, 189.
77. K. Shankland, W. I. F. David and T. Csoka, *Z. Kristallogr*., 1997, **212**, 550.
78. K. D. M. Harris, R. L. Johnston and B. M. Kariuki, *Acta Crystallogr., Sect. A*, 1998, **54**, 632.
79. G. W. Turner, E. Tedesco, K. D. M. Harris, R. L. Johnston and B. M. Kariuki, *Chem. Phys. Lett*., 2000, **321**, 183.
80. R. Storn and K. V. Price, *J. Global Optimization*, 1997, **11**, 341.
81. M. Tremayne, C. C. Seaton and C. Glidewell, *Acta Crystallogr., Sect. B*, 2002, **58**, 823.
82. J. C. Johnston, W. I. F. David, A. J. Markvardsen and K. Shankland, *Acta Crystallogr., Sect. A*, 2002, **58**, 441.
83. S. Brenner, L. B. McCusker and C. Baerlocher, *J. Appl. Crystallogr*., 1997, **30**, 1167.
84. S. Brenner, "Structure Envelopes and their Application in Structure Determination from Powder Diffraction Data", PhD Thesis, 1999, ETH, Zürich.
85. S. Brenner, L. B. McCusker and C. Baerlocher, *J. Appl. Crystallogr*., 2002, **35**, 243.
86. A. Altomare, C. Giacovazzo, A. Guagliardi, A. G. G. Moliterni and R. Rizzi, *J. Appl. Crystallogr*., 2000, **33**, 1305.
87. A. Altomare, R. Caliandro, M. Camalli, C. Cuocci, C. Giacovazzo, A. G. G. Moliterni and R. Rizzi, *J. Appl. Crystallogr*., 2004, **37**, 1025.
88. A. Altomare, C. Cuocci, C. Giacovazzo, A. G. G. Moliterni and R. Rizzi, *J. Appl. Crystallogr*., 2002, **35**, 422.
89. M. A. Estermann, L. B. McCusker and C. Baerlocher, *J. Appl. Crystallogr*., 1992, **25**, 539.
90. Y. Tanahashi, H. Nakamura, S. Yamazaki, Y. Kojima, H. Saito, T. Ida and H. Toraya, *Acta Cyrstallogr., Sect. B*, 2001, **57**, 184.

91. A. Altomare, R. Caliandro, C. Giacovazzo, A. G. G. Moliterni and R. Rizzi, *J. Appl. Crystallogr.*, 2003, **36**, 230.
92. H. Nowell, J. P. Attfield, J. C. Cole, P. J. Cox, K. Shankland, S. J. Manginn and W. D. S. Motherwell, *New J. Chem.*, 2002, **26**, 469.
93. W. D. S. Motherwell, H. L. Ammon, J. D. Dunitz, A. Dzyabchenko, P. Erk, A. Gavezzotti, D. W. M. Hofmann, F. J. J. Leusen, J. P. M. Lommerse, W. T. M. Mooij, S. L. Price, H. Scheraga, B. Schweizer, M. U. Schmidt, B. P. van Eijck, P. Verwer and D. E. Williams, *Acta Crystallogr., Sect. B*, 2002, **58**, 647.
94. A. Gavezzotti, *J. Am. Chem. Soc.*, 1991, **113**, 4622.
95. B. P. van Eijck and J. Kroon, Acta Crystallogr., *Sect. B*, 2000, **56**, 535.
96. P. Verwer and F. J. J. Leusen, *Rev. Comput. Chem.*, 1998, **12**, 327.
97. J. D. Gale, *J. Chem. Soc., Faraday Trans.*, 1997, **93**, 629.
98. A. Le Bail, *IUCr Comp. Comm. Newsletter*, 2004, **4**, 37.
99. K. D. M. Harris, M. Tremayne and B. M. Kariuki, *Angew. Chem., Int. Ed.*, 2001, **40**, 1626.

CHAPTER 9

# Rietveld Refinement

R. B. VON DREELE

IPNS/APS Argonne National Laboratory, Argonne, IL, USA

## 9.1 INTRODUCTION

A polycrystalline powder can be represented in reciprocal space as a set of nested spherical shells positioned with their centers at the origin[1] (Figure 9.1). These shells arise from the reciprocal lattice points from the myriad (*e.g.* $\approx 10^9$ mm $^3$ for 1 μm crystallites) of small crystals, ideally with random orientation, in the sample (Chapter 1). Their magnitude is related to the crystalline structure factors as well as the symmetry driven overlaps (*i.e.* reflection multiplicities) and are affected by systematic effects (*e.g.* Lorentz and polarization, absorption, extinction and preferred orientation). The structure factors and their systematic effects are discussed elsewhere in this volume (Chapter 3). These shells have some thickness or broadening from instrumental effects and the characteristics of the crystalline grains themselves; details are given in Chapters 5, 6 and 13. An experimentally measured powder diffraction pattern is a scan through this suite of shells, which by its nature, is a smooth curve consisting of a sequence of peaks resting upon a slowly varying background.

Techniques for obtaining these data are discussed in Chapter 2.

Early data analysis attempted to extract values of the individual structure factors from peak envelopes and then apply standard single crystal methods to obtain structural information. This approach was severely limited because the relatively broad peaks in a powder pattern resulted in substantial reflection overlap and the number of usable structure factors that could be obtained in this way was very small. Consequently, only very simple crystal structures could be examined by this method. For example, the neutron diffraction study of defects in $CaF_2$-$YF_3$ fluorite solid solutions[2] used 20 reflection intensities to determine values for eight structural parameters. To overcome this limitation, H. M. Rietveld[3,4] realized that a neutron powder diffraction pattern is a smooth curve that consists of Gaussian peaks on top of a smooth background

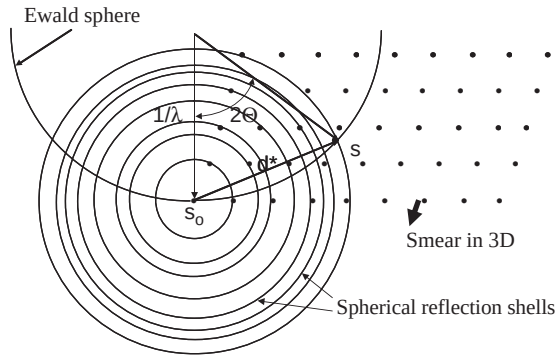



**Figure 9.1** Reciprocal space construction for a powder diffraction experiment. The myriad reciprocal lattice points for the crystallites combine to form nested spherical shells centered at the reciprocal space origin.

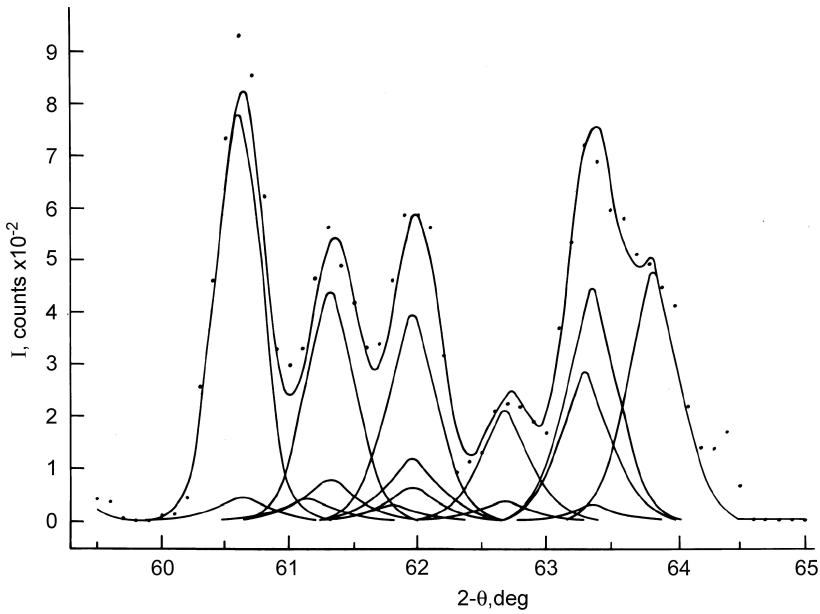



**Figure 9.2** Portion of a powder diffraction pattern showing the contributions to the calculated pattern from 15 reflections above a small flat background.

and that the best way of extracting the maximum information from it was to write a mathematical expression to represent the observed intensity at every step in this pattern:

$$Y_c = Y_b + \sum Y_{\mathbf{h}} \tag{1}$$

This expression has both a contribution from the background ($Y_b$) and each of the Bragg reflections ($Y_{\mathbf{h}}$; $\mathbf{h} = hkl$) that are near the powder pattern step (Figure 9.2).

Each of these components is represented by a mathematical model that embodies both the crystalline and noncrystalline features of a powder diffraction experiment.

The adjustable parameters for this model are refined by a least-squares minimization of the weighted differences between the observed and calculated intensities. The study by Loopstra and Rietveld[5] on $Sr_3UO_6$ with 42 structural parameters clearly showed the power of this technique compared to the integrated intensity methods used earlier. This approach to the analysis of powder patterns has been so successful[6 12] that it led to a renaissance in powder diffraction and this technique of treating powder diffraction data is now known as "Rietveld refinement."

## 9.2 RIETVELD THEORY

### 9.2.1 Least Squares

Since a powder diffraction pattern is a set of peaks, some overlapped, superimposed on a smooth and slowly varying background, a Rietveld refinement can be thought of as a very complex curve fitting problem. The model function [Equation (1)] is parameterized by both the crystal structure (atomic coordinates, thermal displacements and site occupancies) and by the diffraction experiment (unit cell, peak profile broadening, *etc*.) *via* mostly nonlinear and transcendental analytical expressions. Since the powder diffraction pattern is usually obtained *via* particle (X-ray photon or neutron) counting techniques (Chapter 2), the intensities have a Poisson distribution about their expected value. Given sufficient counts ($>20$) in every powder profile step this distribution is indistinguishable from a Gaussian one and in any case has a well-defined 2nd moment. Consequently, when the number of observations (powder profile points in this case) exceeds the number of parameters, a minimization of:

$$M = \sum w(Y_o - Y_c)^2 \tag{2}$$

by least-squares will give parameter estimates of minimum variance in any linear combination.[13] The weight, $w$, is computed from the variance in $Y_o$ and it is generally assumed that there are no nonzero covariances between different $Y_o$ across the powder pattern. The calculated powder profile intensity, $Y_c$, is given by:

$$Y_c = K|F_{\mathbf{h}}|^2 H(\Delta T_{\mathbf{h}}) \tag{3}$$

where $K$ is the product of the various correction and scaling factors to the reflection intensities $|F_{\boldsymbol{h}}|^2$ (Chapter 3) and $H(\Delta T_{\mathbf{h}})$ is the value of the profile function for the location of the profile point relative to the reflection Bragg position (Chapters 5, 6 and 13).

One can think of the minimization Equation (2) as describing a slightly noisy multidimensional surface with a very small number of very deep minima that correspond to the possible solutions to the problem. Notably, the minima are

not always equivalent; some may be "false minima" and describe incorrect solutions.

Since Equation (3) is nonlinear and transcendental (*i.e.* invokes trigonometric functions), the usual linear version of least-squares analysis can not be used. The method is to approximate the expression for $Y_c$ as a Taylor series and only retain the first term:

$$Y_c(p_i) = Y_c(a_i) + \sum_i \frac{\partial Y_c}{\partial p_i} \Delta p_i \tag{4}$$

The minimum is found from the first derivative of Equation (2):

$$\sum w(Y_o - Y_c) \frac{\partial Y_c}{\partial p_j} = 0 \tag{5}$$

or by substitution:

$$\sum w \left[ \Delta Y - \sum_i \frac{\partial Y_c}{\partial p_i} \Delta p_i \right] \frac{\partial Y_c}{\partial p_j} = 0 \quad \Delta Y = Y_o - Y_c(a_i) \tag{6}$$

After rearrangement:

$$\sum w \frac{\partial Y_c}{\partial p_j} \left( \sum_i \frac{\partial Y_c}{\partial p_i} \Delta p_i \right) = \sum w \Delta Y \frac{\partial Y_c}{\partial p_j} \tag{7}$$

This is the suite of normal equations; there is one for each parameter shift, $\Delta p_i$. By accumulating terms, these equations can be given, in matrix form, from the following:

$$a_{i,j} = \sum w \frac{\partial Y_c}{\partial p_i} \frac{\partial Y_c}{\partial p_j} \quad x_j = \Delta p_j \quad v_i = \sum w(\Delta Y) \frac{\partial Y_c}{\partial p_i} \tag{8}$$

to give:

$$\mathbf{Ax} = \mathbf{v} \tag{9}$$

This matrix equation is solved for the desired parameter shifts by:

$$\mathbf{A}^{-1}\mathbf{Ax} = \mathbf{A}^{-1}\mathbf{v} \quad \mathbf{x} = \mathbf{A}^{-1}\mathbf{v} = \mathbf{Bv} \quad x_j = \Delta p_j \tag{10}$$

The inverse matrix, **B**, is normalized by the reduced $\chi^2$ [Equation (13)] to give the variance-covariance matrix. The square roots of the diagonal elements of this normalized matrix are the estimated errors in the values of the shifts and, thus, those for the parameters themselves. These error estimates are based solely on the statistical errors in the original powder diffraction pattern intensities and can not accommodate the possible discrepancies arising from systematic flaws in the model. Consequently, the models used to describe the powder diffraction profile must accurately represent a close correspondence to

the scattering process that gives rise to features in the observed pattern to avoid significant systematic errors.

The result of a Taylor series approximation is that the computed shifts, $\Delta p_i$, is not accurate yielding a fully minimized solution to the problem, but are a (hopefully) better approximation. Consequently, the new parameter values are used for a subsequent refinement cycle; this process is repeated until the parameter shifts are less than some fraction of their estimated errors as obtained from the diagonal elements of the **B** matrix.

Implicit in this approach is that an initial estimate of all the parameters [$a_i$, Equation (4)] must be provided beforehand. These estimates must place the value of the minimization function within one (preferably the "best") well in the $M$-surface.

The quality of the least squares refinement is indicated by some residual functions:

$$R_p = \frac{\sum |Y_o - Y_c|}{\sum Y_o} \tag{11}$$

and:

$$R_{wp} = \sqrt{\frac{M}{\sum w Y_o^2}} \tag{12}$$

Notice that the "weighted" residual, $R_{wp}$, contains the factor, $M$, that is minimized by the least squares; thus it is the only statistically relevant residual. The reduced $\chi^2$ or "goodness of fit" is defined from the minimization function as:

$$\chi^2 = M/(N_{\text{obs}} - N_{\text{var}}) \tag{13}$$

and the "expected $R_{wp}$" from:

$$R_{wp(\text{exp})} = R_{wp} \Big/ \sqrt{\chi^2} \tag{14}$$

If the weights for the observations are chosen "properly" (*i.e.* as reciprocal variances) then the value of reduced $\chi^2$ will be somewhat greater than unity for an optimal refinement. Misscaled variances will drive this value away from unity without affecting the value of $R_{wp}$. As recently noted by Mercier *et al.*,[14,15] inversion of the **A** matrix developed in a Rietveld refinement is frequently plagued by poor numerical conditioning due to the extreme range of the individual partial derivatives. This had been noted for some time by many developers of the Rietveld refinement codes (*e.g.* GSAS by Larson and Von Dreele[16]) and one solution is to employ a normalization process to the matrix before inversion. The simplest is to apply the following:

$$A'_{ij} = \frac{A_{ij}}{\sqrt{A_{ii} A_{jj}}} \tag{15}$$

After inversion of $\mathbf{A}'$, the required inverse matrix is obtained by applying the same correction to every element:

$$B_{ij} = \frac{B'_{ij}}{\sqrt{A_{ii}A_{jj}}} \tag{16}$$

This eliminates those least squares instabilities in Rietveld refinements that arise from rounding error limitations in computer calculations.

## 9.3 CONSTRAINTS AND RESTRAINTS

### 9.3.1 Introduction

A crystal structure is described by a collection of parameters that give the arrangement of the atoms, their motions and the probability that each atom occupies a given location. These parameters are the atomic fractional coordinates, atomic displacement or thermal parameters, and occupancy factors. A scale factor then relates the calculated structure factors to the observed values. This is the suite of parameters usually encountered in a single crystal structure refinement. In the case of a Rietveld refinement an additional set of parameters describes the powder diffraction profile *via* lattice parameters, profile parameters and background coefficients. Occasionally other parameters are used; these describe preferred orientation or texture, absorption and other effects. These parameters may be directly related to other parameters *via* space group symmetry or by relations that are presumed to hold by the experimenter. These relations can be described in the refinement as "constraints" and as they relate the shifts, $\Delta p_i$, in the parameters, they can be represented by

$$\Delta p'_j = k_{ij}\, \Delta p_i \tag{17}$$

The $k_{ij}$ are then the elements of a sparse rectangular matrix that relates the suite of parameters of interest to a smaller set that are actually refined. This reduces the number of partial derivatives *via*:

$$\frac{\partial Y_c}{\partial p'_i} = \frac{1}{k_{ij}} \frac{\partial Y_c}{\partial p_j} \tag{18}$$

In their simplest form, these constraints can be used for atomic sites on special positions (*e.g.* *x*,*x*,*x* positions in cubic space groups) where there are special relationships between the individual atomic coordinates and also among the individual anisotropic thermal motion parameters (*e.g.* $U_{11} = U_{22} = U_{33}$ and $U_{12} = U_{13} = U_{23}$ for cubic *x*,*x*,*x* sites).

### 9.3.2 Rigid Body Refinement

For large structures, the number of parameters required to describe them is greater than can be determined from the diffraction data obtained in a single experiment. This can be resolved by providing additional information to the

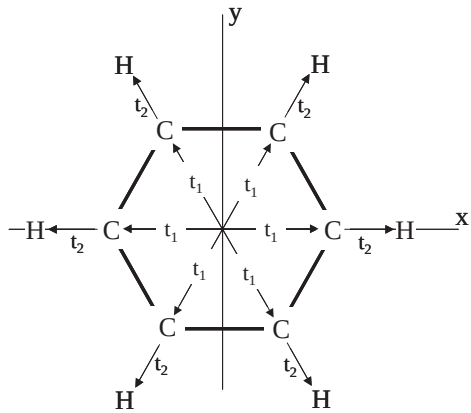



**Figure 9.3** A benzene ring developed in Cartesian coordinates by two translations, one to place the C atoms and the other to further place the H atoms.

refinement problem. Very frequently some part of the structure has well-known stereochemical features. For example, it may have one (or more) phenyl (-$C_6H_5$) groups, which can be assumed to be flat with uniform C–C, and C–H distances. This information can be provided by various techniques, depending on the effect one desires as well as the level of confidence in these data. One way is to describe the molecular fragment as a ''rigid body'' that is oriented and positioned within the crystal structure. The fragment is first described in a local Cartesian coordinate system. Although this could be a simple list of *xyz* coordinates, an alternative description can be made by successive translations of the atoms from the Cartesian origin. For example, a benzene ring can be built by two translations for the six carbon atoms and the six hydrogen atoms starting from the centroid of the molecule (Figure 9.3).

In the first step the six C atoms and six H atoms are translated by $t_1$ along the vectors (1,0,0), (cos60,sin60,0), (−cos60,sin60,0), (−1,0,0), (−cos60,−sin60,0), (cos60,–sin60,0). For the second step only the H atoms are translated by $t_2$ along these vectors. The two translations can potentially be parameters in the refinement, and this model preserves the $D_{6h}$ symmetry of the benzene molecule. Alternative descriptions are possible in which the group is built by a different sequence of translation scales and vectors from a different choice of origin that gives a different flexibility to the model. For example, the $C_6H_5$ phenyl group may be built from the C atom that forms the attachment point with a sequence of four translations that follow the bonding pattern and allow the three types of C–C bond lengths and the C–H bond length to be refined separately. In more general terms the position of any atom, $\mathbf{X} = (X,Y,Z)$, in a rigid body is given by:

$$\mathbf{X} = \sum_{i=1}^{N_t} t_i \mathbf{v}_i \tag{19}$$

where the $t_i$ are the translation scalars and $\mathbf{v}_i$ are the associated vectors.

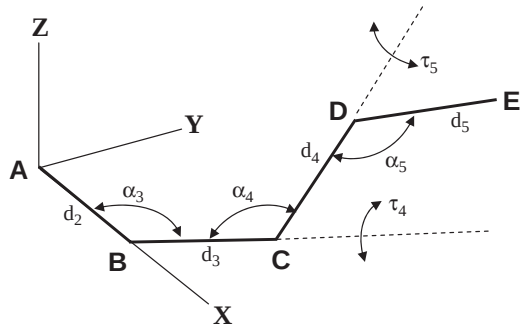



**Figure 9.4** A Z matrix representation of a molecular chain.

The Cartesian atom coordinates can also be developed by a sequence of bond translations, each with associated bond and torsion angles with respect to previously placed atoms. This "Z-matrix" description[17] is most useful for relatively short chains of atoms; in long chains small changes in bond or torsion angles at one end will induce very large atom position shifts at the other. It also is not easily applied to cyclic molecules. For the Z-matrix scheme in Figure 9.4, the first atom (A) is placed at the Cartesian origin and the second (B) is placed along the X axis at the presumed bond distance ($d_2$). The third atom (C) is placed in the X,Y plane at the presumed bond distance ($d_3$) from B and the presumed angle ($\alpha_3$) with respect to the B–A bond. The fourth atom (D) is then placed at a bond distance ($d_4$) from the previously placed one, the bond angle ($\alpha_4$) from the previous two and at a torsion angle ($\tau_4$) with respect to the previous three atoms. Succeeding atoms are placed *via* selection of three parameters $d_n$, $\alpha_n$, and $\tau_n$.

The rigid body is then oriented in preparation for inclusion within the crystallographic unit cell by a sequence of rotations. These are defined as rotations of the coordinate system about the Cartesian axes {X,Y,Z}:

$$R_x(\alpha_1) = \begin{pmatrix} 1 & 0 & 0 \\ 0 & \cos\alpha_1 & -\sin\alpha_1 \\ 0 & \sin\alpha_1 & \cos\alpha_1 \end{pmatrix} \quad \text{for a rotation } \alpha_1 \text{ about the X axis} \qquad (20a)$$

$$R_y(\alpha_2) = \begin{pmatrix} \cos\alpha_2 & 0 & \sin\alpha_2 \\ 0 & 1 & 0 \\ -\sin\alpha_2 & & \cos\alpha_2 \end{pmatrix} \quad \text{for a rotation } \alpha_2 \text{ about the Y axis} \qquad (20b)$$

$$R_z(\alpha_3) = \begin{pmatrix} \cos\alpha_3 & -\sin\alpha_3 & 0 \\ \sin\alpha_3 & \cos\alpha_3 & 0 \\ 0 & 0 & 1 \end{pmatrix} \quad \text{for a rotation } \alpha_3 \text{ about the Z axis} \qquad (20c)$$

The order and number of these rotations is selected to properly orient the group within the crystal structure. Although only three rotations at most are required for any conceivable molecular orientation, additional rotations could be used to allow "preorientation" of a group so that a refined rotation can occur about some "natural" direction in the crystal structure. The rigid body coordinates then transform by:

$$\mathbf{X}' = \mathrm{R_a}(\alpha_3)\mathrm{R_a}(\alpha_2)\mathrm{R_a}(\alpha_1)\mathbf{X} \text{ where a is one of X, Y or Z} \tag{21}$$

The coordinates of oriented rigid body group are then transformed into the crystallographic coordinate system defined by the unit cell axes {**a,b,c**} and then the origin of the group is translated to the appropriate location within the unit cell. Given the crystal to Cartesian transformation matrix:

$$\mathbf{L} = \begin{pmatrix} a & b\cos\gamma & c\cos\beta \\ 0 & b\sin\alpha^*\sin\gamma & 0 \\ 0 & -b\cos\alpha^*\sin\gamma & c\sin\beta \end{pmatrix} \tag{22}$$

the rigid body atom locations in the crystal structure are given by:

$$\mathrm{x} = \mathrm{L}\ {}^1\mathrm{X}' + \mathrm{t} \tag{23}$$

Thus, a small set of parameters can be used to describe the position and orientation of a large group of atoms. Equations (19–23) are used to form elements of the sparse matrix that transforms the set of atomic coordinate parameters into a smaller set of variables determined by the least squares refinement *via* Equations (17) and (18).

### 9.3.3 Rigid Body Refinement of $Fe[OP(C_6H_5)_3]_4Cl_2FeCl_4$

As an example we describe the refinement of $Fe[OP(C_6H_5)_3]_4Cl_2FeCl_4$, employing rigid body descriptions of the various molecular fragments that make up this structure.[18] As seen in Figure 9.5, this structure is composed of two molecular fragments; one is a simple $FeCl_4$ tetrahedron and the other is a six-coordinate iron complex with four triphenylphosphine oxide, $OP(C_6H_5)_3$, ligands and two chlorides. A "free" refinement of this crystal structure requires the adjustment of the positions of 88 non-hydrogen atoms or 264 parameters. The X-ray diffraction data obtained from this material with $CoK_\alpha$ radiation on a laboratory instrument was insufficient ($d_{min} = 1.39$ Å) to allow a meaningful refinement for this problem. Thus, a rigid body description was constructed using the software program GSAS[16] that fixes the stereochemistry of those parts of this structure that are assumed to be well known from comparison with other structures.

The $FeCl_4$ anion is assumed to have an idealized tetrahedral symmetry, thus forming one rigid body with only its position, angular orientation and the Fe–Cl bond length as adjustable parameters (Figure 9.6). Thus 15 atomic coordinates are replaced by seven rigid body parameters. In this figure the five atoms are represented by five vectors, one null for the Fe atom and four that

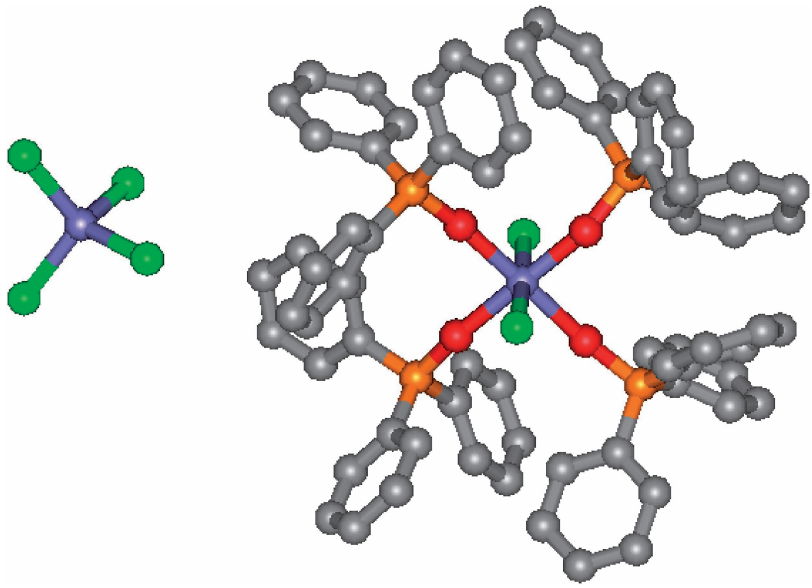
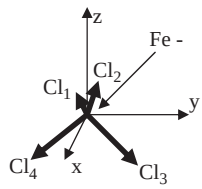


**Figure 9.5** Molecular structure of $Fe[OP(C_6H_5)_3]_4Cl_2^{+}FeCl_4^{-}$.




1 translation, 5 vectors

Fe [ 0, 0, 0 ]

$Cl_1$ [ sin(54.75), 0, cos(54.75)]

$Cl_2$ [ -sin(54,75), 0, cos(54.75)]

$Cl_3$ [ 0, sin(54.75), -cos(54.75)]

$Cl_4$ [ 0, -sin(54.75), -cos(54.75)]

D=2.1Å

**Figure 9.6** Rigid body description of $FeCl_4^{-}$ anion.

point to the vertices of a tetrahedron over a distance of 2.1 Å for the four Cl atoms. This distance will be adjusted in the rigid body refinement. The Fe atom is then at the origin of this rigid body and six parameters will be used to describe its location and orientation.

A more complex model is required for the triphenylphosphine oxide group (Figure 9.7). Two rigid bodies are defined both with the P atom as their origin. The first consists of just the P and O atoms as a simple linear group oriented along the positive Cartesian Z-axis; the P–O bond (1.4 Å) is refined. The second describes the position of the six C atoms relative to the P atom position arranged along the negative Z-axis; the P–C (1.6 Å) and C–C (1.38 Å) bond lengths are refined. This choice of common origin is important as the rigid body translations and rotations are all defined about their respective origins.

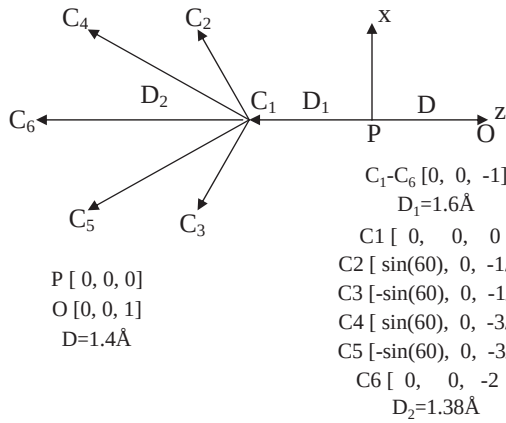



**Figure 9.7** Rigid body descriptions of the PO and $PC_6$ groups.

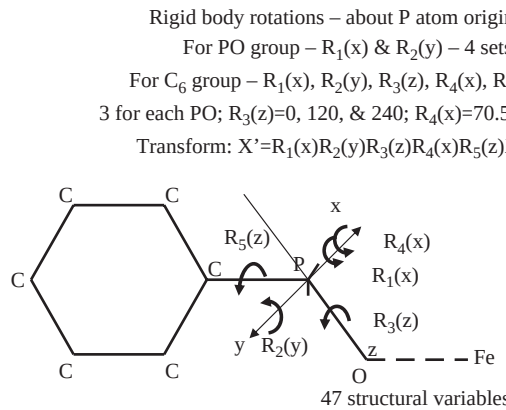



**Figure 9.8** Assembly of PO and $C_6$ rigid bodies with applied rotations.

Each triphenylphosphine oxide ligand is then assembled from one PO and three $C_6$ rigid bodies (Figure 9.8). The first two rotations, $R_1(x)$ and $R_2(y)$ position the OP group about the P atom position such that the O atom forms a reasonable bond with Fe; there are four sets of these for the four $OP(C_6)_3$ ligands giving eight parameters. Each P atom has an $x,y,z$ crystallographic coordinate for 12 more parameters. The three additional rotations $R_3(z)$, $R_4(x)$ and $R_5(z)$ are applied to each of the three $C_6$ groups to position them about each P atom. The $P_5(z)$ rotations describe the "twist" of each $C_6$ group about its P–C bond; these are 12 more parameters. The initial $P_4(x)$ rotation is 70.55° and $P_3(z)$ rotations are 0°, 120° and 240° apart to give tetrahedral stereochemistry for the $POC_3$ bonds. These are refined so that the $P_4(x)$ rotation is identical for all four $OP(C_6)_3$ ligands and the three $P_3(z)$ rotations on each ligand retain their relative 120° differences; this yields five more parameters. Figure 9.8 shows the

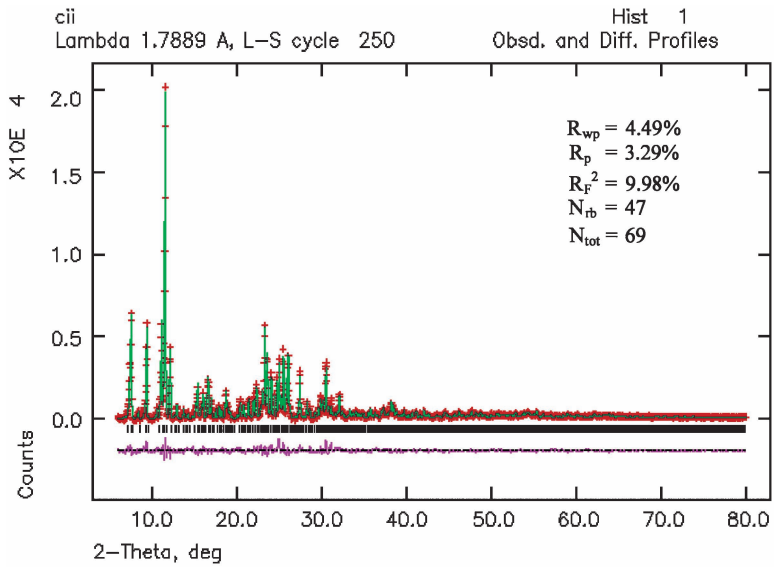



**Figure 9.9** Result of final rigid body refinement of $Fe[OP(C_6H_5)_3]_4Cl_2[FeCl_4]$. Observed profile is indicated by (+), calculated and difference curves are shown and reflection positions are marked as (|).

order of the coordinate transforms for the five rotations. These can be understood easily by considering them in reverse ($R_5$ to $R_1$); the rotation $R_5$ twists the $C_6$ group about the P–C bond, $R_4$ then tilts the $C_6$ group to a near tetrahedral angle (70.6°), $R_3$ then positions each of the three $C_6$ groups on the three legs of the tetrahedron, $R_2$ and $R_1$ then position the $P(C_6)_3$ on the complex with iron. With this model the structure is described by 47 rigid body parameters with an additional nine $x,y,z$ parameters (for the $FeCl_2$ part of the complex) compared to 264 required for a completely free refinement of 88 atoms. Figure 9.9 shows the powder profile fit with this model.

### 9.3.4 Stereochemical Restraint Refinement

An alternative method for providing the additional information to a structure refinement is to include as additional observations the values and associated estimates of their errors of various stereochemical features. These additional observations provide additional terms to the least-squares minimization function:

$$M = \sum w_{Yi}(Y_{oi} - Y_{ci})^2 + f_a \sum w_{ai}(a_{oi} - a_{ci})^2 + f_d \sum w_{di}(d_{oi} - d_{ci})^2 + f_p \sum w_{pi}(-p_{ci})^2 \quad (24)$$

For the minimization function in a Rietveld refinement including stereochemical restraints, the terms are: $Y$ – powder pattern, $a$ – bond angles,

*d* – bond distances, and *p* – deviations from best plane. The weight factors, ***f***, are chosen to balance the various contributions and prevent any excess impact by any suite of terms. The individual observation weights are determined from the standard uncertainty associated with each observation.

Unlike the rigid body formulation, the use of restraints does not result in a reduction in the number of parameters used to describe a crystal structure, but it includes additional stereochemical information to augment the suite of diffraction observations (*i.e.* the powder pattern), thus permitting a full refinement of the structure.

For the $Fe[OP(C_6H_5)_3]_4FeCl_4$ example considered above, bond length restraints for six Fe–Cl (2.21 Å), four P–O (1.48 Å), 12 P–C (1.75 Å), and 72 C–C (1.36 Å) can be used along with tetrahedral angles (109.5°) for the 12 O–P–C, 12 C–P–C and six Cl–Fe–Cl angles and the hexagonal value (120°) for 72 C–C–C and 24 P–C–C angles. In addition the six C atoms in each phenyl ring can be considered to be coplanar, giving an additional 72 restraints on their positions. Thus, a total of 290 stereochemical restraint terms are added to the minimization function for the refinement of the 264 atomic coordinates needed for the 88 atoms in this complex. The powder profile fit for this refinement is shown in Figure 9.10 and a comparison between the two refinements is shown in Figure 9.11. A closer fit as indicated by the profile residuals was obtained here, most likely due to the larger number of parameters in the refinement. The results are very similar; the small differences arise from the difference between the rigid

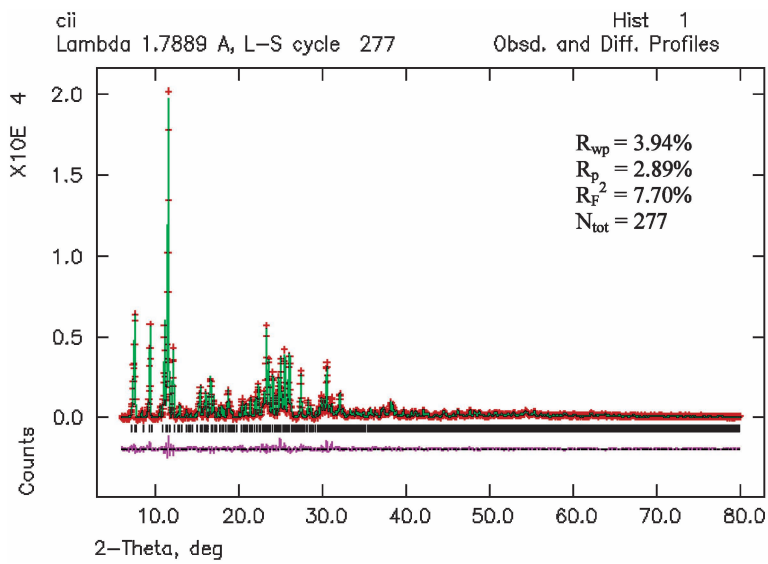



**Figure 9.10** Result of final stereochemical restraint refinement of the complex $Fe[OP(C_6H_5)_3]_4Cl_2[FeCl_4]$. Observed profile is indicated by (+), calcu lated and difference curves are shown and reflection positions are marked as (|).

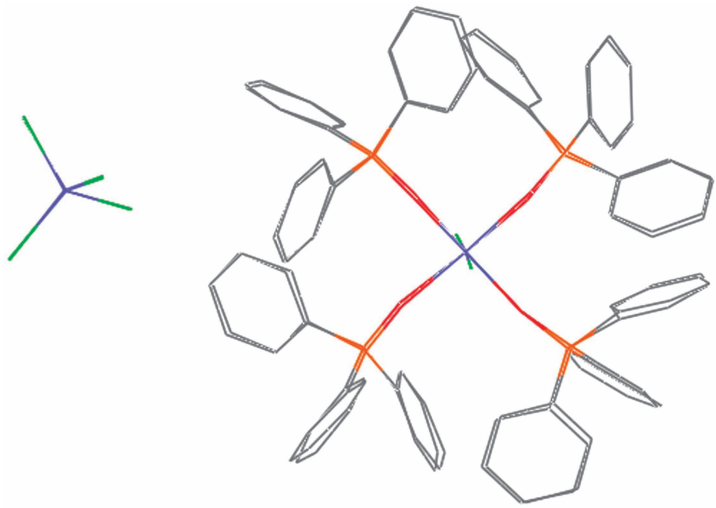


**Figure 9.11** Superposition of the rigid body and stereochemical restrained refinements of $Fe[OP(C_6H_5)_3]_4Cl_2[FeCl_4]$.

body model and the stereochemical restraint model. These constrain/restrain the refinement in slightly different ways.

### 9.3.5 Protein Powder Refinements

The crystal structures of proteins represent an extreme in the number of atom positions needed to describe them compared to those structures more commonly studied by powder diffraction. For example, the well-known tetragonal crystal structure of hen egg white lysozyme has 1001 nonhydrogen atoms within the protein molecule; another 100 or so water molecules and salt ions are also present. This gives over 3000 atomic $x,y,z$ coordinates. Nonetheless, a Rietveld refinement of these structures from powder diffraction data can be performed by extending the suite of restraints to include all stereochemical features that show characteristic values.[19,20] The suite of restraints given in Equation (24) is then:

$$\begin{aligned} M = &\sum w_{Yi}(Y_{oi} - Y_{ci})^2 + f_a \sum w_{ai}(a_{oi} - a_{ci})^2 + f_d \sum w_{di}(d_{oi} - d_{ci})^2 \\ &+ f_p \sum w_{pi}(-p_{ci})^2 + f_x \sum w_{xi}(x_{oi} - x_{ci})^2 + f_v \sum w_{vi}(v_{oi} - v_{ci})^4 \\ &+ f_h \sum w_{hi}(h_{oi} - h_{ci})^2 + f_t \sum w_{ti}(-t_{ci})^2 + f_R \sum w_{Ri}(-R_{ci})^2 \end{aligned} \quad (25)$$

with additional terms for chiral volume, $x$, van der Waals "bump", $v$, hydrogen bond, $h$, torsion angle, $t$, and torsion angle pair, $R$, restraints. The characteristic values for these restraints are obtained from the results of high-resolution single-crystal protein structures[21] and those of small peptides.[22] The torsion angle and paired torsion angle restraints present a particular difficulty as these

have no single preferred value (unlike, for example, a bond angle).[23] These restraints can be formulated as pseudopotentials[19,20,24] determined from the observed distribution of these values in high-resolution protein structures. This allows the restraint to have multiple preferred values and can accommodate the coupling of the two torsion angles, $\phi$ and $\psi$, as present in, for example, the protein backbone.[25]

## ACKNOWLEDGEMENT

This work was supported by the U. S. DOE/OS/BES under Contract No. DE-AC-02-06CH11357.

## REFERENCES

1. B. E. Warren, *X-ray Diffraction*, Dover, New York, 1990.
2. A. K. Cheetham, B. E. F. Fender and M. J. Cooper, *J. Phys. C: Solid St. Phys.*, 1971, **4**, 3107–3121.
3. H. M. Rietveld, *J. Appl. Cryst.*, 1969, **2**, 65–71.
4. H. M. Rietveld, *Acta Crystallogr.*, 1967, **22**, 151–152.
5. B. O. Loopstra and H. M. Rietveld, *Acta Crystallogr., Sect. B*, 1969, **25**, 787–791.
6. A. K. Cheetham and J. C. Taylor, *J. Solid State Chem.*, 1977, **21**, 253–275.
7. A. W. Hewat, *Chem. Script., A*, 1985, **26**, 119–130.
8. J. E. Post and D. L. Bish, *Modern Powder Diffraction*, ed. D. L. Bish and J. E. Post, Mineralogical Society of America, Washington, 1989, Reviews in Mineralogy, vol. 20, pp. 277–308.
9. R. A. Young (ed), *The Rietveld Method*, IUCr Monograph on Crystallography 5, Oxford University Press, Oxford, 1993.
10. K. D. M. Harris and M. Tremayne, *Chem. Mater.*, 1996, **8**, 2554–2570.
11. D. M. Poojary and A. Clearfield, *Acc. Chem. Res.*, 1997, **30**, 414–422.
12. H.-R. Wenk, (ed), *Neutron Scattering in Earth Sciences*, Mineralogical Society of America, Washington, 2006, Reviews in Mineralogy and Geochemistry, vol. 63.
13. W. C. Hamilton, *Statistics in Physical Science*, Ronald Press, New York, 1964.
14. P. H. J. Mercier, Y. Le Page, P. S. Whitfield and L. D. Mitchell, *J. Appl. Crystallogr.*, 2006, **39**, 369–375.
15. P. H. J. Mercier, Y. Le Page, P. S. Whitfield and L. D. Mitchell, *J. Appl. Crystallogr.*, 2006, **39**, 458–465.
16. A. C. Larson and R. B. Von Dreele, *General Structure Analysis System (GSAS)*, Los Alamos National Laboratory Report LA-UR 86-748, 2004.
17. K. Shankland, L. McBride, W. I. F. David, N. Shankland and G. Steele, *J. Appl. Crystallogr.*, 2002, **35**, 443–454.
18. V. Jorík, I. Ondrejkovicová1, R. B. Von Dreele and H. Ehrenberg, *Cryst. Res. Technol.*, 2003, **38**, 174–181.
19. R. B. Von Dreele, *J. Appl. Crystallogr.*, 1999, **32**, 1084–1089.

20. R. B. Von Dreele, *J. Appl. Crystallogr.*, 2007, **40**, 133–143.
21. A. L. Morris, M. W. MacArthur, E. G. Hutchinson and J. M. Thornton, *Proteins*, 1992, **12**, 345–364.
22. R. A. Engh and R. Huber, *Acta Crystallogr., Sect. A*, 1991, **47**, 392–400.
23. E. Dodson, *Acta Crystallogr., Sect. D*, 1998, **54**, 1109–1118.
24. R. B. Von Dreele, *Acta Crystallogr., Sect. D*, 2005, **61**, 22–32.
25. G. N. Ramachandran, C. Ramakrishnan and V. Sasisekharan, *J. Mol. Biol.*, 1963, **7**, 95–99.

CHAPTER 10

# The Derivative Difference Minimization Method

LEONID A. SOLOVYOV

Institute of Chemistry and Chemical Technology, K. Marx av., 42, 660049 Krasnoyarsk, Russia

## 10.1 INTRODUCTION

The extensive practice of using the full-profile approach to powder diffraction data analysis has validated it to be the best way of extracting precise and comprehensive information. An evident advantage of this approach is the possibility of using experimental data in the original form of a whole diffraction pattern. This advantage is utilized in the Rietveld[1] method of structure refinement from powder data and in many other techniques of structural, microstructural, and quantitative phase analysis. Most generally applied routines of full-profile fitting are based on the minimization of the squared differences between the observed and calculated powder profiles at each data point. Achieving this goal requires the modelling of all of the scattering contributions to a powder pattern, including the background. In simple cases, the background can be estimated and subtracted from the experimental pattern,[2–5] or modelled by physically based functions.[6,7] However, as a rule, the background line is very difficult to describe correctly, since it is a complex convolution of diverse components originating from the sample itself, amorphous and semi-crystalline admixtures, the sample holder and other sources. The problem of the background curve ambiguity, which increases with increasing diffraction peak overlap, is commonly approached by applying empirical functions such as polynomial or Fourier series. None of these approximations can provide an adequate general description of the background line. As a result, systematic errors caused by inadequate background definitions limit the precision and applicability of full-profile data analysis.

This chapter is devoted to the recently proposed derivative difference minimization (DDM) method,[8] which allows full-profile refinement independently of the background. In this method the refinement is aimed not at minimizing the absolute difference between the observed and calculated patterns, but at minimizing the oscillations (or curvature) of the difference curve. The difference curve is considered as an estimation of background which, in the absence of crystalline admixtures, usually varies much less rapidly along the powder profile than does the diffraction pattern. Thus, the DDM procedure is aimed at finding such a calculated diffraction pattern that gives the smoothest difference after being subtracted from the observed powder profile. This procedure does not involve background line modelling or approximations, thus avoiding the background-related systematic errors.

## 10.2 DERIVATIVE DIFFERENCE MINIMIZATION PRINCIPLE

As a measure of the difference curvature and oscillations, the squared values of its derivatives may be used. The respective minimization function is given by:

$$\mathrm{MF} \quad \sum \left\{ w^1 \left[ \frac{\partial}{\partial \theta} (Y_\mathrm{o} \quad Y_\mathrm{c}) \right]^2 + w^2 \left[ \frac{\partial^2}{\partial \theta^2} (Y_\mathrm{o} \quad Y_\mathrm{c}) \right]^2 + \ldots + w^k \left[ \frac{\partial^k}{\partial \theta^k} (Y_\mathrm{o} \quad Y_\mathrm{c}) \right]^2 \right\} \qquad (1)$$

where $Y_\mathrm{o}$ and $Y_\mathrm{c}$ are the observed and calculated profile intensities, respectively, $\theta$ is the diffraction angle, $w$ is the weight and the sum is over the entire powder profile. Applying the Savitzky–Golay (SG) formalism[9] for calculating derivatives, the minimization function may be rewritten as:

$$\mathrm{MF} = \sum_{i=m+1}^{N} \sum_{k}^{m} w_i^k \left( \sum_{j=\ m}^{m} c_j^k \Delta_{i+j} \right)^2 \qquad (2)$$

where $c_j^k$ are the SG coefficients for the derivative of order $k$ with the profile convolution interval $[-m, m]$, $N$ is the number of profile points, and $\Delta$ is the profile difference ($\Delta = Y_\mathrm{o} - Y_\mathrm{c}$). The refinement of variable parameters, $v_r$, is carried out by solving the normal equations corresponding to the minimum of Equation (2):

$$\sum_{k} \sum_{i=m+1}^{N} \sum_{m}^{m} w_i^k \left( \sum_{j=\ m}^{m} c_j^k \Delta_{i+j} \right) \cdot \left( \sum_{j=\ m}^{m} c_j^k \frac{\partial Y_{c,i+j}}{\partial v_r} \right) = 0 \qquad (3)$$

$$w_i^k = \left[ \sum_{j=\ m}^{m} (c_j^k)^2 (\sigma_{i+j})^2 \right]^{\ 1} \qquad (4)$$

where $\sigma_i$ is the variance in the observed profile intensity $Y_{\mathrm{o}i}$. The sum in Equation (4) represents the estimated squared variance in the SG derivative of order $k$ for the $i$th profile point. The standard deviations of the refined

parameters are estimated from Equation (5):

$$s_i = \left[A_{ii}^{-1}\mathrm{MF}/(N - P + C)\right]^{1/2} \tag{5}$$

where $A_{ii}^{-1}$ is the diagonal element in the inverted normal matrix, $N$ is the number of observations, $P$ is the number of refined parameters and $C$ is the total number of constraints.

For a practical application, the set of $k$ derivatives needs to be restricted to a finite number. Test runs of the procedure gave satisfactory results using the first and second derivatives calculated applying the SG coefficients for the second-degree polynomial. When minimizing only the first-order derivative, the refinement was less stable since, presumably, the first derivative has values close to zero in the regions of the diffraction peak maxima, thus reducing the contribution of these regions to the minimization function. The SG coefficients for the first and second derivatives with the convolution interval $[-m, m]$ can be expressed as:

$$c_j^1 = \frac{3j}{m(m+1)(2m+1)} \tag{6}$$

$$c_j^2 = \frac{45j^2 - 15m(m+1)}{m(m+1)(2m+1)[4m(m+1) - 3]} \tag{7}$$

Equation (7) contained an error in the original paper on DDM,[8] which was later corrected.[10]

The reliability factor for DDM may be calculated analogously to that for Rietveld refinement as a normalized sum of the squared derivative difference over the powder profile. However, the value of such a reliability factor will depend on the convolution interval choice. For instance, for wider convolution intervals the $R$ factor will be lower, as the wider the intervals the smoother the derivative curve. A less interval-dependent $R$ factor can be calculated as:

$$R_{\mathrm{DDM}} = \sqrt{\frac{\sum_k \sum_{i=m+1}^{N-m} w_i^k \left(\sum_{j=-m}^{m} c_j^k \Delta_{i+j}\right)^2}{\sum_k \sum_{i=m+1}^{N-m} w_i^k \left(\sum_{j=-m}^{m} c_j^k Y_{o,i+j}\right)^2} + \frac{\sum_{i=m+1}^{N-m} w_i \left(Y_{oi} - \sum_{j=-m}^{m} c_j^0 Y_{o,i+j}\right)^2}{\sum_{i=m+1}^{N-m} w_i Y_{oi}^2}} \tag{8}$$

The second summand in Equation (8) characterizes the quality of the SG smoothing of the observed profile. This term will increase with increasing convolution interval, since with wider convolution intervals the quality of the SG polynomial fit is worse. Such a composite $R$ factor allows a partial compensation of the $R_{\mathrm{DDM}}$ dependence on the convolution interval.

The choice of the convolution intervals for each data point requires special consideration since it influences the results of the DDM application. On the one hand, the intervals should be narrow enough to provide an adequate calculation of the derivatives. On the other hand, they should be wide enough to take into account long modulations of the difference curve. A derivative of the profile difference can, alternatively, be considered as a difference in the derivatives of the observed and the calculated profiles. Since the SG coefficients are calculated from a polynomial fitted to the convoluted profile region, the optimal interval should be the maximal one that provides an adequate polynomial fitting of the observed profile. For simplicity, the intervals can be chosen to be equal to the average full-width at half-maximum (FWHM) of the diffraction peaks. Preliminary tests of the procedure showed that such a choice provided stable refinement. However, better results were achieved by applying flexible convolution intervals for each profile point.

The optimal intervals can be assigned on the basis of the counting statistics. The assignment procedure consists in finding the widest interval for which the average deviation of the observed profile intensities from the SG polynomial does not exceed their variances at each point of the convoluted profile region. Such a procedure generates narrower convolution intervals for the powder pattern regions with intense well-resolved diffraction peaks, and wider intervals for the regions with small and/or overlapped peaks. For noisy data and when the background curvature is apparently high the maximal allowed interval width should be restricted to a reasonable value to let the difference be adequate by curvature with the background line. Figure 10.1 shows a fragment of an XRD pattern of $[Pt(NH_3)_2(C_2O_4)]$ after the DDM refinement of the structure with different maximal convolution intervals ($C$-max) allowed. One may see that with wider $C$-max the difference profile has higher oscillations but lower overall curvature. With narrower $C$-max the difference profile is less oscillatory, but of higher overall curvature. Notably, the quality of structural parameters obtained by DDM with $C\text{-max} = 0.4^\circ\ 2\theta$ was somewhat better than that with wider $C$-max, which was also reflected in lower $R$ factors. In this example the choice of narrower $C$-max led to better DDM refinement results due to the presence of local background maxima on the XRD pattern attributed, presumably, to an amorphous admixture. In other cases, however, when the real background curvature is apparently low, the choice of wider $C$-max intervals may be more appropriate.

## 10.3 DDM DECOMPOSITION PROCEDURE

The initial stages of powder diffraction structure analysis often require the decomposition of the powder pattern into individual Bragg components without reference to a structural model. The DDM-based decomposition procedure[11] consists in finding additions to the calculated (or initially set) reflection intensities for minimizing the squared derivatives of the difference

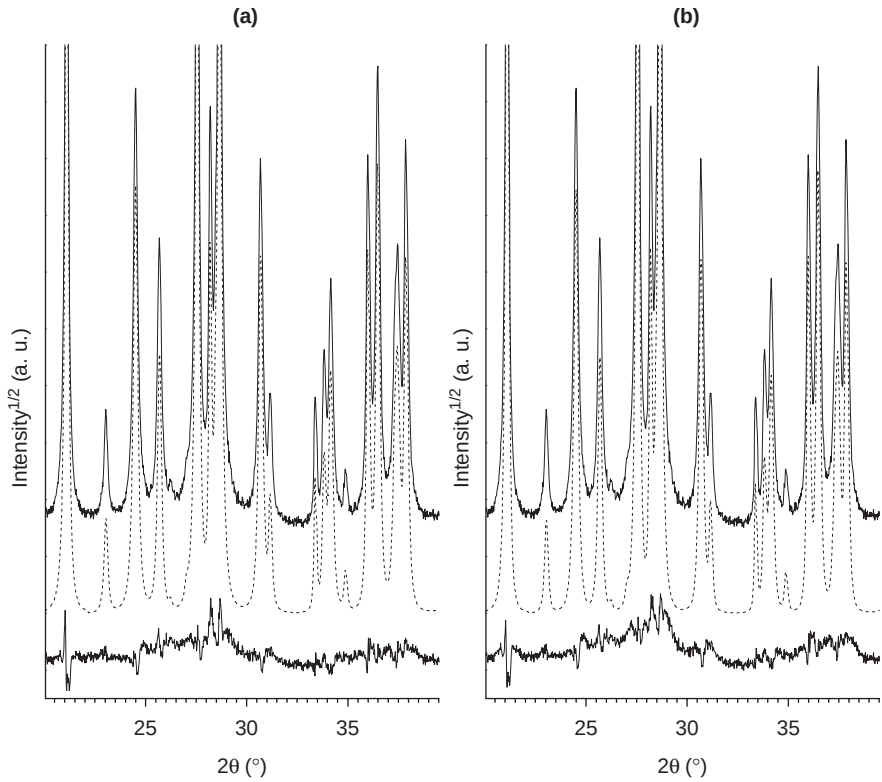



**Figure 10.1** Fragment of weighted observed (top solid), calculated (middle dashed), and difference (bottom solid) XRD powder profiles for $[Pt(NH_3)_2(C_2O_4)]$ after DDM refinement with different maximal convolution intervals $C$ max allowed. (a) $C$ max $= 2^\circ$ $2\theta$, $R_{DDM} = 0.075$, $R_B = 0.030$; (b) $C$ max $= 0.4^\circ$ $2\theta$, $R_{DDM} = 0.063$, $R_B = 0.026$.

diffraction profile. The calculated profile intensity in the $i$th profile point is defined as:

$$Y_{ci} = \sum_n I_{cn} f_n(\theta_i) \tag{9}$$

where $I_{cn}$ is the calculated intensity of the $n$th reflection, $f(\theta)$ is the peak-shape function, and the sum is over the whole set of reflections contributing to the profile point. In accordance with the DDM methodology, the minimization function for an individual reflection can be written as:

$$\begin{aligned} \mathrm{MF} = \sum_i \Bigg\{ & w_i^1 \left[ \frac{\partial}{\partial\theta} (\Delta_i - f(\theta_i)\delta) \right]^2 + w_i^2 \left[ \frac{\partial^2}{\partial\theta^2} (\Delta_i - f(\theta_i)\delta) \right]^2 \\ & + \ldots + w_i^k \left[ \frac{\partial^k}{\partial\theta^k} (\Delta_i - f(\theta_i)\delta) \right]^2 \Bigg\} \end{aligned} \tag{10}$$

where $\delta$ is the sought addition to the reflection intensity and the sum is over the profile area to which the reflection contributes. Restricting the derivatives in MF to first and second order and minimizing with respect to $\delta$ gives:

$$\frac{\partial}{\partial\delta}\mathrm{MF} \quad 2\sum_i \left[ w_i^1 \delta \frac{\partial}{\partial\theta} f(\theta_i) \frac{\partial}{\partial\theta}(\Delta_i \quad f(\theta_i)\delta) + w_i^2 \delta \frac{\partial^2}{\partial\theta^2} f(\theta_i) \frac{\partial^2}{\partial\theta^2}(\Delta_i \quad f(\theta_i)\delta) \right] \quad 0 \quad (11)$$

from which:

$$\delta = \frac{\sum_i \left\{ w_i^1 \frac{\partial}{\partial\theta} f(\theta_i) \frac{\partial}{\partial\theta} \Delta_i + w_i^2 \delta \frac{\partial^2}{\partial\theta^2} f(\theta_i) \frac{\partial^2}{\partial\theta^2} \Delta_i \right\}}{\sum_i \left\{ w_i^1 \left[ \frac{\partial}{\partial\theta} f(\theta_i) \right]^2 + w_i^2 \left[ \frac{\partial^2}{\partial\theta^2} f(\theta_i) \right]^2 \right\}} \quad (12)$$

Using the SG coefficients one may rewrite Equation (12) as:

$$\delta = \frac{\sum_i \left\{ w_i^1 \sum_{j=\ m}^{m} c_j^1 f(\theta_{i+j}) \sum_{j=\ m}^{m} c_j^1 \Delta_{i+j} + w_i^2 \sum_{j=\ m}^{m} c_j^2 f(\theta_{i+j}) \sum_{j=\ m}^{m} c_j^2 \Delta_{i+j} \right\}}{\sum_i \left\{ w_i^1 \left[ \sum_{j=\ m}^{m} c_j^1 f(\theta_{i+j}) \right]^2 + w_i^2 \left[ \sum_{j=\ m}^{m} c_j^2 f(\theta_{i+j}) \right]^2 \right\}} \quad (13)$$

Considering the peak overlap, because of which several reflections may contribute to the same profile area, the addition $\delta$ should be reduced by an appropriate overlap correction. Finally, the estimated "observed" reflection intensity is given by:

$$I_{\mathrm{obs}} = I_c + \delta \frac{f(\theta^0) I_c}{Y_c^0} \quad (14)$$

$$Y_c^0 = \sum_n I_{cn} f_n(\theta^0) \quad (15)$$

where $\theta^0$ is the reflection position, $f(\theta^0)$ and $Y_c{}^0$ are the values of the peak-shape function and the calculated profile intensity in the position $\theta^0$; $\delta$ is obtained from Equation (13). The multiplier after $\delta$ in Equation (14) represents the overlap correction factor.

The result of the application of the DDM decomposition formula Equation (14) is similar to that of Rietveld's approximation for $I_{\mathrm{obs}}$,[1] except that it is DDM-oriented and thus does not require a background definition. In the DDM program[12] the formula is also used for the Bragg $R$ factor calculation. For single non-overlapped peaks or a set of peaks with the same position, the DDM decomposition directly gives the best estimate for $I_{\mathrm{obs}}$. For partly overlapped peaks it should be iterated to arrive at an optimized set of $I_{\mathrm{obs}}$ similarly to the Le Bail method.[13] The starting intensities $I_{\mathrm{c}}$ can either be calculated from an existing structure model or set arbitrarily when the model is absent. Notably, for fully overlapped peaks the DDM decomposition

procedure automatically preserves the initial set ratio of intensities, which is important when the values of $I_{obs}$ are used in the difference Fourier map calculations.

## 10.4 RESULTS AND DISCUSSION

### 10.4.1 Tests on Simulated and Real Data

The DDM algorithm can be readily adapted to any full-profile refinement routine. It was included into the computer program DDM,[12] which is based on a modified and corrected code of BDWS-9006PC.[14] A variant of DDM has recently been implemented in the BGMN[15] program.

The method was initially tested using simulated powder X-ray diffraction (XRD) patterns. Numerous DDM runs starting from randomly altered structure and profile parameters showed stable and correct refinement, equivalent by the convergence rate to the least-squares Rietveld refinement. The original structure models used for generating the test simulated patterns were reproduced by DDM completely up to the isotropic displacement parameters. Comparative Rietveld and DDM refinements were performed on simulated data with added statistical noise and a polynomial background of moderate curvature. In these tests both DDM and Rietveld procedures were shown to have the same accuracy.[8] Figure 10.2 illustrates the results of DDM run on a simulated XRD pattern of $Ag_2[Pd(NH_3)_2(SO_3)_2]$[16] with an added randomly modulated highly curved background and statistical noise. DDM was started from randomly altered parameters (with 0.5–1.0 Å displacement of the atomic positions) and demonstrated a stable convergence. The test structure model was reproduced with less than 0.01 Å deviations in the interatomic distances. The only notable bias from the test model was in lower (by $\sim$0.5–0.7 Å$^2$) isotropic displacement parameters, $B_{iso}$. The randomly curved background line was rendered by the difference curve in detail.

The first tests of DDM on experimental XRD data of $[Pd(NH_3)_4](C_2O_4)$ and neutron diffraction data of $(C_5H_6N)Al_3F_{10}$ have validated its capacities for high precision structural analysis.[8] The crystal structure of $[Pd(NH_3)_4](C_2O_4)$ was earlier solved by Patterson search and refined by Rietveld method.[17] Its re-refinement by DDM gave a better structural geometry. A smaller imbalance in the C–O distances and O–C–C angles of the oxalate molecule was obtained, and the C–C distance was much closer to that usually determined for oxalates. The problem with the Rietveld refinement in this case was, in particular, due to a local maximum of the background curve, which was not adequately modelled by the polynomial function applied in the earlier study. The structure solution and Rietveld refinement of $(C_5H_6N)Al_3F_{10}$, performed in the framework of the "DuPont Powder Challenge", was seriously complicated by the low quality of the diffraction data (Figure 10.3) as a result of strong anisotropic peak broadening and complex background curvature.[18] In the process of structure determination, the background was approximated by an enhanced variant of the algorithm described by Sonneveld and Visser.[2] Rietveld refinement of the

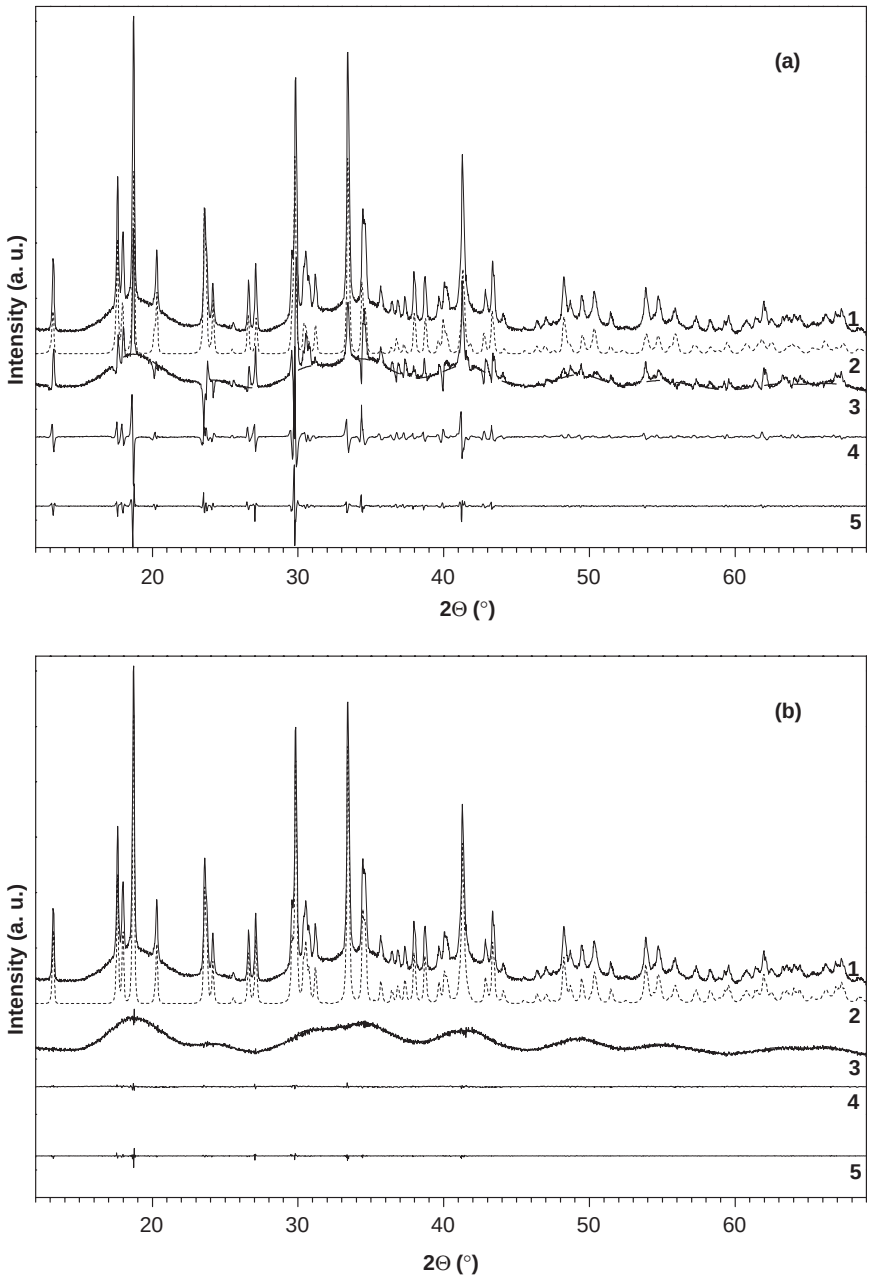



**Figure 10.2** Results of DDM refinement for simulated XRD pattern with randomly modulated background and statistical noise added. The simulated (1), calculated (2), difference (3), difference first derivative (4) and difference second derivative (5) profiles are shown at the initial stage (a) and after 15 cycles of DDM (b). The bold dashed line depicts the background curve added.

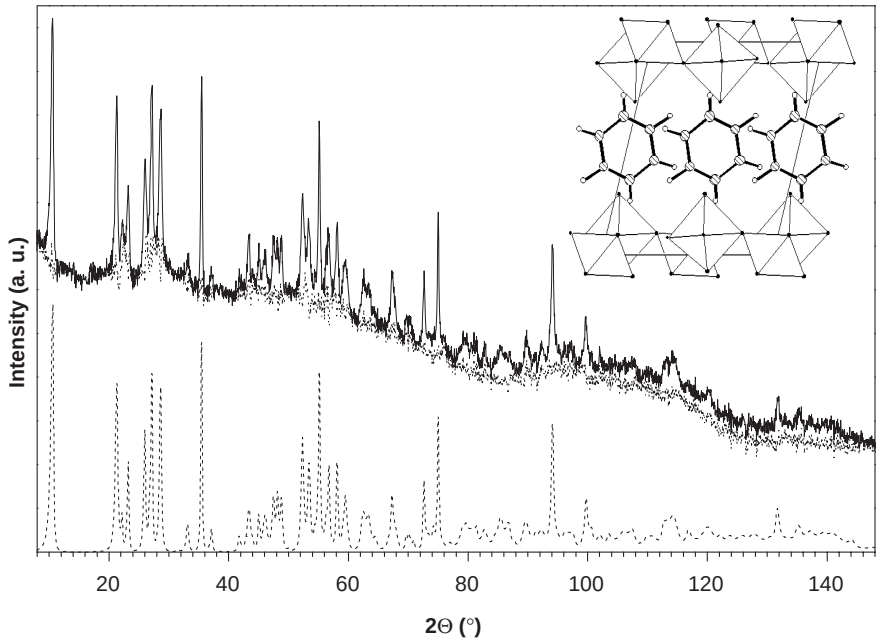



**Figure 10.3** Experimental (top), calculated (bottom) and difference (middle dotted) neutron powder diffraction profiles after DDM refinement of the $(C_5H_6N)Al_3F_{10}$ structure (shown in insert).

structure was performed using the shifted Chebyshev background functions and applying constraints on interatomic distances, without which the structure geometry was not satisfactory. With DDM, the structure was refined successfully without geometrical constraints and without background modelling.[8]

The sensitivity of DDM refinement to light atom positions, namely to H atoms, was examined on laboratory XRD data for *trans*-$[Pd(NH_3)_2(NO_2)_2]$. The Rietveld refinement of this structure was earlier carried out with rigid constraints on the $NH_3$ geometry.[19] Attempts at unconstrained Rietveld refinement of H-atom positions resulted in a serious distortion of the amino-group geometry. By applying DDM, the H-atom positions were refined successfully, giving an acceptable molecular geometry and a reasonable hydrogen bonding system. This example is included into the DDM program package.[12] Additionally, the Rietveld and DDM procedures were tested on simulated XRD data for the same compound. The simulated XRD profile was generated from the structure model with an idealized geometry of $NH_3$ and added by a polynomial background and statistical noise. The results are summarized in Table 10.1. For the simulated data both Rietveld refinement and DDM demonstrated the same accuracy, but for real data the geometric parameters of H atoms obtained by DDM were essentially better. In these tests, the same set of structural and profile parameters were refined by both Rietveld and DDM methods, except the polynomial background parameters used in the

**Table 10.1** Geometric parameters of the $NH_3$ group in *trans*-$[Pd(NH_3)_2(NO_2)_2]$ obtained from unconstrained DDM and Rietveld refinements for real and simulated powder XRD data.

| | *Bond length (Å)* | | | *Bond angles (°)* | | |
|---|---|---|---|---|---|---|
| *Source of data* | *N H1* | *N H2* | *N H3* | *H1 N H2* | *H2 N H3* | *H3 N H1* |
| DDM, real data | 0.88(15) | 0.84(12) | 1.09(14) | 106(11) | 119(10) | 98(11) |
| Rietveld, real data | 0.99(8) | 1.32(9) | 1.11(8) | 129(6) | 89(5) | 91(5) |
| DDM, simulated data | 0.97(4) | 0.97(5) | 0.89(5) | 118(4) | 108(4) | 101(4) |
| Rietveld, simulated data | 0.93(4) | 0.94(5) | 0.83(5) | 112(4) | 103(4) | 112(4) |
| Expected | 0.9 | 0.9 | 0.9 | 110 | 110 | 110 |

Rietveld refinement. Evidently, the reason for the problematic Rietveld refinement of H-atom positions in this example was in the inaccuracy of the background model.

The successful testing of DDM method for structure refinement purposes allows us to predict its applicability in other fields of powder diffraction, such as the analysis of microstructure and quantitative phase analysis (QPA). Trial runs of DDM for the XRD data supplied by the International Union of Crystallography Commission on Powder Diffraction for the Size-Strain and QPA round-robins gave encouraging results. Respective examples are included in the DDM program package.[12] In particular, the biases in the phase contents determined by DDM refinement for the QPA round-robin samples from the weighted amounts were less than 1 wt.%.

### 10.4.2 Applications of DDM

The first applications of DDM in the structural studies of polycrystalline[8,11,20] and mesostructured substances[21 23] have demonstrated its capacities for obtaining precise structure characteristics from diffraction data with various background complexities. DDM was used in the structure refinement and analysis of a series of nickel and iron methylimidazole hexafluorophosphates and tetrafluoroborates obtained in a sonochemical reaction.[20] Due to the specific synthesis procedure, the substances were highly disordered and their XRD powder patterns contained a background of complex curvature, indicating the presence of an amorphous admixture. Despite these difficulties, the structures were successfully refined by DDM and analyzed in detail.

The crystal structure of the potassium salt of 1-(tetrazol-5-yl)-2-nitroguanidine $[K(C_2H_3N_8O_2)]$ was solved and refined from laboratory X-ray powder diffraction data by applying the DDM decomposition and refinement methods.[11] The structure model was found from a Patterson search, for which the reflection intensities were derived from the powder profile by the DDM decomposition. The use of DDM allowed successful location and unconstrained refinement of all the atomic positions, including those of three

independent H atoms. An ambiguous position of one of the H atoms was explicitly resolved from the difference Fourier map. The advantages of DDM in terms of the precision and reproducibility of the structural parameters were discussed in comparison to Rietveld refinement results. The failure to refine the H-atom positions by the Rietveld method was attributed to systematic errors associated with the background modelling, which were avoided by DDM. Figure 10.4 shows the final DDM plots after the decomposition and structure refinement. The difference curves on the plots reveal two broad maxima in the region between 20 and 50° $2\theta$ that could not be adequately modelled by the polynomial function used in the Rietveld refinement. For the same reason, the reproducibility of the Rietveld refinement results for two differently prepared samples was shown to be worse than that of DDM. Specifically, the overall mean difference in the interatomic distances determined for the two samples was *ca.* 0.016 Å for DDM and *ca.* 0.032 Å for Rietveld refinement. Notably, the complexity of the background line was not apparent from a visual examination of the XRD patterns. Only after the DDM refinement did the background modulations become noticeable.

The opportunity of full-profile refinement independently of the background curve allowed by DDM is especially important for studies of semi-crystalline substances, such as polymers, organized amphiphilic liquid crystals, block copolymers, mesostructured materials *etc.*, for which the contribution of amorphous and disordered fractions to the background line is essential. A particular problem with mesostructured materials, for which the DDM method was originally designed, is that they exhibit diffraction peaks at very low angles, where the background scattering is especially complex and difficult to model. In the first applications of the full-profile structure analysis of mesoporous mesostructured materials using the continuous density function method[24 27] the background line was subtracted from the powder profile by the enhanced algorithm of Sonneveld and Visser.[2] This approximation was rough, but attempts of background modelling with polynomials and other functions gave unsatisfactory results because of its very sharp change and complexity in the low-angle region. The use of DDM has given a solution to these problems.

First preliminary variants of DDM were applied in the full-profile X-ray diffraction structure analysis of a series of new silica mesoporous materials[28] and ordered nanopipe mesostructured carbons.[29] DDM allowed stable background-independent full-profile refinement of the structure parameters of these advanced nanomaterials, a result that was unattainable by any other method. To date, DDM has been applied to many various mesoporous and mesostructured substances. The structural parameters of a series of face-centred cubic (*Fm*3*m*), body-centred cubic (*Im*3*m*), and two-dimensional hexagonal (*p*6*mm*) mesoporous silicates were determined by DDM from synchrotron XRD.[22] A comprehensive structural analysis of mesoporous silicates SBA-16 (cage-type cubic *Im*3*m*), their carbon replicas, and silica/carbon composites was performed by applying DDM.[23] The structure of MCM-48 mesoporous silicate materials was analysed in detail by DDM from different laboratory and synchrotron XRD data.[21] The pore wall thickness of both as-made and

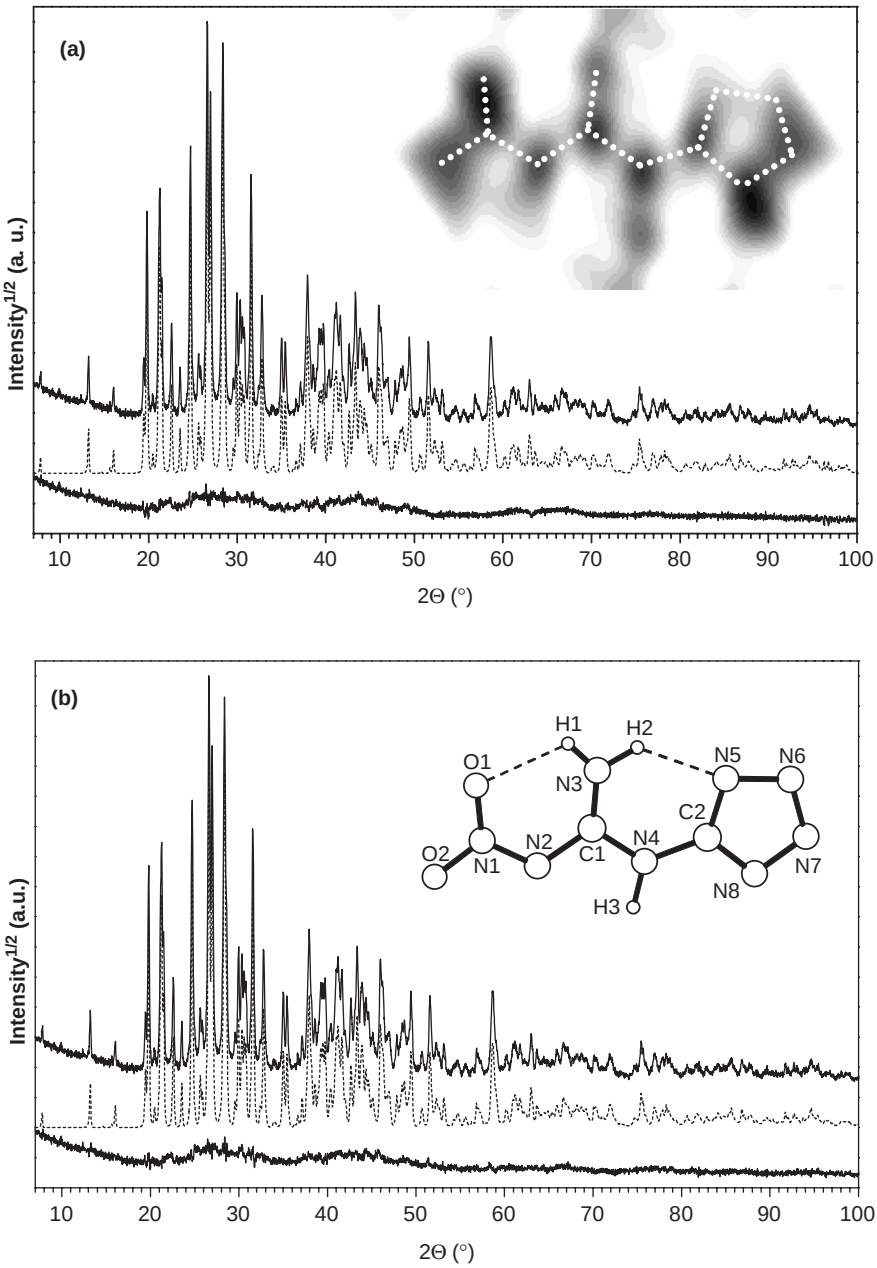



**Figure 10.4** Weighted observed (top), calculated (middle), and difference (bottom) XRD powder profiles for 1 (tetrazol 5 yl) 2 nitroguanidine potassium after (a) DDM decomposition and (b) DDM refinement. Inserts: Patterson map section with the superimposed sketch of the anion and the molecular conformation.

calcined MCM-48 was determined with high precision to be 8.0(1) Å. Detailed density distribution analysis revealed that the low-curvature segments of the pore wall were *ca*. 10% denser than the curved ones, which could be related to a more compact atomic packing of silica allowed by the flat-wall geometry. The surfactant density distribution in the pores was analysed and found to have a distinct minimum in the pore centre similar to that detected previously in MCM-41.[24] A new extended model function of the density distribution in MCM-48 was proposed on the basis of the structural features revealed. The reliability of the results was supported by the reproducibility of the structural characteristics obtained by DDM from different XRD data sets. The agreement between the observed and calculated synchrotron XRD patterns of MCM-48 and its carbon mesostructured replica[30] achieved by DDM refinement is illustrated by Figure 10.5. The modulations of the difference profile indicated the presence of a disordered fraction in the sample, which is, in general, very difficult to exclude in the synthesis of mesostructured materials. The sharp increase of background for the carbon replica in the low-angle area is due to density fluctuations in the carbon nanoframeworks.

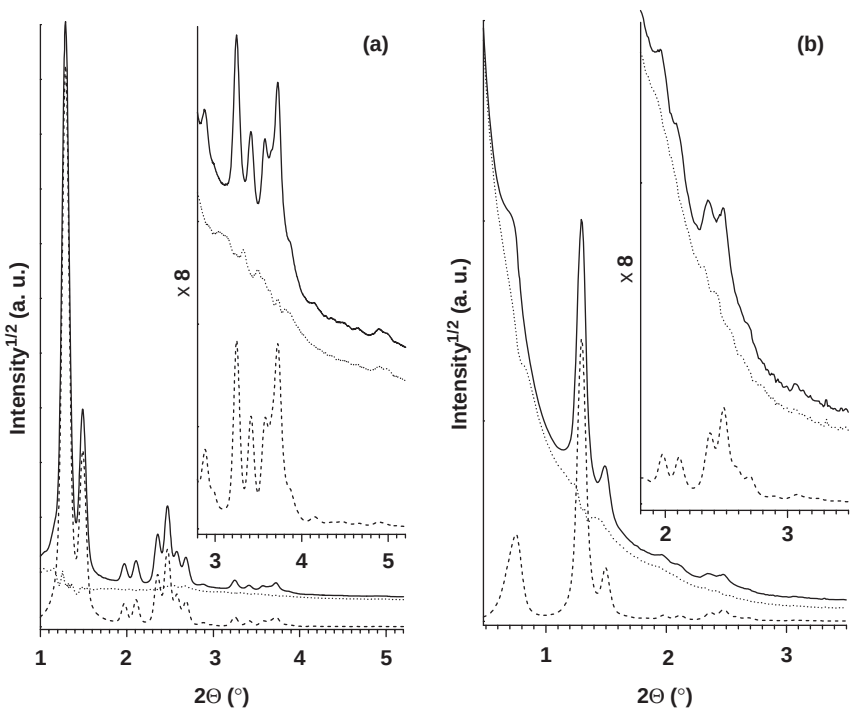



**Figure 10.5** Weighted observed (solid), calculated (dashed), and difference (dotted) synchrotron XRD patterns for MCM 48 mesoporous silica (a) and its carbon replica (b) after DDM refinement.

## 10.5 CONCLUSIONS

The derivative difference minimization method of full-profile refinement has been shown to be a powerful and efficient tool of powder diffraction analysis. The most attractive advantage of DDM is the possibility of profile refinement without the background line modelling, which presents a generally recognized problem. Moreover, in comparison to the Rietveld refinement involving empirical background modelling, DDM can provide structural characteristics with higher precision, reproducibility and comprehension.

While the derivative difference method was primarily designed for cases of complex modulated background, it has also been demonstrated to be advantageous in common cases of seemingly flat background line. Notably, even when the background contribution to a powder pattern is apparently simple it may have (and normally has) modulations that are invisible due to peak overlap. Inadequate background modelling and/or approximations give rise to systematic errors that are avoided in the scheme of DDM. The improvement of the precision provided by the derivative difference method is, evidently, of high importance for powder diffraction analysis.

The residual difference after a successful DDM refinement or/and decomposition can be considered as a scattering component of the powder pattern free of Bragg diffraction. The separation of this component would facilitate the analysis of the amorphous fraction of the sample, the radial distribution function of the non-crystalline scatterers, the thermal diffuse scattering properties and other non-Bragg features of powder patterns. The background-independent profile treatment can be especially desirable in quantitative phase analysis when amorphous admixtures must be accounted for. Further extensions of DDM may involve Bayesian probability theory, which has been utilized efficiently in background estimation procedures[3–5] and Rietveld refinement in the presence of impurities.[31] DDM will also be useful at the initial steps of powder diffraction structure determination when the structure model is absent and the background line cannot be determined correctly. The direct space search methods of structure solution, in particular, may efficiently utilize DDM.

The principles of DDM are universal and may be used in many diverse areas of powder diffraction and beyond. Future developments will be focused on studying the properties of this procedure and its efficiency in applications to different data. Various options for calculating the derivative difference minimization function and optimal refinement strategies should be subjected to methodical analysis.

## REFERENCES

1. H. M. Rietveld, *J. Appl. Crystallogr.*, 1969, **2**, 65.
2. E. J. Sonneveld and J. V. Visser, *J. Appl. Crystallogr.*, 1975, **8**, 1.
3. W. von der Linden, V. Dose, J. Padayachee and V. Prozesky, *Phys. Rev. E*, 1999, **59**, 6527.

4. R. Fischer, K. M. Hanson, V. Dose and W. von der Linden, *Phys. Rev. E*, 2000, **61**, 1152.
5. W. I. F. David and D. S. Sivia, *J. Appl. Crystallogr.*, 2001, **34**, 318.
6. P. Riello, G. Fagherazzi, D. Clemente and P. Canton, *J. Appl. Crystallogr.*, 1995, **28**, 115.
7. J. W. Richardson, in *The Rietveld Method*, ed. R. A. Young, Oxford University Press, Oxford, 1993, 102.
8. L. A. Solovyov, *J. Appl. Crystallogr.*, 2004, **37**, 743.
9. A. Savitzky and M. J. E. Golay, *Anal. Chem.*, 1964, **36**, 1627.
10. L. A. Solovyov, *J. Appl. Crystallogr.*, 2005, **38**, 401.
11. L. A. Solovyov, A. M. Astachov, M. S. Molokeev and A. D. Vasiliev, *Acta Crystallogr., B*, 2005, **61**, 435.
12. L. A. Solovyov, Institute of Chemistry and Chemical Technology, Krasnoyarsk, Russia, 2004, (DDM program is available from http://icct.krasn.ru/eng/content/persons/Sol_LA/ ddm.html).
13. A. Le Bail, H. Duroy and J. L. Fourquet, *Mater. Res. Bull.*, 1988, **23**, 447.
14. D. B. Wiles and R. A. Young, *J. Appl. Crystallogr.*, 1981, **14**, 149.
15. J. Bergmann, P. Friedel and R. Kleeberg, *Commission Powder Diffraction Newsletter*, International Union of Crystallography, 1998, no. 20, 5.
16. L. A. Solovyov, A. I. Blokhin, R. F. Mulagaleev and S. D. Kirik, *Acta Crystallogr., Sect. C*, 1999, **55**, 293.
17. L. A. Solovyov, M. L. Blochina, S. D. Kirik, A. I. Blokhin and M. G. Derikova, *Powder Diffr.*, 1996, **11**, 13.
18. R. L. Harlow, N. Herron, Z. Li, T. Vogt, L. Solovyov and S. Kirik, *Chem. Mater.*, 1999, **11**, 2562.
19. A. I. Blokhin, L. A. Solovyov, M. L. Blokhina, I. S. Yakimov and S. D. Kirik, *Russ. J. Coord. Chem.*, 1996, **22**, 185.
20. D. S. Jacob, S. Makhluf, I. Brukental, R. Lavi, L. A. Solovyov, I. Felner, I. Nowik, R. Persky, H. E. Gottlieb and A. Gedanken, *Eur. J. Inorg. Chem.*, 2005, 2669.
21. L. A. Solovyov, O. V. Belousov, R. E. Dinnebier, A. N. Shmakov and S. D. Kirik, *J. Phys. Chem. B*, 2005, **109**, 3233.
22. F. Kleitz, L. A. Solovyov, G. M. Anilkumar, S. H. Choi and R. Ryoo, *Chem. Commun.*, 2004, 1536.
23. T.-W. Kim, R. Ryoo, K. P. Gierszal, M. Jaroniec, L. A. Solovyov, Y. Sakamoto and O. Terasaki, *J. Mater. Chem.*, 2005, **15**, 1560.
24. L. A. Solovyov, S. D. Kirik, A. N. Shmakov and V. N. Romannikov, *Microporous Mesoporous Mater.*, 2001, **44**, 17.
25. L. A. Solovyov, S. D. Kirik, A. N. Shmakov and V. N. Romannikov, *Adv. X-ray Anal.*, 2001, **44**, 110.
26. L. A. Solovyov, A. N. Shmakov, V. I. Zaikovskii, S. H. Joo and R. Ryoo, *Carbon*, 2002, **40**, 2477.
27. L. A. Solovyov, V. I. Zaikovskii, A. N. Shmakov, O. V. Belousov and R. Ryoo, *J. Phys. Chem. B*, 2002, **106**, 12198.

28. F. Kleitz, D. Liu, G. M. Anilkumar, I.-S. Park, L. A. Solovyov, A. N. Shmakov and R. Ryoo, *J. Phys. Chem. B*, 2003, **107**, 14296.
29. L. A. Solovyov, T.-W. Kim, F. Kleitz, O. Terasaki and R. Ryoo, *Chem. Mater*., 2004, **16**, 2274.
30. L. A. Solovyov, J. Parmentier, F. Ehrburger-Dolle, J. Werckmann, C. Vix-Guterl and J. Patarin, Fourth International Mesostructured Materials Symposium, Cape Town, South Africa, Abstracts, 2004, 358.
31. W. I. F. David, *J. Appl. Crystallogr*., 2001, **34**, 691.

CHAPTER 11

# Quantitative Phase Analysis

IAN C. MADSEN AND NICOLA V. Y. SCARLETT

CSIRO Minerals, Box 312 Clayton South 3169, Victoria, Australia

## 11.1 INTRODUCTION

Measurement of the elemental composition of materials is a relatively mature art. In the natural world there are 92 elements with methods for their quantitative determination generally well established and, in many cases, the subject of internationally accepted standards. However, the physical properties of minerals and materials formed by these elements, and the manner in which they react, is not solely dependant on their chemical composition but on how the constituent elements are arranged; that is, their structural form. This finite number of known elements combine into some 230 crystallographic forms with almost infinite variability induced by solid solution, degree of crystallinity, morphology and so on. Therefore, the measurement of the form and amount of the various crystalline and amorphous components is considerably more complex than the measurement of the constituent chemistry.

In industry, many manufacturing or processing lines are controlled by measurement of chemistry alone simply because these values can be readily obtained to a high degree of accuracy and precision. When quantification of crystal form, or *phase*, is used in plant optimization and control it is often derived from bulk chemical analysis rather than being measured directly. This is achieved by normative calculation where particular elements are assigned to specific phases based on an assumed knowledge of individual phase composition.

While there are several methods that can be used to obtain phase related information, diffraction methods are the most direct. This is because diffraction information is produced by the crystal structure of each phase rather than being derived from secondary information (*e.g.*, chemistry).

Crystal structures of individual phases have traditionally been obtained *via* single-crystal diffraction methods. However, in both the natural and

synthesized material world, many compounds are only present as fine-grained materials and are ideally suited to characterization using powder diffraction methodology. Powder diffraction is also the only diffraction technique suited to multi-phase samples where the emphasis is to derive phase identification and quantification. This is possible since the observed powder diffraction pattern of a multi-phase sample is the sum of the diffraction patterns of the component phases.

The fundamental relationships between diffracted peak intensity in a powder diffraction pattern and the quantity of phase in a mixture producing that peak are well established. However, many factors impinge upon these relationships. These are generally experimental and arise from sample and instrument related effects.[1] Such factors include counting errors, particle statistics, preferred orientation, microabsorption and, the most hazardous of all, operator error.

This chapter focuses on the application of quantitative phase analysis (QPA) techniques for the extraction of phase abundance from diffraction data. Rather than repeat the extensive coverage of the QPA methodology covered in other texts,[2–5] the focus will be on the basis and application of the most commonly used techniques. These were identified from participant responses to the recent round robin on QPA sponsored by the International Union of Crystallography (IUCr) Commission on Powder Diffraction (CPD).[6,7] By far the greatest number of participants in that study used whole pattern (Rietveld based) methods but there are still several users of traditional single peak based methods and there are still many applications for which these methods suffice. Issues in the measurement of precision and accuracy will also be discussed.

## 11.2 PHASE ANALYSIS

There are several traditional methods for the estimation of phase abundance in multi-phase materials.[4] In summary, these can be divided into two groups:

- *Indirect methods* – these are usually based on the measurement of total chemistry which is then apportioned according to an assumed composition for each phase. A very widely used form of this "normative calculation" is the Bogue method[8] for the estimation of Portland cement phases. The limitations in this approach arise when the actual compositions of individual phases vary from those assumed in the calculation. This frequently occurs in the cement industry, where variance in local materials and production conditions can affect detailed phase compositions. In addition, normative calculation has the potential to be unstable when several phases in the mixture have similar chemical composition.
- *Direct methods* – these are based on a property specific to phases of interest in the sample. These methods are often not generally applicable, but are useful in estimating abundances of selected components. Examples include (i) magnetism – applicable to samples in which phases have different magnetic susceptibilities, (ii) selective dissolution – where the rate and extent of dissolution can be phase dependant, (iii) density – involving the

physical separation of phases with different densities, (iv) image analysis – for estimation of phase abundance from optical and electron-beam images, and (v) thermal analysis – where the magnitude of endo- and exothermic features during phase transitions are proportional to the amount of the phases present. Powder diffraction may be included in this category as it distinguishes and quantifies phases on the basis of their unique crystal structures, giving the technique broad applicability for crystalline materials.

Quantification of powder diffraction data is reliant on determination of the contribution of each component phase in a mixture to the final pattern. Commonly used methods can be divided into two distinct groups:

- The so-called "single peak" methods which rely on the measurement of a peak, or group of peaks, for each phase of interest and assumes that the intensity of these peaks are representative of the amount of the individual phases. This is often not the case due to peak overlap and phase-dependant factors (*e.g.*, preferred orientation and microabsorption) which affect the relative intensities.
- Whole pattern methods which rely on the comparison of wide range diffraction data with a calculated pattern formed from the summation of individual phase components that have either been (i) measured from pure phase samples or (ii) calculated from crystal structure information.

## 11.3 MATHEMATICAL BASIS

The integrated intensity $I$ of reflection $hkl$ for phase $\alpha$ in a multi-phase mixture measured on a flat-plate sample of infinite thickness can be calculated from:

$$I_{(hkl)\alpha} = \left[\frac{I_0\lambda^3}{32\pi r}\frac{e^4}{m_e^2c^4}\right] \cdot \left[\frac{M_{hkl}}{2V_\alpha^2}\left|F_{(hkl)\alpha}\right|^2\left(\frac{1+\cos^2 2\theta\,\cos^2 2\theta_m}{\sin^2\theta\,\cos\theta}\right)\right] \cdot \left[\frac{W_\alpha}{\rho_\alpha \mu_m^*}\right] \quad (1)$$

where $I_0$ is the incident beam intensity, $e$ is the charge on an electron, $m_e$ is the mass of an electron, $r =$ the distance from the scattering electron and the detector and $c =$ the speed of light. $M$ and $F$ are the multiplicity and structure factor of the reflection $hkl$ respectively, $V$ is the unit cell volume and $\theta$ and $\theta_m$ are the diffraction angles for the $hkl$ reflection and the monochromator, respectively. $W_\alpha$ and $\rho_\alpha$ are the weight fraction and density of phase $\alpha$, respectively, while $\mu_m^*$ is the mass absorption coefficient of the entire sample.

For Bragg–Brentano geometry, the path lengths of the incident and diffracted beams are equal for all values of $2\theta$ and, consequently, the effect of increased sample absorption is a decrease in the overall intensity of the pattern.

This is accounted for in Equation (1) by:

$$\frac{1}{2\mu_m^*} \tag{2}$$

However, for some instrument geometries, there is an angular dependence on observed intensity due to sample absorption, which must be allowed for in the calculation of $I$. This is the case where a flat plate sample is examined using a fixed angle of incidence or where a capillary sample is used.

A fixed angle of incidence arises when a flat plate sample is examined in an instrument such as the Inel powder diffractometer incorporating the CPS120 position sensitive detector (detector produced by Inel, Z.A.-C.D. 405, 45410 Artenay, France. http://www.inel.fr/en/accueil/). In this case, the absorption term above takes the form:[9]

$$\frac{\sin\beta}{\mu_m^*(\sin\alpha + \sin\beta)} \tag{3}$$

Where $\alpha$ is the angle between the incident beam and the sample surface and $\beta$ is the angle between the diffracted beam and the sample surface. In this geometry, $\alpha$ is set to a fixed value and $\beta$ varies with diffraction angle according to $\beta = 2\theta - \alpha$. In Bragg–Brentano geometry $\alpha = \beta = \theta$ and Equation (3) reduces to the expression in Equation (2).

For cylindrical samples, Sabine, *et al.*[10] define the absorption factor as the ratio between the "integrated intensity when no radiation removal processes are operative" and the observed intensity. This factor is given by:

$$A(\theta) = A_L \cos^2(\theta) + A_B \sin^2(\theta) \tag{4}$$

where $A_L$ and $A_B$ are the absorption factors at the Laue condition, $\theta = 0^\circ$, and the Bragg condition, $\theta = 90^\circ$ respectively.

For quantitative phase analysis, the expression in the first square bracket of Equation (1) can be reduced to a constant for a particular experimental set-up while the expression in the second square bracket is a constant for reflection *hkl* for phase $\alpha$. Therefore, the intensity, $I$, of a reflection (or group of reflections), $i$, can be reduced to:

$$I_{i\alpha} = C_{i\alpha}\frac{W_\alpha}{\rho_\alpha \mu_m^*} \tag{5}$$

where $C_{i\alpha}$ = constant for reflection (or group of reflections) $i$ of phase $\alpha$.

Application of Equation (5) can be seen in the absorption–diffraction method[3] for QPA. This method requires:

(i) The determination of $C_{i\alpha}$ by (i) the preparation of standards with known additions $W_\alpha$ of phase $\alpha$, (ii) measurement of peak intensity $I$ for the standards, and (iii) estimation of the standard sample mass absorption coefficient $\mu_m^*$.

(ii) Measurement of $I_{i\alpha}$ and estimation of $\mu_m^*$ for the unknown samples and calculation of $W_\alpha$ use a rearranged Equation (5).

The value of $\mu_m^*$ can be estimated through direct measurement of beam intensity through a sample of known thickness $t$ in a beam of the same wavelength as that used in the XRD data collection. Following measurement of the beam intensity with sample in ($I$) and out ($I_0$) of the beam, $\mu_m^*$ can be calculated using:

$$\frac{I}{I_0} = \exp(-\mu_m^* \rho \cdot t) \tag{6}$$

Alternatively, $\mu_m^*$ can be calculated from the sum of the products of the theoretical mass absorption coefficient ($\mu_j^*$) of each element (or phase) and the weight fractions ($W_j$) of all $n$ elements (or phases) in the sample. Elemental composition may be determined, for example, by X-ray fluorescence (XRF) measurement and use of this is more accurate than the use of phase composition as it takes into account any amorphous material not represented by peaks in the diffraction pattern but which still contribute to $\mu_m^*$.

$$\mu_m^* = \sum_{j=1}^{n} \mu_j^* W_j \tag{7}$$

Notably, measurement *via* Equation (6) produces an accurate estimate of $\mu_m^*$ while calculation *via* Equation (7) gives only a theoretical $\mu_m^*$ and does not include sample porosity. All of this presumes that the sample used to measure beam attenuation is the same as that used to collect the diffraction pattern, otherwise variations in packing density need to be taken into account.

A more general, and experimentally simpler, approach is to eliminate $\mu_m^*$ from the analysis altogether *via* the inclusion of an internal standard $s$ in known weight fraction $W_s$. Substitution of the measured intensity of the $j^{th}$ reflection (or group of reflections) of the standard phase, $I_{js}$, into Equation (5) yields:

$$I_{js} = C_{js} \frac{W_s}{\rho_s \mu_m^*} \tag{8}$$

The ratio of Equations (5) and (8) gives:

$$\frac{I_{i\alpha}}{I_{js}} = \frac{C_{i\alpha} \rho_s \mu_m^*}{C_{js} \rho_\alpha \mu_m^*} \frac{W_\alpha}{W_s} \tag{9}$$

Since $\mu_m^*$ now appears both in the numerator and denominator, its effect on the analysis is removed from the calculation. The weight fraction of the unknown, $W_\alpha$, can be determined from:

$$W_\alpha = K_{\alpha s}^{ij} \cdot W_s \cdot \frac{I_{i\alpha}}{I_{js}} \tag{10}$$

where:

$$K_{\alpha s}^{ij} = \frac{C_{js}}{C_{i\alpha}} \cdot \frac{\rho_\alpha}{\rho_s}$$

$K_{\alpha s}^{ij}$ can be determined by making known mixtures of standard and analyte phases. Notably, the presence of systematic errors (such as preferred orientation and microabsorption) which vary as a function of $W_\alpha$ will not be detected through application of Equation (10). The use of consistent sample preparation and presentation techniques is required to minimize the effect of these aberrations on the analysis.

### 11.3.1 Reference Intensity Ratio (RIR) Methods

Rearranging Equation (10) allows the definition of the so-called Reference Intensity Ratio (RIR)[11,12] as the ratio of strongest peak of phase $\alpha$ to the strongest peak of standard $s$. Since the generally accepted standard for QPA is corundum, the RIR equates to $I/I_c$ for the phase (where $I$ is the intensity of the strongest peak of the phase $\alpha$ and $I_c$ is the intensity of the strongest peak of corundum):

$$\frac{1}{K_{\alpha s}^{ij}} = \frac{I_{i\alpha}}{I_{js}} \cdot \frac{W_s}{W_\alpha} = RIR_{\alpha s} \equiv \frac{I}{I_c} \tag{11}$$

Quantification of the unknown phase in the presence of a known standard addition can be achieved by the rearrangement of Equation (11):

$$W_\alpha = \frac{I_{i\alpha}}{I_{js}} \cdot \frac{W_s}{RIR_{\alpha s}} \tag{12}$$

Hubbard and Snyder[12] describe modifications to Equation (11) that allow the use of peaks other than the strongest peak. Values for RIR can be obtained by (i) measurement using known mixtures of the standard and analyte phases or (ii) calculation from crystal structure information using, for example, Rietveld analysis software set to pattern calculation mode. Collated lists of RIR values for frequently encountered phases can be found in the ICDD database[13] and Smith *et al.*[14] Importantly, though, the user must be very careful in their selection of an appropriate RIR value for their particular experiment. The values of RIR will depend upon the analytical strategy employed (*e.g.* peak height, peak area, whole pattern, X-ray wavelength) in their derivation. This must match the conditions used in the experiment to which the value is to be applied. An important feature of RIR based techniques is that, once they are determined for the analyte phases of interest, the standard phase does not need to be present in the sample.

Chung[15,16] has demonstrated that for a system consisting of $n$ phases in which all components are crystalline and included in the analysis, an additional

constraint can be included of the form:

$$\sum_{k=1}^{n} W_k = 1.0 \tag{13}$$

The effects due to sample $\mu_m^*$ can be removed during calculation by the application of this so-called matrix flushing (or normalized RIR) method which combines Equations (12) and (13) and replaces the terms related to the standard phase according to:

$$\frac{W_s}{I_{js}} = \left( \sum_{k=1}^{n} \frac{I_k}{RIR_{ks}} \right)^{1} \tag{14}$$

Thus the weight fraction of phase α can be calculated from:

$$W_\alpha = \frac{I_{i\alpha}}{RIR_{\alpha s}} \times \left( \sum_{k=1}^{n} \frac{I_{ik}}{RIR_{ks}} \right)^{1} \tag{15}$$

The application of Equation (15) assumes that all phases are crystalline and included in the analysis with the result that the sum of the $W_j$'s is normalized to 1.0. While the technique leads to derivation of the correct relative phase abundances, the absolute values may be overestimated if non-identified or amorphous materials are present. The addition of an internal standard to the system allows calculation of the absolute amount of each phase [Equation (16)] and thus the derivation of the amount of amorphous and/or non-analysed components [Equation (17)]:

$$W_{\alpha(\text{abs})} = W_\alpha \times \frac{W_{\text{std(known)}}}{W_{\text{std(meas)}}} \tag{16}$$

$$W_{(\text{unk})} = 1.0 - \sum_{k=1}^{n} W_{k(\text{abs})} \tag{17}$$

where $W_{\alpha(\text{abs})}$ is the absolute weight fraction of phase $\alpha$; $W_{\text{std(known)}}$ is the known weight fraction of the standard added to the sample; $W_{\text{std(meas)}}$ is the weight fraction of the standard reported by Equation (15); $W_{\text{unk}}$ is the weight fraction of the unknown (unidentified) and/or amorphous component in the mixture.

If an internal standard has been used, then initial calculation of its concentration *via* Equation (15) may be (i) the same as the weighed amount, indicating that no amorphous/unidentified phases are present, (ii) greater than the weighed amount, indicating that amorphous/unidentified phases may be present, or (iii) less than the weighed amount indicating operator error or the use of invalid RIR values.

### 11.3.2 Rietveld-based Methods

Whole pattern (especially Rietveld-based) methods for the determination of phase abundance have the potential to produce more accurate and precise

results than those obtained from conventional single peak methods. This improvement derives from the fact that (i) all of the peaks in the pattern contribute to the analysis, regardless of the degree of overlap, and (ii) the impact of some sample related effects, such as preferred orientation, are minimized by the inclusion of all reflections. The application of models for correction of certain residual aberrations serves to further improve the analysis.

While the Rietveld technique was initially developed for the refinement of crystal structure, other parameters that must be refined to ensure best fit between the observed and calculated patterns contain useful, non-structural information that can be of interest to the analyst. These include peak width and shape, which can be related to crystallite size and strain (see Chapter 13), and the Rietveld scale factor, which, in a multiphase mixture, relates to the amount of the phase present.

Recalling Equation (1), the expression in the second square bracket shows that the constant $C$ in Equation (5) is inversely proportional to the square of the unit cell volume ($V^2$), while Hill[17] has demonstrated that the individual reflection intensity $I$ is proportional to the Rietveld scale factor, $S$:

$$C_\alpha \propto \frac{1}{V_\alpha^2} \quad \text{and} \quad I_\alpha \propto S_\alpha \tag{18}$$

Coupled with the knowledge that the phase density $\rho_\alpha$ (g cm $^3$) can be calculated from the mass of the unit cell contents ($ZM$, where $Z =$ the number of formula units in the unit cell and $M =$ the molecular mass of the formula unit) and the unit cell volume ($V$):

$$\rho_\alpha = 1.6604 \cdot \frac{ZM_\alpha}{V_\alpha} \tag{19}$$

(The value $1.6604 = 10^{24}/6.022 \times 10^{23}$ is needed to convert $\rho$ in AMU Å $^3$ into gm cm $^3$.) Substitution and rearrangement of Equations (18) and (19) in Equation (5) shows that:

$$W_\alpha = \frac{S_\alpha (ZMV)_\alpha \mu_m^*}{K} \tag{20}$$

where $K$ is a "scaling factor" which is used to put $W_\alpha$ on an absolute basis. O'Connor and Raven[18] have demonstrated that $K$ is dependant only on the instrumental conditions and is independent of individual phase and overall sample-related parameters. Therefore, a single measurement is sufficient to determine the value of $K$ for a given instrumental configuration. In this context, $(ZMV)_\alpha$ is the "calibration constant" for phase $\alpha$ and can be calculated from published crystal structure information alone. Measurement of $K$ in this way may be carried out on a standard mixture separately from the measurement of the actual unknown mixture in question. This standard mixture then constitutes an "external standard". The value of $K$ calculated for the external standard will be appropriate for the calibration of subsequent measurements as long as all instrumental conditions remain the same as those used for its determination.

In a similar manner to that used for the single peak approach, the need to measure $K$ and measure or calculate $\mu_m^*$ can be eliminated by the addition of an

internal standard $s$ in known amount $W_s$ and taking the ratio of Equation (20) for analyte and standard phases:

$$W_\alpha = W_s \cdot \frac{S_\alpha (ZMV)_\alpha}{S_s (ZMV)_s} \tag{21}$$

Hill and Howard[19] have applied the matrix flushing method of Chung[15,16] to the Rietveld analysis context and shown that the weight fraction of phase $\alpha$ in an $n$ phase mixture can be given by the relationship:

$$W_\alpha = \frac{S_\alpha (ZMV)_\alpha}{\sum_{k=1}^{n} S_k (ZMV)_k} \tag{22}$$

The use of Equation (22) in QPA once again eliminates the need to measure the instrument calibration constant and the sample mass absorption coefficient. However, in a similar manner to Equation (15), the method normalizes the sum of the analysed weight fractions to 1.0. Thus, if the sample contains amorphous phases, and/or minor amounts of unidentified crystalline phases, the analysed weight fractions will be overestimated. Once again this can be addressed by inclusion of an internal standard and modification of the measured $W_\alpha$'s *via* Equations (16) and (17).

*11.3.2.1 Application to Phases of Poor Crystallinity or Unknown Structure.* As a general rule, the Rietveld method requires the phases being analysed to be crystalline and of known structure, although amorphous and unidentified phases may be quantified as a group by the use of either internal or external standard methods. However, if phases of interest are poorly ordered or have only partially known structures, it is still useful to be able to quantify them separately from the bulk of truly amorphous material.

Phases with partially known structures have had their unit cell dimensions and space group determined, allowing the assignment of indices to the reflections. If the phase of interest can be "indexed" in this manner, analysis can be achieved by substituting the structure factors in Equation (1) with values derived from measurement of peak intensities.[20] Application of a Le Bail *et al.*[21] approach (see Chapter 5) permits the constraint of peak positions according to the assigned space group and unit cell parameters while allowing individual peak intensities to vary to achieve the best fit to the pattern.

If the phase cannot be indexed, it can be defined as a related series of peaks that may be scaled as a single entity during refinement. The relative peak intensities can be derived through peak fitting to a diffraction pattern in which the phase is a major component.

In either case, the lack of a complete crystal structure precludes the calculation of the ZMV calibration constant, requiring additional measurement steps for the calibration of the model. The following steps describe the

procedure necessary for the generation of such a calibrated model:

1. Collect a diffraction pattern from the pure phase. If pure phase material is not available, then the phase should constitute the bulk of the sample.
2. Run the Rietveld program in the LeBail fitting mode using the assigned space group and unit cell parameters. From the refined list of intensities, create a file containing $h$, $k$, $l$, $M$, $d$, $2\theta$ and $I$, where $h$, $k$ and $l$ are the Miller indices of the reflection, $M$ is the reflection multiplicity, $d$ is the $d$-spacing of the reflection, $2\theta$ is the Bragg angle and $I$ is the reflection intensity.
3. Depending on which Rietveld program has been used, it might be necessary to remove the effect of the Lorentz-polarization ($Lp$) factor from each observed peak intensity:

$$Lp = \frac{1 + \cos^2 2\alpha \cdot \cos^2 2\theta}{4 \cos\theta \sin^2\theta \cdot (1 + \cos^2 2\alpha)} \tag{23}$$

   where $\alpha$ is the diffraction angle of the monochromator.

   Note that Equation (23) refers to Bragg–Brentano geometry.
4. Removal of the contribution of the $Lp$ factor from the measured intensities *via*:

$$I'_{\text{meas}} = \frac{I_{\text{meas}}}{Lp} \tag{24}$$

   These modified intensities can now replace the intensities in the *hkl* file.
5. To achieve quantification *via* Equation (22), it is necessary to calculate a ZMV calibration constant that can be used with this *hkl* file. This can be achieved through the addition of an internal standard in known amount and rearrangement of Equation (21):

$$(ZM)_\alpha = \frac{w_\alpha}{w_s} \cdot \frac{S_s}{S_\alpha} \cdot \frac{(ZMV)_s}{V_\alpha} \tag{25}$$

   where $\alpha$ is the unknown and $s$ is the standard.

The $ZM$ value calculated in Step 5 will be appropriate for quantification of mixtures using the *hkl* file created in Step 4, but will not be physically realistic in its magnitude since the intensity values used are not true structure factors. A physically meaningful number may be determined from the measured density of the phase, $\rho_\alpha$, using:

$$(ZM)_{\alpha(\text{true})} = \frac{\rho_\alpha V_\alpha}{1.6604} \tag{26}$$

The peak intensity values in the *hkl* file can then be scaled according to the ratio of $ZM_{\alpha(\text{true})}/ZM_\alpha$. These values will then approximate "real" structure factors for this material.

Further details of this approach to the calibration of poorly ordered materials can be found in Scarlett and Madsen.[22]

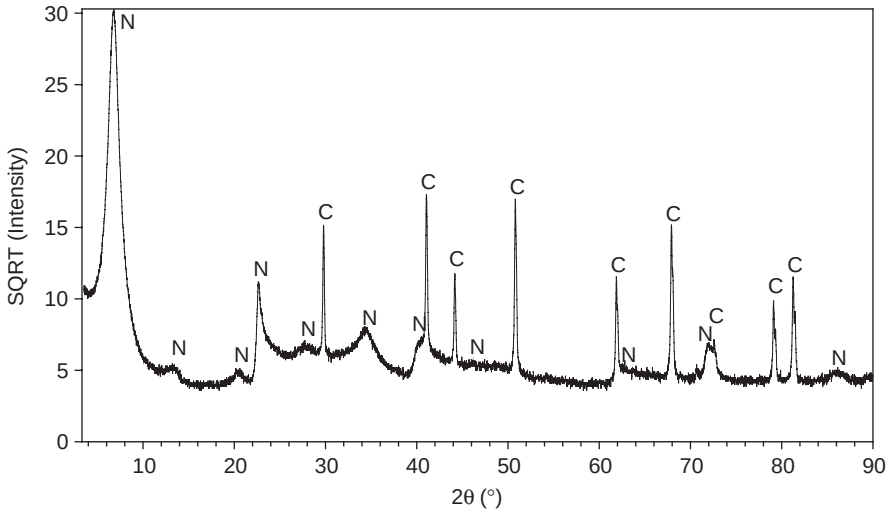



**Figure 11.1** X Ray diffraction pattern (Co Kα) for a sample of 3 : 1 nontronite (N) : corundum (C). The poor crystallinity of the nontronite is evident from the peak broadening in the diffraction peaks. The lack of an adequate crystal structure for nontronite precluded the use of a conventional Rietveld analysis technique.

The following example demonstrates the application of the peak model technique to the poorly ordered clay phase nontronite, for which accurate crystal structure models are not available (Figure 11.1). In this instance, the phase model was obtained by Le Bail extraction of peaks using nontronite cell data and X-ray diffraction data obtained from relatively pure nontronite. Synthetic mixtures of this material and corundum ($Al_2O_3$) were prepared and a value for $ZM_{\text{nontronite}}$ calculated from the refinement of the 50/50 mixture. Figure 11.2 shows the good agreement between weighed and measured amounts of nontronite for the series of synthetic mixtures.

## 11.4 FACTORS LIMITING ACCURACY

### 11.4.1 Particle Statistics

For quantitative phase analysis it is generally accepted that the peak intensities need to be measured to an accuracy of about $\pm 1 - 2\%$ relative. The ability to achieve this is strongly influenced by the size of the crystallites in the sample: reproducible diffraction intensities require a small crystallite size to ensure that there is uniform intensity around the Debye–Scherrer cone.

Elton and Salt[23] have used both theoretical and experimental methods to estimate the number of crystallites diffracting ($N_{\text{diff}}$) in a sample. Fluctuations in line intensity between replicate samples arise largely from statistical variation in the number of particles contributing to the diffraction process. It has been shown that small changes to the instrumental and sample configurations can

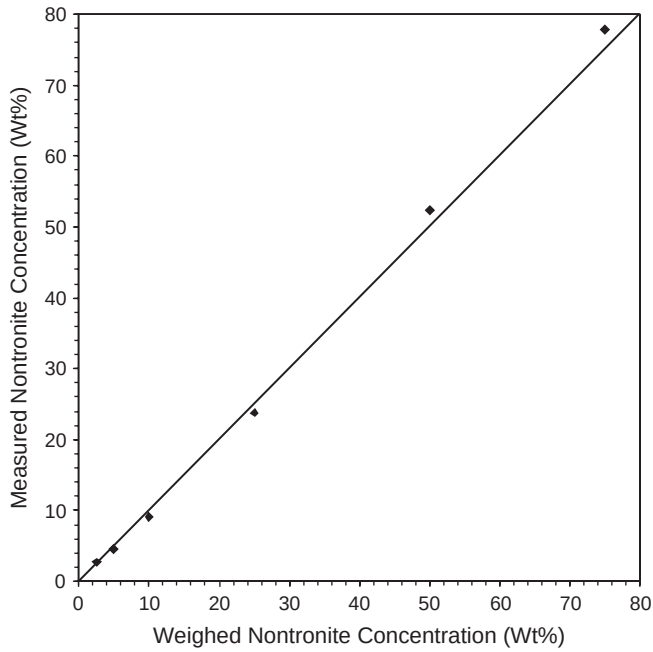



**Figure 11.2** Comparison of weighed and measured values for the series of synthetic mixtures of nontronite and corundum. The analyses were derived using a modified Rietveld approach in which nontronite is defined using a file of reflection *hkl*'s and intensities rather than the full crystal structure. The line represents a 1 : 1 relationship.

**Table 11.1** Relationship between crystallite diameter and the number diffracting (after Smith[24]).

| *Crystallite diameter (μm)* | *40* | *10* | *1* |
|---|---|---|---|
| **Crystallites (20 mm$^3$)** | $5.97 \times 10^5$ | $3.82 \times 10^7$ | $3.82 \times 10^{10}$ |
| **Number diffracting** | 12 | 760 | 38 000 |
| $\sigma_{PS}$ | 0.289 | 0.036 | 0.005 |

significantly improve the sample's particle statistics. An estimate of the fractional particle statistics error, $\sigma_{PS}$, is given by:

$$\sigma_{PS} = \sqrt{N_{\text{diff}}} \Big/ N_{\text{diff}} \tag{27}$$

Table 11.1 summarizes the work of Smith[24] into the effect of particle statistics in a static sample. This work showed that a powder of particle size 40 μm may have as few as 12 crystallites diffracting in a sample volume of 20 mm$^3$. This results in a value of $\sigma_{PS}$ of about 0.3, which is insufficient for reproducible pattern statistics. Reduction of the particle size to 1 μm reduces $\sigma_{PS}$ to a more acceptable value of 0.005. Notably, the number of diffracting

crystallites will be affected by the absorption coefficient ($\mu$) of the sample and that the figures given in Table 11.1 are for a particular value of $\mu$.

For a given sample, several methods can be used to increase the number of crystallites contributing to the diffraction pattern, including:

(i) Increase the instrument beam divergence. Some of the ways of achieving this for a laboratory source are to use a broad focus rather than a fine focus tube, or to use wider divergence and receiving slits. Elton and Salt[23] have demonstrated that $\sigma_{PS}$ can be reduced by a factor of about two times by using a broad focus tube with a 1.2 mm receiving slit instead of a long fine focus tube with a 0.3 mm receiving slit. However, notably, such steps may reduce the overall instrument resolution and lead to greater peak overlap.

(ii) Rotate the sample about the normal to the sample surface for a flat plate sample or the sample axis for a capillary sample. This increases the irradiated volume and reduces $\sigma_{PS}$ by a factor of about 5–6 times.

(iii) Oscillate the sample about the theta axis (flat plate geometry). Note that this motion removes the exact $\theta/2\theta$ relationship between sample and receiving slit and may lead to aberrations in the peak intensities, positions and profile shapes when using non-parallel laboratory source X-ray beams. The degree of improvement in $\sigma_{PS}$ will depend on the range of oscillation used.

(iv) Repack the sample, recollect and reanalyse the diffraction data. Averaging the results from each analysis will produce more meaningful parameter values and will allow independent determination of their estimated standard deviations (esd's).

(v) Reduce the average crystallite size by mechanical comminution of the sample. This is the most effective method of increasing the number of crystallites examined. However, caution must be exercised in the choice of mill since many grinding techniques introduce peak broadening through both the reduced crystallite size and the introduction of lattice strain. In addition, some phases can undergo solid-solid phase transitions or dehydration during grinding. These problems are significantly reduced by grinding in a liquid (*e.g.* alcohol or acetone) which tends to reduce local heating of the sample in the grinding vessel. The McCrone micronising mill is effective in reducing the particle size to around 10 μm or less in times of 1–20 min, depending on material hardness (Produced by McCrone Research Associates Ltd, 2 McCrone Mews, Belsize Lane, London NW3 5BG, England). Further details of sample preparation techniques and their effect on diffraction data can be found in Buhrke *et al.*[25] and Hill and Madsen.[26]

### 11.4.2 Preferred Orientation

The basis for calculation of powder diffraction intensities relies on the sample being a randomly orientated powder; that is, all reflections have an equal

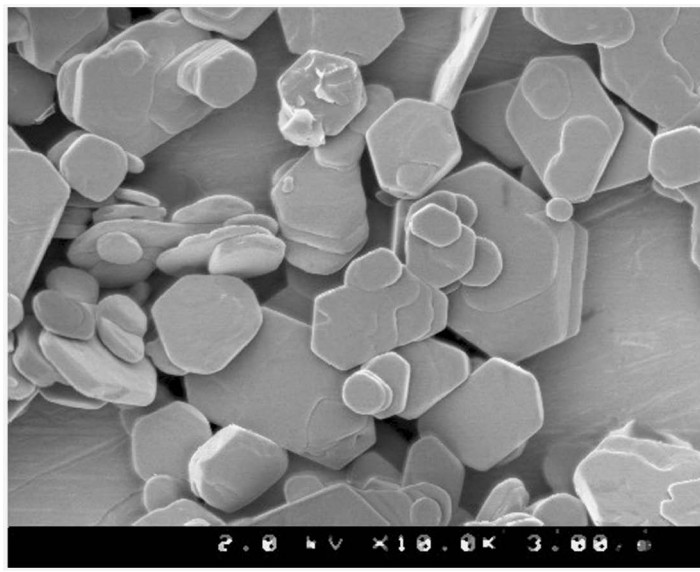


**Figure 11.3** Brucite, $Mg(OH)_2$, morphology showing the flat, hexagonal plates that lead to the preferred orientation along the [00l] direction.

probability of meeting the diffraction condition. However, the morphology of some materials often makes this difficult to achieve since they have a natural inclination to align themselves along a particular crystallographic direction. This causes a preponderance of one set of reflections to be presented to the beam and the relative intensities of the pattern to be skewed accordingly. Materials that crystallize as needles or plates are particularly susceptible to this and tend to align themselves during sample packing.

Figure 11.3 shows a scanning electron image of the mineral brucite ($Mg(OH)_2$), which exhibits anisotropic crystal growth resulting in relatively large dimensions in the (*hk*0) plane relative to the (00*l*) plane. During sample packing, the natural tendency is for these plates to orient with the large flat (*hk*0) surfaces aligned with the sample surface. This leads to preferred orientation, and hence intensity enhancement, of the (00*l*) reflections.

This misrepresentation of relative intensity causes significant problems for the application of single peak methods in that no single peak is truly representative of the amount of the material present. Whole pattern methods are, in general, more accurate for these types of materials since (i) all peaks in the pattern contribute to the analysis, and (ii) they generally incorporate some form of correction algorithm to compensate for such intensity aberrations. The most commonly used (Madsen *et al.*[26] and Scarlett *et al.*[17]) correction algorithm for preferred orientation is the March–Dollase[27,28] model given in Equation (28):

$$P(\alpha) = (r^2 \cos^2 \alpha + r^{-1} \sin^2 \alpha)^{-\frac{3}{2}} \tag{28}$$

where $\alpha$ is the angle between the preferred orientation vector and the reciprocal lattice vector direction of the Bragg peak being corrected and $r$ is a refinable parameter indicating the degree of preferred orientation. In an ideal, randomly orientated powder, $r = 1$.

Notably, the correction algorithms are only approximations and may not adequately correct for extreme preferred orientation. In this case it may be better to eliminate, or at least minimize, preferred orientation before data collection begins through appropriate selection of sample packing technique or instrument geometry.[26]

### 11.4.3 Microabsorption

The most problematic factor affecting accuracy in QPA *via* XRD is that of microabsorption. While the application of whole pattern, Rietveld based techniques for QPA[19,29] may allow for the correction of some sample related aberrations (such as preferred orientation), it does not adequately counter the effects of microabsorption. A detailed discussion of the effect can be found in Zevin and Kimmel[4] and references therein and will not be repeated here. In summary, the effect arises when the sample contains phases with different mass absorption coefficients and/or particle size distributions. The result is that the intensities of reflections from the heavily absorbing phases are suppressed while those from lighter absorbers are effectively enhanced. This subsequently misrepresents the derived relative abundance of the phases.

For those samples where the effects of microabsorption absorption are present Brindley[30] has defined the so-called particle absorption factor $\tau$ as:

$$\tau_\alpha = \frac{1}{Vol_k} \int_0^{Vol_k} \exp[-(\mu_\alpha - \mu)D] \cdot dVol_k \tag{29}$$

where $\mu_\alpha$ is the linear absorption coefficient (LAC) of phase $\alpha$, $\mu$ is the average linear absorption coefficient of the entire sample and $D$ is the "effective dimension" of the particles and $Vol$ is the particle volume.

Taylor and Matulis[31] have shown that Brindley microabsorption corrections can be incorporated into Equation (22) according to:

$$W_\alpha = \frac{\frac{S_\alpha (ZMV)_\alpha}{\tau_\alpha}}{\sum_{j=1}^{n} \frac{S_j (ZMV)_j}{\tau_j}} \tag{30}$$

Since $\tau_\alpha$ is a function of the weight fractions, $W$, of all phases, $W$ is derived through iterative calculation of the $\tau$'s and $W$'s.

There are severe limitations in the Brindley correction that arise from the range of applicability of the model (for coarse samples, $\mu D$ is typically in the range 0.1 to 1.0) and the difficulty in defining an appropriate value for $D$.

All materials subject to size reduction through grinding will exhibit a distribution of particle sizes, often skewed in shape, with the result that a single estimate of size will not represent the sample as a whole. In addition, the grinding of multiphase samples most often results in differential size reduction of "hard" and "soft" phases. In practice, the difficulty in obtaining an accurate estimate of individual particle sizes usually means that analysts make an informed guess at the value of $D$. Thus, the value used may be empirically based to achieve a desired phase abundance rather than a value based on sound measurement. Widespread misuse of microabsorption correction was clearly demonstrated in the IUCr quantitative phase analysis round robin.[6,7]

Given the limitations of current microabsorption correction algorithms, the best approach is to minimize the effect where possible before data collection is undertaken. Examination of Equation (29) shows that this can be achieved in two ways, namely:

- Reduction of particle size. Further discussion can be found Section 11.4.1 (Particle Statistics) and in Buhrke *et al*.[25]
- Reduction of the absorption contrast. Sometimes this can be simply achieved through a change in the wavelength used to collect the diffraction data. Table 11.2 shows that for a mixture containing corundum ($\alpha$-$Al_2O_3$) and hematite ($\alpha$-$Fe_2O_3$) there is a factor of about 10× in the linear absorption coefficient if Cu K$\alpha$ radiation is used to collect the data. However, if Co K$\alpha$ radiation is used, the LAC's of the two phases are almost equal. Thus, there will be minimal preferential absorption if the particle sizes are similar. While the absorption contrast remains high for short wavelengths such as Mo K$\alpha$, the lower values of LAC means that a larger volume of material will contribute to the pattern, resulting in benefits deriving from the improved particle statistics. Notably, the penetrating power of neutrons is such that the often debilitating effects of microabsorption present in X-ray data are very significantly reduced in neutron diffraction data. The results of the QPA round robin[7] showed that for Sample 4 (designed to exacerbate the microabsorption effect) those participants who collected and analysed neutron diffraction data performed significantly better than all other participants.

**Table 11.2** Linear absorption coefficients for corundum ($\alpha$-$Al_2O_3$) and hematite ($\alpha$-$Fe_2O_3$) at a range of wavelengths.

| | *X Ray linear absorption coefficient ($cm^{-1}$)* | | | *Neutron cross section (cm)* |
|---|---|---|---|---|
| Wavelength | Cu K$\alpha$ | Co K$\alpha$ | Mo K$\alpha$ | 1.54 Å |
| Corundum | 125.4 | 194.7 | 12.6 | 0.005 |
| Hematite | 1145.9 | 238.4 | 139.2 | 0.039 |

### 11.4.4 Precision, Accuracy and the Calculation of Error

The question of precision and accuracy in QPA *via* XRD is a difficult one. It is simple enough to calculate errors on the basis of replication or precision in the mathematical fit. However, determination of the actual *accuracy* of the analysis is no trivial task in a standardless method. In fact, it cannot be achieved without recourse to some other measure of the sample that does incorporate standards. Too often, analysts will report Rietveld errors (see Appendix A) calculated during refinement as the errors in the final quantification.[6,7] These numbers relate purely to the mathematical fit of the model and have no bearing on the accuracy or otherwise of the quantification itself.

Consider, for example, a three-phase mixture of corundum, magnetite and zircon. Such a sample was presented as Sample 4 in the IUCr CPD round robin on quantitative phase analysis.[7] Its components were chosen with the deliberate aim of creating a sample in which severe microabsorption occurs. Table 11.3 shows the weighed amounts of each component and the results of replicate analyses of three different sub-samples of this material.

In this context, the Rietveld error represents the uncertainty in the mathematical fit between the observed and calculated patterns and is the value most often quoted as the error in the phase abundance. Contrasting with this is the standard deviation of the mean abundances, which represents the expected precision in the analysis and is 3 to 4 times greater than the Rietveld derived errors. The good level of fit achieved in conducting these analyses (evidenced in the low *R*-factors) could lead the analyst to conclude that the mean value $\pm$ the standard deviation of the mean is an adequate measure of the phase abundances and their errors. However, the Rietveld errors and the replication errors are at least an order of magnitude smaller than the bias (measured – weighed). The bias, due to the presence of severe microabsorption, represents the true accuracy that can be achieved in this system if the analyst takes no further steps to identify the cause and minimize the effect of absorption contrast or other aberrations which may affect accuracy.

**Table 11.3** Comparison of errors generated during the analysis of XRD data (Cu K$\alpha$) from three sub-samples of Sample 4 from the IUCr CPD round robin on quantitative phase analysis. The bias values are (measured – weighed) while the values denoted "XRF" are the phase abundances generated from elemental concentrations measured by X-ray fluorescence methods.

| *Parameter* | *Phase* | | |
|---|---|---|---|
| $N = 3$ | Corundum | Magnetite | Zircon |
| Weighed | 50.46 | 19.46 | 29.90 |
| Mean measured wt.% | 56.52 | 17.06 | 26.42 |
| Mean of Rietveld errors | 0.15 | 0.11 | 0.11 |
| S.D. of measured wt.% | 0.63 | 0.41 | 0.35 |
| Mean of bias | 6.06 | 2.58 | 3.48 |
| XRF | 50.4(2) | 19.6(1) | 29.5(1) |

**Table 11.4** Comparison of errors generated during the analysis of the same XRD data (Cu K$\alpha$) presented in Table 11.3 using the Brindley correction method for microabsorption. As in Table 11.3, the mean is based upon three replicate measurements and the bias is the measured value – the weighed.

| *Parameter* | *Phase* | | |
|---|---|---|---|
| $N = 3$ | Corundum | Magnetite | Zircon |
| Weighed | 50.46 | 19.46 | 29.90 |
| Brindley correction, $D = 1\,\mu m$ | | | |
| Mean measured wt.% | 55.76 | 17.81 | 26.43 |
| Mean of bias | 5.30 | 1.83 | 3.47 |
| Brindley correction, $D = 5\,\mu m$ | | | |
| Mean measured wt.% | 52.49 | 21.18 | 26.33 |
| Mean of bias | 2.03 | 1.54 | 3.57 |
| Brindley correction, $D = 10\,\mu m$ | | | |
| Mean measured wt.% | 47.76 | 26.15 | 26.08 |
| Mean of bias | 2.70 | 6.51 | 3.82 |

In the example above, the phases are such that the chemistry is unambiguous and the phase quantification could have been derived by normative calculation from bulk elemental analysis (XRF). This is not often the case, but it is frequently possible to establish the composition of each phase within a system *via* electron probe microanalysis or similar and conduct the inverse of a normative calculation to derive the bulk chemistry from the XRD QPA. This can then be compared with the results of a standards based technique such as XRF to obtain a measure of the accuracy of the XRD analysis. Examples of such calculations are given later in the sections dealing with application in mineralogical and industrial situations. Where this is not possible or practical, it is better to consider XRD QPA as a "semi-quantitative" technique at best.

As an addendum to the above example, Table 11.4 shows the effect of the use of the Brindley correction on the mean measured weight percentages and bias values. The difficulty in establishing an appropriate value of $D$ has been discussed in the preceding section on microabsorption, and Table 11.4 shows the considerable effect on quantification of different, arbitrarily chosen values. The magnitude of the change in bias between no correction and a correction for a particle size of 10 μm, serves to illustrate the need for extreme caution in the application of this technique. Notably, a mean particle size of 10 μm is typical for samples prepared using a common milling device such as the McCrone micronising mill discussed in Section 11.4.1 (Particle Statistics).

## 11.5 EXAMPLES OF QPA *VIA* POWDER DIFFRACTION

### 11.5.1 Application in Mineralogical Systems

*11.5.1.1 A Simple Three-phase Mixture.* The first sample of the IUCr CPD round robin on QPA[6] summarized the results obtained from the analysis of a

three-phase mixture (Figure 11.4) prepared with eight different compositions so that each phase was represented at concentration levels ranging from about 1.3 to 95 wt.%. The purpose of the study was to determine the level of precision and accuracy of the quantitative phase determinations of the three components in terms of the variation due to (a) pure sampling and testing errors within a typical laboratory and (b) differences in the analytical procedures between laboratories.

The materials used in the study (corundum – $\alpha$-$Al_2O_3$, zincite – ZnO, and fluorite – $CaF_2$) provided a relatively "simple" analytical system to determine the levels of accuracy and precision that could be expected under ideal conditions. Rather than being too prescriptive in the detail of the techniques to be used for analysis, the round robin organizers allowed the participants to select and report their own methodology. Thus, the RR also served as a survey of commonly used techniques for QPA.

A summary of all the results returned shows that while the mean values approximate the weighed values, there is a very wide range of values, indicating that many participants were unable to accurately quantify the amounts of materials present even in this relatively simple phase system. Among the significant causes of deviation from the weighed values were operator errors.

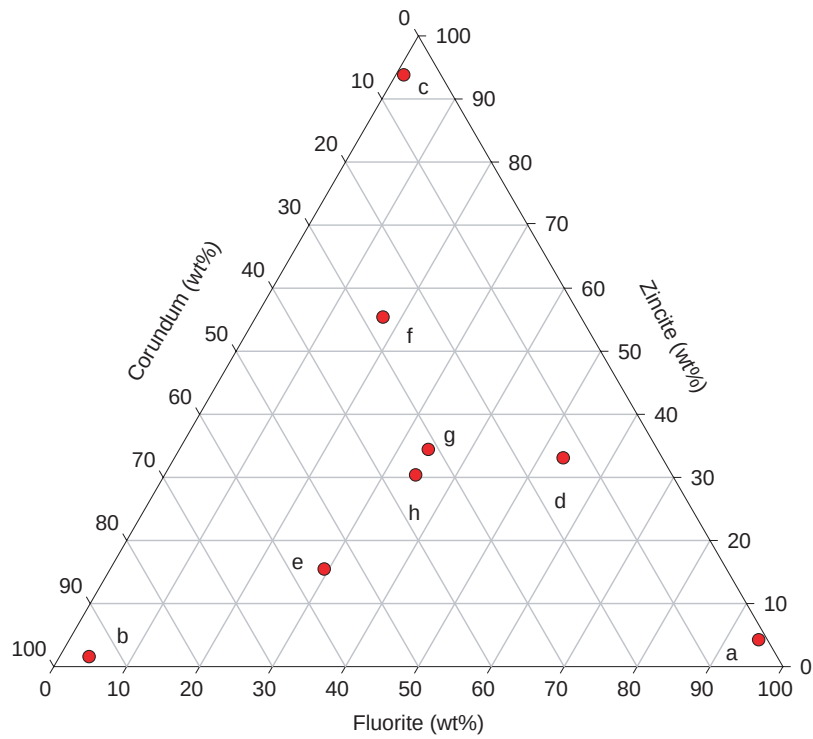



**Figure 11.4** Composition of mixtures contained within the Sample 1 suite from the IUCr CPD round robin on quantitative phase analysis.

These were largely due to inappropriate use of the method being applied. For the Rietveld based techniques, these errors included (i) entry of incorrect crystal structure information, including atom coordinates and thermal vibration parameters, (ii) incorrect space group notation, (iii) incorrect atom site occupation parameters, (iv) allowing structure parameters (especially thermal parameters) to refine to physically unrealistic values, and (v) not completing the refinement.

To test the validity of Rietveld based methods for QPA, the round robin organizers undertook the analysis of all eight mixtures in the Sample 1 suite using the following refinement strategy:

(i) For all samples, parameters included in the refinement included (i) pattern background, modelled with a polynomial in $2\theta$, (ii) sample offset, and (iii) sample absorption coefficient.

(ii) For Rietveld programs that used the fundamental parameters approach[32,33] to peak modelling, the instrument component was defined using data collected from a sample of highly crystalline of $Y_2O_3$. The instrument parameters (divergence slit aperture, receiving slit width, axial divergence and so on) released in this step were then fixed at their refined values and used to define the instrument contribution to peak width for the remaining samples in the analysis.

(iii) For Sample 1a ($\sim$95 wt.% fluorite), parameters included in the refinement were the unit cell dimensions and crystallite size for each of the three phases. In addition, the thermal vibration parameters for Ca and F were released. The thermal parameters were then fixed at their refined values and used in the model for fluorite in all other samples.

(iv) For Sample 1b ($\sim$95 wt.% corundum), Step 3 was repeated but this time allowing refinement of Al and O thermal parameters as well as the Al $z$ and O $x$ coordinates. These parameters were then fixed at their refined values and used in the model for corundum in all other samples.

(v) For Sample 1c ($\sim$95 wt.% zincite), Step 3 was repeated but this time allowing refinement of Zn and O thermal parameters. Once again, these parameters were then fixed at their refined values and used in the model for zincite in all other samples.

(vi) In each of steps 3 to 5, the refined thermal parameters were checked for agreement with literature values. This is a critical step, since thermal parameters that deviate significantly from expected values may point to errors in the models that generate the calculated pattern intensity. Since all phases in this study are well-ordered materials, isotropic thermal parameters ($B_{eq}$) in the range = 0.3–0.5 Å$^2$ are expected. However, participants in the RR returned results based on structures with $B_{eq}$ values ranging from 0.0 to 10.0 Å$^2$. Since the thermal parameters correlate strongly with the Rietveld scale factor, any errors in $B_{eq}$ will be reflected in the reported quantitative phase abundances.

(vii) For all eight Sample 1 data sets, the refinable parameters for each phase included (i) unit cell dimensions, (ii) crystallite size, and (iii) an overall

scale factor. By following the procedure detailed above, refinement stability, even for the minor phases, was assured through the minimization of the number of parameters in the refinement.

The data sets distributed by the CPD for the QPA round robin are a useful resource for users aiming to develop and test their skills in applying various techniques. All data sets, in formats suitable for most of the commonly used software, can be found at http://www.mx.iucr.org/iucr-top/comm/cpd/QARR/data-kit.htm.

Phases present only in minor amounts are more difficult to determine than the phases present in medium to major amounts. This is especially true in this example for corundum, which, for X-ray radiation, has the lowest average scattering power and hence the lowest observed intensities of the three phases.

*11.5.1.2 Internal Standard Addition.* An example of the use of an internal standard for phase quantification is the recent work by Madsen *et al.*[34] in their study of the reaction mechanism of pressure acid leaching (PAL) of nickel laterite ores. This was an *in situ* study in which nickel laterites were reacted with sulfuric acid at elevated temperature and hydrothermal pressure to prevent the boiling of the acid. The purpose of pressure acid leaching is to dissolve any nickel-bearing phases into the acid and subsequently treat this with solvent extraction for the recovery of the nickel. There has been much *ex situ* work done to the reaction mechanisms of this system,[35,36] but these studies have relied on the cooling of the system prior to any analytical work.

The aim of the *in situ* XRD study was to examine the phase changes occurring in the system at processing temperature and pressure to remove any artefacts induced by cooling. The reaction products formed during PAL of one particular laterite ore, saprolite, were believed to undergo considerable change upon cooling and as such its phase chemistry had not been confirmed. This dynamic study allowed that system to be examined directly. To obtain kinetic information from experiments such as this, it is important that phase quantification be carried out throughout the reaction. In this example, datasets of two minutes duration were collected throughout the experiment using a position sensitive detector (Inel CPS120). Each dataset was quantified using the Rietveld method.

The reaction mechanism of this system involved the transfer of phases across the solid–liquid interface. Hence, quantification using Equation (22) produced values that were overestimated. To determine the absolute phase abundances, powdered diamond was selected as an inert internal standard and was weighed into the starting solids. Acid was then added to this mixture and the standard concentration taken as its weight fraction of the sample in its entirety, *i.e.*, solids and liquids in total. For each dataset the results of the quantitative phase analysis were adjusted according to the known amount of standard present in the system [Equation (16)]. This allowed the determination of variation in the amorphous content of the system to be assessed [*via* Equation (17)] as well as the formation and consumption of crystalline phases. The amorphous content

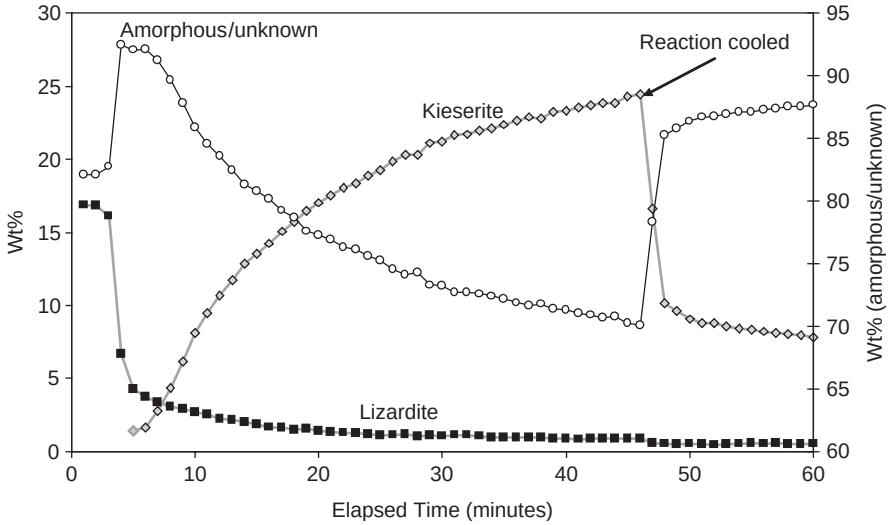



**Figure 11.5** Results of quantitative phase analysis during pressure acid leaching of saprolitic nickel laterite ore.

of the sample included any amorphous solid material as well as the liquid phase.

Figure 11.5 shows the results of QPA of a PAL experiment (data collected at Beamline 6.2, Daresbury SRS under grant number 42028). The dissolution of lizardite [nominally $Mg_3Si_2O_5(OH)_4$] and subsequent crystallization of kieserite ($MgSO_4.H_2O$) is immediately apparent. These reactions correspond with an increase and decrease in amorphous content, respectively. Kieserite is only observed during *in situ* studies as it has a negative temperature coefficient of solubility and redissolves on cooling during extraction for *ex situ* study.

*11.5.1.3 External Standard.* The recent work of Scarlett *et al.*[37,38] in the determination of reaction sequences in the formation of iron ore sinter phases (SFCA) highlighted some of the difficulties in determining the absolute abundances of phases in complex mineralogical systems. The work consisted of laboratory-based, *in situ* analysis of XRD data collected during the heating to $\sim$1200 °C of a mixture of $SiO_2$, $Fe_2O_3$, CaO (added as calcite – $CaCO_3$), and $Al_2O_3$ [added as gibbsite – $Al(OH)_3$]. Initially, quantification was carried out using the ZMV algorithm of Hill and Howard[19] given in Equation (22). However, during the reaction, there are several significant phase changes that have the potential to affect the accuracy of phase abundances derived in this manner. These include:

- Decomposition of gibbsite at about 220 °C with an accompanying loss of water from the sample. The product of this decomposition is a finely-divided Al-oxide which is effectively amorphous and hence cannot be

included in a conventional analytical method based on the Hill/Howard ZMV algorithm.

- The decomposition of calcite at about 650 °C with an accompanying loss of $CO_2$ from the sample. In this case, crystalline CaO in the form of lime is formed and can be included in the analysis.

Since the ZMV algorithm normalizes the sum of the analysed weight fractions to 1.0, the loss of part of the sample or the generation of amorphous phases will result in the overestimation of the analysed phases. The black circles and line in Figure 11.6 show the analysed amount of the major phase (hematite – $Fe_2O_3$) calculated using Equation (22). At the start of the reaction, the amount of hematite is ~69 wt.% (from known weight additions), but appears to increase in concentration as the gibbsite and calcite decompose during the reaction sequence. While the relative phase abundances in the sample at each step are correct, the absolute amounts are needed to derive the reaction mechanism.

To put the phase abundances on the absolute scale, Equation (20) was used by first determining the scaling factor $K$ based on the known amount of hematite in the sample at the start of the reaction. This makes the initial measurement of hematite effectively an external standard for the rest of the experiment. The results of this quantification method are shown by the crosses in Figure 11.6 and give a more realistic indication of the amount of hematite present in the sample at each step in the reaction.

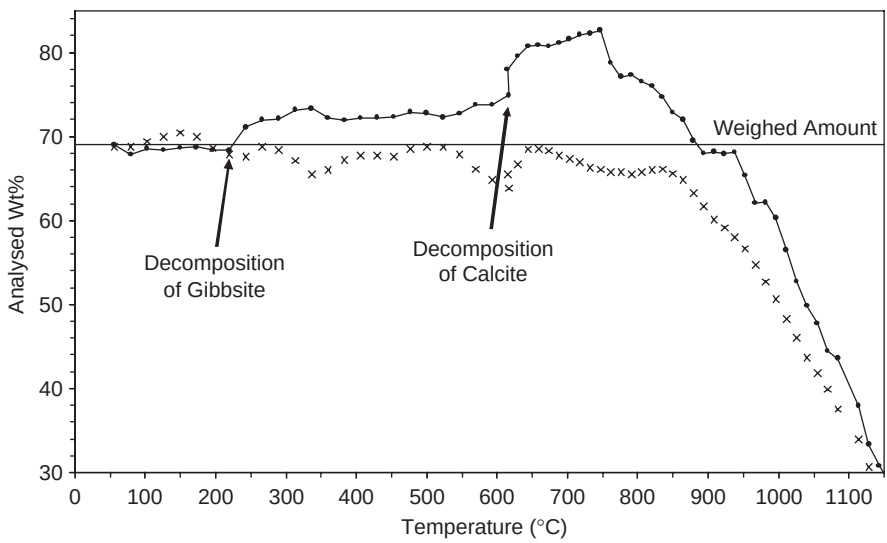



**Figure 11.6** Results of QPA of hematite in the formation reaction of SFCA by (i) the ZMV algorithm given in Equation (22) (filled circles and line) and (ii) the external standard method given in Equation (20) (crosses).

In dynamic experiments of this nature, phase identification and quantification of complex mixtures is made more difficult by the poor quality of the rapidly accumulated data. It is, therefore, critically important to cross check the analyses wherever possible. In this example, calculation of bulk chemistry at each data point was possible as the starting materials were synthetics of known composition. This calculation involves knowing or determining (*via* electron probe microanalysis or similar) the chemical composition of each phase identified within the mixture, calculating its contribution to each element present in the mixture and summing the individual elements to give the bulk chemistry. Figure 11.7 shows the results of such calculations for Fe, Ca and O for the SFCA mixture described above. The match between calculated chemistry and weighed (or theoretical) chemistry is quite reasonable. This is a good confirmation of the XRD QPA throughout this reaction. Note that there is a discrepancy between the calculated and theoretical values at elevated temperature due to the formation of SFCA and SFCA-I of unknown and probably variable chemical composition.

Such calculations can be used, not only for verification, but as part of the phase identification process. For example, Figure 11.8 again shows the calculated chemistry (Fe, Ca and O only) from the XRD QPA during the reaction of the mixture described above. This calculation was carried out prior to completion of the analysis of this reaction and represents a time at which phase identification, and thus the Rietveld model, was incomplete. Compared with Figure 11.7, there is a clear discrepancy between the theoretical and calculated amounts of Ca, Fe and O from about 1000 °C. This suggests that a phase of composition $Ca_xFe_yO_z$ is missing from the analytical method. Inclusion of

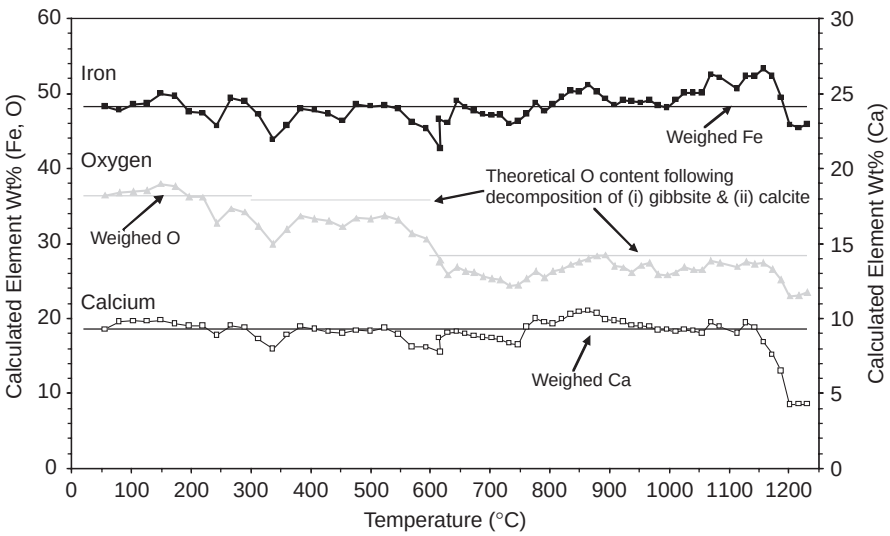



**Figure 11.7** Chemistry calculated from the XRD QPA of the *in situ* heating of an SFCA mixture.

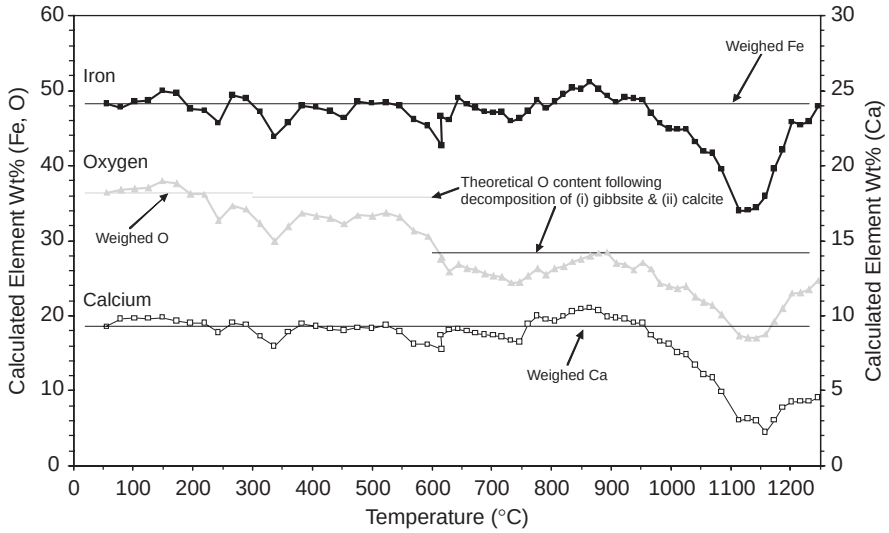



**Figure 11.8** Chemistry calculated from the XRD QPA of the *in situ* heating of an SFCA mixture prior to the inclusion of $CaFe_2O_4$ in the Rietveld refine ment model.

$CaFe_2O_4$ and recalculation of the chemistry produces the agreement shown in Figure 11.7.

### 11.5.2 Applications in Industrial Systems

The emergence of interest in XRD as a tool for monitoring phase abundances in industrial processing plants has led to the development of on-line measurement systems. These instruments are required to take XRD data from a continuously flowing stream of material, derive a quantitative estimate of the minerals present and to report the results to the plant control room in a totally automatic manner that does not require operator intervention. To achieve this, a robust analytical regime is required to minimize the possibility of erroneous results being produced. For methods that rely on a Rietveld based approach to the analysis, careful optimization of the input conditions (including crystal structures for all phases and minimization of the number of parameters being refined) is required for refinement stability.

By way of example Scarlett *et al.*[39] and Manias *et al.*[40] have described an on-line XRD analyser designed for use in monitoring the abundance of the major phases in finished Portland cement. The instrument is placed at the exit of an operational cement mill and passes some 30 kg h $^{1}$ of material on a continuous basis while obtaining XRD data and quantitative phase abundances every 1 to 2 min. Portland cement is a mineralogically complex material consisting of some 10 to 15 phases of interest that vary in concentration from 60 wt.% down to $\approx$0.2 wt.%. The physical and chemical characteristics of the component

phases, including the detailed chemical composition, crystallite size and ratio of polymorphs, depend on the nature of the starting materials and the production conditions present in a specific plant.[41,42]

To produce the most reliable analyses under these conditions, especially for the minor phases, Rietveld-based analytical conditions need to be developed using the following steps:

(i) The ferrite and aluminate phases, C4AF and C3A, are present in cement clinker at about 10 to 15 wt.% in total. (Cement industry nomenclature has been used when referring to the phases present in cement and clinker. $C = CaO$, $S = SiO_2$, $A = Al_2O_3$, $F = Fe_2O_3$.) Hence their diffraction patterns are normally dominated by the more abundant silicate phases, C3S and C2S. Taylor[41] describes a method where C3S and C2S can be extracted from the sample using a mixture of salicylic acid and methanol (SAM), leaving a residue (denoted Residue #2) in which C4AF and C3A are the major phases remaining. Collection and analysis of high quality, laboratory based XRD data from this residue (Figure 11.9C) allows refinement of parameters for the C4AF and C3A. In addition, this pattern can be used to identify whether (i) C3A is present as more than one polymorph – cubic and orthorhombic are the most commonly occurring forms – and (ii) C4AF exhibits a range of compositions with varying Fe/Al ratios – some cement plants produce C4AF with two distinct compositions which have different unit cell dimensions and are readily analysed as separate phases. During on-line analysis, the crystallite size and unit cell parameters are fixed at the values determined from the residues or, at the very least, constrained to vary within a small range near the determined values.

(ii) There is also a high degree of peak overlap between C3S and the next most abundant phase (C2S) normally present in clinker at about 10 to 15 wt.%. A separate chemical extraction, using different ratios of salicylic acid and methanol, allows the removal of only C3S, leaving a residue (Residue #1, Figure 11.9B) in which the major phase is C2S. Collection of XRD data from this material allows refinement of the crystallite size and unit cell dimensions for C2S. This is a critical step in the development of a robust method since the high degree of overlap between the C3S and C2S patterns leads to ambiguities in the partitioning of peak intensity, and hence the derived phase abundances, between the two major silicate phases. Notably, in the determination of parameters for C2S, the parameters determined for C4AF and C3A (step i above) are utilized in the refinement method as these phases are also present in this residue.

(iii) Since C3S is the major phase in clinker (typically present at about 50 to 70 wt.%), its parameters, including crystallite size and unit cell dimensions, can be refined by collecting XRD data from a representative sample of the plant's clinker production (Figure 11.9A). During this step, the unit cell and crystallite size parameters for the other phases are fixed at the values determined during steps i and ii above.

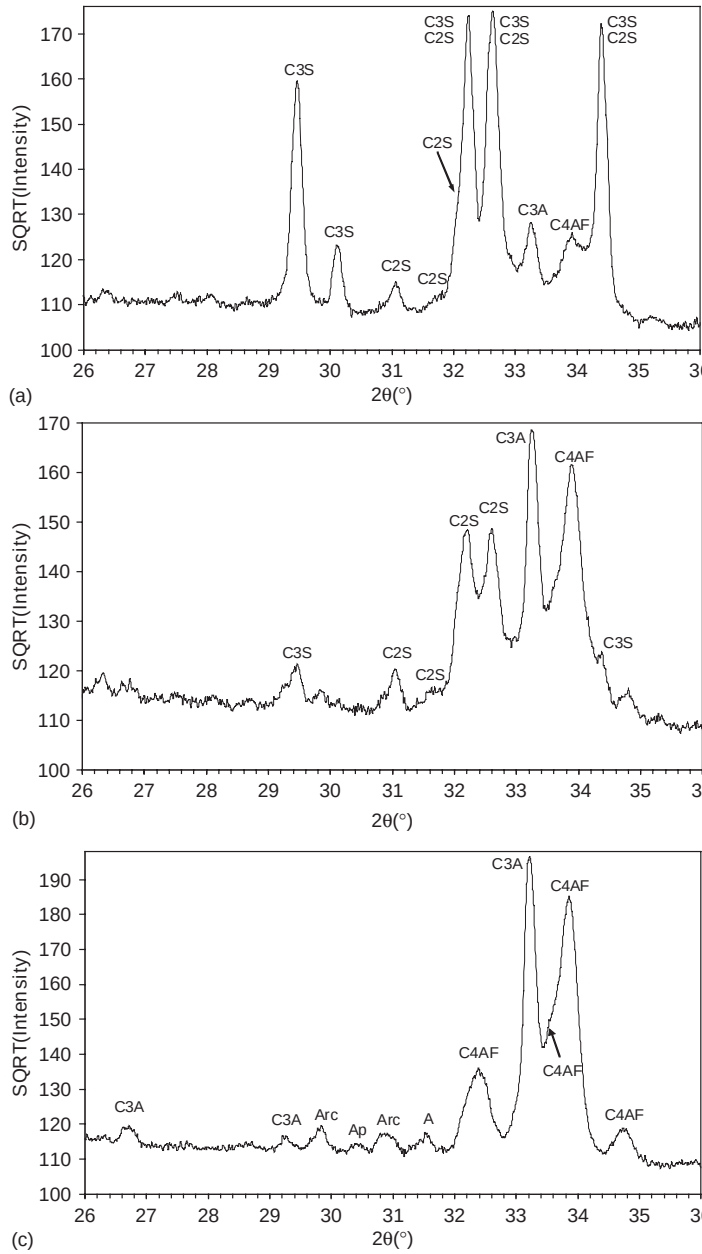



**Figure 11.9** XRD (Cu Kα) data for (A) raw Portland cement clinker, (B) Residue #1 from which most of the C3S has been removed and (C) Residue #2 from which C3S and C2S have been removed. Silicate phase extraction was conducted using a salicylic acid methanol (SAM) mixture using the method described by Taylor.[41] In Residue #2 the presence of the alkali sulfate phases [denoted Arc for arcanite $K_2SO_4$ and Ap for aphthitalite $K_3Na(SO_4)_2$] is clearly evident. Notably, the material used in these plots was derived from a different cement plant to the one illustrated in Figure 10.

(iv) Any other materials added to clinker to make Portland cement, especially gypsum ($CaSO_4.2H_2O$), must also be defined crystallographically. Care must be taken in the sample preparation stage as gypsum can partially dehydrate to hemihydrate ($CaSO_4.\frac{1}{2}H_2O$) and anhydrite ($CaSO_4$) during grinding. Since all three calcium sulfate phases may be present in finished cement, samples of hemihydrate and anhydrite can be prepared by heating two sub-samples of the gypsum to 125 and 600 °C respectively. The unit cell parameters and crystallite sizes of the three sulfate phases can be refined from respective XRD data sets and fixed for on-line use. However, the tendency for gypsum to orientate preferentially along the (0*k*0) crystallographic direction necessitates the inclusion of a refinable preferred orientation parameter for this phase.

*11.5.2.1 Alkali Sulfates.* Since the silicate phases (C3S and C2S), present in total at up to 85 wt.%, normally dominate clinker samples, all minor phases are significantly concentrated in Residue #2. This includes the important alkali sulfate phases which can (i) affect setting times and final strength, and (ii) be used to assess kiln operating conditions. Since these are normally present at a total of about 0.5 wt.% in clinker, and are often distributed across several Na and K sulfate phases, they are not easily identified in raw clinker XRD patterns. However, their presence may be more easily detected in the XRD pattern of Residue #2. By optimizing the parameters of the alkali sulfates from Residue #2 data, and then constraining them in the on-line analysis system, these phases can be measured at the $<0.5$ wt.% level (Madsen, Scarlett and Storer 2001, unpublished results) even when rapidly collected on-line data is used.

The inclusion of the alkali sulfate phases in an automatic, on-line analysis method has the potential to produce meaningless results, especially under conditions where data quality may not be optimal for the analysis of minor phases. Therefore, it is essential that some verification of the results be obtained. Figure 11.10 shows the concentration of $K_2O$ (i) from chemical (XRF) analysis and (ii) calculated from the quantitative phase abundances measured using an on-line XRD instrument installed in an operational cement plant. Up to the 5th of June 2002, alkali sulfates were not included in the analytical method, resulting in a clear underestimation of $K_2O$ calculated from the XRD results relative to those obtained by XRF. In this particular cement plant, the only alkali sulfate phase identified was arcanite ($K_2SO_4$). After the 5th June, arcanite was included in the method, resulting in excellent agreement between the calculated and observed $K_2O$ values. This agreement gives both the analyst and plant operators confidence that the XRD derived phase abundances, even at this low level, are accurate and can be used to either control plant parameters or predict downstream properties of the material.

For Portland cement, the removal of the major phases to leave a residue in which the minor phases are concentrated relies on a chemical extraction process. Clearly, this approach will not be suitable for all phase systems. In some cases, concentration of minor phases can be achieved by magnetic, density or grain size

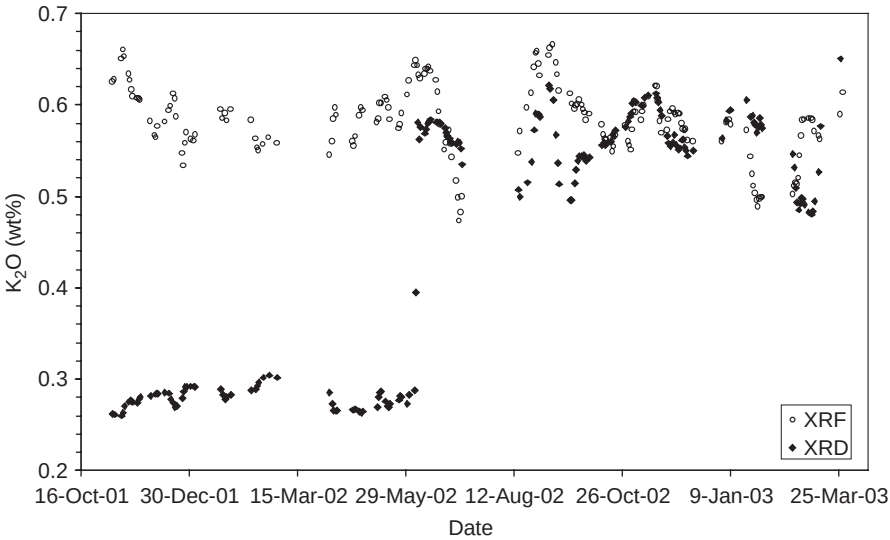



**Figure 11.10** Comparison of $K_2O$ values calculated from the XRD phase abundances with measurements from XRF chemical analysis. The alkali sulfate phase arcanite ($K_2SO_4$) was only included in the analytical method in June 2002.

separation from the major phases. Whichever method is selected, the importance of obtaining detailed parameters from all phases in the material cannot be overstated if a reliable and stable on-line analysis regime is to be achieved.

## 11.6 SUMMARY

The value in using diffraction based methods for the determination of phase abundance arises from the fact that diffraction information is derived directly from the crystal structure of each phase rather than from secondary parameters such as measurement of total chemistry. However, the methodology of quantitative phase estimation is fraught with difficulties, many of which are experimental or derive from sample related issues. Hence it is necessary to verify diffraction based phase abundances against independent methods. In those circumstances where this is not possible, the QPA values should be regarded only as semi-quantitative. While such values may be useful for deriving trends within a particular system, they cannot be regarded as an absolute measure.

## ACKNOWLEDGEMENTS

The authors gratefully acknowledge Drs Brian O'Connor, Ian Grey and Matthew Rowles for critical reading of an early version of this chapter and Dr Thaung Lwin for assistance in the derivation of the equations used to calculate the errors in phase abundance.

## APPENDIX A: DERIVATION OF ERRORS IN RIETVELD-BASED QUANTITATIVE PHASE ANALYSIS

### Relative Phase Abundances

The following section describes the derivation of errors in the quantitative phase abundances resulting from the Hill and Howard[19] algorithm. Notably, these errors only reflect the uncertainty generated by the mathematical fitting process in the Rietveld minimization process. It should also be reiterated that other sources of error, such as the presence of microabsorption, may generate errors that exceed the magnitude of those calculated here.

The weight fraction $W_\alpha$ of phase $\alpha$ is calculated using:

$$W_\alpha = \frac{S_\alpha (ZMV)_\alpha}{\sum_{j=1}^{n} S_j (ZMV)_j} \tag{A1}$$

The variance in the weight fraction of phase $\alpha$, $\mathrm{Var}(W_\alpha)$, is calculated from:

$$\mathrm{Var}(W_\alpha) = \frac{(S_\alpha ZMV_\alpha)^2}{\left(\sum_{j=1}^{n} S_j ZMV_j\right)^2} \times \left[\frac{\delta S_\alpha^2}{S_\alpha^2} + \frac{\sum_{j=1}^{n} \delta S_j^2 ZMV_j^2}{\left(\sum_{j=1}^{n} S_j ZMV_j\right)^2}\right] \tag{A2}$$

where $\delta S$ is the error in the Rietveld scale factor.

The error in the determination of the weight fraction for phase $\alpha$ is then:

$$\delta(W_\alpha) = \sqrt{\mathrm{Var}(W_\alpha)} \tag{A3}$$

### Absolute Phase Abundances

Equation (A1) can only be used to determine the *relative* phase abundance since the total of the measured weight fractions is summed to 1.0. The addition of an internal standard phase to the sample in a known amount $W_s^{\mathrm{weigh}}$ can be used to determine the absolute amount of the phases present. The corrected (absolute) concentration $\mathrm{Cor}(W_\alpha)$ for phase $\alpha$ is given by:

$$\mathrm{Cor}(W_\alpha) = W_\alpha \times \frac{W_s^{\mathrm{weigh}}}{W_s^{\mathrm{measure}}} \tag{A4}$$

where $W_s^{\mathrm{measure}}$ is the measured weight fraction for the standard phase derived using Equation (A1).

The variance in the corrected weight fractions can be calculated from:

$$\mathrm{Var}(\mathrm{Cor}(W_\alpha)) = [W_s^{\mathrm{weigh}}]^2 \times \frac{(W_\alpha)^2}{\left(W_s^{\mathrm{measure}}\right)^2} \times \left[\frac{(\delta(W_\alpha))^2}{(W_\alpha)^2} + \frac{\left(\delta(W_s^{\mathrm{measure}})\right)^2}{(W_s^{\mathrm{measure}})^2}\right] \tag{A5}$$

where $\delta(W_\alpha)$ is the error in the weight fraction of phase $\alpha$ calculated using Equation (A3); $\delta(W_s^{\mathrm{measure}})$ is the error in the measured weight fraction of the standard phase calculated using Equation (A3).

The error in the corrected weight fraction is:

$$\delta(\mathrm{Cor}(W_\alpha)) = \sqrt{\mathrm{Var}(\mathrm{Cor}(W_\alpha))} \tag{A6}$$

The concentrations of the phases in the sample before the addition of the internal standard, *i.e.* on the "as-received" basis can then be calculated using:

$$\mathrm{AsRec}(W_\alpha) = \frac{\mathrm{Cor}(W_\alpha)}{1.0 - W_s^{\mathrm{weigh}}} \tag{A7}$$

The variance in the "as received" concentrations can be calculated from:

$$\mathrm{Var}(\mathrm{AsRec}(W_\alpha)) = \left(\frac{1.0}{1.0 - W_s^{\mathrm{weigh}}}\right)^2 \times (\delta\mathrm{Cor}(W_\alpha))^2 \tag{A8}$$

where $\delta\mathrm{Cor}(W_\alpha)$ is the error in the corrected weight fraction of phase $\alpha$ calculated from Equation (A6).

The error in the "as-received" concentrations is then:

$$\delta(\mathrm{AsRec}(W_\alpha)) = \sqrt{\mathrm{Var}(\mathrm{AsRec}(W_\alpha))} \tag{A9}$$

**Amorphous Content**

The difference between 1.0 and the sum of the "as-received" components represents the total amount of amorphous material in the sample and/or non-included phases in the analysis and can be calculated from:

$$W_{\mathrm{amorphous}} = 1.0 - \sum_{j=1}^{n\ 1} \mathrm{AsRec}(W_j) \tag{A10}$$

Note that Equation (A10) is only summed over $n-1$ phases since the internal standard phase is now omitted from the calculation.

The variance in the amorphous content is calculated from:

$$\mathrm{Var}(W_{\mathrm{amorphous}}) = \sum_{j=1}^{n\ 1} \left(\delta(\mathrm{AsRec}(W_j))\right)^2 \tag{A11}$$

where $\delta(\mathrm{AsRec}(W_j))$ is the error in the corrected weight fraction of phase $j$ calculated from Equation (A9).

The error in the amorphous content is then:

$$\delta\left(W_{\text{amorphous}}\right) = \sqrt{\mathrm{Var}\left(W_{\text{amorphous}}\right)} \tag{A12}$$

## REFERENCES


1. F. H. Chung and D. K. Smith, in *Industrial Applications of X-Ray Diffraction*, ed. F. H. Chung and D. K. Smith, Marcel Dekker, New York, 2000.
2. H. P. Klug and L. E. Alexander, *X-Ray Diffraction Procedures*, Wiley-Interscience, New York, 1974.
3. R. Jenkins and R. L. Snyder, *Introduction to X-Ray Powder Diffractometry*, Wiley-Interscience, New York, 1996.
4. L. S. Zevin and G. Kimmel, *Quantitative X-Ray Diffractometry*, Springer-Verlag, New York, Inc., 1995.
5. B. D. Cullity, *Elements of X-Ray Diffraction*, Addison-Wesley, Reading, Massachusetts, 1978.
6. I. C. Madsen, N. V. Y. Scarlett, L. M. D. Cranswick and T. Lwin, Outcomes of the International Union of Crystallography Commission on powder diffraction round robin on quantitative phase analysis: Samples 1a to 1h, *J. Appl. Crystallogr.*, 2001, **34**, 409–426.
7. N. V. Y. Scarlett, I. C. Madsen, L. M. D. Cranswick, T. Lwin, E. Groleau, G. Stephenson, M. Aylmore and N. Agron-Olshina, Outcomes of the International Union of Crystallography Commission on powder diffraction round robin on quantitative phase analysis: Samples 2, 3, 4, synthetic bauxite, natural granodiorite and pharmaceuticals, *J. Appl. Crystallogr.*, 2002, **35**, 383–400.
8. R. H. Bogue, Calculation of the compounds in Portland cement, *Ind. Eng. Chem., Anal.*, 1929, **1**, 192–197.
9. H. Toraya, T. C. Huang and Y. Wu, Intensity enhancement in asymmetric diffraction with parallel-beam synchrotron radiation, *J. Appl. Crystallogr.*, 1993, **26**, 774–777.
10. T. M. Sabine, B. A. Hunter, W. R. Sabine and C. J. Ball, Analytical expressions for the transmission factor and peak shift in absorbing cylindrical specimens, *J. Appl. Crystallogr.*, 1998, **31**, 47–51.
11. C. R. Hubbard, E. H. Evans and D. K. Smith, The reference intensity ratio I/Ic for computer simulated powder patterns, *J. Appl. Crystallogr.*, 1976, **9**, 169–174.
12. C. R. Hubbard and R. L. Snyder, Reference intensity ratio measurement and use in quantitative XRD, *Powder Diffr.*, 1988, **3**, 74–77.
13. ICDD, The Powder Diffraction File, Database of the International Center for Diffraction Data, Sets 1–49 and 70–86, ICDD, 12 Campus Boulevard, Newton Square, Pennsylvania 19073-3273, USA, 1999.

14. D. K. Smith, G. G. Johnson, A. Scheible, A. M. Wims, J. L. Johnson and G. Ullmann, Quantitative X-ray powder diffraction method using the full diffraction pattern, *Powder Diffr.*, 1987, **2**, 73–77.
15. F. H. Chung, Quantitative interpretation of X-ray diffraction patterns of mixtures. I. Matrix-flushing method for quantitative multicomponent analysis, *J. Appl. Crystallogr.*, 1974, **7**, 519–525.
16. F. H. Chung, Quantitative interpretation of X-ray diffraction patterns of mixtures. II. Adiabatic principle of X-Ray diffraction analysis of mixtures, *J. Appl. Crystallogr.*, 1974, **7**, 526–531.
17. R. J. Hill, Expanded use of the Rietveld method in studies of phase abundance in multiphase mixtures, *Powder Diffr.*, 1991, **6**, 74–77.
18. B. H. O'Connor and M. D. Raven, Application of the Rietveld refinement procedure in assaying powdered mixtures, *Powder Diffr.*, 1988, **3**, 2–6.
19. R. J. Hill and C. J. Howard, Quantitative phase analysis from neutron powder diffraction data using the Rietveld method, *J. Appl. Crystallogr.*, 1987, **20**, 467–474.
20. J. C. Taylor and R. Zhu, Simultaneous use of observed and calculated standard profiles in quantitative XRD analysis of minerals by the multiphase Rietveld method: the determination of pseudorutile in mineral sands products, *Powder Diffr.*, 1992, **7**, 152–161.
21. A. Le Bail, H. Duroy and J. L. Fourquet, *Ab-initio* structure determination of $LiSbWO_6$ by X-ray powder diffraction, *Mater. Res. Bull.*, 1988, **23**, 447–452.
22. N. V. Y. Scarlett and I. C. Madsen, Quantification of phases with partial or no known crystal structures, *Powder Diffr.*, 2006, **21**, 278–284.
23. N. J. Elton and P. D. Salt, Particle statistics in quantitative X-ray diffractometry, *Powder Diffr.*, 1996, **11**, 218–229.
24. D. K. Smith, Particle statistics and whole pattern methods in quantitative X-ray powder diffraction analysis, *Adv. X-Ray Anal.*, 1992, **35**, 1–15.
25. V. E. Buhrke, R. Jenkins and D. K. Smith, *A Practical Guide for the Preparation of Specimens for X-Ray Fluorescence and X-Ray Diffraction Analysis*, Wiley-VCH, New York, 1998.
26. R. J. Hill and I. C. Madsen, in *Structure Determination from Powder Diffraction Data*, ed. W. David, K. Shankland, L. McCusker and C. Baerlocher, Oxford University Press, New York, 2002.
27. A. March, Mathematische theorie der regelung nach der korngestalt bei affiner deformation, *Z. Kristallogr.*, 1932, **81**, 285–297.
28. W. A. Dollase, Correction of intensities for preferred orientation in powder diffractometry: Application of the March model, *J. Appl. Crystallogr.*, 1986, **19**, 267–272.
29. D. L. Bish and S. A. Howard, Quantitative phase analysis using the Rietveld method, *J. Appl. Crystallogr.*, 1988, **21**, 86–91.
30. G. W. Brindley, The effect of grain or particle size on X-ray reflections from mixed powders and alloys, considered in relation to the quantitative determination of crystalline substances by X-ray methods, *Philos. Mag.*, 1945, **36**, 347–369.

31. J. C. Taylor and C. E. Matulis, Absorption contrast effects in the quantitative XRD analysis of powders by full multi-phase profile refinement, *J. Appl. Crystallogr.*, 1991, **24**, 14–17.
32. R. W. Cheary and A. A. Coelho, A fundamental parameters approach of X-ray line-profile fitting, *J. Appl. Crystallogr.*, 1992, **25**, 109–121.
33. R. W. Cheary, A. A. Coelho and J. P. Cline, Fundamental parameters line profile fitting in laboratory diffractometers, *J. Res. Natl. Inst. Stand. Technol.*, 2004, **109**, 1–25.
34. I. C. Madsen, N. V. Y. Scarlett and B. I. Whittington, Pressure acid leaching of nickel laterite ores: an *in-situ* diffraction study of the mechanism and rate of reaction, *J. Appl. Crystallogr.*, 2005, **38**, 927–933.
35. B. I. Whittington, J. A. Johnson, L. P. Quan, R. G. McDonald and D. M. Muir, Pressure acid leaching of arid-region nickel laterite ore part II. Effect of ore type, *Hydrometallurgy*, 2003, **70**, 47–62.
36. B. I. Whittington, R. G. McDonald, J. A. Johnson and D. M. Muir, Pressure acid leaching of arid-region nickel laterite ore part I: Effect of water quality, *Hydrometallurgy*, 2003, **70**, 31–46.
37. N. V. Y. Scarlett, I. C. Madsen, M. I. Pownceby and A. N. Christensen, *In-situ* X-ray diffraction analysis of iron ore sinter phases, *J. Appl. Crystallogr.*, 2004, **37**, 362–368.
38. N. V. Y. Scarlett, M. I. Pownceby, I. C. Madsen and A. N. Christensen, Reaction sequences in the formation of silico-ferrites of calcium and aluminium in iron ore sinter, *Metall. Mater. Trans. B*, 2004, **35**, 929–936.
39. N. V. Y. Scarlett, I. C. Madsen, C. Manias and D. Retallack, On-line X-ray diffraction for quantitative phase analysis: application in the Portland cement industry, *Powder Diffr.*, 2001, **16**, 71–80.
40. C. Manias, I. C. Madsen and D. Retallack, Plant optimisation and control using continuous on-line XRD for mineral phase analysis, *ZKG Int.*, 2001, **54**, 138–145.
41. H. F. W. Taylor, *Cement Chemistry*, Academic Press, London, 1990.
42. I. C. Madsen and N. V. Y. Scarlett, in *Industrial Applications of X-Ray Diffraction*, ed. F. H. Chung and D. K. Smith, Marcel Dekker, New York, 2000.

CHAPTER 12

# Microstructural Properties: Texture and Macrostress Effects

NICOLAE C. POPA

National Institute for Materials Physics, P.O. Box MG-7, Bucharest, Romania

## 12.1 TEXTURE

Frequently, polycrystalline specimens exhibit a preferred orientation of the crystallites or polycrystalline texture. In addition, many manufacturing processes of technological materials can induce texture. In comparison with specimens having randomly oriented crystallites, the relative intensities of the diffraction lines of textured samples are modified. As a consequence the structural and quantitative phase analysis of polycrystalline samples becomes impossible without proper modeling of the texture.

Texture can influence many macroscopic properties of materials. Strain, stress and the elastic constants, as well as sound propagation in samples, depend strongly on the preferred orientation of crystallites. To calculate the pyroelectric and piezoelectric coefficients of polycrystalline specimens the orientation distribution function of the crystallites is needed. Some properties such as macroscopic magnetic anisotropy do not exist if the sample is not textured. Other properties like ionic conductivity or critical current in high-temperature superconductors are texture dependent. By studying the texture of rocks important information can be obtained about the geological history of a given region of the Earth. Consequently, texture analysis is needed not only to correct for preferred orientation in the structural and phase analysis of powders but also is a vital step in materials characterization.

### 12.1.1 The Orientation Distribution Function and the Pole Distributions

The texture of a polycrystalline sample is commonly described by the orientation distribution function (ODF). To define this function two orthogonal

coordinate systems must be introduced, the system ($\mathbf{x}_1$, $\mathbf{x}_2$, $\mathbf{x}_3$) linked to the crystallite and ($\mathbf{y}_1$, $\mathbf{y}_2$, $\mathbf{y}_3$) linked to the sample. The Euler matrix $\mathbf{a}(\varphi_1, \Phi_0, \varphi_2)$ connects the two systems:

$$\mathbf{x}_i = \sum_{j=1}^{3} a_{ij}(\varphi_1, \Phi_0, \varphi_2)\mathbf{y}_j \tag{1}$$

$$\mathbf{a}(\varphi_1, \Phi_0, \varphi_2) = \begin{pmatrix} \cos\varphi_1 \cos\varphi_2 & \sin\varphi_1 \cos\varphi_2 & \sin\varphi_2 \sin\Phi_0 \\ -\sin\varphi_1 \sin\varphi_2 \cos\Phi_0 & +\cos\varphi_1 \sin\varphi_2 \cos\Phi_0 & \\ -\cos\varphi_1 \sin\varphi_2 & -\sin\varphi_1 \sin\varphi_2 & \cos\varphi_2 \sin\Phi_0 \\ -\sin\varphi_1 \cos\varphi_2 \cos\Phi_0 & +\cos\varphi_1 \cos\varphi_2 \cos\Phi_0 & \\ \sin\varphi_1 \sin\Phi_0 & -\cos\varphi_1 \sin\Phi_0 & \cos\Phi_0 \end{pmatrix} \tag{2}$$

Here $0 \leq \varphi_1 \leq 2\pi$ is a simple rotation of ($\mathbf{y}_1$, $\mathbf{y}_2$, $\mathbf{y}_3$) around $\mathbf{y}_3$ transforming this system into $\mathbf{y}'_1$, $\mathbf{y}'_2$, $\mathbf{y}_3$. Further, the angle $0 \leq \Phi_0 \leq \pi$ rotates this system around $\mathbf{y}'_1$ transforming it into $\mathbf{y}'_1$, $\mathbf{y}''_2$, $\mathbf{x}_3$) and, finally, by rotating this last system around $\mathbf{x}_3$ by $0 \leq \varphi_2 \leq 2\pi$ one obtains ($\mathbf{x}_1$, $\mathbf{x}_2$, $\mathbf{x}_3$).

The orientation distribution function $f(\varphi_1, \Phi_0, \varphi_2)$ is defined by the volume fraction of the crystallites having the orientations in the range ($\varphi_1$, $\varphi_1 + d\varphi_1$), ($\Phi_0$, $\Phi_0 + d\Phi_0$), ($\varphi_2$, $\varphi_2 + d\varphi_2$):

$$\left(1/8\pi^2\right) f(\varphi_1, \Phi_0, \varphi_2) \sin\Phi_0 \mathrm{d}\varphi_1 \mathrm{d}\Phi_0 \mathrm{d}\varphi_2 = dV(\varphi_1, \Phi_0, \varphi_2)/V \tag{3}$$

From the definition the following normalization condition follows:

$$\left(1/8\pi^2\right) \int_0^{2\pi} \int_0^{\pi} \int_0^{2\pi} f(\varphi_1, \Phi_0, \varphi_2) \sin\Phi_0 d\varphi_1 d\Phi_0 d\varphi_2 = 1 \tag{4}$$

If the crystal and sample symmetries are higher than triclinic, the multiple physically equivalent choices of the coordinate systems ($\mathbf{x}_i$) and ($\mathbf{y}_i$) impose constraints on the ODF. The symmetry group of the ODF must be the product of the proper subgroups (only pure rotations) of the crystal and sample point groups.

In the diffraction measurements of textured polycrystals the ODF is not observed, but a two-dimensional projection of the ODF called pole distribution. Diffraction occurs when the Bragg condition $\mathbf{Q}_B = 2\pi\mathbf{H}$ is (nearly) fulfilled (Chapter 1). By $\mathbf{Q}_B$ and $\mathbf{H}$ we denoted the Bragg scattering vector and the reciprocal lattice vector; $\mathbf{y} = \mathbf{Q}_B/Q_B$ and $\mathbf{h} = \mathbf{H}/H$ are their unit vectors. Let us denote by $I^R_{\mathbf{H}}(\Delta s)$ the diffracted intensity of the randomly oriented polycrystal, where $s$ is the scanning variable (scattering angle, energy, time-of-flight), and by $I^T_{\mathbf{H}}(\Delta s)$ the diffracted intensity of the textured polycrystal. The ratio $p_{\mathbf{h}}(\mathbf{y}) = I^T_{\mathbf{H}}(\Delta s)/I^R_{\mathbf{H}}(\Delta s)$ is equal to the ratio between the volumes of crystallites in reflection for the textured and non-textured sample. This ratio is called the pole

distribution function and has the following expression:

$$p_{\mathbf{h}}(\mathbf{y}) = (1/2\pi) \int_{\mathbf{h}||\mathbf{y}} f(\varphi_1, \Phi_0, \varphi_2) d\omega = (1/2\pi) \int_0^{2\pi} f(\varphi_1', \Phi_0', \varphi_2') d\omega \tag{5}$$

The angles $\varphi_1', \Phi_0', \varphi_2'$ in Equation (5) are the Euler angles for which $\mathbf{h}||\mathbf{y}$ and the angle $\omega$ denote the rotation of the crystallite around this direction. The unit vectors $\mathbf{h}$ and $\mathbf{y}$ can be represented in the coordinate systems $(\mathbf{x}_i)$ and $(\mathbf{y}_i)$ by the pairs of polar and azimuthal angles $(\Phi, \beta)$ and $(\Psi, \gamma)$, respectively, or by triplets of direction cosines $a_i$ and $b_i$:

$$\mathbf{h} = \sum_{i=1}^{3} a_i \mathbf{x}_i = \cos\beta \sin\Phi \mathbf{x}_1 + \sin\beta \sin\Phi \mathbf{x}_2 + \cos\Phi \mathbf{x}_3 \tag{6}$$

$$\mathbf{y} = \sum_{i=1}^{3} b_i \mathbf{y}_i = \cos\gamma \sin\Psi \mathbf{y}_1 + \sin\gamma \sin\Psi \mathbf{y}_2 + \cos\Psi \mathbf{y}_3 \tag{7}$$

With these definitions the Euler matrix with the constraint $\mathbf{h}||\mathbf{y}$ becomes:

$$\mathbf{a}(\varphi_1', \Phi_0', \varphi_2') = \mathbf{m}^t(\Phi, \beta)\mathbf{n}(\omega)\mathbf{m}(\Psi, \gamma) \tag{8}$$

The index $t$ in Equation (8) stands for transpose and the matrices $\mathbf{m}$ and $\mathbf{n}$ are:

$$\mathbf{m}(\Psi, \gamma) = \begin{pmatrix} \cos\Psi\cos\gamma & \cos\Psi\sin\gamma & -\sin\Psi \\ -\sin\gamma & \cos\gamma & 0 \\ \sin\Psi\cos\gamma & \sin\Psi\sin\gamma & \cos\Psi \end{pmatrix},$$
$$\mathbf{n}(\omega) = \begin{pmatrix} \cos\omega & \sin\omega & 0 \\ -\sin\omega & \cos\omega & 0 \\ 0 & 0 & 1 \end{pmatrix} \tag{9a, b}$$

The peaks marked $\mathbf{H}$ and $-\mathbf{H}$ are not distinguishable in position and for regular scattering (anomalous scattering negligibly small) the Friedel law holds (Chapter 7), then $I^R_{\mathbf{H}}(\Delta s) = I^R_{\mathbf{H}}(\Delta s)$. As a consequence the measured intensity for the textured sample is:

$$I^T_{\mathbf{H}}(\mathbf{y}, \Delta s) = I^R_{\mathbf{H}}(\Delta s) P_{\mathbf{h}}(\mathbf{y}) \tag{10}$$

$$P_{\mathbf{h}}(\mathbf{y}) = (1/2)[p_{\mathbf{h}}(\mathbf{y}) + p_{\mathbf{h}}(\mathbf{y})] = (1/2)[p_{\mathbf{h}}(\mathbf{y}) + p_{\mathbf{h}}(-\mathbf{y})] \tag{11}$$

The function $P_{\mathbf{h}}(\mathbf{y})$ defined by Equation (11) is called the reduced pole distribution (pole figure). Hereafter we will call it, simply, the pole distribution (or pole density), because $p_{\mathbf{h}}(\mathbf{y})$ will be used very rarely. The pole distribution is centrosymmetric and for crystal and sample symmetry higher than triclinic it

has the symmetries of the corresponding Laue groups. The normalization condition is:

$$(1/4\pi)\int_0^{2\pi}\int_0^{\pi} P_{\mathbf{h}}(\mathbf{y})\sin\Psi d\gamma d\Psi = 1 \tag{12}$$

According to Equation (10) the diffracted intensity of a textured polycrystal is the diffracted intensity of the randomly oriented polycrystal multiplied by the pole density in the direction of the scattering vector in sample. The pole density $P_{\mathbf{h}}(\mathbf{y})$ is the unique function connected with the preferred orientation that is accessible to a direct measurement by diffraction.

### 12.1.2 Two Goals in Texture Analysis

Concerning interest in texture analysis, the community of diffractionists can be roughly divided in two categories. For the first category the goal is a quantitative texture analysis. The texture can have important effects on some physical properties of manufactured materials. Consequently, the texture determination is a necessary step in material characterization.

Quantitative texture analysis means the determination of the ODF. It presumes the measurement by X-ray or neutron diffraction of several pole distributions. In the traditional constant wavelength diffraction method, the detector is positioned on the center of the diffraction peak and the sample is rotated on a goniometer to obtain as many points as possible in a hemisphere of ($\Psi$, $\gamma$) space. For neutron time-of-flight, a well-separated peak of strong intensity can be selected for which the integral intensity is extracted. The pole distributions obtained for several peaks are further processed to obtain the ODF. This operation is named inversion of the pole figures. Many mathematical methods have been proposed for this purpose. A largely used method is by Fourier analysis, as described in the book by Bunge.[1] Other methods solve the integral Equation (5) + (11) directly, like the WIMV method (Williams,[2] Imhof,[3] Matthies and Vinel[4]), which uses an iterative procedure assuring a positive solution for ODF. Matthies, Wenk and Vinel[5] give a comparison of three methods for inversion of pole figures in a paper where the reader can find also a comprehensive bibliography for this specific problem.

The traditional method to measure the pole distributions becomes unsatisfactory if the peaks are overlapped. This happens for low symmetry compounds or when the sample contains many phases. In addition, by using a position sensitive detector or neutron time-of-flight diffraction, a large segment or the whole pattern can be recorded simultaneously, and using only a small number of peaks, a large volume of information is lost. To eliminate these drawbacks, Wenk, Matthies and Lutterotti[6,7] proposed a combination of the WIMV procedure (or other inversion method) with the Rietveld method – more exactly with the Le Bail[8] (Chapter 8) routine for peak intensity extraction. In this combined method it is presumed that the structural parameters, or

Bragg peak intensities for the random sample, are known and then are not refined.

Those interested mostly in structure determination from powder diffraction see the texture problem differently. The presence of the preferred orientation makes a good pattern fitting difficult or even impossible and, consequently, a procedure is needed to correct for the texture effect in the Rietveld codes. For that it is not necessary to find the ODF, but to have a reliable model of the pole distribution whose parameters are refined together with the structure and other parameters.

In the 1970s and early 1980s in the Rietveld programs an empirical Gaussian model was used for the pole distribution. In 1986 Dollase[9] proposed the March model[10] describing the texture resulting from the packing of platelets or needles and having cylindrical sample symmetry. Details on this model are given below. For Bragg–Brentano geometry the Dollase–March model has a simple form that was implemented in the Rietveld programs DBWS[11] and GSAS.[12]

Ahtee, Nurmela, Suortti and Jarvinen[13] (1989) described the pole distribution in their Rietveld program by a series of symmetrized spherical harmonics in the angles ($\Phi$, $\beta$), the series coefficients being refinable parameters. This means that only the dependence on **h** of $P_{\mathbf{h}}(\mathbf{y})$ was modeled, and not the dependence on **y**. Consequently, the model works for any texture only if the direction in the sample of the scattering vector is constant on the whole pattern, as in the Bragg–Brentano geometry or in the time-of-flight diffraction with only one detector. For Debye–Scherrer geometry or for time-of-flight with multi-detectors in the same scattering plane the model only works for texture of cylindrical sample symmetry, if the cylinder axis is normal to the scattering plane. In this case $P_{\mathbf{h}}$ depends only on $\Psi$ that is kept constant ($\pi/2$) in the whole pattern.

In 1992 Popa[14] reported the implementation in the Rietveld refinement of the general description of texture by spherical harmonics. This means that the dependence of $P_{\mathbf{h}}(\mathbf{y})$ on both **h** and **y** was considered. The author used a sample of cylindrical symmetry but the diffraction pattern was recorded in a non-conventional focusing geometry in which the angle $\Psi$ depends on the Bragg angle. Consequently, both directions **h** and **y** are involved and then there is no loss of generality. It is impossible to fit such patterns if the general representation of texture by spherical harmonics is not considered, even if the sample symmetry is cylindrical.

Later Von Dreele[15] implemented the general description of texture by spherical harmonics in GSAS. Von Dreele proved that, by using this description, beside the robustness of the texture correction in the Rietveld method it is also possible to perform a reliable quantitative texture analysis. He measured by neutron time-of-flight diffraction a standard calcite sample previously used for a texture round robin.[16] The patterns from different detector banks and sample orientations were processed by GSAS, refining the harmonic coefficients simultaneously with the structural and other parameters. Six pole distributions calculated from the refined harmonic coefficients and used as input in the

WIMV routine gave similar ODF to those obtained from individual pole figure measurement.

In connection with the implementation in the Rietveld codes, the Dollase–March model and the spherical harmonics approach, for pole distributions determination, is developed in the next two parts. The problem of pole figure inversion is outside the scope of this chapter.

### 12.1.3 Dollase–March Model

The Dollase approach[9] is based on the observation that, if the distribution of a given pole $\mathbf{h}_0$ is known, the distribution of any other pole $\mathbf{h}$ can be derived. Let us denote by $\alpha$ the angle between $\mathbf{h}$ and $\mathbf{h}_0$. For the crystallites that have $\mathbf{h}$ parallel to $\mathbf{y}$, the pole $\mathbf{h}_0$ lies on the surface of a cone of axis $\mathbf{y}$ and angle $2\alpha$. On the other hand, the pole $\mathbf{h}$ is a member of a family of $m_{\mathbf{h}}$ equivalents making different angles $\alpha_k$ with $\mathbf{h}_0$. Then we can write:

$$P_{\mathbf{h}}(\Psi,\gamma) = (1/m_{\mathbf{h}}) \sum_{k=1}^{m_{\mathbf{h}}} (1/2\pi) \int_0^{2\pi} P_{\mathbf{h}_0}[\Psi_{0k}(\omega), \gamma_{0k}(\omega)] \mathrm{d}\omega \tag{13}$$

Here the angle $\omega$ denotes the rotation of $\mathbf{h}_0$ on the surface of the cone of angle $2\alpha_k$ and the angles $\Psi_{0k}$, $\gamma_{0k}$ of $\mathbf{y}_0 || \mathbf{h}_0$ are:

$$\cos\Psi_{0k} = \cos\alpha_k \cos\Psi - \sin\alpha_k \sin\Psi \cos\omega \tag{14}$$

$$\tan\gamma_{0k} = \frac{\sin\alpha_k \cos\Psi \sin\gamma \cos\omega + \sin\alpha_k \cos\gamma \sin\omega + \cos\alpha_k \sin\Psi \sin\gamma}{\sin\alpha_k \cos\Psi \cos\gamma \cos\omega - \sin\alpha_k \sin\gamma \sin\omega + \cos\alpha_k \sin\Psi \cos\gamma} \tag{15}$$

Note that $\mathbf{h}_0$ is also a member of a family of equivalents. If the pattern indexation is changed into an equivalent indexation the terms in the sum in Equation (13) permute but the sum remains unchanged.

In general it is impossible to know any pole distribution prior to a measurement, and then Equation (13) seems useless. But, as Dollase remarked,[9] if, on average, the crystallites are disc shaped or rods (needles), the preferred orientation of a prominent, cleavage or growing plane $(h_0k_0l_0)$ can be predicted. This plane is the disc surface and, respectively, the plane normal to the rod axis. When the powder is settled and compacted on a flat surface, the pole $\mathbf{h}_0(h_0k_0l_0)$ distributes preferentially along the surface normal for discs, and perpendicular to this normal for needles. Around this normal the distribution is uniform. This results a specimen with cylindrical sample symmetry, the symmetry axis being the normal to the compaction surface. According to March[10] and taking the symmetry axis as $\mathbf{y}_3$, the distribution of $\mathbf{h}_0$ is:

$$P_{\mathbf{h}_0}(\mathbf{y}) = P_{\mathbf{h}_0}(\Psi) = \left[1/r + (r^2 - 1/r)\cos^2\Psi\right]^{3/2} \tag{16}$$

The March distribution fulfills the normalization condition Equation (12) and is monotonic in the limits $1/r^3$ for $\Psi = 0$ and $r^{3/2}$ for $\Psi = \pi/2$. The maximum is

in $\Psi = 0$ if $r < 1$, and in $\Psi = \pi/2$ if $r > 1$. Consequently, $r < 1$ corresponds to disc shaped crystallites and $r > 1$ corresponds to needles. The parameter $r$, refinable in the Rietveld method, has a physical significance. It represents the ratio between the thickness in the preferred orientation direction of the textured and of a hypothetical not-textured specimen under the condition of volume conservation.

By replacing Equation (16) in Equation (13) one obtains:

$$P_{\mathbf{h}}(\Psi) = (1/m_{\mathbf{h}}) \sum_{k=1}^{m_{\mathbf{h}}} (1/\pi) \int_0^{\pi} \left[1/r + (r^2 - 1/r) \cos^2 \Psi_{0k}(\omega)\right]^{3/2} d\omega \qquad (17)$$

Here $\cos \Psi_{0k}$ is given by Equation (14); $\gamma_{0k}$ given by Equation (15) is no longer necessary because the sample symmetry is cylindrical. Also, the range for integration is constrained to $(0,\pi)$ because in Equation (14) $\cos(2\pi - \omega) = \cos\omega$. Equation (17) gives the pole density in the limits of the March model of texture for any diffraction geometry. For any diffraction geometry the angle $\Psi$ can be calculated from two pairs of polar and azimuthal angles describing the orientations in the laboratory coordinate system ($\mathbf{l}_1$, $\mathbf{l}_2$, $\mathbf{l}_3$) of the symmetry axis $\mathbf{y}_3$ and of the scattered beam $\mathbf{k}_2$. To define the laboratory system we presume, without loss of generality, that the incident beam is horizontal. The axis $\mathbf{l}_1$ is taken along the incident beam from source to sample, $\mathbf{l}_3$ is taken in the vertical direction and then $\mathbf{l}_2 = \mathbf{l}_3 \times \mathbf{l}_1$. The vector $\mathbf{k}_2$ from sample to detector (pixel, if the detector is position sensitive) is defined by the scattering angle $2\theta$, a polar angle with respect to $\mathbf{l}_1$, and by the azimuthal angle $\zeta$ measured anticlockwise from $\mathbf{l}_2$ to the projection of $\mathbf{k}_2$ on the plane ($\mathbf{l}_2$, $\mathbf{l}_3$). Consequently, in the laboratory system, the unit vector of the scattering vector is:

$$\mathbf{y} = \mathbf{Q}_B/Q_B = -\sin\theta \mathbf{l}_1 + \cos\theta\cos\zeta \mathbf{l}_2 + \cos\theta \sin\zeta \mathbf{l}_3 \qquad (18)$$

If the sample symmetry axis $\mathbf{y}_3$ is defined by the standard polar and azimuthal angles ($\Psi_s$, $\gamma_s$), then the angle $\Psi$ can be generally written as follows:

$$\cos\Psi = -\sin\theta \sin\Psi_s \cos\gamma_s + \cos\theta\cos\zeta \sin\Psi_s \sin\gamma_s + \cos\theta \sin\zeta \cos\Psi_s \qquad (19)$$

For particular diffraction geometries $\zeta$, $\Psi_s$, $\gamma_s$ take specific values. In the Bragg–Brentano geometry $\zeta = 0$, $\Psi_s = \pi/2$ and $\gamma_s = \pi/2 + \theta$, then $\Psi = 0$ and Equation (17) takes a simple form:

$$P_{\mathbf{h}}(0) = (1/m_{\mathbf{h}}) \sum_{k=1}^{m_{\mathbf{h}}} \left[1/r + (r^2 - 1/r) \cos^2 \alpha_k\right]^{3/2} \qquad (20)$$

Only for the Bragg–Brentano geometry, the Dollase–March texture multiplier has a simple expression. For any other diffraction geometry the integral over $\omega$ cannot be removed. In the Debye–Scherrer geometry $\zeta = 0$, $\Psi_s = 0$, then from Equation (19) $\Psi = \pi/2$, and in place of Equation (17) we have:

$$P_{\mathbf{h}}(\pi/2) = (1/m_{\mathbf{h}}) \sum_{k=1}^{m_{\mathbf{h}}} (2/\pi) \int_0^{\pi/2} \left[1/r + (r^2 - 1/r) \sin^2 \alpha_k \cos^2 \omega\right]^{3/2} d\omega \qquad (21)$$

Howard and Kisi[17] have found that Equation (21) can be reasonably approximated by Equation (20) if the March parameter $r$ is replaced by $r^{1/2}$. Consequently, many Rietveld programs use Equation (20) for both Bragg–Brentano and Debye–Scherrer geometry. The approximation is good for $r$ not far from 1 but becomes too rough for medium and strong texture. For geometries other than Bragg–Brentano (including Debye–Scherrer) it would be better to implement in the Rietveld programs the exact formula Equation (17). As the integrant is a "quiet" function, the integral can be calculated by a Gauss quadrature formula with a small number of nodes.

Sometimes, even if the crystallites are disc-shaped or needles, the description of the texture starting from a single distribution of a single prominent plane is inadequate. It is possible that volume fractions of crystallites in the specimen have different prominent, cleavage or growing planes ($h_{0i}$, $k_{0i}$, $l_{0i}$) with the same sample symmetry axis and different or identical strength parameters $r_i$, or the prominent plane is the same for all fractions but the strength parameters $r_i$ are different. In these cases the integrant in Equation (13) must be replaced as follows:

$$P_{\mathbf{h}_0}(\Psi, r) \Rightarrow \sum_{i=1}^{n} w_i P_{\mathbf{h}_{0i}}(\Psi, r_i) \tag{22}$$

Here $n$ is the number of distinct fractions, $w_i$ the fraction weights and $P_{\mathbf{h}_{0i}}(\Psi, r_i)$ March distributions. The refinable parameters are $n-1$ weights plus the distinct strength parameters $r_i$.

The Dollase–March model to describe the texture in the Rietveld method has become very attractive due to the small number of refinable parameters. Nevertheless, frequently it produces an incomplete texture correction, even if complex variants like Equation (22) are used. In fact the condition of disc-shaped crystallites or needles is not fulfilled in general and the specimen does not have cylindrical sample symmetry. In principle, by spinning the specimen, an apparent cylindrical texture is obtained, but in this case there is no prominent plane ($h_0k_0l_0$) as required by the Dollase approach. Any diffraction plane can be used as a placeholder, but it is highly improbable that the corresponding pole $\mathbf{h}_0$ has a monotonic distribution in the range $0 \leq \Psi \leq \pi/2$, which is described by the March formula Equation (16). For a general type of texture, only a mathematical description independent of any physical model can guarantee a reliable correction in the Rietveld method. Such a description is the Fourier analysis by using symmetrized spherical harmonics.

### 12.1.4 The Spherical Harmonics Approach

*12.1.4.1 Description of the Texture by Spherical Harmonics.* The description of the texture by spherical harmonics was first reported by Roe[18] and Bunge[19] and later developed by Bunge.[1,20] According to Bunge[1] the orientation distribution

function can be expanded in a series of generalized spherical harmonics:

$$f(\varphi_1, \Phi_0, \varphi_2) = \sum_{l=0}^{\infty} \sum_{m=}^{l} \sum_{l\, n=}^{l} c_l^{mn} \exp(im\varphi_2) P_l^{mn}(\Phi_0) \exp(in\varphi_1) \tag{23}$$

Denoting $x = \cos\Phi_0$, the functions $P_l^{mn}(x)$ are defined as follows:

$$\begin{aligned} P_l^{mn}(x) = & \frac{(-1)^{l\ \ m} i^{n\ \ m}}{2^l (l-m)!} \left[\frac{(l-m)!(l+n)!}{(l+m)!(l-n)!}\right]^{1/2} (1-x)^{\ \ (n\ \ m)/2} (1+x)^{\ \ (n+m)/2} \\ & \times \frac{d^{l\ \ n}}{dx^{l\ \ n}} \left[(1-x)^{l\ \ m} (1+x)^{l+m}\right] \end{aligned} \tag{24}$$

The functions $P_l^{mn}$ are real for $m + n$ even and imaginary for $m + n$ odd. They have the following properties:

$$P_l^{mn*}(\Phi) = (-1)^{m+n} P_l^{mn}(\Phi) \tag{25}$$

$$P_l^{nm}(\Phi) = P_l^{mn}(\Phi) = P_{l\ \ }^{m,\ \ n}(\Phi) \tag{26}$$

$$P_l^{mn}(\pi - \Phi) = (-1)^{l+m+n} P_{l\ \ }^{\ mn}(\Phi) \tag{27}$$

$$\int_0^{\pi} P_l^{mn}(\Phi) P_{l'}^{mn*}(\Phi) \sin\Phi d\Phi = \frac{2}{2l+1} \delta_{ll'} \tag{28}$$

The last equation says that the functions $P_l^{mn}$ of different harmonics indices $l$ are orthogonal. By using the Equation (25) and taking account that the ODF is a real function one obtains the following condition for the complex coefficients $c_l^{mn}$:

$$c_{l\ \ }^{m,\ \ n} = (-1)^{m+n} c_l^{mn*} \tag{29}$$

On the other hand, the normalization condition (4) for the ODF together with Equation (28) impose $c_0^{00} = 1$.

According to equation (14.160) of Bunge,[1] the pole distribution function defined by Equation (5) becomes:

$$p_{\mathbf{h}}(\mathbf{y}) = \sum_{l=0}^{\infty} [2/(2l+1)] \sum_{m=}^{l} \sum_{l\, n=}^{l} c_l^{mn} \exp(-im\beta) P_l^m(\Phi) \exp(in\gamma) P_l^n(\Psi) \tag{30}$$

In this equation $P_l^m$ is the adjunct Legendre function defined as follows ($x = \cos\Phi$):

$$P_l^m(x) = \frac{(-1)^{l\ \ m}}{2^l l!} \left(\frac{2l+1}{2}\right)^{1/2} \left[\frac{(l+m)!}{(l-m)!}\right]^{1/2} (1-x^2)^{\ \ m/2} \frac{d^{l\ \ m}}{dx^{l\ \ m}} (1-x^2)^l \tag{31}$$

There is an obvious relation between the functions $P_l^{m0}$ and $P_l^m$:

$$P_l^{m0}(\Phi) = P_l^{0m}(\Phi) = i^{\ m}[2/(2l+1)]^{1/2} P_l^m(\Phi) \tag{32}$$

By replacing Equation (32) in Equations (26), (27) and (28) one obtains the following properties for $P_l^m$:

$$P_l^m(\Phi) = (-1)^m P_l^{\ m}(\Phi) \tag{33}$$

$$P_l^m(\pi - \Phi) = (-1)^{l+m} P_l^m(\Phi) \tag{34}$$

and:

$$\int_0^\pi P_l^m(\Phi) P_{l'}^m(\Phi) \sin\Phi d\Phi = \delta_{ll'} \tag{35}$$

The reduced pole distribution $P_{\mathbf{h}}(\mathbf{y})$ accessible to the diffraction measurement is obtained from Equation (30) according to Equation (11). When $\mathbf{h}$ is changed in $-\mathbf{h}$, $\Phi$ pass into $\pi - \Phi$ and $\beta$ pass into $\pi + \beta$. By using the property Equation (34) one obtains for $p_{\ \mathbf{h}}(\mathbf{y})$ Equation (30) with a supplementary factor $(-1)^l$ inside the sum over $l$. Consequently, in $P_{\mathbf{h}}(\mathbf{y})$ only the terms with $l$ even remain from Equation (30). It is convenient to rearrange Equation (30) to contain only real functions and positive indices $m$, $n$. By using Equations (29) and (33), $P_{\mathbf{h}}(\mathbf{y})$ becomes:

$$P_{\mathbf{h}}(\mathbf{y}) = \sum_{l=0}^{\infty} [4/(2l+1)] t_l(\mathbf{h}, \mathbf{y}), l = \text{even} \tag{36}$$

$$t_l(\mathbf{h}, \mathbf{y}) = A_l^0(\mathbf{y}) P_l^0(\Phi) + \sum_{m=1}^{l} \left[A_l^m(\mathbf{y}) \cos m\beta + B_l^m(\mathbf{y}) \sin m\beta\right] P_l^m(\Phi) \tag{37}$$

$$A_l^m(\mathbf{y}) = \alpha_l^{m0} P_l^0(\Psi) + \sum_{n=1}^{l} \left(\alpha_l^{mn} \cos n\gamma + \beta_l^{mn} \sin n\gamma\right) P_l^n(\Psi), (m = 0, l) \tag{38}$$

$$B_l^m(\mathbf{y}) = \gamma_l^{m0} P_l^0(\Psi) + \sum_{n=1}^{l} \left(\gamma_l^{mn} \cos n\gamma + \delta_l^{mn} \sin n\gamma\right) P_l^n(\Psi), (m = 1, l) \tag{39}$$

The coefficients $\alpha_l^{mn}$, $\beta_l^{mn}$, $\gamma_l^{mn}$, $\delta_l^{mn}$ are obtained from the coefficients $c_l^{mn}$ by the linear transformations given in Table 12.1.

If both the crystal and sample symmetry are triclinic, there are $(2l + 1)^2$ coefficients for a given value of $l$. For higher symmetries the number of coefficients is reduced, some coefficients being zero and some being correlated. Before finding the selection rules of the coefficients for all Laue classes, we must

**Table 12.1** The relations between the coefficients $\alpha_l^{mn}$, $\beta_l^{mn}$, $\gamma_l^{mn}$, $\delta_l^{mn}$ and $c_l^{mn} = a_l^{mn} + ib_l^{mn}$.

| | | |
|---|---|---|
| $\alpha_l^{00} = a_l^{00}/2$ | $\alpha_l^{0n} = a_l^{0n}$ | $\beta_l^{0n} = \quad b_l^{0n}$ |
| $\alpha_l^{m0} = a_l^{m0}$ | $\alpha_l^{mn} = a_l^{mn} + (\quad 1)^n a_l^{m,-n}$ | $\beta_l^{mn} = \quad b_l^{mn} + (\quad 1)^n b_l^{m,-n}$ |
| $\gamma_l^{m0} = b_l^{m0}$ | $\gamma_l^{mn} = b_l^{mn} + (\quad 1)^n b_l^{m,-n}$ | $\delta_l^{mn} = a_l^{mn} \quad (\quad 1)^n a_l^{m,-n}$ |

show how the crystal and the sample systems ($\mathbf{x}_i$) and ($\mathbf{y}_i$) are defined and, consequently, how the polar and azimuthal angles of **h** and **y**, respectively, are calculated.

*12.1.4.2 Crystal and Sample Coordinate Systems, Calculation of the Polar and Azimuthal Angles.* As a rule the axis $\mathbf{x}_3$ of the crystal orthogonal system is taken along the *r*-fold axis, ($r = 2,3,4,6$), and $\mathbf{x}_1$ along the two-fold axis normal to the *r*-fold axis, if it exists, which is the case of the Laue classes *mmm*, 4/*mmm*, 3*m*, 6/*mmm* and the cubic classes. For the Laue classes 2/*m*, 4/*m*, 3 and 6/*m* there is no two-fold axis normal to the *r*-fold axis and $\mathbf{x}_1$ can have an arbitrary direction. For simplicity $\mathbf{x}_1$ is taken, if possible, like in the first case. Once the crystal coordinate system ($\mathbf{x}_i$) is fixed the direction cosines ($a_i$) of **h** are calculated from the lattice parameters and the Miller indices. Finally, the corresponding polar and azimuthal angles are:

$$\cos\Phi = a_3, \ \tan\beta = a_2/a_1 \tag{40}$$

Table 12.2 gives the crystal system ($\mathbf{x}_i$) and the corresponding direction cosines for all Laue classes.

The sample coordinate system ($\mathbf{y}_i$) is defined in a manner similar with ($\mathbf{x}_i$) but not totally identical. The axis $\mathbf{y}_3$ is taken along the sample *r*-fold axis or along the cylindrical axis for a fibre texture, and $\mathbf{y}_1$ along the two-fold axis normal to the *r*-fold axis, if this axis exists; if not, $\mathbf{y}_1$ has an arbitrary direction. A significant difference from the crystal case is that the symmetry directions in the sample are in general not known, although sometimes we can guess them. As a consequence it is necessary to find these directions by Rietveld refinement together with the spherical harmonics parameters. Let us consider the general diffraction geometry described in Section 12.1.3. To change the sample orientation in the laboratory system the specimen is rotated on a goniometer with the standard Euler angles ($\omega$, $\chi$, $\phi$). When the goniometer is set to zero the axis $\omega$ is coincident with $\phi$ and parallel to the axis $\mathbf{l}_3$ of the laboratory system and the axis $\chi$ is parallel to $\mathbf{l}_1$. If we denote by ($\omega_s$, $\chi_s$, $\phi_s$) three standard Euler angles defining the orientation of the sample system ($\mathbf{y}_i$) with respect to the laboratory system ($\mathbf{l}_i$) when the goniometer is set to zero, then after the rotations ($\omega$,$\chi$,$\phi$) the sample system becomes:

$$\mathbf{y}_i = \sum_{j=1}^{3} M_{ij}(\omega_s, \chi_s, \phi_s; \omega, \chi, \phi)\mathbf{l}_j \tag{41}$$

**Table 12.2** Crystal axes ($\mathbf{x}_i$) and the direction cosines ($a_i$) as function of the lattice parameters and Miller indices for all Laue classes; $d$ is the interplanar distance, $2/m$ (**c**) means monoclinic unique axis **c**, and $3(R)$ denotes trigonal in rhombohedral setting.

| *Laue group* | *Lattice par.* | $x_3$ | $x_1$ | $a_1$ | $a_2$ | $a_3$ |
|---|---|---|---|---|---|---|
| $\bar{1}$ | $a, b, c, \alpha, \beta, \gamma$ | **c*** | **a** | $hd/a$ | $(ka \quad hb\cos\gamma)d/(ab\sin\gamma)$ | $(ha^*\cos\beta^* + kb^*\cos\alpha^* + lc^*)d$ |
| $2/m$ (**c**) | $a, b, c, \gamma$ | **c** | **a** | $hd/a$ | $(ka \quad hb\cos\gamma)d/(ab\sin\gamma)$ | $ld/c$ |
| $2/m$ (**b**) | $a, b, c, \beta$ | **b** | **c** | $ld/c$ | $(hc \quad la\cos\beta)d/(ac\sin\beta)$ | $kd/b$ |
| $mmm$ | $a, b, c$ | **c** | **a** | $hd/a$ | $kd/b$ | $ld/c$ |
| $4/m$, $4/mmm$ | $a, c$ | **c** | **a** | $hd/a$ | $kd/a$ | $ld/c$ |
| $\bar{3}, \bar{3}m1, 6/m, 6/mmm$ | $a, c$ | **c** | **a** | $hd/a$ | $(h+2k)d/(a\sqrt{3})$ | $ld/c$ |
| $\bar{3}1m$ | $a, c$ | **c** | $2\mathbf{a} + \mathbf{b}$ | $(2h+k)d/(a\sqrt{3})$ | $kd/a$ | $ld/c$ |
| $\bar{3}(R), \bar{3}m1(R)$ | $a, \alpha$ | $\mathbf{a} + \mathbf{b} + \mathbf{c}$ | $\mathbf{a} \quad \mathbf{b}$ | $(h \quad k)d/a/\sqrt{2(1 \quad \cos\alpha)}$ | $(h+k \quad 2l)d/a/\sqrt{2(1 \quad \cos\alpha)}$ | $(h+k+l)d/a/\sqrt{3(1+2\cos\alpha)}$ |
| $m\bar{3}, m\bar{3}m$ | $a$ | **c** | **a** | $hd/a$ | $kd/a$ | $ld/a$ |

$$\mathbf{M}(\omega_s, \chi_s, \phi_s; \omega, \chi, \phi) = \mathbf{a}(\omega_s, \chi_s, \phi_s)\mathbf{a}(\omega, \chi, \phi) \tag{42}$$

In Equation (42) **a** is the standard Euler matrix given by Equation (2) with ($\phi_1$, $\Phi_0$, $\phi_2$) replaced by ($\omega_s$, $\chi_s$, $\phi_s$) and by ($\omega$, $\chi$, $\phi$). Now by using Equations (18) and (41) one obtains the direction cosines of the scattering vector in the sample and, further, the angles ($\Psi$, $\gamma$):

$$b_i = \mathbf{y}\mathbf{y}_i = -\sin\theta M_{i1} + \cos\theta\cos\zeta M_{i2} + \cos\theta\sin\zeta M_{i3} \tag{43}$$

$$\cos\Psi = b_3,\ \tan\gamma = b_2/b_1 \tag{44}$$

Note that any point ($\Psi$, $\gamma$) can be reached by varying only two Euler angles, ($\omega$, $\chi$) or ($\chi$, $\phi$), the third angle being fixed at a convenient value. The sample initial orientation angles ($\omega_s$, $\chi_s$, $\phi_s$) are refinable parameters. If the sample symmetry belongs to a Laue class with an $r$-fold axis and a two-fold axis normal to it, all three parameters must be refined. If the two-fold axis is absent $\mathbf{y}_1$ has an arbitrary direction and one parameter must be fixed to an arbitrary value. Finally, if the sample has a triclinic symmetry, all three-sample orientation parameters must be fixed in the refinement. In practice the sample symmetry is not known, *a priori*, and is found by successive trials starting the refinement from a higher symmetry.

*12.1.4.3 Selection Rules for all Laue Classes.* The selection rules for the harmonic coefficients are derived from the invariance of the pole distribution to the operations of the crystal and sample Laue groups. The invariance conditions are applied to every function $t_l$ (**h**, **y**) from Equation (36), as the terms of different $l$ in this equation are independent. If we compare Equations (38) and (39) with (37) we observe that they have an identical structure. On the other side the sample and the crystal coordinate systems were similarly defined. As a consequence the selection rules for the coefficients $\alpha_l^{mn}$, $\beta_l^{mn}$, and respectively $\gamma_l^{mn}$, $\delta_l^{mn}$ resulting from the sample symmetry must be identical with the selection rules for the coefficients $A_l^m$ and $B_l^m$ resulting from the crystal symmetry, if the sample and the crystal Laue groups are the same. The exception is the case of cylindrical sample symmetry that has no correspondence with the crystal symmetry. In this case, only the coefficients $\alpha_l^{m0}$ and $\gamma_l^{m0}$ are different from zero, if they are not forbidden by the crystal symmetry.

An $r$-fold axis along $\mathbf{x}_3$ transforms $\beta$ into $\beta + 2\pi/r$ and leaves $\Phi$ unchanged. The invariance condition is:

$$t_l(\Phi, \beta + 2\pi/r, \mathbf{y}) = t_l(\Phi, \beta, \mathbf{y}) \tag{45}$$

The first term on the right-hand side of Equation (37) always fulfills this condition; the rest only for $A_l^m$ and $B_l^m$ that satisfy the following system of linear homogenous equations:

$$\begin{aligned} A_l^m(\mathbf{y})[\cos(2\pi m/r) - 1] + B_l^m(\mathbf{y})\sin(2\pi m/r) = 0 \\ -A_l^m(\mathbf{y})\sin(2\pi m/r) + B_l^m(\mathbf{y})[\cos(2\pi m/r) - 1] = 0 \end{aligned} \tag{46}$$

If $m = kr$, where $k$ is an integer, the system has a non-trivial solution for both $A_l^m$ and $B_l^m$. If, besides an $r$-fold axis in $\mathbf{x_3}$, there is a two-fold axis in $\mathbf{x_1}$, then $t_l(\mathbf{h},\mathbf{y})$ must fulfill a supplementary invariance condition:

$$t_l(\pi - \Phi, -\beta, \mathbf{y}) = t_l(\Phi, \beta, \mathbf{y}) \tag{47}$$

Replacing Equation (37) in (47) and taking into account Equation (34) and that $l$ is an even number one obtains:

$$(-1)^m A_l^m(\mathbf{y}) = A_l^m(\mathbf{y}),\ (-1)^{m+1} B_l^m(\mathbf{y}) = B_l^m(\mathbf{y}) \tag{48}$$

It means that $A_l^m$ is different from zero only for $m$ even and $B_l^m$ only for $m$ odd. Table 12.3 summarizes the selection rules for all non-cubic Laue groups.

The cubic groups $m3$ and $m3m$ are obtained by adding a three-fold axis on the big diagonal of the orthorhombic and, respectively, of the tetragonal $4/mmm$ prism. By adding this axis some coefficients become zero and other coefficients become correlated. To find them we cannot use the same procedure as before because the transformations of $\Phi$ and $\beta$ by the diagonal three-fold axis are no longer linear. To solve the problem Bunge[1] uses the Fourier coefficients of the Legendre functions and the transformation $(\Phi,0) \rightarrow (\pi/2,\Phi)$. An alternative approach by Popa and Balzar[21] does not need the Fourier coefficients. In place of $\Phi$ and $\beta$, Equation (37) for $mmm$ is evaluated in terms of direction cosines $a_1$, $a_2$, $a_3$. In these variables $t_l$ is a homogenous polynomial of degree $l$, the polynomial coefficients being linear combinations of $A_l^m$. The diagonal three-fold axis transforms $(a_1, a_2, a_3)$ into $(a_2, a_3, a_1)$ and setting the invariance condition to this transformation results in a system of linear homogenous equations for the coefficients $A_l^m$. By solving this system one obtains zero for some coefficients and linear correlations for other coefficients. At least two coefficients are involved in every correlation. The selection rules for the group $m3m$ are found from those of $m3$ by setting to zero the coefficients whose harmonic index $m$ is not a multiple of 4. The functions $t_l(\mathbf{h},\mathbf{y})$ for the cubic groups are given in the Table 12.4 for $l = 2,8$.

**Table 12.3** Selection rules for the non-cubic Laue groups. The symbols $A$ and $B$ designate $A_l^m(\mathbf{y})$ and $B_l^m(\mathbf{y})$ for the crystal symmetry or $\alpha_l^{mn}$, $\beta_l^{mn}$ and $\gamma_l^{mn}$, $\delta_l^{mn}$ for the sample symmetry.

| $m,n \rightarrow$ | 0 | 1 | 2 | 3 | 4 | 5 | 6 | 7 | 8 | 9 | 10 | 11 | 12 |
|---|---|---|---|---|---|---|---|---|---|---|---|---|---|
| 1 | $A$ | $AB$ | $AB$ | $AB$ | $AB$ | $AB$ | $AB$ | $AB$ | $AB$ | $AB$ | $AB$ | $AB$ | $AB$ |
| $2/m$ | $A$ | | $AB$ | | $AB$ | | $AB$ | | $AB$ | | $AB$ | | $AB$ |
| $mmm$ | $A$ | | $A$ | | $A$ | | $A$ | | $A$ | | $A$ | | $A$ |
| 3 | $A$ | | | $AB$ | | | $AB$ | | | $AB$ | | | $AB$ |
| $3m$ | $A$ | | | $B$ | | | $A$ | | | $B$ | | | $A$ |
| $4/m$ | $A$ | | | | $AB$ | | | | $AB$ | | | | $AB$ |
| $4/mmm$ | $A$ | | | | $A$ | | | | $A$ | | | | $A$ |
| $6/m$ | $A$ | | | | | | $AB$ | | | | | | $AB$ |
| $6/mmm$ | $A$ | | | | | | $A$ | | | | | | $A$ |

**Table 12.4** Functions $t_l(\mathbf{h},\mathbf{y})$, $l=2,8$ for the cubic group $m3$. For $m3m$, $A_6^2(\mathbf{y})=0$.

| |
|---|
| $t_2(\mathbf{h},\mathbf{y})=0$ |
| $t_4(\mathbf{h},\mathbf{y})=A_4^0(\mathbf{y})[P_4^0(\Phi)+\sqrt{10/7}P_4^4(\Phi)\cos 4\beta]$ |
| $t_6(\mathbf{h},\mathbf{y})=A_6^0(\mathbf{y})[P_6^0(\Phi) \quad \sqrt{14}P_6^4(\Phi)\cos 4\beta]+A_6^2(\mathbf{y})[P_6^2(\Phi)\cos 2\beta \quad \sqrt{5/11}P_6^6(\Phi)\cos 6\beta]$ |
| $t_8(\mathbf{h},\mathbf{y})=A_8^0(\mathbf{y})[P_8^0(\Phi)+\sqrt{56/99}P_8^4(\Phi)\cos 4\beta+\sqrt{130/99}P_8^8(\Phi)\cos 8\beta]$ |

After application of the selection rules the pole distribution Equation (36) becomes:

$$P_{\mathbf{h}}(\mathbf{y})=1+\sum_{l=2}^{\infty}[4/(2l+1)]\sum_{\mu=1}^{M(l)}\sum_{\nu=1}^{N(l)}\varepsilon_l^{\mu\nu}C_l^{\mu}(\Phi,\beta)S_l^{\nu}(\Psi,\gamma),\ l=\text{even} \tag{49}$$

Here $C_l^{\mu}$ and $S_l^{\nu}$ are symmetrized spherical harmonics that have the crystal and, respectively, the sample symmetry. The indices $\mu$ and $\nu$ count these functions for a given $l$. By taking Equation (35) into account we can prove that for different indices $l$, $\mu$, $\nu$ the symmetrized spherical harmonics are orthogonal:

$$\int_0^{\pi}\int_0^{2\pi}C_l^{\mu}(\Phi,\beta)C_{l'}^{\mu'}(\Phi,\beta)\sin\Phi d\Phi d\beta\sim\delta_{ll'}\delta_{\mu\mu'} \tag{50}$$

A similar equation holds for $S_l^{\nu}(\Psi,\gamma)$. The coefficients $\varepsilon_l^{\mu\nu}$ in Equation (49) are the non-zero, independent coefficients $\alpha_l^{mn}$, $\beta_l^{mn}$, $\gamma_l^{mn}$ $\delta_l^{mn}$. As an example, let us presume $m3$ and $3m$ the crystal and the sample symmetry, respectively. For $l=6$, and taking into account Tables 12.3 and 12.4, $M=2$ and $N=3$; the corresponding symmetrized harmonics and coefficients are:

$$C_6^1(\Phi,\beta)=P_6^0(\Phi)-\sqrt{14}P_6^4(\Phi)\cos 4\beta$$

$$C_6^2(\Phi,\beta)=P_6^2(\Phi)\cos 2\beta-\sqrt{5/11}P_6^6(\Phi)\cos 6\beta$$

$$S_6^1(\Psi,\gamma)=P_6^0(\Psi),\ S_6^2(\Psi,\gamma)=P_6^3(\Psi)\sin 3\gamma,\ S_6^3(\Psi,\gamma)=P_6^6(\Psi)\cos 6\gamma$$

$$\varepsilon_6^{1\nu}(\nu=1,3):\ \alpha_6^{00},\beta_6^{03},\alpha_6^{06};\ \varepsilon_6^{2\nu}(\nu=1,3):\ \alpha_6^{20},\beta_6^{23},\alpha_6^{26}$$

*12.1.4.4 Implementation in the Rietveld Method.* When implemented in the Rietveld codes the series Equation (49) is truncated at $l=L$. The harmonics coefficients $\varepsilon_l^{\mu\nu}$ (together with the structural and other parameters) and the optimum value of $L$ are found by successive refinements by increasing $L$ from a small value up to a value for which the added coefficients do not improve the fit.

Once the series convergence is reached the pole distributions can be calculated from the refined harmonic coefficients. The standard error of the calculated pole distribution is given by:

$$\sigma^2[P_{\mathbf{h}}(\mathbf{y})] = \sum_{l=2}^{L} [4/(2l+1)]^2 \sum_{\mu=1}^{M(l)} \sum_{\nu=1}^{N(l)} \sigma^2(\varepsilon_l^{\mu\nu})[C_l^{\mu}(\Phi,\beta) S_l^{\nu}(\Psi,\gamma)]^2 \qquad (51)$$

When Equation (51) was derived the correlation matrix of $\varepsilon_l^{\mu\nu}$ was considered diagonal because the symmetrized spherical harmonics are orthogonal. In practice some correlations exists [because only discrete points ($\Phi$, $\beta$) and ($\Psi$, $\gamma$) are involved] but they are small. We can also calculate the texture index $J$ and the texture strength $J^{1/2}$. According to Bunge[1] the texture index is defined as follows:

$$\begin{aligned} J &= (1/8\pi^2) \int_0^{2\pi} \int_0^{\pi} \int_0^{2\pi} f^2(\varphi_1, \Phi_0, \varphi_2) \sin\Phi_0 d\varphi_1 d\Phi_0 d\varphi_2 \\ &= 1 + \sum_{l\ 2}^{L} (2l+1)\ {}^{1}\left\{ \begin{array}{l} 4(\alpha_l^{00})^2 + 2\sum\limits_{m\ 1}^{l} \left[(\alpha_l^{m0})^2 + (\gamma_l^{m0})^2\right] + 2\sum\limits_{n\ 1}^{l} \left[(\alpha_l^{0n})^2 + (\beta_l^{0n})^2\right] \\ + \sum\limits_{m\ 1}^{l} \sum\limits_{n\ 1}^{l} \left[(\alpha_l^{mn})^2 + (\beta_l^{mn})^2 + (\gamma_l^{mn})^2 + (\delta_l^{mn})^2\right] \end{array} \right\} \end{aligned} \qquad (52)$$

To derive the right-hand side of Equations (52), (28) and Table 12.1 were used. Note that the texture index contributes not only to the refined coefficients but also the coefficients linearly correlated from the cubic groups ($\alpha_6^{00}$ and also $\alpha_6^{40} = -\sqrt{14}\alpha_6^{00}$ in the example above).

Implementation in the Rietveld method of the general representation of the texture by symmetrized spherical harmonics made possible a robust texture correction in the structure refinement and transformed the Rietveld method into a powerful tool for a quantitative determination of the texture itself. The robustness of the texture correction is a direct consequence of the fact that the symmetrized spherical harmonics are orthogonal functions.

For the determination of the orientation distribution function it is necessary to record diffraction patterns successively by rotating the sample on a goniometer, as was shown in Section 12.1.4.2. The patterns must be measured in a large number of points ($\Psi$, $\gamma$) scattered more or less uniformly on a hemisphere. It is difficult to evaluate beforehand how many such points are necessary for a reliable determination of the ODF. For a calcite sample previously used in a texture round robin[16] Von Dreele[15] recorded neutron time of flight diffraction patterns in about 50 points ($\Psi$, $\gamma$). All patterns were processed by GSAS simultaneously and six pole distributions calculated from the refined harmonic coefficients were further used as input in the WIMV inversion routine. An ODF similar to those obtained in the texture round robin resulted, but its dependence on the number of points in the space ($\Psi$, $\gamma$) was not examined.

If the quantitative texture analysis is not of interest the sample is not rotated on a goniometer and only one or a small number of patterns are recorded. Because the number of points in the space ($\Psi$, $\gamma$) is not sufficient, one expects that the refined harmonic coefficients give only a rough description of the texture, even if the texture correction is very good. An extreme case is the Bragg–Brentano geometry. In this case in Equations (41–43) we must take $\omega = \theta$, $\chi = \phi = 0$, $\zeta = 0$ and consequently Equation (44) becomes:

$$\cos \Psi_0 = a_{32}(\omega_s, \chi_s, \phi_s),\ \tan \gamma_0 = a_{22}(\omega_s, \chi_s, \phi_s)/a_{12}(\omega_s, \chi_s, \phi_s)$$

Only one direction in sample is involved for the whole pattern and in place of Equation (49) in the Rietveld programs one uses the density of poles in this single direction:

$$P_{\mathbf{h}} = 1 + \sum_{l=2}^{\infty} [4/(2l+1)] \sum_{\mu=1}^{M(l)} \varepsilon_l^{\mu} C_l^{\mu}(\Phi, \beta), l = \text{even} \tag{53}$$

The refinable parameters are $\varepsilon_l^{\mu}$ defined as follows:

$$\varepsilon_l^{\mu} = \sum_{\nu=1}^{N(l)} \varepsilon_l^{\mu\nu} S_l^{\nu}(\Psi_0, \gamma_0) \tag{54}$$

We can have a good texture correction but no information about the texture itself because the coefficients $\varepsilon_l^{\mu\nu}$ cannot be refined. A similar situation appears for the pattern recorded on a neutron time of flight diffractometer equipped with only one detector battery.

## 12.2 MACROSCOPIC STRAIN AND STRESS

The stress state, where the stress can be both applied and residual, and the associated strain influence many different material properties, which is especially important in engineering and technological applications. The residual stress and strain can be advantageous or, on the contrary, can provoke a faster failure of machine parts or other manufactured materials. There are different methods to determine the strain and stress in materials: mechanical, acoustical, optical and the diffraction of X-ray and neutrons. The diffraction method is applicable for crystalline materials and is based on the measurements of the elastic strain effects on the diffraction lines. There are two kinds of such effects, a peak shift and a peak broadening. The strain modifies the interplanar distances $d$. In a polycrystalline specimen a peak shift is produced if the average of the interplanar distance modifications on the crystallites in reflection is different from zero. If the dispersion of interplanar distance modifications is different from zero, then a peak broadening occurs. The effect of the strain on the peak breadth is described in Chapter 13. Here we deal only with the peak shift effect caused by the macroscopic, or Type I strain/stress. There is a substantial amount of literature on this subject. The comprehensive

monographs by Noyan and Cohen[22] and by Hauk[23] are strongly recommended. A rich reference list can be found in a recent review by Welzel *et al.*[24]

### 12.2.1 Elastic Strain and Stress in a Crystallite – Mathematical Background

If we denote by $\mathbf{u}(\mathbf{r}) = u_1(\mathbf{r})\mathbf{x}_1 + u_2(\mathbf{r})\mathbf{x}_2 + u_3(\mathbf{r})\mathbf{x}_3$ the vector of a small deformation in the point $\mathbf{r}$ of the crystallite, the strain tensor is:

$$\varepsilon_{ij} = (1/2)\left(\partial u_i/\partial x_j + \partial u_j/\partial x_i\right),\ (i,j = 1,3) \tag{55}$$

By definition it is a symmetric second-rank tensor. The stress tensor $\sigma_{ij}$, $(i, j = 1,3)$, is also a symmetric second-rank tensor defined as follows (Landau and Lifchitz[25]): the element $\sigma_{ij}$ is the $i$ component of the force acting on the unit area normal to the axis $\mathbf{x}_j$. The symmetry of the stress tensor is imposed by the condition of mechanical equilibrium.

In different reference systems the strain and stress tensors have different components, the transformation being easily derived starting from the definitions. Let us consider, for example, the sample reference system $(\mathbf{y}_i)$ and denote by Latin letters $e_{km}$ and $s_{km}$ the components of the strain and stress tensors in this system. If the transformation of the sample reference system $(\mathbf{y}_i)$ into the crystal reference system $(\mathbf{x}_i)$ is given by Equation (1) then the transformations of the strain tensors are the following:

$$\varepsilon_{il} = \sum_{k=1}^{3}\sum_{m=1}^{3} a_{ik}a_{lm}e_{km},\ e_{km} = \sum_{i=1}^{3}\sum_{l=1}^{3} a_{ik}a_{lm}\varepsilon_{il} \tag{56a, b}$$

Similar transformations occur between $\sigma_{il}$ and $s_{km}$.

The $d$-spacing variation caused by a strain along the lattice vector $\mathbf{H}(hkl)$ is observable in a diffraction experiment:

$$[d(hkl) - d_0(hkl)]/d_0(hkl) = \Delta d/d_0 = -\Delta H/H_0 = \varepsilon_{hh} \tag{57}$$

To calculate this quantity from the strain tensor components $\varepsilon_{ij}$ we must define the reference system $(\mathbf{k}, \mathbf{l}, \mathbf{h})$ with the axis $\mathbf{k}$ in the plane $(\mathbf{x}_3, \mathbf{h})$ and normal to $\mathbf{h}$ and $\mathbf{l} = \mathbf{h} \times \mathbf{k}$. The systems $(\mathbf{k}, \mathbf{l}, \mathbf{h})$ and $(\mathbf{x}_i)$ are connected by the matrix $\mathbf{m}$ defined before by Equation (9a):

$$\begin{pmatrix} \mathbf{k} \\ \mathbf{l} \\ \mathbf{h} \end{pmatrix} = \mathbf{m}(\Phi, \beta) \begin{pmatrix} \mathbf{x}_1 \\ \mathbf{x}_2 \\ \mathbf{x}_3 \end{pmatrix} \tag{58}$$

A comparison of Equation (58) with Equation (1) shows how to obtain $\varepsilon_{hh}$ by using Equation (56a):

$$\varepsilon_{hh} = \sum_{k=1}^{3}\sum_{m=1}^{3} m_{3k}(\Phi, \beta)m_{3m}(\Phi, \beta)\varepsilon_{km} = \sum_{k=1}^{3}\sum_{m=1}^{3} a_k a_m \varepsilon_{km} \tag{59}$$

Note that we used for this tensor element a notation with a Greek letter because the system (**k**, **l**, **h**) is linked to the crystallite. Hereafter we will denote $\varepsilon_{hh}$ simply by $\varepsilon_{\mathbf{h}}$. If the $\varepsilon_{km}$ on the right-hand side of Equation (59) are replaced by Equation (56a) one obtains an equivalent expression for $\varepsilon_{\mathbf{h}}$ but with the strain tensor components and the direction cosines of **h** from the sample reference system:

$$\varepsilon_{hh} = \varepsilon_{\mathbf{h}} = \sum_{k=1}^{3}\sum_{m=1}^{3} b_k b_m e_{km} \tag{60}$$

As we will see later, sometimes it is advantageous to use Equation (60), whereas at other times a large amount of calculation is saved by starting from Equation (59).

The stress and strain tensors are connected by the Hooke equations. In the crystallite reference system these are the following:

$$\sigma_{ij} = \sum_{k=1}^{3}\sum_{l=1}^{3} C_{ijkl}\varepsilon_{kl},\ \varepsilon_{ij} = \sum_{k=1}^{3}\sum_{l=1}^{3} S_{ijkl}\sigma_{kl},\ (i,j=1,3) \tag{61a, b}$$

Here $C_{ijkl}$ are the stiffness constants and $S_{ijkl}$ are the compliance constants. They form two symmetric fourth-rank tensors with 81 elements inverse one to another. For the triclinic symmetry only 21 elements are independent because the strain and stress tensors are symmetric. Consequently the indices $i, j$ and $k, l$ can be permuted and also can be permuted one pair with another. For a crystal symmetry higher than triclinic the number of independent elastic constants is less than 21.

We can take advantage of the symmetry of the strain, stress and elastic constants tensors by using the reduced indices defined as follows:

$$11 \to 1, 22 \to 2, 33 \to 3, 23 = 32 \to 4, 13 = 31 \to 5, 12 = 21 \to 6 \tag{62}$$

By using the reduced indices the strain and stress tensors are represented as vectors of dimension 6 and the elastic constant tensors as symmetrical matrices of dimensions $6 \times 6$. In the literature two conventions can be found for expressing the strain, stress and the elastic constants tensors in the reduced indices. The first convention is:[26]

$$\begin{cases} \varepsilon_{ij} \to \varepsilon_m & \text{if } m = 1,2,3 \\ 2\varepsilon_{ij} \to \varepsilon_m & \text{if } m = 4,5,6 \\ C_{ijkl} \to C_{mn}, & m,n = 1,6 \end{cases} \qquad \begin{cases} \sigma_{ij} \to \sigma_m, & m = 1,6 \\ S_{ijkl} \to S_{mn} & \text{if } m,n = 1,2,3 \\ 2S_{ijkl} \to S_{mn} & \text{if } m \text{ or } n = 4,5,6 \\ 4S_{ijkl} \to S_{mn} & \text{if } m \text{ and } n = 4,5,6 \end{cases}$$

We prefer to use the second convention[27] that keeps the values of the tensor elements and, for crystal symmetry higher than triclinic, gives the same structure for the matrices **C** and **S**:

$$\begin{array}{llll} \varepsilon_{ij} \to \varepsilon_m, & m = 1,6 & \sigma_{ij} \to \sigma_m, & m = 1,6 \\ C_{ijkl} \to C_{mn}, & m,n = 1,6 & S_{ijkl} \to S_{mn}, & m,n = 1,6 \end{array} \tag{63}$$

**Table 12.5** The matrix **C** of the stiffness constants for all Laue classes. The matrix **S** of the compliance constants is identical, only $C$ is replaced by $S$. The last column gives the number of the independent constants.

| | | |
|---|---|---|
| $\bar{1}$ | | 21 |
| $2/m$ (**c**) | $C_{14}$ $C_{15}$ $C_{24}$ $C_{25}$ $C_{34}$ $C_{35}$ $C_{46}$ $C_{56}$ 0 | 13 |
| $mmm$ | $2/m + C_{16}$ $C_{26}$ $C_{36}$ $C_{45}$ 0 | 9 |
| $4/m$ | $2/m + C_{36}$ $C_{45}$ 0, $C_{22}$ $C_{11}$, $C_{23}$ $C_{13}$, $C_{26}$ $C_{16}$, $C_{55}$ $C_{44}$ | 7 |
| $4/mmm$ | $4/m + C_{16}$ 0 | 6 |
| $\bar{3}$ | $C_{16}$ $C_{26}$ $C_{34}$ $C_{35}$ $C_{36}$ $C_{45}$ 0, $C_{22}$ $C_{11}$, $C_{23}$ $C_{13}$, $C_{24}$ $C_{14}$, $C_{25}$ $C_{15}$, $C_{46}$ $C_{15}$, $C_{55}$ $C_{44}$, $C_{56}$ $C_{14}$, $C_{66}$ $(C_{11}$ $C_{12})/2$ | 7 |
| $\bar{3}m$ | $\bar{3} + C_{15}$ 0 | 6 |
| Hexag. | $\bar{3}m + C_{14}$ 0 | 5 |
| Cubic | $4/mmm + C_{13}$ $C_{12}$, $C_{33}$ $C_{11}$, $C_{66}$ $C_{44}$ | 3 |
| Isotropic | Cubic + $C_{44}$ $(C_{11}$ $C_{12})/2$ | 2 |

By using Equation (63) the inversion relations between the matrices **C** and **S** are $\mathbf{S} = (\mathbf{C}')^{-1}$ and $\mathbf{C} = (\mathbf{S}')^{-1}$, where $\mathbf{C}'$ and $\mathbf{S}'$ are obtained by partitioning **C** and **S** in four blocks and multiplying the elements as follows: by 1 in the upper left block, by 2 in the upper right and lower left blocks and by 4 in the lower right block. Table 12.5 gives the matrices **C** for all Laue classes. The matrices **S** have exactly the same structure. The elastic constant matrices, as given in Table 12.5, were obtained by choosing the crystal reference system ($\mathbf{x}_i$) according to Section 12.1.4.2 (Table 12.2) and by setting the condition of invariance of the elastic free energy per unit volume to the operations of the crystal point group.

We can resume now the basic equations that will be used later. They are obtained by applying Equations (62) and (63) to Equations (56), (59), (60) and (61) : the Hooke equations:

$$\sigma_i = \sum_{j=1}^{6} C_{ij}\rho_j\varepsilon_j, \quad \varepsilon_i = \sum_{j=1}^{6} S_{ij}\rho_j\sigma_j \tag{64a, b}$$

the transformations of the strain and stress tensors from crystal (Greek) to sample (Latin) reference system and back:

$$e_i = \sum_{j=1}^{6} P_{ij}\varepsilon_j, \ \varepsilon_i = \sum_{j=1}^{6} Q_{ij}e_j \tag{65a, b}$$

$$s_i = \sum_{j=1}^{6} P_{ij}\sigma_j, \ \sigma_i = \sum_{j=1}^{6} Q_{ij}s_j \tag{66a, b}$$

and the strain along the reciprocal lattice vector:

$$\varepsilon_{\mathbf{h}} = \sum_{j=1}^{6} E_j\rho_j\varepsilon_j, \ \varepsilon_{\mathbf{h}} = \sum_{j=1}^{6} F_j\rho_j e_j \tag{67a, b}$$

In Equations (64) and (67) the following notation was used:

$$(\rho_1, ....., \rho_6) = (1, 1, 1, 2, 2, 2) \tag{68}$$

$$(E_1, ...., E_6) = (a_1^2, a_2^2, a_3^2, a_2a_3, a_1a_3, a_1a_2) \tag{69}$$

$$(F_1, ...., F_6) = (b_1^2, b_2^2, b_3^2, b_2b_3, b_1b_3, b_1b_2) \tag{70}$$

In Equations (65) and (66) the matrices $\mathbf{Q}$ and $\mathbf{P} = \mathbf{Q}^{-1}$ of dimensions (6,6) can be expressed by four other matrices of dimensions (3,3):

$$\mathbf{Q} = \begin{pmatrix} \mathbf{L} & 2\mathbf{M} \\ \mathbf{N} & \mathbf{O} \end{pmatrix}, \ \mathbf{P} = \begin{pmatrix} \mathbf{L}^t & 2\mathbf{N}^t \\ \mathbf{M}^t & \mathbf{O}^t \end{pmatrix} \tag{71a, b}$$

$$\left.\begin{array}{l} L_{kl} = a_{kl}^2, M_{lk} = a_{li}a_{lj}, N_{kl} = a_{il}a_{jl} \\ O_{ij} = a_{kk}a_{ji} + a_{ki}a_{jk}, O_{kk} = a_{ii}a_{jj} + a_{ij}a_{ji} \end{array}\right\}, \left\{\begin{array}{l} i,j,k,l = 1,3 \\ i \neq j \neq k \end{array}\right. \tag{72}$$

Finally, the Hooke equations in a crystallite can be written by using the components of the strain and stress tensors in the sample reference system. Denoting by $g$ the triplet of Euler angles ($\varphi_1$, $\Phi_0$, $\varphi_2$) and using Equations (64–66) we have:

$$s_i = \sum_{j=1}^{6} C_{ij}(g)\rho_j e_j, \ e_i = \sum_{j=1}^{6} S_{ij}(g)\rho_j s_j \tag{73a, b}$$

Here $C_{il}(g)$ and $S_{il}(g)$ are the single-crystal stiffness and compliance tensors in the sample reference system. They have the following expressions:

$$C_{il}(g) = \rho_l^{-1} \sum_{j=1}^{6}\sum_{k=1}^{6} C_{jk}\rho_k P_{ij}Q_{kl}, \ S_{il}(g) = \rho_l^{-1} \sum_{j=1}^{6}\sum_{k=1}^{6} S_{jk}\rho_k P_{ij}Q_{kl} \tag{74a, b}$$

### 12.2.2 Strain and Stress in Polycrystalline Samples

*12.2.2.1 Strains and Stresses of Types I, II and III.* The elastic strain and stress state of a crystallite is determined by the Hooke equations together with the boundary conditions. In a polycrystalline sample the boundary conditions are the result of the interaction of the crystallite with its neighbors and this interaction depends on the crystallite shape and orientation. The resulting strain and stress in the crystallite are not homogenous and in the most general case are described by functions depending not only on the crystallite orientation but also on the position vector in the crystallite. Let us denote by $\mathbf{R}_k$ the position vector with respect to the sample reference system of the crystallite $k$ having the orientation in the range ($g$, $g + dg$). The position vector of a point within this crystallite will be $\mathbf{R}_k + \mathbf{r}$ and the strain at this point is $\varepsilon_i(\mathbf{R}_k + \mathbf{r}, g)$.

Denoting the volume of this crystallite by $V_k$ the average strain in this crystallite is:

$$\varepsilon_i(\mathbf{R}_k, g) = V_k{}^{-1} \int \varepsilon_i(\mathbf{R}_k + \mathbf{r}, g) d\mathbf{r} \tag{75}$$

The micro-strain or the Type III strain is the difference between $\varepsilon_i$ ($\mathbf{R}_k + \mathbf{r}$, $g$) and this average:

$$\Delta\varepsilon_i(\mathbf{R}_k + \mathbf{r}, g) = \varepsilon_i(\mathbf{R}_k + \mathbf{r}, g) - \varepsilon_i(\mathbf{R}_k, g) \tag{76}$$

Obviously, the average over $\mathbf{r}$ of the Type III strain is zero. Let us now denote by $N_g$ the total number (presumed large) of crystallites from the group of orientation $g$ and define the following average and difference:

$$\varepsilon_i(g) = N_g{}^{-1} \sum_{k=1}^{N_g} \varepsilon_i(\mathbf{R}_k, g) \tag{77}$$

$$\Delta\varepsilon_i(\mathbf{R}_k, g) = \varepsilon_i(\mathbf{R}_k, g) - \varepsilon_i(g) \tag{78}$$

The strain $\varepsilon_i(g)$ defined by Equation (77) is a macroscopic quantity called Type I strain. The difference Equation (78) between the average strain on the crystallite $k$ of the group $g$ and the Type I strain is a sub-macroscopic quantity called Type II strain. Obviously, the average over $k$ of the Type II strain is also zero. Taking account of Equations (76) and (78) we can write the strain at the point $\mathbf{r}$ of the crystallite $k$ from the group $g$ as a sum of these three types of strains:

$$\varepsilon_i(\mathbf{R}_k + \mathbf{r}, g) = \varepsilon_i(g) + \Delta\varepsilon_i(\mathbf{R}_k, g) + \Delta\varepsilon_i(\mathbf{R}_k + \mathbf{r}, g) \tag{79}$$

Similar expressions can be written for any strain or stress component in any reference system. In Equation (79) $\varepsilon_i$ is in fact a placeholder for $\varepsilon_i$, $e_i$, $\sigma_i$, $s_i$ and also for $\varepsilon_{\mathbf{h}}$ that gives the diffraction peak shift caused by the strain in a crystallite. To calculate the peak shift for a polycrystalline sample, $\varepsilon_{\mathbf{h}}$ ($\mathbf{R}_k + \mathbf{r}$, $g$) given by Equation (79) must be averaged over $\mathbf{r}$, $k$ and $g'$, where $g'$ represents those crystallite orientations for which $\mathbf{h}$ is parallel to $\mathbf{y}$, the direction in the sample of the scattering vector. Taking account that the sample could be textured this multiple average is the following:

$$\begin{aligned} \langle \varepsilon_{\mathbf{h}}(\mathbf{y}) \rangle &= \int d\omega\, f(g') N_{g'}{}^{-1} \sum_{k=1}^{N_{g'}} V_k{}^{-1} \int d\mathbf{r} \varepsilon_{\mathbf{h}}(\mathbf{R}_k + \mathbf{r}, g') / \int d\omega\, f(g') \\ &= (1/2\pi) \int d\omega\, f(g') \varepsilon_{\mathbf{h}}(g') / p_{\mathbf{h}}(\mathbf{y}). \end{aligned} \tag{80}$$

The contributions to the peak shift of the third and of the second terms from Equation (79) are zero because the average of these terms over $\mathbf{r}$ and $k$,

respectively, are zero. The peak shift is exclusively caused by the Type I strain, in which case we will retain only the first term from the right-hand side of Equation (79). Type II and Type III strains contribute only to the peak broadening that is described in Chapter 13.

*12.2.2.2 Macroscopic and Intergranular Strain/Stress.* Similar to the case of texture we can call $\varepsilon_i(g) = \varepsilon_i(\varphi_1, \Phi_0, \varphi_2)$ the strain/stress orientation distribution functions (SODF) ($\varepsilon_i$ is still a placeholder). In contrast to the texture case, the average of the SODF over all variables is not unity but is the macroscopic strain/stress:

$$\varepsilon_i = (1/8\pi^2) \int_0^{2\pi} \int_0^{\pi} \int_0^{2\pi} \varepsilon_i(\varphi_1, \Phi_0, \varphi_2) f(\varphi_1, \Phi_0, \varphi_2) \sin \Phi_0 d\varphi_1 d\Phi_0 d\varphi_2 \tag{81}$$

The SODF is itself a macroscopic quantity, as is the following difference, called intergranular strain/stress:

$$\Delta\varepsilon_i(\varphi_1, \Phi_0, \varphi_2) = \varepsilon_i(\varphi_1, \Phi_0, \varphi_2) - \varepsilon_i \tag{82}$$

Obviously, the integral over all variables of the intergranular strain/stress weighted by texture is zero. The intergranular strain/stress may be originated by elastic and plastic deformations, phase transformations, thermal treatments, mismatch of *d*-spacing in composite materials and differences in the coefficients of thermal expansion. In general both mean values Equation (81) and intergranular strains/stresses Equation (82) are necessary for a complete description of the strain/stress state in a material.

The SODF is not accessible directly in diffraction measurements but the strain pole distribution given by Equation (80). The strain pole distribution is for the SODF the equivalent of the pole distribution for texture with an important difference: in place of one distribution, six separate SODFs in a well-defined linear combination [Equation (67)] are projected on the space ($\Psi$, $\gamma$). The strain pole distribution given by Equation (80) contains as a normalizing factor the texture pole distribution $p_{\mathbf{h}}(\mathbf{y})$ that is not accessible to the diffraction measurements. This can be replaced by the reduced pole distribution because the peak positions for $-\mathbf{h}$ and $\mathbf{h}$ are not distinguishable. Therefore, the strain pole distribution becomes:

$$\langle \varepsilon_{\mathbf{h}}(\mathbf{y}) \rangle = \frac{1}{2P_{\mathbf{h}}(\mathbf{y})} \begin{bmatrix} (1/2\pi) \int\limits_{\mathbf{h}\|\mathbf{y}} d\omega \varepsilon_{\mathbf{h}}(\varphi_1, \Phi_0, \varphi_2) f(\varphi_1, \Phi_0, \varphi_2) \\ +(1/2\pi) \int\limits_{\mathbf{h}\|\mathbf{y}} d\omega \varepsilon_{\mathbf{h}}(\varphi_1, \Phi_0, \varphi_2) f(\varphi_1, \Phi_0, \varphi_2) \end{bmatrix} \tag{83}$$

Note that angular brackets $<\ldots>$ are used for the average over the orientations of crystallites in reflection and a bar on the averaged quantity for the average over all orientations in the Euler space.

### 12.2.3 Status of the Strain/Stress Analysis by Diffraction

For many decades the principal aim of strain/stress analysis by diffraction was the determination of the average strain and stress tensors $\overline{\mathbf{e}}$ and $\overline{\mathbf{s}}$ in materials. The determination was based on the supposition that the elastic strain and stress tensors $\mathbf{e}(g)$, $\mathbf{s}(g)$ in a crystallite are connected to the average tensors $\overline{\mathbf{s}}$, $\overline{\mathbf{e}}$ as follows:

$$\mathbf{e}(g) = \mathbf{S}^*(g)\overline{\mathbf{s}},\ \mathbf{s}(g) = \mathbf{C}^*(g)\overline{\mathbf{e}} \tag{84a, b}$$

Here $\mathbf{S}^*(g)$ and $\mathbf{C}^*(g)$ are fourth-rank tensors describing the elastic behavior of the crystallites in the polycrystalline material [not necessarily the single-crystal compliance and stiffness tensors as in Equation (73)]. If Equations (84) are true then the average strain measured by diffraction has the following expression:

$$\langle \varepsilon_{\mathbf{h}}(\mathbf{y}) \rangle = \sum_{j=1}^{6} R_j(\Psi, \gamma; \Phi, \beta) s_j \tag{85}$$

The coefficients $R_j$ are called diffraction stress factors. The relations (84) are only true if the elastic interactions of crystallites are considered. In other words the right-hand sides in Equation (84) represent the elastically induced parts of strain and stress in crystallites. Classical models like Voigt,[28] Reuss[29] and Kroner[30] describe these elastic interactions and the diffraction stress factors $R_j$ can be calculated analytically or numerically by using Equation (83). The average stresses can be obtained by fitting Equation (85) to the measured data for several peaks and directions in the sample. For isotropic (not-textured) samples Equation (85) becomes linear in $\sin^2\Psi$ and $\sin 2\Psi$ and is the basic equation of the traditional "$\sin^2\Psi$" method.[31,32] Most experimental data can be processed by this method, even if the sample has a weak texture.

For textured samples the relation between the peak shifts and $\sin^2\Psi$ becomes nonlinear and analytical expressions can be found only by approximating the texture pole distribution by $\delta$ functions on some prominent sample directions.[33] This could be a rough approximation, especially if the grain elastic interactions are not of the Reuss type, and numerical calculations of the diffraction stress factors are preferable.

Determination of the stress in textured sample requires a prior, accurate determination of the texture. To eliminate this time consuming step and to increase the accuracy of the stress determination Ferrari and Lutterotti[34] proposed to include the stress analysis into the Rietveld method, the stress parameters being refined together with the texture spherical harmonics coefficients and the structural parameters. Balzar and coworkers[35] also used the Rietveld method with a Voigt type formula implemented in GSAS to determine the average strain tensor from multiple time-of-flight neutron diffraction patterns on Al/SiC composites. In GSAS [profile #5 (ref. [36])] are also implemented formulae for all Laue groups describing the peak shift caused by a hydrostatic pressure. These are useful to fit the effect of thermal expansion and some solvent-dependent effects in highly hydrated crystals.

Sometimes the dependence of the measured strain on $\sin^2\Psi$ becomes strongly nonlinear, especially in metals after plastic deformation, and cannot be explained by the texture or by the stress gradient effect. In general, Equations (84) are too restrictive because they do not take into account the plastically induced part of the strain and stress. They must be replaced by the exact Equations (73):

$$\mathbf{e}(g) = \mathbf{S}(g)[\bar{\mathbf{s}} + \Delta\mathbf{s}(g)],\ \mathbf{s}(g) = \mathbf{C}(g)[\bar{\mathbf{e}} + \Delta\mathbf{e}(g)] \tag{86}$$

In other words, the averaged strain and stress tensors and the whole intergranular strains and stresses must be considered to explain the strongly nonlinear dependence of the measured strain on $\sin^2\Psi$. There are two possibilities to account for the whole intergranular stress. The first is to calculate the plastically induced part of the stress starting from the models of the plastic flow of crystallites within a polycrystalline sample.[37,38] The second possibility is to construct the strain/stress orientation distribution functions $\varepsilon_i(\varphi_1, \Phi_0, \varphi_2)$ by inverting the strain pole distributions $\langle\varepsilon_{\mathbf{h}}(\mathbf{y})\rangle$ measured for several poles and in a large number of points $(\Psi, \gamma)$. No model is necessary to assume for the elastic or plastic interactions of crystallites. Conversely, determination of the SODF on elastically loaded or plastically deformed samples gives essential information on the mechanisms of crystallite interactions.

To determine the SODF, Wang and coworkers[39–42] and Behnken[43] proposed and tested an approach based on the representation of these functions by generalized spherical harmonics. The Wang and the Behnken approaches presume a prior determination of the ODF (texture) and individual peak fitting to find the peak position. Only isolated peaks can be used for accurate position determination, and then a large part of information contained in the diffraction pattern is lost. To eliminate these drawbacks Popa and Balzar[21] proposed to implement the spherical harmonic analysis of the strain in the Rietveld method. The strain harmonic coefficients are refined simultaneously with the texture coefficients and with the structural and other parameters. In place of the SODF, Popa and Balzar used WSODF, the strain orientation function weighted by texture, and performed the spherical harmonic analysis for all Laue classes. Note that in the Wang and Behnken approach only the cubic crystal symmetry and the orthorhombic sample symmetry were considered. The strain harmonic coefficients refined in the Rietveld method are further used to construct the WSODF, and then the SODF, by Fourier synthesis or by direct inversion methods such as WIMV. For every tensor component $\varepsilon_i$ several pole figures $\langle\varepsilon_i(\mathbf{h}, \mathbf{y})\rangle$ are calculated from the refined coefficients. Further, these pole figures are used as input in the WIMV routine.

The following sections develop three subjects: the classical approximations for the strain/stress in isotropic polycrystals, isotropic polycrystals under hydrostatic pressure and the spherical harmonic analysis to determine the average strain/stress tensors and the intergranular strain/stress in textured samples of any crystal and sample symmetry. Most of the expressions that are obtained for the peak shift have the potential to be implemented in the Rietveld routine, but only a few have been implemented already.

### 12.2.4 Strain/Stress in Isotropic Samples – Classical Approximations

The term isotropic for a polycrystalline sample denotes the absence of the preferred orientation, in which case $f(\varphi_1,\ \Phi_0,\ \varphi_2) = 1$. Concerning the elastic properties, on average this sample is isotropic but the behavior of crystallites, with rare exceptions, is anisotropic. For this reason a non-textured polycrystalline sample can be also called quasi-isotropic.

*12.2.4.1 Voigt Model.* According to Voigt[28] the intergranular strain in the sample reference system is zero and then the strain tensor in the crystallite is identical with the macroscopic strain:

$$e_i(\varphi_1, \Phi_0, \varphi_2) = e_i \tag{87}$$

To find the stress tensor in the same system we place Equation (87) into Equation (73a) and one obtains an expression similar to Equation (84b). To obtain the macroscopic stress we must integrate this expression over the Euler space. The integral acts only on the single-crystal stiffness tensor elements Equation (74a) and can be calculated analytically. The macroscopic stress is:

$$s_i = \sum_{j=1}^{6} C_{ij}^{V} \rho_j e_j \tag{88}$$

In Equation (88) the $C_{ij}^{V}$ are the averaged elastic stiffness constants for the isotropic polycrystal. They can be calculated from the single-crystal stiffness constants as follows:

$$C_{11}^{V} = (C_{11} + C_{22} + C_{33})/5 + 2(C_{12} + C_{13} + C_{23} + 2C_{44} + 2C_{55} + 2C_{66})/15 \tag{89a}$$

$$C_{12}^{V} = (C_{11} + C_{22} + C_{33} - 2C_{44} - 2C_{55} - 2C_{66})/15 + 4(C_{12} + C_{13} + C_{23})/15 \tag{89b}$$

The index $V$ was added to distinguish these constants from the stiffness constants obtained by inverting the tensor of averaged compliance constants, calculated by integrating Equation (74b) over the Euler space.

To find the peak shift for the Voigt model, Equation (87) must be replaced in Equation (67b) and further Equation (67b) in Equation (83). The average (83) is trivial and one obtains:

$$\langle \varepsilon_{\mathbf{h}}(\mathbf{y}) \rangle = \sum_{j=1}^{6} F_j \rho_j e_j \tag{90}$$

Equation (90) can be arranged similar to Equation (85). By inverting Equation (88) and replacing $e_j$ in Equation (90) this equation becomes:

$$\langle \varepsilon_{\mathbf{h}}(\mathbf{y}) \rangle = [F_1 S_{11}^{V} + (F_2 + F_3) S_{12}^{V}] s_1 + [F_2 S_{11}^{V} + (F_1 + F_3) S_{12}^{V}] s_2 + [F_3 S_{11}^{V} + (F_1 + F_2) S_{12}^{V}] s_3 + 2(S_{11}^{V} - S_{12}^{V})(F_4 s_4 + F_5 s_5 + F_6 s_6) \tag{91}$$

In Equation (91), $S_{ij}^V$ is the compliance tensor obtained by inverting the stiffness tensor $C_{ij}^V$:

$$S_{11}^V = (C_{11}^V + C_{12}^V)/[C_{11}^V(C_{11}^V + C_{12}^V) - 2(C_{12}^V)^2] \tag{92a}$$
$$S_{12}^V = -C_{12}^V/[C_{11}^V(C_{11}^V + C_{12}^V) - 2(C_{12}^V)^2] \tag{92b}$$

We can see from Equations (90) or (91) that in the frame of the Voigt model of the crystallite interactions the relative peak shifts do not depend on the Miller indices, which frequently is contradicted by experiment. The Reuss model gives such a dependence.

*12.2.4.2 Reuss Model.* In the Reuss[29] hypothesis the intergranular stress in the sample system is zero and then:

$$s_i(\varphi_1, \Phi_0, \varphi_2) = s_i \tag{93}$$

To find the macroscopic strain, Equation (93) is placed in Equation (73b) which is integrated on the Euler space and one obtains:

$$e_i = \sum_{j=1}^{6} S_{ij}^R \rho_j s_j \tag{94}$$

Here $S_{ij}^R$ are the averaged compliance constants for the isotropic polycrystals. They are calculated from the single-crystal compliances with formulae similar to Equations (89):

$$S_{11}^R = (S_{11} + S_{22} + S_{33})/5 + 2(S_{12} + S_{13} + S_{23} + 2S_{44} + 2S_{55} + 2S_{66})/15 \tag{95a}$$

$$S_{12}^R = (S_{11} + S_{22} + S_{33} - 2S_{44} - 2S_{55} - 2S_{66})/15 + 4(S_{12} + S_{13} + S_{23})/15 \tag{95b}$$

Note that $S_{ij}^R$ and $S_{ij}^V$ are different. Also the stiffness constants $C_{ij}^R$ obtained by inverting $S_{ij}^R$ are different from $C_{ij}^V$ defined before.

To calculate the peak shift there are two possibilities that should give the same result: starting from Equation (67b) as we did for the Voigt approximation or starting from Equation (67a). In the first case Equation (93) is replaced in Equation (73b) and both Equations (73b) and (74b) are replaced in Equation (67b); the peak shift becomes:

$$\langle \varepsilon_{\mathbf{h}}(\mathbf{y}) \rangle = \sum_{i=1}^{6} F_i \rho_i \sum_{l=1}^{6} s_l \sum_{j=1}^{6} \sum_{k=1}^{6} S_{jk} \rho_k \langle P_{ij} Q_{kl} \rangle \tag{96}$$

In the second case Equation (93) is replaced in Equation (66b), (66b) in Equation (64b), (64b) in (67a) and the peak shift is:

$$\langle \varepsilon_{\mathbf{h}}(\mathbf{y}) \rangle = \sum_{i=1}^{6} E_i \rho_i \sum_{l=1}^{6} s_l \sum_{j=1}^{6} S_{ij} \rho_j \langle Q_{jl} \rangle \tag{97}$$

Obviously, Equation (97) is much more convenient than Equation (96) as there are only 36 integrals to calculate in place of 1296. Behnken and Hauk[44] adopted a derivation path starting from the strain components in the sample reference system. In this report the condition of invariance of the peak shift to the operations of the point group is violated for some Laue classes. Later, Popa[45] reported invariant expressions for all Laue groups that were derived starting from Equation (97). Here we follow this derivation.

The averages in the right-hand side of Equation (97) are the following:

$$\langle Q_{ij} \rangle = (1/2\pi) \int_0^{2\pi} \mathrm{d}\omega \, Q_{ij}(\varphi_1', \Phi_0', \varphi_2') \tag{98}$$

The matrix elements $Q_{ij}$ under the integral are given by Equations (71) and (72) and the Euler matrices of angles $(\varphi_1', \Phi_0', \varphi_2')$ for which $\mathbf{h}$ is parallel to $\mathbf{y}$ are given by Equations (7) and (8). The integrals (98) can be calculated analytically and one obtains Equation (99):

$$\langle Q_{ij} \rangle = \begin{cases} (3F_j - 1)E_i/2 + \delta_i(1 - F_j)/2 & \text{for} \quad j = 1, 2, 3 \\ 3F_j E_i - \delta_i F & \text{for} \quad j = 4, 5, 6 \end{cases} \tag{99}$$
$$(\delta_1, \ldots\ldots, \delta_6) = (1,\ 1,\ 1,\ 0,\ 0,\ 0)$$

By replacing Equation (99) in Equation (97) and rearranging the terms the last expression becomes:

$$\langle \varepsilon_{\mathbf{h}}(\mathbf{y}) \rangle = (t_s - s_{\mathbf{y}}) r_2/2 + (3s_{\mathbf{y}} - t_s) r_4/2 \tag{100}$$

Here $t_s$ and $s_{\mathbf{y}}$ are the trace of $\bar{\mathbf{s}}$ and, respectively, the macroscopic stress along $\mathbf{y}$:

$$t_s = s_1 + s_2 + s_3, \ s_{\mathbf{y}} = \sum_{i=1}^{6} F_i \rho_i s_i \tag{101a, b}$$

The dependence of the peak shifts on the Miller indices is given by the factors $r_2$ and $r_4$ that are quadratic and quartic forms, respectively, of the direction cosines $a_i$. For the triclinic symmetry these factors are the following:

$$\begin{aligned} r_2 =& (S_{11} + S_{12} + S_{13})a_1^2 + (S_{12} + S_{22} + S_{23})a_2^2 + (S_{13} + S_{23} + S_{33})a_3^2 \\ &+ 2(S_{14} + S_{24} + S_{34})a_2 a_3 + 2(S_{15} + S_{25} + S_{35})a_1 a_3 \\ &+ 2(S_{16} + S_{26} + S_{36})a_1 a_2 \end{aligned} \tag{102}$$

$$
\begin{aligned}
r_4 =& S_{11}a_1^4 + S_{22}a_2^4 + S_{33}a_3^4 + 2(S_{23} + 2S_{44})a_2^2a_3^2 + 2(S_{13} + 2S_{55})a_1^2a_3^2 \\
&+ 2(S_{12} + 2S_{66})a_1^2a_2^2 + 4(S_{14} + 2S_{56})a_1^2a_2a_3 + 4(S_{25} + 2S_{46})a_1a_2^2a_3 \\
&+ 4(S_{36} + 2S_{45})a_1a_2a_3^2 + 4S_{24}a_2^3a_3 + 4S_{34}a_2a_3^3 + 4S_{15}a_1^3a_3 + 4S_{35}a_1a_3^3 \\
&+ 4S_{16}a_1^3a_2 + 4S_{26}a_1a_2^3
\end{aligned} \tag{103}
$$

For higher symmetries $r_2$ and $r_4$ can be derived taking account Table 12.5. They are given in Tables 12.6 and 12.7, respectively.

In Table 12.7 we see that $r_4$ for the group $4/m$ differs by one term from $r_4$ for the group $4/mmm$. The extra-term in $4/m$ splits those reflections that are non-equivalent but coincident in the absence of the macrostress. The same is valid for the trigonal group 3. The anisotropic peak broadenings caused by micro-stress are also different for coincident but non-equivalent peaks.[46]

*12.2.4.3 The Hill Average.* The Voigt and the Reuss models are two extreme cases of crystallite interactions that roughly describe the strain/stress state of isotropic polycrystalline samples. Concerning the elastic constants calculated with the two models Hill[47] observed that they are the upper and the lower limits of the real elastic constants, and the arithmetic averages are close enough to the real values. Consequently, a very good description of the peak shift is obtained in practice by using the arithmetic average of the Voigt and Reuss peak shifts Equations (91) and (100). Even better is to use a weighted average with the weight $w$ ($0 < w < 1$) refinable in a least-square analysis:

$$
\langle \varepsilon_{\mathbf{h}}(\mathbf{y}) \rangle = w \langle \varepsilon_{\mathbf{h}}(\mathbf{y}) \rangle^V + (1 - w) \langle \varepsilon_{\mathbf{h}}(\mathbf{y}) \rangle^R \tag{104}
$$

*12.2.4.4 Kroner Model.* A model for crystallite interaction that is better than the Voigt or the Reuss models was proposed by Kroner.[30] According to Kroner every crystallite is an inclusion in a continuous and homogenous matrix that has the elastic properties of the polycrystal. For the isotropic polycrystal the strain in the inclusion is the following:

**Table 12.6** Quadratic forms $r_2$ for symmetries higher than triclinic.

| | |
|---|---|
| $2/m$ **(c)** | $(S_{11} + S_{12} + S_{13})a_1^2 + (S_{12} + S_{22} + S_{23})a_2^2 + (S_{13} + S_{23} + S_{33})a_3^2 + 2(S_{16} + S_{26} + S_{36})a_1a_2$ |
| $2/m$ **(b)** | $(S_{11} + S_{12} + S_{13})a_1^2 + (S_{12} + S_{22} + S_{23})a_2^2 + (S_{13} + S_{23} + S_{33})a_3^2 + 2(S_{15} + S_{25} + S_{35})a_1a_3$ |
| *mmm* | $(S_{11} + S_{12} + S_{13})a_1^2 + (S_{12} + S_{22} + S_{23})a_2^2 + (S_{13} + S_{23} + S_{33})a_3^2$ |
| Tetrag., Trig., Hex. | $(S_{11} + S_{12} + S_{13})(a_1^2 + a_2^2) + (2S_{13} + S_{33})a_3^2$ |
| Cubic | $S_{11} + 2S_{12}$ |

**Table 12.7** Quartic forms $r_4$ for symmetries higher than triclinic. In square brackets is the term to be added to $r_4$ of $4/mmm$ and of $3m$ to obtain $r_4$ of $4/m$ and of 3, respectively.

| | |
|---|---|
| $2/m$ (**c**) | $S_{11}a_1^4 + S_{22}a_2^4 + S_{33}a_3^4 + 2(S_{23} + 2S_{44})a_2^2a_3^2 + 2(S_{13} + 2S_{55})a_1^2a_3^2 + 2(S_{12} + 2S_{66})a_1^2a_2^2 + 4(S_{36} + 2S_{45})a_1a_2a_3^2 + 4S_{16}a_1^3a_2 + 4S_{26}a_1a_2^3$ |
| $2/m$ (**b**) | $S_{11}a_1^4 + S_{22}a_2^4 + S_{33}a_3^4 + 2(S_{23} + 2S_{44})a_2^2a_3^2 + 2(S_{13} + 2S_{55})a_1^2a_3^2 + 2(S_{12} + 2S_{66})a_1^2a_2^2 + 4(S_{25} + 2S_{46})a_1a_2^2a_3 + 4S_{15}a_1^3a_3 + 4S_{35}a_1a_3^3$ |
| $mmm$ | $S_{11}a_1^4 + S_{22}a_2^4 + S_{33}a_3^4 + 2(S_{23} + 2S_{44})a_2^2a_3^2 + 2(S_{13} + 2S_{55})a_1^2a_3^2 + 2(S_{12} + 2S_{66})a_1^2a_2^2$ |
| $4/mmm$<br>$4/m$ | $S_{11}(a_1^4 + a_2^4) + S_{33}a_3^4 + 2(S_{13} + 2S_{44})(a_1^2 + a_2^2)a_3^2 + 2(S_{12} + 2S_{66})a_1^2a_2^2$<br>$+ [4S_{16}(a_1^2 \quad a_2^2)a_1a_2]$ |
| $3m$<br>3 | $S_{11}(a_1^2 + a_2^2)^2 + S_{33}a_3^4 + 2(S_{13} + 2S_{44})(a_1^2 + a_2^2)a_3^2 + 4S_{14}(3a_1^2 \quad a_2^2)a_2a_3$<br>$+ [4S_{15}(a_1^2 \quad 3a_2^2)a_1a_3]$ |
| Hexagonal | $S_{11}(a_1^2 + a_2^2)^2 + S_{33}a_3^4 + 2(S_{13} + 2S_{44})(a_1^2 + a_2^2)a_3^2$ |
| Cubic | $S_{11}(a_1^4 + a_2^4 + a_3^4) + 2(S_{12} + 2S_{44})(a_2^2a_3^2 + a_1^2a_3^2 + a_1^2a_2^2)$ |

$$e_i(g) = \sum_{j=1}^{6} \left[ S_{ij}^R + t_{ij}(g) \right] \rho_j s_j \tag{105}$$

In this expression, similar to Equation (84a), the first term is the strain of the isotropic matrix given by Equation (94). The second term is the strain induced in crystallite by the matrix and is given by the Eshelby[48] theory for an ellipsoidal inclusion. The tensor $t_{ij}(g)$ accounts for the differences between the compliances of the inclusion and of the matrix and has the property $t_{ij} = 0$. To calculate the peak shift, Equation (105) is replaced in Equation (67b), which is further replaced in Equation (83). Analytical calculations can be performed only for a spherical crystalline inclusion that has a cubic symmetry. For the peak shift an expression similar to Equation (91) is obtained but with different compliances. According to Bollenrath *et al.*[49] the compliance constants in Equation (91) must be replaced as follows:

$$S_{11}^V \to S_{11}^R + T_{11} - 2T_0\Gamma, \; S_{12}^V \to S_{12}^R + T_{12} + T_0\Gamma \tag{106a, b}$$

$$T_0 = T_{11} - T_{12} - 2T_{44}, \; \Gamma = a_2^2a_3^2 + a_1^2a_3^2 + a_1^2a_2^2 \tag{106c, d}$$

The compliances $T_{11}$, $T_{12}$ and $T_{44}$ are calculated from the single-crystal compliances by bulky algebraic expressions reproduced in many papers.[24,33,49,50]

The matrix compliances $S_{11}^R$ and $S_{12}^R$ are given by Equation (95) for the special case of cubic symmetry.

*12.2.4.5 The Method "sin$^2\Psi$".* The peak shift Equations (91) and (100) can be arranged in the following form, which is convenient for experimental data processing:

$$\begin{aligned}\langle \varepsilon_{\mathbf{h}}(\mathbf{y})\rangle =& S_1(s_1+s_2+s_3)+(1/2)S_2s_3\\ &+(1/2)S_2(s_1\cos^2\gamma+s_2\sin^2\gamma-s_3+s_6\sin 2\gamma)\sin^2\Psi\\ &+(1/2)S_2(s_4\sin\gamma+s_5\cos\gamma)\sin 2\Psi\end{aligned} \tag{107}$$

The factors $S_1$ and $S_2$ are called diffraction elastic constants. For the models examined above they are the following:

$$\begin{array}{ll} S_1=\bar{S}_{12}^V,\ S_2=2(\bar{S}_{11}^V-\bar{S}_{12}^V) & -\text{Voigt}\\ S_1=(r_2-r_4)/2,\ S_2=3r_4-r_2 & -\text{Reuss}\\ S_1=\bar{S}_{12}^R+T_{12}+T_0\Gamma,\ S_2=2(\bar{S}_{11}^R-\bar{S}_{12}^R+T_{11}-T_{12}-3T_0\Gamma) & -\text{Kroner (cubic)}\end{array} \tag{108}$$

Except for the Voigt model, the diffraction elastic constants are dependent on the Miller indices.

If we consider the peak shifts for $\gamma$ and $\gamma+\pi$ at the same value of $\Psi$, Equation (107) is split into two linear equations, one in $\sin^2\Psi$ and the other in $\sin 2\Psi$:

$$\begin{aligned}\langle \varepsilon_{\mathbf{h}}\rangle^+=&\langle \varepsilon_{\mathbf{h}}(\Psi,\gamma)\rangle+\langle \varepsilon_{\mathbf{h}}(\Psi,\gamma+\pi)\rangle=2S_1(s_1+s_2+s_3)+S_2s_3\\ &+S_2(s_1\cos^2\gamma+s_2\sin^2\gamma-s_3+s_6\sin 2\gamma)\sin^2\Psi\end{aligned} \tag{109}$$

$$\langle \varepsilon_{\mathbf{h}}\rangle = \langle \varepsilon_{\mathbf{h}}(\Psi,\gamma)\rangle-\langle \varepsilon_{\mathbf{h}}(\Psi,\gamma+\pi)\rangle=S_2(s_4\sin\gamma+s_5\cos\gamma)\sin 2\Psi \tag{110}$$

Consequently, if the peak shifts for one or more peaks are measured as a function of $\Psi$ in the range $(0, \pi/2)$ at $\gamma$ and $\gamma+\pi$ for three fixed values of $\gamma$ (*e.g.*, 0, $\pi/4$ and $\pi/2$) the stress tensor elements $s_i$ can be determined from the intercept and the slopes of these lines. It is presumed that the single-crystal elastic constants are known and the diffraction elastic constants in Equations (109) and (110) can be calculated following one of the models presented before. This is the conventional "sin$^2$ $\Psi$"method. Alternatively Equation (107) can be used in a least-square analysis or implemented in the Rietveld codes. If diffraction patterns measured in several points ($\Psi$, $\gamma$) are available the stress tensor elements $s_i$ can be refined together with the structural and other parameters. The implementation in GSAS is the Voigt formula Equation (90) and not Equation (107). In this case refinable parameters are the strain tensor elements $e_i$.

*12.2.4.6 Determination of the Single-crystal Elastic Constants.* The dependence of the diffraction elastic constants on the Miller indices can be exploited to find the single-crystal elastic constants from powder diffraction data. Indeed,

let us presume that an axial, known stress $s_3$ is applied to a polycrystalline sample. All other components of the stress tensor are zero and then Equation (107) becomes:

$$\langle \varepsilon_{\mathbf{h}}(\mathbf{y}) \rangle = [S_1 + (1/2)S_2 \cos^2 \Psi] s_3$$

By measuring the peak shift for $\Psi = 0$ and $\Psi = \pi/2$ both $S_1$ and $S_2$ can be determined. If the measurement is repeated for many peaks the single-crystal elastic constants can be calculated by minimizing a $\chi^2$ calculated with the differences between the measured diffraction elastic constants and those calculated with one of the models presented above (except Voigt). For a given Laue group the number of measured diffraction peaks must be greater than the number of independent single-crystal elastic constants. A comparison of the single-crystal elastic constant determined in this way on aluminium, copper and steel[50] with those measured on a single-crystal by ultrasonic pulse proved the reliability of the diffraction method.

### 12.2.5 Hydrostatic Pressure in Isotropic Polycrystals

A hypothesis not yet examined in the literature is that the intergranular strain in the crystallite reference system is zero and then:

$$\varepsilon_i(\varphi_1, \Phi_0, \varphi_2) = \varepsilon_i \tag{111}$$

To obtain the strain tensor in the sample reference system, Equation (111) is replaced in Equation (65a); to obtain the stress tensor, Equation (111) is replaced in Equation (64a) and (64a) in (66a). We have:

$$e_i(g) = \sum_{j=1}^{6} P_{ij}(g)\varepsilon_j, \; s_i(g) = \sum_{l=1}^{6} \rho_l \varepsilon_l \sum_{j=1}^{6} P_{ij}(g) C_{jl} \tag{112a, b}$$

To calculate the macroscopic strains and stresses, Equations (112) are averaged over the Euler space. The average acts only on the matrix **P** and, presuming isotropic polycrystals, one obtains:

$$P_{ij} = \begin{cases} 1/3 & \text{if } i, \, j = 1, 3 \\ 0 & \text{if } i \text{ or } j > 3 \end{cases} \tag{113}$$

The macroscopic strains and stresses are then the following:

$$e_1 = e_2 = e_3 = e = (\varepsilon_1 + \varepsilon_2 + \varepsilon_3)/3, \; e_4 = e_5 = e_6 = 0 \tag{114a}$$

$$s_1 = s_2 = s_3 = s = (1/3) \sum_{l=1}^{6} \rho_l \varepsilon_l (C_{1l} + C_{2l} + C_{3l}), \; s_4 = s_5 = s_6 = 0 \tag{114b}$$

The structure of Equations (114) is specific for the strain/stress state in a sample under a hydrostatic pressure.

To calculate the peak shift we replace Equation (111) in Equation (67a), (67a) in (83) and one obtains:

$$\langle \varepsilon_{\mathbf{h}} \rangle = \varepsilon_1 a_1^2 + \varepsilon_2 a_2^2 + \varepsilon_3 a_3^2 + 2\varepsilon_4 a_2 a_3 + 2\varepsilon_5 a_1 a_3 + 2\varepsilon_6 a_1 a_2 \qquad (115)$$

As expected, the peak shift is independent of direction in sample. The peak shift must be invariant to the operations of the Laue group that imposes constraints on the strains $\varepsilon_i$. For crystal symmetries higher than triclinic the peak shift is given in Table 12.8.

These formulae can be easily implemented in Rietveld codes with $\varepsilon_i$ refinable parameters. In fact they were already implemented in GSAS (profile #5) but the derivation presented in the GSAS manual[36] is different, the concrete connection of the refined parameters with the macroscopic hydrostatic strain and stress not being revealed.

The present hypothesis fully describes the hydrostatic strain/stress state in isotropic samples. Indeed, from the refined parameters $\varepsilon_i$ the macroscopic strain and stress $e$, $s$ can be calculated and also the intergranular strains and stresses $\Delta e_i(g)$, $\Delta s_i(g)$, both different from zero. Note that nothing was presumed concerning the nature of the crystallite interaction, which can be elastic or plastic. From Equations (112) it is not possible to obtain relations of the type (84) but only of the type (86). For this reason a linear homogenous equation of the Hooke type between the macroscopic stress and strain cannot be established.

Finally, we note that the hydrostatic state can be also described in the frame of the classical models, but this is not a full description as one or another intergranular strain/stress is ignored. If in Equation (107) we set $s_1 = s_2 = s_3 = s, s_4 = s_5 = s_6 = 0$, one obtains $\langle \varepsilon_{\mathbf{h}} \rangle = (3S_1 + S_2/2)s$. There is no dependence of $\langle \varepsilon_{\mathbf{h}} \rangle$ on the Miller indices for the Voigt and the Kroner model. For the Reuss model the dependence is similar to those from Equation (115) and Table 12.8 but with only one refinable parameter for all Laue groups, the macrostress $s$, and very probably the refined value of $s$ will be wrong.

**Table 12.8** Peak shift $\langle \varepsilon_{\mathbf{h}} \rangle$ caused by hydrostatic stress in isotropic samples for all Laue groups higher than triclinic. Parameters $\varepsilon_i$ are refinable in the Rietveld codes.

| | |
|---|---|
| $2/m$ (**c**) | $\varepsilon_1 a_1^2 + \varepsilon_2 a_2^2 + \varepsilon_3 a_3^2 + 2\varepsilon_6 a_1 a_2$ |
| $2/m$ (**b**) | $\varepsilon_1 a_1^2 + \varepsilon_2 a_2^2 + \varepsilon_3 a_3^2 + 2\varepsilon_5 a_1 a_3$ |
| *mmm* | $\varepsilon_1 a_1^2 + \varepsilon_2 a_2^2 + \varepsilon_3 a_3^2$ |
| Tetrag., Trig., Hex. | $\varepsilon_1 (a_1^2 + a_2^2) + \varepsilon_3 a_3^2$ |
| Cubic | $\varepsilon_1$ |

### 12.2.6 The Macroscopic Strain/Stress by Spherical Harmonics

Arguments for recent developments of the spherical harmonics approach for the analysis of the macroscopic strain and stress by diffraction were presented in Section 12.2.3. Resuming, the classical models describing the intergranular strains and stresses are too rough and in many cases cannot explain the strongly nonlinear dependence of the diffraction peak shift on $\sin^2 \Psi$, even if the texture is accounted for. A possible solution to this problem is to renounce to any physical model to describe the crystallite interactions and to find the strain/stress orientation distribution functions SODF by inverting the measured strain pole distributions $\langle \varepsilon_{\mathbf{h}}(\mathbf{y}) \rangle$. The SODF fully describe the strain and stress state of the sample.

Similar to the ODF for texture, SODF can be subjected to a Fourier analysis by using generalized spherical harmonics. However, there are three important differences. The first is that in place of one distribution (ODF), six SODFs are analyzed simultaneously. The components of the strain, or the stress tensor can be used for analysis in the sample or in the crystal reference system. The second difference concerns the invariance to the crystal and the sample symmetry operations. The ODF is invariant to both crystal and sample symmetry operations. By contrast, the six SODFs in the sample reference system are invariant to the crystal symmetry operations but they transform similarly to Equation (65) if the sample reference system is replaced by an equivalent one. Inversely, the SODFs in the crystal reference system transform like Equation (65) if an equivalent one replaces this system and remain invariant to any rotation of the sample reference system. Consequently, for the spherical harmonics coefficients of the SODF one expects selection rules different from those of the ODF. As the third difference, the average over the crystallites in reflection (83) is structurally different from Equations (5) + (11). In Equation (83) the products of the SODFs with the ODF are integrated, which, in comparison with Equation (5), entails a supplementary difficulty.

In the literature three different approaches were reported based on the spherical harmonics representation of the SODFs: by Wang *et al.*,[39,40] by Behnken[43] and by Popa and Balzar.[21] Wang *et al.*[39,40] represent by spherical harmonics the stress tensor $s_i(g)$ in the sample reference system. Consequently, the harmonic coefficients of $l = 0$ are the macroscopic stresses $s_i$, but to calculate the macroscopic strains $e_i$ the coefficients with $l = 0,2,4$ are necessary. Behnken[43] proposed to expand in spherical harmonics both $e_i(g)$ and $s_i(g)$ independently. In this case $e_i$ and $s_i$ are the coefficients with $l = 0$ of the two series but the volume of calculations by least square to find the harmonic coefficients is higher. In Equation (83), both Wang and Behnken used for $\varepsilon_{\mathbf{h}}(g)$ the expression given by Equation (67b). Then, when the strain pole distribution $\langle \varepsilon_{\mathbf{h}}(\mathbf{y}) \rangle$ is calculated starting from the harmonic series of $s_i(g)$, the single-crystal compliances in the sample reference system appear in Equation (83) as supplementary factors to SODF and ODF. Behnken performs the integrals of Equation (83) numerically. Wang *et al.* used the spherical harmonics representation of the ODF and the Clebsch–Gordan coefficients to express the product

of the SODF, ODF and single-crystal compliances in a series that is further integrated like the ODF for texture. Both Wang and Behnken considered only the case of cubic crystal symmetry and orthorhombic sample symmetry and constructed the corresponding symmetrized spherical harmonics according to the invariance and non-invariance properties in the Euler space described before. The third approach reported by Popa and Balzar[21] is similar to those of Wang and Behnken, but with an important distinction that makes the problem of determination of components of the strain tensor equivalent to the texture problem and significantly simplifies the mathematical formalism. This approach, described below, is extended to any crystal and sample symmetry and has the potential to be implemented in the Rietveld codes.

*12.2.6.1 Strain Expansion in Generalized Spherical Harmonics.* In the approach by Popa and Balzar[21] the representation by spherical harmonics is performed not on the SODFs but on the product of the SODFs and the ODF, that is the SODFs weighted by texture (WSODF):

$$\tau_i(\varphi_1, \Phi_0, \varphi_2) = \varepsilon_i(\varphi_1, \Phi_0, \varphi_2)\, f(\varphi_1, \Phi_0, \varphi_2) \tag{116}$$

In this product the strain tensor components in the crystallite reference system are used for the SODFs. With this choice the calculation of the macroscopic strains and stresses $e_i$ and $s_i$ requires only the harmonic coefficients of $l=0$ and $l=2$ (see Section 12.2.6.3). Similar to the ODF [Equation (23)], the WSODFs are expanded in a series of generalized spherical harmonics:

$$\tau_i(\varphi_1, \Phi_0, \varphi_2) = \sum_{l=0}^{\infty} \sum_{m=}^{l} \sum_{n=}^{l} c_{il}^{mn} \exp(im\varphi_2) P_l^{mn}(\Phi_0) \exp(in\varphi_1) \tag{117}$$

The integral over the Euler space gives $c_{i0}^{00} = \tau_i = \varepsilon_i$, and then the term $l=0$ of Equation (117) represents the hydrostatic strain/stress state of the isotropic polycrystal discussed in Section 12.2.5. The rest of the terms describe the deviation of the real strain/stress state from the hydrostatic state of the isotropic polycrystal. To calculate the peak shift, Equation (67a) is replaced in Equation (83) and $\tau_i$ which appear after this operation are replaced by Equation (117). The calculations follow those in Section 12.1.4.1 and one obtains:

$$\langle \varepsilon_{\mathbf{h}}(\mathbf{y}) \rangle P_{\mathbf{h}}(\mathbf{y}) = \sum_{l=0}^{\infty} [4/(2l+1)] I_l(\mathbf{h}, \mathbf{y}), l = \text{even} \tag{118}$$

$$\begin{aligned} I_l(\mathbf{h}, \mathbf{y}) =& a_1^2 t_{1l}(\mathbf{h}, \mathbf{y}) + a_2^2 t_{2l}(\mathbf{h}, \mathbf{y}) + a_3^2 t_{3l}(\mathbf{h}, \mathbf{y}) \\ &+ 2a_2 a_3 t_{4l}(\mathbf{h}, \mathbf{y}) + 2a_1 a_3 t_{5l}(\mathbf{h}, \mathbf{y}) + 2a_1 a_2 t_{6l}(\mathbf{h}, \mathbf{y}) \end{aligned} \tag{119}$$

$$t_{il}(\mathbf{h}, \mathbf{y}) = A_{il}^0(\mathbf{y}) P_l^0(\Phi) + \sum_{m=1}^{l} \left[ A_{il}^m(\mathbf{y}) \cos m\beta + B_{il}^m(\mathbf{y}) \sin m\beta \right] P_l^m(\Phi) \tag{120}$$

$$A_{il}^{m}(\mathbf{y}) = \alpha_{il}^{m0} P_l^0(\Psi) + \sum_{n=1}^{l} \left(\alpha_{il}^{mn} \cos n\gamma + \beta_{il}^{mn} \sin n\gamma\right) P_l^n(\Psi), (m = 0, l) \qquad (121)$$

$$B_{il}^{m}(\mathbf{y}) = \gamma_{il}^{m0} P_l^0(\Psi) + \sum_{n=1}^{l} \left(\gamma_{il}^{mn} \cos n\gamma + \delta_{il}^{mn} \sin n\gamma\right) P_l^n(\Psi), (m = 1, l) \qquad (122)$$

The coefficients $\alpha_{il}^{mn}$, $\beta_{il}^{mn}$, $\gamma_{il}^{mn}$, $\delta_{il}^{mn}$ are obtained from the coefficients $c_{il}^{mn}$ by linear transformations similar to those given in Table 12.1. Equations (118–122) are the general formulae for the diffraction line shift determination valid for triclinic crystal and sample symmetries. For a given value of $l$ the total number of coefficients is $6(2l + 1)^2$. If the crystal and sample symmetries are higher than triclinic, the number of coefficients is reduced, some coefficients being zero and some being correlated.

*12.2.6.2 Selection Rules for all Laue Classes.* To find the selection rules for all Laue classes the invariance conditions to rotations are applied to the peak shift weighted by texture $\langle \varepsilon_{\mathbf{h}}(\mathbf{y}) \rangle P_{\mathbf{h}}(\mathbf{y})$. As the terms of different $l$ in Equation (118) are independent, the invariance conditions must be applied to every $I_l$.

We begin with the selection rules imposed by the crystal symmetry. An $r$-fold axis along $\mathbf{x}_3$ transforms $\Phi$, $\beta$, $a_1$, $a_2$ as follows: $\Phi \to \Phi$, $\beta \to \beta + 2\pi/r$, $a_1 \to a_1 \cos(2\pi/r) - a_2 \sin(2\pi/r)$ and $a_2 \to a_1 \sin(2\pi/r) + a_2 \cos(2\pi/r)$. By applying the invariance conditions to Equation (119) one obtains a system of six linear equations:

$$t_{il}(\Phi, \beta + 2\pi/r, \mathbf{y}) = \sum_{k=1}^{6} f_{ik}(r) t_{kl}(\Phi, \beta, \mathbf{y}) \qquad (123)$$

These equations are just the transformations Equation (65) for a particular value of $r$. Further, if Equation (120) is replaced in Equation (123) one obtains a system of homogenous equations in $A_{il}^{m}$ and $B_{il}^{m}$ that has a non-trivial solution only for certain values of $m$. If, besides the $r$-fold axis in $\mathbf{x}_3$, there is an 2-fold axis along $\mathbf{x}_1$, then $A_{il}^{m}$ and $B_{il}^{m}$ must fulfill supplementary conditions resulting from the invariance of $I_l$ to the transformations $\Phi \to \pi - \Phi$, $\beta \to -\beta$, and $(a_2, a_3) \to (-a_2, -a_3)$. Tables 12.9–12.12 give the selection rules imposed by the crystal symmetry for the non-cubic Laue groups.

Note that coefficients belonging to different strain tensor components are correlated, but in all correlations only two coefficients are involved. The three-fold axis added on the main diagonal of the *mmm* and 4/*mmm* prism to obtain the cubic groups *m*3 and *m*3*m* introduces supplementary correlations between the coefficients $A_{il}^{m}$ and $B_{il}^{m}$ of the orthorhombic and tetragonal group, respectively. These correlations involve more than two coefficients and are found by evaluating $I_l$ in terms of the direction cosines $a_i$ and setting the condition of invariance to the transformation $(a_1, a_2, a_3) \to (a_2, a_3, a_1)$. Tables 12.13 and 12.14 give the supplementary correlations added to *mmm* and 4/*mmm*, respectively, by the cubic three-fold axis.

**Table 12.9** Selection rules imposed by the crystal symmetry for the Laue groups $2/m$ and $mmm$.

| $2/m$ | $mmm$ |
|---|---|
| $i = 1,2,3,6 : \begin{cases} A^0_{il} \\ A^m_{il}, B^m_{il}, m = 2k \end{cases}$ | $i = 1,2,3 : \begin{cases} A^0_{il} \\ A^m_{il}, m = 2k \end{cases}$ |
| $i = 4,5 : \quad A^m_{il}, B^m_{il}, \quad m = 2k \quad 1$ | $B^m_{4l}, m = 2k \quad 1$ |
| | $A^m_{5l}, m = 2k \quad 1$ |
| | $B^m_{6l}, m = 2k$ |

**Table 12.10** Selection rules imposed by the crystal symmetry for the Laue groups $4/m$ and $4/mmm$.

| $4/m$ | $4/mmm$ |
|---|---|
| $\begin{cases} A^0_{1l} \\ A^m_{1l}, B^m_{1l}, \ m = 2k \end{cases}$ | $\begin{cases} A^0_{1l} \\ A^m_{1l}, \ m = 2k \end{cases}$ |
| $\begin{cases} A^0_{2l} = A^0_{1l} \\ A^m_{2l} = (\ \ 1)^k A^m_{1l}, \ B^m_{2l} = (\ \ 1)^k B^m_{1l}, \ m = 2k \end{cases}$ | $\begin{cases} A^0_{2l} = A^0_{1l} \\ A^m_{2l} = (\ \ 1)^k A^m_{1l}, \ m = 2k \end{cases}$ |
| $\begin{cases} A^0_{3l} \\ A^m_{3l}, B^m_{3l}, \ m = 4k \end{cases}$ | $\begin{cases} A^0_{3l} \\ A^m_{3l}, \ m = 4k \end{cases}$ |
| $A^m_{4l}, B^m_{4l}, \ m = 2k \quad 1$ | $B^m_{4l}, \ m = 2k \quad 1$ |
| $A^m_{5l} = (\ \ 1)^{k-1} B^m_{4l}, \ B^m_{5l} = (\ \ 1)^k A^m_{4l}, \ m = 2k \quad 1$ | $A^m_{5l} = (\ \ 1)^{k-1} B^m_{4l}, \ m = 2k \quad 1$ |
| $A^m_{6l}, B^m_{6l}, \ m = 4k \quad 2$ | $B^m_{6l}, \ m = 4k \quad 2$ |

For textured samples under stress two sample symmetries must be distinguished: texture and strain/stress sample symmetry. Sometimes they are identical, but generally the strain/stress sample symmetry is lower. A simple example is offered by Equation (107). The texture has a spherical symmetry but the strain sample symmetry is in general triclinic. The texture sample symmetry must form a super group of the strain sample symmetry because $P_{\mathbf{h}}(\mathbf{y})$ must be invariant to both sample symmetries. Concerning the selection rules imposed by the sample symmetry, one expects them to be identical to those for the texture of the same sample symmetry. Indeed, the invariance conditions act directly on Equation (121) and (122) that are identical to Equations (38) and (39). Hence, the selection rules in the index $n$ for the coefficients $\alpha^{mn}_{il}$, $\beta^{mn}_{il}$, $\gamma^{mn}_{il}$ and $\delta^{mn}_{il}$ are those from the Table 12.3.

**Table 12.11** Selection rules imposed by the crystal symmetry for the Laue classes 3 and 3*m*. For 3*m* there are two distinct situations: for *m* even, at the left-hand side of the vertical bar, and for *m* odd, at the right-hand side of the bar.

| $\bar{3}$ | $\bar{3}m$ |
|---|---|
| $\begin{cases} A^0_{1l} \\ A^m_{1l}, B^m_{1l},\ m \quad 3k \quad 2,\ 3k \quad 1,\ 3k \end{cases}$ | $\begin{cases} A^0_{1l} \\ A^m_{1l} \vert B^m_{1l},\ m \quad 3k \quad 2,\ 3k \quad 1,\ 3k \end{cases}$ |
| $\begin{cases} A^0_{2l} \quad A^0_{1l} \\ A^m_{2l} \quad A^m_{1l}, B^m_{2l} \quad B^m_{1l},\ m \quad 3k \\ A^m_{2l} \quad A^m_{1l}, B^m_{2l} \quad B^m_{1l},\ m \quad 3k \quad 2,\ 3k \quad 1 \end{cases}$ | $\begin{cases} A^0_{2l} \quad A^0_{1l} \\ A^m_{2l} \quad A^m_{1l} \vert B^m_{2l} \quad B^m_{1l},\ m \quad 3k \\ A^m_{2l} \quad A^m_{1l} \vert B^m_{2l} \quad B^m_{1l},\ m \quad 3k \quad 2,\ 3k \quad 1 \end{cases}$ |
| $\begin{cases} A^0_{3l} \\ A^m_{3l}, B^m_{3l},\ m \quad 3k \end{cases}$ | $\begin{cases} A^0_{3l} \\ A^m_{3l} \vert B^m_{3l},\ m \quad 3k \end{cases}$ |
| $A^m_{4l}, B^m_{4l},\ m \quad 3k \quad 2,\ 3k \quad 1$ | $A^m_{4l} \vert B^m_{4l},\ m \quad 3k \quad 2,\ 3k \quad 1$ |
| $\begin{cases} A^m_{5l} \quad B^m_{4l}, B^m_{5l} \quad A^m_{4l},\ m \quad 3k \quad 2 \\ A^m_{5l} \quad B^m_{4l}, B^m_{5l} \quad A^m_{4l},\ m \quad 3k \quad 1 \end{cases}$ | $\begin{cases} B^m_{5l} \quad A^m_{4l} \vert A^m_{5l} \quad B^m_{4l},\ m \quad 3k \quad 2 \\ B^m_{5l} \quad A^m_{4l} \vert A^m_{5l} \quad B^m_{4l},\ m \quad 3k \quad 1 \end{cases}$ |
| $\begin{cases} A^m_{6l} \quad B^m_{1l}, B^m_{6l} \quad A^m_{1l},\ m \quad 3k \quad 2 \\ A^m_{6l} \quad B^m_{1l}, B^m_{6l} \quad A^m_{1l},\ m \quad 3k \quad 1 \end{cases}$ | $\begin{cases} B^m_{6l} \quad A^m_{1l} \vert A^m_{6l} \quad B^m_{1l},\ m \quad 3k \quad 2 \\ B^m_{6l} \quad A^m_{1l} \vert A^m_{6l} \quad B^m_{1l},\ m \quad 3k \quad 1 \end{cases}$ |

**Table 12.12** Selection rules imposed by the crystal symmetry for the Laue classes 6/*m* and 6/*mmm*.

| $6/m$ | $6/mmm$ |
|---|---|
| $\begin{cases} A^0_{1l} \\ A^m_{1l}, B^m_{1l},\ m \quad 6k \quad 4,\ 6k \quad 2,\ 6k \end{cases}$ | $\begin{cases} A^0_{1l} \\ A^m_{1l},\ m \quad 6k \quad 4,\ 6k \quad 2,\ 6k \end{cases}$ |
| $\begin{cases} A^0_{2l} \quad A^0_{1l} \\ A^m_{2l} \quad A^m_{1l}, B^m_{2l} \quad B^m_{1l},\ m \quad 6k \\ A^m_{2l} \quad A^m_{1l}, B^m_{2l} \quad B^m_{1l},\ m \quad 6k \quad 4,\ 6k \quad 2 \end{cases}$ | $\begin{cases} A^0_{2l} \quad A^0_{1l} \\ A^m_{2l} \quad A^m_{1l},\ m \quad 6k \\ A^m_{2l} \quad A^m_{1l},\ m \quad 6k \quad 4,\ 6k \quad 2 \end{cases}$ |
| $\begin{cases} A^0_{3l} \\ A^m_{3l}, B^m_{3l},\ m \quad 6k \end{cases}$ | $\begin{cases} A^0_{3l} \\ A^m_{3l},\ m \quad 6k \end{cases}$ |
| $A^m_{4l}, B^m_{4l},\ m \quad 6k \quad 5,\ 6k \quad 1$ | $B^m_{4l},\ m \quad 6k \quad 5,\ 6k \quad 1$ |
| $\begin{cases} A^m_{5l} \quad B^m_{4l}, B^m_{5l} \quad A^m_{4l},\ m \quad 6k \quad 5 \\ A^m_{5l} \quad B^m_{4l}, B^m_{5l} \quad A^m_{4l},\ m \quad 6k \quad 1 \end{cases}$ | $\begin{cases} A^m_{5l} \quad B^m_{4l},\ m \quad 6k \quad 5 \\ A^m_{5l} \quad B^m_{4l},\ m \quad 6k \quad 1 \end{cases}$ |
| $\begin{cases} A^m_{6l} \quad B^m_{1l}, B^m_{6l} \quad A^m_{1l},\ m \quad 6k \quad 4 \\ A^m_{6l} \quad B^m_{1l}, B^m_{6l} \quad A^m_{1l},\ m \quad 6k \quad 2 \end{cases}$ | $\begin{cases} B^m_{6l} \quad A^m_{1l},\ m \quad 6k \quad 4 \\ B^m_{6l} \quad A^m_{1l},\ m \quad 6k \quad 2 \end{cases}$ |

**Table 12.13** Selection rules imposed by the crystal symmetry for the cubic $m3$: the following constraints must be added to the selection rules for $mmm$.

| | | |
|---|---|---|
| $l$ 0 | $A_{30}^0$ | $A_{20}^0 \quad A_{10}^0$ |
| $l$ 2 | $A_{12}^2$ | $(2/3)^{1/2}(A_{12}^0 + 2A_{32}^0), \quad A_{22}^2 \quad (2/3)^{1/2}(A_{22}^0 + 2A_{32}^0)$ |
| | $A_{32}^2$ | $(2/3)^{1/2}(A_{12}^0 \quad A_{22}^0) + 2(B_{42}^1 \quad A_{52}^1)$ |
| | $B_{62}^2$ | $(3/2)^{1/2}(A_{12}^0 + A_{22}^0 + A_{32}^0)/2 + (B_{42}^1 + A_{52}^1)/2$ |
| $l$ 4 | $A_{14}^4$ | $3(2/35)^{1/2}A_{14}^0 + 8(2/35)^{1/2}A_{34}^0 + 2A_{14}^2/7^{1/2}$ |
| | $A_{24}^4$ | $3(2/35)^{1/2}A_{24}^0 + 8(2/35)^{1/2}A_{34}^0 \quad 2A_{24}^2/7^{1/2}$ |
| | $B_{44}^3$ | $2(A_{14}^0 + 3A_{24}^0)/35^{1/2} + (27/4)A_{34}^0/35^{1/2} \quad (1/2)(6A_{24}^2 + 5A_{34}^2)/14^{1/2}$ |
| | | $(3B_{44}^1 + 4A_{54}^1)/7^{1/2} + (1/4)A_{34}^4/2^{1/2}$ |
| | $A_{54}^3$ | $2(3A_{14}^0 + A_{24}^0)/35^{1/2} \quad (27/4)A_{34}^0/35^{1/2} \quad (1/2)(6A_{14}^2 + 5A_{34}^2)/14^{1/2}$ |
| | | $+ (4B_{44}^1 + 3A_{54}^1)/7^{1/2} \quad (1/4)A_{34}^4/2^{1/2}$ |
| | $B_{64}^2$ | $(2/5)^{1/2}(A_{14}^0 + A_{24}^0 \quad 2A_{34}^0) \quad (A_{14}^2 \quad A_{24}^2)/2 \quad 2^{1/2}(B_{44}^1 + A_{54}^1)$ |
| | $B_{64}^4$ | $(2/35)^{1/2}(A_{14}^0 \quad A_{24}^0) + (A_{14}^2 + A_{24}^2 + 3A_{34}^2/2)/7^{1/2} \quad (2/7)^{1/2}(B_{44}^1 \quad A_{54}^1)$ |

**Table 12.14** Selection rules imposed by the crystal symmetry for the cubic $m3m$: the following constraints must be added to the selection rules for $4/mmm$.

| | | |
|---|---|---|
| $l = 0$ | $A_{30}^0 = A_{10}^0$ | |
| $l = 2$ | $A_{12}^2 = (2/3)^{1/2}(A_{12}^0 + 2A_{32}^0), \quad B_{62}^2 = (3/2)^{1/2}(A_{12}^0 + A_{32}^0/2) + B_{42}^1$ | |
| $l = 4$ | $A_{14}^4 =$ | $3(2/35)^{1/2}A_{14}^0 + 8(2/35)^{1/2}A_{34}^0 + 2A_{14}^2/7^{1/2}$ |
| | $B_{44}^3 =$ | $8A_{14}^0/35^{1/2} + (27/4)A_{34}^0/35^{1/2} + 3A_{14}^2/14^{1/2} \quad 7^{1/2}B_{44}^1 + (1/4)A_{34}^4/2^{1/2}$ |
| | $B_{64}^2 =$ | $2(2/5)^{1/2}(A_{14}^0 \quad A_{34}^0) \quad A_{14}^2 \quad 8^{1/2}B_{44}^1$ |

*12.2.6.3 Determination of the Average Strains and Stresses.* For the calculation of both $e_i$ and $s_i$, only the coefficients $\alpha_{il}^{mn}$, $\beta_i^{mn}$, $\gamma_{il}^{mn}$ and $\delta_{il}^{mn}$ with $l = 0$ and $l = 2$ are needed. This is easy to see by combining Equations (117) and (65a) into Equation (81) written for $e_i$ and Equations (117), (66a) and (64a) into Equation (81) written for $s_i$ [remember that in Equation (81) $\varepsilon_i$ is a placeholder for any strain or stress component]. The integrals of the terms with $l = 1$ and $l > 2$ are zero because the elements of the matrix $\mathbf{P}$ are the sum of products of two Euler matrix elements and the generalized harmonics are orthogonal. So, retaining from Equation (117) only the terms with $l = 0$ and $l = 2$, and rearranging to have only positive indices $m$, $n$, in place of Equation (117) in

Equation (81) is replaced the following truncated WSODF:

$$\tau_i'(\varphi_1, \Phi_0, \varphi_2) = \sum_{k=0}^{25} g_{ik} R_k(\varphi_1, \Phi_0, \varphi_2) \tag{124}$$

Here the functions $R_k$ ($\varphi_1$, $\Phi_0$, $\varphi_2$) are linear combinations of terms like $\cos(m\varphi_2 \pm n\varphi_1)$ $Q_l^{mn}$ ($\pm\cos\ \Phi_0$) or $\sin(m\varphi_2 \pm n\varphi_1)$ $Q_l^{mn}$ ($\pm\cos\ \Phi_0$), where $Q_l^{mn} = P_l^{mn}$ for $m + n$ even and $Q_l^{mn} = iP_l^{mn}$ for $m + n$ odd. The elements of the matrix $\mathbf{g}$ are the harmonic coefficients with $l = 0,2$. The row $i$ of this matrix is the following:

$$\mathbf{g}_i = \begin{pmatrix} \alpha_{i0}^{00}, \alpha_{i2}^{00}, \alpha_{i2}^{01}, \beta_{i2}^{01}, \alpha_{i2}^{02}, \beta_{i2}^{02}, \alpha_{i2}^{10}, \alpha_{i2}^{11}, \beta_{i2}^{11}, \alpha_{i2}^{12}, \beta_{i2}^{12}, \gamma_{i2}^{10}, \gamma_{i2}^{11}, \\ \\ \delta_{i2}^{11}, \gamma_{i2}^{12}, \delta_{i2}^{12}, \alpha_{i2}^{20}, \alpha_{i2}^{21}, \beta_{i2}^{21}, \alpha_{i2}^{22}, \beta_{i2}^{22}, \gamma_{i2}^{20}, \gamma_{i2}^{21}, \delta_{i2}^{21}, \gamma_{i2}^{22}, \delta_{i2}^{22} \end{pmatrix} \tag{125}$$

After combining Equation (124) with Equation (65a) or with (66a) and (64a) into Equation (81) there are 936 integrals to calculate on the Euler space of the products of the functions $P_{ij}$ and $R_k$. Although an analytical calculation is possible they were calculated numerically. Only 73 are different from zero. The macroscopic strain tensor is the following:

$$\begin{aligned} e_1, e_2 =& (2/3)(g_{10} + g_{20} + g_{30}) + (1/15)(g_{11} + g_{21} - 2g_{31}) \\ & - (\sqrt{3}/2/30)(\pm g_{14} \pm g_{24} \mp 2g_{34} + 2g_{4,11} + g_{1,16} - g_{2,16} + 2g_{6,21}) \\ & \pm (1/20)(2g_{59} + 2g_{4,14} + g_{1,19} - g_{2,19} + 2g_{6,24}) \end{aligned} \tag{126a}$$

$$\begin{aligned} e_3 =& (2/3)(g_{10} + g_{20} + g_{30}) - (2/15)(g_{11} + g_{21} - 2g_{31}) \\ & + (\sqrt{3}/2/15)(2g_{4,11} + g_{1,16} - g_{2,16} + 2g_{6,21}) \end{aligned} \tag{126b}$$

$$\begin{aligned} e_4 =& -(\sqrt{3}/2/30)(g_{13} + g_{23} - 2g_{33}) \\ & + (1/60)(g_{58} + g_{4,13} + 3g_{1,18} - 3g_{2,18} + 6g_{6,23}) \end{aligned} \tag{126c}$$

$$\begin{aligned} e_5 =& -(\sqrt{3}/2/30)(g_{12} + g_{22} - 2g_{32}) \\ & + (1/60)(g_{57} + g_{4,12} + 3g_{1,17} - 3g_{2,17} + 6g_{6,22}) \end{aligned} \tag{126d}$$

$$\begin{aligned} e_6 =& -(\sqrt{3}/2/30)(g_{15} + g_{25} - 2g_{35} + g_{16} + g_{26} - 2g_{36}) \\ & + (1/20)(2g_{5,10} + 2g_{4,15} + g_{1,20} - g_{2,20} + 2g_{6,25}) \end{aligned} \tag{126e}$$

The elements of the macroscopic stress tensor $s_i$ have exactly the same expressions; only the matrix $\mathbf{g}$ must be replaced by $\mathbf{g}'$ defined as follows:

$$g_{jk}' = \sum_{l=1}^{6} C_{jl} \rho_l g_{lk} \tag{127}$$

In Equation (127) $C_{jl}$ are the single-crystal stiffness constants.

*12.2.6.4 Simplified Harmonics Representation of the Peak Shift.* When it is not necessary to find the WSODFs and the average strain and stress tensors is not of interest, one can choose a different approach that corrects only for the line shifts caused by stress. In this case, an alternative representation for $I_l$ with fewer parameters is possible. To accomplish this, the angles ($\Phi$, $\beta$) in Equation (120) are replaced by the direction cosines $a_i$. After introducing this into Equation (119) and rearranging, $I_l$ becomes:

$$I_l(\mathbf{h},\mathbf{y}) = \sum_{k=1}^{k_l} M_{kl}(\Psi,\gamma) J_{k,l+2}(a_1,a_2,a_3) \tag{128}$$

Here $J_{k,l+2}$ are homogenous polynomials of degree $l+2$ in the variables $a_1$, $a_2$, $a_3$, invariant to the Laue class symmetry operations. For $l=0$ and $l=2$ they can be extracted from Tables 12.6 and 12.7, for $l=4$ these polynomials are given in Table 12.15.

The functions $M_{kl}(\Psi,\gamma)$ are linear combinations of $A_{il}^{mn}(\Psi,\gamma)$ and $B_{il}^{mn}(\Psi,\gamma)$ and then can be written as follows:

$$M_{kl}(\Psi,\gamma) = \mu_{kl}^0 P_l^0(\Psi) + \sum_{n=1}^{l} \left(\mu_{kl}^n \cos n\gamma + \nu_{kl}^n \sin n\gamma\right) P_l^n(\Psi) \tag{129}$$

For sample symmetries higher than triclinic the coefficients $\mu_{kl}^n$ and $\nu_{kl}^n$ follow the selection rules of the texture with the same sample symmetry. The maximum number $k_l$ of functions $M_{kl}$ in the series expansion Equation (128) must be

**Table 12.15** Invariant polynomials $J_{k,6}$ for all Laue classes. Additional terms that should be added to *mmm* to obtain 2/*m*, *etc*. are enclosed in square brackets.

| | |
|---|---|
| *mmm* | $a_1^6,\ a_2^6,\ a_3^6,\ a_1^4a_2^2,\ a_1^2a_2^4,\ a_1^4a_3^2,\ a_1^2a_3^4,\ a_2^4a_3^2,\ a_2^2a_3^4,\ a_1^2a_2^2a_3^2,$ |
| + [2/*m*] | $[a_1^5a_2,\ a_1a_2^5,\ a_1^3a_2^3,\ a_1^3a_2a_3^2,\ a_1a_2^3a_3^2,\ a_1a_2a_3^4]$ |
| 4/*mmm* | $a_1^6+a_2^6,\ a_3^6,\ (a_1^4+a_2^4)a_3^2,\ (a_1^2+a_2^2)a_3^4,\ a_1^2a_2^2a_3^2,\ (a_1^2+a_2^2)a_1^2a_2^2,$ |
| + [4/*m*] | $[(a_1^2 \quad a_2^2)a_1a_2a_3^2,\ (a_1^4 \quad a_2^4)a_1a_2]$ |
| 3*m* | $(a_1^2+a_2^2)^3,\ a_3^6,\ (a_1^2+a_2^2)^2a_3^2,\ (a_1^2+a_2^2)a_3^4,\ (a_1^2+a_2^2)(3a_1^2 \quad a_2^2)a_2a_3,$ |
| + [3] | $(3a_1^2 \quad a_2^2)a_2a_3^3,\ a_1^6 \quad 15a_1^4a_2^2+15a_1^2a_2^4 \quad a_2^6,$ |
| | $[(a_1^2+a_2^2)(a_1^2 \quad 3a_2^2)a_1a_3,\ (a_1^2 \quad 3a_2^2)a_1a_3^3,\ (3a_1^2 \quad a_2^2)(a_1^2 \quad 3a_2^2)a_1a_2]$ |
| 6/*mmm* | $(a_1^2+a_2^2)^3,\ a_3^6,\ (a_1^2+a_2^2)^2a_3^2,\ (a_1^2+a_2^2)a_3^4,\ a_1^6 \quad 15a_1^4a_2^2+15a_1^2a_2^4 \quad a_2^6,$ |
| + [6/*m*] | $[(3a_1^2 \quad a_2^2)(a_1^2 \quad 3a_2^2)a_1a_2]$ |
| *m*3 | $a_1^4a_2^2+a_2^4a_3^2+a_3^4a_1^2, \quad a_1^4a_3^2+a_2^4a_1^2+a_3^4a_2^2$ |
| *m*3*m* | $a_1^4a_2^2+a_2^4a_3^2+a_3^4a_1^2+a_1^4a_3^2+a_2^4a_1^2+a_3^4a_2^2$ |

equal or smaller than the total number of functions $A_{il}^{mn}$, $B_{il}^{mn}$ in Equations (119) and (120), but for crystal symmetry higher than triclinic, it is frequently much smaller. For example, for the Laue class 3 and $l=4$ the total number of $A_{il}^{mn}$, $B_{il}^{mn}$ is 18 but $k_4=10$. This is important in Rietveld refinement, as the number of refinable parameters must be kept to a minimum. On the other hand, it is not possible to obtain the WSODFs and the average strain and stress tensors from the coefficients $\mu_{kl}^{n}$ and $\nu_{kl}^{n}$.

*12.2.6.5 Implementation in the Rietveld Codes.* In the practical applications reported to date by Behnken[43] by Wang *et al.*[41,42,51] and recently by Popa *et al.*[52] the least-square method was used to fit the calculated peak shifts with the measured peak shifts determined by individual peak fitting. This procedure presumes a prior determination of the pole distribution $P_{\mathbf{h}}(\mathbf{y})$. The procedure is time consuming and only a limited number of peaks can be used because the extraction of position becomes inaccurate for overlapped peaks.

The variant of the spherical harmonics analysis of the WSODFs presented above is similar to those of the ODF and consequently is suitable for implementation in Rietveld codes that would allow the use of all the information contained in the diffraction patterns. The strain parameters are refined together with the texture, the structure and other parameters. There are three possible levels of implementation. The easiest is to implement Equations (118) + (128) for any value of $l$. This allows a fit of the peak positions shifted by stress, but the average strain and stress tensors as well as the WSODFs are not accessible. A mixed implementation with the term $l=2$ according to Equations (118) + (119), the rest by using Equations (118) + (128), allows a fit of the peak positions and to determine $e_i$ and $s_i$, but without reconstruction of the WSODF. Implementation of Equations (118) + (119) for any value of $l$ allows a full determination of the average and the intergranular strain and stress tensors. By using the coefficients with $l$ even obtained from the Rietveld refinement, the WSODFs can be calculated directly from Equation (117) and then $e_i(g)$, $s_i(g)$. Alternatively, as for texture,[15] with the refined strain harmonic coefficients the weighted strain pole distribution $\tau_i(\mathbf{h},\mathbf{y})$ can be constructed and further the strain and stress pole distributions $e_i(\mathbf{h},\mathbf{y})$ and $s_i(\mathbf{h},\mathbf{y})$. An inversion of these strain/stress pole figures by a direct inversion method like WIMV should be possible, in principle, but so far this possibility has not been examined.

## REFERENCES

1. H. J. Bunge, *Texture Analysis in Material Science*, Butterworth, London, 1982.
2. R. D. Williams, *J. Appl. Phys.*, 1968, **39**, 4329.
3. J. Imhof, *Textures Microstruc.*, 1982, **5**, 73.
4. S. Matthies and G. W. Vinel, *Phys. Status Solidi B*, 1982, **112**, K111.
5. S. Matthies, H. R. Wenk and G. W. Vinel, *J. Appl. Crystallogr.*, 1988, **21**, 285.

6. H. R. Wenk, S. Matthies and L. Lutterotti, *Mater. Sci. Forum*, 1994, **157–162**, 473.
7. S. Matthies, L. Lutterotti and H. R. Wenk, *J. Appl. Crystallogr.*, 1997 **30**, 31.
8. A. Le Bail, H. Duroy and J. R. Fourquet, *Mater. Res. Bull.*, 1988, **23**, 447.
9. W. A. Dollase, *J. Appl. Crystallogr.*, 1986, **19**, 267.
10. A. March, *Z. Kristallogr.*, 1932, **81**, 285.
11. R. A. Young and D. B. Wiles, *J. Appl. Crystallogr.*, 1982, **10**, 262.
12. A. C. Larson and R. B. Von Dreele, *GSAS – General Structure Analysis System*, Report LAUR 86-748, Los Alamos National Laboratory, New Mexico, 1986.
13. M. Ahtee, M. Nurmela, P. Suortti and M. Jarvinen, *J. Appl. Crystallogr.*, 1989, **22**, 261.
14. N. C. Popa, *J. Appl. Crystallogr.*, 1992, **25**, 611.
15. R. B. Von Dreele, *J. Appl. Crystallogr.*, 1997, **30**, 517.
16. H. R. Wenk, *J. Appl. Crystallogr.*, 1991, **24**, 920.
17. C. J. Howard and E. H. Kisi, *J. Appl. Crystallogr.*, 2000, **33**, 1434.
18. R. J. Roe, *J. Appl. Phys.*, 1965, **36**, 2024.
19. H. J. Bunge, *Z. Metallkd.*, 1965, **56**, 872.
20. H. J. Bunge, *Mathematische Methoden der Texturanalyse*, Akademieverlag, Berlin, 1969.
21. N. C. Popa and D. Balzar, *J. Appl. Crystallogr.*, 2001, **34**, 187.
22. I. C. Noyan and J. B. Cohen, *Residual Stress*, Springer-Verlag, New York, 1987.
23. V. Hauk, *Structural and Residual Stress Analysis by Nondestructive Methods*, Elsevier, Amsterdam, 1997.
24. U. Welzel, J. Ligot, P. Lamparter, A. C. Vermeulen and E. J. Mittemeijer, *J. Appl. Crystallogr.*, 2005, **38**, 1.
25. L. Landau and E. Lifchitz, *Theorie de l'elasticite*, Edition Mir, Moscow, 1967.
26. J. F. Nye, *Physical Properties of Crystals*, University Press, Oxford, 1957.
27. W. A. Wooster, *Tensors and Group Theory for Physical Properties of Crystals*, Clarendon Press, Oxford, 1973.
28. W. Voigt, *Lehrbuch der Kristallphysik*, Teubner Verlag, Berlin-Leipzig, 1928.
29. A. Reuss, *Z. Angew. Math. Mech.*, 1929, **9**, 49.
30. E. Kroner, *Z. Phys.*, 1958, **151**, 504.
31. V. Hauk, *Arch. Eisenhuttenwesen*, 1952, **23**, 353.
32. A. L. Christenson and E. S. Rowland, *Trans. ASM*, 1953, **45**, 638.
33. H. Dolle, *J. Appl. Crystallogr.*, 1979, **12**, 489.
34. M. Ferrari and L. Lutterotti, *J. Appl. Phys.*, 1994, **76**, 7246.
35. D. Balzar, R. B. Von Dreele, K. Bennett and H. Ledbetter, *J. Appl. Phys.*, 1998, **84**, 4822.
36. R. B. Von Dreele, http://www.ccp14.ac.uk/ccp/ccp14/ftp-mirror/gsas/public/gsas/manual/, 2004.

37. A. Baczmanski, K. Wierzbanowski and J. Tarasiuk, *Z. Metallkd.*, 1995, **86**, 507.
38. K. Van Acker, J. Root, P. Van Houtte and E. Aernoudt, *Acta Mater.*, 1996, **44**, 4039.
39. Y. D. Wang, R. Lin Peng and R. McGreevy, *Proceedings of the Twelfth International Conference on Textures of Materials ICOTOM – 12, Canada, August 9-13*, NRC Research Press, Ottawa, 1999, p. 553.
40. Y. D. Wang, R. Lin Peng, X. H. Zeng and R. McGreevy, *Mater. Sci. Forum*, 2000, **347–349**, 66.
41. Y. D. Wang, R. Lin Peng and R. McGreevy, *Philos. Mag. Lett.*, 2001, **81**, 153.
42. Y. D. Wang, X. L. Wang, A. D. Stoica, J. W. Richardson and R. Lin Peng, *J. Appl. Crystallogr.*, 2003, **36**, 14.
43. H. Behnken, *Phys. Stat. Sol. A*, 2000, **177**, 401.
44. H. Behnken and V. Hauk, *Z. Metallkd.*, 1986, **77**, 620.
45. N. C. Popa, *J. Appl. Crystallogr.*, 2000, **33**, 103.
46. N. C. Popa, *J. Appl. Crystallogr.*, 1998, **31**, 176.
47. R. Hill, *Proc. Phys. Soc. London Ser. A*, 1952, **65**, 349.
48. J. D. Eshelby, *Proc. Phys. Soc. London Ser. A*, 1957, **241**, 376.
49. F. Bollenrath, V. Hauk and E. H. Muller, *Z. Metallkd.*, 1967, **58**, 76.
50. T. Gnaupel-Herold, P. C. Brand and H. J. Prask, *J. Appl. Crystallogr.*, 1998, **31**, 929.
51. Y. D. Wang, R. Lin Peng, X. L. Wang and R. McGreevy, *Acta Mater.*, 2002, **50**, 1717.
52. N. C. Popa, D. Balzar, G. Stefanic, S. Vogel, D. Brown, M. Bourke and B. Clausen, *Adv. X-Ray Anal.*, 2005, **47**, CD–ROM.

CHAPTER 13

# Microstructural Properties: Lattice Defects and Domain Size Effects

PAOLO SCARDI

Department of Materials Engineering and Industrial Technologies,
University of Trento, 38050 via Mesiano 77, Trento, Italy

## 13.1 INTRODUCTION

The analysis of line profiles in Powder Diffraction patterns is a topic nearly as old as diffraction itself. However, despite the long time that has passed since the pioneering studies of Scherrer (1918),[1] and the rich literature and textbooks[2–5] produced over many decades, line profile analysis is still a subject of active research.[6,7]

LPA is used to investigate features of the microstructure and lattice defects in materials. The main applications concern the study of: crystalline domain size and shape, also considering dispersion effects (*i.e.* presence of a size distribution);[2,5,8,9] the nature and density of line defects (typically dislocations, but also disclinations);[10–12] planar defects (*e.g.* twin and stacking faults);[2,3,6,13] anti-phase domains in materials undergoing disorder/order transformations;[2,3,14–16] microstrains produced by misfitting inclusions;[17,18] grain surface relaxation in nanocrystalline materials;[19] and compositional fluctuations.[20]

This chapter briefly describes the origin of line broadening in PD, considering the most common sources, and illustrates the potential of LPA, especially in relation to the current development towards full pattern methods.[7]

After the Introduction (Section 13.1), the useful concept of PD in reciprocal space is used to discuss the origin of line broadening, mostly concerning size and strain broadening; some additional sources (faulting, anti-phase domains and instrument) are outlined (Section 13.2). Traditional methods are then briefly reviewed, before describing the general philosophy of present-day methods, which tend to rely on a full pattern analysis for studying microstructure and lattice defects, very much like the Rietveld method[21] is used for

structural refinement (Section 13.3). The last part is dedicated to some applications of full pattern modelling methods (Section 13.4).

## 13.2 ORIGIN OF LINE BROADENING

### 13.2.1 Size Broadening

As described in Chapter 1, for a perfect, infinite crystal the reciprocal lattice is made of points, each representing a set of planes with Miller indices (*hkl*). The diffraction condition in reciprocal space is then defined in terms of a geometrical relation: diffraction takes place when incident and diffracted beam are such that the scattering vector $\underline{d}^* = (\underline{v} - \underline{v}_0)/\lambda$ connects the origin with an (*hkl*) point:

$$\frac{\underline{v} - \underline{v}_0}{\lambda} = \underline{d}^*_{hkl} \tag{1}$$

For PD, the fact that this condition, represented in Figure 13.1, holds for all equivalent points laying on the diffraction, or Ewald, sphere (Chapter 1), leads to the concept of peak multiplicity and systematic overlap.[22]

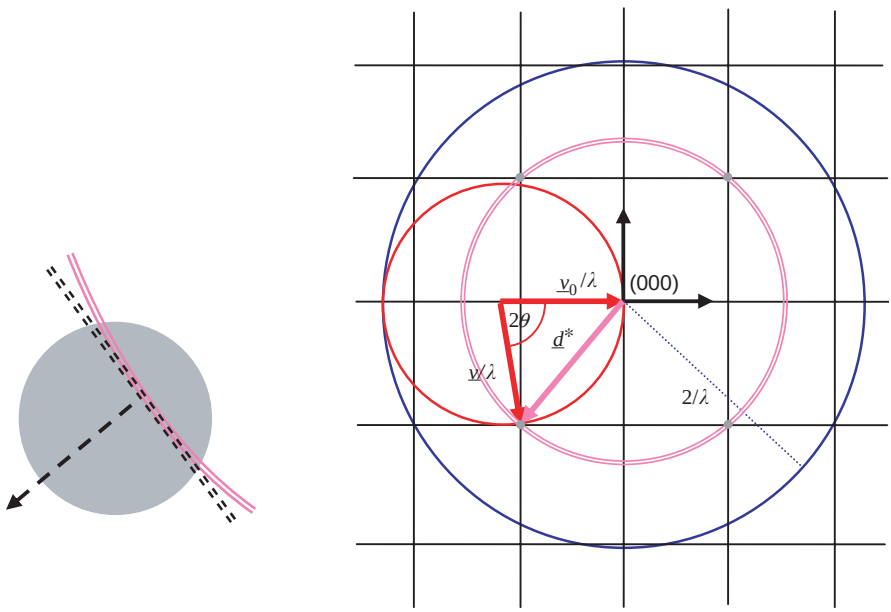



**Figure 13.1** Reciprocal space (2D) representation of the diffraction condition: Ewald sphere (radius $1/\lambda$), limiting sphere (radius $2/\lambda$) and PD sphere (double line, radius $\underline{d}^*$). Left: Enlargement of the intersection between PD sphere and reciprocal space point, with approximating tangent plane (dash). The arrow shows the direction of expansion of the diffraction sphere during a PD measurement.

The size of the points, for a perfect crystal, is uniquely determined by instrumental factors (including radiation emission and optics) and absorption, so the diffracted intensity is confined to a small region around each point (Figure 13.2a), and the FWHM is quite small. Instrumental effects on peak broadening and line-shape are described in greater detail in Chapters 4 and 5.

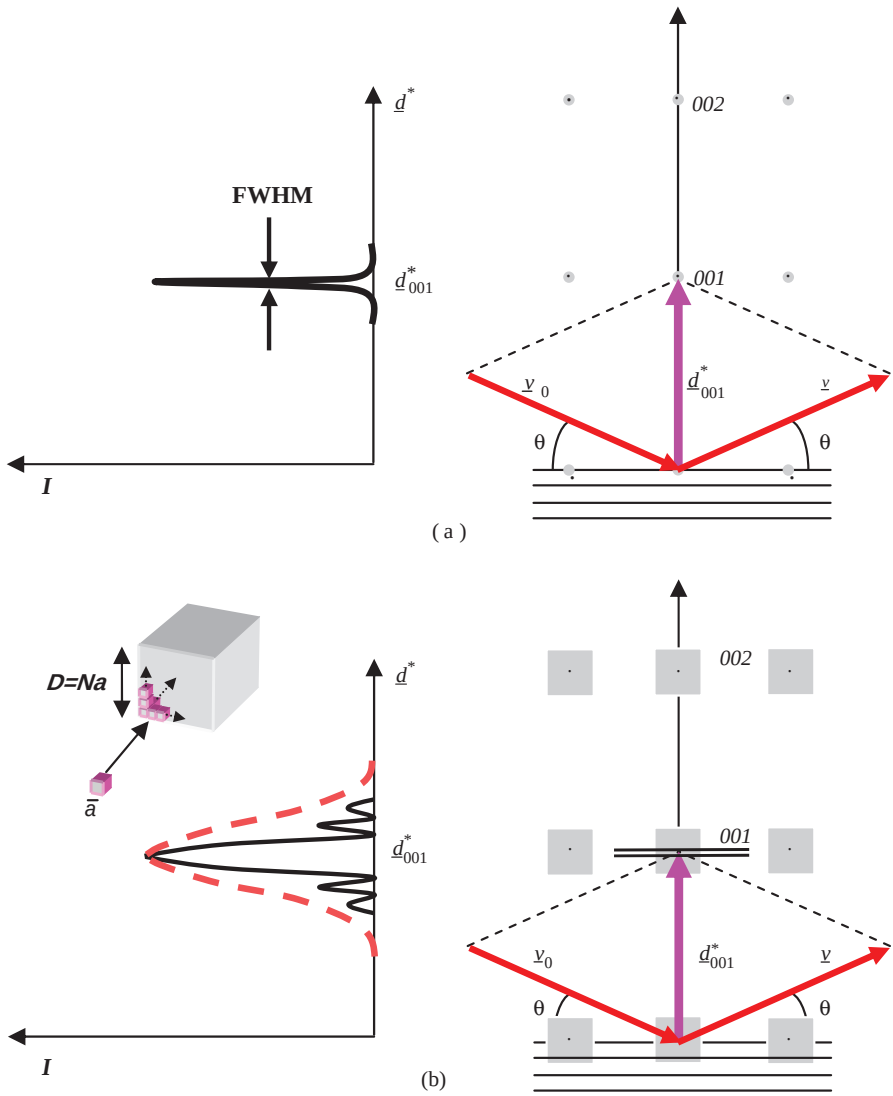



**Figure 13.2** Schematic representation of the (001) diffraction condition (right) and amplitude of the diffracted intensity (left) in reciprocal space for an ideally perfect crystal (a) and for cubic crystalline domains of edge $D$ [inset of (b)]. The profile for a dispersed system of cubic crystallites (dashed line) is also sketched out in (b).

When the crystalline domains (or crystallites, *i.e.* coherently scattering regions) have a finite extension, the diffracted intensity is no longer confined to a point, but spreads over a region whose size and shape are related to the crystallite size and shape.[22]

For example, if crystalline domains of a cubic phase are cubes of edge $D = Na$ (where $N$ is a positive integer), the corresponding reciprocal space points have the same symmetry and the diffracted intensity in reciprocal space is given by the so-called interference function.[3] For a (00$l$) point, as in Figure 13.2b, the intensity can be written as:

$$Y(d^*) \propto \frac{\sin^2(\pi N a s_{00l})}{(\pi a s_{00l})^2} \tag{2}$$

The expression is different for other ($hkl$) and crystallite shapes, thus providing intensity profiles with different width and shape.

During a powder diffraction measurement the Ewald sphere expands in reciprocal space, crossing points whenever Equation (1) is satisfied. This means that the signal collected in a powder measurement is the integral of the diffracted intensity in reciprocal space, over the intersection surface between the diffraction sphere and the reciprocal space points (Figure 13.1). This rather cumbersome integration over a spherical cross section of each reciprocal space point can be replaced, with minimal consequences, with an integration over the cross section given by the plane tangent to the Ewald sphere at that point (Figure 13.1).[2,23,†]

For the specific case shown in Figure 13.2 the intersection surface has a constant square shape, independent of $s_{00l}$, and the integration simply results in scaling Equation (2) by a constant term. The peak profile observed in a PD pattern is, therefore, given by the same functional form as that of Equation (2). For different ($hkl$) the integration surface is a function of the reciprocal space variable $s_{hkl}$, and the PD peak profile is also different in width and shape. As an example, Figure 13.3 shows the (100), (110) and (111) PD profiles for a powder made of cubic crystallites with edge $D = 10\,\text{nm}$.

The integral breadth, defined as the ratio between integrated intensity (peak area) and peak maximum, is frequently considered as a measure of the peak width. For the case of (00$l$) reflections from cubic crystallites of edge $D = Na$, the IB of the PD peak profile is readily obtained using the properties of the profile function of Equation (2):

$$\beta(s) = \frac{\int_{\infty}^{\infty} I(s)ds}{I(0)} = \frac{\int_{\infty}^{\infty} \frac{\sin^2(\pi N a s)}{(\pi a s)^2} ds}{\underset{s \to 0}{Lim} \frac{\sin^2(\pi N a s)}{(\pi a s)^2}} = \frac{Na}{(Na)^2} = \frac{1}{D} \tag{3}$$

[†] The tangent plane approximation is valid for sufficiently small points with equiaxial shapes. It cannot be used, for example, when faulting is present and some reciprocal space points are rods extended along the stacking direction (Section 13.2.3). In this case, integration over a spherical (or at least cylindrical) cross section is necessary.[2]

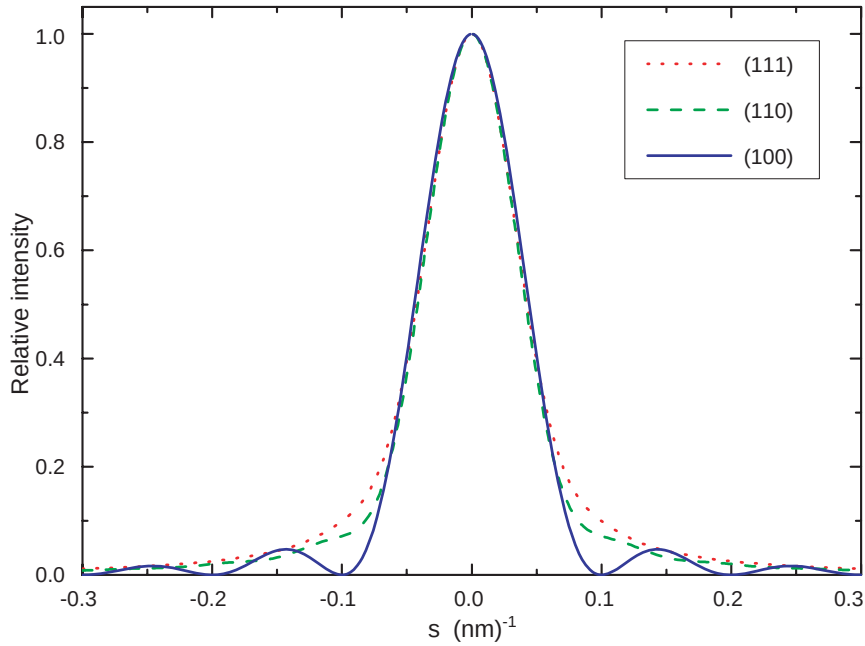



**Figure 13.3** PD (100) (line), (110) (dash) and (111) (dot) peak profiles for a system made of cubic crystallites (edge $D = 10$ nm). Normalized profiles in reciprocal space.

This is the well-known Scherrer equation, relating the peak width with the crystallite size, in this case IB in reciprocal space and cube edge, respectively. The inverse proportionality between IB and domain size is valid whatever the crystal shape (and symmetry of the lattice).[24,25] In a more general form, Equation (3) can be written as:

$$\beta(s) = \frac{K_\beta}{D} \tag{4}$$

where the Scherrer constant, $K_\beta$, can be calculated for different ($hkl$) reflections and crystallite shapes[2,8,9] [$K_\beta = 1$ for (00$l$) lines from cubic crystallites].

It may be more convenient to consider the IB in $2\theta$ space, directly referred to the peak profiles observed in a powder pattern. The change of variable from reciprocal to $2\theta$ space can be made according to:

$$\begin{aligned} ds = d\left(\frac{1}{d} - \frac{1}{d_{hkl}}\right) = d\left(\frac{2\sin\theta}{\lambda} - \frac{2\sin\theta_{hkl}}{\lambda}\right) &= (2\cos\theta/\lambda)d\theta \\ &= (\cos\theta/\lambda)d2\theta \end{aligned} \tag{5}$$

Even if Equation (5) is formally valid for infinitesimal quantities, in the limit of not too large profiles, it can also be used for the IB in Equation (4), leading to:

$$\beta(2\theta) = \frac{\lambda K_\beta}{D\cos\theta} \tag{6}$$

In real life one is not likely to observe fine features like those of the $(00l)$ profile (Figure 13.3), because crystallites, even if may have the same shape, tend to have a distribution of sizes. As a consequence, the peak profile is smeared into a bell-shaped curve, as shown schematically in Figure 13.2b.

For polydisperse systems the Scherrer equation is still valid, *i.e.* peak width is still inversely proportional to domain size, but the meaning of the size parameter changes. For instance, if the crystallites have the same shape but different sizes, it can be shown that:

$$\beta(2\theta) = \frac{\lambda}{< L >_V \cos\theta} \tag{7}$$

where $< L >_V = M_4/K_\beta M_3$, with $M_3$ and $M_4$, respectively, third and fourth moments of the size distribution.[8,9] For this reason $< L >_V$ is considered a volume-weighted mean size. Evidently, from these considerations, the interpretation of the size parameter of the Scherrer equation may not be straightforward as it depends on the features of the studied material. As a consequence $< L >_V$ is also called the *apparent* domain size. The simple case of Equation (6) is obtained only for monodisperse systems, *i.e.* when the size distribution is a delta function centred in $D$: the meaning of the size parameter is quite different for samples with arbitrary crystallite shape and size distributions.

The inverse proportionality between peak width and mean size stated by the Scherrer equation places practical limits to the range of domain sizes that produce measurable effects in a powder pattern. While the lower bound [a few ($\approx$2) nm, depending on the specific phase] is related to the approximations used,[2,26‡] the upper bound depends on the instrumental resolution, *i.e.* on the width of the instrumental profile. Traditional laboratory powder diffractometers, using standard commercial optics, typically allow the detection of domain sizes up to $\approx$200 nm. Above this value, domain size effects can hardly be distinguished from the instrumental broadening. This limit, however, can considerably be extended by using suitable high resolution optics, as is the case of many diffractometers in use with synchrotron radiation. In this case the practical limit can reach several micrometres.

### 13.2.2 Strain Broadening

Most real crystals contain imperfections producing local distortions of the lattice, resulting in a non-homogeneous strain field. The effect on position, shape and extension of reciprocal space points, and consequently on PD peak profiles, is usually more complex than that of the domain size. A formal treatment of the strain broadening is beyond the scope of the present book: interested readers can refer to the cited literature.[2 4,10] In the following a simplified, heuristic approach is proposed.[2,27]

‡For domain sizes of the order of a few nanometers surface effects become important, and basic diffraction laws, like the Bragg's law, need to be reconsidered.[26]

First consider the effect of a macroscopically homogeneous strain (or macrostrain), expressed as $\varepsilon = \Delta d/d$. By differentiating Bragg's law (assuming a constant wavelength):

$$0 = 2\Delta d \sin\theta + 2d\Delta\theta \cos\theta \tag{8}$$

Introducing the strain and rearranging the terms:

$$\Delta 2\theta = -2\tan\theta \frac{\Delta d}{d} = -2\varepsilon \tan\theta \tag{9}$$

This well-known result is the foundation of the residual stress (actually residual strain) analysis by diffraction techniques, dealt with in Chapter 12. As shown schematically in Figure 13.4b, macrostrain produces a shift in PD reflections. The effect can be measured for different sample orientations and different

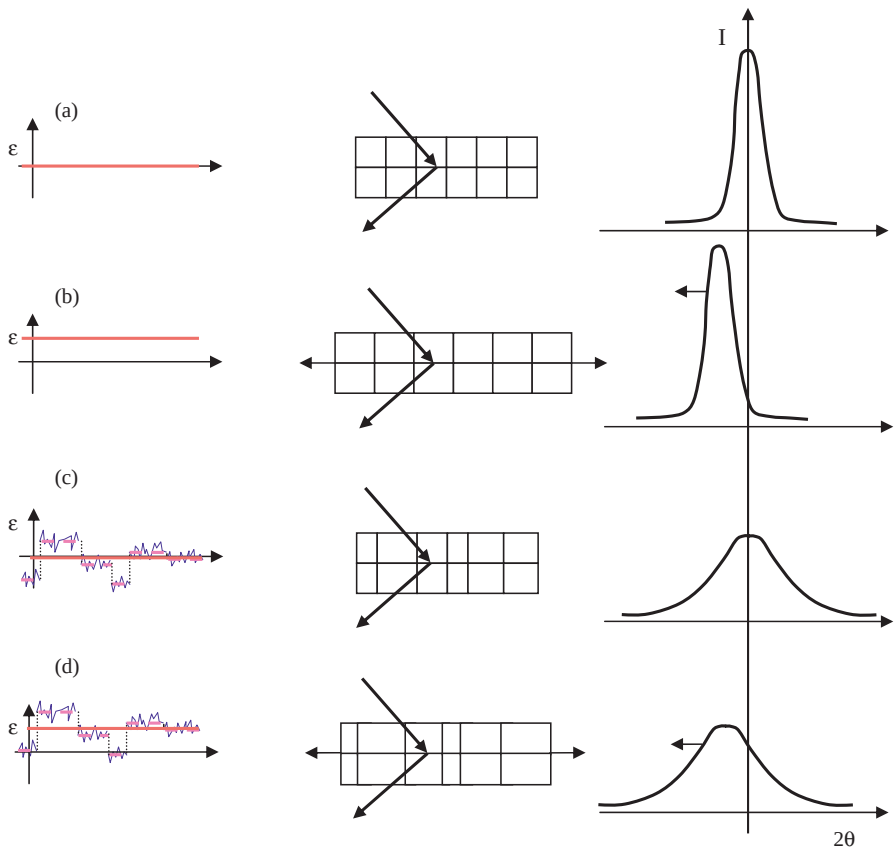



**Figure 13.4** PD peak profile for zero strain (no macrostrain and no microstrain) (a), (tensile) macrostrain (b), microstrain (c) and combined effect of micro strain and macrostrain (d). Strain ($\varepsilon$) is plotted on the left as a function of the position within a material microstructure sketched in the middle drawing.

peaks, thus providing a rather detailed amount of information on the strain tensor and, after suitable modelling, on the stress tensor.[28]

If the strain field is not homogeneous on the length scale of the crystallite size or smaller, according to Equation (9), different parts of the material diffract at slightly different angles, thus producing a broadened profile. Profile width and shape will evidently depend on the strain distribution across the sample.[2] Considering the root mean square strain (or microstrain), $\langle \varepsilon^2 \rangle^{1/2}$, Equation (9) suggests that:

$$\beta(2\theta) \propto \langle \varepsilon^2 \rangle^{1/2} \tan\theta \tag{10}$$

Microstrain has a rather peculiar effect on reciprocal lattice points – taking into account the $\cos\theta/\lambda$ transformation factor [Equation (5)] from $2\theta$ to reciprocal space, Equation (10) implies that:

$$\beta(s) \propto \frac{2\sin\theta_{hkl}}{\lambda} = d^*_{hkl}$$

Therefore, while domain size gives the same effect (*i.e.* same width and shape) for all reciprocal space points (Figure 13.2), strain broadening varies from point to point, generally increasing with the diffraction order (Figure 13.5).

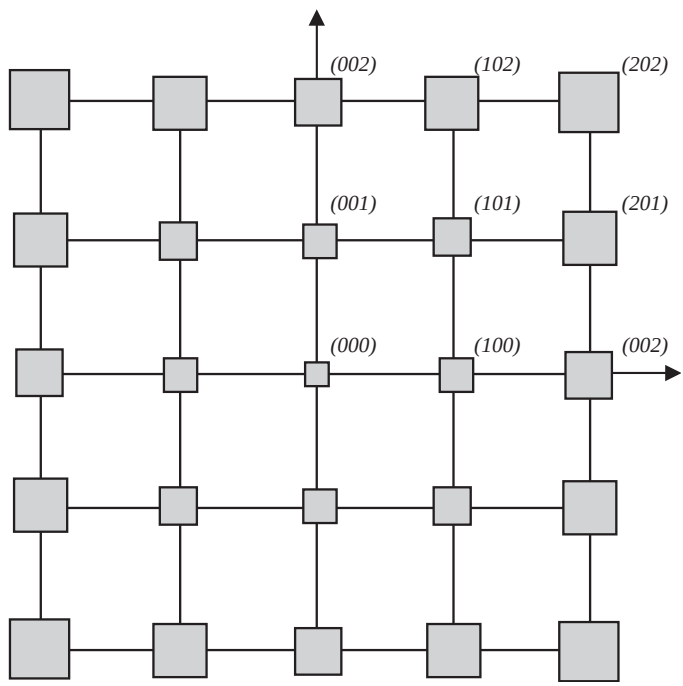



**Figure 13.5** Strain broadening effect in reciprocal space. In this schematic picture, according to Equation (10), points spread increasingly with the distance from the origin.

As shown schematically in Figure 13.4c, the strain can change among different crystallites, *e.g.* as a consequence of plastic deformation in an elastically anisotropic medium, but can also vary across each crystallite, *e.g.* because of the presence of dislocations (the two terms are sometimes referred to as strain of the second and third kind, respectively). Notably, a strain broadening effect can be observed even if the macrostrain (mean value of the strain distribution) is zero (Figure 13.4c), as in a powder sample. Otherwise, the simultaneous effect of macrostrain and microstrain results in a shift and broadening of the diffraction profile (Figure 13.4d).

### 13.2.3 Other Sources of Line Broadening

As discussed in Section 13.1, line broadening sources are manifold. In the previous subsections two of the most common ones were considered: "size" (Section 13.2.1) and "strain" (Section 13.2.2) broadening. It is therefore legitimate to wonder to what extent different line broadening sources can be distinguished from the effects observed in a PD pattern. To discuss this point, two types of lattice defects that affect the line profile are considered.

Faulting, a two-dimensional "mistake" in the crystal structure, is a frequent defect in materials. The characteristic of faulting is that the disorder along the direction of stacking of atomic planes alters, or even destroys, the coherency of diffraction along that direction.[2] It is, therefore, possible to observe that some points are extended into rods along a given direction in reciprocal space, whereas some other points are unaffected. This feature gives a distinctive mark to the diffraction line broadening, so that faulting can be studied in detail.[2,7]

In general, the presence of faulting acts as limiting the coherence length, thus reducing the apparent domain size along specific directions. In a simplified form, valid in the limit of low staking ($\alpha$) and twin ($\beta$) fault probabilities,[3] the measured domain size can be regarded as an effective size, $L_{\text{eff}}$, related to the actual mean size, $< L >$, and to a mean faulting size, $< L >_{\text{F}}$, as:

$$\frac{1}{L_{\text{eff}}} \approx \frac{1}{< L >} + \frac{1}{< L >_{\text{F}}} \tag{11}$$

where $< L >_{\text{F}}$ depends on $\alpha$, $\beta$, and ($hkl$). Selection rules for fcc, bcc and hcp, determining which reflection is broadened and by what amount, can be found in the literature.[3] It is worth underlining that selection rules may be different for different ($hkl$) combinations of a $\{hkl\}$ reflection: consequently, faulting causes a complex change in peak shape in a powder pattern, even more so if one considers the slight peak shift and asymmetry also due to faulting.[29]

Anti-phase domain boundaries, are three-dimensional mistakes typical of several intermetallic systems undergoing disorder/order transformations. APBs also act on the apparent domain size, but selection rules are totally different

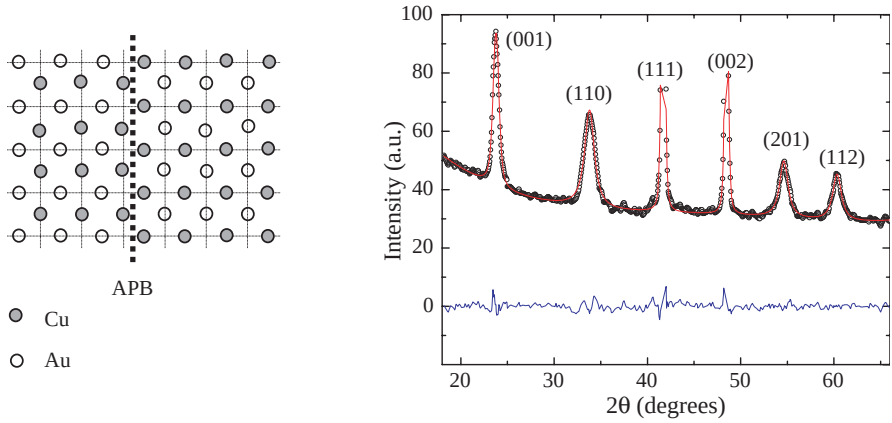



**Figure 13.6** Antiphase domains and APB in $Cu_3Au$ (left). Diffraction pattern of the ordered phase (right). Superstructure lines (sharp and very intense) are truncated. Data (○) from Figure 12.9 of ref. 3. The WPPM result (line) is also shown, with the difference between experimental and modelled data (residual, lower line).[16a]

from those of faulting.[3,14,15] $Cu_3Au$ is a typical example of a material forming APBs: the disordered structure is fcc, and turns into a $L1_2$ ordered superstructure below 390 °C. As a consequence, the disorder/order transition is accompanied by the appearance of superstructure lines in addition to the fundamental reflections observed also for the disordered phase [(111) and (002) in Figure 13.6]. On cooling from the high-temperature disordered phase, the ordering process starts at several positions in the material, thus forming domains that grow and eventually come in contact, forming boundaries.

Since the ordering process can start at non-equivalent atomic sites, the boundary can result in a discontinuity, dividing regions with a different phase relation. Such boundaries are therefore called APBs (Figure 13.6).

For energetic reasons, APBs in $Cu_3Au$ are more likely to occur on the {001} planes, corresponding to a half diagonal glide, in such a way to avoid gold atoms becoming first neighbours.[2,3] The effect on PD peak profiles is rather peculiar, as it only concerns superstructure reflections, whereas fundamental reflections are unaffected by the APBs. For the {00*l*} APBs in $Cu_3Au$ the IB of superstructure reflections is related to $\gamma$, the probability of crossing an APB:

$$\beta(2\theta) = \frac{\lambda\gamma(|h| + |k|)}{a\cos\theta(h^2 + k^2 + l^2)^{1/2}} \tag{12}$$

where Miller indices must be selected so that $h$ and $k$ have the same parity.[3] Figure 13.6 shows the PD pattern of an ordered $Cu_3Au$ phase obtained by cooling from the high-temperature disordered phase and annealing at 360 °C for 1/2 h. Detection of APBs is supported by the different width of superstructure lines and absence of line broadening in fundamental lines. Even if APBs

give an apparent size effect, it is quite evident that this type of line broadening cannot be mistaken for the domain size effect of Section 13.2.1.

In conclusion, different line broadening sources – *e.g.* size, strain, faulting, APBs, ... – tend to produce different effects on the line profiles. Consequently, all these features can be studied by profiting from the specific dependence of line broadening on the scattering vector and on the Miller indices of each given diffraction peak. Most LPA methods, as shown in the following section, are then based on using the line broadening information from several peak profiles to separate the various contributing effects.

To conclude this overview on the most common sources of line broadening it is worth considering the instrumental profile. As discussed in Chapters 5 and 6, wavelength dispersion, sample absorption and instrument optics generally produce a finite width IP[2,5] that is regarded as an extrinsic profile, even if absorption is actually a sample related property. The IP is always present in a PD pattern, combined with the intrinsic profile produced by microstructural features and lattice defects present in the studied sample.

The traditional approach to treat the IP is based on deconvolution techniques. In fact, it can be shown that the PD profile is a convolution ($\otimes$) of profile components produced by different sources [IP, size (S), strain (D), faulting (F), *etc.*]:[5]

$$I(s) = I^{IP}(s) \otimes I^{S}(s) \otimes I^{D}(s) \otimes I^{F}(s) \otimes \ldots \tag{13}$$

The Fourier Transform of $I(s)$ is equal to the product of the FTs of the various profile components on the right-hand side of Equation (13). This makes it possible to separate the extrinsic component following the Stokes procedure.[3,5,30] In addition to the PD pattern of the sample under study, it is necessary to collect a pattern of the same sample after a suitable treatment to remove any source of intrinsic line broadening, *e.g.* by means of a high-temperature annealing.[5] Assuming that peak profiles are sufficiently well separated, and that the background is properly removed, one can obtain the FT of a profile, both for the studied sample and for the corresponding annealed sample. The ratio between the FTs of the studied sample and annealed sample gives the FT of the intrinsic profile component, which can be used directly for a LPA (*e.g.* using Fourier methods, see Section 13.3) or to reconstruct a purely intrinsic profile by Fourier back-transform.

In principle this is a robust method, but it has several practical drawbacks. Eliminating background and overlap with other peak profiles can be difficult, if not impossible in many cases of practical interest: the broader the profiles (*i.e.* the more suitable to a LPA) the more peak overlapping is inevitably present in the PD pattern. In addition, the Stokes method involves a numerical procedure for the Fourier analysis, so it is exposed to all the downsides related to signal sampling and truncation.[31]

Two valid alternatives have been proposed so far. The first relies on a profile fitting stage, preliminary to the LPA.[32] The IP of most PD instruments can be satisfactorily modelled by simple analytical profile functions, like Voigt,

pseudo-Voigt or Pearson VII [see Chapter 4]. By using profile fitting for the pattern of a suitable line profile standard (*e.g.* $LaB_6$ SRM 660a distributed by the NIST[33]), one can obtain a parametric description of the IP for the instrument used, *i.e.* the trend of the IP parameters, typically width and shape, as a function of the PD angle $2\theta$. The so-determined IP can then be used for a deconvolution procedure (numerical or analytical[32,34,35]).

A viable alternative is using the so-called Fundamental Parameters Approach to synthesize the IP (Chapters 5 and 6). In fact, the IP is itself given by a convolution of profiles, chiefly those produced by wavelength dispersion, optical components and absorption.[5] If the geometry of the PD instrument is known and sufficiently accurate, the FPA can provide a calculated IP without the need for using powder standards.[36,37]

It is, finally, worth mentioning that in addition to deconvolution methods it is also possible to use a convolution approach. The advantage of the latter is that LPA can be performed in a one-step procedure, directly on the measured data, provided that the procedure can make use of a parametric description of the IP preliminarily determined. Software packages are available for this type of analysis.[38]

## 13.3 TRADITIONAL *VERSUS* INNOVATIVE METHODS

### 13.3.1 Integral Breadth Methods

As a natural extension of the methods shown in Section 13.2, IB expressions for the various sources of line broadening can be combined. This is the basis of the Williamson–Hall method, introduced in the late 1940s.[5,39 41] Considering Equations (7) and (10), size and strain contributions can be combined as:

$$\beta(s) \approx \frac{1}{< L >_V} + 2e \cdot d^*_{hkl} \tag{14}$$

where $e$ should be regarded as an upper limit of the microstrain[2,5] (within the limits of the assumptions of Stokes and Wilson:[5,42] $e = 1.25 < \varepsilon^2 >^{1/2}$).

According to this expression, the slope of a regression line in a plot of $\beta(s)$ *versus* $d^*_{hkl}$ (known as a WH plot) gives $2e$, whereas the intercept gives the inverse of the apparent size, $< L >_V$. It is implicitly assumed that $\beta(s)$ refers to the intrinsic profile, *i.e.* the IP component has been removed.

As an example of the application of the WH method, Figure 13.7 shows the diffraction pattern of a ceria stabilized-zirconia powder sample [with a 20 wt.% addition of standard silicon (SRM 640b distributed by the NIST)], together with the corresponding WH plot for the tetragonal zirconia phase. The WH plot points out the presence of both size and strain effects (respectively, non-zero intercept and slope), and the best fit of Equation (14) gives: $< L >_V = 18(1)$ nm and $e = 0.0024(3)$.[38]

Equation (14) can also be modified to include terms accounting for faulting.[43 45] It is also possible to consider the strain anisotropy arising from the

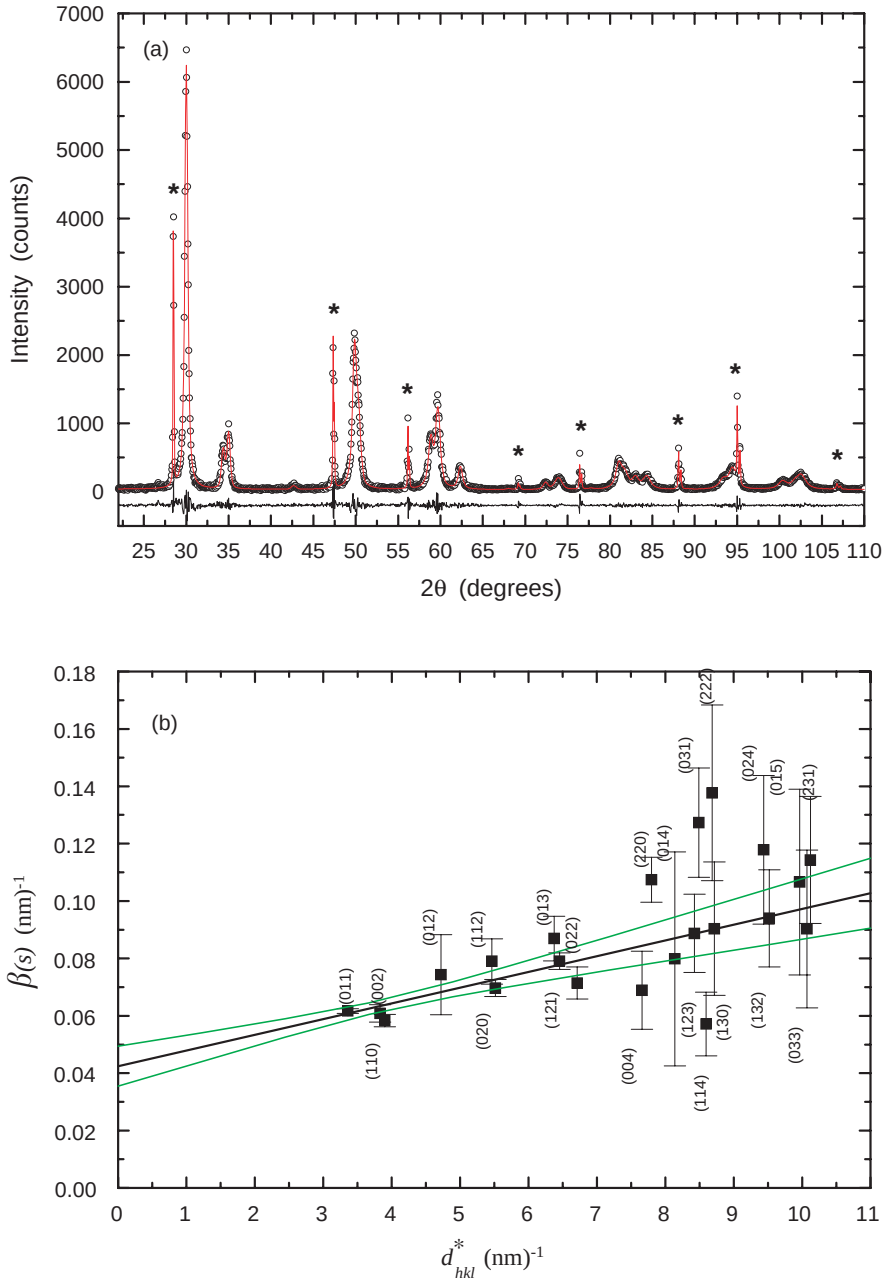



**Figure 13.7** XRD pattern of a ceria stabilized zirconia powder mixed with 20 wt.% of standard silicon (asterisks).[38] Experimental data (○) profile fitting result (line) and difference between data and fit (residual, lower line) (a); WH plot for the stabilized zirconia phase, with indication of Miller indices, regression line and 95% confidence range (b). (Reprinted from ref. 38 with the permission of the International Union of Crystallography.)

anisotropy of the elastic medium and of the specific defect considered[42] (*e.g.* dislocations[43 47]).

The weak point of Equation (14) is that the additivity of integral breadths is an arbitrary choice, valid only under rather restrictive conditions. In fact, owing to the mechanism of convolution of various profile components shown by Equation (13), the way the IB components add up depends on specific features of the broadening sources (and relevant profile components). In particular, Equation (14) can be justified if $I^S(s)$ and $I^D(s)$ both have a Lorentzian shape. For Gaussian profiles, instead, one should write:[5]

$$\beta^2(s) \approx \left(\frac{1}{<L>_V}\right)^2 + 4e^2 \cdot d^{*2} \tag{15}$$

Unfortunately, few cases can be properly described under the assumptions of Equations (14) or (15) (or by other possible combinations[5,39,47]): real life cases usually do not match perfectly any simple combination of Lorentzian or Gaussian profiles. Generally speaking the additivity rule for different IB components is not known *a priori*, so using Equations (14), (15) or other combinations of terms is somewhat arbitrary, unless specific assumptions are made on the line broadening sources.[45]

Despite all of this, IB methods are very popular, because they are simple and can provide a quick estimate of the main sources of line broadening. When properly used, IB methods can also be rather informative and resolutive.[48] However, as a general rule, IB methods should be regarded only as simple and useful tools for a qualitative, preliminary assessment of the main sources of line broadening.

### 13.3.2 Fourier Methods

As suggested by Equation (13) and the related discussion in Section 13.2.3, Fourier analysis is a natural choice for treating line profiles that makes it possible to separate the various sources of line broadening in a much better and more general way than using IB methods.

The Warren–Averbach method[3] starts from this consideration and takes into account the simultaneous presence of size and strain effects. Once the IP has been properly considered (*e.g.* by a deconvolution procedure), the Fourier expansion of the intrinsic profile can be written as:

$$I(s) = k(s) \sum_{L=-\infty}^{\infty} A_L e^{2\pi i L s} \tag{16}$$

where $L = n \cdot d_{hkl}$ (with $n$ integer) is the Fourier length and $k(s)$ groups constants and known functions of $s$ (Lorentz-polarization factor, square of the structure factor, *etc.*). Owing to the convolution principle expressed by Equation (13), the Fourier coefficients $A_L$ can be written as the product of the

coefficients for the contributing size (S) and strain (D) effects:

$$A_L = A_L^S A_L^D \tag{17}$$

The WA method gives an approximate expression for the strain coefficients in terms of the r.m.s. strain $<\varepsilon_{hkl}^2(L)>^{1/2}$. Written in logarithmic form, Equation (17) becomes:[3]

$$\ln(A_L) \cong \ln\left(A_L^S\right) - 2\pi^2 L^2 \left\langle \varepsilon_{hkl}^2(L) \right\rangle d_{hkl}^{*2} \tag{18}$$

Profiting from the fact that only the strain term depends on the scattering vector, Equation (18) can be used to separate domain size and microstrain terms: at least two reflections of the same (*hkl*) plane family are necessary to solve Equation (18) for $A_L^S$ and $<\varepsilon_{hkl}^2(L)>^{1/2}$.

The WA plot[3] is shown in Figure 13.8 for the stabilized-zirconia powder of Figure 13.7: $\ln(A_L)$ is plotted as a function of $d_{0ll}^{*2}$ for three reflections of the (0*ll*) family, (011), (022) and (033). According to Equation (18), from the intercept and slope of the regression lines, respectively, size Fourier coefficients and microstrain can be obtained for different Fourier lengths, *L*.

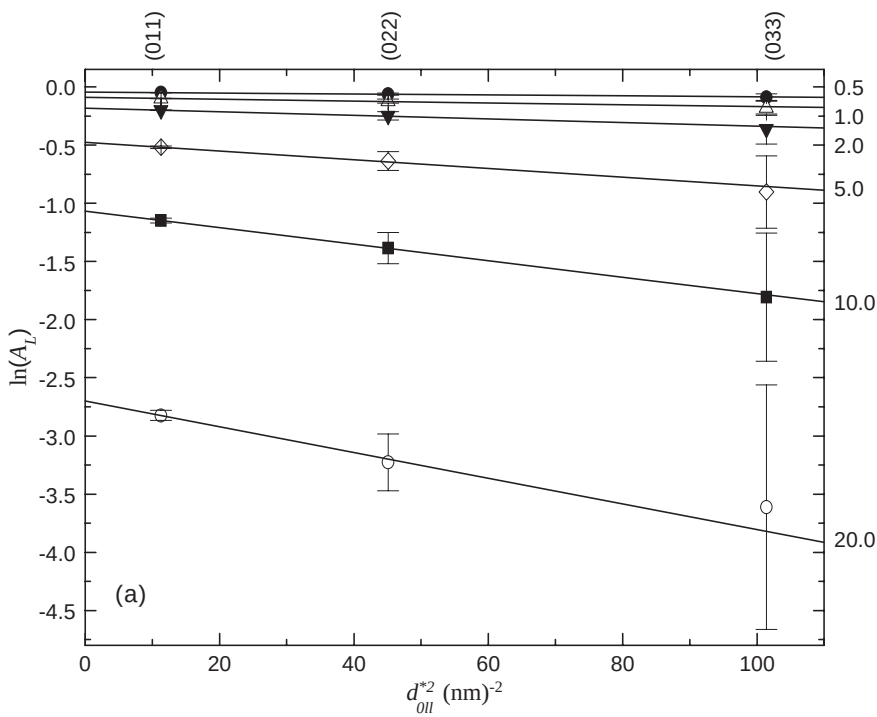



**Figure 13.8** WA plot for the sample of Figure 13.7: Logarithm of the Fourier coefficients of the (0*ll*) profiles of the stabilized zirconia phase for several values of Fourier length (on the right, in nm), plotted as a function of the square of the reciprocal space variable. (Reprinted from ref. 38 with the permission of the International Union of Crystallography.)

The results of the WA analysis for the (*0ll*) planes are shown in Figure 13.9, where $A_L^S$ (a) and $<\varepsilon_{hkl}^2(L)>^{1/2}$ (r.m.s.) (b) are plotted as a function of the Fourier length.

Instead of an average microstrain ($<\varepsilon^2>^{1/2}$) or an upper limit ($e$) given by IB methods (Section 13.3.1), the WA method provides much more detailed

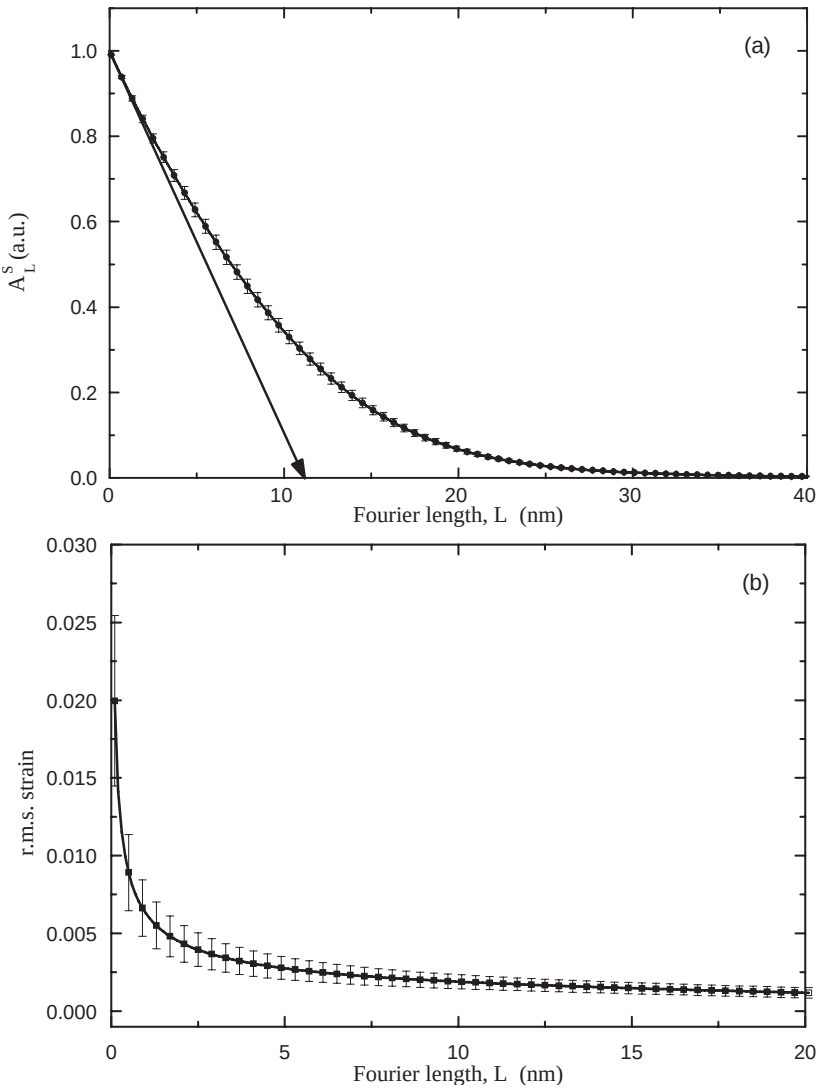



**Figure 13.9** Results of the WA analysis of the data of Figures 13.7 and 13.8: Size Fourier coefficients (a) and r.m.s. strain (b) as a function of the Fourier length. The arrow in (a) shows the tangent at $L=0$ [see text and Equation (20)]. (Reprinted from ref. 38 with the permission of the International Union of Crystallography.)

information, *i.e.* r.m.s. strains for each distance $L$ between cells along the scattering directions. Also, the information on domain sizes is much richer, as we now have the entire representation, in Fourier space, of the domain size contribution to the PD profile.

Using the properties of the Fourier coefficients and the normalization condition ($A_{L\ 0}^{S}=1$), the equivalent of the IB result for the mean domain size is given by:[2,4,9,24]

$$< L >_V = \sum_L A_L^S \tag{19}$$

where the sum extends to all (positive and negative) values of $L$ for which $A_L^S \neq 0$ ($A_L^S$ is by definition an even function of $L$).[2]

As pointed out by Bertaut,[3,4,49] the derivative of the size Fourier coefficients (Figure 13.9) is also related to a mean domain size according to:

$$-\left.\frac{dA_L^S}{dL}\right|_{L=0} = \frac{1}{< L >_S} \tag{20}$$

The mean size $< L >_S$ in Equation (20) is an area-weighted mean size, and should not be confused with $< L >_V$ given by Equation (19) and by IB methods. The two quantities are generally different, the difference being smaller for narrow size distributions.[24]

If one considers each crystalline domain as made of columns of unit cells (actually the unit cells are projected along the specific [*hkl*] direction considered), then the scattering domain can be described by a column length distribution $p(L)$, which gives the fraction of columns of length $L$. Continuing the analysis introduced by Bertaut it can be demonstrated that $p(L)$ is proportional to the second derivative of $A_L^S$:[3,4,49]

$$p(L) \propto \frac{d^2 A_L^S}{dL^2} \tag{21}$$

The distribution $L \cdot p(L)$ shown in Figure 13.10 was obtained from the size Fourier coefficients of Figure 13.9a: in this specific context, $L$ is called column length. From this distribution one can obtain both the area-weighted mean size [same as that of Equation (20)] and the volume-weighted mean size [same as that of Equation (19)], which are likewise called area-weighted and volume-weighted mean column lengths, respectively:[3,4]

$$< L >_S = \sum_L Lp(L) \Big/ \sum_L p(L) \tag{22a}$$

$$< L >_V = \sum_L L^2 p(L) \Big/ \sum_L Lp(L) \tag{22b}$$

Values obtained from Equation (19) and (20) [or by Equation (22)] are, for the case shown in Figure 13.7, $< L >_S = 11(1.5)$ nm, $< L >_V = 17(1)$ nm. Even if

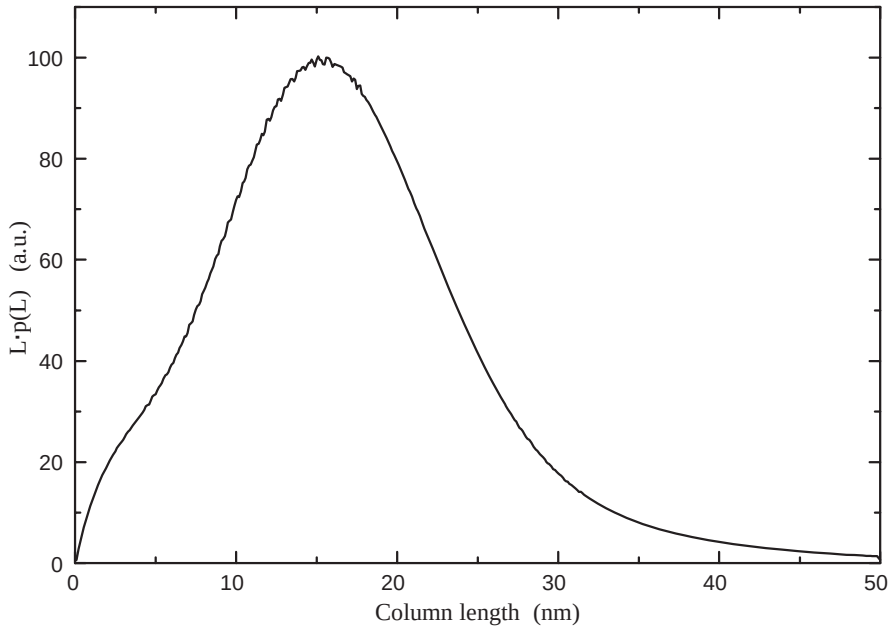



**Figure 13.10** Column length distribution $[L \cdot p(L)]$ obtained from the size Fourier coefficients of Figure 13.9. (Reprinted from ref. 38 with the permission of the International Union of Crystallography.)

the WA analysis is referred to a specific (*hkl*), whereas the IB method gives a sort of average over different (*hkl*), the volume-weighted mean size given by the WA is in good agreement with the value obtained from the IB analysis (Figure 13.7).

Microstrains are also in reasonable agreement: the IB value [0.0024(3)] corresponds to the r.m.s. strain around $L \approx < L >_S$ in Figure 13.9b. In this case WH and WA methods give consistent results, but this should not be considered a rule. As the underlying hypotheses of the two LPA methods are different, results may not necessarily agree.

The discussion above explains why the LPA results may require some further analysis to be compared with size values obtained by other techniques (*e.g.* HREM). The mean size values of Equation (22) are not referred to the dimensions (*e.g.* the diameter) of crystalline domains observable in a TEM picture. The interpretation of the size effect in terms of column length distribution is quite general, but requires some assumption on the actual domain shape and possibly on the size distribution to give a result directly comparable with those of other techniques. For polydisperse systems made of crystalline domains with the same shape, one can write:[9]

$$< L >_S = \frac{1}{K_k} \frac{M_3}{M_2} \tag{23a}$$

$$< L >_V = \frac{1}{K_\beta} \frac{M_4}{M_3} \tag{23b}$$

where $K_k$ is the Scherrer constant for the area-weighted mean size, which can be found in the literature for several simple crystallite shapes,[2,8,9] and the $M_i$ are moments of the size distribution as in Equation (7). For domain shapes with just one length parameter (*e.g.* sphere, cube, tetrahedron, octahedron,...) dispersed according to a simple, two-parameter (*e.g.* mean and variance) distribution, the equation system (23) can be solved: if the two weighted mean sizes are known from the LPA, the domain size distribution can be obtained. For example, for the specific case of spherical domains with a lognormal distribution of diameters, the system:[9,50]

$$< L >_S = \frac{2}{3}\exp[\mu + (5/2)\sigma^2] \tag{24a}$$

$$< L >_V = \frac{3}{4}\exp[\mu + (7/2)\sigma^2] \tag{24b}$$

can be solved for the lognormal mean $\mu$ and variance $\sigma$.

Also the interpretation of the r.m.s. strain (Figure 13.9b) is not straightforward. To obtain information on the excess energy of the lattice defects responsible for the observed microstrain, it is necessary to make some assumptions on the specific defect type and relative strain field.[17] Examples are considered in the next section.

Finally, even if the WA analysis is considered a robust LPA method, it is important to recognize that its applicability is in any case limited by the validity of the underlying hypotheses and approximations.[3,11,17,31] Besides the theoretical issues, some practical considerations are also important: as observed for the IB methods, peak profile overlap and background can make it difficult, if not impossible, to reliably extract the information on single peak profiles, as required by the traditional WH and WA methods, without truncating the important information in the peak tails. To circumvent this problem, most of the present day LPA procedures use a profile fitting stage (see Chapters 4 and 5), whose application in conjunction with LPA is the subject of the next section.

### 13.3.3 Profile Fitting and Traditional LPA Methods

Owing to the presence of a complex background, and to peak overlap, most traditional LPA methods cannot be reliably applied in interesting cases such as nanocrystals and heavily deformed materials, and in general to the most interesting cases, *i.e.* when peak profiles are broad.

A handy solution is using profile fitting to decompose the PD pattern into its constituent profiles and background, and then use LPA methods (IB or Fourier analysis). This procedure is used for the example discussed so far: Figure 13.7a shows the results of a Whole Powder Pattern Fitting obtained using the *MarqX* code.[38]

Advantages of using a profile fitting stage, and a WPPF in particular, are many: patterns with peak overlap, complex background, and multiple phases can be readily analysed; the procedure is fast and flexible, in the sense that it can be used on various different problems, even in absence of detailed structural

information on the present phases; the IP can be included in the analysis, as in the case shown in Figure 13.7: a parameterized expression of the IP, obtained from a preliminary analysis of a profile standard (Section 13.2.3) can be used to account for the extrinsic profile components; if necessary, integrated intensities can be constrained by a suitable structural model, then transforming the WPPF into a Rietveld method (see Chapter 9).

Further aspects, pros and cons of WPPF, are discussed in Chapter 5. Here it is important to underline the fact that the validity of profile fitting is limited by the basic assumption of using an *a priori* selected profile function without any sound hypothesis that the specific functional form is appropriate to the case of study. The consequence of this arbitrary assumption can be quite different. For example, in most practical cases, profile fitting can provide reliable values of peak position and area, whereas the effects on the profile parameters are less known and rarely considered. The arbitrary choice of a profile function tends to introduce systematic errors in the width and shape parameters, which invariably introduce a bias in a following LPA, whose consequences can hardly be evaluated. It is therefore a natural tendency, for complex problems and to obtain more reliable results, to remove the *a priori* selected profile functions – leading to the following section dedicated to "Whole Powder Pattern Modelling" methods.

### 13.3.4 Whole Powder Pattern Modelling

To avoid using arbitrary (*a priori* selected) profile functions, whose parameters are not directly and univocally related to physically observable quantities, a different approach can be followed: line profiles can be described directly in terms of physical models of the microstructure and lattice defects present in the studied material. This is the foundation of the WPPM method:[9,16a,51 57] in this respect, *modelling* is opposed to *fitting* as the former involves the use of physical information at all stages of the analysis, whereas the latter uses an *a priori* selected (though flexible) form for the PD profiles.

A brief overview of the physical basis of WPPM is given here, together with some examples of applications to real cases of study. Interested readers can find further details in the cited literature.[9,16a,51 57] The basic expression of WPPM considers the FT of a $\{hkl\}$ peak profile:

$$I_{\{hkl\}}(s_{hkl}) = k(s_{hkl}) \cdot \sum_{hkl} w_{hkl} \int_{\infty}^{\infty} \mathbb{C}_{hkl}(L)\exp[2\pi i L(s_{hkl} - \delta_{hkl})]\mathrm{d}L \qquad (25)$$

The sum extends to all equivalent $(hkl)$ planes composing a $\{hkl\}$ family (that for a cubic system means all permutations of $h,k,l$, sign included). $w_{hkl}$ and $\delta_{hkl}$ are, respectively, weight and shift from the Bragg condition (caused by lattice defects, *e.g.* by faulting)[3] for the $(hkl)$ component. In this way the possibility that lattice defects might produce different effects on different $(hkl)$s is explicitly considered.

The core of Equation (25) is the FT, $\mathbb{C}_{hkl}(L)$, which, owing to Equation (13), can be written as the product of the FTs of all contributing extrinsic and intrinsic profile components:

$$\mathbb{C}_{hkl}(L) = T_{pV}^{IP} \cdot A_{\{hkl\}}^{S} \cdot A_{\{hkl\}}^{D} \cdot (A_{hkl}^{F} + iB_{hkl}^{F}) \cdot A_{\{hkl\}}^{APB} \cdot \ldots \qquad (26)$$

Terms included in Equation (26) are the IP, which can be expressed by the FT of a pseudo-Voigt function ($T_{pV}^{IP}$) obtained from a suitable line profile standard (Section 13.2.3), contributions from size ($A_{\{hkl\}}^{S}$), dislocations ($A_{\{hkl\}}^{D}$), faulting ($A_{hkl}^{F} + iB_{hkl}^{F}$), anti-phase domain boundaries ($A_{\{hkl\}}^{APB}$). Expressions for various FTs are reported in the Appendix.

The advantage of this formulation, which is implicit in Equation (13), is that additional line broadening sources can easily be included by adding corresponding terms to Equation (26).[19] Peak areas may be free modelling parameters or may be constrained by a structural model[54] (as in the Rietveld method),[21] whereas the background can be modelled by a suitable polynomial (power or Chebyshev).[57] Bragg peak positions are related to the lattice parameters (also considered as modelling parameters). Typical instrumental aberrations of the powder diffraction geometry (*e.g.* $2\theta$ zero and sample displacement from instrument axis)[57] can also be considered.

All in all, the WPPM approach can provide a simultaneous structure and microstructure refinement, based on physical models of the phases under study, without using any arbitrary profile function. Considering the terms of Equation (26), refinement parameters to be optimized in a least-squares analysis are relatively few, namely, mean ($\mu$) and variance ($\sigma$) of a suitable distribution of coherent domain sizes, dislocation density ($\rho$), effective outer cut-off radius ($R_e$) and character ($f_E$, effective fraction of edge dislocations), twin fault ($\beta$), deformation fault ($\alpha$) and APB ($\gamma$) probabilities.

## 13.4 WPPM: EXAMPLES OF APPLICATION

### 13.4.1 Heavily Deformed Metal Powders

WPPM applications have been reported in several recent publications concerning nanocrystalline powders[19,54,56,58] and heavily deformed ceramic[57,59] and metallic materials.[53,55,60]

Ball-milled metal powders are among the best case studies to illustrate the potential of WPPM. The example shown in the following is taken from a more general work on the microstructure and lattice defects of ball milled metals.[61]

The material considered is an iron alloy ($Fe_{1.5}Mo$) powder with the α-Fe bcc structure. The metal powders were ground in a planetary ball mill (Fritsch Pulverisette 4) using tempered Cr steel balls (100Cr6) and jars (X210Cr12, 80 mL volume), with a 10 : 1 ratio between ball and powder weight. Different powder samples were ball milled in a sealed Ar atmosphere for increasing times, keeping a $\Omega = 300$ rpm rotation speed for the main disk and a ratio $\omega/\Omega = -1.8$ between jar revolution and main disk speed.

Powder diffraction measurements were carried out at the ID31 beamline of ESRF, Grenoble (F), using the standard capillary geometry. Powder samples were loaded into borosilicate glass capillaries (diameter 0.3–0.5 mm, depending on powder size). Sealed capillaries were spun at 3000 rpm during the data collection between 4° and 100° ($2\theta$) at 4° min$^{-1}$, using monochromatic radiation with wavelength $\lambda = 0.063250$ nm. Details of the beamline geometry and procedures can be found elsewhere.[62] The instrumental profile had been previously measured using the NIST $LaB_6$ standard powder (SRM 660a)[33] following the procedure outlined in Section 13.2.3.

Data were analysed by WPPM, considering the 28 bcc reflections, from (110) to (444), encompassing the 4–100° range. Structural constraints were used to refine the intensities of overlapping reflections [*e.g.* (330) and (411)], thus reducing further the number of free modelling parameters. As an example of graphical result of the WPPM analysis, Figure 13.11 shows the experimental and modelled pattern of two powder samples ball milled for 2 h (a) and 96 h (b), respectively. The log scale plots in the insets are shown to highlight details in the peak tail and background region. The modelling result is quite good: besides the peculiarities of the ID31 instrument – high flux, high energy, monochromaticity, high resolution – that provide unique conditions of counting statistics and instrumental resolution, WPPM is particularly effective because the patterns include several multiple order reflections for different crystallographic directions: (110)/(220)/(330)/(440), (200)/(400)/(600), (211)/(422), (310)/(620) and (222)/(444). The anisotropic line broadening due to dislocations can then be separated reliably from the other sources of broadening.

Figure 13.12 shows the domain size distributions for some of the samples ball milled for different times. The WPPM analysis was carried out assuming spherical domains and a lognormal distribution of diameters, a model supported by several literature observations (see ref. 55 and references therein). Ball milling causes a rapid reduction of domain size from $\sim 120$ nm of the starting powder to 40–50 nm, and this value is approximately constant up to 32 h. During this initial stage a strong plastic deformation occurs: electron microscopy shows a dramatic shape change of the metal particles, which take a plate-like aspect and a tendency to incorporate smaller particles and to partly solder. After this plasticity region, extended work hardening causes grain comminution to start, leading to the formation of nearly equiaxial grains. Correspondingly, after 32 h of ball milling the domain size distributions in Figure 13.12 become narrower and shift to smaller values, down to $\sim 18$ nm of mean final dimension.

Even if both size and dislocation effects contribute to the observed line broadening, the main contribution in this case is that of dislocations generated by the heavy mechanical treatment. The dislocation type corresponds to the $\{110\}\langle\overline{1}11\rangle$ primary slip system of bcc α-Fe (Burgers vector modulus $|\boldsymbol{b}| = a\sqrt{3}/2$), for which the average contrast factor $\overline{C}_{\{hkl\}}$ was calculated using the elastic constants of pure iron ($c_{11} = 237$, $c_{12} = 141$, $c_{44} = 116$ GPa). Calculated values of $\overline{C}_{\{hkl\}}$ are shown in Figure 13.13 as a function of

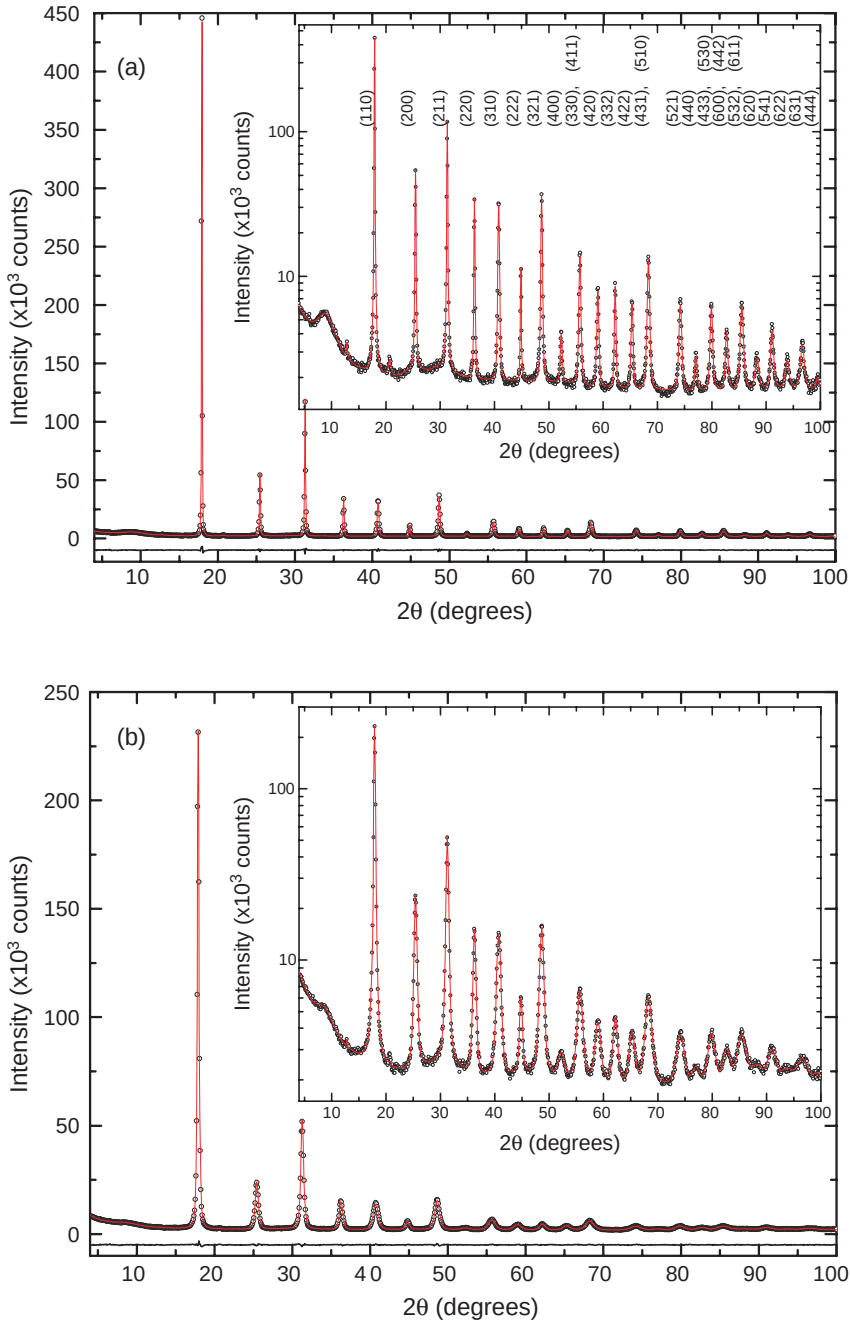



**Figure 13.11** WPPM results for $Fe_{1.5}Mo$ powders ball milled for 2 h (a) and 96 h (b). Experimental data (○) profile fitting result (line) and difference between data and fit (residual, lower line). Insets: Log scale plots and Miller indices of Bragg peaks.

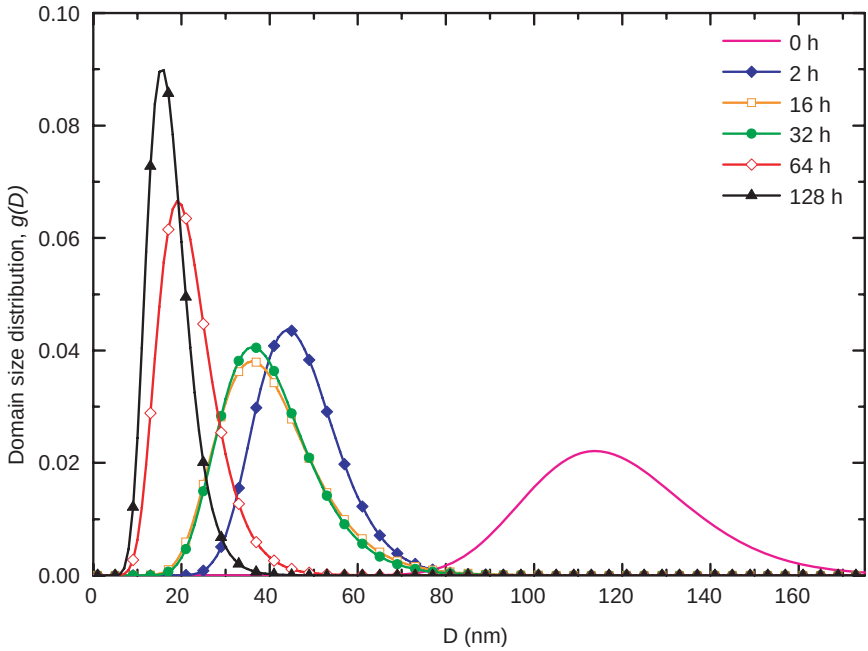



**Figure 13.12** Domain size distribution for $Fe_{1.5}Mo$ powder samples having undergone ball milling for increasing times from 0 (starting powder) to 128 h.

$H = h^2k^2 + k^2l^2 + l^2h^2/(h^2 + k^2 + l^2)^2$ [according to Equation (A10) in the Appendix].

The values in Figure 13.13 for edge and screw dislocations define upper and lower bounds for $\overline{C}_{\{hkl\}}$. As the average contrast factors for the limiting cases of screw and edge dislocations are given, the dislocation character, expressed as the effective edge dislocation fraction $f_E$ [see Equation (A11) in the Appendix], can be refined by WPPM together with the average dislocation density, $\rho$, and the effective outer cut-off radius, $R_e$.

WPPM refined values of dislocation densities are plotted together with the mean domain size in Figure 13.14. The trend of the dislocation density is somewhat opposite to that observed previously for the domain size: after an initial increase up to $\rho \approx 0.3 \times 10^{16}\,\mathrm{m}^{-2}$, the dislocation density is about constant up to 32 h of ball milling, then it increases again reaching values around $2.0 \times 10^{16}\,\mathrm{m}^{-2}$ for extensive grinding up to 128 h.

Figure 13.15 shows the refined values of the effective edge dislocation fraction for increasing ball milling time. The so-called Wilkens parameter, $R_e\sqrt{\rho}$, is also shown, which is a measure of the dislocation interaction and screening effects.[11,63] A physical interpretation of these two parameters should always be considered carefully, as the basic hypotheses of the underlying Wilkens–Krivoglaz model for the dislocation line broadening are usually rather idealized with respect to the real world. Line defects can be much more complex and heterogeneous than the straight edge or screw dislocations considered here,

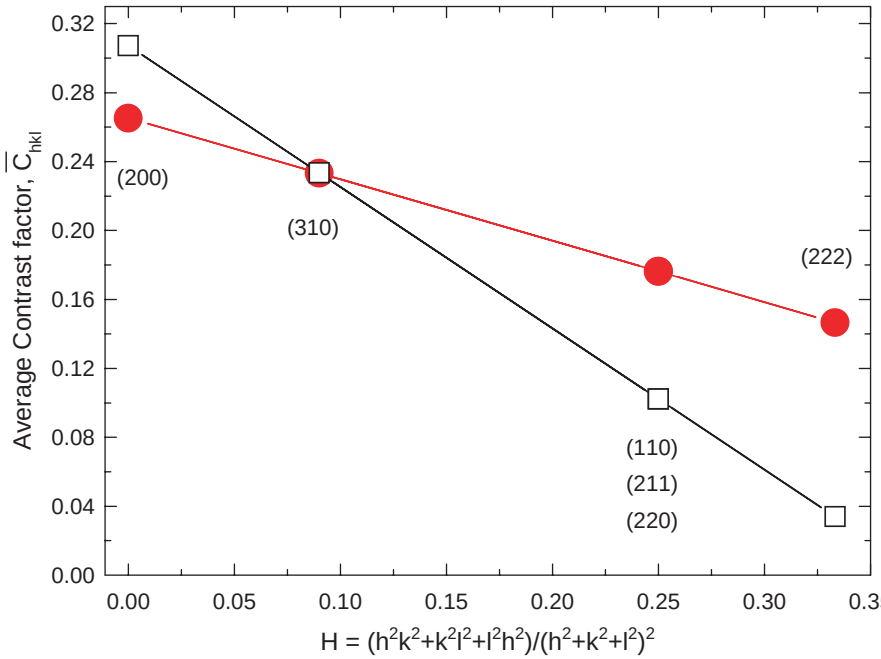



**Figure 13.13** Average contrast factor for screw (□) and edge (●) dislocations in iron ($\{110\}\langle 111\rangle$ primary slip system) as a function of $H = h^2k^2 + k^2l^2 + l^2h^2/(h^2 + k^2 + l^2)^2$.

and the dislocation system can be quite far from resembling the restrictedly random distribution assumed by Wilkens.[11,63]

Beyond any possible physical interpretation, the results of Figure 13.15 provide information on the plausibility of the adopted models. The choice of the dislocation model and of the $\{110\}\langle \bar{1}11\rangle$ slip system is supported by the refined values of $f_E$, between 0.5 and 0.6, within the limits of the pure edge or pure screw dislocation cases. The Wilkens parameter, being always well above unity, confirms that the Wilkens–Krivoglaz approach is appropriate to treat this case. The decrease observed in $R_e\sqrt{\rho}$ above 32 h suggests an increase in the dislocation interaction for extensive ball milling, and nicely matches the trend of the dislocation density, domain size and grain morphology with the treatment time.

Measuring lattice parameters of heavily deformed, nanocrystalline materials can be a difficult task on a laboratory instrument with the usual flat-sample Bragg–Brentano geometry. Errors due to sample morphology (roughness) and positioning inside the instrument can be rather large and affect systematically the peak positions. From this point of view the capillary-sample, parallel-beam geometry of ID31 provides much more reliable results. It is therefore possible to observe, as shown in Figure 13.16, the slight but progressive increase of lattice parameters, mimicking the trend observed for the dislocation density. In addition to the effects of progressive contamination due to ball milling,[61] the

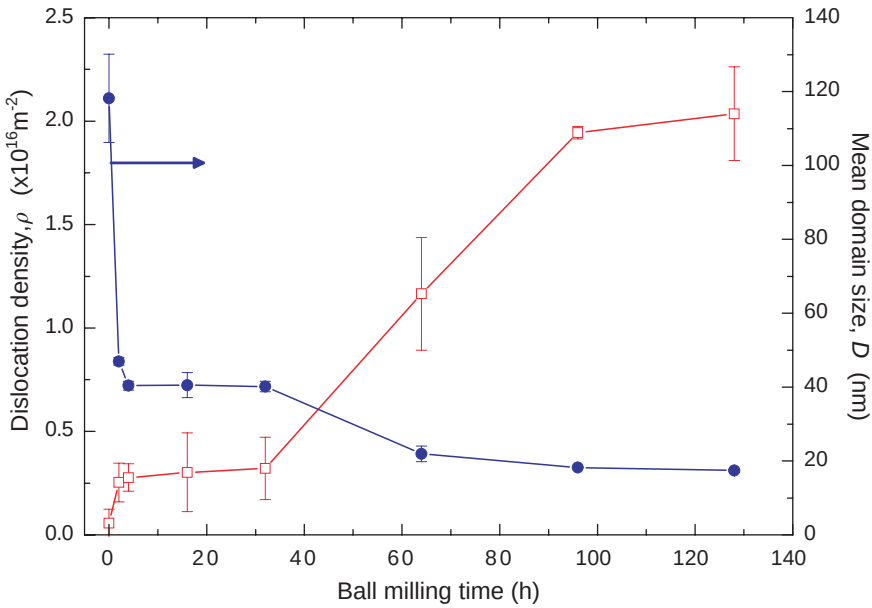



**Figure 13.14** Average dislocation density (left axis, □) and mean domain size (right axis, ●) for increasing ball milling time.

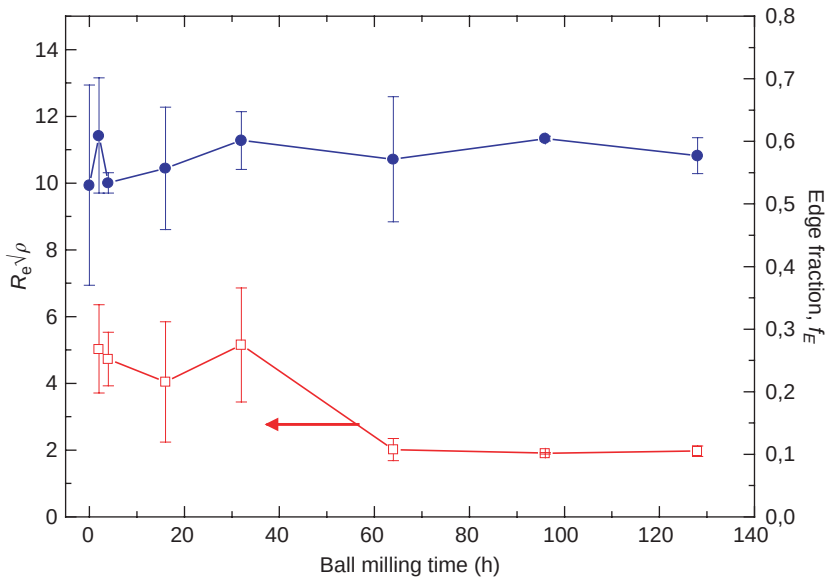



**Figure 13.15** Wilkens parameter, $R_e\sqrt{\rho}$ (left axis, □) and effective edge fraction, $f_E$ (right axis, ●) for samples ball milled for increasing time.

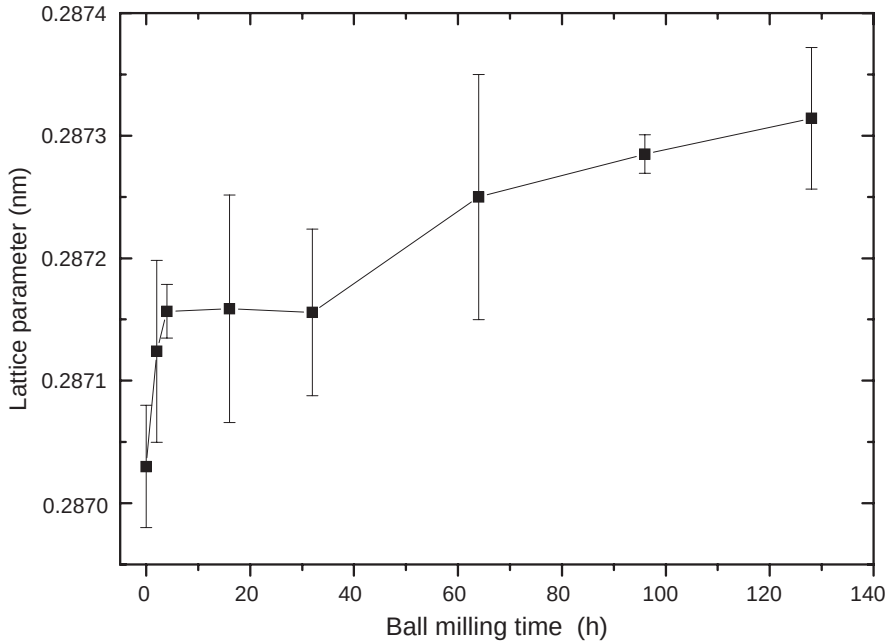



**Figure 13.16** Lattice parameter of the $Fe_{1.5}Mo$ powders for increasing ball milling time.

lattice parameter increase can be related to the volume change produced by lattice defect incorporation.[55]

Further speculation is possible using the WPPM results. For instance one could be interested in comparing domain size and dislocation density to estimate the number of dislocations present in each crystalline domain. Assuming a random distribution of straight dislocations, which is of course a rather crude approximation, the mean dislocation distance is given by $1/\sqrt{\rho}$. The parameter $\langle D \rangle \sqrt{\rho}$ can therefore provide an estimate of the mean number of random dislocations per crystalline domain. Despite the complex evolution of $\rho$ and $\langle D \rangle$ with the ball milling time, a roughly constant $\langle D \rangle \sqrt{\rho} \approx 2-3$ is obtained from the values of Figure 13.14.

### 13.4.2 Nanocrystalline Cerium Oxide Powder

One of the major motivations for the development of the WPPM approach is provided by the growing field of nanomaterials. Knowing the distribution of crystalline domains is a basic piece of information in nanotechnology. In many cases, as in the example considered below, this information is particularly valuable because it is equivalent to the grain size distribution. It is frequently observed in nanocrystalline materials that grains are single crystalline domains: in these cases, one can expect a close match between WPPM results and a size distribution obtained by other techniques, like HREM.

This is the case of a sol–gel derived powder of cerium oxide analysed recently by WPPM.[58] In the sample considered, a xerogel heat-treated at 400 °C, the main line broadening effect is that of domain size, even if a comparatively small but non-negligible contribution is given by microstrain, presumably due to growth dislocations.[19,56] TEM pictures show that particles are actually single equiaxial crystalline domains; therefore, the WPPM approach can be used assuming the presence of spherical crystallites with a distribution $g(D)$ of diameters. Given the preponderance of the size effect, it is worth studying in more detail the size distribution, possibly without constraining the analysis by using an *a priori* decided distribution curve. To this purpose (see Appendix), $g(D)$ is represented by a histogram, to be refined during the WPPM procedure. The starting (prior) $g(D)$ is a uniform distribution, representing the most general and unbiased condition: the least-squares minimization gives the final shape to the $g(D)$, refining independently each column height.

Figure 13.17 shows the WPPM result: despite the strong overlap between line profiles, there is a fairly good agreement between model and experimental data. Even if the pattern was collected on a traditional laboratory instrument using copper radiation,[58] the number of reflections is sufficiently high to model reliably.

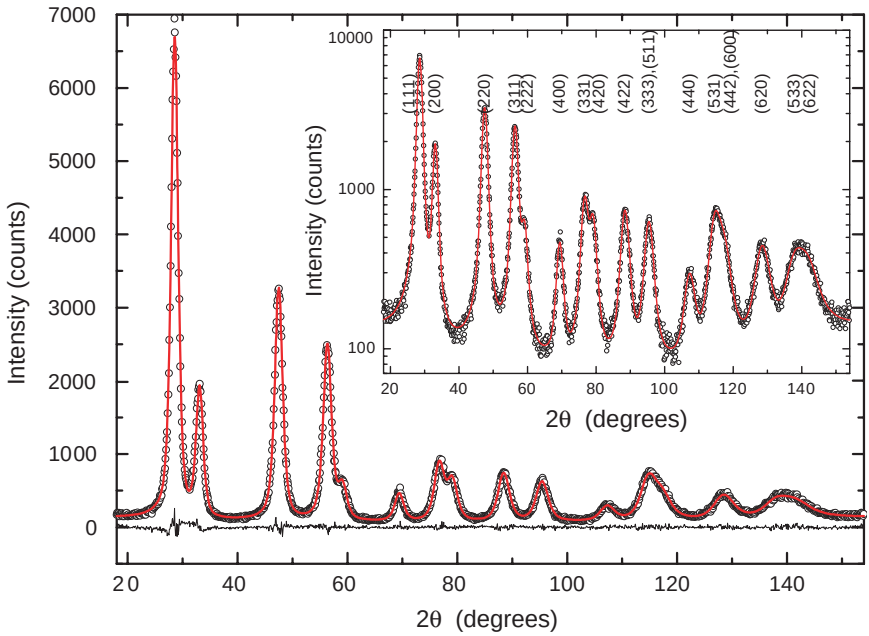



**Figure 13.17** WPPM results for a nanocrystalline cerium oxide powder. Experimental data (○) profile fitting result (line) and difference between data and fit (residual, lower line). Inset: Log scale plot and Miller indices of Bragg peaks. (Reprinted from ref. 58 with the permission of the International Union of Crystallography.)

The corresponding domain size distribution is shown in Figure 13.18, together with the distribution obtained from HREM pictures.[19,56,58] In the same figure we also show the (uniform) prior $g(D)$. WPPM and HREM are in remarkably good agreement, and show a distribution approximately log–normal, with a mean size slightly below 5 nm.

Despite the preponderance of the size effect, a small but non-negligible microstrain effect could be measured. Assuming the presence of growth dislocations[19,56] an average dislocation density of $1.4(4) \times 10^{16}\,\mathrm{m}^{-2}$ was refined. Such a relatively high value can in part be due to the corresponding (abnormally) low values of effective outer cut-off radius ($\rho$ and $R_e$ tend to correlate), but is in any case not so unrealistic considering the small domain size. In general, however, when the size effect prevails, as in this case, the microstrain effect gives just a correction to the profile modelling: numerical results derived by minority strain terms are very likely affected by large errors and should be considered with caution, more as correction terms than as sound physical information.

Notably, such detailed information on the size distribution shown by the example of Figures 13.17 and 13.18 can only be obtained under specific conditions:

a. In general, sufficient information must be available; the pattern must include as many reflections as possible, to reduce errors and to stabilize the modelling algorithm.

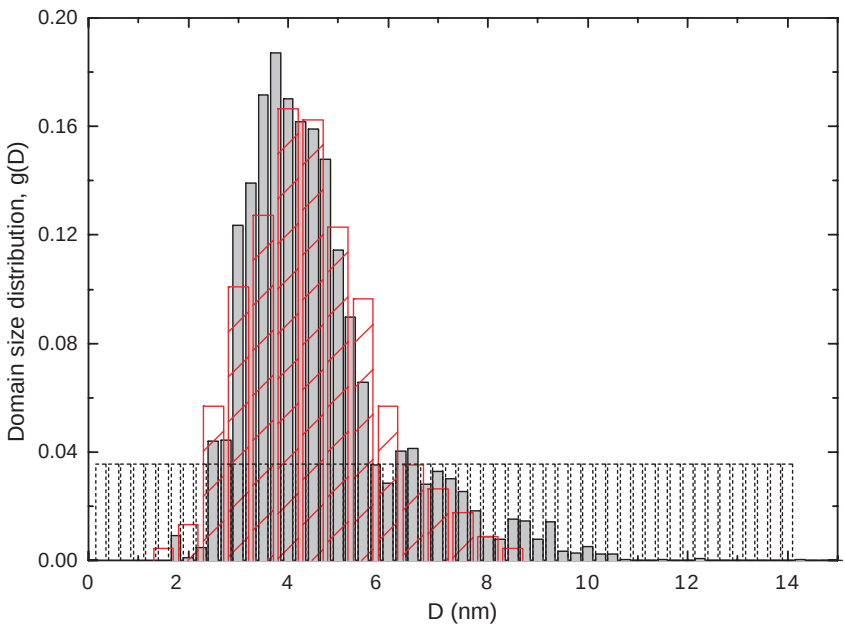



**Figure 13.18** Domain size (diameter) distribution for the nanocrystalline cerium oxide powder of Figure 13.17. WPPM result (plain bar), HREM result (hatched bar) and WPPM starting $g(D)$ (dotted bar). (Reprinted from ref. 58 with the permission of the International Union of Crystallography.)

b. The statistical quality of the data must be high; this is also a general point, not strictly related to WPPM. Fine details such as the shape of the size distribution can only be studied on high quality diffraction patterns.
c. Point (b) is even more true when broad or multimodal distributions are present. Noise in the data has a tremendous impact on the modelling of line broadening from complex distributions of domain size.[58]
d. The possibility of separating size, strain, faulting and the many other possible sources of line broadening is also limited by the quantity and quality of available information. In any case, best results are obtained for the dominant effect, even if correlations among different effects can be limited by rules [*e.g.* (*hkl*) dependent] valid for specific line broadening sources, like those involved in Equations (A5)–(A7) or in Equations (A8)–(A11) for faulting and dislocations, respectively.

## ACKNOWLEDGEMENTS

I am particularly grateful to M. Leoni, for suggestions and critical review of the text, and M. D'Incau for technical support in the ball milling and in the collection of diffraction data. The support of the ID31 staff is also acknowledged, as well as the support from the European Community for the measurements carried out at ESRF, Grenoble.

This work was partially supported by the basic research funds of the Italian Ministry for Education, University and Research, PRIN project (2005-2006) "Microstructure, morphology, and reactivity: modelling and evaluation of crystallization and dissolution processes in minerals".

## LIST OF PRINCIPAL SYMBOLS

| | |
|---|---|
| $a$ | Unit cell parameter of a cubic phase |
| $A^S_{\{hkl\}}$, $A^D_{\{hkl\}}$, $A^{APB}_{\{hkl\}}$, $A^F_{hkl} + iB^F_{hkl}$, $A^C_{\{hkl\}}$ | Fourier Transform of the profile component due to, respectively, domain size, dislocations, APB, faulting and stoichiometry fluctuations |
| APBs | Anti-Phase Domain Boundaries |
| $\boldsymbol{b}$ | Burgers vector |
| $\mathbb{C}_{hkl}(L)$ | Fourier Transform for the (*hkl*) profile component |
| $\overline{C}_{\{hkl\}}$ | Average dislocation contrast factor |
| $d_{hkl}$ | Interplanar distance between (*hkl*) planes |
| $\underline{d}^*$ | Scattering (reciprocal space) vector ($d^* = 2\sin\theta/\lambda$) |
| $\underline{d}^*_{hkl}$ | Scattering vector in Bragg condition for the (*hkl*) planes |
| $f^*(\eta)$ | Wilkens function |
| $f_E$ | Effective fraction of edge dislocations |
| FPA | Fundamental Parameters Approach |

| | |
|---|---|
| FT | Fourier Transform |
| FWHM | Full Width at Half Maximum |
| $g(D)$ | Distribution of diameters of spherical crystalline domains |
| HREM | High-resolution Transmission Electron Microscopy |
| $I(\theta)$, $I(s)$ | Diffracted intensity in a powder pattern (in $2\theta$ or in reciprocal space unit) |
| IB | Integral Breadth |
| IP | Instrumental Profile |
| $K_\beta$, $K_k$ | Scherrer constant for volume-weighted and area-weighted mean size, respectively |
| $L = n \cdot d_{hkl}$ | (with $n$ integer) Fourier length |
| $< L >_S$ | Surface-weighted mean column length |
| $< L >_V$ | Volume-weighted mean column length |
| LPA | Line Profile Analysis |
| $M_i$ | $i$th Moment of the size distribution |
| $p(L)$ | Column length distribution |
| PD | Powder Diffraction |
| pV | pseudo-Voigt profile function |
| $R_e$ | Dislocation effective outer cut-off radius |
| $\underline{s}_{hkl} = \underline{d}^* - \underline{d}^*_{hkl}$ | Distance, along $\underline{d}^*$, from the $(hkl)$ reciprocal space point |
| $T^{IP}_{pV}$ | Fourier Transform of the pV function modelling the IP |
| TEM | Transmission Electron Microscopy |
| $V(D)$ | Crystallite volume ($D$ length parameter) |
| $w_{hkl}$, $\delta_{hkl}$ | Weight and shift, respectively, from Bragg condition of the $(hkl)$ component |
| WA | Warren–Averbach |
| WH | Williamson–Hall |
| WPPF | Whole Powder Pattern Fitting |
| WPPM | Whole Powder Pattern Modelling |
| $Y(d^*)$ | Diffracted intensity in reciprocal space |
| $\alpha$, $\beta$ | Deformation and twin fault probability, respectively |
| $\beta(s)$, $\beta(2\theta)$ | Integral breadths in reciprocal and $2\theta$ space, respectively |
| $\beta_G$, $\beta_C$ | Gaussian and Lorentzian IB components, respectively |
| $\gamma$ | Probability of crossing an APB |
| $\langle \varepsilon^2 \rangle^{1/2}$ | Root mean square strain (microstrain) |
| $\eta$ | Mixing parameter of the pV profile function |
| $\theta_{hkl}$ | Bragg angle for the $(hkl)$ planes |
| $\lambda$ | Radiation wavelength |
| $\mu$, $\sigma$ | Mean and variance of the coherent domain size distribution, respectively, |

| | |
|---|---|
| $\underline{v}_0$, $\underline{v}$ | Incident and diffracted beam unit vectors (versors), respectively |
| $\rho$ | Average dislocation density |
| $\sigma_s$ | HWHM in reciprocal space |
| $\omega$ | (HWHM) Half Width at Half Maximum |

## APPENDIX: FOURIER TRANSFORMS OF PROFILE COMPONENTS

### Instrumental Profile (IP)

A parametric description of the IP can be obtained by modelling the pattern of a line profile standard with pseudo-Voigt functions (see Chapters 4 and 5 and Section 13.2.3 in this chapter):[35]

$$pV(x) = I_0\left\{(1-\eta)\exp\left(-\frac{\pi x^2}{\beta_G^2}\right) + \eta\left[1+\left(\frac{\pi x}{\beta_C}\right)^2\right]^{-1}\right\} \tag{A1}$$

where $x = s_{hkl}$ or $x = 2\theta - 2\theta_{hkl}$, according to whether the integral breadths of the Gaussian ($\beta_G$) and Lorentzian ($\beta_C$) components are written in reciprocal or in $2\theta$ space, respectively; $\eta$ is the mixing parameter (or Lorentzian fraction) and $I_0$ is the peak maximum intensity. If $\omega$ is the half width at half maximum, then $\beta_G = \omega \cdot \sqrt{\pi/Ln(2)}$, and $\beta_C = \omega \cdot \pi$. In this way, the trend of $\omega$ and $\eta$ with $2\theta$ can be determined and used to calculate the FT of the pV:

$$T_{pV}^{IP} = (1-k)\exp\left(-\pi^2\sigma_s^2 L^2/\ln 2\right) + k\exp(-2\pi\sigma_s L) \tag{A2}$$

where $k = \left[1+(1-\eta)\Big/\left(\eta\sqrt{\pi\ln 2}\right)\right]^{-1}$ and $\sigma_s = \omega\cos\theta_{hkl}/\lambda$ is the half-width at half-maximum (HWHM) in reciprocal space.

### Domain Size (S)

The FT of the domain size component produced by a system of crystallites of volume $V(D)$ and size dispersed according to a $g(D)$ distribution can be written in the general form:

$$A_{\{hkl\}}^S(L) = \frac{\int_{L\cdot K^c(hkl)}^{\infty} A_c^S(L,D)g(D)V(D)\mathrm{d}D}{\int_0^{\infty} g(D)V(D)\mathrm{d}D} \tag{A3}$$

where crystallites have simple one-parameter ($D$) convex shapes (*e.g.* sphere, cube, tetrahedral, octahedral).[9] $A_c^S(L, D)$ is the FT of a single crystallite, easily calculated using Wilson's common-volume function,[2,24] whereas $K^c(hkl)$ is a function of the crystallite shape and ($hkl$) considered. Expressions of $A_c^S(L, D)$ and $K^c(hkl)$ can be found in the literature.[9,55]

Equation (A3) can be dealt with analytically, assuming a given $g(D)$,[24] or numerically, considering $g(D)$ as a generic histogram whose column heights are to be refined.[58] As an example of the former option, considering a system of spheres distributed according to a lognormal $g(D)$ with mean $\mu$ and variance $\sigma$:

$$A_l^S(L) = \frac{1}{2} Erfc\left[\frac{\ln|L| \quad \mu \quad 3\sigma^2}{\sigma\sqrt{2}}\right] \quad \frac{3}{4}|L| Erfc\left[\frac{\ln|L| \quad \mu \quad 2\sigma^2}{\sigma\sqrt{2}}\right] \exp\left[\quad \mu \quad \frac{5}{2}\sigma^2\right] + \frac{1}{4}|L|^3 Erfc\left[\frac{\ln|L| \quad \mu}{\sigma\sqrt{2}}\right] \exp\left[\quad 3\mu \quad \frac{9}{2}\sigma^2\right] \tag{A4}$$

The subscript $\{hkl\}$ was omitted as superfluous for the case considered (spherical crystallites). Expressions for other distributions are also available:[9,55] the extension of Equation (A3) to the case of more complex grain shapes and distributions can be cumbersome, but is always possible in principle.

### Faulting (F)

Faulting can be treated according to different approaches.[2,3,13,64] Within the limit of small probabilities, twin ($\beta$) and deformation ($\alpha$) faults in fcc materials can be dealt with using a corrected version of Warren's theory,[3,29] leading to the following expressions for the real and imaginary parts of the FT:

$$A_{hkl}^F(L) = \left(1 - 3\alpha - 2\beta + 3\alpha^2\right)^{\left|\frac{1}{2}Ld^*_{\{hkl\}} \cdot \frac{L_o}{h_o^2}\sigma_{L_o}\right|} \tag{A5a}$$

$$B_{hkl}^F(L) = -\sigma_{L_o} \cdot \frac{L}{|L|} \cdot \frac{L_o}{|L_o|} \cdot \beta \Big/ \left(3 - 6\beta - 12\alpha - \beta^2 + 12\alpha^2\right)^{1/2} \tag{A5b}$$

where $L_0 = h + k + l$, $h_0^2 = h^2 + k^2 + l^2$, and $\sigma_{L_o}$ is a sign function, defined as:

$$\sigma_{L_0} = \begin{cases} +1 \rightarrow L_0 = 3N + 1 \\ 0 \rightarrow L_0 = 3N \\ -1 \rightarrow L_0 = 3N - 1 \end{cases} \qquad N = 0, \pm 1, \pm 2, \ldots \tag{A6}$$

Faulting also produces a shift from the Bragg position given by:

$$\delta_{hkl} = \left\{\frac{1}{2\pi}\arctan\left[\frac{\left(3 - 12\alpha - 6\beta + 12\alpha^2 - \beta^2\right)^{1/2}}{1 - \beta}\right] - \frac{1}{6}\right\} d^*_{\{hkl\}} \cdot \frac{L_o}{h_o^2}\sigma_{L_o} \tag{A7}$$

### Dislocations (D)

Generalized line defects, like dislocations and disclinations, are known to produce a markedly anisotropic line broadening, *i.e.* a line broadening dependent on the observed [*hkl*] direction in the crystalline domain. This is due to the combined effect of the anisotropy of the elastic medium (described by the

elastic tensor, *e.g.* the stiffness $c_{ij}$) and of the orientational anisotropy of the line defect (*e.g.* dislocation line and Burgers vector).

According to the Wilkens–Krivoglaz approach,[10,11,63] the FT of the diffraction profile produced by a system of dislocations with average density $\rho$, Burgers vector $\boldsymbol{b}$ and effective outer cut-off radius $R_e$, can be written as:[11,63]

$$A^D_{\{hkl\}}(L) = \exp\left[-\tfrac{1}{2}\pi|b|^2\overline{C}_{\{hkl\}}\rho d^{*2}_{\{hkl\}} \cdot L^2 f^*(L/R_e)\right] \tag{A8}$$

where $f^*(\eta)$ is the Wilkens function,[11,63] given by:

$$f^*(\eta) = \frac{256}{45\pi\eta} - \frac{1}{\eta^2}\left(\frac{11}{24} + \frac{\ln 2\eta}{4}\right) \quad \text{for } \eta > 1 \tag{A9a}$$

and:

$$\begin{aligned} f^*(\eta) = &\frac{7}{4} - \ln 2 - \ln\eta + \frac{256}{45\pi\eta} + \frac{2}{\pi}\left(1 - \frac{1}{4\eta^2}\right)\int_0^{\eta}\frac{\arcsin x}{x}dx \\ &- \frac{1}{90\pi}\left(\frac{769}{2\eta} + 41\eta + 2\eta^3\right)\sqrt{1-\eta^2} \\ &- \frac{1}{\pi}\left(\frac{11}{12\eta^2} + \frac{7}{2} + \frac{\eta^2}{3}\right)\arcsin\eta + \frac{\eta^2}{6} \quad \text{for} \quad 0 \le \eta < 1 \end{aligned} \tag{A9b}$$

$\overline{C}_{\{hkl\}}$ is the average contrast factor, which accounts for the main effect of anisotropy.[11,65,66] It can be shown that the contrast factor can be written in terms of the fourth order crystallographic invariant for the Laue group of the studied phase.[66] In other words, $\overline{C}_{\{hkl\}}$ can be written for any lattice symmetry, for instance using the invariants given by Popa.[66,67]

Explicit expressions for the average contrast factor and calculated values for any symmetry can be found in the literature.[66,68,69] For the cubic case the invariant form is:[53]

$$\overline{C}_{\{hkl\}} = A + BH = A + B\frac{h^2k^2 + k^2l^2 + l^2h^2}{(h^2 + k^2 + l^2)^2} \tag{A10}$$

where $A$ and $B$ can be calculated given the elastic tensor for the studied phase for any dislocation slip system $(hkl)[h'k'l']$ (*i.e.* knowing dislocation line and Burgers vector).[66] A general expression for the cubic case, considering edge ($E$) and screw ($S$) dislocations, is:

$$\begin{aligned} \overline{C}_{\{hkl\}} =& f_E\overline{C}_{E,\{hkl\}} + (1-f_E)\overline{C}_{S,\{hkl\}} \\ =& [f_E A_E + (1-f_E)A_S] + [f_E B_E + (1-f_E)B_S]H \end{aligned} \tag{A11}$$

where $f_{\mathrm{E}}$, the edge fraction, can be regarded as an effective parameter representing the mean dislocation character. If the contrast factor for edge and screw dislocations ($A_E$, $B_E$, $A_S$, $B_S$) is known, line broadening can be described by just three modelling parameters in Equation (A8): $\rho$, $R_e$ and $f_{\mathrm{E}}$.

Further consideration and a more rigorous implementation of Wilkens' theory can be found in the cited literature.[65]

### Anti-phase Domain Boundaries (APB)

Line broadening due to APBs is somewhat similar to faulting,[3] even if the FT in this case is real and there is no peak shift. According to Wilson, $A^{APB}_{\{hkl\}}(L)$ can be written as an exponential function of $L$. For the case of APBs in $Cu_3Au$ (Section 13.2.3):[2,14]

$$A^{APB}_{\{hkl\}}(L) = \exp\left[-2\gamma d^*_{hkl} L \cdot f(h,k,l)\right] \tag{A12}$$

where the $f(h,k,l)$ depends on the specific APB considered. $A^{APB}_{\{hkl\}}(L) = 1$ for the fundamental lines. For APBs in $Cu_3Au$ along {100} with no gold-gold contact (Section 13.2.3), $f(h,k,l) = (|h| + |k|)/(h^2 + k^2 + l^2)$ (with $l$ as unpaired index). $f(h,k,l)$ expressions for different APB orientations are given in the literature.[14,15]

### Stoichiometry Fluctuation (C)

Stoichiometry fluctuations are also responsible for a line broadening effect that, with the exception of cubic phases, is also ($hkl$) dependent.[20] The effect on the line profile is directly related to the nature of the fluctuation: if the compositional variation is described by a suitable function, *e.g.* a Gaussian curve, then the resulting peak profile component is also Gaussian and the FT for this effect can be written as:

$$A^{C}_{\{hkl\}}(L) = \mathrm{e}^{\ \pi\beta^2 L^2} \tag{A13}$$

where the integral breadth $\beta$ is related to the invariant for the corresponding Laue group:[20]

$$\beta^2 \propto \sum_{H+K+L=4} S_{HKL} \cdot h^H k^K l^L \tag{A14}$$

The $S_{HKL}$ can be treated as refinement parameters, subject to the symmetry restriction of the specific Laue group. For example, for an hexagonal phase:

$$\begin{aligned}\sum_{H+K+L=4} S_{HKL} \cdot h^H k^K l^L = {} & S_{400}\left(h^4 + k^4 + 3h^2k^2 + 2h^3k + 2hk^3\right) \\ & + S_{202}\left(h^2l^2 + k^2l^2 + hkl^2\right) + S_{004}l^4\end{aligned} \tag{A15}$$

with the additional condition: $S_{202} = \pm 2(S_{400}S_{004})^{1/2}$. If the relation between lattice parameters and composition is known (*e.g.* see the case of $a$ and $c$ parameters in $\varepsilon$-$FeN_x$)[20] a further constraint can be added to the modelling.

One can think of several other possible line broadening sources. Expressions for the FT may be analytical but also numerical in some cases, as for the grain

surface relaxation effect.[19] In any case, the way each line broadening contribution enters the WPPM algorithm is the same, as described by Equation (26). Combining different line broadening sources is straightforward in WPPM.

## REFERENCES


1. P. Scherrer, *Göttingen Nachrichten*, 1918, **2**, 98.
2. A. J. C. Wilson, *X-ray Optics*, 2nd edn., Methuen, London, 1962.
3. B. E. Warren, *X-ray Diffraction*, Addison-Wesley, Reading, MS, 1969.
4. A. Guinier, *X-ray Diffraction in Crystals, Imperfect Crystals and Amorphous Bodies*, Freeman, San Francisco, 1963. Reprinted by Dover, New York, 1994.
5. H. P. Klug andL. E. Alexander, *X-ray Diffraction Procedures for Polycrystalline and Amorphous Materials*, 2nd edn., Wiley, New York, 1974.
6. *Defect and Microstructure Analysis by Diffraction*, ed. R. L. Snyder, J. Fiala, H. J. Bunge, IUCr series, Oxford University Press, New York, 1999.
7. *Diffraction Analysis of the Microstructure of Materials*, ed. E. J. Mittemeijer and P. Scardi, Springer Series in Materials Science, vol. 68, Springer-Verlag, Berlin, 2004.
8. J. I. Langford and A. J. C. Wilson, *J. Appl. Crystallogr.*, 1978, **11**, 102.
9. P. Scardi and M. Leoni, *Acta Crystallogr., Sect. A*, 2001, **57**, 604.
10. M. A. Krivoglaz, *X-Ray and Neutron Diffraction in Nonideal Crystals*, Springer-Verlag, Berlin, 1996.
11. M. Wilkens, in *Fundamental Aspects of Dislocation Theory*, ed. J.A. Simmons, R. de Wit, R. Bullough, Vol. II, National Bur. Stand., (US) Special Publication No 317, Washington, D.C. 1970, p. 1195.
12. P. Klimanek, V. Klemm, M. Motylenko and A. Romanov, *Adv. Eng. Mater.*, 2004, **6**, 861.
13. M. Leoni, A. F. Gualtieri and N. Roveri, *J. Appl. Crystallogr.*, 2004, **37**, 166.
14. A. J. C. Wilson, *Proc. R. Soc. London, Ser. A*, 1943, **181**, 360.
15. A. J. C. Wilson and L. Zsoldos, *Proc. R. Soc. London, Ser. A*, 1966, **290**, 508.
16. (a) P. Scardi and M. Leoni, *CPD Newsletter*, 2002, **28**, 8; (b) P. Scardi and M. Leoni, *Acta Mater.*, 2005, **53**, 5229.
17. J.G.M. van Berkum, ''Strain Fields in Crystalline Materials'', PhD Thesis, Technische Universiteit Delft, Delft, The Netherlands, 1994. ISBN 90-9007196-2.
18. T. C. Bor, ''Strain Fields in Crystalline Solids'', PhD Thesis, Technische Universiteit Delft, Delft, The Netherlands, 2000. ISBN 90-9013758-0.
19. M. Leoni and P. Scardi, in *Diffraction Analysis of Materials Microstructure*, ed. E. J. Mittemeijer and P. Scardi, Springer Series in Materials Science, vol. 68, Springer-Verlag, Berlin, 2004, p. 413.
20. A. Leineweber and E. J. Mittemeijer, *J. Appl. Crystallogr.*, 2004, **37**, 123.

21. *The Rietveld Method*, ed. R. A. Young, Oxford University Press, Oxford, 1993.
22. C. Giacovazzo, H. L. Monaco, G. Artioli, D. Viterbo, G. Ferrari, G. Gilli, G. Zanotti and M. Catti, *Fundamentals of Crystallography*, 2nd edn., IUCr, Oxford University Press, New York, 2002.
23. A. L. Patterson, *Phys. Rev.*, 1939, **56**, 972.
24. A. R. Stokes and A. J. C. Wilson, *Proc. Cam. Phil. Soc.*, 1942, **38**, 313.
25. A. R. Stokes and A. J. C. Wilson, *Proc. Cam. Phil. Soc.*, 1944, **40**, 197.
26. E. Grzanka, B. Palosz, S. Gierlotka, S. Stel'makh, R. Pielaszek, U. Bismayer, J. Neuefeind, P. Jovari and W. Palosz, *Mater. Sci. Forum*, 2004, **443–444**, 39.
27. L. H. Schwartz and J. B. Cohen, *Diffraction from Materials*, Springer-Verlag, Berlin, 1987.
28. I. C. Noyan and J. B. Cohen, *Residual Stress*, Springer-Verlag, New York, 1987.
29. L. Velterop, R. Delhez, Th. H. de Keijser, E. J. Mittemeijer and D. Reefman, *J. Appl. Crystallogr.*, 2000, **33**, 296.
30. A. R. Stokes, *Proc. Phys. Soc. London*, 1948, **61**, 382.
31. R. Delhez, T. H. de Keijser and E. J. Mittemeijer, in *Accuracy in Powder Diffraction*, ed. S. Block and C. R. Hubbard, NBS Special Publication No. 567, US Dept of Commerce, Gaithersburg MA, 1980, p. 213.
32. S. Enzo, G. Fagherazzi, A. Benedetti and S. Polizzi, *J. Appl. Crystallogr.*, 1988, **21**, 536.
33. J. P. Cline, R. D. Deslattes, J.-L. Staudenmann, E. G. Kessler, L. T. Hudson, A. Henins and R. W. Cheary, *Certificate SRM 660a*. NIST, Gaithersburg, MD, 2000.
34. M. Leoni, P. Scardi and J. I. Langford, *Powder Diffr.*, 1998, **13**, 210.
35. P. Scardi and M. Leoni, *J. Appl. Crystallogr.*, 1999, **32**, 671.
36. R. W. Cheary and A. A. Coehlo, *J. Appl. Crystallogr.*, 1992, **25**, 109.
37. Bruker AXS, *TOPAS V2.1: General Profile and Structure Analysis Software for Powder Diffraction Data.-User's Manual*, Bruker AXS, Karlsruhe, Germany, 2003.
38. Y. H. Dong and P. Scardi, *J. Appl. Crystallogr.*, 2000, **33**, 184.
39. W. H. Hall, *Proc. Phys. Soc. London, A*, 1949, **62**, 741.
40. G. K. Williamson and W. H. Hall, *Acta Metall.*, 1953, **1**, 22.
41. J. I. Langford, in *Accuracy in Powder Diffraction II*, ed. E. Prince and J. K. Stalick, NIST Spec. Pub. No.846, US Dept of Commerce, Gaithersburg MA, 1992, p. 110.
42. A. R. Stokes and A. J. C. Wilson, *Proc. Phys. Soc. London*, 1944, **56**, 174.
43. T. Ungár, S. Ott, P. G. Sanders, A. Borbely and J. R. Weertman, *Acta Mater.*, 1998, **46**, 3693.
44. R. Kužel, J. Čížek, J. Procházka, F. Chmelík, R. K. Islamgaliev and N. M. Amirkhanov, *Mater. Sci. Forum*, 2001, **378–381**, 463.
45. P. Scardi, M. Leoni and R. Delhez, *J. Appl. Crystallogr.*, 2004, **37**, 381.
46. T. Ungár and A. Borbely, *Appl. Phys. Lett.*, 1996, **69**, 3173.
47. T. Ungár, J. Gubicza, G. Ribarik and A. Borbely, *J. Appl. Crystallogr.*, 2001, **34**, 298.

48. D. Louër, J. P. Auffrédic, J. I. Langford, D. Ciosmak and J. P. Niepce, *J. Appl. Crystallogr.*, 1983, **16**, 183.
49. F. Bertaut, *C.R. Acad. Sci. Paris*, 1949, **228**, 492.
50. C. E. Krill and R. Birringer, *Philos. Mag.*, 1998, **77**, 621.
51. P. Scardi, M. Leoni and Y. H. Dong, *Mater. Sci. Forum*, 2001, **378–381**, 132.
52. P. Scardi, M. Leoni and Y. H. Dong, *CPD Newsletter*, 2001, **24**, 23.
53. P. Scardi and M. Leoni, *Acta Crystallogr., Sect. A*, 2002, **58**, 190.
54. P. Scardi, *Z. Kristallogr.*, 2002, **137**, 420.
55. P. Scardi and M. Leoni, in *Diffraction Analysis of Materials Microstructure*, ed. E. J. Mittemeijer and P. Scardi, Springer Series in Materials Science, vol. 68, Springer-Verlag, Berlin, 2004, p. 51.
56. M. Leoni, R. Di Maggio, S. Polizzi and P. Scardi, *J. Am. Ceram. Soc.*, 2004, **87**, 1133.
57. M. Leoni, T. Confente and P. Scardi, *Z. Kristallogr. Suppl.*, 2006, **23**, 249.
58. M. Leoni and P. Scardi, *J. Appl. Crystallogr.*, 2004, **37**, 629.
59. M. Leoni, G. De Giudici, R. Biddau and P. Scardi, *Z. Kristallogr. Suppl.*, 2006, **23**, 111.
60. P. Scardi, *Z. Metall.*, 2005, **96**, 698.
61. M. D'Incau, M. Leoni and P. Scardi, *J. Mater. Res.*, 2007, **22**, 1744.
62. O. Masson, E. Dooryhée, R. W. Cheary and A. N. Fitch, *Mater. Sci. Forum*, 2001, **378–381**, 300.
63. M. Wilkens, *Phys. Status Solidi A*, 1970, **2**, 359.
64. E. Estevez-Rams, M. Leoni, P. Scardi, B. Aragon-Fernandez and H. Fuess, *Philos. Mag.*, 2003, **83**, 4045.
65. N. Armstrong, M. Leoni and P. Scardi, *Z. Kristallogr. Suppl.*, 2006, **23**, 81.
66. M. Leoni, J. Martinez-Garcia and P. Scardi, *J. Appl. Crystallogr.*, 2007, **40**, 719.
67. N. Popa, *J. Appl. Crystallogr.*, 1998, **31**, 176.
68. P. Klimanek and R. Kužel, *J. Appl. Crystallogr.*, 1988, **21**, 59.
69. R. Kužel and P. Klimanek, *J. Appl. Crystallogr.*, 1988, **21**, 363.

CHAPTER 14

# Two-dimensional Diffraction Using Area Detectors

BERND HINRICHSEN, ROBERT E. DINNEBIER AND MARTIN JANSEN

Max Planck Institute for Solid State Research, Stuttgart, Germany

## 14.1 TWO-DIMENSIONAL DETECTORS

The first two-dimensional detector in X-ray diffraction was conventional film. It remained for decades the detector of choice for both single crystal as well as powder diffraction experiments. In the field of two-dimensional detection it was surpassed initially by image plates and later by CCD cameras (Figure 14.1). Today virtually no film is in use, with perhaps the exception of Polaroid used for single-crystal images. To be able to compare various detectors with one another, and to select the most appropriate detector for a specific experiment, certain key technical qualities are important. These are in general the detective quantum efficiency, the spatial response characteristics, the size, speed and dynamic range.[1]

The *detective quantum efficiency* $(DQE)^2$ is a measure of the signal-to-noise degradation caused by the instrument. It is defined in Equation (1):

$$DQE = \frac{\left[\frac{I_{\text{out}}^2}{\sigma_{\text{out}}^2}\right]}{\left[\frac{I_{\text{in}}^2}{\sigma_{\text{in}}^2}\right]} = \frac{1}{NR_{\text{out}}^2} \tag{1}$$

where $I$ and $\sigma$ represent the input ($I_{\text{in}}$) and output ($I_{\text{out}}$) intensities and the input ($\sigma_{\text{in}}$) and output ($\sigma_{\text{out}}$) standard deviations of the signal intensities, $N$ is the number of incident X-ray photons and $R_{\text{out}}$ is the relative variance of the output signal. A detector with a DQE of 50% has to count twice the time a detector with a DQE of 100% has to count to record a signal of equal variance.

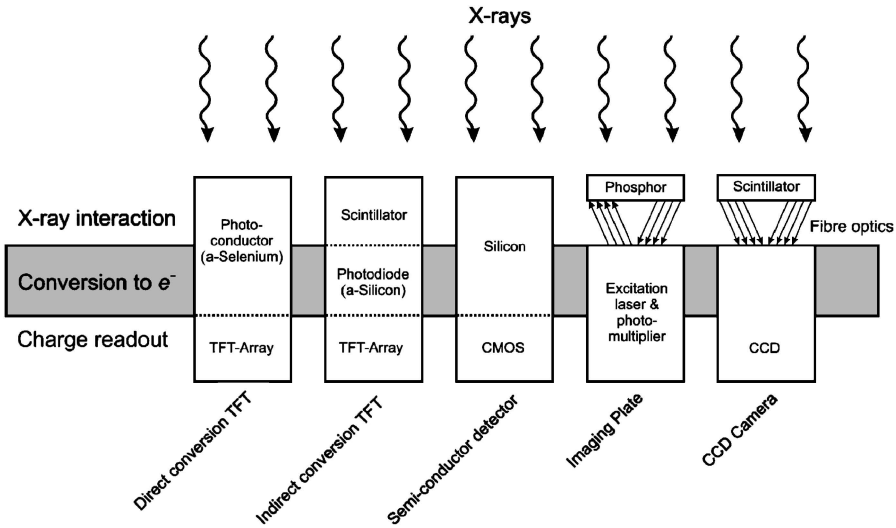



**Figure 14.1** Detector types. Five different detector designs are shown in their fundamental units. (This is an adaptation of an image in ref. 4.)

The *spatial response* characteristics[3] are normally characterized by the point spread function (PSF) – the detector's signal following a delta function stimulus. Ideally the point spread is also a delta function. Experimentally this is seldom the case as detector characteristics generally give the signal a Gaussian spread. It is often the point spread function that is the main cause of the limited resolution in powder diffraction experiments.

The *size* of the detector is an important factor, determining the size of the accessible reciprocal (or q-) space. Larger detectors offer a greater area and thus a greater q-space that can be imaged in one exposure. Greater size also opens the possibility of moving the detector further from the sample to improve resolution.

*Speed* is of ultimate importance when acquiring data at a synchrotron beam line. The readout time should be minimal to ensure a high time resolution for *in situ* experiments and a most efficient use of the costly synchrotron rays.

The *dynamic range* of the detector limits the intensity differences that are recordable on one image. The higher the dynamic range the better one is able to characterize signals having a strong contrast.

### 14.1.1 CCD Detectors

Probably the most widely used detector type in X-ray crystallography is the CCD camera. These detectors are in use in many fields and their general ongoing development has been of benefit to the relatively small X-ray detector segment. The great advantages of these detectors are their high resolution and short readout times. This is of importance especially in single-crystal diffraction in which dead-times can make up a great part of the measurement time. The

drawbacks stem from three basic elements of the detector. First, the fluorescent screen has to be optimized for the required wavelength: higher energy radiation requires a thicker layer to fully absorb the incident rays. Thicker layers are disadvantageous as the PSF increases with the thickness of the layer due to the spherical dissipation of excited electrons within the fluorescent layer. Second, fibre optical tapers channel the light from the large fluorescent layer to the smaller CCD chip. The tapering often leads to an imperfect representation of the original image onto the CCD. This has to be corrected as much as possible within the detector electronics (firmware). Some detectors have a CCD area of equal size to the fluorescent layer and can circumvent this source of errors. Finally, one major drawback is the substantial dark current from the CCD chip, which requires permanent cooling to reduce.

### 14.1.2 Imaging Plate Detectors

Imaging plates were the first digital technology to replace films in synchrotron and laboratory equipment. The concept is extremely simple. A layer of $BaF(Br,I):Eu^{2+}$ which contains colour centres is deposited on a robust film-like base "plate". The plate is then exposed to X-rays. The image is later scanned by an online, or a more cumbersome offline, scanner. Scanning the image consists of exciting the colour centres and then detecting the induced radiation. Stimulating colour centres does not require much energy, generally red lasers suffice. The stimulated green light is detected by a photomultiplier following the path of the laser.

The great advantages of imaging plates are their large size, low cost and their high dynamic range. The latter quality has made it the detector of choice for two-dimensional powder diffraction. Their major drawback is the high dead time associated with the time-consuming scanning. This can take the best part of two minutes for large images. Rigaku MSC has developed a practical solution to this problem. The detector system consists of two or even three detectors. When one is being scanned the other can be exposed. A precision rotation system transports the imaging plate from one position to the other. The future for this detector type does seem rather bleak, though, especially in view of flat panel detectors and the single photon counting hybrid pixel detectors.

### 14.1.3 Flat Panel Detectors

Thin film transistor (TFT) arrays are produced inexpensively and in large numbers for use in modern computer monitors and televisions. This readout system can be combined with amorphous hydrated silicon or amorphous selenium which is deposited over the large surface of the TFT array and acts as the X-ray conversion layer. Having established themselves firmly as an X-ray detector for medical imaging already, they have until now failed to make an impact on the field of crystallography,[5] their high noise level being the main drawback. It can be surmised with some confidence that this type of detector will become standard equipment in the near future.

A very general categorization into direct and indirect conversion types can be made for these detectors.[4] With direct converters X-rays are transformed into electrons in a single step, *e.g.* by a layer of amorphous selenium. One further step is required for the indirect sensors: here a scintillating layer (photoconductor) converts the X-rays into visible light, which is in turn converted into an electronic charge by a further amorphous silicon layer. This brings with it the inevitable resolution loss associated with the radial diffusion of photons and again their interaction with the amorphous silicon. As with all detection layer systems they can be optimized using various layer thicknesses and scintillating substances, which can be selected according to the X-ray wavelength and the photon detection properties of the lower layer. Currently, vapour grown CsI:Tl is an extremely popular material. It grows in columnar structures and can act as a guide in a similar fashion to fibre optics, thereby reducing lateral scattering. Its high atomic number secures a high X-ray absorption and thus good conversion. Other materials under study as possible photoconductors are $HgI_2$, $PbI_2$ and CdZnTe (CZT). Especially, CZT, grown using a high-pressure Bridgeman technique, has been rapidly implemented in a wide variety of medical detectors.[6]

### 14.1.4 Hybrid Pixel Detectors

Silicon pixel array detectors are based, as the name suggests, on silicon as the primary detecting layer. The photoelectric effect causes one electron/hole pair to be created for each 3.65 eV of incident X-rays. This leads to 3220 electrons from each X-ray photon at 12 keV in a one millimetre layer, which absorbs 98% of that radiation. In contrast a CCD would only produce roughly 10 electrons. The readout time of a few nanoseconds also contrasts impressively with all other detector systems. Further, no distortions are to be expected as no intermediary tapering or disconnected readout systems are involved. Despite these overwhelming advantages the price of prototyping and the expense of the readout electronics design has inhibited the speedy development of this detector type. Nevertheless, a few groups have been working on realizing a detector specifically for crystallography. Christian Broennimann *et al.*[7,8] have succeeded in building a six mega-pixel detector for protein crystallography with a pixel size of $172 \times 172\,\mu m^2$. Although this might be larger than the pixels of a CCD the perfect point spread function of a single pixel still represents a marked resolution improvement over the CCD detector types. The detector was built up of an array of 18 modules covering a total area of $210 \times 240\,mm^2$. A full frame readout time of this detector takes 6.7 ms, allowing a continual rotation single-crystal data collection without the shutter closing between frames.

Detectors of this type are already in operation[9] in the field of powder diffraction. Large manufacturers of diffraction equipment have these detectors among their products, disappointingly, though, reduced to point detectors and not implemented as area detectors. An installation at the material science beam line at the Swiss Light Source (SLS) of the Paul Scherrer Institute (PSI) in Switzerland is an equatorial type detector, covering a fixed angle of 60° in $2\theta$. Again, this is not a real two-dimensional detector. It has a faster readout time

than the two-dimensional detector mentioned earlier and can acquire entire diffractograms in a fraction of a second. Most probably this type of detector will establish itself in the field of two-dimensional diffraction.

## 14.2 DIFFRACTION GEOMETRY

Early powder diffraction experiments relied mostly on the Debye–Scherrer experiment to record a diffractogram. A broad film strip set into a cylindrical chamber produced the first known two-dimensional powder diffraction data. In contrast to modern methods the thin equatorial strip was the only part of interest and intensities merely optically and qualitatively analysed. This changed drastically with the use of electronic scintillation counters. Intensities were no longer a matter of quality but quantity. Inevitably the introduction of intensity correction functions long known to the single-crystal *metier*, *i.e.* Lorentz and polarization corrections (see Section 14.3), made their way into the field of powder diffraction.

Continuous detector development brought about the next revolution in the field of powder diffraction. Large area detectors made their debut in powder diffraction at synchrotron beam-lines in the beginning of the 1990s, having first been used in the field of single-crystal diffraction. First experiments only utilized thin equatorial strips[10] of the image but with the introduction of freely available software,[11] the integration of the entire image to a standard one-dimensional powder diffraction pattern became commonplace.

The term two-dimensional powder diffraction does not imply any specific geometry; it merely states the two-dimensionality of the detected signal. Conceivably, this detector could be cylindrical, as in a Weissenberg camera. Such detectors are still common in modern single-crystal diffractometers in both standard laboratories[12] as well as at neutron beam-lines;[13] however, the concept has never gained great popularity in the modern powder diffraction field. The ubiquity of large flat image plate detectors, their unparalleled dynamic range as well as a speedy read-out time are the reasons for their current prominence in the field.

A precise determination of the experimental geometry is a prerequisite for highly accurate and well-resolved diffraction angles, peak profiles, absorption effects or even good filtering. Especially, the separation of micro-structural effects from the instrumental contribution to the peak profile needs exact $2\theta$ values. An accurate calibration remains the single most significant factor in the extraction of high quality powder diffractograms from two-dimensional images.

Generally the detectors are set up perpendicular to the primary beam, with the intersection of the primary beam at the detector centre. This setting has some advantages: the entire Bragg cones are detected and the deviation of the cone projection from an ideal circle is usually small. Sometimes a detector can be placed off-centre and non-orthogonally to the primary beam. This can enlarge the detectable q-space in a very cost effective manner. The downsides are the strongly elliptical conical projections and the loss of the entire azimuthal information of a diffraction cone.

Extraction of standard powder diffractograms from two-dimensional images requires knowledge of the diffraction angle at each pixel. These angles have to be known to a precision equal to or less than the detector resolution. The detector resolution is mainly governed by the point spread function (PSF). In addition the calculation of air absorption would require the sample to pixel distance in each case. The azimuthal angle is vital for the application of the Lorentz and polarization corrections, as is the incident angle for a detector dependent correction. The next section deals with the derivation of all possible geometrical values that could be of importance during data reduction.

### 14.2.1 Resolution and FWHM in Two-dimensional Diffraction

The resolution of a two-dimensional detector is governed to a dominant extent by the PSF. This can be very well observed by the behaviour of the FWHM distribution of reflections over an image plate. The PSF of a standard image plate is roughly 300 μm. The projection $\Delta l$ of the diffracted beam width $d$ on the image plate in the case of a fully parallel beam is given by:

$$\frac{d}{\cos(\Psi)} = \Delta l \tag{2}$$

This would result in the projection of the diffracted beam leaving a larger footprint on the image plate at higher incident angles ($\Psi$); we should therefore expect higher FWHM of the diffracted beams at higher incident angles. Experimentally we find an inverted relation. How can this seemingly aberrant behaviour be explained? The answer lies in the PSF of the detector. Detectors do not resolve differences in the half-width of the incident beam if they lie well below the point spread of the detector. The increasing footprint of the incident beam is overshadowed by the detectors point spread, thus leading to no discernable angle dependence. So it is no surprise that with changing incident angle and sample distance the "number of points (pixels) across the peak . . . is not changed".[10] The reduction in the FWHM of the diffracted X-rays at higher incident angles is more intrinsically connected to the angular resolution per pixel (Figure 14.2).

Taking into account both the effect of the incident angle and the distance of the detector from the sample, the resolution of an experimental set-up can be calculated as the half-width (FWHM) of the diffracted beam by its diffraction angle ($2\theta$), the PSF of the detector and the sample to detector distance ($D$) (Figure 14.3). For simplicity we assume that the detector tilt is negligible. The radius is then related to the sample detector distance and the diffraction angle by the following equation (see Figure 14.5):

$$D \tan 2\theta = r \tag{3}$$

Adding the FWHM resulting from the point spread contribution would lead to:

$$D \tan(2\theta + FWHM) = r + PSF \tag{4}$$

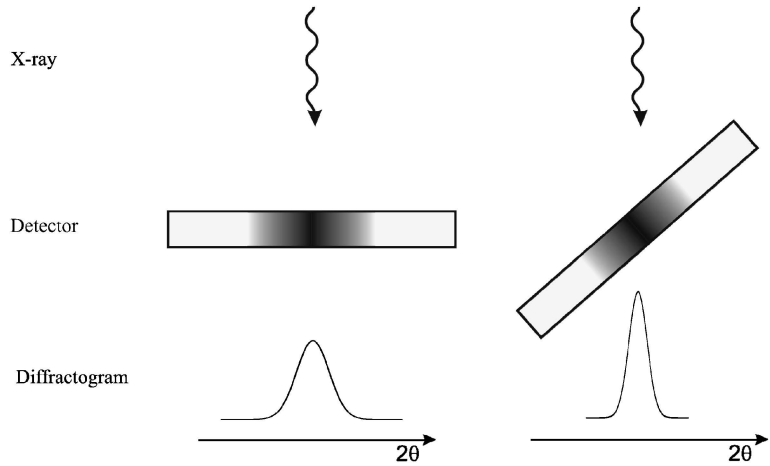



**Figure 14.2** Effect of the incident angle on the sharpness of the final angular projection. The point spread of the detector does not change. The difference in the angular resolution between the perpendicular and the tilted detector is the cause of the sharper peak.

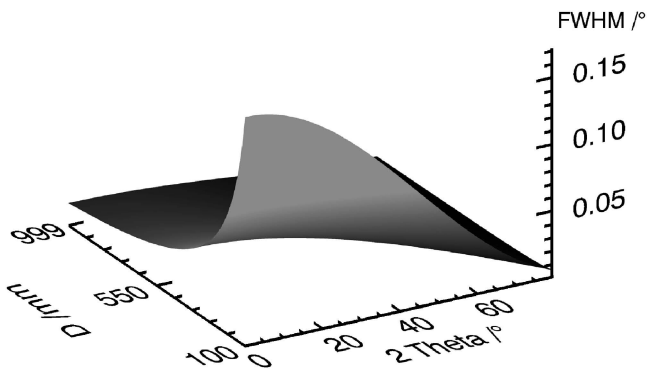



**Figure 14.3** Effect of the point spread of a two dimensional detector upon the FWHM of a diffracted beam. The detector is assumed to be ideally aligned normal to the primary beam. The point spread is taken to be 300 μm. Sample contributions to the peak width have not been considered.

As Equation (3) still holds Equation (4) would become:

$$D\tan(2\theta + FWHM) = D\tan 2\theta + PSF \tag{5}$$

Solving for FWHM in terms of $2\theta$ and the PSF then leads to:

$$FWHM = \arctan\left(\frac{D\tan 2\theta + PSF}{D}\right) - 2\theta \tag{6}$$

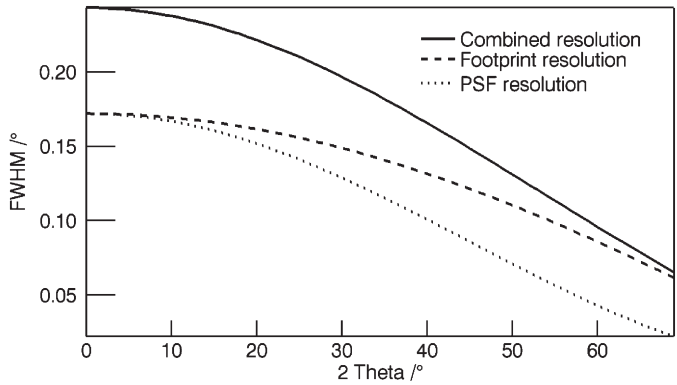



**Figure 14.4** An example of the resolution contributions of an ideally aligned typical image plate detector placed 100 mm from the sample. The footprint of a 0.3 mm diffracted beam and the PSF of 0.3 mm of the detector contribute varying amounts to the resolution over the diffraction angle range.

To show the effect of the PSF on the FWHM of a diffracted beam a surface spanning a $2\theta$ range from $0^\circ$ to $80^\circ$ and a detector distance range from 100 to 1000 mm has been calculated, estimating the point spread to be 300 μm (see Figure 14.4)

The detector resolution can be estimated as a convolution of the footprint with the PSF. Placing this in Equation (6) would lead to the following formula, again for an idealized non-tilted detector:

$$FWHM = \arctan\left(\frac{D\tan 2\theta + PSF_{conv}}{D}\right) - 2\theta \tag{7}$$

As both the footprint and the PSF can be described by a Gaussian function the FWHM of their convolution is given by:

$$PSF_{conv} = \sqrt{PSF^2 + (d\sec 2\theta)^2} \tag{8}$$

The resolution is computed for a typical image plate PSF of 0.3 mm, a FWHM of the diffracted beam of 0.3 mm, and a sample to detector distance of 100 mm, for a diffraction angle range from $0^\circ$ to $70^\circ$ (see Figure 14.4).

It is possible to estimate the line width of the diffraction experiment by knowing the width of the diffracted beam, the PSF of the detector and the distance to the detector. Adding tilt to the two-dimensional detector makes the situation a lot more complicated. Essentially an azimuthal factor is added to the incident angle as well as to the angular resolution, which results in an azimuth-dependent FWHM of the diffraction image. The dependence of the line width on the detector orientation is given in its complete form by Equation (9). This equation is deduced in the same manner as Equation (6), starting, however, from the more complex formulation of a tilted detector given

by Equation (13):

$$\begin{aligned} FWHM = & \\ & \arctan\sqrt{\frac{(x_{PSF}\cos(rot)+y_{PSF}\sin(rot))^2\cos^2(tilt)+(y_{PSF}\cos(rot)\quad x_{PSF}\sin(rot))^2}{(D+(x_{PSF}\cos(rot)+y_{PSF}\sin(rot))\sin(tilt))^2}} \\ & -\arctan\sqrt{\frac{(x\cos(rot)+y\sin(rot))^2\cos^2(tilt)+(y\cos(rot)\quad x\sin(rot))^2}{(D+(x\cos(rot)+y\sin(rot))\sin(tilt))^2}}, \\ & x_{PSF}=x+PSF, y_{PSF}=y+PSF \end{aligned} \tag{9}$$

For a precise explanation of the terms *rot* and *tilt* please refer to Figures 14.6 and 14.8. The line width can also be expressed in the more general terms of diffraction angle ($2\theta$), azimuthal angle ($\alpha$), detector orientation ($D$, *rot*, *tilt*) and the detector point spread (*PSF*). To deduce the formula we start with Equation (3) but alter it to fit a tilted detector. This implies adding a distance $z$ to the sample to detector distance. It represents the change of the distance to the reflection point on the detector projected onto the primary beam vector. This change is brought about by the tilt and can easily be derived as is shown in Figure 14.7a. The factor narrowing the effective width of the tilted beam (Figure 14.2) has to be added, leading to the modified form of Equation (5):

$$(D+z)\tan(2\theta + FWHM\cos(tilt(\cos\alpha))) = (D+z)\tan 2\theta + PSF \tag{10}$$

The change in distance is given by the following equation:

$$z = r\sin(tilt) \tag{11}$$

The radius has been derived and is given below by Equation (38). Substituting all values of $z$ and $r$ in Equations (11) and (10), solving for the FWHM and simplifying leads to the fundamental formulation of Equation (10):

$$\begin{aligned} FWHM &= \operatorname{arc\,cot}\left(\frac{num}{den}\right)\sec(tilt\cos\alpha) - 2\theta, \\ num &= D + D(\cos\alpha + \cos(tilt)\tan(tilt)\tan 2\theta, \\ den &= PSF + \tan 2\theta\begin{pmatrix} D + D\sin(tilt)\tan 2\theta \\ +\cos\alpha\tan(tilt)(PSF + D\tan 2\theta) \end{pmatrix} \end{aligned} \tag{12}$$

Such a situation can be simplified only if a thin Debye–Scherrer type strip along an azimuthal angle is considered.[10]

When using focusing optics[14] the detector distance to the optics is fixed and the focal spot of the beam well below the PSF of the detector. The resolution is governed solely by the PSF of the detector. To decrease the resulting line width the only solution is to increase the distance between the sample and the detector, as tilting the detector would move it out of the focal point.

### 14.2.2 Diffraction Angle Transformation

The fundamental function relating the non-orthogonality of the detector to the primary beam and the sample to detector distance into diffraction angles is

given by Equation (13). This equation can easily be deduced from two rotations of the plane out of its position orthogonal to the cone axis. The first rotation is performed around the $x$-axis. As can be seen in Figure 14.5, it causes the conic section to become elliptical. The axis of the cone now intersects the plane at a focal point of the ellipse. What was the radius in the circular conic section now has become the semi-latus rectum (Figure 14.10). A second rotation is performed around the plane normal centred on the focal point which is the intersection of the cone axis. The effect of this rotation is shown in Figure 14.8. This transformation provides a general formulation of a conic section using experimentally accessible parameters,

$$2\theta = \arctan\sqrt{\frac{\cos^2(tilt)\Big((x\cos(rot)+y\sin(rot))^2+(-x\sin(rot)+y\cos(rot))\Big)^2}{(D+\sin(tilt)(x\cos(rot)+y\sin(rot)))^2}} \tag{13}$$

The parameters $x$, $y$, *tilt*, *rotation* and $D$ are depicted in Figures 14.5–14.8. A derivation of this equation is given in ref. 11 and is described with the aid of Figures 14.5–14.8. A good overview of the transformations involved in calculating the conic section can be found in ref. 15. However, in that work three angles are used to describe the detector orientation relative to the

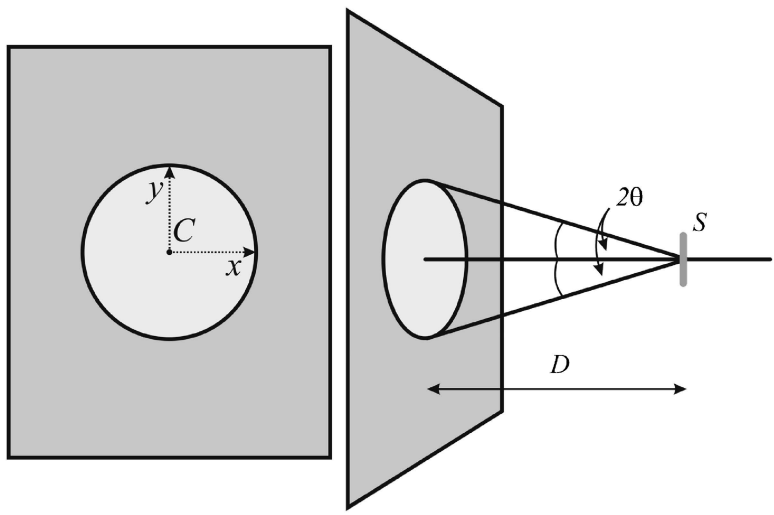



**Figure 14.5** A circular conic section resulting from an orthogonal detector to primary X ray beam setting. On the left is a view perpendicular to the detector, on the right is a side view, showing the primary beam entering from the right. The primary and diffracted beams from the sample S intersect the detector on the detector plane. The primary beam intersects the detector at the centre of the circle. For clarity only one diffraction cone has been drawn. The distance from the sample to the detector along the primary beam is given by $D$. The detector coordinate system is denoted in $x$ and $y$ relative to the beam centre.

scattering cone. As any detector orientation can be described by two angles alone, this is the transformation we chose to use.

Figure 14.5 displays a conic section normal to the cones axis. The diffraction angle, which is half the cone opening angle, is given by Equation (14). All the coordinates are given in the cone coordinate system wherein $z$ is the cone axis, and $x$ and $y$ describe the plane perpendicular to it. The position of the plane is at a distance $D$ from the cone's apex along the cone axis:

$$x^2 + y^2 = D^2 \tan^2 2\theta \tag{14}$$

In our case the cone axis is synonymous with the primary beam. For the conic section to change from a circle to an ellipse the angle between the plane normal and the cone axis has to be greater than zero.

This is realized in Figures 14.6 and 14.7 by rotating the cone axis around the horizontal plane axis, this is equal to the $x$-axis. For compatibility with the established formulation[11] the detector is tilted around the $y$-axis. The coordinate system changes to that of the tilted detector and is denoted by $x'$ and $y'$ (Figure 14.7):

$$\left(\frac{Dx'\cos(tilt)}{D + x'\sin(tilt)}\right)^2 + \left(\frac{Dy'}{D + x'\sin(tilt)}\right)^2 = D^2 \tan^2 2\theta \tag{15}$$

Equation (15) then simplifies to Equation (16):

$$x'^2 \cos^2(tilt) + y'^2 = (D + x'\sin(tilt))^2 \tan^2 2\theta \tag{16}$$

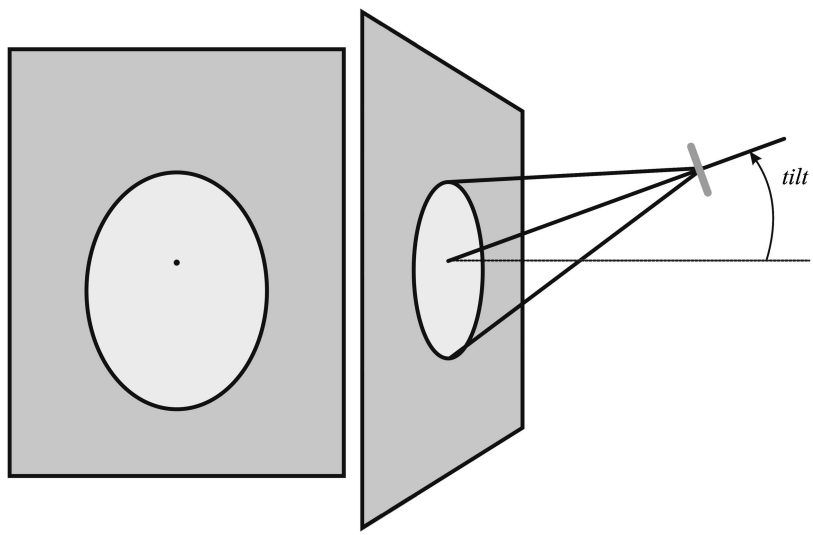



**Figure 14.6** Elliptical conic section resulting from a tilting of the detector around a horizontal axis. This results in an ellipse that is mirror symmetrical along the central vertical axis.

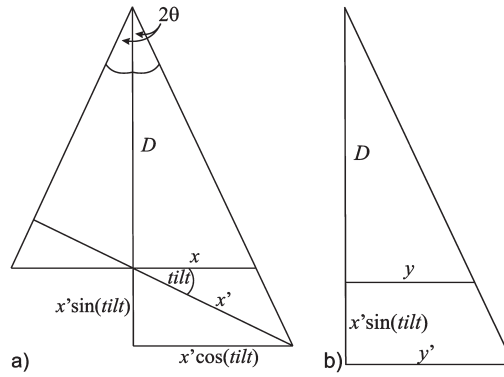



**Figure 14.7** Constructions after Kumar[15] to deduce the tilted $x'$ and $y'$ values in terms of the orthonormal $x$ and $y$ values. (a) The construction used to calculate the relation between $x$ and $x'$. The similarity of the triangle spanned by $D$ and $x$ (small triangle), and the triangle spanned by $D + x\ \sin(tilt)$ and $x'\cos(tilt)$ is used to set up the relation. (b) The construction used to elucidate the relation between $y$ and $y'$. Here again the similarity of the smaller and larger triangles is used to set up the relation.

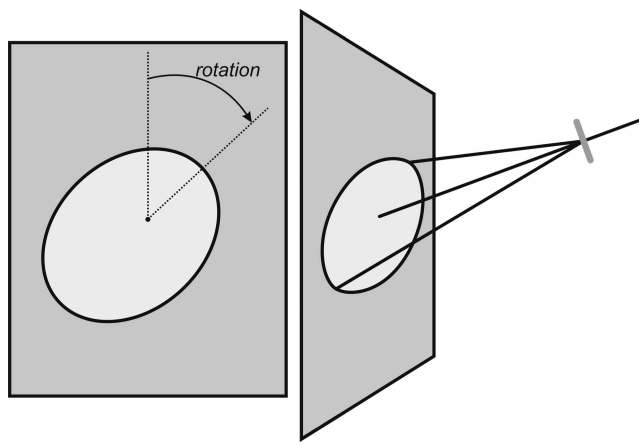



**Figure 14.8** General description of an arbitrary tilt. The added rotation angle suffices to describe any possible detector tilt.

Adding a rotation angle around the normal to the focus of the ellipse leads us to the general ellipse represented in Figure 14.8.

This adds a cosine and a sine term of the rotation to the $x$ and $y$ values in the following form. Again a separate notation is used to denote the rotated values $x''$ and $y''$:

$$\begin{aligned} x' &= x'' \cos(rot) + y'' \sin(rot) \\ y' &= y'' \cos(rot) - x'' \sin(rot) \end{aligned} \tag{17}$$

On inserting these rotational equations into Equation (16) one obtains Equation (18):

$$\begin{aligned}&(x''\cos(rot)+y''\sin(rot))^2\cos^2(tilt)+(y''\cos(rot)-x''\sin(rot))^2\\&\quad=(D+(x''\cos(rot)+y''\sin(rot))\sin(tilt))^2\tan^2 2\theta\end{aligned}\tag{18}$$

Equation 18 can be rearranged to the initial form equalling Equation (13).

$$2\theta=\arctan\sqrt{\frac{(x''\cos(rot)+y''\sin(rot))^2\cos^2(tilt)+(y''\cos(rot)-x''\sin(rot))^2}{(D+(x''\cos(rot)+y''\sin(rot))\sin(tilt))^2}}\tag{19}$$

### 14.2.3 Incident Angle and Ray Distance Calculations

The incident angle of the reflected beam onto the detector is utilized in a factor often described as correcting for the flatness of a detector. The diffracted beam penetrates into the image plate or fluorescent layer of the detector. The penetration length depends on the angle of incidence and the linear attenuation factor for the utilized wavelength and fluorescent material.

As can be seen from Figure 14.9 the minimum and the maximum incident angle are given by Equation (20):

$$\begin{aligned}\Psi_{\min}&=2\theta-tilt\\\Psi_{\max}&=2\theta+tilt\end{aligned}\tag{20}$$

The tilt can be replaced with the effective tilt, $tilt_{eff}$ according to:

$$tilt_{eff}=tilt\sin(\alpha-rot)\tag{21}$$

resulting in an effective incident angle of:

$$\Psi_{eff}=2\theta-tilt\sin(\alpha-rot)\tag{22}$$

To determine the distance of the diffracted ray from the sample to each point on the detector we use the construction presented in Figure 14.9. Application of the sine rule results in Equation (23):

$$\frac{\sin(90^\circ-\Psi)}{D}=\frac{\sin(180^\circ-2\theta-(90^\circ-\Psi))}{\text{ray distance}}\tag{23}$$

This simplifies to:

$$\text{ray distance}=D(\cos 2\theta+\sin 2\theta\tan\Psi)\tag{24}$$

### 14.2.4 General Transformations

As most pattern recognition algorithms use conventional geometric parameters of ellipses, namely semi-major and semi-minor axes and eccentricity, this section will deduce all the necessary transformations between the

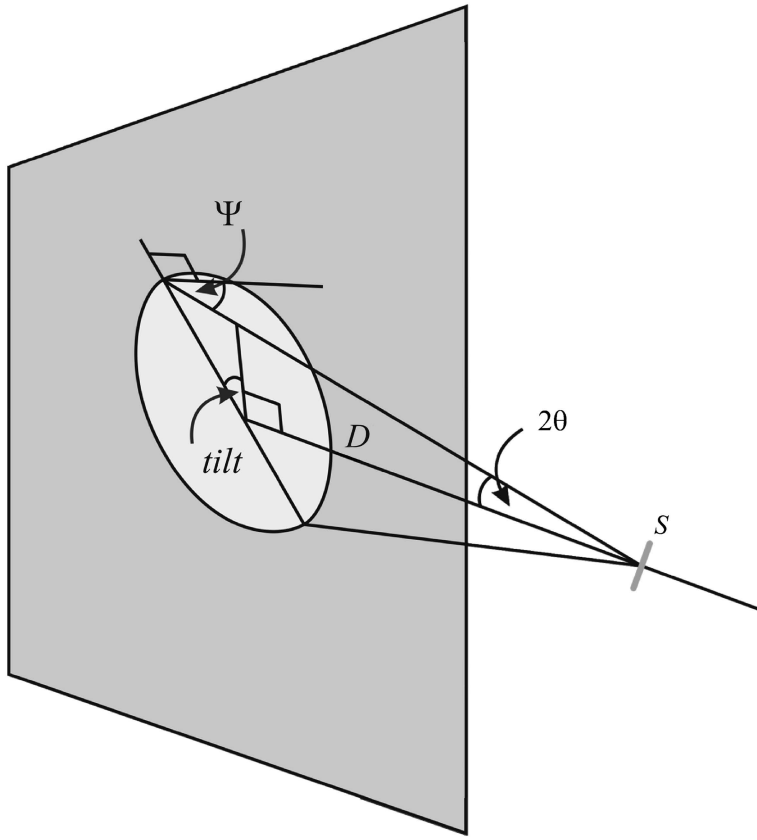



**Figure 14.9** Incident angle calculation. The small triangle containing the complementary angle to the incident angle Ψ and *tilt* is used to deduce the formula for the calculation of the incident angle.

crystallographic and standard systems. Further transformations are needed to calculate the exact Cartesian coordinates of a reflection on the detector. This corresponds to the determination of $x,y = f(2\theta,\alpha,D,tilt,rot,X_0,Y_0)$. This information is important for calculating and plotting theoretical ellipse positions.

The semi-latus rectum is independent of the tilt and can be given in terms of the scattering angle and the sample to detector distance as in Equation (25):

$$D \tan 2\theta = l \tag{25}$$

From Figures 14.9, 14.10 and the sine rule we can deduce the following relation:

$$\frac{\sin(2\theta)}{a-c} = \frac{\sin(90^\circ - 2\theta + tilt)}{D} \tag{26}$$

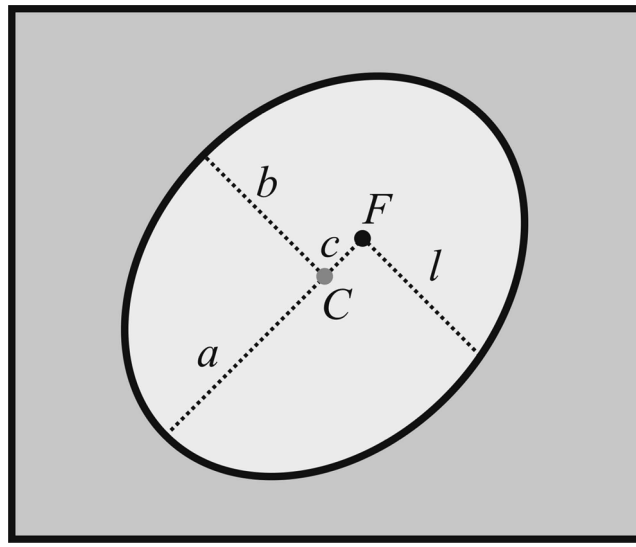



**Figure 14.10** Common ellipse parameters. The centre is denoted by $C$, one focal point by $F$, the semi major axis by $a$, the semi minor axis by $b$ and the semi latus rectum by $l$.

This can be reformulated as:

$$c = a - D\sec(tilt - 2\theta)\sin 2\theta \tag{27}$$

However, we also know from Figures 14.9, 14.10, and the sine rule, that the following relation holds:

$$\frac{\sin(2\theta)}{a+c} = \frac{\sin(90^\circ - 2\theta - tilt)}{D} \tag{28}$$

This can be reformed to:

$$c = -a + D\sec(tilt - 2\theta)\sin 2\theta \tag{29}$$

Setting Equations (27) and (29) and equal and solving for $a$ leads to the following formulation:

$$\frac{D\cos(tilt)\sin 4\theta}{\cos(2tilt) + \cos 4\theta} = a \tag{30}$$

The same method can be used to find an expression of $c$ in alignment variables. This leads to the very similar formulation:

$$\frac{2D\sin(tilt)\sin^2 2\theta}{\cos(2tilt) + \cos 4\theta} = c \tag{31}$$

$$al = b^2 \tag{32}$$

Because of the well-known identity Equation (32) the semi-minor axis can be described using the scattering angle, the tilt and the detector to sample distance, as given in Equation (33):

$$\frac{D\sqrt{\cos(tilt)}\sqrt{\sin 2\theta}\sqrt{\tan 2\theta}}{\sqrt{\cos(2tilt)+\cos 4\theta}} = b \tag{33}$$

Now $a$ and $c$ can be inserted into the well-known identity $e = c/a$ to denote the eccentricity in calibration parameters:

$$\tan(tilt)\tan 2\theta = e \tag{34}$$

*14.2.4.1 Detector Coordinate Transformations.* We now attempt to deduce the detector coordinates from the calibration values and the reflection parameters. Some well-known elliptical identities:

$$e = \sqrt{1-\frac{b^2}{a^2}} \tag{35}$$

$$c = \sqrt{a^2 - b^2} \tag{36}$$

shall be used in these calculations. The ellipse radius as measured from the focus can be described in terms of eccentricity, semi-major axis and the angle of the azimuth:

$$r_{focus\ \ ellipse} = \frac{a(1-e^2)}{1+e\cos(\alpha)} \tag{37}$$

Inserting Equation (34) into Equation (37) leads to:

$$r_{focus\ \ ellipse} = \frac{D\tan 2\theta}{1+\cos\alpha\tan(tilt)\tan 2\theta} \tag{38}$$

The Cartesian coordinates take the following values:

$$y_d = r_{focus\ \ ellipse}\sin(\alpha - rot) \tag{39}$$

$$x_d = r_{focus\ \ ellipse}\cos(\alpha - rot) \tag{40}$$

Here $x_d$ and $y_d$ are the $x$ and $y$ positions relative to the focus. The ellipse has been made non-parallel to the axes by subtracting the rotation from the azimuth angle.

## 14.3 INTENSITY CORRECTIONS

As important as the diffraction angles are to the exact lattice parameters, the intensities are crucial for the precise determination of atomic position,

elemental species, and their occupation and displacement parameters. The great popularity of equatorial point detectors and later one-dimensional position sensitive detectors in laboratory diffractometers has hindered the spread of generally applicable correction formulae for 2D geometries and canonized equatorial specific corrections. These are often incorrectly applied to data collected from two-dimensional detectors. Important experimental factors influencing the intensity of a diffracted beam are discussed and the corresponding two-dimensional correction functions are given.

### 14.3.1 Lorentz Corrections

Lorentz corrections applied to powder diffraction data are slightly different to those applied to single-crystal data. Whereas the single-crystal correction only consists of a rotational factor, the powder correction contains an additional statistical factor.[24] This corrects for the likelihood of a crystallite being in diffraction position. This factor has a simple $(\sin\theta)^{-1}$ dependence, and is found in the common Lorentz correction

$$L^{-1} = \sin 2\theta \sin\theta \tag{41}$$

The well-known correction for the speed of the transition of a reflection through the Ewald membrane is attributed to a lecture given by Lorentz.[25] In its form applicable to a perfect single crystal it normalizes the intensity of a single reflection to the shortest traversal of the Ewald sphere. This motion is brought about by the rotation of the crystal in direct space. A consequence is that the correction is not only dependent upon the rotation vector of the crystal but also on the detection method. The general formulation takes the form:

$$|F_{hkl}|^2 \propto (\mathrm{d}z/\mathrm{d}s) \int I_{xy}(s)\mathrm{d}s \tag{42}$$

Here $I_{xy}$ is the reflection intensity measured as a function of a scan variable $s$; $z$ is the direction normal to the Ewald sphere at the reflection position. Integrating over $s$ for a typical four-circle diffractometer[26] and approximating sine and cosine values for the small angular range of a reflection leads to the following formalism:

$$L^{-1} = -\begin{pmatrix} \Delta\omega_i \sin\gamma \cos\nu + \Delta\chi_i \sin\omega \sin\nu + \\ \Delta\varphi_i(\cos\chi \sin\gamma \cos\nu - \cos\omega \sin\chi \sin\nu) \end{pmatrix} \tag{43}$$

When regarding rotation around a single axis, an experimental set-up most commonly used in two-dimensional powder diffraction, the function reduces to:[16]

$$L^{-1} = \cos\mu \sin\gamma \cos\nu \tag{44}$$

where $\mu$ = angle between axis of sample rotation and the primary beam normal plane, $\gamma$ = angle of horizontal reflection displacement and $\nu$ = angle of vertical reflection displacement.

The well-known equatorial form of Equation (44) is obtained when setting the axis of rotation perpendicular to the primary beam and reducing the vertical displacement to zero. $\gamma$ is then the diffraction angle:

$$L^{-1} = \sin 2\theta \tag{45}$$

Reduction from the two-dimensional form to the one-dimensional equatorial form was a requirement of the equatorial diffractometer geometries utilizing point detectors or at most linear position sensitive detectors. Importantly, this correction is neither applicable to the Bragg–Brentano nor to the flat transmission geometry, but is only valid for the Debye–Scherrer geometry.

With the onset of area detection in powder diffraction a two-dimensional correction has to be applied (Figure 14.11). A formulation of Equation (44) independent of the more accessible scattering angle $2\theta$ and the azimuthal angle $\alpha$ has been derived:

$$L^{-1} = \cos\mu \frac{\cos\alpha \tan 2\theta}{\sqrt{1 + \cos^2\alpha \tan^2 2\theta}\sqrt{1 + \sin^2\alpha \tan^2 2\theta}} \tag{46}$$

Combining this with the statistical factor leads to the general formulation of the Lorentz correction for powder samples rotated within the beam:

$$L^{-1} = \sin\theta \cos\mu \frac{\cos\alpha \tan 2\theta}{\sqrt{1 + \cos^2\alpha \tan^2 2\theta}\sqrt{1 + \sin^2\alpha \tan^2 2\theta}} \tag{47}$$

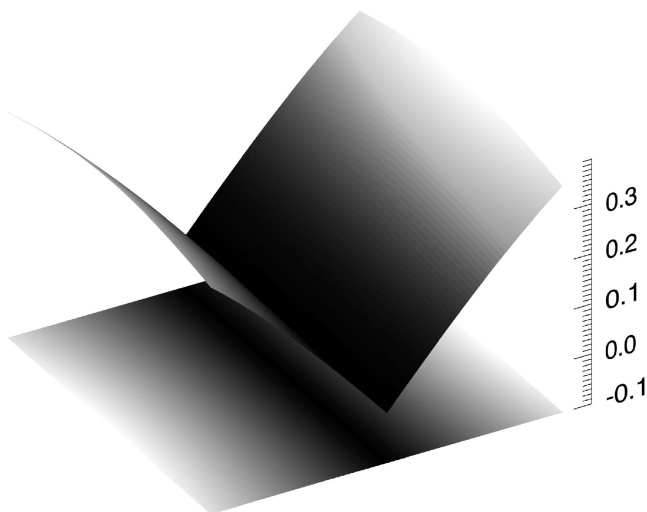



**Figure 14.11** Two dimensional single crystal Lorentz correction for an ideally aligned detector. Note the zero values in the central valley. These cause divergent intensities as they are multiplied with the inverse of the Lorentz correction. Therefore, the intensities in that region have no meaning. The central valley is parallel to the sample rotation axis.

*Lorentz Correction for Highly Collimated Beams.* The rotational correction should be used if the powder sample is rotated within the beam *in the single crystal sense*, *i.e.* all crystallites should complete their rotation within the beam. Should the beam be collimated to dimensions below those of the sample containment then this further reduces the rotational impact on the cumulative Lorentz factor. A term $R_L$ can be introduced to quantify the rotational Lorentz factor from 0 for no rotational element to 1 for full rotation of all crystallites within the beam (Figure 14.12). The introduction of this factor leads to:

$$L^{-1} = \sin\theta R_L \cos\mu \frac{\cos\alpha \tan 2\theta}{\sqrt{1+\cos^2\alpha\tan^2 2\theta}\sqrt{1+\sin^2\alpha\tan^2 2\theta}} \tag{48}$$

$R_L$ has been deduced for the case of the rotational axis being normal to the primary beam. The common Lorentz formulation is valid if a crystallite is rotated within the beam by $\omega = 2\pi$. For a certain number of crystallites with a rotational radius less than the beam radius this is true. Crystallites outside this radius experience a rotation $\omega_{\text{eff}}$ that is dependent upon their rotational radius and the width of the primary beam. It can be given as:

$$\omega_{eff} = 4\arcsin(W/R) \tag{49}$$

where $W$ is the beam width and $R$ is the rotational radius. As all crystallites between $R = W$ and $R = L$ (where L is capillary diameter) are affected differently by rotational radius an integration over that range has to be made:

$$\Omega_{eff} = \int_{y}^{1} \omega_{eff}(y)\mathrm{d}y = 2(\pi - 2\sqrt{1-y^2} - 2y\arcsin y), y = W/L \tag{50}$$

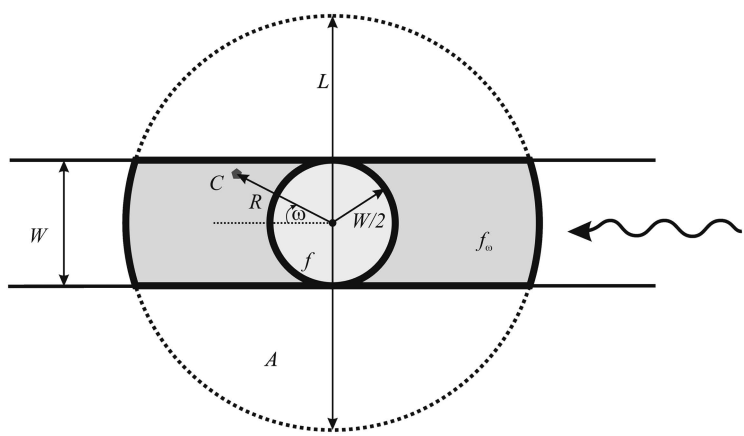



**Figure 14.12** Relative Lorentz factor. The image depicts a perpendicular section of a capillary of diameter $L$ being illuminated by a beam of width $W$. Only crystallites falling in the light grey inner circle are rotated completely (2π) within the beam. Crystallites outside this region but still within the beam path only experience a limited rotation $\omega$, thus reducing the effective single crystal Lorentz factor to be applied to them.

Interestingly, the integration tends to a value of roughly 33° as the beam width to sample radius ratio tends to zero:

$$\lim_{y\to 0}\int_{y}^{1}\omega_{eff}(y)\mathrm{d}y = \pi/2 - 1 \tag{51}$$

Now this rotation needs to be put into relation to the entire illuminated area. The normalization takes the form of the average rotational angle of the entire illuminated area relative to the full $2\pi$ rotation of the standard Lorentz correction:

$$R_L = \frac{2\pi f + \Omega_{eff} f_\omega}{2\pi(f + f_\omega)} \tag{52}$$

where $f$ is the area in which the crystallites experience a complete rotation in the collimated primary beam and $f_\omega$ is the area in which the crystallites only experience a partial rotation within the beam (Figure 14.13). These are computed in the following manner:

$$A = 1/4\left(L^2 \cos^{\ 1}\left(\frac{W}{L}\right) - W\sqrt{L^2 - W^2}\right) \tag{53}$$

$$f = 2\pi(W/2)^2 \tag{54}$$

$$f_\omega = 2\pi(L/2)^2 - f - 2A \tag{55}$$

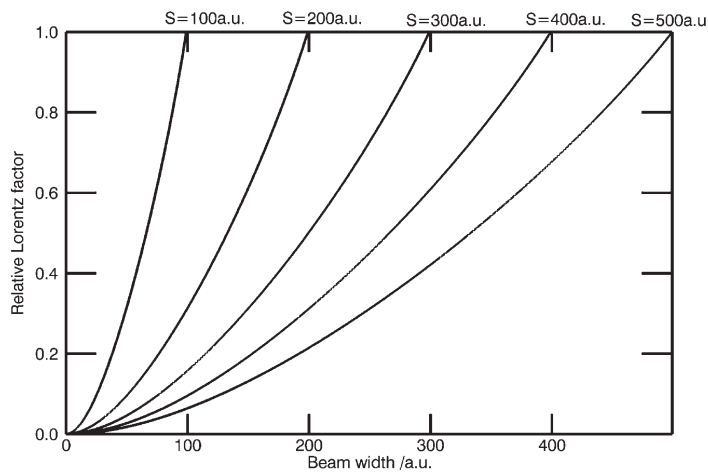



**Figure 14.13** Relative Lorentz factor. The image depicts the surface of the correction factor for a primary beam that is collimated to below the sample size. Should the primary beam be larger than the sample, the factor is unity.

Reforming Equation (55) and simplifying leads to Equation (56):

$$f_\omega = 1/2\left(L^2\pi + W\left(-\pi W + \sqrt{L^2 - W^2}\right) - L^2\cos^{\ 1}\left(\frac{W}{L}\right)\right) \tag{56}$$

Equation (52) then becomes:

$$R_L = \frac{2\pi f + \Omega_{eff} f_\omega}{2\pi\left(2\pi(L/2)^2 - 2A\right)} \tag{57}$$

When reduced to the fundamental parameters the function takes the final form of:

$$R_L \quad \frac{\pi^2 W^2 + \frac{1}{4}\left(L^2\pi + W\left(\ \pi W + \sqrt{L^2}\quad W^2\right)\quad L^2\arccos\left(\frac{W}{L}\right)\right)\left(\pi\quad 2\sqrt{1}\quad \frac{W^2}{L^2}\quad \frac{2W\arcsin\left(\frac{W}{L}\right)}{L}\right)}{\pi\left(L^2\pi + W\sqrt{L^2}\quad W^2\quad 2L^2\arccos\left(\frac{W}{L}\right)\right)} \tag{58}$$

To see the effect this correction factor has for differing beam sizes and capillaries a simple two-dimensional plot has been made. In Figure 14.13 you can see that as the beam size approaches zero so does $R_L$ approach zero, whereas when the beam size equals or is larger than the sample diameter the standard correction factor of unity is applied.

### 14.3.2 Polarization Correction

When X-rays are diffracted by a lattice plane they are partially polarized. This leads to an intensity reduction that can be expressed as a function of the diffraction angle. For a completely unpolarized primary beam this leads to the following correction:[17]

$$P = \frac{1}{2}\left(1 + \cos^2 2\theta\right) \tag{59}$$

Should the primary beam be polarized this changes the correction to:[18 21]

$$P = P_0 - P' \tag{60}$$

$$P_0 = \frac{1}{2}\left(1 + \cos^2 2\theta\right) \tag{61}$$

$$P' = \frac{1}{2}\mathrm{J}'\cos 2\alpha \sin^2 2\theta \tag{62}$$

where:

$$\mathrm{J}' = \frac{I_\pi - \mu I_\sigma}{\mu(I_\pi + I_\sigma)} \tag{63}$$

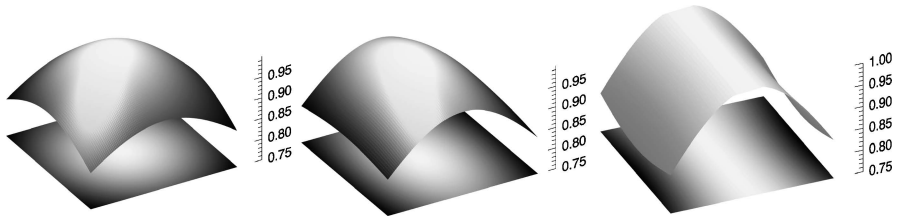



**Figure 14.14** Two dimensional polarization correction for an ideally aligned detector. The polarization factor has been set (from left to right) to 0.1, 0.5 and 0.99. The polarization correction is displayed as a three dimensional rendered surface hovering over an image depicting the same information in greyscale. The correction is applied by dividing the intensities by the displayed correction values.

Here $I_\pi$ and $I_\sigma$ are the vertical and horizontal intensities, respectively. The monochromator angle is related to $\mu$ by:

$$\mu = \cos^2 2\theta_m \tag{64}$$

With knowledge of the monochromator angle ($2\theta_m$) and that of the initial polarization of the X-ray beam one can calculate the effective polarization factor. However, it is possible to refine this parameter against two-dimensional reflection intensities, and thereby retrieve a reliable value (Figure 14.14).

### 14.3.3 Incident Angle Correction

An intensity correction based on the angle at which the reflected beam strikes the detector plane was initially proposed by Gruner[2] in his work on CCD detectors. Since then the development of this correction has been mainly driven by electron density researchers striving to attain high quality intensity data from area detectors. From Figure 14.15 it becomes clear how the incident angle affects the path of the beam through the detecting layer. The distance traversed by the beam in the detecting layer is $d/\cos\Psi$, where $\Psi$ is the incident angle and $d$ is the thickness of the detecting layer.

If the absorption of the visible light generated within the layer is disregarded then the correction[22] is independent of the detector type (CCD or IP) (Figure 14.16):

$$\begin{aligned} K &= \frac{1 - e^{\left(\frac{\mu d}{\cos\Psi}\right)}}{1 - e^{\ \mu d}} \\ &= \frac{1 - e^{\left(\frac{\ln T_\downarrow}{\cos\Psi}\right)}}{1 - T_\downarrow} \end{aligned} \tag{65}$$

with:

$$I_{\text{corr}} = I_{\text{obs}}/K \tag{66}$$

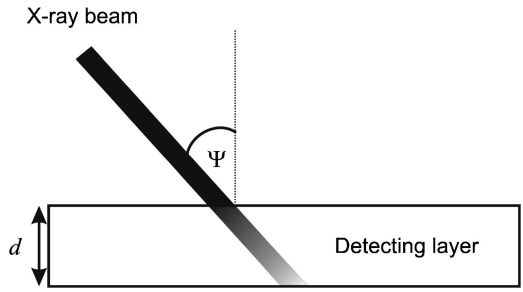



**Figure 14.15** Incident angle correction. The path of the incident ray through the detecting layer of thickness $d$ depends upon the incident angle $\Psi$. The length travelled within the layer is then $d/\cos\Psi$. This correction is necessary should the beam not be completely absorbed by the layer. Reflections at high incident angles would have a falsified higher intensity because of the greater detection length. This correction attempts to normalize the intensity to an incident reflection normal to the plain.

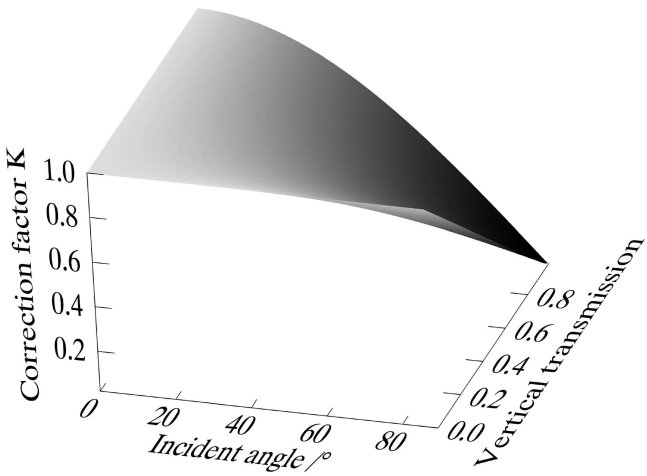



**Figure 14.16** Incident angle correction factor. The correction factor of ref. 22 has been calculated for an incident angle range from 0° to 90° and for a vertical transmission ratio from 0 to 1. The correction is applied by dividing the observed intensities by correction factor $K$. Clearly, the correction factor remains unity for complete X ray absorption as well as for incident angles of 0°.

and $T_\downarrow$ being the transmission of the detector layer at normal incidence. This leads to the complete correction function of:

$$I_\downarrow = I_{\text{obs}} \frac{1 - T_\downarrow}{1 - \mathrm{e}^{\left(\ln T_\downarrow / \cos\Psi\right)}} \tag{67}$$

An empirical correction that is used by some single-crystal diffractometers equipped with CCD cameras takes the following form:

$$K = 1 + m(1 - \cos\Psi) \tag{68}$$

Here $m$ is a coefficient that parameterizes a detector–wavelength combination. For example, a CCD detector optimized for copper radiation used $m = 0.1763$. One optimized for molybdenum radiation had $m = 0.3274$. No derivation of this formulation has to date been published.

The correction implemented in the Fit2D package[11] is given by:

$$K = \cos^3\Psi \tag{69}$$

Again no formal derivation of this correction has been published.

A more complex function for imaging plates taking into consideration additional absorption of the excitation and emitted light has been proposed:[23]

$$\begin{aligned} I_f^F(x, y, z, \nu, \kappa, \Psi) &= kI_z^x I_y^\varepsilon \\ &= kI(x, y)\exp\left[\left(-\mu_g/\cos\nu + \mu_p/\cos\kappa - \mu_y/\cos\Psi\right)z_p\right] \end{aligned} \tag{70}$$

This was reported to provide a better normalization when applied to single-crystal data collected for electron density studies of $CeB_6$. In Equation (70), $\mu_g$, $\mu_p$ and $\mu_y$ represent the linear absorption coefficients of the excitation, X-ray and emitted light within the image plate layer. The corresponding incident angles are $\nu$, $\kappa$ and $\Psi$. The vector of the incident X-ray is given by $z$.

## REFERENCES


1. E. M. Westbrook, *Detectors for Crystallography and Diffraction Studies at Synchrotron Sources*, SPIE, Denver, CO, 1999.
2. S. M. Gruner, J. R. Milch and G. T. Reynolds, *IEEE Trans. Nucl. Sci.*, 1978, **25**, 562–565.
3. C. Ponchut, *J. Synchrotron Radiat.*, 2006, **13**, 195–203.
4. H. G. Chotas, J. T. Dobbins III and C. E. Ravin, *Radiology*, 1999, **210**, 595.
5. S. Ross, G. Zentai, K. S. Shah, R. W. Alkire, I. Naday and E. M. Westbrook, *Nucl. Instrum. Methods Phys. Res. Sect. A*, 1997, **399**, 38.
6. D. G. Darambara, *Nucl. Instrum. Methods Phys. Res. Sect. A*, 2006, **569**, 153.
7. C. Broennimann, E. F. Eikenberry, B. Henrich, R. Horisberger, G. Huelsen, E. Pohl, B. Schmitt, C. Schulze-Briese, M. Suzuki, T. Tomizaki, H. Toyokawa and A. Wagner, *J. Synchrotron Radiat.*, 2006, **13**, 120–130.
8. G. Hulsen, C. Broennimann, E. F. Eikenberry and A. Wagner, *J. Appl. Crystallogr.*, 2006, **39**, 550–557.

9. F. Fauth, B. Patterson, B. Schmitt and J. Welte, *Acta Crystallogr., Sect. A*, 2000, **56**, s223.
10. P. Norby, *J. Appl. Crystallogr.*, 1997, **30**, 21–30.
11. A. P. Hammersley, S. O. Svensson, M. Hanfland, A. N. Fitch and D. Häusermann, *High Pressure Res.*, 1996, **14**, 235–248.
12. Rigaku, *Rigaku J.*, 2004, **21**, 39–42.
13. J. M. Cole, G. J. McIntyre, M. S. Lehmann, D. A. A. Myles, C. Wilkinson and J. A. K. Howard, *Acta Crystallogr., Sect. A*, 2001, **57**, 429–434.
14. R. B. von Dreele, P. L. Lee and Y. Zhang, *Z. Kristallogr.*, 2006, **23**, 3–8.
15. A. Kumar, PhD Thesis, Austin College, USA, 2006.
16. M. Buerger, *Contemporary Crystallography*, McGraw-Hill, New York, 1970.
17. H. Lipson and J. I. Langford, in *International Tables for Crystallography, Vol. C*, eds. A. J. C. Wilson and E. Prince, Springer, Chester, 1999, pp. 590–591.
18. L. Azaroff, *Acta Crystallogr.*, 1955, **8**, 701–704.
19. L. Azaroff, *Acta Crystallogr.*, 1956, **9**, 315.
20. R. Kahn, R. Fourme, A. Gadet, J. Janin, C. Dumas and D. Andre, *J. Appl. Crystallogr.*, 1982, **15**, 330–337.
21. E. Whittaker, *Acta Crystallogr.*, 1953, **6**, 222–223.
22. J. Zaleski, G. Wu and P. Coppens, *J. Appl. Crystallogr.*, 1998, **31**, 302–304.
23. K. Tanaka, T. Yoshimi and N. Morita, *Acta Crystallogr., Sect. A*, 2005 **61**, C146.
24. L. Zevin, *Acta Crystallographica, Section A*, 1990, **46**, 730–734.
25. L. Azaroff, *Elements of X-Ray Crystallography,* McGraw-Hill, 1968, New York.
26. W. R. Busing and H. A. Levy, *Acta Crystallographica*, 1967, **22**, 457–464.

CHAPTER 15

# Powder Diffraction under Non-ambient Conditions

POUL NORBY[a] AND ULRICH SCHWARZ[b]

[a] Department of Chemistry and Centre for Materials Science and Nanotechnology, University of Oslo, P.O. Box 1033, Blindern, N-0315 Oslo, Norway; [b] Max-Planck-Institut für, Chemische Physik fester Stoffe, Nöthnitzer Strasse 40, 01187 Dresden, Germany

## 15.1 INTRODUCTION

Powder diffraction is very well suited for studies at non-ambient conditions. Naturally, one of the early applications of powder diffraction was high temperature studies of phase transformations. Development of equipment for low temperature and high-pressure studies quickly followed. Later, application of powder diffraction for *in situ*, time-resolved and *in operando* studies were successfully pursued.

Powder diffraction is a non-contact and non-destructive characterization method, which allows a great deal of information regarding crystal structure, phase composition and microstructure to be obtained. It is possible to construct sample environment chambers for many types of non-ambient studies. One of the challenges in using X-ray powder diffraction for non-ambient and *in situ* studies is the need to penetrate containers and sample holders. This is for instance the case in high-pressure experiments, where X-ray radiation must penetrate, for example, a diamond anvil cell, or for *in situ* studies of catalysts, where the reaction cell may be a steel container. In addition, the need for good time resolution for time-resolved experiments has been a limiting factor. The use of neutrons, which will easily penetrate most metal containers, has made *in situ* studies of materials inside containers possible. However, large samples are needed and the low neutron flux limits the time resolution considerably. The development of synchrotron X-ray sources has had a major impact on non-ambient powder diffraction. The very high X-ray intensity of synchrotron

sources and the development of powerful insertion devices make it possible to perform time-resolved experiments with very good time resolution. In addition, by using high energy synchrotron X-ray radiation it is possible to obtain information from materials contained in even fairly thick-walled metal containers. By using a focussed high energy X-ray beam, it is also possible to obtain good diffraction data from tiny amounts of materials inside a high-pressure diamond anvil cell.

In parallel with the development of powerful X-ray and neutron sources, development of increasingly more efficient detectors has made it possible to obtain very good powder diffraction data in a very short time. The use of position sensitive and area detectors allow a large part of the diffraction pattern to be collected simultaneously. Therefore, non-ambient and *in situ* powder diffraction studies which were unthinkable a few decades back can now be performed routinely.

## 15.2 *IN SITU* POWDER DIFFRACTION

The term "*in situ* powder diffraction" is used for many different types of experiments, and there is no strict agreement on the definition. It may be argued that all non-ambient experiments are by definition *in situ*, as they must be performed at the required conditions, *e.g.* high temperature or high pressure.

High-pressure studies are described later in the chapter. Here we discuss:

- Dynamic powder diffraction where time-resolved experiments are performed to follow materials during chemical or physical reactions and processes.
- Static experiments where information about materials under steady-state conditions in a complex system is obtained, *e.g.* catalysts in a reactor at operating conditions.

In *in situ* experiments a system or a material is studied at non-ambient conditions where chemical or physical processes occur. This could be time-resolved studies of chemical reactions, such as in materials synthesis (solid state, sol/gel, hydrothermal, thin film growth *etc.*), cathode and anode materials in lithium batteries during charge/discharge cycles, adsorption/desorption, ion exchange and intercalation reactions of layered or microporous materials. It could be studies of catalysts under operating conditions, hydrogen storage materials during uptake and release of hydrogen or studies of electrochemical reactions just to mention a few. It could also be studies of materials during physical processes or interactions. For instance, piezoelectric materials in oscillating electrical fields, studies of strain/stress development during mechanic treatment of metals or reaction to changes in an external magnetic field.

We have not made any distinction between *in situ* and *in operando* experiments. *In operando* requires the system studied to be under identical conditions as in, for example, an industrial process, while *in situ* could describe simulated conditions such as time-resolved studies of synthesis and chemical reactions.

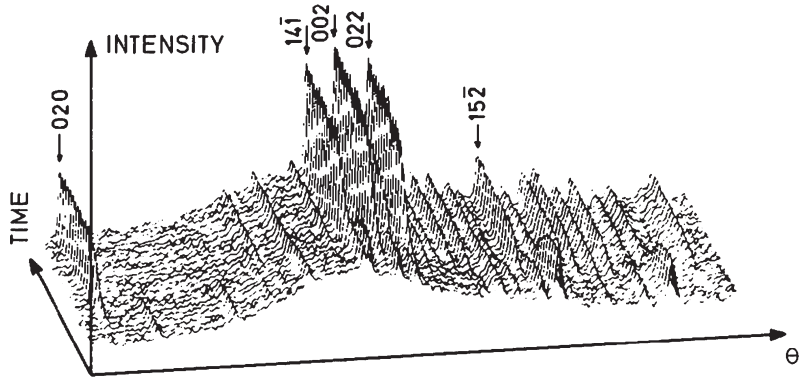



**Figure 15.1** Example of the changes in diffraction pattern from a sample undergoing reaction. Each pattern is separated in time by 5 min. The sample is $CaSO_4$ at different levels of hydration.[2]

It is difficult to pinpoint the emergence of *in situ* powder diffraction to one particular event. However, some of the very early *in situ* experiments aimed at obtaining structural information and kinetic data were performed using neutron powder diffraction.[1 3] The possibility of using metal containers and large sample volumes made neutron diffraction a favourable choice, despite the low flux, which limits the time resolution obtainable. The use of a position sensitive detector at the neutron powder diffractometer D1B at ILL made it possible to follow, for example, the hydration of gypsum[2] with a time resolution of 3–5 min. Figure 15.1 shows a three-dimensional representation of time-resolved powder diffraction patterns during reaction, where the formation of the hydrated phase is clearly visible.

These studies were of great interest to understand cement hydration and since then many *in situ* studies have been performed following the reactions using neutron and synchrotron X-ray powder diffraction. The development in time resolution is demonstrated by a synchrotron study of the hydration of tricalcium aluminate, $C_3A$, which is an important component of Portland cement.[4] Using a time resolution of down to 0.3 s a hitherto unknown short-lived intermediate phase was detected in the very early stage of hydration.

The early experiments spurred a great interest in using *in situ* powder diffraction for many other systems. *In situ* powder diffraction is still a fast developing research field, which has expanded to increasingly more challenging experiments.

The main reason for the explosive development in *in situ* powder diffraction experiments is the development of high intensity synchrotron X-ray sources. The very high intensity allows good time resolution, which makes it possible to follow even very fast reactions. In addition, the accessibility of high energy X-ray radiation has enabled *in situ* studies in even thick walled steel containers, making it possible to study materials under operating conditions.

Due to the large number of *in situ* powder diffraction experiments being performed, the following will not attempt to present a comprehensive record of *in situ* experiments, but will try to focus on important aspects that should be considered when performing *in situ* powder diffraction experiments.

### 15.2.1 Techniques and Instrumentation

*15.2.1.1 Synchrotron X-ray Radiation.* Both energy dispersive and angle dispersive diffraction is used for *in situ* powder diffraction studies using synchrotron X-ray radiation.

In energy dispersive X-ray diffraction (EDXRD), a beam containing a broad spectrum of X-ray energies (white beam) is incident on the sample. An energy discriminating detector, *e.g.* a solid state Si or Ge detector, is positioned at a fixed angle, and the energy/intensity distribution of the scattered beam is analysed. By using multiple detectors at different scattering angles, a wider range of *d*-spacings may be covered, and interference from fluorescence and absorption edges in the material or container can be reduced. In *in situ* energy dispersive powder diffraction the use of multiple detectors is now common, *e.g.* experiments at Daresbury,[5,6] where a three-element detector system was developed for *in situ* studies (Figure 15.2).

There are many advantages of using energy dispersive diffraction for *in situ* studies. There are no moving parts during exposure, and fixed angles are used. This makes it less complicated to design specific reaction cells and also makes it easier to combine experimental techniques in one experiment. By using low detector angles, diffraction occurs at high energies, which has the added benefit of allowing for the use of thick containers. Another important aspect is that it is

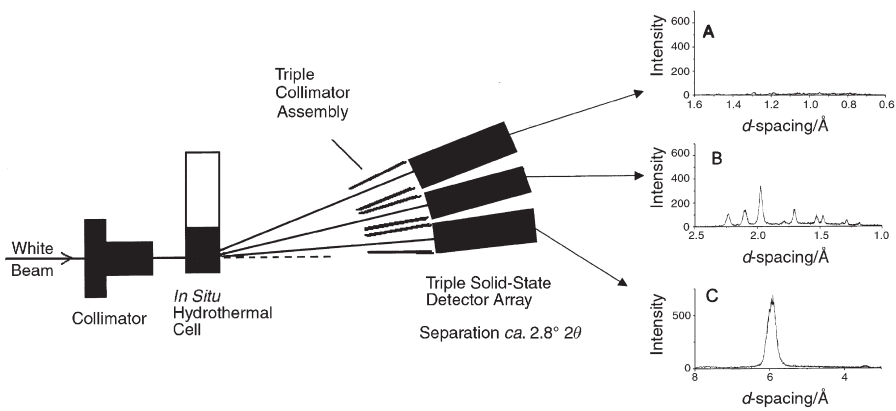



**Figure 15.2** Schematic diagram of the three element detector at Station 16.4 of the Daresbury Laboratory, employed for the study of the synthesis of microporous materials. Note that the bottom detector is kept at an angle of between 1.1° and 1.4° so that reflections having d spacings in the range 0.5 20 Å can be observed.[6]

possible to obtain diffraction selectively from a small volume element in the sample by using collimators on the incident and diffracted beam. This may be used to eliminate diffraction from container materials or other materials in the system, which is a great advantage when studying buried interfaces, multi-layered structures (*e.g.* batteries or fuel cells) or hydrothermal synthesis. Short exposure may be used and the readout time is short, resulting in good time resolution.

Disadvantages of energy dispersive powder diffraction are the low resolution obtained due to the limited energy resolution of the detectors, making it difficult to determine accurate unit cell parameters. Fluorescence lines and absorption edges will also influence the collected spectrum and it is generally difficult to obtain structural information, *e.g.* from Rietveld refinement, from energy dispersive diffraction data.

Angle dispersive diffraction is used for most X-ray powder diffraction experiments using conventional or synchrotron sources. A monochromatic X-ray beam is used, and the scattered intensity is recorded as a function of diffraction angle. Very good unit cell parameters can be obtained and it is possible to collect data that are suitable for structural investigations using Rietveld refinement. The time resolution obtained depends strongly on the detector system. The detector may be a point detector, a one-dimensional (position sensitive) detector or an area detector. The use of one- or two-dimensional detectors significantly increases the counting efficiency, as a large part of the pattern is collected simultaneously. In addition, it is important for time-resolved (and temperature resolved) powder diffraction experiments to collect the total powder diffraction pattern in the shortest possible time, preferably simultaneously collecting the entire pattern. This is not only to improve the time resolution; if a scanning detector (point detector or small position sensitive detector) is used, the material may change between the start and the end of the scan. Thus, analyses of the patterns, especially when extracting structural information, may be problematic. When collecting the entire pattern using a large position sensitive or area detector, any changes taking place during measurement/exposure is reflected in the entire collected pattern.

It is important to realize that when using a one- or two-dimensional detector (without focusing geometry), the angular resolution (*i.e.* the width of the diffraction peaks) obtained is to a large extent determined by the size of the sample. Therefore, the sample size must be kept small, which makes the design of reaction cells for *in situ* studies a challenge. In addition, it is more difficult to design environmental cells or to perform combined experiments without obstructing the diffracted beam path. The angular resolution may be improved by increasing the distance between the sample and the detector. However, this limits the angular range available due to the limited size of the detector. When using a one-dimensional detector, a longer sample–detector distance also means that a smaller fraction of the Debye–Scherrer ring is sampled. Thus, it is often necessary to find a compromise between resolution, angular range sampled and intensity. In general, the angular resolution obtained using an area detector on

the synchrotron is comparable to high-resolution laboratory powder diffractometers using CuK$\alpha_1$ radiation.

The use of two-dimensional detectors, where the entire, or a significant part of, the Debye–Scherrer rings are collected will, in addition to improved counting statistics, limit the negative effect of small samples, *i.e.* non-statistical number of crystallites and, to some extent, texture. Geometric effects of these detectors are described in detail in Chapter 14.

The use of high-resolution synchrotron X-ray powder diffraction for time-resolved *in situ* studies is limited by the obtained intensity, and thereby the time resolution. The use of multiple analyser crystals will reduce the time required for each data set. In addition, the availability of high-resolution powder diffractometers on insertion device beam lines (wiggler or undulator) with multiple analyser crystals, such as ID31 at ESRF or 11-ID at APS, makes it possible to perform experiments where very high-resolution data are obtained with good time resolution. This development will significantly contribute to the use of *in situ* powder diffraction for attacking increasingly more complex problems.

*15.2.1.2 Home Laboratory X-ray Sources.* It must be emphasized that laboratory X-ray sources, either sealed tube or rotating anode, in many cases will be excellent for *in situ* experiments, especially when equipped with a position sensitive detector. There are of course many challenges and limitations regarding time resolution and absorption in the sample or container. Most powder diffractometers use copper radiation, which will be attenuated significantly by thick samples. However, it is often sufficient to collect data over a limited $2\theta$ range, which is useful for experiments where one follows the development of a few reflections. By using a point detector fast scans may be made. When using a small position sensitive detector, the detector may be in a fixed position, which will make it possible to obtain a time resolution below 1 min.

Notably, in many cases a single-crystal diffractometer with Mo-radiation and an area detector is available in the home laboratory. This may be an excellent instrument for *in situ* powder diffraction studies. It is often possible to build a heating system for capillary samples, and to incorporate a reaction cell on the instrument. The higher energy of the molybdenum X-ray radiation compared to copper radiation reduces the problems with absorption. The collection of the entire Debye–Scherrer rings gives data with good statistics using short exposure times. The readout time for most systems is short, making it possible to obtain a good time resolution. However, the angular resolution of powder diffraction data collected on a standard single-crystal diffractometer with a divergent beam is not very good, resulting in diffraction patterns with broad reflections. It is in most cases not possible to obtain reliable unit cell parameters. Often, however, the phases involved are well known, and the poor resolution is not a big obstacle. When following the development or transformation of phases, high intensity is often more important than good resolution.

The time resolution obtainable using a laboratory source is in many cases sufficient to follow chemical reactions and to study materials in a given environment. Many chemical reactions and synthesis may take hours to complete, and here good results may be obtained using the laboratory experiment. In addition it is a valuable tool when preparing for synchrotron experiments.

*15.2.1.3 Neutron Diffraction.* The use of neutron diffraction for *in situ* studies offers many advantages. The scattering power is not a function of the atomic number, as neutrons scatter on the nuclei. Neutron scattering is sensitive to some light atoms as hydrogen and deuterium, and neutron diffraction is for instance very suitable for *in situ* studies of hydrogen storage materials. The penetrating power of neutrons means that large samples may be used, and that containers may be penetrated easily, when the container material is chosen carefully. Vanadium is often used due to the low scattering cross section. A reaction cell developed for *in situ* neutron powder diffraction studies of hydrothermal reactions was constructed from a null scattering Ti-Zr alloy (67.7 at.% Ti, 32.2 at.% Zr)[7,8] (Figure 15.3). The null scattering refers to the fact that the coherent scattering cross-section is zero due to the opposite signs

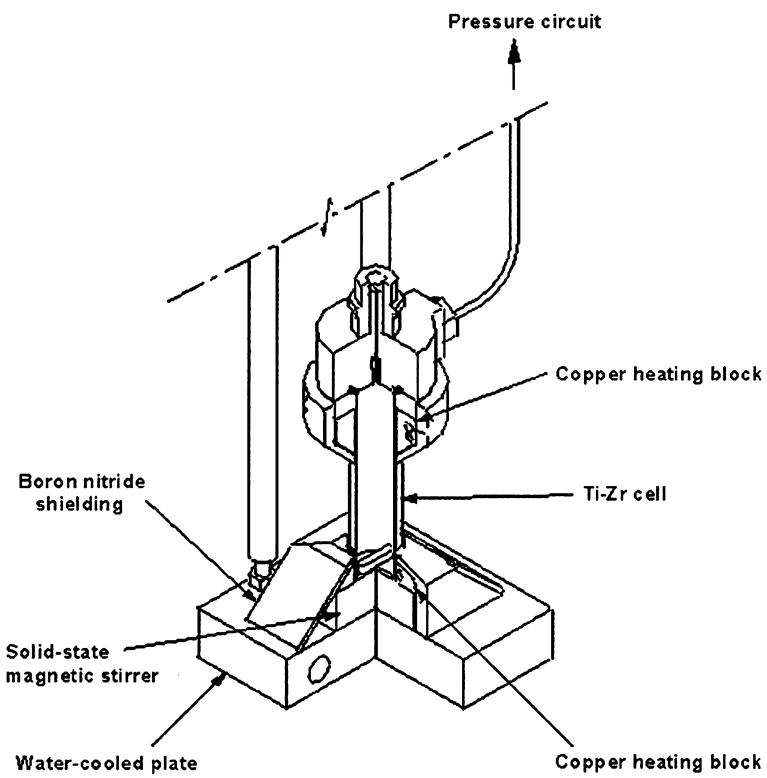



**Figure 15.3** Schematic of the Oxford/ISIS hydrothermal reaction cell for recording *in situ* neutron powder diffraction data.

of the scattering factor for Ti and Zr, such that the resulting intensity for all Bragg reflections from the autoclave material is zero.

The neutron flux from neutron sources is much lower than for X-ray sources, and the interactions are weaker. The time resolution obtainable is therefore lower than for X-ray sources, and efficient detectors (one- or two-dimensional) and/or high-flux neutron sources (*e.g.* spallation sources) are necessary for time-resolved studies.

*15.2.1.4 Reaction Cells and Sample Setup.* A great deal of ingenuity is being displayed in developing setup and reaction cells for attacking specific materials science problems using *in situ* powder diffraction. *In situ* studies are often demanding, and many studies require development of a custom-made setup for a single or a series of experiments. However, several more generally applicable sample holders and reactors have been developed, which are versatile enough to be used for many different experiments. Many of the *in situ* powder diffraction studies, which have been performed previously, have been devoted to developing and refining techniques for studies of materials under various conditions. This has created an experience basis, and the number and complexity of the problems that may be investigated is expanding. The field has matured, and now more and more studies result in new knowledge of the processes studied. The development of the technique will continue, and significant emphasis will be on combining experimental techniques, so that complementary information may be extracted from a single experiment. A few examples of reaction cells are given below.

Reactions between solids and gases are common in *in situ* powder diffraction studies, whether studying catalysts under real or realistic conditions, oxidation/reduction of solids, adsorption/desorption under controlled conditions or synthesis involving gaseous species.

Several cells are available; the simplest is to use a generally available high-temperature chamber where a solid is deposited on a platinum strip that is heated by passing a current through it. The chamber is usually filled or flushed with an inert gas, but the sample may be exposed to other atmospheres. The method is limited to gases that do not attack the filament or the chamber. This means, for example, that hydrogen at high temperature is not feasible, as it will destroy the platinum strip. Likewise, care must be exercised when using very oxidizing and corrosive gases. In this setup large temperature gradients exist, and the conditions and concentrations experienced by the sample are not very well defined.

Improved control over the reaction conditions may be obtained by using flow-through cells, where temperature and concentration gradients are reduced. Many reaction cells have been developed for both reflection and transmission geometry.

Pioneering development of a capillary based micro reaction cell was published by Clausen et al.,[9,10] for studies of catalysts under real operating conditions. The reaction cell was suited for both *in situ* EXAFS and transmission geometry powder diffraction studies (and was also used for combined

XAS/XRD experiments). The reaction cell was based on standard quartz glass capillaries mounted in Swagelok fittings using ferrules. This allows a gas flow to be directed through the cell, making it possible to analyse the exhaust gas to correlate observed changes to catalytic reactivity. Part of the capillary is heated using a hot air blower or a resistance heater. This setup makes it possible to use also aggressive or reducing gasses; the volume of gas is very small and the gas is in contact only with the capillary and the sample at high temperature. Furthermore, very good control over pressure and gas composition is obtained. It is also possible to obtain a specific water vapour pressure by moisturizing or by using a mass flow controller for liquids to introduce controlled amounts of water into the gas stream. Standard quartz glass capillaries (0.5 or 0.7 mm o.d.) may withstand a pressure of up to 50–100 bar (depending on reaction conditions), making it possible to study even medium-pressure catalytic reactions. The capillary walls are 0.01 mm (10 μm) thick, which makes absorption very low. If higher pressures are needed, the reaction cell may be made of steel tubing, but then higher energy (and high intensity) radiation must be used to penetrate the sample holder and obtain diffraction patterns from the sample within. Recent developments in this setup has been the use of single-crystal sapphire (corundum) tubes.[11] These have a larger wall thickness than the quartz glass capillaries, but allow higher pressures to be used. These cells are suitable mainly for synchrotron based *in situ* powder diffraction experiments.

Reaction cells for reflection geometry have been developed based on a setup where gas is passed through a ceramic frit with the powder placed on top (*e.g.* ref. 12 and Figure 15.4).

The X-ray radiation must be able to pass into the sample cell, and the cells are often covered by a dome of a weakly scattering and absorbing materials such as boron nitride, making it possible to control the flow and environment in the cell. The pressure is limited due to the large surface area of the dome enclosing the cell. By using a dome shaped enclosure, the reflected beam is perpendicular to the enclosure wall at all scattering angles, reducing the absorption and ensuring that the absorption is not angle dependent.

Reaction cells have been developed also for time-resolved studies of hydrothermal and solvothermal synthesis. In addition to obtaining kinetics information on the crystallization of the materials, intermediate or transient phases may be identified. To study crystallization involving liquids above its boiling point, it is necessary to apply a pressure. Two approaches to studying hydrothermal and solvothermal reactions have been followed.

One type of micro-reaction cell has been developed based on the capillary cell for studies of catalysts described above. Instead of using a flow-through cell, a closed quartz glass capillary (*e.g.* 0.7 mm o.d.) is filled with the reaction mixture and mounted in a Swagelok fitting. A pressure of an inert gas (*e.g.* $N_2$) is applied to the surface of the reaction mixture, and a part of the capillary is heated to the desired temperature (Figure 15.5).

When the applied pressure is higher than the vapour pressure of the reaction mixture at the reaction temperature, hydrothermal or solvothermal conditions

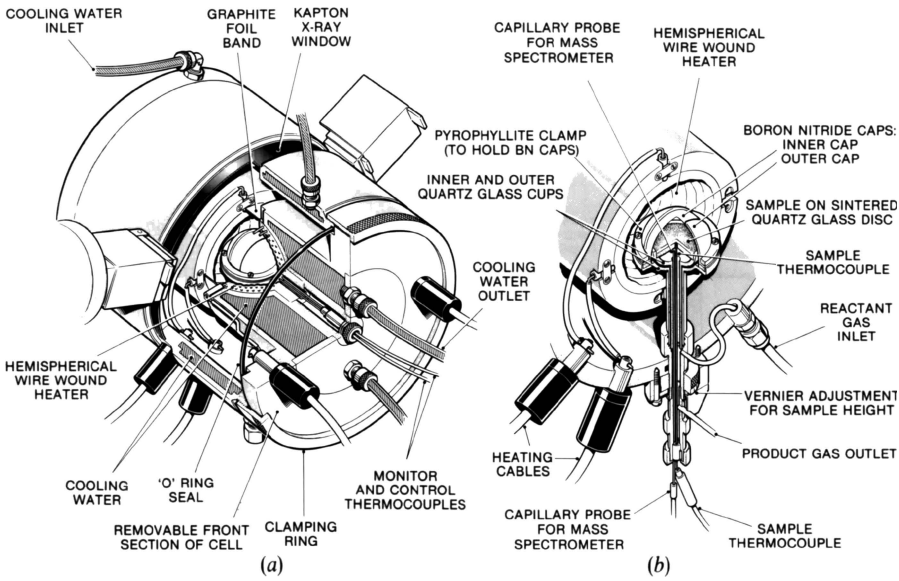



**Figure 15.4** Cutaway view of a high temperature cell fit on a Siemens D 500 gonio meter. The image on the right (b) is a blow up of the sample chamber at the centre of the furnace shown on the left (a).[12]

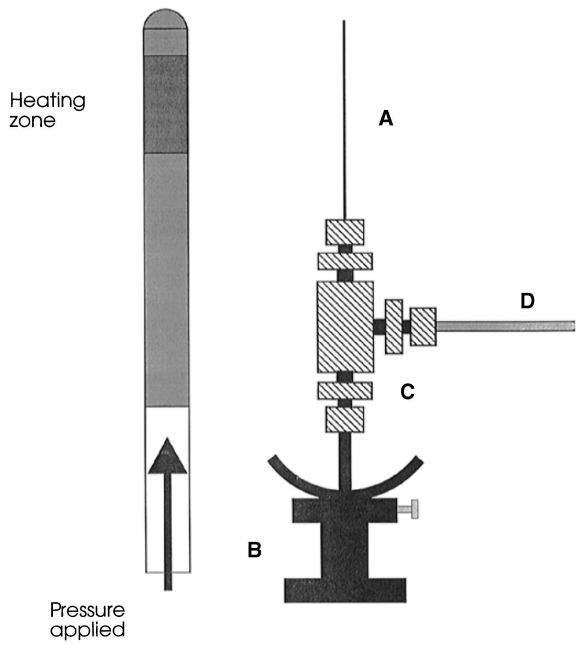



**Figure 15.5** Schematic of a glass capillary (A) mounted on a goniometer head (B) with a Swagelok T piece (C). A nitrogen pressure can be applied through the con nected tubing (D). An expanded view of the capillary is shown on the left.[13]

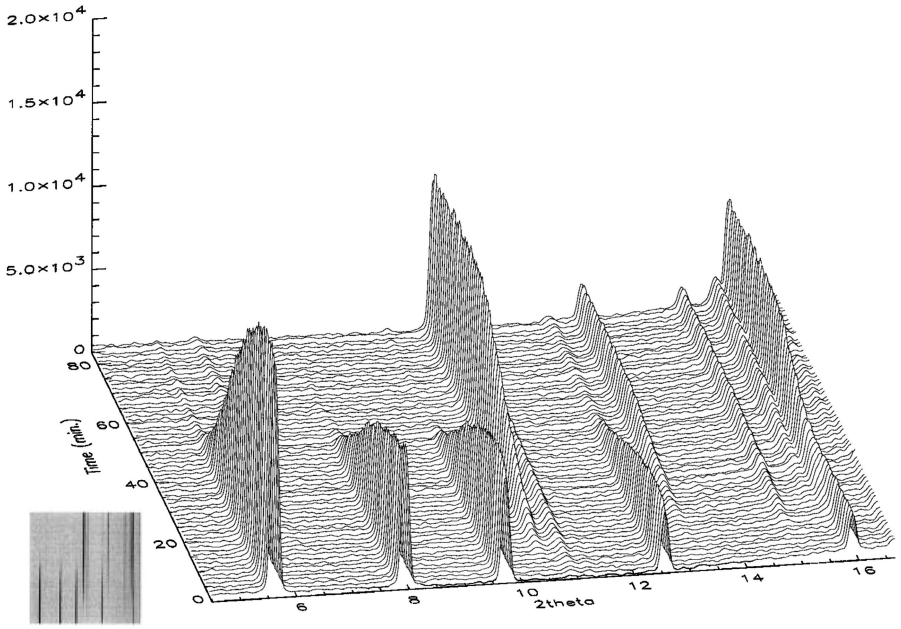



**Figure 15.6** Three dimensional plot of powder diffraction profiles as a function of time during the hydrothermal conversion of zeolite Li/Na LTA to zeolite Li A(BW). The temperature was ramped to 200 °C in 5 min and kept at that temperature.[13]

are obtained.[13,14] Figure 15.6 shows one example of time-resolved *in situ* powder diffraction data obtained for hydrothermal conversion of a zeolite.

The quartz glass capillary cell can withstand pressures of up to at least 25 bar (depending on the chemical environment; when using alkaline conditions at high temperature the quartz glass is attacked and the capillary may break after a short time). This means that hydrothermal reactions up to *ca.* 260 °C may be studied. If higher temperature, and consequently higher pressure, is needed, a steel tube and a hydraulic pressure may be used. This was, for example, used for studies of high temperature hydrothermal reaction at temperatures above 350 °C and pressures of several hundred bar.[15]

One disadvantage of the capillary based system is the small volume compared to laboratory synthesis, which may influence the crystallization mechanisms. In addition, only a small part of the capillary is heated, so care must be taken to avoid convection effects due to thermal gradients. To minimize effects from thermal gradients, the heated part of the capillary must be much larger than the X-ray beam.

Another approach to studies of hydrothermal and solvothermal reactions is to use energy dispersive diffraction. A normal size laboratory autoclave is used with a thinning of a small part to allow X-rays to penetrate the wall.[6] Collimated slits are used to obtain diffraction from only a small volume element inside the autoclave. Stirring is necessary to prevent sedimentation of the materials.

## 15.3 POWDER DIFFRACTION AT HIGH PRESSURE

### 15.3.1 Introduction

Pressure is a fundamental state variable like temperature or composition and is, thus, a suitable means to modify the properties of solids. Its application induces a continuous shortening of interatomic distances, within the stability ranges of structural phases. Different types of chemical bonding will generally exhibit dissimilar changes upon application of pressure, resulting in different compressibility for covalent and metallic solids (Figure 15.7), for example.

Correspondingly, low-symmetry atomic or molecular arrangements comprising different types of chemical bonds normally exhibit pronounced anisotropy of the compressibility. Structural reorganizations due to pressure-induced phase transitions are associated with discontinuous volume decreases and normally increasing coordination numbers. These structural changes not only modify the coordination environment in the crystal structure but frequently also the electronic properties of the solid.

Since the 1990s the combination of diamond anvil cell (DAC) techniques with imaging plate detectors has turned the investigation of compressibility and

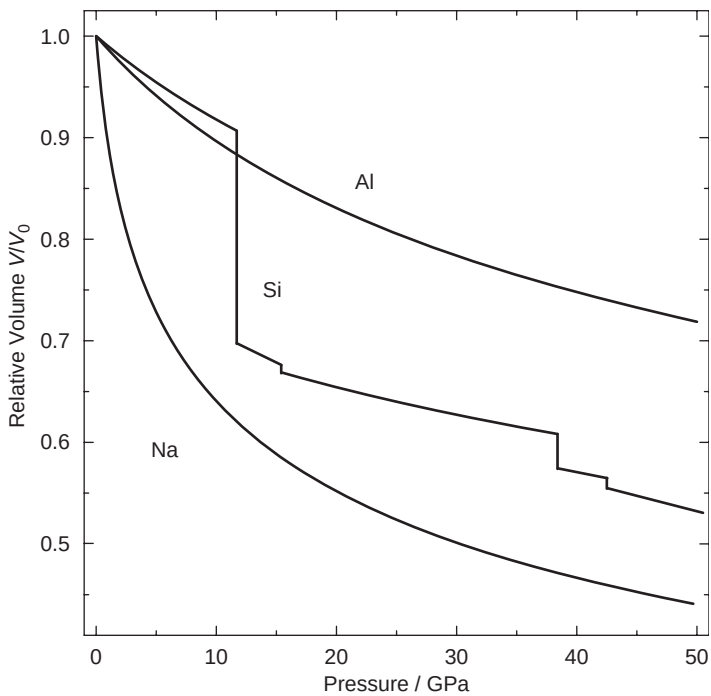



**Figure 15.7** Pressure volume relation of three main group elements. Aluminium and sodium exhibit continuous compression behaviour in the selected pres sure range. The discontinuous volume changes of silicon are caused by structural phase transitions.

structural changes almost into a routine procedure. The accessible pressure range amounts to about 50 GPa with a standard laboratory sealed-source setup and up to several hundred GPa at third-generation synchrotron sources when specially designed pressure cells are used. Experiments exceeding 100 GPa frequently end with a destruction of the anvils made from diamonds. Temperatures between approximately 4 K and several thousand K can be realized with specially designed cryostat systems or heating devices (laser, electrical resistance).

In the following sections we assume that the application of pressure is non-directed, *i.e.* hydrostatic or quasi-hydrostatic (see below). The usual unit of pressure is the Giga-Pascal GPa ($1\,\mathrm{Pa} = 1\,\mathrm{N\,m^{-2}}$), but older literature often refers to kbar ($1\,\mathrm{kbar} = 0.1\,\mathrm{GPa}$).

### 15.3.2 The Diamond Anvil Cell

For pressure generation in X-ray diffraction and spectroscopy, the Diamond Anvil Cell is the most versatile tool. Using diamond as the anvil material combines the advantages of mechanical hardness and transparency for electromagnetic radiation.[16]

The principle of the DAC as a high-pressure tool for X-ray diffraction is given below (Figure 15.8).

The diamonds have typical sizes of a few millimetres with masses of about 0.2 to 0.5 carat. During the initial development of DAC techniques, the tips of brilliant-cut diamonds were removed so that culets with typical diameters between 0.1 and 1 mm resulted. Today, simplified shapes providing an improved performance are used. The anvils are located on seats that transmit the force from the cell body to the diamond tables. The supports are subject to maximal forces of typically 10 kN and stresses of about 2 GPa for customarily sized diamonds. Thus, seats are often made from a hard material like tungsten carbide, although steel or materials prepared from elements with a low atomic number like beryllium or boron are also used. Within the holders, cylindrical or conical holes provide optical access to anvil tips and sample. The diamonds are frequently fixed with commercial epoxy glue onto the seats, but for certain experiments, *e.g.*, at high temperatures, metal rings machined from copper or steel keep the anvils in place. The design of the support usually provides possibilities for aligning orientation (parallel tables with minimized tilt) and lateral position (congruent table location) of the diamonds.

Between the diamonds a metallic seal is positioned that is typically 0.2 mm thick. This metal foil is pre-indented to characteristically 40 μm by cold pressing between the diamond anvils. The resulting shape is optimally fitted to the diamonds and guarantees the required lateral support for the conical faces of the diamonds in the regions close to the tips. To reach ultrahigh pressures exceeding 100 GPa (Figure 15.9), small culets $< 0.3$ mm are used and the outer part of the diamond tip is beveled by at obtuse angle.

The seal is normally manufactured from metals like stainless steel or beryllium, but hard metals like molybdenum, tungsten, scandium or rhenium have

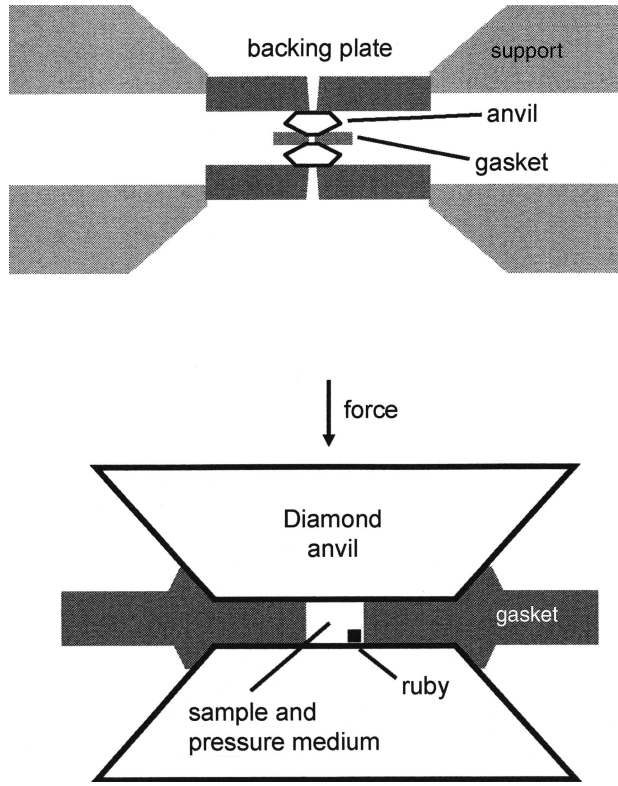



**Figure 15.8** Details of a Diamond Anvil Cell. Top: Set up with supports. Bottom: Inner part with diamonds and gasket.

also been used, especially for reaching ultrahigh pressures. A hole drilled in the centre serves as the high-pressure chamber for sample, pressure sensor and medium. Centering of the hole with respect to the indented polygon is essential for the stability under load. The volume not taken by the sample is filled with a pressure medium that is usually a liquid. When force is applied by the parallel oriented diamond tips, the gasket is deformed plastically and the pressure that results from the reduction of volume is transferred to the sample by the medium. To reach high pressures, stability of the hole diameter and position upon compression is essential. It requires some experience to reach the maximal possible pressure since the stability is dependent on the compressibility of sample, pressure medium and gasket material, the size-ratio of hole and tips, which must not exceed 1/3, the height of the cylindrical drilling (the thickness of the gasket) and the friction coefficient between anvil faces and gasket. The small tips of the diamonds (culets) have to be exactly aligned, *i.e.* oriented absolutely parallel and positioned precisely on top of each other. Even small misalignments can cause large shear forces and, thus, fatal failure of the anvils.

The force to produce the pressure may be generated by screws[17,18] or gas membranes[19] and is transferred to the diamonds by the seats. The different

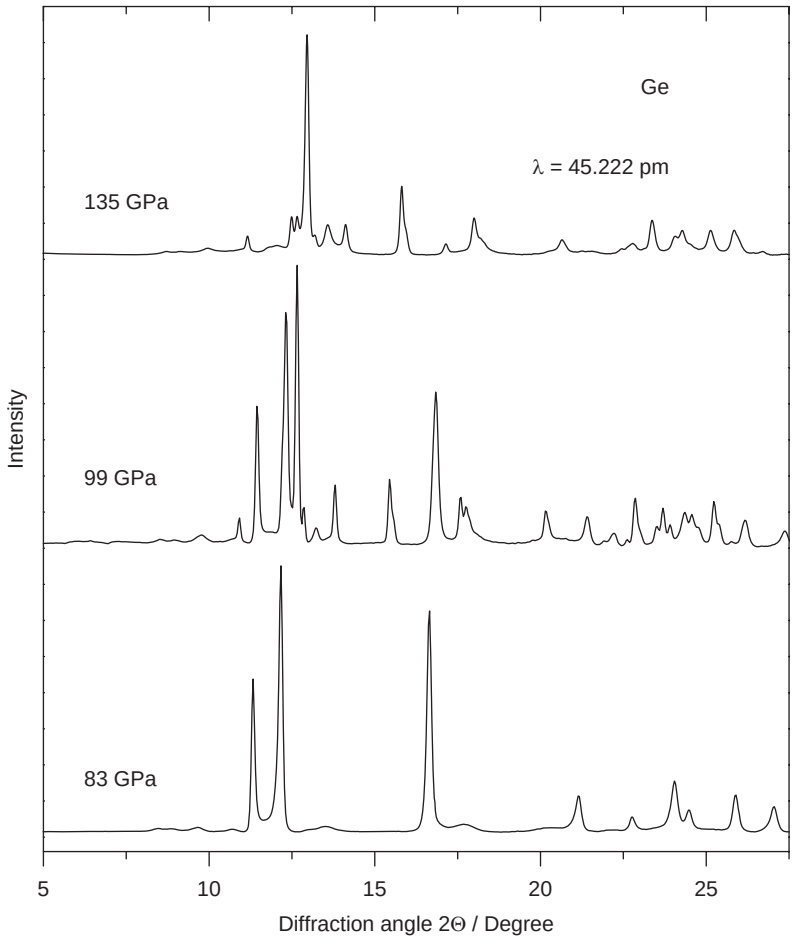



**Figure 15.9** Diffraction diagrams of germanium in the megabar (100 GPa) region measured with synchrotron radiation. The intensity changes indicate a structural phase transition from a primitive hexagonal arrangement into an orthorhombic crystal structure.[44]

diamond anvil cell designs and the alignment procedures have been reviewed in detail.[20]

### 15.3.3 Pressure Media

Within the cylindrical hole serving as a sample chamber, a suitable, normally liquid, pressure transmitting medium is used to provide hydrostatic pressure conditions. However, soft salts like CsCl with low shear strength have also been employed in some experiments. One of the conditions for a suitable pressure medium is that even under irradiation by X-rays it does not undergo chemical reactions with the investigated sample.

Upon pressure increase, liquid media tend to solidify and the samples are subject to some directed pressure components, *i.e.* stress and strain. This compression condition is often labelled as quasi-hydrostatic. The frequently used mixture methanol/ethanol in a ratio of 1 : 4 undergoes a transition into a glass at approximately 10 GPa.[21] The solidified mixture may exhibit pressure gradients of up to 15% in typically-sized gasket holes at a pressure around 50 GPa.[22] The radial pressure distribution in a DAC at even higher pressures is a serious issue that has been investigated experimentally.[23] If the positions of pressure sensor and X-ray beam differ significantly, the pressure differences due to the gradient cause a systematic error of the measurement. Pronounced pressure inhomogeneity can cause a destruction of sample crystals and a severe profile broadening in X-ray powder diffraction diagrams. These problems can be lessened by using nitrogen or noble gases as pressure transmitting media. Although they also solidify at high pressures, their low shear strength impedes the transmission of significant strain forces so that they represent widely accepted pressure media.[24,25] Especially, helium is well suited with respect to its quasi-hydrostatic behaviour (even at low temperatures), but the procedures to load the noble gas into the sample chamber are technically demanding. They involve either liquefaction by cooling down to 4 K or pressurizing to approximately 0.2 GPa.

### 15.3.4 Diffraction Measurements

The design of the pressure cell means that the X-ray beam penetrates those parts that are machined from materials with low atomic number like beryllium or diamond. However, for molybdenum K$\alpha$ radiation between 50% and 90% of the primary intensity are absorbed. The exact amount depends on the design of the pressure cell and especially the size of the diamonds. Furthermore, the accessible scattering angle is limited by the highly absorbing parts of the pressure device, which are manufactured from steel or tungsten carbide. This shading at high scattering angles can be compensated by using hard X-rays. The utilization of short wavelengths enables measurements of diffraction lines down to small *d*-values (Figure 15.10).

Synchrotron sources combine the advantages of tunable wavelength with high-brilliance and low-divergence so that diffraction images with superb resolution and signal-to-noise ratio can be recorded. Moreover, typical beam diameters of 30 μm or even less permit one to measure just the area close to the centre of the diamond anvil cell where pressure gradients are small. The result is a well-resolved diffraction pattern with significantly smaller line-widths than those of sealed-source measurements. However, the small beam diameter may cause the problem of a poor powder average, *i.e.* there are not a sufficient number of crystallites fulfilling the reflection condition to guarantee a random distribution of orientation. Thus, synchrotron diffraction experiments require a reduction of the average powder particle size well below 10 μm and oscillation of the diamond anvil cell during the measurement by typically $\pm 3^{\circ}$. In combination with modern 2D detectors, most samples can be prepared with a

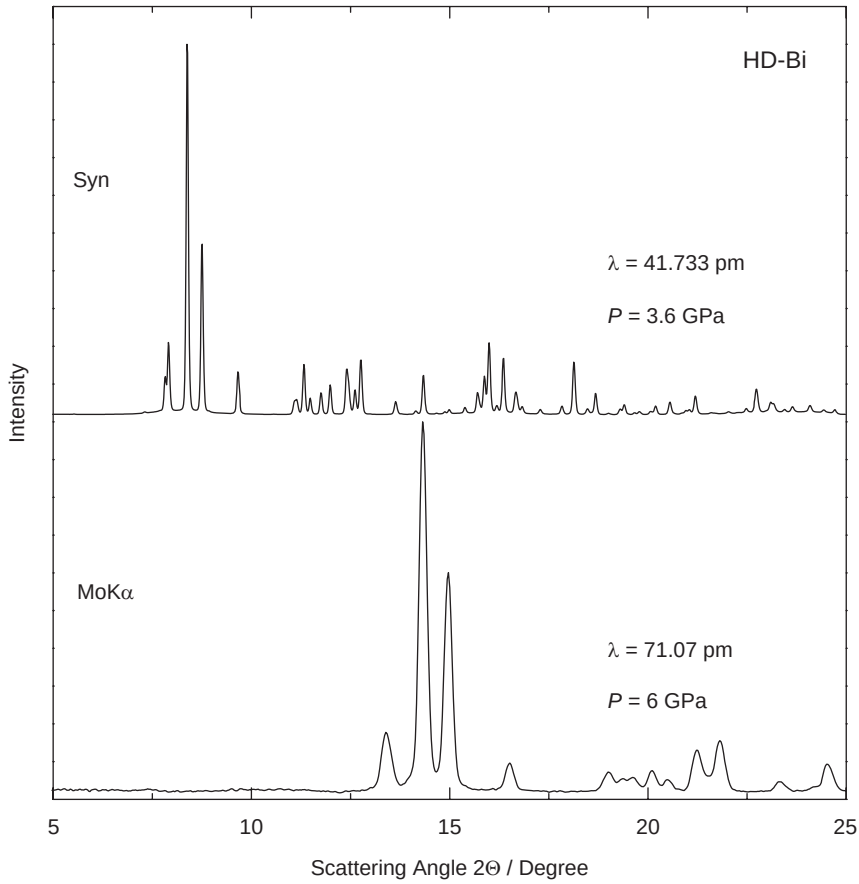



**Figure 15.10** Diffraction diagrams of a high pressure modification of bismuth. The lower diagram shows diffraction data recorded with a conventional sealed source, the upper one data measured with synchrotron radiation (unpublished results).

quality that is sufficient for measuring diffraction patterns suitable for least-squares refinements using full diffraction profiles (Figure 15.11).

The introduction of two-dimensional imaging plates as X-ray detectors has considerably reduced the problems associated with missing powder average. Additionally, the gain in sensitivity and the recording of complete diffraction rings, or large parts thereof, has significantly improved the realized signal-to-noise ratio in powder diffraction experiments. For data analysis, the 2D images are converted into conventional one-dimensional (intensity versus diffraction angle) data by azimuthal integration of the intensities.[26] Today, even elements with low scattering power like hydrogen or lithium can be measured using area detectors in combination with third-generation synchrotron sources (Figure 15.12).

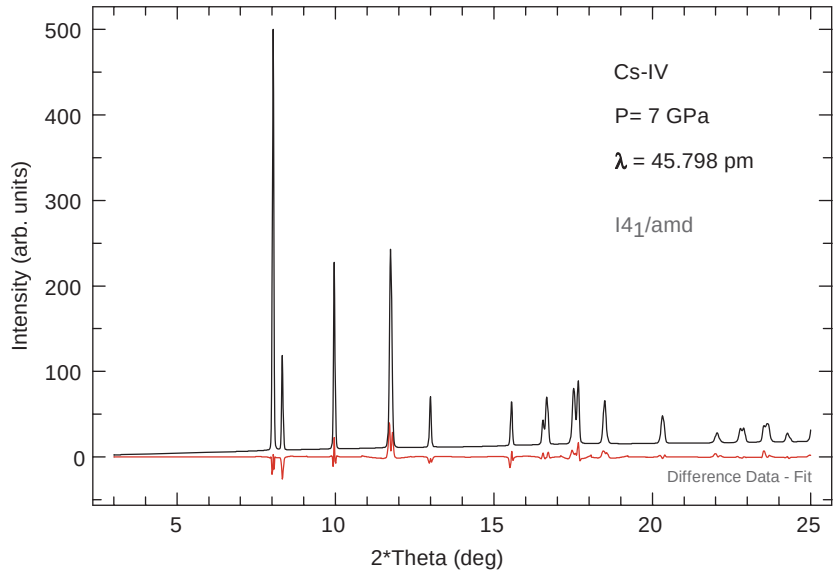



**Figure 15.11** Structure refinement using full diffraction profiles of a tetragonal high pressure modification of caesium (unpublished results).

Single-crystal measurements at high pressures are complicated by the high refractive index of diamond, which hampers the procedure of optical sample centering. Additionally, the mechanical set-up of diamond anvil cells constrains the optical access to certain directions. Thus, a preliminary orientation matrix is determined by measuring the exact positions of symmetry equivalent reflections. The exact position of the single crystal and the required translation for an alignment in the center is calculated from these data.[27] After an adjustment, the procedure is repeated several times so that a centering is achieved by an iterative procedure.

The limits of the accessible scattering angles cause a shading of parts of the Ewald sphere in high-pressure experiments. When the geometry of the set-up is exactly known, the shaded areas can be calculated and reflections located in these regions are either excluded from the measurement or removed in the process of data reduction. Finally, the absorption effects of diamond and beryllium have to be taken into account. A solution for the generally complex absorption problem is the use of backing plates with a large conical opening and diamonds with an almost spherical shape so that the absorption becomes direction independent.[28]

Crystals with high symmetry allow for a collection of complete data sets within the accessible angle range in many cases. For compounds with low symmetry, the crystal can be re-oriented and re-measured after the first data collection. Since this process is in many cases fatal for the investigated specimen, it is often preferred to perform the least-squares refinements with a smaller number of reflections and, correspondingly, a reduced number of

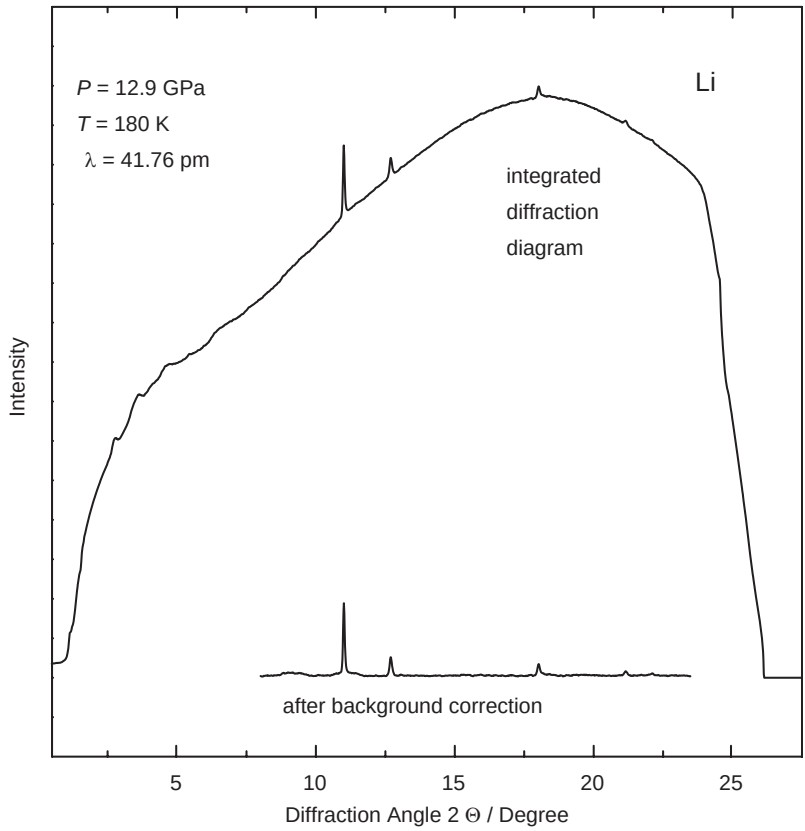



**Figure 15.12** Diffraction diagram of lithium measured at high pressures and low temperatures. The upper diagram shows the raw data after integration of a 2D imaging plate pattern, the lower intensities result after back ground correction. The background is attributed to the Compton scattering of the diamonds.

parameters, by using an isotropic description of the atomic displacement and by further constraining of parameters. To record diffraction data in an acceptable time, large crystals are preferred. However, the specimen cannot be larger than half the size of the pressure chamber since the available volume may be significantly reduced upon application of force and a squeezing of the sample by the diamonds or the metallic gasket results in destruction of the crystal.

### 15.3.5 Pressure Measurement

*In situ* pressure measurements within the diamond anvil cell are performed by means of calibration substances that are embedded in the pressure chamber together with the sample and the transmitting medium. Frequently used

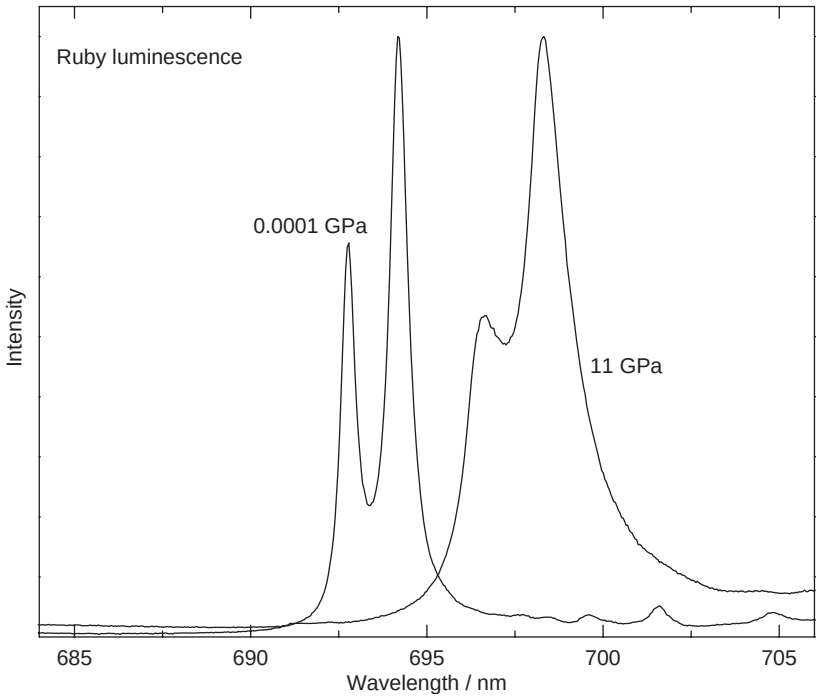



**Figure 15.13** Luminescence spectra of ruby chips irradiated with the blue 488 nm line of an argon ion laser. The double line structure shifts with pressure in the direction of increasing wavelength by 2.74 GPa $nm^{-1}$ (ref. 30). The broadening visible in the measurement performed at 11 GPa is attri buted to pressure inhomogeneity and strain in the employed pressure medium paraffin.

techniques are the laser induced luminescence of a ruby crystal.[29,30] The wavelength of the emission maximum is strongly pressure dependent and even with small crystals the signal is intense enough to be recorded with a standard optical spectrometer (Figure 15.13).

Also the pressure-dependent wavelength of the fluorescence maximum of a samarium-doped borate has been calibrated. The compound has the advantage of allowing for more precise determinations at very high pressures (above approximately 100 GPa) and it was demonstrated that, in contrast to ruby, the line position exhibits only a negligible temperature dependence.[31]

Another method for pressure calibration is to add a powdered salt[32] or metal[33] for which the equation of state has been determined precisely. In these experiments, the diffraction lines of the calibrant have to be measured simultaneously with the sample. The observed line positions are used to calculate lattice parameters by application of least-squares refinements and, thus, experimental volumes are determined that can be used to calculate the pressure by employing a calibrated equation of state. At extremely high-pressures, microcrystalline powder of metals like tantalum[34] may be used. A disadvantage of

this type of pressure measurement is that the diffraction lines of the calibrant may overlap the intensity data of the sample.

### 15.3.6 Thermodynamic Considerations

Diffraction experiments at high pressures provide information concerning the compression-induced changes of lattice parameters and, thus, sample volume. In pure phases of constant chemical composition and in the absence of external fields, the thermodynamic parameters volume $V$, temperature $T$ and pressure $P$ are related by equations of state, *i.e.* each value of a state variable can be defined as a function of the other two parameters. Some macroscopic quantities are partial differentials of these equations of state, *e.g.* the frequently used isothermal bulk modulus $B_0$ of a phase at a defined temperature and zero pressure $B_0 = -V_0\,(\partial P/\partial V)$ for $T =$ constant and $P = 0$, with the reciprocal of $B_0(V)$ being the isothermal compressibility $\kappa$. Equations of state can also be formulated as derivatives of thermodynamic functions like the internal energy $U$ or the Helmholtz free-energy $F$. However, for practical use the macroscopic properties of solids are often described by means of semi-empirical equations, some of which will be discussed in more detail.

For small volume changes, the bulk modulus can be expanded as a power series of the pressure at $P = 0$:

$$B(P) = -V(dP/dV) = B_0 + B_0'P + \ \ldots \tag{1}$$

$$\text{with}: B_0 = -V(\partial P/\partial V) \text{ at } V = V_0 \tag{2}$$

$$\text{and}: B_0'P = (\partial B/\partial P) \text{ at } P = 0 \tag{3}$$

$B_0'$ describes the pressure-dependent change of the isothermal bulk modulus $B_0$, *i.e.* the stiffening of a material upon application of pressure. If only the first two terms of the expansion series are taken into consideration, integration for constant temperature leads to the well-known Murnaghan equation of state:[35]

$$P(V) = (B_0/B_0') \times [(V_0/V)B_0' - 1] \tag{4}$$

Solving the equation for $P$ results in the frequently-used inverse Murnaghan equation:

$$V(\mathrm{P}) = V_0[1 + P(B_0'/B_0)]^{\ -1/B_0'} \tag{5}$$

An independent approach for the derivation of the relation between pressure and volume was developed by Birch. Under the assumption of isotropic deformation the strain tensor $e_{ij}$ can be treated as a scalar quantity $e$.[36] Then, the Helmholtz free energy is expanded as a power series of this isostatic strain $e$

and the relation between elastic deformation and volume:

$$V_0/V = (1 - 2e)^{3/2} \tag{6}$$

is taken into account. Differentiation of the first three terms of the sum for $V$ leads under the assumption of constant temperature to the Birch equation:

$$\begin{aligned} P(V) =& 3/2B_0[(V_0/V)^{7/3} - (V_0/V)^{5/3}]\{1 - 3/4(4 - B_0')\\ &\times [(V_0/V)^{2/3} - 1]\} \end{aligned} \tag{7}$$

It can be shown that for $\Delta V_0/V_0 \to 0$ Murnaghan- and Birch-type equations of state are equivalent.

In an alternative microscopic model,[37 42] a universal relation between binding energy and interatomic distance is presumed. The validity of this assumption was demonstrated for interfaces between metals, gases absorbed on metals and finally pure metals. The interdependence of binding energy $E$(a) and distance $a$ can be decomposed into a product of a function $E^*(a^*)$ and the cohesion energy $E_0$ at equilibrium distance $a_0$:

$$E(a) = E_0 E^*(a^*) \tag{8}$$

$$a^* = (a - a_0)/L \tag{9}$$

The adjustment of the universal function $E(a^*)$ is realized by a determination of a scaling length $L$. For covalent solids, the same type of relation between binding energy and bond length holds whereas the potentials for Coulomb and van der Waals interactions are different for increasing interatomic distances. However, for decreasing volumes the overlap of wave functions dominates the pressure–volume relation for all types of bonding, thus causing a universal behaviour concerning the compression of solids. The pressure $P$ can be calculated as a derivative of the cohesion energy function with respect to the volume:

$$P(V) = -(E_0/4\pi r^2)(1/L)E^{*\prime}(a^*) \tag{10}$$

After introducing a function for the force and using Hook's law, application of a scaling procedure results in a universal function that can be simplified into a pressure–volume relation:

$$P = 3B_0(V/V_0)^{2/3}[1 - (V/V_0)^{1/3} \times e^{\eta}] \tag{11}$$

with:

$$\eta = 1.5(B_0{}' - 1) \times [1 - (V/V_0)^{1/3}] \tag{12}$$

A discussion of a large number of equations of state and various theoretical as well as experimental aspects can be found in an earlier review.[43]

For reversible phase transitions in thermodynamic equilibrium conditions, the relation between Gibb's free energy $G$, internal energy $U$, temperature $T$,

entropy $S$, volume $V$ and pressure $P$ is given by the expression:

$$\Delta G = \Delta U - T\Delta S + P\Delta V = 0 \tag{13}$$

or:

$$\Delta U = T\Delta S - P\Delta V \tag{14}$$

Temperature-induced phase transitions are typically associated with small volume changes so that the change of the internal energy is dominated by the entropy term $T\Delta S$. For pressure-induced phase transitions with volume changes of the order of 10%, the $P\Delta V$ term dominates and the entropy term can be neglected at room temperature. The corresponding work $\Delta W$ is defined as:

$$\Delta W = -\int P\,\partial V \text{ at } T = \text{constant} \tag{15}$$

and amounts to approximately 1% of the Madelung part of the lattice energy for typical ionic crystals such as ZnS.

## SELECTED REVIEWS

### *In-situ* diffraction

P. Norby, *in-situ* XRD as a tool to understanding zeolite crystallization, *Curr. Opin. Colloid Interface Sci.*, 2006, **11**, 118–125.

J. Munn, P. Barnes, D. Häusermann, S. A. Axon and J. Klinowski, *in-situ* studies on the hydrothermal synthesis of zeolites using synchrotron energy-dispersive X-ray diffraction, *Phase Trans.*, 1992, **39**, 129–134.

R. I. Walton and D. O'Hare, Watching solids crystallise using *in situ* powder diffraction, *Chem. Commun.*, 2000, 2283–2291.

R. J. Francis and D. O'Hare, The kinetics and mechanisms of the crystallisation of microporous materials, *J. Chem. Soc., Dalton Trans.*, 1998, 3133–3148.

### High-pressure Diffraction

*High-pressure Crystallography*, ed. A. Katrusiak and P. McMillan, NATO Science Series 2, 2003, vol. 140.

M. I. McMahon, *Z. Kristallogr.*, 2004, **219**, 742.

M. I. McMahon and R. J. Nelmes, *Chem. Soc. Rev.*, 2006, **35**, 943.

R. J. Nelmes and M. I. McMahon, *Semiconductors Semimetals*, 1998, **54**, 145.

U. Schwarz, *Z. Kristallogr.*, 2004, **219**, 376.

U. Schwarz, *Z. Kristallogr.*, 2006, **221**, 420.

K. Syassen, *Physica B&C*, 1986, **139**, 277.

## REFERENCES


1. C. Riekel and R. Schollhorn, *Mater. Res. Bull.*, 1976, **11**, 369–376.
2. A. N. Christensen, M. S. Lehmann and J. Pannetier, *J. Appl. Crystallogr.*, 1985, **18**, 170–172.
3. A. N. Christensen, H. Fjellvåg and M. S. Lehmann, *Acta Chem. Scand. Ser. A*, 1985, **39**, 593–604.
4. A. C. Jupe, X. Turrillas, P. Barnes, S. L. Colston, C. Hall, D. Hausermann and M. Hanfland, *Phys. Rev. B*, 1996, **53**, R14697.
5. P. Barnes, A. C. Jupe, S. L. Colston, S. D. Jacques, A. Grant, T. Rathbone, M. Miller, S. M. Clark and R. J. Cernik, *Nucl. Instrum. Methods Phys. Res. Sect. B*, 1998, **134**, 310–313.
6. G. Muncaster, A. T. Davies, G. Sankar, C. R. A. Catlow, J. M. Thomas, S. L. Colston, P. Barnes, R. I. Walton and D. O'Hare, *Phys. Chem. Chem. Phys.*, 2000, **2**, 3523–3527.
7. R. I. Walton, R. J. Francis, P. S. Halasyamani, D. O'Hare, R. I. Smith, R. Done and R. Humpreys, *Rev. Sci. Instrum.*, 1999, **70**, 3391.
8. R. I. Walton, R. I. Smith and D. O'Hare, *Microporous Mesoporous Mater.*, 2001, **48**, 79–88.
9. B. S. Clausen, G. Steffensen, B. Fabius, J. Villadsen, R. Feidenhans and H. Topsoe, *J. Catal.*, 1991, **132**, 524–535.
10. B. S. Clausen, L. Grabaek, G. Steffensen, P.L. Hansen and H. Topsoe, *Catal. Lett.*, 1993, **20**, 23–36.
11. D. G. Medvedev, A. Tripathi, A. Clearfield, A. J. Celestian, J. B. Parise and J. Hanson, *Chem. Mater.*, 2004, **16**, 3659–3666.
12. D. C. Puxley, G. D. Squire and D. R. Bates, *J. Appl. Crystallogr.*, 1994, **27**, 585–594.
13. P. Norby, *J. Am. Chem. Soc.*, 1997, **119**, 5215–5221.
14. P. Norby, A. Nørlund Christensen and J.C. Hanson, *Inorg. Chem.*, 1999, **38**, 1216–1221.
15. P. Norby, J. C. Hanson, A. N. Fitch, G. Vaughan, L. Flaks and A. Gualtieri, *Chem. Mater.*, 2000, **12**, 1473.
16. A. van Valkenburg, *Diamond Res.*, 1964, 17.
17. L. Merrill and W. A. Bassett, *Rev. Sci. Instrum.*, 1974, **45**, 290.
18. D. M. Adams, A. G. Christy and A. J. Norman, *Measurement Sci. Technol.*, 1993, **4**, 422.
19. R. Letoullec, J. P. Pinceaux and P. Loubeyre, *High Pressure Res.*, 1988, **1**, 77.
20. *High-pressure Techniques in Chemistry and Physics*, ed. W. B. Holzapfel and N. S. Isaacs, Oxford University Press, Oxford, 1997.
21. G. J. Piermarini, S. Block and J. D. Barnett, *J. Appl. Phys.*, 1973, **44**, 5377.
22. J. W. Otto, J. K. Vassiliou and G. Frommeyer, *Phys. Rev. B*, 1998, **57**, 3253.
23. L. Goettel, H. K. Mao and P. M. Bell, *Rev. Sci. Instrum.*, 1985, **56**, 1422.
24. K. Takemura, *J. Appl. Phys.*, 2001, **89**, 662.
25. R. J. Angel, M. Bujak, J. Zhao, G. D. Gatta and St. D. Jacobsen, *J. Appl. Cryst.*, 2007, **40**, 26.

26. R. O. Piltz, M. I. McMahon, J. Crain, P. D. Hatton, R. J. Nelmes, R. J. Cernik and G. Bushnell-Wye, *Rev. Sci. Instrum.*, 1992, **63**, 700.
27. H. E. King and L. W. Finger, *J. Appl. Crystallogr.*, 1979, **12**, 374.
28. H. Ahsbahs, *Z. Kristallogr.*, 2004, **219**, 305.
29. R. A. Forman, G. J. Piermarini, J. D. Barnett and S. Block, *Science*, 1972, **176**, 284.
30. G. J. Piermarini, S. Block, J. D. Barnett and R. A. Forman, *J. Appl. Phys.*, 1975, **46**, 2774.
31. F. Datchi, R. LeToullec and P. Loubeyre, *J. Appl. Phys.*, 1997, **81**, 3333.
32. D. L. Decker, *J. Appl. Phys.*, 1971, **42**, 3239.
33. H. K. Mao, P. M. Bell, J. W. Shaner and D. J. Steinberg, *J. Appl. Phys.*, 1978, **49**, 3276.
34. M. Hanfland, K. Syassen and J. Köhler, *J. Appl. Phys.*, 2002, **91**, 4143.
35. F. D. Murnaghan, *Proc. Natl. Acad. Sci. U.S.A.*, 1944, **50**, 244.
36. F. Birch, *Phys. Rev.*, 1947, **71**, 809.
37. J. H. Rose, J. Ferrante and J. R. Smith, *Phys. Rev. Lett.*, 1981, **47**, 675.
38. J. R. Smith, J. Ferrante and J. H. Rose, *Phys. Rev. B*, 1982, **25**, 1419.
39. J. Ferrante, J. R. Smith and J. H. Rose, *Phys. Rev. Lett.*, 1983, **50**, 1385.
40. J. H. Rose, J. R. Smith and J. Ferrante, *Phys. Rev. B*, 1983, **28**, 1835.
41. J. H. Rose, J. R. Smith, F. Guinea and J. Ferrante, *Phys. Rev. B*, 1984, **29**, 2963.
42. P. Vinet, J. Ferrante, J. R. Smith and J. H. Rose, *J. Phys. C*, 1986, **19**, L467.
43. W. B. Holzapfel, *High Pressure Res.*, 1998, **16**, 81.
44. K. Takemura, U. Schwarz, K. Syassen, M. Hanfland, N. E. Christensen, D. L. Novikov and I. Loa, *Phys. Rev. B*, 2000, **62**, R10603.

CHAPTER 16

# Local Structure from Total Scattering and Atomic Pair Distribution Function (PDF) Analysis

SIMON BILLINGE

Department of Physics and Astronomy, 4268 Biomedical Phys. Sciences Building, Michigan State University, East Lansing, MI 48824, USA

## 16.1 INTRODUCTION

Increasingly, the materials that are under study for their interesting technological or scientific properties are highly complex. They are made of multiple elements, have large unit cells and often low dimensional or incommensurate structures.[1] Increasingly also, they have aperiodic disorder: some aspect of the structure that is different from the average crystal structure. In the case of nanoparticles the very concept of a crystal is invalid as the approximation of infinite periodicity is no longer a good one. Still we would like to study the structure of these materials. Powder diffraction is an important method for characterizing these materials, but we have to go beyond the Bragg equation and crystallographic analysis.

The "total scattering" approach treats both the Bragg and diffuse scattering on an equal basis.[2] Powder diffraction data are measured in much the same way as in a regular powder measurement. However, explicit corrections are made for extrinsic contributions to the background intensity from such things as Compton scattering, fluorescence, scattering from the sample holder, and so on, and the measured intensity is normalized by the incident flux. The resulting coherent scattered intensity, $I(Q)$, is a continuous function of $Q$, the magnitude of the scattering vector, where:

$$Q = |\boldsymbol{Q}| = 2k \sin\theta = \frac{4\pi \sin\theta}{\lambda}$$

Sharp intensities are observed where there are Bragg peaks with broad features, the diffuse scattering, in between. In general we like to work with a normalized version of this scattering intensity, $S(Q)$, that is in absolute units of scattering-per-atom.[2] To obtain this we divide $I(Q)$ by the number of scatterers, $N$, and the average scattering power per atom. In the case of X-rays the average scattering per atom is given by the square of the atomic form factor, $f(Q)$, and in the case of neutrons it is the coherent scattering cross-section. If more than one type of atom (or in the case of neutrons, more than one isotope) is present, an additional incoherent scattering term (the Laue monotonic diffuse scattering) must also be subtracted. The resulting $S(Q)$ is known as the ''total-scattering structure function''. It is a dimensionless quantity and the normalization is such that the average value, $\langle S(Q)\rangle = 1$. Here the angle brackets indicate an average over $Q$. Despite the tricky definition, it is worth remembering that $S(Q)$ is nothing other than the powder diffraction pattern that has been corrected for experimental artifacts and suitably normalized. There is no reason why one could not carry out a Rietveld refinement directly on $S(Q)$, though in practice this is never done as there is little point in making all the explicit corrections that are accounted for with parameterized equations in the Rietveld refinement code. This may change in the future as computing power increases and we push towards solving problems of greater complexity. An example of $S(Q)$ is shown in Figure 16.1.

In practice, the $S(Q)$ determined for total scattering studies is measured over a wide range of $Q$-values. The coherent intensity (the features) in $S(Q)$ dies out with increasing $Q$ due to the Debye–Waller factor, which comes from thermal and quantum zero-point motion of the atoms as well as any static displacive disorder in the material. By a $Q$-value of 30–50 $\text{Å}^{-1}$ (depending on temperature and stiffness of the bonding) there are no more features in $S(Q)$ and there is no need to measure to higher-$Q$. Still, this is much higher than conventional powder diffraction experiments using laboratory X-rays or reactor neutrons. The maximum $Q$ attainable in back-scattering from a copper $K_\alpha$ tube is around 8 $\text{Å}^{-1}$ and from a Mo $K_\alpha$ tube, 16 $\text{Å}^{-1}$. Routine total-scattering measurements can be made using laboratory sources with Mo or Ag tubes; however, for the highest real-space resolution, and the best statistics, synchrotron data are preferred. In the case of neutron scattering, spallation neutron sources, which have large fluxes of short-wavelength epithermal neutrons, are ideal for this type of experiment.

Total scattering $S(Q)$ functions appear different to standard powder diffraction measurements because of the $Q$-range studied, but also because of an important aspect of the normalization: the measured intensity is divided by the total scattering cross-section of the sample. For neutrons, this scattering cross-section is simply $\langle b\rangle^2$, where $b$ is the coherent neutron scattering length of the atoms of the material in units of barns. The angle brackets denote an average over the different types of nuclei (chemical and isotopic variants) in the sample. This will be discussed in greater detail later. The scattering length, $b$, is constant as a function of $Q$ and so is just part of the overall normalization coefficient. However, in the case of X-ray scattering, the sample scattering cross-section is the square of the atomic form-factor, $\langle f(Q)\rangle^2$, which becomes very small at

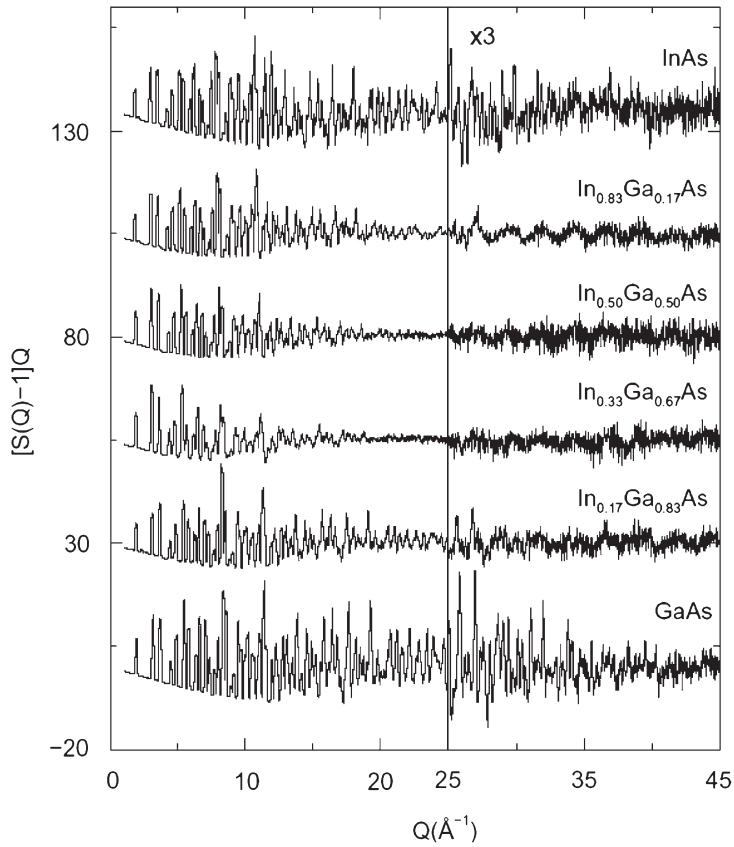



**Figure 16.1** Examples of reduced $S(Q)$ functions ($Q[S(Q)$ 1]) from semiconductor alloy samples from the system $In_xGa_{1-x}$ As. Data were measured using X rays at the CHESS synchrotron source at Cornell University in New York. (Reprinted with permission from ref. 4, © 2001, American Physical Society.)

high-$Q$. Thus, during the normalization process the data at high-$Q$ are amplified (by being divided by a small number). This has the effect that even rather weak intensities at high-$Q$, which are totally neglected in a conventional analysis of the data, become rather important in a total-scattering experiment. Because the signal at high-$Q$ is weak it is important to collect the data in that region with good statistics and so one runs into the somewhat paradoxical situation that a large amount of counting time can be devoted to measuring rather flat and relatively featureless data in the high-$Q$ region, to the surprise of colleagues visiting the beamline or laboratory. This is illustrated in Figure 16.2.

Thus, the value added of a total scattering experiment over a conventional powder diffraction analysis is both in the inclusion of diffuse scattering and Bragg peak intensities in the analysis, and also the wide range of $Q$ over which data are measured and the increased weighting given to the high-Q

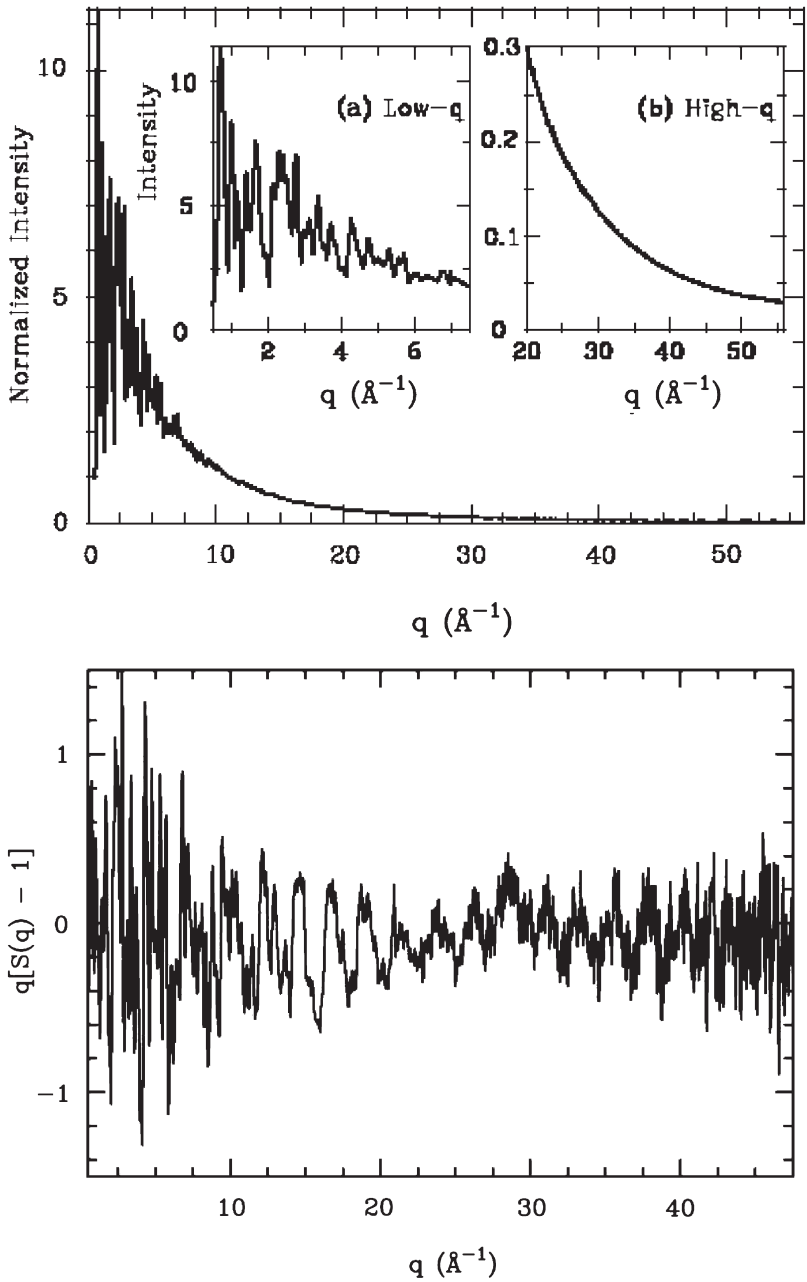



**Figure 16.2** Comparison of raw data and normalized reduced total scattering structure function $F(Q) = Q[S(Q) \quad 1]$. The sample is a charge density wave organic and the data are X ray data from CHESS synchrotron source. The raw data are shown in the top panel, on expanded scales in the insets. The high $Q$ data in the region $20 < Q < 45$ is smooth and featureless. However, after normalizing and dividing by the square of the atomic form factor, important diffuse scattering is evident in this region of the diffraction pattern (lower panel).[2]

information. In fact, the total scattering name comes from the fact that *all* the coherent scattering in *all* of $Q$-space is measured.

Total scattering data can be analyzed by fitting models directly in reciprocal-space [*i.e.*, the $S(Q)$ function is fit]. However, an alternative and intuitive approach is to Fourier transform the data to real-space to obtain the atomic pair distribution function (PDF), which is then fit in real-space. The reduced pair distribution function, $G(r)$, is related to $S(Q)$ through a sine Fourier transform according to:

$$G(r) = \frac{2}{\pi}\int_0^\infty Q[S(Q) - 1]\sin(Qr)dQ \tag{1}$$

Figure 16.3 shows examples of $G(r)$ functions. These were obtained from the same data as shown in Figure 16.1.

The PDF is a probability distribution function in real-space. It is a measure of the probability of finding pairs of atoms in the material separated by a

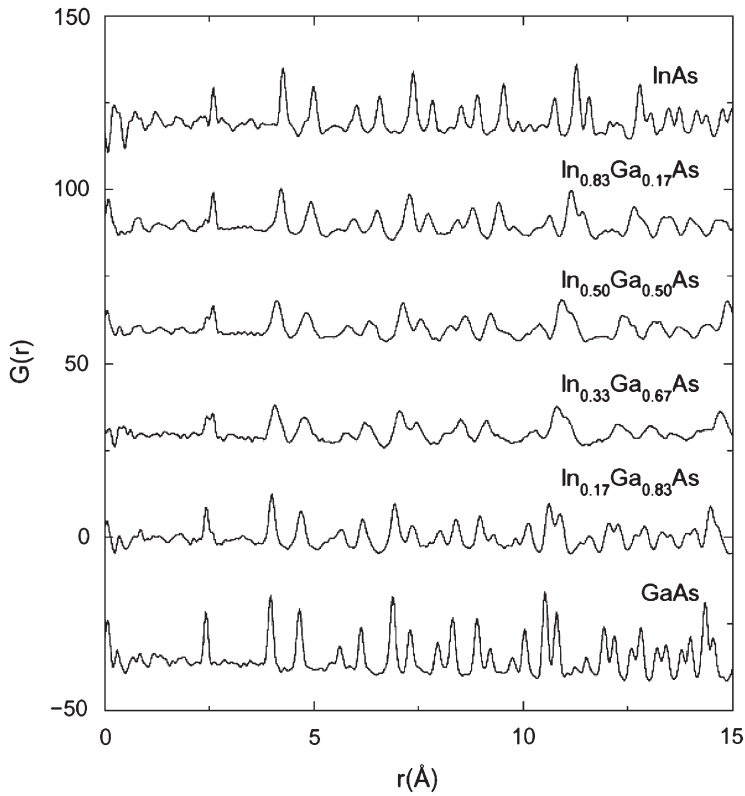



**Figure 16.3** $G(r)$ functions obtained from the structure functions in Figure 16.1 for the semiconductor alloy $In_xGa_{1-x}As$. (Reprinted with permission from ref. 4, © 2001, American Physical Society.)

distance, $r$. Peaks in the function coincide with a high probability and the function returns to its baseline if there is zero probability of finding atoms separated by that distance. There are a whole family of distribution functions that are used in different circumstances, all with subtly different definitions and normalizations (and units),[2,3] but they all contain the same information: the probability of finding atoms at separation $r$.

To find our way around this function we can consider Figure 16.3. There are no peaks (other than low-$r$ measurement artifacts) below the nearest neighbor peak at $\sim$2.5 Å,[4] which is the Ga–As separation in GaAs and at slightly larger-$r$ for the In–As separation in InAs. This is because atoms cannot approach each other closer than this nearest neighbor separation and there is, therefore, a zero probability of finding two atoms separated by that distance. There is a high probability of finding atoms at exactly the nearest neighbor distance of $\sim$2.5 Å as they are bonded to each other precisely at that distance, then a zero probability of finding atoms at any other distance until we find the second-neighbor coordination shell at around 3.5 Å, then the third neighbor coordination shell at 4.5 Å and so on. This pattern is characteristic of a crystalline material, with sharp, well-defined coordination shells whose position is determined by the crystal structure. Fitting these peaks therefore allows us to learn about the crystal structure. In more disordered materials, such as liquids and amorphous materials, the second and third neighbor shells become broad and the features in the PDF smear out rapidly with increasing $r$.

In crystals, in addition to the nearest-neighbor information, valuable structural information is contained in the pair-correlations extending to much higher values of $r$. In fact, with high $Q$-space resolution data, PDFs can be measured out to tens to hundreds of nanometres (hundreds to thousands of angstroms) and the structural information remains quantitatively reliable (Figure 16.4).[5]

As we discuss later, PDFs can be fit using structural models, allowing us to extract quantitative structural information about the local and intermediate

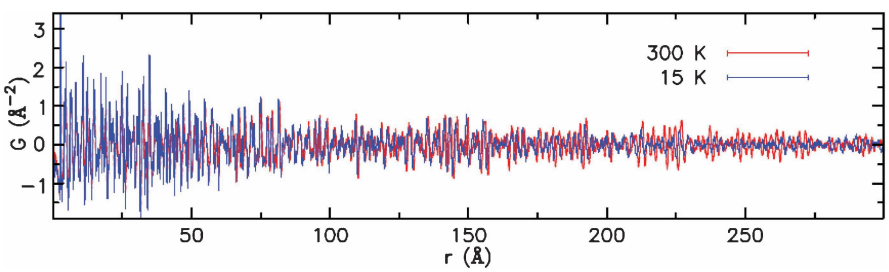



**Figure 16.4** PDF shown extending out to high $r$. The PDF is from $Zn_4Sb_3$ taken at two different temperatures as shown. See ref. 5 for details. The range of the data is limited only by the resolution of the measurement. The high resolution neutron data were collected at the NPDF instrument at Los Alamos National Laboratory Higher resolutions, and, therefore, wider ranges of $r$ for the PDF are possible at X ray synchrotron sources.

range structure. Recently, *ab initio* structure determination from the PDF has also been demonstrated for a nanoparticle.[6]

What do we gain scientifically from taking this approach? We will discuss this in more detail below, but the diffuse scattering gives information about local distortions to the structure that are not periodic. One can think of crystallography as giving the average, or mean-field, structural solution. In physics, the mean-field approximation in a model neglects fluctuations. Going beyond the mean-field means exploring local fluctuations that are sometimes important, *e.g.*, near a second-order phase transition. This may also be the case structurally where local deviations from the average structure can give rise to important properties in the material (an example is the insulating phase of colossal magnetoresistant manganites[7]). A second important asset of this approach is that Bragg and diffuse intensity is treated in an unbiased way, which means that samples that contain both Bragg and diffuse intensities, or features that are half way between Bragg and diffuse scattering such as from nanoparticles, can be treated straightforwardly.

There are now many classes of problems that have been studied using total scattering analysis. Traditionally it was used for liquids and amorphous materials,[12,13] more recently for the study of disorder in crystalline materials, and now with increasing popularity it is used to study nanostructured materials. Several recent reviews[2,8,9] give examples of modern applications of the PDF method.

## 16.2 THEORY

### 16.2.1 Single Component Systems

*16.2.1.1 The PDF is an Experimentally Measurable Function.* The basis of the total scattering method is the normalized, measured, scattering intensity from a sample: the total scattering structure function, $S(\mathbf{Q})$.[2,10,11] The wavevector, $\mathbf{Q}$, is a vector quantity and in general the intensity variation, $S(\mathbf{Q})$, will depend on which direction one looks in $Q$-space. However, when the sample is isotropic, for example, a powder, it depends only on the magnitude of $Q$ and not its direction. The greatest utility of the technique to date has been to study the isotropic scattering from powdered, liquid or glassy samples. In this case, the scattered intensity from a sample is given by the Debye Equation:[14]

$$I_{coh}(Q) = \sum_{m,n} f_m(Q) f_n^*(Q) \frac{\sin Qr}{Qr} \tag{2}$$

where each of the sums runs over all scattering centers in the sample. This equation is obtained from an orientational average of the standard scattering equation:

$$I_{coh}(\mathbf{Q}) = \sum_{m,n} f_m(Q) f_n^*(Q) \mathrm{e}^{\mathbf{Q}.(\mathbf{r}_m \ \ \mathbf{r}_n)} \tag{3}$$

Here $\mathbf{r}_m$ is the position vector of the $m$th atom, and again each of the sums run over every atom in the solid.

Finally, $S(Q)$ can be written in terms of the coherent scattering intensity from Equation (2) as:

$$S(Q) = \frac{1}{N\langle f(Q)\rangle^2}\left[I_{coh}(Q) + \langle f(Q)\rangle^2 - \langle f^2(Q)\rangle\right] \tag{4}$$

The angle brackets denote an average over atom types (and isotopes in the case of neutrons). In the most general case, close to an absorption edge, the X-ray scattering factors, $f$, are complex [see Equation (30) below] and for completeness we reproduce these averages explicitly here:

$$\langle f(Q)\rangle^2 = \sum_{\alpha\beta} c_\alpha c_\beta \left[(f_\alpha(Q) + f'_\alpha)(f_\beta(Q) + f'_\beta) + f''_\alpha f''_\beta\right] \tag{5}$$

and:

$$\langle f^2(Q)\rangle = \sum_{\alpha\beta} c_\alpha^2 \left[\left(f_\alpha(Q) + f'_\alpha\right)^2 + \left(f''_\alpha\right)^2\right] \tag{6}$$

It is readily seen that for a single element system $\langle f(Q)\rangle^2 = \langle f^2(Q)\rangle$ and:

$$S(Q) = \frac{I_{coh}(Q)}{N\langle f(Q)\rangle^2}$$

The other terms account for an incoherent elastic background that comes about because of the different scattering length of atoms on different sites.

Similarly, the Fourier transform of the scattered intensity in the form of $S(Q)$, yields the reduced atomic pair distribution function, $G(r)$, defined by Equation (1). This is strictly correct when the sample is made of a single element. We will discuss later an approximate extension, which works excellently in practice, to the more interesting case of multiple elements.

The inverse transformation of Equation (1) can be defined and it yields the structure function $S(Q)$ in terms of $G(r)$:

$$S(Q) = 1 + \frac{1}{Q}\int_0^\infty G(r)\sin(Qr)\,dr \tag{7}$$

There are several similar correlation functions related to $G(r)$ by multiplicative and additive constants. They contain the same structural information but are subtly different in some detail. Their interrelationship has been discussed in detail in the literature.[3] $G(r)$ is the function obtained directly from the Fourier transform of the scattered data. The function oscillates around zero and asymptotes to zero at high-$r$. It also tends to zero at $r = 0$ with the slope $-4\pi\rho_0$, where $\rho_0$ is the average number density of the material. From a practical point of view $G(r)$ is an attractive function because the random uncertainties on the data (propagated from the measurement) are constant in $r$. This means that fluctuations in the difference between a calculated and measured $G(r)$ curve have the same significance at all values of $r$. Thus, for example, if the observed fluctuations in the

difference curve decrease with increasing $r$, this implies that the model is providing a better fit at longer distances (perhaps it is a model of the average crystallographic structure). This inference cannot be made directly from a difference curve to other differently normalized functions [such as $\rho(r)$ or $g(r)$ (ref. 2)]. A further advantage of the $G(r)$ function is that the amplitude of the oscillations gives a direct measure of the structural coherence of the sample. In a crystal with perfect structural coherence, oscillations in $G(r)$ extend to infinity with a constant peak–peak amplitude.[15] In a real measurement, the $G(r)$ peak–peak amplitude of the signal gradually falls off due to the finite $Q$-resolution of the measurement, which is then the limitation on the spatial coherence of the measurement rather than the structural coherence itself. A higher $Q$-resolution results in data extending over a wider range of $r$. In samples with some degree of structural disorder, the signal amplitude in $G(r)$ falls off faster than dictated by the $Q$-resolution and this becomes a useful measure of the structural coherence of the sample. For example, it can be used to measure the diameter of nanoparticles.

Another function often denoted $g(r)$ is called the pair distribution function. It is normalized so that, as $r \to \infty$, $g(r) \to 1$ and has the property that for $r$ shorter than the distance of closest approach of pairs of atoms $g(r)$ becomes zero. It is closely related to the pair density function, $\rho(r) = \rho_0 g(r)$. Clearly, $\rho(r)$ oscillates about, and then asymptotes to, the average number density of the material, $\rho_0$ at high-$r$ and becomes zero as $r \to 0$. The relationship between these correlation functions is given by:

$$G(r) = 4\pi r(\rho(r) - \rho_0) = 4\pi\rho_0 r(g(r) - 1) \tag{8}$$

Finally, we describe the radial distribution function (RDF), $R(r)$ given by:

$$R(r) = 4\pi r^2 \rho(r) \tag{9}$$

which is related to $G(r)$ by:

$$G(r) = \frac{R(r)}{r} - 4\pi r\rho_0 \tag{10}$$

The $R(r)$ function is important because it is the most closely related to the physical structure since $R(r)dr$ gives the number of atoms in a spherical shell of thickness $dr$ at distance $r$ from another atom. For example, the coordination number, or the number of neighbors, $N_C$, is given by:

$$N_C = \int_{r_1}^{r_2} R(r)dr \tag{11}$$

where $r_1$ and $r_2$ define the beginning and ending positions of the RDF peak corresponding to the coordination shell in question.

*16.2.1.2 The PDF is a Structurally Determined Function.* This suggests a scheme for calculating PDFs from atomic models. Consider a model consisting of a large number of atoms situated at positions $\mathbf{r}_v$ with respect to some origin.

Expressed mathematically, this amounts to a series of delta functions, $\delta(\boldsymbol{r}-\boldsymbol{r}_v)$. The RDF is then given as:

$$R(r)=\frac{1}{N}\sum_{\nu}\sum_{\mu}\delta(r-r_{\nu\mu}) \tag{12}$$

where $r_{\nu\mu}=|\boldsymbol{r}_\nu-\boldsymbol{r}_\mu|$ is the magnitude of the separation of the $\nu$-th and $\mu$-th atoms and the double sum runs twice over all atoms in the sample. Later we address explicitly samples with more than one type of atom, but for completeness we give here the expression for $R(r)$ in this case:

$$R(r)=\frac{1}{N}\sum_{\nu}\sum_{\mu}\frac{b_\nu b_\mu}{\langle b\rangle^2}\delta(r-r_{\nu\mu}) \tag{13}$$

where the $b$'s are the $Q$-independent coherent scattering lengths for the $\nu$th and $\mu$th atoms and $\langle b\rangle$ is the sample average scattering length. In the case of X-rays the $b$'s are replaced with atomic number, $Z$.

The specification of $R(r)$ given in Equation (12) has the required property that if we integrate $R(r)\mathrm{d}r$ over some range, for example the near-neighbor coordination shell, we get the average number of atom neighbors in that range (*i.e.*, the coordination number), since the integral of a delta-function is unity and there is one delta-function for each atom-pair.

### 16.2.2 Multicomponent Systems

For a single element sample the properly normalized $R(r)$ gives directly the coordination number through Equation (11). For multi-element systems we have defined $R(r)$ according to Equation (13). If this is substituted into Equation (11) we do not get the coordination number directly, but a coordination weighted by the scattering lengths of the atoms involved. If we know the atomic species involved we can extract the coordination, but not otherwise. Also, we could have chosen a different weighting scheme. The one used is by far the most common and is due to Faber and Ziman.[16] We define a *partial pair distribution function*, $G_{\alpha\beta}(r)$, that is equivalent to $G(r)$ but gives the distribution of atom pairs in the material coming only from atoms of type $\beta$ around atoms of type $\alpha$.[17] The total $G(r)$ is then simply the properly weighted sum, over the atom types $\alpha$, of all the partials.

There is an equivalent relationship between the partial structure functions, $S_{\alpha\beta}(Q)$ and the total structure function, $S(Q)$. In the Faber–Ziman scheme, the weighting is chosen such that each partial structure factor, $S_{\alpha\beta}(Q)$, has the same property of the total structure factor that as $Q\to\infty$, $S_{\alpha\beta}(Q)=1$. This means that we can define the Fourier couple between $S_{\alpha\beta}(Q)$ and $G_{\alpha\beta}(r)$ in the same way as for the total structure function, *i.e.*:

$$G_{\alpha\beta}(r)=\frac{2}{\pi}\int_0^\infty Q[S_{\alpha\beta}(Q)-1]\sin(Qr)dQ \tag{14}$$

The price we pay for this convenience is that the total functions, $S(Q)$ and $G(r)$, are not simply the sum of the partials, but weighted sums:

$$\begin{aligned} S(Q) &= \sum_{\alpha}\sum_{\beta}\frac{c_\alpha c_\beta b_\alpha b_\beta}{\langle b\rangle^2}S_{\alpha\beta}(Q) \\ G(r) &= \sum_{\alpha\beta}\frac{c_\alpha c_\beta b_\alpha b_\beta}{\langle b\rangle^2}G_{\alpha\beta}(r), \end{aligned} \tag{15}$$

where $\langle b\rangle = \sum_\alpha c_\alpha b_\alpha$ and $c_\alpha$ is the atomic fraction of species $\alpha$ in the sample. In this case we get the partial radial distribution function:

$$R_{\alpha\beta}(r) = \frac{1}{N}\frac{\left(\sum_\alpha c_\alpha b_\alpha\right)^2}{c_\alpha c_\beta b_\alpha b_\beta}\sum_{\nu\in\{\alpha\}}\sum_{\mu\in\{\beta\}}\delta\left(r - r_{\nu\mu}\right) \tag{16}$$

and:

$$G_{\alpha\beta}(r) = \frac{\left(\sum_\alpha c_\alpha b_\alpha\right)^2}{c_\alpha c_\beta b_\alpha b_\beta}\frac{1}{Nr}\sum_{\nu\in\{\alpha\}}\sum_{\mu\in\{\beta\}}\delta\left(r - r_{\nu\mu}\right) - 4\pi r\rho_0 \tag{17}$$

the number of $\beta$ atoms around an $\alpha$ atom is given by $N_C^{\alpha\beta}$ from which we get:

$$N_C = \sum\frac{c_\alpha c_\beta b_\alpha b_\beta}{\langle b\rangle^2}N_C^{\alpha\beta}(r) \tag{18}$$

A problem arises in the case of X-rays because the X-ray equivalent of the scattering length, $b$, is the $Q$-dependent scattering factor, $f(Q)$. Having this factor $Q$-dependent breaks the simple Fourier couple in Equation (1), an approximation, since the structure function is given by:

$$S(Q) = \sum_{\alpha\beta}\frac{c_\alpha c_\beta f_\alpha(Q)f_\beta^*(Q)}{\langle f(Q)\rangle^2}S_{\alpha\beta}(Q) \tag{19}$$

where the asterisk denotes the complex conjugate and the weighting factor:

$$w_{\alpha\beta}(Q) = \frac{c_\alpha c_\beta f_\alpha(Q)f_\beta^*(Q)}{\langle f(Q)\rangle^2}$$

is $Q$-dependent. In this case the total PDF is not exactly the weighted sum of partial PDFs. It can be made to approximate this situation by separating the absolute value of $f(Q)$ and its $Q$-dependence: the so-called Morningstar–Warren approximation.[18] The $Q$-dependence of the *average* form factor is found according to:

$$\bar{f}(Q) = \frac{\sum_\alpha c_\alpha f_\alpha(Q)}{\sum_\alpha c_\alpha f_\alpha(0)} \tag{20}$$

and the approximation is then made that $f_\alpha(Q) = Z_\alpha \bar{f}(Q)$, where $Z_\alpha$ is the atomic number of the $\alpha$-th element, which is approximately equal to $f_\alpha(0)$. Now the weighting factors, $w_{\alpha\beta}$, are then roughly $Q$-independent. Although this appears to be a somewhat poor approximation, the success with which multiple element X-ray PDFs from multicomponent systems can be fit by structural models suggests that it is valid.

Other weighting schemes are possible, *e.g.*, the Bathia and Thornton scheme that is sometimes used in binary systems. Interested readers are referred to other sources for details.[2,10]

A normal total-scattering powder diffraction measurement measures the chemically unresolved total-PDF. Chemically resolved information can be recovered through modeling and this is done routinely with profile-fitting programs such as PDFfit.[19] However, for complex materials, sometimes it is desirable to recover chemically resolved information directly to help in the analysis. This information is available on a very local scale in complementary measurements such as extended X-ray absorption fine structure (EXAFS).[20] It is also possible to determine chemically resolved information in a PDF measurement. This is done using differential methods.[17] Two measurements are made that are identical except that the scattering power of one of the chemical constituents changes. By taking a difference between these two measurements the differential PDF can be recovered that gives the structural environment around the target chemical species. In terms of the partial PDFs defined above, the differential PDF (DPDF), $G_\alpha$, is:

$$G_\alpha(r) = \sum_\beta \frac{c_\beta b_\beta}{\langle b \rangle} G_{\alpha\beta}(r) \tag{21}$$

In terms of DPDFs the total PDF is given by:

$$G(r) = \sum_\alpha \frac{c_\alpha b_\alpha}{\langle b \rangle} G_\alpha(r) \tag{22}$$

The DPDF is related to the differential structure function (DSF):

$$S_\alpha(Q) = \sum_\beta \frac{c_\beta b_\beta}{\langle b \rangle} S_{\alpha\beta}(Q) \tag{23}$$

through the Fourier-transformation:

$$G_\alpha(r) = \frac{2}{\pi} \int_0^\infty Q[S_\alpha(Q) - 1] \sin(Qr) dQ \tag{24}$$

Similarly, the DSF is related to the total structure function by:

$$S(Q) = \sum_\alpha \frac{c_\alpha b_\alpha}{\langle b \rangle} S_\alpha(Q) \tag{25}$$

In principal, the partial PDFs can be determined by taking second and higher order differences. For an $n$-element compound there are $n(n+1)/2$ partials and therefore $n(n+1)/2$ independent measurements of the same sample are required to determine the full set of partials. For example, for a binary $n=2$ and 3 therefore independent data-sets are required to recover the three partials.

Experimentally, the differential PDF can be determined using isotopic substitution in the case of neutrons, and using anomalous X-ray scattering in the X-ray case. The neutron case is the more straightforward. Different isotopes of an element are chemically identical but have different scattering powers for neutrons. Thus, two identical samples can be synthesized using different isotopes (or different levels of isotopic enrichment) of a particular element. If we define the scattering from the sample with isotope 1 of species $\alpha$ with scattering length $b_{\alpha 1}$ we get:

$$S_1(Q) = \frac{1}{\langle b_1 \rangle^2}\left[(c_\alpha b_{\alpha 1})^2 S_{\alpha\alpha}(Q) + 2c_\alpha b_{\alpha 1}\sum_{\beta\neq\alpha} c_\beta b_\beta S_{\alpha\beta}(Q) + \sum_{\beta\gamma\neq\alpha} c_\beta c_\gamma b_\beta b_\gamma S_{\beta\gamma}(Q)\right] \tag{26}$$

with:

$$\langle b_1 \rangle = c_\alpha b_{\alpha 1} + \sum_{\beta\neq\alpha} c_\beta b_\beta \tag{27}$$

The difference in the intensity, $\Delta I$, between two experiments carried out with isotopes 1 and 2 of element $\alpha$ is:

$$\Delta I(Q) = \langle b_1 \rangle^2 S_1(Q) - \langle b_2 \rangle^2 S_2(Q) \tag{28}$$

which after, substituting in Equation (26) and simplifying, gives:

$$\Delta I(Q) = 2c_\alpha(b_{\alpha 1} - b_{\alpha 2})S_\alpha(Q) \tag{29}$$

The difference in intensity, therefore, directly yields the differential structure function, $S_\alpha(Q)$, and by Fourier transformation the DPDF.

This method is more commonly applied in measurements of glasses and liquids but can be equally well applied to complex crystals or nanocrystals. The principle problem with this approach is the cost and availability of suitable isotopes and the effort required in synthesizing multiple samples. A poor man's version is the chemical substitution method in which an element is replaced by another element with very similar chemical nature and different scattering length.

In the X-ray anomalous scattering method[21] we make use of the fact that the scattering length of an element changes appreciably near an absorption resonance and is given by:

$$f(Q,E) = f_0(Q) + f'(E) + if''(E) \tag{30}$$

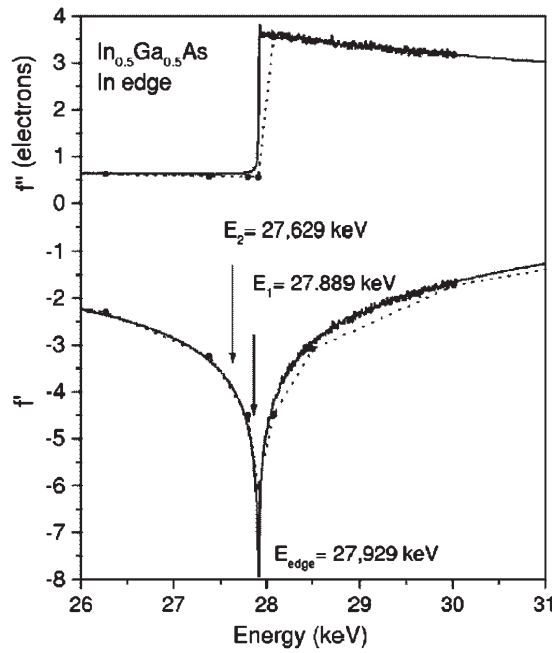



**Figure 16.5** Anomalous dispersion of In scattering factors calculated near the K absorption edge. (Top) imaginary part, $f''$; (bottom) real part, $f'$. (Reprinted with permission from ref. 22, © 2000, American Institute of Physics.)

$f'(E)$ and $f''(E)$ are the real and imaginary parts of the anomalous scattering factor, which are zero away from a resonance but become finite near the absorption edge. Figure 16.5 shows an example of the energy dependence of $f'$ and $f''$.[22]

From Equation (15) we get that the total $S(Q)$ determined at energy 1 is given by:

$$S_1(Q) = \frac{1}{\langle f \rangle_1^2} \sum_{\alpha\beta} c_\alpha c_\beta f_\alpha f_\beta^*(Q) S_{\alpha\beta}(Q),$$
$$= \frac{1}{\langle f \rangle_1^2} \left( c_A f_{A1} \sum_\beta c_\beta f_\beta^*(Q) S_{A\beta}(Q) + c.c. + \sum_{\alpha,\beta \neq A} c_\alpha c_\beta f_\alpha f_\beta^*(Q) S_{\alpha\beta}(Q) \right), \tag{31}$$

where *c.c.* denotes the complex conjugate, and we have separated out the terms involving element A from the double sum. Similarly at energy 2 we get:

$$S_2(Q) = \frac{1}{\langle f \rangle_2^2} \left( c_A f_{A2} \sum_\beta c_\beta f_\beta^*(Q) S_{A\beta}(Q) + c.c. + \sum_{\alpha,\beta \neq A} c_\alpha c_\beta f_\alpha f_\beta^*(Q) S_{\alpha\beta}(Q) \right) \tag{32}$$

After rescaling to put these functions on the same scale we can define the difference:

$$\Delta S(Q) = \langle f \rangle_1^2 S_1(Q) - \langle f \rangle_2^2 S_2(Q) \tag{33}$$

which from Equations (31) and (32) is given by:

$$\Delta S(Q) = c_A \Delta f_A \sum_\beta c_\beta f_\beta^*(Q) S_{A\beta}(Q) + c.c. \tag{34}$$

where $\Delta f_A = f_{A1} - f_{A2}$. The only changes in the scattering factor, $\Delta f$, are due to the anomalous corrections, which, after taking the real part results in:

$$\Delta S(Q) = 2c_A \Delta f'_A \sum_\beta c_\beta \left( f_{0\beta}(Q) + f'_\beta \right) S_{A\beta}(Q) + 2c_A \Delta f''_A \sum_\beta c_\beta f''_\beta S_{A\beta}(Q) \tag{35}$$

We seek the differential structure function given by Equation (23) above. Combining Equations (23) and (35) and rearranging we get the differential, $S_A(Q)$:

$$S_A(Q) = \frac{\Delta S(Q)}{2c_A \Delta f'_A \sum_\beta c_\beta \left( f_{0\beta}(Q) + f'_\beta \right) + 2c_A \Delta f''_A \sum_\beta c_\beta f''_\beta} \tag{36}$$

In general we can use the fact that $\Delta f''_A \ll \Delta f'_A$ giving an approximate expression:[17]

$$S_A(Q) = \frac{\Delta S(Q)}{2c_A \Delta f'_A \sum_\beta c_\beta \left( f_{0\beta}(Q) + f'_\beta \right)} \tag{37}$$

The differential PDF can be obtained directly by Fourier transformation according to Equation (1).

Experimentally we determine $\Delta S(Q)$ by taking two data-sets at different energies, one close to the absorption edge and another some distance away. From Equation (37) we see that the signal in $\Delta S(Q)$ scales with $\Delta f'_A$ and the best experiment would be made when this is as large as possible. Looking at the shape of $f'_A(E)$ in Figure 16.5 we see that for the edge-measurement it is important to get as close as possible to the cusp in $f'_A(E)$ that is centered at the absorption edge. However, for practical reasons even though $f'$ changes most rapidly right at the edge, it is advisable to stay a little below the edge. One reason is that the absorption factor changes rapidly near the edge, making the absorption correction very difficult. Additionally, in the region below the edge $f''_A(Q)$ changes very slowly, which makes the approximation used to get Equation (37) much better, and the fluorescence from the sample is much less than in the region right above the edge; experiments are carried out below the absorption edge of the sample.

## 16.3 EXPERIMENTAL METHODS

The objective of total scattering experiments is to measure $S(Q)$ of a sample with high accuracy. Total scattering measurements have basically the same requirements as any powder diffraction measurement and the methods are described in detail in Chapter 2. However, total scattering measurements have special additional requirements for high-quality data and often the geometries and setups used are somewhat different. Requirements for high quality total scattering data include:

1. Data measured over a wide $Q$-range. This requires wide scattering angles and/or short-wavelength incident radiation.
2. Good statistics, especially at high-$Q$ where the scattering signal is weak.
3. Low background scattering. It is important to measure weak diffuse scattering signals accurately, which is difficult on top of high backgrounds.
4. Stable set-up and accurate incident intensity monitoring. The data are normalized by incident intensity. It is important that the incident beam and detector characteristics do not change in an uncontrolled way during the experiment, or that this can be corrected, *e.g.* by monitoring the incident beam intensity as is done at synchrotron X-ray and spallation neutron measurements.

X-ray experiments can be carried out using laboratory diffractometers with Mo or Ag sources, which give $Q$-ranges up to $Q_{max} \approx 14\,\text{Å}^{-1}$ and $20\,\text{Å}^{-1}$, respectively. These are less than optimal values for $Q_{max}$, but acceptable for straightforward characterization of nanostructured materials at room temperature. Experiments have also been attempted using tungsten sources, though these are currently not standard in diffraction and it is not possible to buy diffraction grade high-voltage power supplies for this type of source and there are no off-the-shelf diffraction instruments with tungsten sources.

Optimally, total scattering X-ray experiments are carried out at X-ray synchrotron sources using high incident energy X-rays. These can be done with incidence energies in the vicinity of 30–45 keV in conventional Debye–Scherrer geometry (for instance using beamline X7A at NSLS, or beamlines such as X31 at ESRF or X11A at APS that are constructed for regular powder diffraction). However, increasingly common these days is to use the rapid acquisition PDF (RAPDF) mode[23] in which data for a PDF is collected in a single-shot using a planar 2D detector. This is illustrated in Figure 16.6.

A dedicated beamline has been constructed at APS for this purpose (ID11B) with similar beamlines planned for NSLS and ESRF. In this geometry, incident X-rays of energy 70–150 keV are fired through a sample and collected on a large area image-plate detector placed behind the sample. The experiment consists of ensuring that the beam is perpendicular and centered on the detector and the sample, then exposing the image plate. Depending on the strength of scattering and the sensitivity of the detector, exposures for good PDFs in excess of

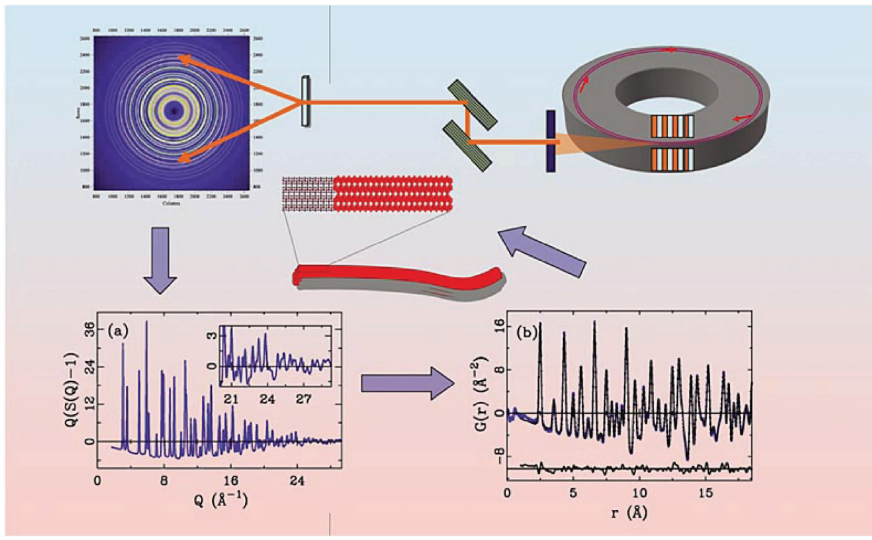



**Figure 16.6** Schematic of the rapid acquisition RAPDF X ray data collection method. Intense high energy X ray beams that emerge from the synchrotron (top right) are collimated and monochromated before passing through the sample, where they are scattered into the 2D detector behind. Moving anticlockwise around the figure we see that the 2D data are reduced to a 1D function that is corrected and normalized to obtain the total scattering structure function, which is Fourier transformed to obtain the PDF. This can be fit to gain structural information about the material. (Figure adapted from ref. 8.)

$Q_{max} = 30$ Å$^{-1}$ can be obtained in as little as 30 ms, and typically a few seconds to minutes. This compares to data collection times of 8–12 hours with conventional non-parallel counting (*i.e.*, point detector) approaches, even at the synchrotron. The RAPDF measurement is ideal for time-resolved and parametric measurements,[57] of local structure through phase transitions for example. The *Q*-resolution of these measurements is very poor because of the geometry, and this limits the *r*-range of the resulting PDFs from crystalline materials. However, most modeling is carried out over rather narrow ranges of *r* and this represents a very good tradeoff. Where a wide *r*-range is necessary for the measurement (to study some aspect of intermediate range order on length-scales of 5–10 nm, for example) the Debye–Scherrer geometry diffractometers described in Chapter 2 can be used. In this case the counting-time is slower and often a lower $Q_{max}$ is accessible as they cannot be operated at very high X-ray energies. Combining data from both methods gives data with high resolution in both real- and reciprocal-spaces, which will increasingly be important in studies of complex materials.

For neutron measurements, the requirement of short-wavelength really limits experiments to time-of-flight spallation neutron sources. Reactor sources with hot moderators would give good quality data for PDF studies, but are in short supply. The requirements for a spallation neutron powder diffractometer are laid out in the list of experimental requirements above. Normal t-o-f powder

diffractometers can be used provided the length of the flight-path and frequency of operation are such to allow good fluxes of neutrons with short wavelength (0.1–0.4 Å). Currently, neutron guides do not propagate these short-wavelength neutrons effectively and so shorter flight-path diffractometers with, or without, guides give the best data. At present, the instruments of choice are NPDF at the Lujan Center at Los Alamos National Laboratory in the USA and GEM at ISIS, Rutherford Laboratory, in the UK. The former was upgraded with PDF experiments in mind and has excellent stability on a water moderator and low backgrounds, though data collection time is not quite at the level of GEM. Instruments suitable for total scattering are under construction at next generation spallation neutron sources: SNS in the US and J-PARC in Japan.

Once the data are collected they must be corrected and normalized. Several data correction programs are available for free download and these take care of the corrections and normalizations needed to obtain PDFs from raw data. These can be browsed at the ccp14 software website.[24] Currently, the easiest and most commonly used programs are PDFgetN[25] and Gudrun[26] for spallation neutron data and PDFgetX2 (refs. 27,28) for X-ray data. PDFgetX2 has the corrections implemented for accurate analysis of RAPDF data from 2D detectors, though currently the data must be preprocessed using the 2D data analysis suite FIT2D.[29] Details of the corrections are beyond the scope of this chapter, but can be found in some detail in Egami and Billinge.[2]

## 16.4 STRUCTURAL MODELING

As with any powder diffraction experiment, structural information is extracted through modeling. Modeling is carried out in real-space (by calculating the PDF of the model and comparing it to the PDF determined experimentally) or in reciprocal-space (by calculating the total-scattering structure function using the Debye equation). Although strictly speaking the information is the same in real- and reciprocal-spaces (they are the direct transform of each other) these different modeling approaches lend themselves to extracting different information. Fitting the PDF is generally done with models described by a small number of atoms in a unit cell (which may or may not be the crystalline unit cell) and yields information about the very local structure. Fitting in reciprocal space is generally carried out on larger models of a few thousand atoms using a Monte Carlo simulated annealing type of approach and yields more information about intermediate range order. Both approaches can successfully be used to gain insight about the structure in question. These approaches are briefly described below.

### 16.4.1 Model Independent Structural Information from the PDF

Information can be extracted directly from the PDF in a model-independent way because of its definition as the atom-pair correlation function described in Equation (13).

*Peak position → bond length:* The position of a peak in the PDF indicates the existence of a pair of atoms with that separation. There is no intensity in $R(r)$

for distances less than the nearest-neighbor distance, $r < r_{nn}$ and a sharp peak at $r_{nn}$. This behavior is very general and true even in atomically disordered systems such as glasses, liquids and gasses. In amorphous materials the second neighbor distance is less well defined, the PDF peak being broader, but will still be apparent even in disordered materials. In crystals, because of the long-range order of the structure, all neighbors at all lengths are well defined and give rise to sharp PDF peaks. The positions of these peaks gives the separations of pairs of atoms in the structure directly.

*Peak integrated intensity → coordination number:* When a well-defined PDF peak can be observed, we can determine information about the number of neighbors in that coordination shell around an origin atom by integrating the intensity under that peak, as shown in Equation (11). By way of example we can consider crystalline Ni which has four Ni atoms in the unit cell (fcc structure). Each nickel atom has 12 neighbors at 2.49 Å.[30] When we construct our PDF using Equation (12) we will therefore place 48 units of intensity at position $r = 2.49$ Å. This can be seen as follows. Place one nickel atom at the origin and count the number of neighbors at $r = 2.49$ Å; there are 12. We repeat this process by placing every atom in the material at the origin in turn. In a crystalline material all the atoms with distinct environments are included in the unit cell (by definition) which is periodically repeated to generate the full structure. We can therefore obtain the accurate PDF of the structure by placing at the origin only the atoms in the unit cell. Therefore, in the nickel example we systematically place each of the four atoms in the unit cell at the origin. In fact they are all equivalent with 12 neighbors, so 48 units of intensity appear at $r = 2.49$ Å. We then divide by $N$, the number of atoms that we summed over at the origin [Equation (12)], to obtain the PDF, in this case 4. This gives the nickel coordination as 12, as expected. Thus, integrating the first peak in the properly normalized experimental RDF will yield 12, which is the coordination number of Ni. The same information can be obtained from multi-element samples if the chemical origin of the PDF peak, and therefore the weighting factor, is known. If, as is often the case, PDF peaks from different origins overlap this process becomes complicated. In that case, information can be extracted by measuring the chemical specific differential or partial-PDFs directly, by fitting the peaks with a series of Gaussian functions, or better, by full-scale structural modeling.

*Peak width → thermal or static disorder:* Atomic disorder in the form of thermal and zero-point motion of atoms, and any static displacements of atoms away from ideal lattice sites, gives rise to a distribution of atom–atom distances. The PDF peaks are therefore broadened resulting in Gaussian shaped peaks. The width and shape of the PDF peaks contain information about the real atomic probability distribution. For example, a non-Gaussian PDF peak may suggest an anharmonic crystal potential.

### 16.4.2 Modeling the PDF

Modeling the data reveals much more information that straight model independent analysis. The most popular approach for real-space modeling is to use

a full-profile fitting method analogous to the Rietveld method[31] but where the function being fit is the PDF. This is implemented in the popular PDFfit program.[19] A new version of this program with significant usability enhancements, PDFgui,[32] has recently become available. This is available for free download.[33]

Parameters in the structural model, and other experiment-dependent parameters, are allowed to vary until a best-fit of the PDF calculated from the model and the data derived PDF is obtained, using a least-squares approach. The sample dependent parameters thus derived include the unit cell parameters (unit cell lengths and angles), atomic positions in the unit cell expressed in fractional coordinates, anisotropic thermal ellipsoids for each atom and the average atomic occupancy of each site.

We highlight here the similarities and differences with conventional Rietveld. The main similarity is that the model is defined in a small unit cell with atom positions specified in terms of fractional coordinates. The refined structural parameters are exactly the same as those obtained from Rietveld. The main difference from conventional Rietveld is that the *local* structure is being fit that contains information about short-range atomic correlations. There is additional information in the data, which is not present in the average structure, about disordered and short-range ordered atomic displacements. To successfully model these displacements it is often necessary to utilize a ''unit cell'' that is larger than the crystallographic one. It is also a common strategy to introduce disorder in an average sense without increasing the unit cell. For example, the example where an atom is sitting in one of two displaced minima in the atomic potential, but its probability of being in either well is random, can be modeled as a split atomic position with 50% occupancy in each well. This is not a perfect, but a very good, approximation of the real situation and is very useful as a first order attempt at modeling the data.

This ''Real-space Rietveld'' approach is proving to be very useful and an important first step in analyzing PDFs from crystalline materials. This is because of two main reasons. First, its similarity with traditional Rietveld means that a traditional Rietveld derived structure can be compared *quantitatively* with the results of the PDF modeling. This is an important first step in determining whether there is significant evidence for local distortions beyond the average structure. If evidence exists to suggest that local structural distortions beyond the average structure are present, these can then be incorporated in the PDF model. The second strength of the real-space Rietveld approach is the simplicity of the structural models, making it quick and straightforward to construct the structural models. This also makes it straightforward and quick to gain physical understanding from the models. A screenshot from a PDFgui refinement is shown in Figure 16.7 and the resulting fit of the calculated PDF to the data is shown in Figure 16.8.

PDFfit was originally designed to study disorder and short-range order in crystalline materials with significant disorder such as nanoporous bulk materials. It has also found extensive use in studying more heavily disordered

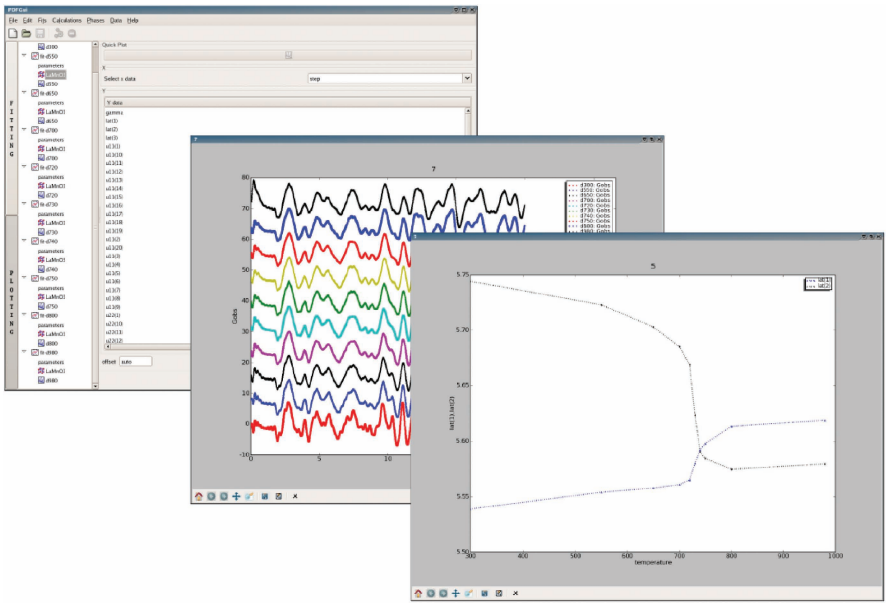


**Figure 16.7** Multiple refinements and plots of refined parameters from a PDFgui modeling project.
(Figure courtesy of Christopher Farrow.)

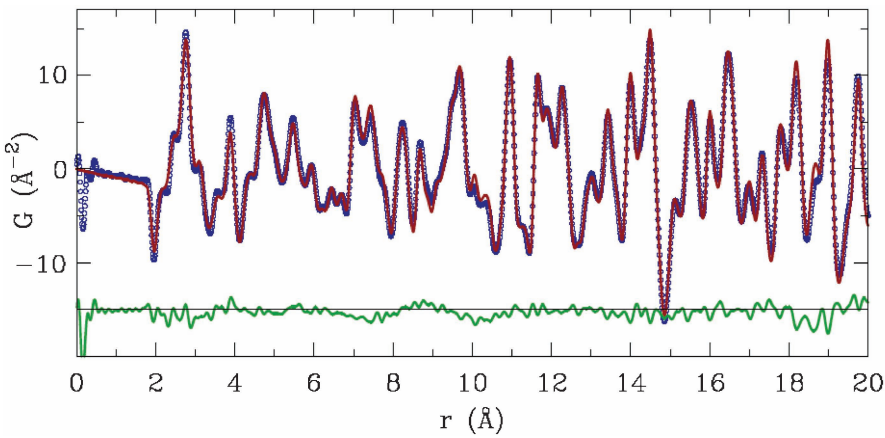



**Figure 16.8** Resulting PDF and fully converged fit with a difference curve below. In this case the data are neutron powder diffraction data from the NPDF instrument from a sample of $La_{0.8}Ca_{0.2}MnO_3$ measured at low temper ature. The nearest neighbor Mn O peak at $r \sim 2$ Å is negative because of the negative neutron scattering length of Mn for neutrons.
(Figure courtesy of Emil Bozin.)

materials such as nanocrystalline materials and nanoporous materials and this looks set to increase in the future.

### 16.4.3 Modeling Total Scattering in Reciprocal Space

Fitting models to reciprocal space total scattering data generally involves larger models of thousands of atoms that are refined using Monte Carlo simulated annealing,[34] or some other global optimization scheme. Conventional simulated annealing is an approach used to find the global minimum in a complicated potential energy landscape. Parameters of the system, such as atom positions, are allowed to vary in some random way. After each change the energy of the system is calculated using the specified potential energy function. If a change reduces the energy of the system it is accepted. If it raises the energy of the system then it can be accepted or rejected. This decision is made randomly according to an underlying probability. In simulated annealing the underlying acceptance probability for bad moves is given by the Boltzmann relation:

$$P = \mathrm{e}^{\left(\frac{\Delta E}{k_{\mathrm{B}}T}\right)} \tag{38}$$

where $\Delta E$ is the change in energy, $k_{\mathrm{B}}$ is the Boltzmann constant and $T$ is the "temperature" of the system, which is initially set by the experimenter. When $T$ is higher, more "bad" moves are accepted and more of the energy landscape is probed by the simulation (it is easier to get out of local minima). The temperature can then be systematically lowered to guide the simulation into the global energy minimum. This is a widely used and powerful method in statistical physics and the computational technology is well developed.[35]

When this approach is used to minimize the difference between a calculated and an experimental diffraction pattern, *i.e.*, to minimize $\chi^2$ instead of an energy, the approach is known as reverse Monte Carlo or RMC.[36] In this case a large box of atoms is used as the structural model. These are allowed to arrange themselves, with the minimum of constraints, in such a way as to give good agreement with the diffraction data. In the most unconstrained case the boundaries of the box and local hard-sphere repulsions, which prevent atoms overlapping, are the only constraints. This approach is very widely used in the sphere of disordered materials, where methods derived from crystallography are not so helpful. A strength of this approach is that it is unbiased. The resulting structural model gives a solution that is unprejudiced but consistent with the data. The expectation is that any structural motifs that emerge in the model, such as local tetrahedral atomic arrangements in network glasses, are probably real. The reason is that the simulated annealing, by its very nature, will find the most probable, and therefore most disordered, structural solution that is consistent with the data. Any atomic correlations (ordered atomic arrangements) that emerge in the model must be more or less uniquely specified in the data themselves. A caveat is that this is an assumption that cannot be

proved and it is possible that more than one distinct structural motif can emerge from the same data. The prerogative is with the user to probe the phase space somewhat by making multiple runs that begin with different random seeds, and to validate results against other knowledge and data on the system. Additional structural constraints can be introduced where necessary to reduce this degeneracy, though at the possible expense of introducing bias. When used carefully, RMC is a powerful method for learning about short *and* intermediate range order in a material.

We note in passing that the ''Monte-Carlo'' aspect of RMC is the choice of Monte Carlo simulated annealing as the regression algorithm. In principle, other global optimizers could be used instead, such as genetic algorithms, and the same structural solution would be found (if indeed all the algorithms found the global, rather than a local, minimum!). Scientifically, the important aspect of this modeling approach is less the Monte Carlo aspect and more that large models are being used to simulate intermediate range order from total scattering data with a goodness-of-fit parameter as the cost function being minimized.

Approaches to modeling the data that are intermediate between the RMC and PDF fitting approaches described above are now appearing that can be thought of as RMC-refinement.[37] In these cases a known structure (*e.g.*, the crystal structure) is given as a starting model which is then refined using Monte Carlo updates without allowing the crystal to melt by keeping it at lower temperature, or by simultaneously fitting diffraction data at low-$Q$ and total-scattering data over a wide range of $Q$. This amounts to using MC as a local search method and other regression methods could also be used. Sometimes data are fit in both real and reciprocal space at the same time,[38] which is a powerful way of satisfying both the long-range and the local order at the same time.

RMC has recently been extended to study not just structure but atom dynamics. The ability to extract phonon and lattice dynamical information from total scattering data has been under debate for some time,[39 42] with the consensus ultimately being that incomplete, but potentially highly useful, lattice dynamical information can be obtained directly from total scattering data. RMC has recently been shown to be useful for extracting that information.[43]

Several RMC modeling and refinement codes are freely available. The list of RMC programs supported by the ISIS group can be found at http://www.isis.rl.ac.uk/rmc/. A versatile and straightforward to use program for data simulation and structure refinement from single crystal and powder/amorphous data, with built in RMC routines based on the McGreevy algorithms, is DISCUS, which is available at http://diffuse.sourceforge.net.

### 16.4.4 Emerging Modeling Approaches

*16.4.4.1 Complex Modeling.* As we seek to model increasingly complex materials, we increasingly run into the situation that data from a single measurement is not sufficient to constrain a unique solution. In this situation the problem is not well conditioned and needs to be regularized. This can be done by adding more independent data to the optimization, or by removing

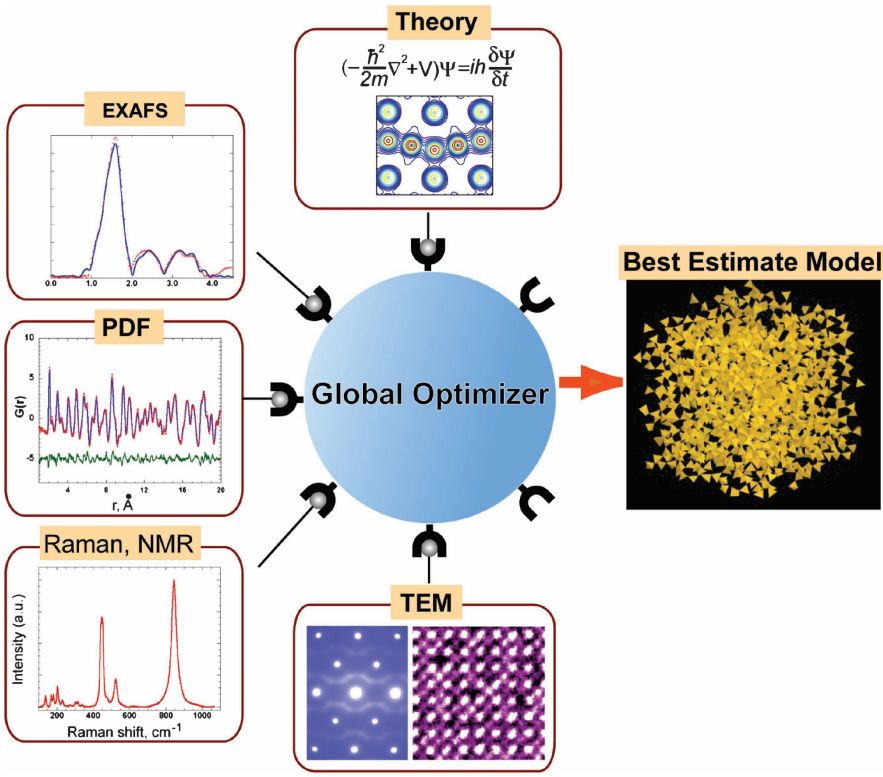



**Figure 16.9** Schematic of the Complex Modeling paradigm. Data from different experiments, as well as theoretical inputs, are used as constraints in a coherent global optimization scheme.
[With help from I. Levin]

degrees of freedom from the model by specifying constraints and bringing to bear other prior knowledge. We refer to this generically as "complex modeling",[1] where the sense of the word "complex" here is not complicated, but mixed; just as a complex number is a mixture of a real and an imaginary part. This is illustrated schematically in Figure 16.9.

Many approaches already do this, for example, by incorporating known chemical constraints, densities or hard-sphere repulsions. Many of the emerging methods described below have this flavor, and as time goes on our ability to complex our data and our modeling approaches will only increase.

*16.4.4.2 Empirical Potential Based Modeling Schemes.* Degrees of freedom in large-scale models can be reduced by incorporating prior information. One way to do this is to specify empirical pair potentials as a function of separation between each atom type. Then the number of atoms the model can be increased but the number of parameters depends only on the number of atomic species. In principle the pair potentials themselves should give the equilibrium structure of

the material and there is no need for an experiment at all! In practice, we still need crystallography because the approximations in first-principles and empirical potentials (for realistic sized systems) give uncertainties that are larger than the differences between competing structures. Total energy minimization of models can therefore only be used as guide without input from data. An attractive approach to incorporate information about the energetics as *a priori* knowledge in a refinement is to make interatomic potential parameters refinable. The process is then to find the arrangement of the atoms that minimizes the energy, calculate the scattering function from this configuration and determine the difference to the measured data, update the potential parameters and iterate until convergence is reached. This has a complete energy minimization calculation in each step of the regression and so efficient convergence of the regression is paramount. Such an approach has been successfully implemented in the empirical potential structure refinement approach, which has been applied principally to liquids.[44] A model is set up with initial values for the pair potential parameters and the potential of mean force, $U(r)$, calculated for each pair of atoms. This is related directly to the measured atomic pair distribution function through:

$$U(r) = -k_B T \ln\left(\frac{\rho(r)}{\rho_0}\right) = -k_B T \ln(g(r)) \tag{39}$$

The reference potential used for the model is denoted $U^m(r)$ and the potential implied from the data $U^D(r)$. We would like to think of a way to modify $U^m(r)$ to bring it closer to $U^D(r)$. To do this we add a perturbation to the original reference potential, $U_0^m(r)$ that is the difference between $U^m(r)$ and $U^D(r)$. *i.e.*, the new potential:

$$U_1^m(r) = U_0^m(r) + kT \ln\left(\frac{g^m(r)}{g^D(r)}\right)$$

Using Monte Carlo, the model is then relaxed using the new potential, resulting in a new calculated $g(r)$. The process is then iterated until it reaches convergence. This approach, known as Empirical Potential Structure Refinement (EPSR) has proved very powerful in the study of complex liquids, and of the solvation states of molecules in solution. It is particularly successful when it has as target functions a number (though not necessarily the complete set) of DPDFs from the system in question.

Along similar lines is the experimentally constrained molecular relaxation (ECMR) that has been used recently to generate both structurally and energetically reasonable models for glasses such as $GeSe_2$.[45] This approach uses an RMC methodology for updating atomic positions, but incorporates a first principles total energy relaxation in the regression cycle to ensure that the resulting configurations are energetically favorable, as well as fitting the data well.

Inverse Monte Carlo approaches have also been used to extract information from single-crystal diffuse scattering data. For example, effective pair interactions were extracted from vanadium hydride, an important potential hydrogen

storage system, using this approach.[46,47] The use of highly simplified "toy model" potentials (*e.g.*, Ising model Hamiltonian and springs between molecular units) combined with Monte Carlo energy minimization has also proved very effective to understand diffuse scattering in crystalline materials.[48] Theory and experiment has also been successfully combined in a highly exhaustive search of the solution space when a large number of experiments and theoretical simulations are brought to bear on the same experimental system, in this case amorphous $Si_3B_3N_7$.[49] Here the experimental data are used to filter the theoretical predictions to find the most appropriate one.

*16.4.4.3 Chemical Constraints.* Rather than using energetics to constrain structural solutions, it is possible to build into the problem aspects of the known chemistry. This is standard in single-crystal structure solutions of organic solids, as discussed in Chapter 9 and ref. 50, and also in macromolecular crystallography, where knowledge of the molecular topology is a prerequisite for many structure solutions. For example, instead of representing a molecule by the coordinates of its atoms, it is possible to represent it as a *Z*-matrix[50] where the atom positions are specified with respect to their neighbors by bond lengths and bond angles. This is a very convenient way of specifying the molecule in terms of its internal degrees of freedom, which may be a small number of internal dihedral rotations about C–C single bonds, for example. In this way the fixed geometry of the molecule appears automatically as a constraint in the problem.

This approach of geometric constraints has been extended to inorganic systems and network systems in an approach called geometric modeling.[51] The difficulty in these systems is that they are 3D infinite networks with bridging atoms. The bridging atoms link two distinct geometric objects (such as tetrahedra or octahedra) at a vertex. If, as is the case in general, the system is not fully relaxed, the bridging atoms will become frustrated. They will not be able to satisfy both of the neighboring geometric objects. The geometric modeling approach creates "ghosts" of the ideal size and shape. The actual atoms in the material are then tethered to the vertices of the ghosts with a harmonic spring. In this way the atoms can move away from the ideal positions that define the geometric object, but only with an energy cost. This is shown schematically in Figure 16.10.[52]

Disorder is introduced into the system and then it is relaxed to find the energy minimum. This approach has recently been extended to solve the inverse problem in a process called geometric refinement.[53] The problem is set up in the same way, but instead of attaching atoms to the vertices with springs the atoms and the geometric templates are moved using a Monte Carlo simulated annealing approach and where acceptance of the moves is governed by a fit to the data: a kind of reverse geometric modeling in analogy with RMC. This approach was recently successful in describing the short-range order of Jahn–Teller distorted octahedra in $LaMnO_3$ at high temperature.[53]

*16.4.4.4 Ab Initio Nanostructure Determination.* The PDF profile fitting methods described earlier are refinement techniques. A good initial guess of

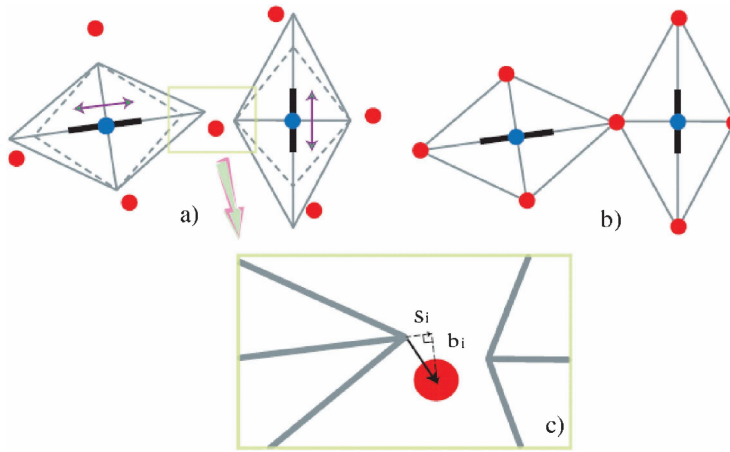



**Figure 16.10** Schematic of the geometric modeling scheme. The grey objects are geometric templates that encode the local structural geometry coming from the chemistry; in this case, corner shared octahedra. The red dots are bridging atoms that are shared by more than one template. The atoms are connected to the templates by springs. The relaxation occurs by an iterative approach of reorienting and shifting the templates to give the best fit to the atoms, then shifting the atoms to minimize the spring energy, then reorienting and shifting the templates, and so on until convergence. (Reprinted with permission from ref. 52, © 2006, American Physical Society.)

the structure is essential and the program "refines" model parameters such as atomic positions and atomic displacement parameters to optimize the fit. The optimization algorithm uses a local search, *i.e.*, finds the nearest local minimum in the parameter space. This is different from an *ab initio* structure solution, where a search for the global minimum is carried out and the structure determined from a completely arbitrary (often random) starting point. This problem is, obviously, much more difficult to solve. The power of crystallography is that this global search problem has been largely solved with, more recently, progress made also in solving this problem from powder diffraction data, as described in Chapter 8. However, these crystallographic methods have not been applied at atomic resolution to reconstruct 3D structures of nanostructured materials. RMC modeling and related methods such as EPSR are, actually, *ab initio* methods: the structural configuration is formed from an initial random (or other) starting point. However, they are only applicable for disordered materials where there are many degenerate solutions that are consistent with the data. These methods are not currently efficient enough to solve nanostructures with unique structural solutions, such as the $C_{60}$ buckyball molecule.

Great progress is being made in this important area. Two-dimensional images with micron[54] to subnanometer[55] resolution have been reconstructed from diffraction data using phase reconstruction in a process known as lensless

imaging.[56] These approaches look promising for structure reconstruction at the atomic scale. Taking a different approach, *ab initio* determination of nanostructure has been demonstrated directly from PDF data. In this case the brute-force Monte Carlo approach failed for small nanoparticles of 20 atoms or so, but a novel algorithm (named "Liga"), developed for the purpose, was successful at reconstructing clusters up to $\sim$200 atoms from synthetic data, and solving the structure of $C_{60}$ uniquely from real PDF data.[6] In the same paper, an adapted genetic algorithm was also successful, though less efficient than Liga. These developments are still at an early stage, but look very promising for the future.

## REFERENCES


1. S. J. L. Billinge and I. Levin, *Science*, 2007, **316**, 561.
2. T. Egami and S. J. L. Billinge, *Underneath the Bragg Peaks: Structural Analysis of Complex Materials*, Pergamon Press, Elsevier, Oxford, England, 2003.
3. D. A. Keen, *J. Appl. Crystallogr.*, 2001, **34**, 172.
4. I.-K. Jeong, F. Mohiuddin-Jacobs, V. Petkov, S. J. L. Billinge and S. Kycia, *Phys. Rev. B*, 2001, **63**, 205202.
5. H. J. Kim, E. S. Bozin, S. M. Haile, G. J. Snyder and S. J. L. Billinge, *Phys. Rev. B*, 2007, **75**, 134103.
6. P. Juhas, D. M. Cherba, P. M. Duxbury, W. F. Punch and S. J. L. Billinge, *Nature*, 2006, **440**, 655.
7. X. Qiu, Th. Proffen, J. F. Mitchell and S. J. L. Billinge, *Phys. Rev. Lett.*, 2005, **94**, 177203.
8. S. J. L. Billinge and M. G. Kanatzidis, *Chem. Commun.*, 2004, 749.
9. T. Proffen, S. J. L. Billinge, T. Egami and D. Louca, *Z. Kristallogr.*, 2003, **218**, 132.
10. B. E. Warren, *X-ray Diffraction*, Dover, New York, 1990.
11. H. P. Klug andL. E. Alexander, *X-Ray Diffraction Procedures for Polycrystalline and Amorphous Materials*, , Wiley, New York, 1974.
12. A. C. Wright, *Glass. Phys. Chem.*, 1998, **24**, 148.
13. A. C. Barnes, H. E. Fischer and P. S. Salmon, *J. Phy. IV*, 2003, **111**, 59.
14. P. Debye, *Annalen der Physik (Berlin, Germany)*, 1915, **46**, 809.
15. V. A. Levashov, S. J. L. Billinge and M. F. Thorpe, *Phys. Rev. B*, 2005, **72**, 024111.
16. T. E. Faber and J. M. Ziman, *Philos. Mag.*, 1965, **11**, 153.
17. D. L. Price and M.-L. Saboungi, in *Local Structure from Diffraction*, ed. S. J. L. Billinge and M. F. Thorpe, Plenum, New York, 1998, p. 23.
18. B. E. Warren, H. Krutter and O. Morningstar, *J. Am. Ceram. Soc.*, 1936, **19**, 202.
19. T. Proffen and S. J. L. Billinge, *J. Appl. Crystallogr.*, 1999, **32**, 572.
20. B. K. Teo, *EXAFS: Basic Principles and Data Analysis*, Springer-Verlag, New York, 1986.

21. P. H. Fuoss, P. Eisenberger, W. K. Warburton and A. I. Bienenstock, *Phys. Rev. Lett.*, 1981, **46**, 1537.
22. V. Petkov, I.-K. Jeong, F. Mohiuddin-Jacobs, T. Proffen and S. J. L. Billinge, *J. Appl. Phys.*, 2000, **88**, 665.
23. P. J. Chupas, X. Qiu, J. C. Hanson, P. L. Lee, C. P. Grey and S. J. L. Billinge, *J. Appl. Crystallogr.*, 2003, **36**, 1342.
24. URL: http://www.ccp14.ac.uk.
25. URL: http://pdfgetn.sourceforge.net/.
26. Information can be found at the ISIS disordered materials group website: http://www.isis.rl.ac.uk/disordered/dmgroup_home.htm.
27. X. Qiu, J. W. Thompson and S. J. L. Billinge, *J. Appl. Crystallogr.*, 2004, **37**, 678.
28. URL: http://www.pa.msu.edu/cmp/billinge-group/programs/PDFgetX2/.
29. A. P. Hammersley, S. O. Svenson, M. Hanfland and D. Hauserman, *High Pressure Res.*, 1996, **14**, 235.
30. R. W. G. Wyckoff, *Crystal Structures*, Wiley, New York, 1967, vol. 1.
31. R. A. Young, *The Rietveld Method*, vol. 5 of International Union of Crystallography Monographs on Crystallography, Oxford University Press, Oxford, 1993.
32. C. L. Farrow, P. Juhas, J. W. Liu, D. Bryndin, E. S. Božin, J. Bloch, T. Proffen and S. J. L. Billinge, *J. Phys: Condens. Matter*, 2007, **129**, 1386–1392.
33. URL: http://www.diffpy.org.
34. N. Metropolis and S. Ulam, *J. Am. Stat. Assoc.*, 1949, **44**, 335–341.
35. K. Binder and D. W. Heerman, *Monte Carlo Simulation in Statistical Physics*, Springer-Verlag, Berlin, 1992.
36. R. L. McGreevy, *J. Phys.: Condens. Matter*, 2001, **13**, R877.
37. M. G. Tucker, M. T. Dove and D. A. Keen, *J. Appl. Crystallogr.*, 2001, **34**, 630.
38. M. G. Tucker, A. L. Goodwin, M. T. Dove, D. A. Keen, S. A. Wells and J. S. O. Evans, *Phys. Rev. Lett.*, 2005, **95**, 255501.
39. D. Dimitrov, D. Louca and H. Röder, *Phys. Rev. B*, 1999, **60**, 6204.
40. W. Reichardt and L. Pintschovius, *Phys. Rev. B*, 2001, **63**, 174302.
41. M. F. Thorpe, V. A. Levashov, M. Lei and S. J. L. Billinge, in *From Semiconductors to Proteins: Beyond the Average Structure*, ed. S. J. L. Billinge and M. F. Thorpe, Kluwer/Plenum, New York, 2002, pp. 105–128.
42. I. K. Jeong, R. H. Heffner, M. J. Graf and S. J. L. Billinge, *Phys. Rev. B*, 2003, **67**, 104301.
43. A. L. Goodwin, M. G. Tucker, E. R. Cope, M. T. Dove and D. A. Keen, *Phys. Rev. B*, 2005, **72**, 214304.
44. A. K. Soper, *Chem. Phys.*, 1996, **202**, 295.
45. P. Biswas, D. Tafen and D. A. Drabold, *Phys. Rev. B*, 2005, **71**, 054204.
46. W. Schweika and M. Pionke, in *Local Structure from Diffraction*, ed. S. J. L. Billinge and M. F. Thorpe, Plenum, New York, 1998, p. 85.
47. W. Schweika, *Disordered Alloys: Diffuse Scattering and Monte Carlo Simulations*, Springer-Verlag, Berlin, 1998.

48. T. R. Welberry, *Diffuse X-Ray Scattering and Models of Disorder*, Oxford University Press, Oxford, 2004.
49. M. Jansen, J. C. Schön and L. van Wüllen, *Angew. Chem., Int. Ed.*, 2006, **45**, 4244.
50. *Structure Determination from Powder Diffraction Data*, ed. W. I. F. David, K. Shankland, L. B. McCusker and C. Baerlocher, Oxford University Press, Oxford, 2002.
51. S. A. Wells, M. T. Dove and M. G. Tucker, *J. Phys.: Condens. Matter*, 2002, **14**, 4567.
52. A. Sartbaeva, S. A. Wells, M. F. Thorpe, E. S. Bozin and S. J. L. Billinge, *Phys. Rev. Lett.*, 2006, **97**, 065501.
53. A. Sartbaeva, S. A. Wells, M. F. Thorpe, E. S. Bozin and S. J. L. Billinge, *Phys. Rev. lett.*, 2007, **99**, 155503.
54. J. Miao, P. Charalambous, J. Kirz and D. Sayre, *Nature*, 1999, **400**, 342.
55. J. M. Zuo, I. Vartanyants, M. Gao, R. Zhang and L. A. Nagahara, *Science*, 2003, **300**, 1419.
56. J. S. Wu and J. C. H. Spence, *Acta Crystallogr. A*, 2005, **61**, 194.
57. P. J. Chupas, K. W. Chapman and P. L. Lee, *J. Appl. Crystallogr.*, 2007, **40**, 463–470.

CHAPTER 17

# Computer Software for Powder Diffraction

LACHLAN M. D. CRANSWICK

Canadian Neutron Beam Centre, National Research Council Canada, Building 459, Chalk River Laboratories, Chalk River ON, Canada, K0J 1J0

## 17.1 INTRODUCTION

Modern powder diffraction necessitates the use of computer software performing a range of data collection and analysis options. As the bulk of a powder diffractionist's working time will be spent performing data analysis, it is advisable to take a keen interest in the range of available software, and to select the most appropriate. The editors requested hints and recommendations to be provided on which software might be most appropriate to use first. The reader should note this is of course rather biased to the limited personal experiences of the author. Space restrictions have also forced overgeneralizations in many cases. References are provided in the tables of the relevant sections, and Internet addresses for the software are given in Appendix 1.

If a reader's favorite program is missing, or functionality not suitably elaborated, the author apologizes in advance and invites comments in the event of a new edition of this book being prepared. Quite radical changes and improvements in software can be announced at the near blink of an eye. Thus keeping an interest in new software developments may offer new methods of more effective analysis that can both save time and/or increase the quality of information obtained from powder diffraction data.

## 17.2 FINDING AND TESTING SOFTWARE

### 17.2.1 Locating New Software

New powder diffraction software tends to be announced in one or all of a small group of publications and forums. The main forums are: the IUCr *Journal of*

*Applied Crystallography*; *IUCr Commission on Powder Diffraction Newsletter*; the SDPD (Structure Determination by Powder Diffractometry) mailing list; the Rietveld Users Mailing list, CCP14 website, and the sci.techniques.xtallography "Usenet" newsgroup. Lists of software are maintained on the CCP14 and IUCr Sincris websites. These sites can be straightforwardly located by using a search engine such as Google. Instructions for joining the Rietveld mailing list can be found at the mailing list home-page:
http://lachlan.bluehaze.com.au/stxnews/riet/intro.htm and the SDPD list at:
http://www.cristal.org/sdpd/

### 17.2.2 Selecting Software

There are two main routes to determine the most appropriate software to use for a particular problem. A quick and effective method is to ask colleagues in the local institute, geographical region, or field of science. The advantage of taking advice from colleagues is it is more likely the most appropriate software will be recommended, and assistance with software problems might be more readily available. Another more rigorous, but time consuming, method is to determine the range of available software and quickly evaluate these for yourself. On evaluation, it can become apparent which packages are more likely to be of immediate assistance. Evaluating a wide range of software can also identify new approaches and analysis methods, and the knowledge gained from personal evaluation can be usefully applied to future problems.

### 17.2.3 Re-locating Software on the Internet

The Internet can be very unstable with respect to weblinks and websites. Scientific software websites can move around due to changed employment of the authors, changes in institute network policies or extinction of research groups or institutes. If known weblinks no longer work, the quickest route to refind software is to use search engines such as Google. If this fails, posting to some relevant mailing lists or Internet newsgroups is the next best method for locating hard to re-find software.

## 17.3 AVAILABLE SOFTWARE

### 17.3.1 Third-party Diffractometer Control Software

A desire for cost effective diffractometer hardware upgrades, or general discontent with vendor control software, may make the use of third-party hardware control software desirable (Table 17.1). Third-party software can often be more intuitive and easier to use than the default vendor diffractometer control software. If non-standard methods of data collection are required, a third-party vendor may be more flexible in making this functionality available. Also, if requested, third-party software is more likely to directly write files in the required analysis formats (*e.g.*, directly into the Rietveld format of interest).

**Table 17.1** Available third-party powder diffractometer control software.

| *Software* | *References* | *Diffractometer/ specializations* |
|---|---|---|
| ADM connect | ADM connect, (2005), RMSKempten, Kaufbeurer Str. 4, D 87437 Kempten, Germany | Many different brands including Philips, PANalytical, Siemens, Bruker, ENRAF (including CPS 120) |
| MDI DataScan | DataScan, Materials Data, Inc., 1224 Concannon Blvd., Livermore, CA 94550, USA | Many different brands including upgrades to non digital diffractometers |
| PC 1710 for Windows/ PC 1800 for Windows | PC 1710 for Windows/ PC 1800 for Windows, Mark Raven, (2005) CSIRO Land and Water, Urrbrae South Australia, 5064, Australia | Philips PW1710 and PW1800 XRDs |
| PW1050 (GPL'd) | PW1050, J. Kopf, (2005), Institut fuer Anorganische Chemie, Roentgenstrukturanalyse, Martin Luther King Platz 6, D 20146 Hamburg, Germany | Interfaces to a UDS2 Programmable Controller for X ray Diffractometers, Steuerungstechnik Skowronek, Antoniusstrasse 3, PO Box 1346, 5170 Julich, Germany, Tel/Fax: +49 (0)2462 55756 (*J. Appl. Crystallogr.* 1992, **25**, 329 330) |
| TXRDWIN | TXRDWIN, Omni Scientific Instruments, Inc. (2005) | Controls various different XRD hardware |
| SPEC | SPEC, Certified Scientific Software, PO Box 390640, Cambridge, MA, 02139 0007, USA | Variety of hardware for synchrotron, neutron and home built laboratory diffractometers |

However, some required methods of data collection may be unavailable from some vendors. For instance, at time of writing, Bede were the only known hardware or software vendor to include a general "Variable Count Time" (VCT) data collection capability.

### 17.3.2 Phase Identification and Search-match Software

The computer based identification of crystalline phases in powder diffraction patterns normally requires two separate components: (a) a powder diffraction database containing reference information and (b) a search-match program that loads the diffractogram and accesses the database to attempt to match the diffraction data to known phases in the database.

*17.3.2.1 Search-match Databases.* By default, it is considered best to obtain the complete ICDD (International Center of Diffraction Data) PDF-2 database of D-spacings (D's), Intensities (I's) and extra phase information. However, the ICDD database is expensive, and it can be initially confusing to determine which ICDD product is the most appropriate to purchase. A newly set up XRD laboratory can face phase identification problems if the "default" purchase of a PDF-1 ICDD database is undertaken, instead of the more comprehensive information within the PDF-2 ICDD database. Owing to the expense of the ICDD, less complete databases may be useable, including the creation of in-house databases when dealing with a small collection of phases (*e.g.*, the limited dozen or so phases commonly found in Lead Acid Batteries) (Table 17.2). Users should be wary that databases can, and do, have errors, more commonly in the form of reference patterns missing trace peaks, or including extra spurious peaks. Pattern calculation or a quick Rietveld refinement can be useful to cross check the results from the Search-Match software.

**Table 17.2** Available search-match databases.

| *Software* | *References* | *Specializations* |
|---|---|---|
| ICDD Powder Diffraction Files on CD ROM | International Centre for Diffraction Data, 12 Campus Boulevard, Newtown Square, PA, 19073 3273, U.S.A. | Comprehensive for X ray powder diffraction data |
| MacDiff | MacDiff a programme for analysis and display of X ray powder diffracto grammes on Apple Macintosh platforms, R. Petschick, Geologisch Paläontologisches Institut, Johann Wolfgang Goethe Universität Frankfurt am Main, Senckenberganlage 32 34, 60054 Frankfurt am Main, Germany | Free mineral database with powder X ray diffraction data of more than 500 minerals for use within the freeware MacDiff software |
| The Nickel Nichols Mineral Database | E. N. Nickel and M. C. Nichols, *Mineral Reference Manual*, Van Nostrand Reinhold, New York, 1991, 250 pp. and The Nickel Nichols Mineral Database, Materials Data, Inc., 1224 Concannon Blvd., Livermore, CA 94550, USA | Mineral database including strongest peaks for X ray diffraction data for Hanawalt type strongest peaks searching |
| Pauling File | The PAULING FILE Binaries Edition, Ed. P. Villars, (2002) ASM International, Materials Park, Ohio, USA, ISBN 0 87170 786 1 | Pure elements and binary compounds with a Hanawalt strongest peaks search option for X ray diffraction data |

Most powder diffraction databases only serve ''angular dispersive'' X-ray diffraction. ''Energy dispersive'' X-ray diffraction data can be transformed into an angular dispersive equivalent that can then be used in conventional search-match software. Users of neutron diffraction data are currently limited to performing phase identification using a list of crystal structures imported into a Rietveld program. It is wise to first run samples destined for neutron diffraction sample in a powder XRD prior to confirm phase purity, and to use calculated patterns to assist in phase identification of possible undesired phases due to ancillary equipment or sample environment.

*17.3.2.2 Search-match and Phase Identification Software.* It would be desirable to have at least two or three search-match programs, as where one program fails to give a good match, another might succeed. However, as most search-match software is commercial and expensive, for a cost conscious institute it can be a struggle to purchase a single search-match program. It can also be impractical to evaluate a range of programs to see which is most appropriate for local usage. Much search-match software is purchased from the hardware vendor with a new X-ray diffractometer. However, there is the increasing practise of third-party vendors to distribute evaluation versions of their programs. The most advanced software tends to use what are called ''third generation'' (or a higher generation number) search-match algorithms. Effective search-match software not only allows for computer searching, but also allows the user to input extra information in an effective manner, such as chemistry or a list of expected phases. A good test for evaluating search-match software is to not only challenge them with difficult multi-phase data, but also examples where you wish to confirm a known answer by requesting specific phases to be displayed from the power diffraction database (Table 17.3). Less effective search-match programs limit the input of user knowledge about the sample, and force the analysis of ''known'' samples via an *ab initio* search-match process.

### 17.3.3 Crystal Structure Databases

The three main databases (Cambridge Organic/Organometallic; ICSD Inorganic/Minerals/Intermetallics and CrystMet Metals/Alloys/Intermetallics) are currently licensed on a yearly basis (Table 17.4). The ICSD is traditionally considered only as containing inorganic phases and minerals, but it has started to add intermetallics. A ''one-time purchase'' database is the Pauling Binaries file, which includes other information such as phase diagrams, but only contains elemental and binary compounds. Several mineral and specialist databases (Zeolites, incommensurate) are freely available on the web. An open source crystal structure database (COD) is also under development. The ICSD has one of the more effective methods of data retrieval via a very friendly web/intranet interface designed by Marcus, Peter and Alan Hewat. Some countries (such as the UK based EPSRC CDS) have national licenses for many of these structure databases, which can be accessed freely via the Internet by academic researchers and students working in these respective countries.

**Table 17.3** Available search-match and phase identification software.

| *Software* | *References or contact information* | *Freely available* |
|---|---|---|
| AXES | H. Mändar and T. Vajakas, AXES a software toolbox in powder diffraction, *Newsletter Int. Union Crystallogr, Commission Powder Diffr.*, 1998, 20, 31 32 and AXES1.9: new tools for estimation of crystallite size and shape by Williamson Hall analysis, H. Mändar, J. Felsche, V. Mikli and T. Vajakas, *J. Appl. Crystallogr.*, 1999, **32**, 345 350 | |
| Bede Search/Match | Bede Scientific Instruments Ltd, Belmont Business Park, Durham, DH1 1TW, U | |
| CMPR & Portable LOGIC | CMPR a powder diffraction toolkit, B. H. Toby, *J. Appl. Crystallogr.*, 2005, **38**, 1040 1041 | Yes |
| Crystallographica Search Match | Oxford Cryosystems Ltd, 3 Blenheim Office Park, Lower Road, Long Hanborough, Oxford OX29 8LN, United Kingdom | |
| DIFFRAC$^{plus}$ SEARCH | Bruker AXS GmbH, Oestliche Rheinbrueckenstr. 49, D 76187 Karlsruhe, Germany | |
| DRXWin | Vicent Primo Martín, El Instituto de Ciencia de los Materiales, Universitat de València Avda. Blasco Ibáñez, 13. 46010, València, Spain | |
| Jade | Jade, Materials Data, Inc., 1224 Concannon Blvd., Livermore, CA 94550, USA | |
| MacDiff | MacDiff a programme for analysis and display of X ray powder diffractogrammes on Apple Macintosh platforms, R. Petschick, Geologisch Paläontologisches Institut, Johann Wolfgang Goethe Universität Frankfurt am Main, Senckenberganlage 32 34, 60054 Frankfurt am Main, Germany | Yes |
| MacPDF | ESM Software, 2234 Wade Court, Hamilton, OH, 45013, USA | |
| MATCH! | CRYSTAL IMPACT, K. Brandenburg & H. Putz GbR, Postfach 1251, D 53002 Bonn, Germany | |
| Pulwin | PULWIN: A program for analyzing powder X ray diffraction patterns, S. Brückner, *Powder Diffr.*, 2000, **15**(4), 218 219 | Yes |
| RayfleX | GE Inspection Technologies, GmbH, Robert Bosch Str. 3, 50354 Huerth, Germany | |

(*Continued*)

**Table 17.3** (*Continued*).

| *Software* | *References or contact information* | *Freely available* |
|---|---|---|
| SIeve | International Centre for Diffraction Data (ICDD), (2005), 12 Campus Boulevard, Newtown Square, PA 19073 3273 U.S.A. | |
| Traces | GBC Scientific Equipment, Monterey Road, Dandenong, Victoria, Australia | |
| TXRDWIN | Omni Scientific Instruments, Inc. | |
| WinDust32 | Ital Structures S.r.l., Via Monte Misone 11/d, 38066 Riva del Garda (TN), Italy | |
| WinX$^{Pow}$ | STOE & Cie GmbH, Hilpertstr. 10, D 64295 Darmstadt, Germany | |
| WinXRD | Thermo Electron Corporation | |
| X′Pert HighScore | PANalytical B.V, Lelyweg 1, 7602 EA Almelo, The Netherlands | |
| Xplot for Windows | Xplot for Windows, Mark Raven, (2005) CSIRO Land and Water, Urrbrae South Australia, 5064, Australia | |
| XPowder | Quetzal Com S.L. La Carrera 5. 18110 HIJAR Las Gabias. Granada, Spain | |
| XSPEX | XSPEX, DIANOCORP, (2005), http://www.dianocorp.com/ | |
| ZDS System | ZDS System, Biskupsky dvur 2, CZ 11000 Praha 1, Czech Republic | |

### 17.3.4 Powder Data Conversion

*17.3.4.1 General Overview*. It is more effective, and time saving, to use data collection software that writes directly into the required data analysis formats. Where this is not possible, or when distributing diffractograms, data conversion may be required. While in theory a trivial operation, when performed routinely on large numbers of data files it can become a significant drain on time. In theory, IUCr CIF (Crystallographic Information File/Crystallographic Information Framework; which includes PowderCIF) is the standard for diffraction data transfer. Nexus is another possible standard, while XML has made an appearance as an Open Format. However, none of these formats have yet to be routinely applied in the powder diffraction community. Vendor hardware or data collection software tends to define the default file formats for most laboratories. Many vendor based XRD data formats are binary, and potentially not readable into the distant future. If using cryptic binary or ASCII file formats, a comprehensive definition of the file formats should be obtained and safely stored. In theory, it would be desirable if all laboratory diffraction data was converted into an open format such as CIF and protected using an appropriate local and offsite backup strategy.

**Table 17.4** Available crystal structure databases and their specializations.

| *Software* | *References or contact information* | *Specialization* | *Freely Available* |
|---|---|---|---|
| American Mineralogist Crystal Structure Database | The American Mineralogist Crystal Structure Database, R. T. Downs and M. Hall Wallace, *Am. Mineral.*, 2003, **88**, 247 250 | Minerals | Yes |
| CCDC/Cambridge Structure Database | The Cambridge Structural Database: a quarter of a million crystal structures and rising, F. H. Allen, *Acta Crystallogr., Sect. B*, 2002, **58**, 380 388 | Organics and Organometallics | |
| CDS (EPSRC funded Chemical Database Service) | "The United Kingdom Chemical Database Service", D. A. Fletcher, R. F. McMeeking, D. J. Parkin, *Chem. Inf. Comput. Sci.*, 1996, **36**, 746 749 | Access to a large number of scientific databases to UK based academics and students, including all the main crystallographic databases | Yes (within the UK) |
| COD (Crystallography Open Database) | Crystallography Open Database, (2005) http://www.crystallography.net/ | Open Access Database including predicted structures | Yes |
| CRYSTMET | CRYSTMET, Toth Information Systems, Inc., 2045 Quincy Avenue, Ottawa, Ontario, K1J 6B2, Canada | Metals and Alloys | |
| ICDD (International Centre for Diffraction Data) PDF 4+ | International Centre for Diffraction Data, 12 Campus Boulevard, Newtown Square, PA, 19073 3273, U.S.A. | Includes crystal structure co ordinates from the Pauling File | |
| ICSD (Inorganic Crystal Structure Database) | CD ROM: http://www.fiz informationsdienste.de/en/DB/icsd/WEB: http://icsd.ill.fr/icsd/ | Inorganic and Minerals | |

(*Continued*)

**Table 17.4** (*Continued*).

| *Software* | *References or contact information* | *Specialization* | *Freely Available* |
|---|---|---|---|
| Incommensurate phases database | A database of incommensurate phases, R. Caracas, *J. Appl. Crystallogr.*, 2002, **35**, 120 121 | Incommensurate | |
| LAMA Incommensurate Structures Database | Incommensurate Structures Database, E. Kroumova, J.A. Luna, G. Madariaga and J.M. Pérez Mato, Bilbao Crystallographic Server, Euskal Herriko Unibertsitatea/ University of the Basque Country, 2005, http:// www.cryst.ehu.es/icsdb/ | Incommensurate and Composites | Yes |
| MINCRYST | Information calculating system on Crystal Structure data for Minerals (MINCRYST), A. V. Chichagov, D. A. Varlamov, R. A. Dilanyan, T. N. Dokina, N. A. Drozhzhina, O. L. Samokhvalova, T. V. Ushakovskaya, *Crystallogr. Rep.*, 2001, **46**(5), 876 879 [translated from *Kristallografiya*, 2001, **46**(5), 950 954] | Minerals | Yes |
| Pauling File | *The PAULING FILE Binaries Edition*, ed. P. Villars, ASM International, Materials Park, Ohio, USA, 2002, ISBN 0 87170 786 1 | Binary Compounds including oxides, alloys; and phase diagrams | |
| PDB (Protein Data Bank) | The Protein Data Bank, H. M. Berman, J. Westbrook, Z. Feng, G. Gilliland, T. N. Bhat, H. Weissig, I. N. Shindyalov and P. E. Bourne, *Nucleic Acids Res.*, 2000, **28**, 235 242 | Proteins and Biological Macromolecules | Yes |
| Zeolite Structures Database | Zeolite Structures Database, Ch. Baerlocher, L. B. McCusker, W. M. Meier and D. H. Olson, http://www.iza structure.org/, 9 October 2003 | Zeolites: known and hypothetical | Yes |

*17.3.4.2 Converting Two-dimensional Powder Diffraction Data into One-dimensional Data.* Fit2D is the benchmark program in use for 2D to 1D conversion due to its age, free availability, recognizing various image formats, running on a range of operating systems and has various other features (Table 17.5). However, some MS-Windows specific conversion programs are more intuitive to use.

*17.3.4.3 Interconverting One-dimensional Powder Diffraction Data.* The ConvX for Windows software can be very effective due to its user friendliness and ability to convert a number of files in a single pass (Table 17.6). The Powder v4 software can be good for converting ill-defined ASCII format data into a standard format while PowDLL can convert some of the latest vendor binary formats. Summing of multiple data files (where different count times may have been used) is available in some converters, but use of a spreadsheet program is recommended as an independent check. The procedure for the general summing of data files and calculation of ESDs is provided on the CCP14 website.

Care must be taken, as many file formats are ill-defined; and where software does not convert some file formats into the described specifications. An example of the later is that of file converters which convert GSAS STD format files without including the "STD" flag in the second header line (line 2).

Some resulting files may require major to minor editing by hand. For the above GSAS example, this would involve adding the STD flag to the end of the second line. Most ASCII data formats are easily checked for starting angle, end angle and step width, by viewing in a text editor (Table 17.7). However, some can be quite cryptic. An example of this is the GSAS Rietveld STD and ESD formats, where the start angle and step is in deci-degrees, and number of datapoints stated instead of an end angle. A moderately common pitfall is that of intermixing UNIX and DOS ASCII files on different computer systems. For MS-Windows, the freeware PFE file editor displays whether the file is UNIX or DOS ASCII and can save into one or the other via the File, Save-As command. For copying or inserting columns of data, the freeware ConTEXT editor is effective and saves time in comparison to importing the file into a spreadsheet program.

### 17.3.5 Structure Data Conversion and Transformation

With CIF becoming a more used standard in the powder diffraction community, structure data conversion is becoming less needed on a day-to-day basis. The Powder Cell format is probably the next best format due to its relative simplicity compared to CIF. Most structure databases can export files into CIF format, and some to Powder Cell format. Eric Dowty's Cryscon software is currently the most comprehensive structure data conversion and transformation (Table 17.8). However, due care should be shown and results checked. Normally, the programs are robust, and it is more a case of users selecting options without understanding the consequences.

**Table 17.5** Available software for integrating of 2D powder diffraction data into 1D data.

| *Software* | *Reference* | *Capability* |
|---|---|---|
| Datasqueeze | Datasqueeze Program for analyzing 2D diffraction data, especially small angle and powder diffraction. Paul Heiney, pheiney@datasqueezesoftware.com, PMB 252, 303 West Lancaster Ave., Wayne, PA 19087 3938 U.S.A. Available at http://www. datasqueezesoftware.com/. First release 2002, last update February 2005 | Can integrate full 2D cones of diffraction |
| FIT2D | FIT2D V9.129 Reference Manual V3.1, A. P. Hammersley, (1998) ESRF Internal Report, ESRF98HA01T and Two Dimensional Detector Software: From Real Detector to Idealised Image or Two Theta Scan, A. P. Hammersley, S. O. Svensson, M. Hanfland, A. N. Fitch, and D. Häusermann, *High Pressure Res*., 1996, **14**, 235 248 | Can integrate full 2D cones of diffraction |
| MAUD | MAUD (Material Analysis Using Diffraction): a user friendly {Java} program for {Rietveld} Texture Analysis and more, L. Lutterotti, S. Matthies and H. R. Wenk, *Proceeding of the Twelfth International Conference on Textures of Materials (ICOTOM 12)*, 1999, Vol. 1, p. 1599 | Debye Scherrer film integration and of full 2D cones of diffraction |
| NIH Image | NIH Image program (developed at the U.S. National Institutes of Health and available on the Internet at http://rsb.info.nih.gov/nih image/) | Usable for Debye Scherrer film integration |
| Powder3D | Powder3D 1.0: A multi pattern data reduction and graphical presentation software, B. Hinrichsen, R.E. Dinnebier and M. Jansen, 2004; http://www.fkf.mpg.de/xray/html/powder3d.html | Integration of full 2D cones of diffraction: under development |
| SImPA | SImPA (Simplified Image Plate Analysis), K. Lagarec and S. Desgreniers (1995 2005), Laboratoire de physique des solides denses, Université d'Ottawa, 150, rue Louis Pasteur, Ottawa, Ontario, Canada, K1N 6N5 | Can integrate full 2D cones of diffraction |
| XRD2DScan | XRD2DScan: new software for polycrystalline materials characterization using two dimensional X ray diffraction, A. B. Rodriguez Navarro, *J. Appl. Crystallogr*., 2006, **39**, 905 909 | Windows software optimized for area detectors |

### 17.3.6 Powder Diffraction Pattern Viewing and Processing

For quick checking of single and multiple diffraction data files, the author has a bias for the XFIT/Koalariet software, but this software is no longer developed (Table 17.9). WinPLOTR, part of the Fullprof Rietveld Suite, is an excellent program for data visualization and processing. It imports various common

**Table 17.6** Available powder diffraction data conversion software and supported file types.

| *Software* | *References* | *Imported file formats* | *Exported file formats* | *Converstion functionality* |
|---|---|---|---|---|
| AXES | H. Mändar and T. Vajakas, AXES a software toolbox in powder diffraction, *Newsletter Int. Union Crystallogr, Commission Powder Diffr.* 1998, **20**, 31 32; and AXES1.9: new tools for estimation of crystallite size and shape by Williamson Hall analysis, H. Mändar, J. Felsche, V. Mikli and T. Vajakas, *J. Appl. Crystallogr.*, 1999, **32**, 345 350 | Siemens Diffrac AT 1 & 3, Bruker DiffracPlus 1.01 RAW, Siemens UXD, DBWS + WYRIET, RIETAN, XRS 82, Allmann DIFFRAC, ICDD *.REF, ICDD *.PD3, SCANPI, Y only, X Y pairs, DiffracINEL, HUBER G600 and G670, Synchrotron SRS, PROFIT, FULLPROF, Guinier Tübingen, GSAS standard, DIFFaX, Philips *.RD, Philips *.UDF, Seifert ASCII, EXTRA, STOE Binary v1.04 | Siemens Diffrac AT 1 & 3, Bruker DiffracPlus 1.01 RAW, Siemens UXD, PEAK 91, DBWS + WYRIET, RIETAN, XRS 82, Allmann DIFFRAC, ICDD *.REF, ICDD *.PD3, Y only, X Y pairs, HUBER G670, PROFIT, FULLPROF, GSAS standard, EXTRA, STOE Binary v1.04 | Summation |
| CMPR | CMPR, Brian Toby, NIST Center for Neutron Research, 100 Bureau Drive, Stop 8562, National Institute of Standards and Technology, Gaithersburg, MD, 20899 8562, USA | SPEC, BT 1, pdCIF, COM CAT, CPI, DBWS/ Fullprof, APS DND, GSAS EXP, GSAS raw data, NIST/ ICP | CSV, TXT, GSAS, XDA | Summation and interpolation of multiple datasets |
| ConvX | ConvX Data File Conversion Software for Windows, M.E. | Philips VAX APD, Philips PC APD (RD | Philips VAX APD, Philips PC APD (RD | |

(*Continued*)

**Table 17.6** (*Continued*).

| *Software* | *References* | *Imported file formats* | *Exported file formats* | *Converstion functionality* |
|---|---|---|---|---|
| | Bowden, *Int. Union Crystallogr., Commission Powder Diffr. Newsletter*, 2000, No. 23, 21 | format), RIET7 Rietveld, GSAS, ASCII 2 theta,I lists, SCANPI, Philips PC APD (SD format) | format), RIET7 Rietveld, GSAS, ASCII 2 theta and I lists, SCANPI, Sietronics CPI, Siemens DiffracPlus, FullProf | |
| Fullprof Suite/ WinPLOTR | WinPLOTR: A Windows tool for powder diffraction pattern analysis, T. Roisnel and J. Rodriguez Carvajal, *EPDIC 7: European Powder Diffraction*, Pts 1 and 2 Materials Science Forum 378 3: 118 123, Part 1&2 2001 | X Y, DBWS/Fullprof, Old D1A (ILL), D1B (ILL), Brookhaven sync, G4.1, D2B/3T2/G4.2, HRPT/ DMC (PSI), RX (Socabim), VCT/SR5 (Variable Count Time Madsen and Hill), GSAS, CPI, PANalytical, ISIS normalized, ESRF multi, LLB Saclay formats, UXD Multscans (Socabim) 6T2 | Multicolumns ASCII, XY INSTM 0, | Normalization and summation of multiple datastes |
| MacDiff | MacDiff a programme for analysis and display of X ray powder diffractogrammes on Apple Macintosh platforms, R. Petschick, Geologisch Paläontologisches Institut, Johann Wolfgang Goethe | Philips ".RD" APD VMS, Philips ".RD" APD MSDOS, Philips APD ASCII MSDOS (APD "View Scan"), Philips APD APD UDF ASCII MSDOS, | Philips APD APD UDF ASCII MSDOS, ".MDI" ASCII, Sietronic ".CPI" ASCII, MacXFit of H.Stanjek, Text ASCII (angle, count [, base] several | |

| | | | | |
|---|---|---|---|---|
| | Universität Frankfurt am Main, Senckenberganlage 32 34, 60054 Frankfurt am Main, Germany | Siemens ".RAW" RAW2 MSDOS, Siemens ".RAW" New RAW1, Siemens ".RAW" Old RAW format, ".MDI" ASCII Text, ".OUT" ASCII Text, Sietronic ".CPI" ASCII Text, Lauterjung ASCII Text, SCINTAG 2000 ASCIII | delimiters possible), MacDiff DIFF format | |
| Powder3D | Powder3D 1.0: A multi pattern data reduction and graphical presentation software, B. Hinrichsen, R. E. Dinnebier and M. Jansen, 2004; http://www.fkf.mpg.de/xray/html/powder3d.html | CHI, XY, XYE, DAT, GSA, UXD | Array, CHI, XYE, GSAS, Fullprof | Normalizing multiple patterns |
| Powder Cell | POWDER CELL a program for the representation and manipulation of crystal structures and calculation of the resulting X ray powder patterns., W. Kraus and G. Nolze, *J. Appl. Crystallogr.*, 1996, **29**, 301 303 | Diffrac AT&Plus, STOE Raw, XY, UDF, CPI, Riet7/ LHPM, APX 63 VAL | X Y, Siemens RAW, CPI | |
| Powder v4 | PowderV2: a suite of applications for powder X ray diffraction | DBWS, GSAS ESD and STD, LHPM, Philips PC UDF, Riet7, | DBWS, GSAS ESD and STD, LHPM, Philips PC UDF, Riet7, | Normalization of multiple datasets |

(*Continued*)

**Table 17.6** (*Continued*).

| *Software* | *References* | *Imported file formats* | *Exported file formats* | *Converstion functionality* |
|---|---|---|---|---|
| | calculations, N. Dragoe, *J. Appl. Crystallogr.*, 2001, **34**, 535 | Scintag, Siemens ASCII, Sietronics CPI, Wppf Profit, Y free ASCII, X,Y free ASCII, X,Y, Z free ASCII, MXP18 UNIX Binary, Mac Science Windows Binary, Philips RD/SD Binary, custom format | Scintag, Siemens, Sietronics CPI, Wppf Profit 1, Wppf Profit 2, Y free ASCII, X,Y free ASCII, X,Y,Z free ASCII, DPLOT, | |
| PowderX | PowderX: Windows 95 based program for powder X ray diffraction data processing, C. Dong, *J. Appl. Crystallogr.*, 1999, **32**, 838 | Mac Science ASCII, BD90 (Raw), X Y, Rigaku (DAT), Sietronics (CPI), TsingHua Rigaku (USR) Siemens ASCII (UXD), Siemens Binary (RAW), Philips ASCII (UDF), Philips Binary (RD) Mac Science Raw, RIET7 (DAT), ORTEC Maestro (CHN) | ALLHKL (POW), Sietronics (CPI), FOURYA/ XFIT/ Koalariet (XDD), Fullprof (DAT), GSAS (DAT), Rietan (INT), Simpro (DUO), X Y (XRD), DBWS (DAT), LHPM (DAT) | |
| PowDLL | PowDLL: A reusable. NET component and XRD data interconversion utility, N. Kourkoumelis (2004 05), http://users.uoi.gr/ nkourkou/powdll.htm | Bruker/Siemens RAW (versions 1 3), Philips RD, Scintag ARD, powderCIF, Sietronics CPI, Riet7 DAT, DBWS, GSAS (CW STD), Jade MDI, Rigaku RIG, Philips | Bruker/Siemens RAW (versions 1 3), Philips RD, Scintag ARD, Sietronics CPI, Riet7 DAT, DBWS, GSAS (CW STD), Jade MDI, Rigaku RIG, Philips | |

| | | | |
|---|---|---|---|
| | | UDF, UXD, XDA, XDD, ASCII XY | UDF, UXD, XDA, XDD, ASCII XY |
| POWF | POWF: a program for powder data file conversion, R.J. Angel, (2005), Virginia Tech Crystallography Laboratory, 3076 Derring Hall, Virgina Tech, Blacksburg, VA 24060, USA; http://www.crystal.vt.edu/crystal/powf.html | ASCII XY, GSAS CW data, Stoe RAW, Siemens UXD, Scintag ARD, DBW, MDI ASCI, MDI MDI, GSAS Cif, Stoe ASCII, Philips UDF | ASCII XY, GSAS CW data, Stoe RAW, Siemens UXD, Scintag ARD, DBW |
| Pulwin | PULWIN: A program for analyzing powder X ray diffraction patterns, S. Brückner, *Powder Diffr.*, 2000, **15**(4), 218 219 | X Y, X, INEL CPS 120 (*.adf), PHILIPS (*.udf), SIEMENS (*.uxd) | X Y, X, INEL CPS 120 (*.adf), PHILIPS (*.udf), SIEMENS (*.uxd) |
| VCTCONV | VCTCONV, M.E. Bowden, CRI IRL, Lower Hutt, New Zealand, (2005) | Variable Count Time RIET7/SR5 | GSAS ESD |
| WinFIT | WinFit 1.2.1, S. Krumm, (June 1997), Institut fur Geologie, Scholssgarten 5, 91054, Erlangen, Germany | DFA, SIEMENS RAW, TRU, X Y, ICDD PD3, ZDS, CRI, Philips UDF and RD, Stoe RAW, MDI Jade, MacDIFF DIF, XDA | SIEMENS (*.raw), PHILIPS (*.rd), ASCII, XDA |

**Table 17.7** Some text editors and spreadsheet programs with useful features for powder diffraction data conversion.

| *Software* | *Useful feature* |
|---|---|
| ConTEXT | Freeware software with good column editing accessible via "[CONTROL] L" |
| DPLOT | User friendly re binning of variable step data into constant 2 theta steps |
| MS Excel | Simple Mathematical operations for summing and data interconversion |
| PFE | Flexible intuitive freeware text editor with good search and replace features, and inter converting DOS ASCII to UNIX ASCII |

formats and can display the data in 2-theta, D-spacing, Q, Sin theta/lambda, making it very useful for comparing data taken at different wavelengths. For large numbers of datasets the new Powder3D is very effective. Powder3D is designed for displaying hundreds to thousands of datasets as part of non-ambient *in situ* diffraction runs. The "2D film mode" within Powder3D is a useful visualization method for obtaining an overview of tens to thousands of datasets.

### 17.3.7 Peak Finding and Peak Profiling

Again, the author has a bias for using XFIT/Koalariet. While peak selection is manual, XFIT's Marquardt fitting is extremely robust and stable compared to other programs, and includes Fundamental Parameters peak profiling for Bragg–Brentano XRD geometries. However, as XFIT is no longer developed, WinPLOTR is actively developed and worth using. WinPLOTR includes automatic and manual peak finding, peak profiling, and passing the results onto several indexing programs. Fityk is an open source GPL'd program for peak fitting. It runs under Linux, FreeBSD, MS Windows and MacOS X, has many common peak-shape functions, and the ability to apply user-defined functions (Table 17.10).

### 17.3.8 Powder Indexing

*17.3.8.1 Powder Indexing Software.* Due to indexing being considered a tedious bottleneck in structure solution from powder diffraction data, it is advisable to use as wide a number of programs as possible (Table 17.11). Traditionally, the three main indexing programs of choice have been Dicvol, Treor and Ito. However, the trend is for indexing programs that are moderately insensitive to impurity peaks, and can handle data of lower quality. Dicvol has been updated with Dicvol2004 and Dicvol 2006; and Treor to Treor2000 (within the EXPO structure solution software). X-Cell, Topas Indexing, MAUD and McMaille are new programs that are more likely to cope with impurity peaks and/or poorer quality data. At present, the indexing options

**Table 17.8** Available structure data conversion and transformation software.

| *Software* | *References* | *Imported file formats* | *Exported file formats* |
|---|---|---|---|
| AXES | H. Mändar and T. Vajakas, AXES a software toolbox in powder diffraction, *Newsletter Int. Union Crystallogr., Commission Powder Diffr*. 1998, **20**, 31 32 and AXES1.9: new tools for estimation of crystallite size and shape by Williamson Hall analysis, H. Mändar, J. Felsche, V. Mikli and T. Vajakas, *J. Appl. Crystallogr*., 1999, **32**, 345 350 | ICSD *.txt, MolDraw, Powder Cell, GSAS EXP, Fullprof PCR | ICSD *.txt, LazyPulvarix, PrecPlot, Schkal, MolDraw, Powder Cell, Fullprof PCR |
| Cryscon | Cryscon: crystallographic conversion and utility software, Eric Dowry, Shape Software, 521 Hidden Valley Road Kingsport, TN, 37663, USA, http://www.shapesoftware.com/ | Freeform, CCDC FDAT, Shelx INS, CIF, DBWS, LHPM, ISCD formats, ORTEP, XtalView, Rietan, GSAS, American Mineralogist Database, Fullprof, PDB, ATOMS, VIBRAT VBR, Raval ATOMS, WIEN2K | Freeform, CCDC FDAT, Shelx INS, CIF, DBWS, LHPM, ISCD formats, ORTEP, Rietan, GSAS, Fullprof, Raval ATOMS. |
| Gretep | LMGP Suite Suite of Programs for the interpretation of X ray Experiments, by J. Laugier and B. Bochu, ENSP/ Laboratoire des Matériaux et du Génie Physique, BP 46. 38042 Saint Martin d′Hčres, France | Gretep, Poudrix, Shelx, Lazy_Pulverix, Powder Cell, CIF | Shelx, GRETEP, CIF |
| MolXtl | MolXtl: molecular graphics for small molecule crystallography, D. W. Bennett, *J. Appl. Crystallogr*., 2004, **37**, 1038 | MolXtl, Shelx, Xmol XYZ, CIF, PDB, Z matrix | MolXtl, Xmol XYZ, CIF, PDB, Z matrix, Xtl Cartesian XTC |
| Open Babel | Open Babel. http://openbabel.sourceforge.net/ (accessed Mar 2005), 2005 | Wide variety of primarily Cartesian molecular modeling formats | Wide variety of primarily Cartesian molecular modeling formats |

(*Continued*)

**Table 17.8** (*Continued*).

| *Software* | *References* | *Imported file formats* | *Exported file formats* |
|---|---|---|---|
| ORTEP III for Windows | ORTEP 3 for Windows a version of ORTEP III with a Graphical User Interface (GUI), L. J. Farrugia, *J. Appl. Crystallogr*., 1997, **30**, 565 | Shelx, CIF, GX, Platon SPF, ORTEP, CSD FDAT, CSSR XR, Crystals, GSAS EXP, Sybyl MOL, Sybyl MOL2, MDL Molfile, XYZ, PDB, Rietica LHPM, Fullprof PCR | ORTEP, Shelx, XYZ |
| Platon | Single crystal structure validation with the program PLATON, A. L. Spek, *J. Appl. Crystallogr*., 2003, **36**, 7 13 | Includes Structure Tidy | |
| Powder Cell | POWDER CELL a program for the representation and manipulation of crystal structures and calculation of the resulting X ray powder patterns., W. Kraus and G. Nolze, *J. Appl. Crystallogr*., 1996, **29**, 301 303 | Powder Cell, Shelx, ICSD (TXT) | Powder Cell, Shelx, Opal (XTL), BGMN (STR) |
| Structure Tidy | STRUCTURE TIDY a computer program to standardize crystal structure data, L. M. Gelato and E. Parthé, *J. Appl. Crystallogr*., 1987, **20**, 139 143 and Inorganic crystal structure data to be presented in a form more useful for further studies, S. Zu Hu and E. Parthe, *Chin. J. Struct. Chem*. 2004, **23**(10), 1150 1160 | Puts crystal structures into standardized co ordinates for comparison with other structures | |
| WinGX | WinGX suite for small molecule single crystal crystallography, L. J. Farrugia, *J. Appl. Crystallogr*., 1999, **32**, 837 838 | CSSR, Shelx, Cif, CSD/CCDC FDAT, GX | Shelx, CIF, GX, SPF/ Platon, CACAO |

**Table 17.9** Available powder diffraction pattern viewing and processing software.

| *Software* | *References* | *Data formats* |
|---|---|---|
| AXES | H. Mändar and T. Vajakas, AXES a software toolbox in powder diffraction, *Newsletter Int. Union Crystallogr., Commission Powder Diffr.*, 1998, **20**, 31 32 and AXES1.9: new tools for estimation of crystallite size and shape by Williamson Hall analysis, H. Mändar, J. Felsche, V. Mikli and T. Vajakas, *J. Appl. Crystallogr.*, 1999, **32**, 345 350 | Siemens Diffrac AT 1 & 3, Bruker DiffracPlus 1.01 RAW, Siemens UXD, DBWS + WYRIET, RIETAN, XRS 82, Allmann DIFFRAC, ICDD *.REF, ICDD *.PD3, SCANPI, Y only, X Y pairs, DiffracINEL, HUBER G600 and G670, Synchrotron SRS, PROFIT, FULLPROF, Guinier Tübingen, GSAS standard, DIFFaX, Philips *.RD, Philips *.UDF, Seifert ASCII, EXTRA, STOE Binary v1.04 |
| CMPR | CMPR, Brian Toby, NIST Center for Neutron Research, 100 Bureau Drive, Stop 8562, National Institute of Standards and Technology, Gaithersburg, MD, 20899 8562, USA | SPEC, BT 1, pdCIF, COM CAT, CPI, DBWS/ Fullprof, APS DND, GSAS EXP, GSAS raw data, NIST/ICP |
| Fityk | Marcin Wojdyr, Institute of High Pressure Physics, Warsaw, Poland, http:// www.unipress.waw.pl/fityk/ | X Y, RIT, CPI, MCA, Siemens/ Bruker RAW |
| Fullprof Suite/ WinPLOTR | WinPLOTR: A Windows tool for powder diffraction pattern analysis, T. Roisnel and J. Rodriguez Carvajal, *EPDIC 7: European Powder Diffraction*, Pts 1 and 2 Materials Science Forum 378 3: 118 123, Part 1&2 2001 | X Y, Old D1A, D1B, Brookhaven Synchrotron, G4.1, D2B, RX (Socabim), VCT, GSAS, CPI, Panalytical, normalized ISIS |
| OpenGenie | Open GENIE Reference Manual, F. A. Akeroyd, R. L. Ashworth, S. I. Campbell, S. D. Johnston, C. M. Moreton Smith, R. G. Sergeant and D. S. Sivia, Rutherford Appleton Laboratory Technical Report RAL TR 1999 031 | ISIS Raw File, GENIE II, Open GENIE |
| Powder 3D | Powder3D 1.0: A multi pattern data reduction and graphical presentation software, B. Hinrichsen, R. E. Dinnebier and M. Jansen, 2004; http://www.fkf.mpg.de/ xray/html/powder3d.html | CHI, XY, XYE, DAT, GSA, UXD |
| Powder Cell | POWDER CELL a program for the representation and manipulation of crystal | Diffrac AT&Plus, STOE Raw, XY, UDF, CPI, Riet7/ LHPM, APX 63 VAL |

(*Continued*)

**Table 17.9** (*Continued*).

| *Software* | *References* | *Data formats* |
|---|---|---|
| | structures and calculation of the resulting X ray powder patterns., W. Kraus and G. Nolze, *J. Appl. Crystallogr.*, 1996, **29**, 301 303 | |
| Powder v4 | PowderV2: a suite of applications for powder X ray diffraction calculations, N. Dragoe, *J. Appl. Crystallogr.*, 2001, **34**, 535 | DBWS, GSAS CW, GSAS CW, GSAS ESD, GSAS ALT, LHPM, Philips RD/SD binary, Philips UDF, MXP18 Binary, RIET7, Scintag, Siemens ASCII, Sietronics CPI, WPPF/Profit, Y free ascii, XY free ascii, XYZ free ascii. Line; X, XY, XYZ. |
| PowderX | PowderX: Windows 95 based program for powder X ray diffraction data processing, C. Dong, *J. Appl. Crystallogr.*, 1999, **32**, 838 | Mac Science ASCII, BD90 (Raw), X Y, Rigaku (DAT), Sietronics (CPI), TsingHua Rigaku (USR) Siemens ASCII (UXD), Siemens Binary (RAW), Philips ASCII (UDF), Philips Binary (RD) Mac Science Raw, RIET7 (DAT), ORTEC Maestro (CHN) |
| Pulwin | PULWIN: A program for analyzing powder X ray diffraction patterns, S. Brückner, *Powder Diffr.*, 2000, **15**(4), 218 219 | X Y, X, INEL CPS 120 (*.adf), PHILIPS (*.udf), SIEMENS (*.uxd) |
| WinFIT | WinFit 1.2.1, S. Krumm, (June 1997), Institut fur Geologie, Scholssgarten 5, 91054, Erlangen, Germany | DFA, SIEMENS RAW, TRU, X Y, ICDD PD3, ZDS, CRI, Philips UDF and RD, Stoe RAW, MDI Jade, MacDIFF DIF, XDA |
| XFIT | Axial Divergence in a Conventional X ray Powder Diffractometer. II. Realization and Evaluation in a Fundamental Parameter Profile Fitting Procedure, R. W. Cheary and A. A. Coelho, *J. Appl. Crystallogr.*, 1998, **31**, 862 868, and R. W. Cheary and A. A. Coelho, 1996, Programs XFIT and FOURYA, deposited in CCP14 Powder Diffraction Library, Engineering and Physical Sciences Research Council, Daresbury Laboratory, Warrington, England | RIET 7, XDD, XDA, SCN, CPI, CAL, CPT, XY |

**Table 17.10** Available peak finding and peak profiling software.

| *Software* | *Reference* | *Peak Find* | *Peak Profiling* | *Data Formats* |
|---|---|---|---|---|
| AXES | H. Mändar and T. Vajakas, AXES a software toolbox in powder diffraction, *Newsletter Int. Union Crystallogr., Commission Powder Diffr.*, 1998, **20**, 31 32 and AXES1.9: new tools for estimation of crystallite size and shape by Williamson Hall analysis, H. Mändar, J. Felsche, V. Mikli and T. Vajakas, *J. Appl. Crystallogr.*, 1999, **32**, 345 350 | | Yes | Siemens Diffrac AT 1 & 3, Bruker DiffracPlus 1.01 RAW, Siemens UXD, DBWS + WYRIET, RIETAN, XRS 82, Allmann DIFFRAC, ICDD *.REF, ICDD *.PD3, SCANPI, Y only, X Y pairs, DiffracINEL, HUBER G600 and G670, Synchrotron SRS, PROFIT, FULLPROF, Guinier Tübingen, GSAS standard, DIFFaX, Philips *.RD, Philips *.UDF, Seifert ASCII, EXTRA, STOE Binary v1.04 |
| CMPR | CMPR and Portable Logic, Brian Toby, NIST Center for Neutron Research, 100 Bureau Drive, Stop 8562, National Institute of Standards and Technology, Gaithersburg, MD, 20899 8562, USA | | Yes | SPEC, BT 1, pdCIF, COM CAT, CPI, DBWS/ Fullprof, APS DND, GSAS EXP, GSAS raw data, NIST/ICP |
| Fitykt | Marcin Wojdyr, Institute of High Pressure Physics, Warsaw, Poland, http:// www.unipress.waw.pl/fityk/ | Yes | Yes | X Y, RIT, CPI, MCA, Siemens/ Bruker RAW |
| Fullprof Suite/ Winplotr | WinPLOTR: A Windows tool for powder diffraction pattern analysis, T. Roisnel and J. Rodriguez Carvajal, *EPDIC 7:* | Yes | Yes | X Y, Old D1A, D1B, Brookhaven Synchrotron, G4.1, D2B, RX (Socabim), VCT, GSAS, CPI, Panalytical, normalized ISIS |

(*Continued*)

**Table 17.10** (*Continued*).

| *Software* | *Reference* | *Peak Find* | *Peak Profiling* | *Data Formats* |
|---|---|---|---|---|
| | *European Powder Diffraction*, Pts 1 and 2 Materials Science Forum 378 3: 118 123, Part 1&2 2001 | | | |
| GSAS RawPlot | General Structure Analysis System (GSAS), A.C. Larson and R.B. Von Dreele, Los Alamos National Laboratory Report LAUR 86 748 (1994) | | Yes | GSAS |
| Powder3D | Powder3D 1.0 : A multi pattern data reduction and graphical presentation software, B. Hinrichsen, R. E. Dinnebier and M. Jansen, 2004; http://www.fkf.mpg.de/xray/html/powder3d.html | Yes | | CHI, XY, XYE, DAT, GSA, UXD |
| Powder v4 | PowderV2: a suite of applications for powder X ray diffraction calculations, N. Dragoe, *J. Appl. Crystallogr.*, 2001, **34**, 535 | Yes | | DBWS, GSAS CW, GSAS CW, GSAS ESD, GSAS ALT, LHPM, Philips RD/SD binary, Philips UDF, MXP18 Binary, RIET7, Scintag, Siemens ASCII, Sietronics CPI, WPPF/Profit, Y free ascii, XY free ascii, XYZ free ascii. Line; X, XY, XYZ |
| PowderX | PowderX: Windows 95 based program for powder X ray diffraction data processing, C. | Yes | | Mac Science ASCII, BD90 (Raw), X Y, Rigaku (DAT), Sietronics (CPI), TsingHua Rigaku (USR) |

| | | | |
|---|---|---|---|
| | Dong, *J. Appl. Crystallogr.*, 1999, **32**, 838 | | Siemens ASCII (UXD), Siemens Binary (RAW), Philips ASCII (UDF), Philips Binary (RD) Mac Science Raw, RIET7 (DAT), ORTEC Maestro (CHN) |
| PRO FIT | Whole powder pattern fitting without reference to a structural model: Application to X ray powder diffractometer data, H. Toraya, *J. Appl. Crystallogr.* 1986, **19**, 440 447 | Yes | Profit |
| PULWIN | PULWIN: A program for analyzing powder X ray diffraction patterns, S. Brückner, *Powder Diffr.*, 2000, **15**(4), 218 219 | Yes | X Y, X, INEL CPS 120 (*.adf), PHILIPS (*.udf), SIEMENS (*.uxd) |
| SHADOW | Simultaneous Crystallite Size, Strain and Structure Analysis from X ray Powder Diffraction Patterns, S. A. Howard and R. L. Snyder, NYS College of Ceramics Technical Publication, New York State College of Ceramics, Alfred University, Alfred, NY 14802, USA | Yes | XDA |
| WinFit | WinFit 1.2.1, S. Krumm, (June 1997), Institut fur Geologie, Scholssgarten 5, 91054, Erlangen, Germany | Yes | DFA, SIEMENS RAW, TRU, X Y, ICDD PD3, ZDS, CRI, Philips UDF and RD, Stoe RAW, MDI Jade, MacDIFF DIF, XDA |

(*Continued*)

**Table 17.10** (*Continued*).

| *Software* | *Reference* | *Peak Find* | *Peak Profiling* | *Data Formats* |
|---|---|---|---|---|
| XFIT | Axial Divergence in a Conventional X ray Powder Diffractometer. II. Realization and Evaluation in a Fundamental Parameter Profile Fitting Procedure, R. W. Cheary and A. A. Coelho, *J. Appl. Crystallogr.*, 1998, **31**, 862 868, and R. W. Cheary and A. A. Coelho, 1996, Programs XFIT and FOURYA, deposited in CCP14 Powder Diffraction Library, Engineering and Physical Sciences Research Council, Daresbury Laboratory, Warrington, England | | Yes | RIET 7, XDD, XDA, SCN, CPI, CAL, CPT |

**Table 17.11** Available powder indexing software.

| *Software* | *References* | *Within suites* |
|---|---|---|
| Dicvol 91 | Indexing of powder diffraction patterns for low symmetry lattices by the successive dichotomy method, A. Boultif and D. Louër, *J. Appl. Crystallogr.*, 1991, **24**, 987 993 | CMPR, Crysfire, Fullprof Suite Winplotr, Powder v4 |
| Dicvol 2004 | Powder pattern indexing with the dichotomy method, A. Boultif and D. Louer, *J. Appl. Crystallogr.*, 2004, **37**, 724 731 | |
| Eflect/Index | EFLECH/INDEX a program pair for peak search/fit and indexing, J. Bergmann and R. Kleeberg, *Newsletter Int. Union Crystallogr., Commission Powder Diffr.*, 1999, No. 21, p. 5 | |
| Fjzn | The Crysfire 2002 System for Automatic Powder Indexing: User's Manual, R. Shirley, (2002) The Lattice Press, 41 Guildford Park Avenue, Guildford, Surrey GU2 7NL, England | Crysfire |
| Ito | A Fully Automatic Program for Finding the Unit Cell from Powder Data, J. W. Visser, *J. Appl. Crystallogr.*, 1969, **2**, 89 95 | Crysfire, Fullprof Suite Winplotr, Powder v4 |
| Kohl/TMO | Trial and error indexing program for powder patterns of monoclinic substances, F. Kohlbeck and E. M. Hörl, *J. Appl. Crystallogr.*, 1978, **11**, 60 61 | Crysfire |
| Lzon | New powder indexing programs for any symmetry which combine grid search with successive dichotomy, R. Shirley and D. Louër, *Acta Crystallogr., Sect. A*, 1978, **34**, S382 | Crysfire |
| MAUD (whole profile indexing) | MAUD (Material Analysis Using Diffraction): a user friendly {Java} program for {Rietveld} Texture Analysis and more, L. Lutterotti, S. Matthies and H. R. Wenk, *Proceeding of the Twelfth International Conference on Textures of Materials (ICOTOM 12)*, 1999, Vol. 1, p. 1599 | |
| McMaille | Monte Carlo Indexing with McMaille, A. Le Bail, *Powder Diffr.* 2004, **19**, 249 254 | Produces Chekcell summary files. |
| Supercell | SuperCell, J. Rodriguez Carvajal, Laboratoire Léon Brillouin, Saclay, France, December 1998 and WinPLOTR: A Windows tool for | Fullprof Suite Winplotr |

(*Continued*)

**Table 17.11** (*Continued*).

| *Software* | *References* | *Within suites* |
|---|---|---|
| | powder diffraction pattern analysis, J. Rodriguez Carvajal and T. Roisnel, *EPDIC 7: European Powder Diffraction*, Pts 1 and 2 Materials Science Forum 378 3: 118 123, Part 1&2 2001 | |
| Taup/Powder | Enhancements in powder pattern indexing, D. Taupin, *J. Appl. Crystallogr.*, 1989, **22**, 455 459 and A powder diagram automatic indexing routine, D. Taupin, *J. Appl. Crystallogr.*, 1973, **6**, 380 385 | Crysfire |
| Topas/Iterative Least Squares SVD Indexing | Indexing of powder diffraction patterns by iterative use of singular value decomposition, A. A. Coelho, *J. Appl. Crystallogr.*, 2003, **36**, 86 95, TOPAS Academic by Alan Coelho, ISIS and TOPAS V3: General profile and structure analysis software for powder diffraction data. User's Manual, (2005) Bruker AXS, Karlsruhe, Germany | |
| Topas/Monte Carlo whole profile indexing | TOPAS Academic by Alan Coelho, ISIS and TOPAS V3: General profile and structure analysis software for powder diffraction data. User's Manual, (2005) Bruker AXS, Karlsruhe, Germany | |
| Treor90 | TREOR, a semi exhaustive trial and error powder indexing program for all symmetries, P. E. Werner, L. Eriksson and M. Westdahl, *J. Appl. Crystallogr.* 1985, **18**, 367 370 | CMPR, Crysfire, Fullprof Suite Winplotr, Powder v4, Powder X |
| Treor 2000 | New techniques for indexing: N TREOR in EXPO, A. Altomare, C. Giacovazzo, A. Guagliardi, A. G. G. Moliterni, R. Rizzi and P. E. Werner, *J. Appl. Crystallogr.*, 2000, **33**, 1180 1186 | EXPO2000 |
| VMRIA/ AUTOX | AUTOX A program for autoindexing reflections from multiphase polycrystals, V. B. Zlokazov, *Comput. Phys. Commun.*, 1995, **85**, 415 422 and Renewed interest in powder diffraction data indexing, J. Bergmann, A. Le Bail, R. Shirley and V. B. Zlokazov, *Z. Kristallogr.*, 2004, **219**, 783 790 | |
| X Cell | X Cell: a novel indexing algorithm for routine tasks and difficult cases, M. A. Neumann, *J. Appl. Crystallogr.*, 2003, **36**, 356 365 | |

within the Topas suite seem the best for difficult data. Topas also includes a whole profile Monte-Carlo indexing where there is no need for the user to select peaks. Failure to index by these various packages can be considered an incentive for the use of Transmission Electron Microscopy (TEM) for obtaining a cell, or putting more effort into the growing of single crystals.

*17.3.8.2 Powder Indexing Suites.* The Crysfire suite by Robin Shirley, linking to over eight different indexing programs, was the main recommended indexing suite. However, with the death of the author from Hepatitis A in March 2005, it is no longer under development. The WinPLOTR software, part of the Fullprof Suite, is a popular, effective and maintained, alternative (Table 17.12).

### 17.3.9 Space Group Assignment

Most indexing programs produce a cell, but not a recommended space group. There are two main methods of determining the space group from powder data, which are discussed below.

*17.3.9.1 Non-whole Profile Space Group Assignment.* Traditional space group assignment involves comparing the list of allowed HKLs to the observed peaks. What was previously a rather manual process has been automated to a large extent by modern software. The author's favorite is the Chekcell program by Jean Laugier and Bernard Bochu, which has a graphical interface for both manual and automatic space group assignment. Chekcell also allows the user to explore possible supercell and subcells, and links to the LEPAGE program of Ton Spek. The Topas indexing software will do this by suggesting a list of possible space groups as part of its solution list. An optimized space group assignment algorithm for powder diffraction exists inside the Extsym program, which uses the output from Pawley fitting to assign the most probable space group(s) (Table 17.13).

*17.3.9.2 Whole Profile Space Group Assignment.* In the case of significant peak overlap, Le Bail or Pawley fitting compatible Rietveld program can perform whole profile space group assignment by manually inputting all the possible space groups. A Le Bail or Pawley fit is performed, and tabulating the fit parameters and Rietveld plot *vs.* the space group. Some Rietveld programs, such as MAUD, will perform this procedure automatically.

### 17.3.10 Space Group Information Software and Databases

Various software exists that outputs information on space groups. It is best to use two or more of these programs in tandem to check for consistency of results (Table 17.14).

**Table 17.12** Available powder indexing suites.

| *Software* | *References* | *Within the suite/feature* |
|---|---|---|
| AXES | H. Mändar and T. Vajakas, AXES a software toolbox in powder diffraction, *Newsletter Int. Union Crystallogr., Commission Powder Diffr.* 1998, **20**, 31 32 and AXES1.9: new tools for estimation of crystallite size and shape by Williamson Hall analysis, H. Mändar, J. Felsche, V. Mikli and T. Vajakas, *J. Appl. Crystallogr.*, 1999, **32**, 345 350 | Dicvol, Ito, Treor |
| CMPR | CMPR, Brian Toby, NIST Center for Neutron Research, 100 Bureau Drive, Stop 8562, National Institute of Standards and Technology, Gaithersburg, MD, 20899 8562, USA | Dicvol, Ito, Treor |
| Crysfire | The Crysfire 2002 System for Automatic Powder Indexing: User's Manual, R. Shirley, (2002) The Lattice Press, 41 Guildford Park Avenue, Guildford, Surrey GU2 7NL, England | Dicvol91, FJZN, Ito12, Kohl/TMO, Lzon, Taup, Treor90 |
| Powder v4 | PowderV2: a suite of applications for powder X ray diffraction calculations, N. Dragoe, *J. Appl. Crystallogr.*, 2001, **34**, 535 | Dicvol, Ito, Treor |
| PowderX | PowderX: Windows 95 based program for powder X ray diffraction data processing, C. Dong, *J. Appl. Crystallogr.*, 1999, **32**, 838 | Treor |
| Fullprof Suite/ Winplotr | WinPLOTR: A Windows tool for powder diffraction pattern analysis, T. Roisnel and J. Rodriguez Carvajal, *EPDIC 7: European Powder Diffraction*, Pts 1 and 2 Materials Science Forum 378 3: 118 123, Part 1&2 2001 | Dicvol, Treor, Ito, Supercell |
| Chekcell | LMGP Suite Suite of Programs for the interpretation of X ray Experiments, by J. Laugier and B. Bochu, ENSP/ Laboratoire des Matériaux et du Génie Physique, BP 46. 38042 Saint Martin d′Hčres, France | Graphical evaluation and analysis of Crysfire and McMaille indexing results |

### 17.3.11 Unit Cell Refinement

Nearly all unit cell refinement programs assume that a list of peak positions will be provided in some form. A personal favorite for quick unit cell refinement is the graphical Celref for Windows software of Jean Laugier and Bernard Bochu. Celref also understands space groups and includes a facility to automatically match HKL positions to observed peaks. For use of internal standard, the XLAT software of Bernhard Rupp, despite its age, is very effective. However,

**Table 17.13** Available non-whole profile space group assignment software and resources.

| *Software* | *References* |
|---|---|
| Absen (within Ortex) | ABSEN a PC computer program for listing systematic absences and space group determination, P. McArdle, *J. Appl. Crystallogr.*, 1996, **29**, 306 |
| Chekcell | LMGP Suite Suite of Programs for the interpretation of X ray Experiments, by J. Laugier and B. Bochu, ENSP/ Laboratoire des Matériaux et du Génie Physique, BP 46. 38042 Saint Martin d′Hčres, France |
| Extsym | A probabilistic approach to space group determination from powder diffraction data, A. J. Markvardsen, W. I. F. David, J. Johnston and K. Shankland, *Acta Crystallogr., Sect. A*, 2001, **57**, 47 |
| International Tables vol A. | *International Tables for Crystallography Volume A: Space group symmetry*, ed. Theo Hahn, Published for the International Union of Crystallography by Springer. Fifth edition, April 2002, ISBN 0 7923 6590 9 |
| ISOTROPY | ISOTROPY, H. T. Stokes and D. M. Hatch, (2002), http://stokes.byu.edu/isotropy.html |
| MAUD | MAUD (Material Analysis Using Diffraction): a user friendly Java program for Rietveld Texture Analysis and more, L. Lutterotti, S. Matthies and H. R. Wenk, *Proceeding of the Twelfth International Conference on Textures of Materials (ICOTOM 12)*, 1999, Vol. 1, p. 1599 |
| Platon | Single crystal structure validation with the program PLATON, A. L. Spek, *J. Appl. Crystallogr.*, 2003, **36**, 7 13 |
| Topas | Indexing of powder diffraction patterns by iterative use of singular value decomposition, A. A. Coelho, *J. Appl. Crystallogr.*, 2003, **36**, 86 95, TOPAS Academic by Alan Coelho, ISIS and TOPAS V3: General profile and structure analysis software for powder diffraction data. User's Manual, (2005) Bruker AXS, Karlsruhe, Germany |
| WinGX | WinGX suite for small molecule single crystal crystallography, L. J. Farrugia, *J. Appl. Crystallogr.*, 1999, **32**, 837 838 |

where speed is an issue, or for unit cell refinement of large numbers of datasets, a whole profile fitting method (such as Le Bail fitting) should be considered (Table 17.15).

### 17.3.12 Full Profile Fitting (Pawley, Le Bail)

Full profile fitting can be useful for various tasks including unit cell refinement involving peak overlap, space group assignment, extracting intensities prior to structure solution, and pre-structure refinement fitting of the powder pattern. The two main methods are listed below.

*17.3.12.1 Le Bail Software*. A Rietveld program could be considered somewhat antiquated if it did not have some form of Le Bail fitting option

**Table 17.14** Available space group information software and databases.

| *Software* | *References* | *Interface* | *Input/caveates* |
|---|---|---|---|
| Bilbao Crystallographic Server | Bilbao Crystallographic Server, Euskal Herriko Unibertsitatea/ University of the Basque Country, 2005, http://www.cryst.ehu.es/ | Web interface | Variety of space group tools: including Space Groups Retrieval Tools, Wyckoff Positions of Space Groups, Group Subgroup Relations of Space Groups |
| cctbx sgtbx Explore symmetry | The Computational Crystallography Toolbox: crystallographic algorithms in a reusable software framework, R. W. Grosse Kunstleve, N. K. Sauter, N. W. Moriarty, P. D. Adams, *J. Appl. Crystallogr.*, 2002, **35**, 126 136 | Web interface. Source code available | Herman Mauguin (H M), Hall Symbol, Space Group number, Schönflies, symmetry operators |
| GETSPEC | A real space computer based symmetry algebra, U. D. Altermatt and I. D. Brown, *Acta Crystallogr., Sect. A*, 1987, **43**, 125 130 | Fortran source code. Standalone version available as LMGP suite Wgetspec | Large variety of different cell settings. Herman Mauguin (H M), Hall Symbol, Space Group number |
| Hypertext Book of Crystallographic Space Group Diagrams and Tables | J. K. Cockcroft, *A Hypertext Book of Crystallographic Space Group Diagrams and Tables*, Dept of Crystallography, Birkbeck College, London, UK, 1999 | On CD Rom and written in HTML: | Includes alternative axes and origins and spacegroup diagrams. Does not include list of general and special positions. |
| International Tables vol A. | *International Tables for Crystallography Volume A: Space group symmetry* ed. Theo Hahn, Published for the International Union of Crystallography by | Book form with spacegroup diagrams and online for IUCr Subscribers | Includes list of general and special positions |

| | | | |
|---|---|---|---|
| | Springer. Fifth edition April 2002, ISBN 0 7923 6590 9 | | |
| SGInfo | Algorithms for Deriving Crystallographic Space Group Information, R. W. Grosse Kunstleve, *Acta Crystallogr., Sect. A*, 1999, **55**, 383 395 | Web interface, standalone program and source code: superceded by cctbx sgtbx | Herman Mauguin (H M), Hall Symbol, Space Group number, Schönflies, symmetry operators |
| Space Group Explorer | Space Group Explorer, (2005), Calidris, http://www.calidris em.com/archive.htm | Standalone MS Windows program | Herman Mauguin (H M), Hall Symbol, Space Group number |
| Space Group Info | Crystallographic Fortran 90 Modules Library (CrysFML): a simple toolbox for crystallographic computing programs, J. Rodríguez Carvajal and J. González Platas, *IUCr Comput. Commission Newsletter*, 2003, **1**, 63 69, and WinPLOTR: A Windows tool for powder diffraction pattern analysis, T. Roisnel and J. Rodriguez Carvajal, *EPDIC 7: European Powder Diffraction*, Pts 1 and 2 Materials Science Forum 378 3: 118 123, Part 1&2 2001 | Standalone program | Herman Mauguin (H M), Hall Symbol, Space Group number |
| Superspace groups for 1D and 2D Modulated Structures | Crystallography of Quasiperiodic Structures, A. Yamamoto, *Acta* | HTML based text | All superspace groups for one dimensionally modulated structures (756 superspace |

(*Continued*)

**Table 17.14** (*Continued*).

| *Software* | *References* | *Interface* | *Input/caveates* |
|---|---|---|---|
| | *Crystallogr*., *Sect*. *A*, 1996, **52**, 509 560 | | groups, excluding enantiomorphic pairs), a provisional list of all (3355) superspace groups for two dimensionally modulated structures (superspace groups, excluding enantiomorphic pairs), a provisional list of all (11764) superspace groups for three dimensionally modulated structures (superspace groups, excluding enantiomorphic pairs) |
| Wgetspec | LMGP Suite Suite of Programs for the interpretation of X ray Experiments, by J. Laugier and B. Bochu, ENSP/Laboratoire des Matériaux et du Génie Physique, BP 46. 38042 Saint Martin d′Hčres, France and A real space computer based symmetry algebra, U. D. Altermatt and I. D. Brown, *Acta Crystallogr*., *Sect*. *A*, 1987, **43**, 125 130 | Standalone Windows binary. | Large variety of different cell settings. Point and click mouse selection of Herman Mauguin (H M), Hall Symbol, Space Group number |

**Table 17.15** Available unit cell refinement software.

| *Software* | *References* | *Can overlay raw diffraction data* | *Can use an internal standard* |
|---|---|---|---|
| Celref | LMGP Suite Suite of Programs for the interpretation of X ray Experiments, by J. Laugier and B. Bochu, ENSP/Laboratoire des Matériaux et du Génie Physique, BP 46. 38042 Saint Martin d′Hčres, France | Yes | |
| Eracel | CELREF unit cell refinement program written in FORTRAN for the IBM360, J. Laugier (1976), CELREF a Fortran program for unit cell refinement, J. Laugier and A. Filhol, 20/10/78 and ERACEL: a port of the CELREF unit cell refinement software, A. Le Bail, 1982 1983, Laboratoire des Oxydes et Fluorures, CNRS UMR 6010, Université du Maine, Faculté des Sciences, Avenue Olivier Messiaen, 72085 LE MANS Cedex 9, France | | |
| LAPOD | Powder pattern programs, J. I. Langford, *J. Appl. Crystallogr.*, 1971, **4**, 259 260 and The accuracy of cell dimensions determined by Cohen's method of least squares and the systematic indexing of powder data, J. I. Langford, *J. Appl. Crystallogr.*, 1973, **6**, 190 196 | | |
| LAPODS | LAPODS: a computer program for refinement of lattice parameters using optimal regression, C. Dong and J. I. Langford, *J. Appl. Crystallogr.*, 2000, **33**, 1177 1179 | | |
| Powder v4 | PowderV2: a suite of applications for powder X ray diffraction calculations, N. Dragoe, *J. Appl. Crystallogr.*, 2001, **34**, 535 | | Yes |
| Refcel | The PROFIL Suite of Programs by Jeremy Karl Cockcroft, Department of Crystallography, Birkbeck College, Malet Street, London WC1E 7HX, United Kingdom | | |
| UNITCELL | Unit cell refinement from powder diffraction data: the use of regression diagnostics, T. J. B. | | |

(*Continued*)

**Table 17.15** (*Continued*).

| *Software* | *References* | *Can overlay raw diffraction data* | *Can use an internal standard* |
|---|---|---|---|
| | Holland and S. A. T. Redfern, *Mineral. Mag.*, 1997, **61**, 65 77 | | |
| UNITCELL | The determination of unit cell parameters from Bragg reflection data using a standard reference material but without a calibration curve, H. Toraya, *J. Appl. Crystallogr.*, 1993, **26**, 583 590 | | |
| XLAT | XLAT Least Squares Refinement of Cell Constants, B. Rupp, *Scripta Metall.*, 1988, **22**, I | | Yes |

(Table 17.16). A feature that increases the stability and effectiveness of the Le Bail fitting process is the ability to recycle the intensities into the next round of fitting. GSAS and Fullprof are two common Rietveld programs with well-developed Le Bail fitting options. With GSAS, the user should be aware that running POWPREF resets the Le Bail intensities, whereas in Fullprof a special flag is used to reset or recycle the Le Bail intensities. Armel Le Bail's "Overlap" program is a small utility that can remove reflections that are excessively overlapped, sometimes aiding the structure solution when using a list of HKLs and intensities.

*17.3.12.2 Pawley Software.* Due to early limitations on computing powder, and relative difficulty of implementation in existing Rietveld software, a less common fitting option is that of Pawley fitting. Pawley fitting is now available in the GSAS Rietveld software (Table 17.17).

### 17.3.13 Texture Analysis Software

A list of traditional pole figure software *vs.* whole profile software analysis is listed in Table 17.18.

### 17.3.14 Size Strain Analysis

Most Rietveld software can perform size-strain analysis, even though this may require some manual calculations based on the software output. Some powder diffraction peak profiling programs also provide simple options for size-strain analysis. Table 17.19 gives a miscellaneous non-comprehensive list of programs.

**Table 17.16** Available software relevant for Le Bail fitting.

| *Software* | *References* |
|---|---|
| ARITVE | Modelling the Silica Glass Structure by the Rietveld Method. A. Le Bail, *J. Non Cryst. Solids*, 1995, **183**, 39 42, and Reverse Monte Carlo and Rietveld Modelling of the NaPbM2F9 (M = Fe, V) Fluoride Glass Structures, A. Le Bail, *J. Non Cryst. Solids*, 2000, **271**, 249 259 |
| BGMN | BGMN a new fundamental parameters based Rietveld program for laboratory X ray sources, its use in quantitative analysis and structure investigations, J. Bergmann, P. Friedel and R. Kleeberg, *Int. Union Crystallogr., Commission Powder Diffr. Newsletter* 1998, No. 20, pp. 5 8 |
| EXPO/EXPO2004 | EXPO: a program for full powder pattern decomposition and crystal structure solution, A. Altomare, M. C. Burla, M. Camalli, B. Carrozzini, G. L. Cascarano, C. Giacovazzo, A. Guagliardi, A. G. G. Moliterni, G. Polidori and R. Rizzi, *J. Appl. Crystallogr.*, 1999, **32**, 339 340 and Automatic structure determination from powder data with EXPO2004, A. Altomare, R. Caliandro, M. Camalli, C. Cuocci, C. Giacovazzo, A. G. G. Moliterni and R. Rizzi, *J. Appl. Crystallogr.*, 2004, **37**, 1025 1028 |
| EXTRACT | EXTRACT A Fortran Program for the Extraction of Integrated Intensities from a Powder Pattern, Ch. Baerlocher, (1990) Institut für Kristallographie, ETH, Zürich, Switzerland |
| Fullprof | FULLPROF. A Program for Rietveld Refinement and Pattern Matching Analysis, J. Rodriguez Carvajal, Abstracts of the Satellite Meeting on Powder Diffraction of the XV Congress of IUCr, (1990) Toulouse, France, p. 127 |
| GeneFP | GENEFP: a full profile fitting program for X ray powder patterns using the genetic algorithm, Z. J. Feng and C. Dong, *J. Appl. Crystallogr.*, 2006, **39**, 615 617 |
| GSAS | General Structure Analysis System (GSAS), A.C. Larson and R.B. Von Dreele, Los Alamos National Laboratory Report LAUR 86 748 (1994) |
| Jana | Jana2000. The crystallographic computing system. V. Petricek, M. Dusek, and L Palatinus, (2000) Institute of Physics, Praha, Czech Republic and Refinement of modulated structures against X ray powder diffraction data with JANA2000, M. Dusek, V. Petrícek, M. Wunschel, R. E. Dinnebier and S. van Smaalen, *J. Appl. Crystallogr.*, 2001, **34**, 398 404 |
| Overlap | Overlap, A. Le Bail, Laboratoire des Fluorures, Université du Maine, 72017 Le Mans Cedex, France 1987, Version D, July 1999 |
| Powder Cell | POWDER CELL a program for the representation and manipulation of crystal structures and calculation of the resulting X ray powder patterns, W. Kraus and G. Nolze, *J. Appl. Crystallogr.*, 1996, **29**, 301 303 |
| RIETAN (GPL'd) | A Rietveld analysis program RIETAN 98 and its applications to zeolites, F. Izumi and T. Ikeda, *Mater. Sci. Forum*, 2000, **321–324**, 198 203 and F. Izumi, "Development and Applications of the Pioneering Technology of Structure Refinement from Powder Diffraction Data," *J. Ceram. Soc. Jpn.*, 2003, **111**, 617 623 |

(*Continued*)

**Table 17.16** (*Continued*).

| *Software* | *References* |
|---|---|
| Rietica | LHPM: a Computer Program for Rietveld Analysis of X ray and Neutron Powder Diffraction Patterns, B. A. Hunter and C. J. Howard (February 2000), Lucas Heights Research Laboratories, Australian Nuclear Science and Technology Organisation and Rietica A visual Rietveld program, Brett Hunter, *Int. Union Crystallogr., Commission Powder Diffr. Newsletter*, 1998, No. 20, p. 21 |
| Topas | TOPAS Academic by Alan Coelho, ISIS and TOPAS V3: General profile and structure analysis software for powder diffraction data. User's Manual, (2005) Bruker AXS, Karlsruhe, Germany |
| WinMprof | WinMProf : a visual Rietveld software, A. Jouanneaux, *Int. Union Crystallogr., Commission Powder Diffr. Newsletter*, 1999, No. 21, p. 13 |
| XND | XND code: from X ray laboratory data to incommensurately modulated phases. Rietveld modelling of complex materials, J. F. Bérar and G. Baldinozzi, *Int. Union Crystallogr., Commission Powder Diffr. Newsletter*, 1998, No. 20, pp. 3 5 |

**Table 17.17** Available software that can perform Pawley fitting.

| *Software* | *References* |
|---|---|
| GSAS | General Structure Analysis System (GSAS), A. C. Larson and R. B. Von Dreele, Los Alamos National Laboratory Report LAUR 86 748 (1994) |
| PRODD | Extraction and use of correlated integrated intensities with powder diffraction data, J. P. Wright, *Z. Kristallogr.*, 2004, **219**(12), 791 802 |
| Simpro | Simultaneous structure refinement of neutron, synchrotron and X ray powder diffraction patterns, J. K. Maichle, J. Ihringer and W. Prandl, *J. Appl. Crystallogr.*, 1988, **21**, 22 27 and A quantitative measure for the goodness of fit in profile refinements with more than 20 degrees of freedom, J. Ihringer, *J. Appl. Crystallogr.*, 1995, **28**, 618 619 |
| Topas | TOPAS Academic by Alan Coelho, ISIS and TOPAS V3: General profile and structure analysis software for powder diffraction data. User's Manual, (2005) Bruker AXS, Karlsruhe, Germany |
| WPPF | Whole powder pattern fitting without reference to a structural model: Application to X ray powder diffractometer data, H. Toraya, *J. Appl. Crystallogr.*, 1986, **19**, 440 447 |

### 17.3.15 Single Crystal Suites useful to Powder Diffraction

Various single crystal suites have programs useful for structure analysis, including finding the reduced cell, checking if the structure has already been solved, structure visualization and structure validation. Most Rietveld

**Table 17.18** Available texture and pole figure analysis software.

| *Software* | *References* |
|---|---|
| BEARTEX | BEARTEX: a Windows based program system for quantitative texture analysis, H. R. Wenk, S. Matthies, J. Donovan and D. Chateigner, *J. Appl. Crystallogr.*, 1998, **31**, 262 269 |
| GSAS | General Structure Analysis System (GSAS), A. C. Larson and R. B. Von Dreele, Los Alamos National Laboratory Report LAUR 86 748 (1994) |
| LABOTEX | LaboTex: The Texture Analysis Software, K. Pawlik and P. Ozga, Göttinger Arbeiten zur Geologie und Paläontologie, SB4, 1999 |
| MAUD for Java (GPL'd) | MAUD (Material Analysis Using Diffraction): a user friendly {Java} program for {Rietveld} Texture Analysis and more, L. Lutterotti, S. Matthies and H. R. Wenk, *Proceeding of the Twelfth International Conference on Textures of Materials (ICOTOM 12)*, 1999, Vol. 1, p. 1599 |
| POFINT | POFINT: a MS DOS program tool for POle Figure INTerpretation and file transformations, D. Chateigner, 1994 2005, http://www.ecole.ensicaen.fr/~chateign/qta/pofint/ |
| PopLA | popLA, Preferred Orientation Package Los Alamos, U. F. Kocks, J. S. Kallend, H. R. Wenk, A. D. Rollett, and S. I. Wright, Los Alamos National Laboratory, Los Alamos, NM, 87545, USA, LA CC 89 18 (1998) |
| STEREOPOLE | STEREOPOLE: software for the analysis of X ray diffraction pole figures with IDL, I. Salzmann and R. Resel, *J. Appl. Crystallogr.*, 2004, **37**, 1029 1033 |
| TexTools | TexTools, Resmat Corporation, (2005) Suite 320, 3637 University Montreal, QC, Canada, H3A 2B3, http://www.resmat.com/ |
| TexturePlus | TexturePlus, M. D. Vaudin, Ceramics Division, National Institute of Standards and Technology, Gaithersburg, MD 20899 8522, USA. Program available on the Web: http://www.ceramics.nist.gov/staff/vaudin.htm. Also on written request: E mail: mark.vaudin@nist.gov; fax: (301) 775 5334 |

programs do not offer various structure validation procedures, and the use of single crystal suites such as WinGX for MS-Windows or Platon/System S for UNIX can be useful (Table 17.20).

### 17.3.16 Powder Diffraction Suites

Suites for powder diffraction that can span a moderately comprehensive range of powder diffraction analysis are relatively uncommon, but some do exist and are listed in Table 17.21.

### 17.3.17 Structure Solution Software Specifically for Powder Diffraction

Various programs exist, many of which focus on specific types of phases (organics, zeolites, *etc.*). When starting out with structure solution, the EXPO Direct Methods software can be the easiest and quickest to use. If direct

**Table 17.19** Available size-strain analysis software.

| *Software* | *References* |
|---|---|
| BGMN | BGMN a new fundamental parameters based Rietveld program for laboratory X ray sources, its use in quantitative analysis and structure investigations, J. Bergmann, P. Friedel and R. Kleeberg, *Int. Union Crystallogr., Commission Powder Diffr. Newsletter*, 1998, No. 20, pp. 5 8 |
| BREADTH | BREADTH a program for analyzing diffraction line broadening, D. Balzar, *J. Appl. Crystallogr.*, 1995, **28**, 244 245 |
| CMWP fit | MWP fit: a program for multiple whole profile fitting of diffraction peak profiles by *ab initio* theoretical functions, G. Ribárik, T. Ungár and J. Gubicza, *J. Appl. Crystallogr.*, 2001, **34**, 669 676 |
| Fullprof Suite | Line broadening analysis using FullProf: Determination of microstructural properties, J. Rodriguez Carvajal and T. Roisnel, *European Powder Diffraction EPDIC 8*, Materials Science Forum 443 4: 123 126, 2004 and WinPLOTR: A Windows tool for powder diffraction pattern analysis, T. Roisnel and J. Rodriguez Carvajal, *EPDIC 7: European Powder Diffraction*, Pts 1 and 2 Materials Science Forum 378 3: 118 123, Part 1&2 2001 |
| GENEFP | GENEFP: a full profile fitting program for X ray powder patterns using the genetic algorithm, Z. J. Feng and C. Dong, *J. Appl. Crystallogr.*, 2006, **39**, 615 617 |
| MAUD | MAUD (Material Analysis Using Diffraction): a user friendly {Java} program for {Rietveld} Texture Analysis and more, L. Lutterotti, S. Matthies and H. R. Wenk, *Proceeding of the Twelfth International Conference on Textures of Materials (ICOTOM 12)*, 1999, Vol. 1, p. 1599 |
| MudMaster | MudMaster: A program for calculating crystallite size distributions and strain from the shapes of X ray diffraction peaks. D. D. Eberl, V. Drits, J. Srodon, and R. Nüesch, U.S. Geological Survey Open File Report 96 171, (1996) 46 pp and XRD measurement of mean thickness, thickness distribution and strain for illite and illite/smectite crystallites by the Bertaut Warren Averbach technique. V. Drits, D. D. Eberl and J. Srodon, *Clays Clay Minerals*, 1998, **46**, 38 50 |
| Powder Cell | POWDER CELL a program for the representation and manipulation of crystal structures and calculation of the resulting X ray powder patterns, W. Kraus and G. Nolze, *J. Appl. Crystallogr.*, 1996, **29**, 301 303 |
| Topas | A fundamental parameters approach to X ray line profile fitting, R. W. Cheary and A. A. Coelho, *J. Appl. Crystallogr.*, 1992, **25**, 109 121, Fundamental Parameters Line Profile Fitting in Laboratory Diffractometers, R. W. Cheary, A. A. Coelho and J. P. Cline, *J. Res. Natl. Inst. Stand. Technol.*, 2004, **109**, 1 25 and Convolution based profile fitting, A. Kern, A. A. Coelho and R. W. Cheary, in *Diffraction Analysis of the Microstructure of Materials*, ed. E. J. Mittemeijer, and P. Scardi, Materials Science, Springer, 2004, ISBN 3 540 40510 4, 17 50 |
| WinFIT | WinFit 1.2.1, S. Krumm, (June 1997), Institut fur Geologie, Scholssgarten 5, 91054, Erlangen, Germany |

**Table 17.20** Available single crystal suites.

| *Software* | *References* | *Included or linked structure solution software* | *Included or linked refinement software* |
|---|---|---|---|
| Crystals | CRYSTALS version 12: software for guided crystal structure analysis, P. W. Betteridge, J. R. Carruthers, R. I. Cooper, K. Prout and D. J. Watkin, *J. Appl. Crystallogr.*, 2003, **36**, 1487 | Sir92, Sir97, Shelxs86, Shelxs97, Superflip | Crystals |
| DS*SYSTEM | DS5: direct searcher automatic system version 5 for small molecules running on Windows personal computers, K. Okada and P. Boochathum, *J. Appl. Crystallogr.*, 2005, **38**, 842 846 | ShakePSD, ShakePSDL, Multan | LSBF |
| LinGX (GPL'd) | LinGX: A free crystallographic GUI, Ralf Müller, (2005), http://www.xtal.rwth aachen.de/LinGX/ | Sir97, Sir2004, Shelxs97 | Shelxl97, Fullprof, Jana2000 |
| NRCVax | NRCVAX an interactive program system for structure analysis, E. J. Gabe, Y. Le Page, J. P. Charland, F. L. Lee and P. S. White, *J. Appl. Crystallogr.*, 1989, **22**, 384 387 | NRCVAX Solver (Multan like) | NRCVax |
| ORTEX | ORTEX2.1 a 1677 atom version of ORTEP with automatic cell outline and cell packing for use on a PC, P. McArdle, *J. Appl. Crystallogr.*, 1994, **27**, 438 439 | Shelxs86, Shelxs97 | Shelxl97 |
| Platon/System S | Single crystal structure validation with the program PLATON, A. L. Spek, *J. Appl. Crystallogr.*, 2003, **36**, 7 13 | Sir97, Sir2004, Shelxs86, Shelxs97, Dirdif, Flipper | Shelxl97 |
| Sir2004/CAOS | SIR2004: an improved tool for crystal structure determination and refinement, M. C. | Sir2004 | CAOS |

(*Continued*)

**Table 17.20** (*Continued*).

| *Software* | *References* | *Included or linked structure solution software* | *Included or linked refinement software* |
|---|---|---|---|
| | Burla, R. Caliandro, M. Camalli, B. Carrozzini, G. L. Cascarano, L. De Caro, C. Giacovazzo, G. Polidori and R. Spagna, *J. Appl. Crystallogr.*, 2005, **38**, 381 388 | | |
| WinGX | WinGX suite for small molecule single crystal crystallography, L. J. Farrugia, *J. Appl. Crystallogr.*, 1999, **32**, 837 838 | Dirdif, Shelxs86, Shelxs97, ShelxD, Patsee, Sir92, Sir97, Sir2004 | Shelxs97, Crystals, Jana2000, Xtal |
| Xtal (GPL'd) | Xtal3.7 System. S. R. Hall, D. J. du Boulay and R. Olthof Hazekamp, Eds., University of Western Australia. (2000) http://xtal.sourceforge.net/ | Crisp, Patsee, Shape | CRILSQ, CRYLSQ, LSLS |

methods fail, a more involved real space program may have to be applied. A real space program of preference for both inorganic and organic materials, is the open-source Fox software (Table 17.22).

### 17.3.18 Structure Solution Using Single Crystal Software

While overshadowed by dedicated powder diffraction based structure solution software, single crystal structure solution programs can still be used where a list of HKLs and intensities are available and can be usefully applied (Table 17.23). This allows not only the use of Direct Methods, but also Patterson and Patterson-based fragment searching. Armel Le Bail's "Overlap" program (listed in Table 17.16) can remove reflections that are excessively overlapped, sometimes aiding single crystal software based structure solution.

### 17.3.19 2D to 3D Molecular Model Generation

For solving organic, and perhaps organometallic, it can be time saving to convert a 2D model into a 3D model suitable for input in some of the available structure solution software (Table 17.24). It is possible that the conversion may get the confirmation of the more complex molecules incorrect. Thus the user must enable the required molecular flexibility within the structure solution software.

**Table 17.21** Available powder diffraction suites.

| *Software* | *References* | *Range of functionality* |
|---|---|---|
| AXES | H. Mändar and T. Vajakas, AXES a software toolbox in powder diffraction, *Newsletter Int. Union Crystallogr., Commission Powder Diffr.*, 1998, No. 20, 31 32 and AXES1.9: new tools for estimation of crystallite size and shape by Williamson Hall analysis, H. Mändar, J. Felsche, V. Mikli and T. Vajakas, *J. Appl. Crystallogr.*, 1999, **32**, 345 350 | Links to a wide range of programs and includes a range of data processing and display functions |
| CPMR/EXPGUI/ GSAS | CMPR and Portable Logic, Brian Toby, NIST Center for Neutron Research, 100 Bureau Drive, Stop 8562, National Institute of Standards and Technology, Gaithersburg, MD, 20899 8562, USA, EXPGUI, a graphical user interface for GSAS, B. H. Toby, *J. Appl. Crystallogr.*, 2001, **34**, 210 213 and General Structure Analysis System (GSAS), A. C. Larson and R. B. Von Dreele, Los Alamos National Laboratory Report LAUR 86 748 (1994) | Importing through to structure refinement, Fourier contour maps and visualization. Routine structure solution performed in other softare |
| DANSE (Distributed Data Analysis for Neutron Scattering Experiments) | A Virtual Test Facility for the Simulation of Dynamic Response in Materials, J. Cummings, M. Aivazis, R. Samtaney, R. Radovitzky, S. Mauch, D. Meiron, *J. Supercomputing*, August 2002, Volume 23, Issue 1 | Framework system for connecting programs for neutron scattering analysis |
| Topas | TOPAS Academic by Alan Coelho, ISIS and TOPAS V3: General profile and structure analysis software for powder diffraction data. User's Manual, (2005) Bruker AXS, Karlsruhe, Germany | Importing through to structure solution, structure refinement, and visualization. No Fourier contour map generation |
| WinPLOTR/ Fullprof | FULLPROF. A Program for Rietveld Refinement and Pattern Matching Analysis, J. Rodriguez Carvajal, Abstracts of the Satellite Meeting on Powder Diffraction of the XV Congress of IUCr, (1990) Toulouse, France, p. 127 and WinPLOTR: A Windows tool for powder diffraction pattern analysis, T. Roisnel and J. Rodriguez Carvajal, *EPDIC 7: European Powder Diffraction*, Pts 1 and 2 Materials Science Forum 378 3: 118 123, Part 1&2 2001 | Importing through to structure refinement, Fourier contour maps and visualization. Routine structure solution performed in other softare |

**Table 17.22** Available powder structure solution software.

| *Software* | *References* | *Methods and/or specialization* |
|---|---|---|
| BGMN | BGMN a new fundamental parameters based Rietveld program for laboratory X ray sources, its use in quantitative analysis and structure investigations, J. Bergmann, P. Friedel and R. Kleeberg, *Int. Union Crystallogr., Commission Powder Diffr. Newsletter*, 1998, No. 20, pp. 5 8 | Direct space and energy minimization |
| Dash | Routine determination of molecular crystal structures from powder diffraction data, W. I. F. David, K. Shankland, N. Shankland, *Chem. Commun.*, 1998, 931 932 | Organics and pharmaceuticals |
| Endeavour | Combined Method for "*Ab initio*" Structure Solution from Powder Diffraction Data, H. Putz, J. C. Schoen, M. Jansen, *J. Appl. Crystallogr.*, 1999, **32**, 864 870 | Direct space and energy minimization |
| EXPO/ EXPO2004 | EXPO: a program for full powder pattern decomposition and crystal structure solution, A. Altomare, M. C. Burla, M. Camalli, B. Carrozzini, G. L. Cascarano, C. Giacovazzo, A. Guagliardi, A. G. G. Moliterni, G. Polidori and R. Rizzi, *J. Appl. Crystallogr.*, 1999, **32**, 339 340 and Automatic structure determination from powder data with EXPO2004, A. Altomare, R. Caliandro, M. Camalli, C. Cuocci, C. Giacovazzo, A. G. G. Moliterni and R. Rizzi, *J. Appl. Crystallogr.*, 2004, **37**, 1025 1028 | Direct methods and real space |
| ESPOIR (GPL'd) | ESPOIR: A program for solving structures by monte Carlo analysis of powder diffraction data, A. Le Bail, *Mater. Sci. Forum*, 2001, **378–381**, 65 70 | Real space |
| Focus | Zeolite structure determination from powder diffraction data: Applications of the FOCUS method, R.W. Grosse Kunstleve, L.B. McCusker, Ch. Baerlocher, *J. Appl. Crystallogr.* 1999, **32**, 536 542 | Chemical Information, Zeolites |
| Fox (GPL'd) | FOX, 'free objects for crystallography': a modular | Real space, dynamic occupancy |

(*Continued*)

**Table 17.22** (*Continued*).

| *Software* | *References* | *Methods and/or specialization* |
|---|---|---|
| | approach to *ab initio* structure determination from powder diffraction, V. Favre Nicolin and R. Cerný, *J. Appl. Crystallogr.*, 2002, **35**, 734 743 | correction and atom merging |
| Fullprof Suite | FULLPROF. A Program for Rietveld Refinement and Pattern Matching Analysis, J. Rodriguez Carvajal, Abstracts of the Satellite Meeting on Powder Diffraction of the XV Congress of IUCr, (1990) Toulouse, France, p. 127 | Direct space for magnetic structures |
| Gest | GEST: a program for structure determination from powder diffraction data using genetic algorithm, Z. J. Feng and C. Dong, *J. Appl. Crystallogr.*, 2007, **40**, 583 588 | Real space, primarily for solving organic structures using a genetic algorithm |
| GRINSP | Inorganic structure prediction with GRINSP, A. Le Bail, *J. Appl. Crystallogr.*, 2005, **38**, 389 395 | Structure prediction of inorganics suitable for "search match" structure solution |
| Organa | Organa a program package for structure determination from powder diffraction data by direct space methods, V. Brodski, R. Peschar and H. Schenk, *J. Appl. Crystallogr.*, 2005, **38**, 688 693 | Direct space |
| Powder Solve | PowderSolve a complete package for crystal structure solution from powder diffraction patterns, G. E. Engel, S. Wilke, O. König, K. D. M. Harris and F. J. J. Leusen, *J. Appl. Crystallogr.*, 1999, **32**, 1169 1179 | Direct space |
| RMCPOW | RMCA Version 3, R. L. McGreevy, M. A. Howe and J. D.Wicks, (1993), available at http:// www.studsvik.uu.se/ and Reverse Monte Carlo modelling of neutron powder diffraction data, A. Mellergård and R. L. McGreevy, *Acta Crystallogr., Sect. A*, 1999, **55**, 783 | Direct Space for magnetic structures |
| Ruby | Ruby, Materials Data, Inc., 1224 Concannon Blvd., Livermore, CA 94550 | Direct Methods and Direct Space |
| SARAh | A new protocol for the determination of magnetic structures using Simulated Annealing and | Direct Space |

(*Continued*)

**Table 17.22** (*Continued*).

| *Software* | *References* | *Methods and/or specialization* |
|---|---|---|
| | Representational Analysis SARAh, A. S. Wills, *Physica B*, 2000, **276**, 680 | |
| Superflip | Superflip computer program for solution of crystal structures by charge flipping in arbitrary dimensions, L. Palatinus and G. Chapuis (2006), http:/ superspace.epfl.ch/superflip and Charge flipping combined with histogram matching to solve complex crystal structures from powder diffraction data, Ch. Baerlocher, L. B. McCusker, L. Palatinus, *Z. Kristallogr.*, 2007, **222**(2), 47 53 | Uses the charge flipping algorithm on extracted intensities to solve in the P1 spacegroup. The algorithm is also use to solve incommensurate and quasicrystal structures |
| TOPAS | Whole profile structure solution from powder diffraction data using simulated annealing, A. A. Coelho, *J. Appl. Crystallogr.*, 2000, **33**, 899 908, TOPAS Academic by Alan Coelho, ISIS and TOPAS V3: General profile and structure analysis software for powder diffraction data. User's Manual, (2005) Bruker AXS, Karlsruhe, Germany | Direct space, energy minimization and charge flipping |
| WinCSD/ CSD | Use of the CSD program package for structure determination from powder data. L. G. Akselrud, P. Zavalii, Yu. N.Grin, V. K. Pecharsky, B. Baumgartner, E. Wolfel, 2nd European Powder Diffraction Conference: Abstract of papers, Enschede, The Netherlands, 41, (1992); *Mater. Sci. Forum*, 1993, **133–136**, 335 340 | Direct methods and Patterson methods |
| ZEFSA II | A biased Monte Carlo scheme for zeolite structure solution, M. Falcioni and M. W. Deem, *J. Chem. Phys.*, 1999, **110**(3), 15 | Real Space, Zeolites |

### 17.3.20 Single Crystal Refinement Programs and Helper Programs to Assist in Building up the Structure

Compared to powder diffraction software, single crystal refinement programs are currently more advanced for routine structure refinement (Table 17.25). Compared to existing Rietveld software, it can be less time consuming to use a

**Table 17.23** Available single crystal structure solution software.

| *Software* | *References* | *Methods and/or specialization* |
|---|---|---|
| Crisp (GPL'd) | CRISP: Crystal Iterative Solution Program, Doug du Boulay & Syd Hall, Xtal3.7 System. Eds. S.R. Hall, D.J. du Boulay & R. Olthof Hazekamp. University of Western Australia | Direct Methods |
| Crunch | CRUNCH: solving structures using Karle Hauptman matrices, R.A.G. de Graaff and R. de Gelder, *Acta Crystallogr. Sect. A*, 1996, **46**(Suppl.), C 53 | Direct Methods |
| Dirdif | The DIRDIF 99 program system, P. T. Beurskens, G. Beurskens, R. de Gelder, S. Garcia Granda, R. O. Gould, R. Israel and J. M. M. Smits (1999), Crystallography Laboratory, University of Nijmegen, The Netherlands | Patterson, Fragment searching |
| Patsee | Structure solution with PATSEE, E. Egert, K. Wagner and J. Hirschler, *Z. Kristallogr.*, 2001, **216**(11), 565 572 | Fragment searching |
| Shake'n'Bake (SnB) | The design and implementation of SnB v2.0, C. M. Weeks and R. Miller, *J. Appl. Crystallogr.*, 1999, **32**, 120 124 | Direct Methods Shake'n'Bake |
| ShakePSD | DS5: direct searcher automatic system version 5 for small molecules running on Windows personal computers, K. Okada and P. Boochathum, *J. Appl. Crystallogr.*, 2005, **38**, 842 846 | Direct Methods Shake'n'Bake |
| Shelxs86/ Shelxs97/ ShelxD | SHELX97 Programs for Crystal Structure Analysis (Release 97 2). G. M. Sheldrick, Institüt für Anorganische Chemie der Universität, Tammanstrasse 4, D 3400 Göttingen, Germany, 1998; SHELXS86. Program for the solution of crystal structures. G. M. Sheldrick, (1986), Univ. of Gottingen, Federal Republic of Germany and Substructure solution with SHELXD, T. R. Schneider and G. M. Sheldrick, *Acta Crystallogr., Sect. D*, 2002, **58**, 1772 1779 | Direct Methods, Patterson, SnB (Shake'n'Bake) |
| Sir92/Sir97/ Sir2004 | SIR92 a program for automatic solution of crystal structures by direct methods, A. Altomare, G. Cascarano, C. Giacovazzo, A. Guagliardi, M. C. Burla, G. Polidori and M. Camalli, *J. Appl. Crystallogr.*, 1994, **27**, 435, SIR97: a new tool for crystal structure determination and refinement, A. Altomare, M. C. Burla, M. Camalli, G. L. Cascarano, C. Giacovazzo, A. Guagliardi, A. G. G. Moliterni, G. Polidori and R. Spagna, *J. Appl. Crystallogr.*, 1999, **32**, 115 119 and SIR2004: an improved tool for crystal structure determination and refinement, M. C. Burla, R. Caliandro, M. Camalli, B. Carrozzini, G. L. Cascarano, L. De Caro, C. Giacovazzo, G. Polidori and R. Spagna, *J. Appl. Crystallogr.*, 2005, **38**, 381 388 | Direct Methods, SnB (Shake'n'Bake) style |

**Table 17.24** Available 2D to 3D molecular model generators.

| *Software* | *References* | *Notes* |
|---|---|---|
| Dirdif | The DIRDIF 99 program system, P. T. Beurskens, G. Beurskens, R. de Gelder, S. Garcia Granda, R. O. Gould, R. Israel and J. M. M. Smits (1999), Crystallography Laboratory, University of Nijmegen, The Netherlands | In built database, and DOS command line style interface |
| Momo | MOMO Molecular Modelling Program, Version 2.00, E. Gemmel, H. Beck, M. Bolte and E. Egert, Universität Frankfurt (1999) | From the makers of Patsee |
| Xdrawchem/ WinDrawChem and Build3D | XDrawChem (software), Bryan Herger, (2002) http://xdrawchem.sourceforge.net/ | Open source with 3D builder option |

**Table 17.25** Available single crystal refinement and structure building software.

| *Software* | *References* |
|---|---|
| Crystals | CRYSTALS version 12: software for guided crystal structure analysis, P. W. Betteridge, J. R. Carruthers, R. I. Cooper, K. Prout and D. J. Watkin, *J. Appl. Crystallogr.*, 2003, **36**, 1487 |
| Platon/System S | Single crystal structure validation with the program PLATON, A. L. Spek, *J. Appl. Crystallogr.*, 2003, **36**, 7 13 |
| Shelxl97 | SHELX97 Programs for Crystal Structure Analysis (Release 97 2). G. M. Sheldrick, Institüt für Anorganische Chemie der Universität, Tammanstrasse 4, D 3400 Göttingen, Germany, 1998 |
| Sir2004/CAOS | SIR2004: an improved tool for crystal structure determination and refinement, M. C. Burla, R. Caliandro, M. Camalli, B. Carrozzini, G. L. Cascarano, L. De Caro, C. Giacovazzo, G. Polidori and R. Spagna, *J. Appl. Crystallogr.*, 2005, **38**, 381 388 and Crystallographic software for a mincomputer, S. Cerrini and R. Spagna (1977), IV Eur. Crystallgr. Meet., Oxford, UK, Abstract A 212 |
| Xtal (GPL'd) | Xtal3.7 System. S. R. Hall, D. J. du Boulay and R. Olthof Hazekamp, Eds., University of Western Australia. (2000) http://xtal.sourceforge.net/ |
| WinGX | WinGX suite for small molecule single crystal crystallography, L. J. Farrugia, *J. Appl. Crystallogr.*, 1999, **32**, 837 838 |

Le Bail or Pawley extracted list of intensities with single crystal software such as Shelxl or Crystals to perform early cycles of refinement to find missing atoms, and graphically examine the structure. This is also an area where it might be helpful to Armel Le Bail's "Overlap" program (listed in Table 17.16) to remove reflections that are excessively overlapped.

### 17.3.21 Rietveld Structure Refinement

While GSAS (using Brian Toby's EXPGUI Graphical User Interface), Fullprof and Topas are generally the most popular "general" Rietveld programs in current use, many Rietveld programs have regionalized followings (*e.g.*, Rietica/LHPM in Australasia; RIETAN in Japan) (Table 17.26). Other Rietveld programs are optimized for certain classes of structures (*e.g.*, Jana and XND for incommensurates, DEBVIN for polymers, XRS-82 for zeolites). As first time use of Rietveld refinement can be quite challenging and intimidating, it can be useful to determine which programs are being used locally and make first use of these. This allows a chance of obtaining tutorial assistance from a local source. An alternative source of tuition is to search for workshops emphasizing computer based hands-on Rietveld tutorials. Participants should not expect too much from "hands-on" Rietveld workshops organized in conjunction with conferences, as often both workshop organizers and attendees find out on the day that access to computers were not arranged.

### 17.3.22 Pair Distribution Function Software

This is an area of powder diffraction that has suffered from a lack of available, user-friendly software for data processing and data analysis. While this is slowly changing, it has mostly been due to the software development efforts of teams led by or involving Robert McGreevy, Simon Billinge, Thomas Proffen, and Reinhard Neder (Table 17.27).

### 17.3.23 Hydrogen Placement Using Single Crystal and Ancillary Software

Automatic and manual hydrogen placement can be tedious when performed within most Rietveld programs. Software made for single crystal applications can be more user-friendly and time-effective. This not only includes the placement of hydrogens off carbons, but that of hydrides. In modern single crystal methods it is generally expected that all hydrogens will be visible in the Fourier map, allowing the validation of calculated hydrogens. This is not the case in powder diffraction and the user should be more cautious in the calculated placement of hydrogens (Table 17.28).

### 17.3.24 Free Standing Powder and Single Crystal Fourier Map Generation and Display Software

While more noisy than single crystal generated Fourier maps, powder diffraction generated Fourier maps are still useful for locating missing atoms. While programs such as Fullprof, BRASS, GSAS and Jana have integrated Fourier Map generation and viewing, there are free standing programs available for the generation of Fourier maps. Free-standing Fourier map viewers are also available, of which DRAWxtl and Marching Cubes are worth a first evaluation. An article by Fujio Izumi was published in the November 2005 issue of the

**Table 17.26** Available Rietveld structure refinement software.

| *Software* | *References* | *Methods and/or specialization* | *Fourier map capability* |
|---|---|---|---|
| ARITVE | ARITVE User Guide, A. Le Bail, Universite du Maine, France (2000) | Modeling glass structures | |
| BGMN | BGMN a new fundamental parameters based Rietveld program for laboratory X ray sources, its use in quantitative analysis and structure investigations, J. Bergmann, P. Friedel and R. Kleeberg, *Int. Union Crystallogr., Commission Powder Diffr. Newsletter* 1998, No. 20, pp. 5 8 | Fundamental parameters Rietveld with macro language | Yes |
| BRASS | BRASS 2003: The Bremen Rietveld Analysis and Structure Suite, J. Birkenstock, R. X. Fischer and T. Messner, *Ber. DMG, Beih. z. Eur. J. Mineral.*, 2003, **15**(1), 21 | Inorganic materials | Yes |
| DBWS | DBWS 9411, an Upgrade of the DBWS, R. A. Young, A. Sakthivel, T. S. Moss and C. O. Paiva Santos (1995) | General refinement | |
| DDM | Full profile refinement by derivative difference minimization, L. A. Solovyov, *J. Appl. Crystallogr.*, 2004, **37**, 743 749 | Derivative Difference Minimization | |
| DEBVIN | DEBVIN a program for Rietveld refinement with generalized coordinates subjected to geometrical restraints, S. Brückner and A. Immirzi, *J. Appl. Crystallogr.*, 1997, **30**, 207 208 | Polymers | |
| DIFFaX+ | Simultaneous refinement of structure and microstructure of layered materials, M. Leoni, A. F. Gualtieri and N. Roveri, *J. Appl. Crystallogr.*, 2004, **37**, 166 173 | Disordered layered materials | |
| EXPGUI | EXPGUI, a graphical user interface for GSAS, B. H. Toby, *J. Appl. Crystallogr.*, 2001, **34**, 210 213 | Windows, Linux and Mac Graphical User Interface for GSAS | |
| EXPO/EXPO2004 | EXPO: a program for full powder pattern decomposition and crystal structure solution, A. Altomare, M. C. Burla, M. Camalli, B. Carrozzini, G. L. Cascarano, C. Giacovazzo, A. Guagliardi, A. G. G. Moliterni, G. Polidori and R. Rizzi, | Refinement of EXPO solved structures | Yes |

| | | | |
|---|---|---|---|
| | *J. Appl. Crystallogr.*, 1999, **32**, 339 340 and Automatic structure determination from powder data with EXPO2004, A. Altomare, R. Caliandro, M. Camalli, C. Cuocci, C. Giacovazzo, A. G. G. Moliterni and R. Rizzi, *J. Appl. Crystallogr.*, 2004, **37**, 1025 1028 | | |
| Fullprof | FULLPROF. A Program for Rietveld Refinement and Pattern Matching Analysis, J. Rodriguez Carvajal, Abstracts of the Satellite Meeting on Powder Diffraction of the XV Congress of IUCr, (1990) Toulouse, France, p. 127 and WinPLOTR: A Windows tool for powder diffraction pattern analysis, T. Roisnel and J. Rodriguez Carvajal, *EPDIC 7: European Powder Diffraction*, Pts 1 and 2 Materials Science Forum 378 3: 118 123, Part 1&2 2001 | Normal, microstructure, magnetic and incommensurates. GUI interface based around the WinPLOTR software | Yes |
| GSAS | General Structure Analysis System (GSAS), A. C. Larson and R. B. Von Dreele, Los Alamos National Laboratory Report LAUR 86 748 (1994) | Combined refinement, proteins, large numbers of restraints. EXPGUI GUI interface by Brian Toby | Yes |
| IC POWLS | IC POWLS: A program for calculation and refinement of commensurate and incommensurate structures using powder diffraction data, W. Kockelmann, E. Jansen, W. Schäfer and G. Will, Berichte des Forschungszentrums Jülich, Report Jül 3024 (1995) | Incommensurate and magnetic structures | Yes |
| Jana | Jana2000. The crystallographic computing system. V. Petricek, M. Dusek, and L Palatinus, (2000) Institute of Physics, Praha, Czech Republic and Refinement of modulated structures against X ray powder diffraction data with JANA2000, M. Dusek, V. Petrícek, M. Wunschel, R. E. Dinnebier and S. van Smaalen, *J. Appl. Crystallogr.*, 2001, **34**, 398 404 | Incommensurate and composite structures | Yes |

(*Continued*)

**Table 17.26** (*Continued*).

| *Software* | *References* | *Methods and/or specialization* | *Fourier map capability* |
|---|---|---|---|
| Koalariet | A fundamental parameters approach to X ray line profile fitting, R. W. Cheary and A. A. Coelho, *J. Appl. Crystallogr.*, 1992, **25**, 109 121 | Fundamental parameters Rietveld. No longer developed. | |
| MAUD for Java (GPL'd) | MAUD (Material Analysis Using Diffraction): a user friendly {Java} program for {Rietveld} Texture Analysis and more, L. Lutterotti, S. Matthies and H. R. Wenk, *Proceeding of the Twelfth International Conference on Textures of Materials (ICOTOM 12)*, 1999, Vol. 1, p. 1599 | GUI Interface and microstructural modeling | |
| MXD (MiXeD crystallographic executive for diffraction) | MXD: a general least squares program for non standard crystallographic refinements, P. Wolfers, *J. Appl. Crystallogr.*, 1990, **23**, 554 557 | Magnetic and incommensurate; single crystal and powder diffraction | |
| PFLS | Application of total pattern fitting to X ray powder diffraction data, H. Toraya and F. Marumo, *Rep. Res. Lab. Engin. Mat., Tokyo Inst. Tech.*, 1980, **5**, 55 64 and Crystal structure refinement of alpha $Si_3N_4$ using synchrotron radiation powder diffraction data: unbiased refinement strategy, H. Toraya, *J. Appl. Crystallogr.*, 2000, **33**, 95 102 | General Rietveld refinement | |
| Powder Cell | POWDER CELL a program for the representation and manipulation of crystal structures and calculation of the resulting X ray powder patterns., W. Kraus and G. Nolze, *J. Appl. Crystallogr.*, 1996, **29**, 301 303 | General Rietveld refinement | |
| PREMOS | Rietveld analysis of the modulated structure in the superconducting oxide $Bi_2(Sr,Ca)_3Cu_2O_{8+x}$, A. Yamamoto, M. Onoda, E. Takayama Muromachi, F. Izumi, T. Ishigaki and H. Asano, *Phys. Rev. B*, 1990, **42**, 4228 4239 | Incommensurately modulated structures | |
| PRODD | PRODD Profile Refinement of Diffraction Data using the Cambridge Crystallographic Subroutine Library (CCSL), J. P. Wright and J. B. Forsyth, Rutherford Appleton Laboratory Report RAL TR 2000 012, Version 1.0, May 2000 | Concepts and algorithms development | |

| | | | |
|---|---|---|---|
| Profil | The PROFIL Suite of Programs by Jeremy Karl Cockcroft, Department of Crystallography, Birkbeck College, Malet Street, London WC1E 7HX, United Kingdom | Organics and organometallics requiring restrained refinement | |
| Riet7/SR5/LHPM | LHPM: a Computer Program for Rietveld Analysis of X ray and Neutron Powder Diffraction Patterns, R. J. Hill, and C. J. Howard (1986) AAEC Report No. M112 and QPDA A User Friendly, Interactive Program for Quantitative Phase and Crystal Size/Strain Analysis of Powder Diffraction Data, I. C. Madsen and R. J. Hill, *Powder Diffr*., 1990, **5**, 195 199 | General refinement | |
| RIETAN (GPL'd) | A Rietveld analysis program RIETAN 98 and its applications to zeolites, F. Izumi and T. Ikeda, *Mater. Sci. Forum*, 2000, **321–324**, 198 203 and F. Izumi, "Development and Applications of the Pioneering Technology of Structure Refinement from Powder Diffraction Data," *J. Ceram. Soc. Jpn*., 2003, **111**, 617 623 | Whole pattern fitting based on the maximum entropy method (MEM). Using PRIMA for MEM analysis and VENUS for structure and map visualization | Yes |
| Rietica/LHPM | LHPM: a Computer Program for Rietveld Analysis of X ray and Neutron Powder Diffraction Patterns, B. A. Hunter and C. J. Howard (February 2000), Lucas Heights Research Laboratories, Australian Nuclear Science and Technology Organisation and Rietica A visual Rietveld program, Brett Hunter, *Int. Union Crystallogr*., *Commission Powder Diffr. Newsletter*, 1998, No. 20, p. 21 | GUI Interface | Yes |
| Simref | Simultaneous structure refinement of neutron, synchrotron and X ray powder diffraction patterns, J. K. Maichle, J. Ihringer and W. Prandl, *J. Appl. Crystallogr*., 1988, **21**, 22 27 and A quantitative measure for the goodness of fit in profile refinements with more than 20 degrees of freedom, J. Ihringer, *J. Appl. Crystallogr*. 1995, **28**, 618 619 | Incommensurate and composite structures, refinement of multiple powder data sets | |

(*Continued*)

**Table 17.26** (*Continued*).

| *Software* | *References* | *Methods and/or specialization* | *Fourier map capability* |
|---|---|---|---|
| Topas | A fundamental parameters approach to X ray line profile fitting, R. W. Cheary and A. A. Coelho, *J. Appl. Crystallogr.*, 1992, **25**, 109 121, Fundamental Parameters Line Profile Fitting in Laboratory Diffractometers, R. W. Cheary, A. A. Coelho and J. P. Cline, *J. Res. Natl. Inst. Stand. Technol.*, 2004, **109**, 1 25, TOPAS Academic by Alan Coelho, ISIS and TOPAS V3: General profile and structure analysis software for powder diffraction data. User's Manual, (2005) Bruker AXS, Karlsruhe, Germany | Fundamental parameters Rietveld with macro language | |
| VMRIA | VMRIA a program for a full profile analysis of powder multiphase, neutron diffraction time of flight (direct and Fourier) spectra, V. B. Zlokazov, V. V. Chernyshev, *J. Appl. Crystallogr.*, 1992, **25**, 447 451 and DELPHI based visual object oriented programming for the analysis of experimental data in low energy physics, V. B. Zlokazov, *Nucl. Instrum. Methods Phys. Res. A*, 2003, **502**(2 3), 723 724 | Rietveld refinement of TOF data | |
| WinMprof | WinMProf : a visual Rietveld software, A. Jouanneaux, *Int. Union Crystallogr.*, *Commission Powder Diffr. Newsletter*, 1999, No. 21, 13 | Organics and organometallics requiring restrained refinement | Yes |
| XND | XND code: from X ray laboratory data to incommensurately modulated phases. Rietveld modelling of complex materials, J. F. Bérar and G. Baldinozzi, *Int. Union Crystallogr.*, *Commission Powder Diffr. Newsletter*, 1998, No. 20, 3 5 | Incommensurate and composite structures, refinement of multiple powder data sets | |
| XRS 82/DLS 76 | The X ray Rietveld System XRS82, Ch. Baerlocher, (1982) Institut für Kristallographie und Petrographie, ETH Zentrum, Zürich and DLS76. A Fortran Program for the Simulation of Crystal Structures by Geometric Refinement. Ch. Baerlocher, A. Hepp and W. M. Meier, (1977) Institut für Knstallographie, ETH, Zürich, Switzerland | Zeolites | |

**Table 17.27** Available pair distribution function software.

| *Software* | *References* |
|---|---|
| DERB and DERFFT | Powerful new software for the simulation of WAXS and SAXS diagrams, D. Espinat, F. Thevenot, J. Grimoud and K. El Malki, *J. Appl. Crystallogr.* 1993, **26**, 368 383 |
| DISCUS | DISCUS, a program for diffuse scattering and defect structure simulations Update, Th. Proffen and R. B. Neder, *J. Appl. Crystallogr.*, 1999, **32**, 838 and DISCUS, a program for diffuse scattering and defect structure simulations, Th. Proffen and R. B. Neder, *J. Appl. Crystallogr.* 1997, **30**, 171 |
| MCGRtof | MCGRtof: Monte Carlo G(r) with resolution corrections for time of flight neutron diffractometers, M. G. Tucker, M. T. Dove and D. A. Keen, *J. Appl. Crystallogr.*, 2001, **34**, 780 782 |
| PDFFIT/ PDFgui | PDFFIT a program for full profile structural refinement of the atomic pair distribution function, Th. Proffen and S. J. L. Billinge, *J. Appl. Crystallogr.* 1999, **32**, 572. PDFgui and PDFfit2 replace PDFFIT: C. L. Farrow, P. Juhas, J. W. Liu, D. Bryndin, E. S. Božin, J. Bloch, Th. Proffen and S. J. L. Billinge, *J. Phys: Condens. Matter*, 2007, **19**, 335219 |
| PDFgetN | PDFgetN: A user friendly program to extract the total scattering structure function and the pair distribution function from neutron powder diffraction data, P. F. Peterson, M. Gutmann, Th. Proffen and S. J. L. Billinge, *J. Appl. Crystallogr.*, 2000, **33**, 1192 |
| PDFgetX2 | PDFgetX2: a GUI driven program to obtain the pair distribution function from X ray powder diffraction data, X. Qiu, J. W. Thompson and S. J. L. Billinge, *J. Appl. Crystallogr.*, 2004, **37**, 678 |
| RAD | RAD, a program for analysis of X ray diffraction data from amorphous materials for personal computers, V. Petkov, *J. Appl. Crystallogr.*, 1989, **22**, 387 |
| RMC | Reverse Monte Carlo modelling of neutron powder diffraction data, A. Mellergård and R. L. McGreevy, *Acta Crystallogr., Sect. A*, 1999, **55**, 783 789 |
| RMC++ | G. Evrard, L. Pusztai, Reverse Monte Carlo Modelling of the structure of disordered materials with RMC++: a new implementation of the algorithm in C++, *J. Phys.: Condens. Matter*, 2005, **17**(5), S1 S13 |
| RMCprofile | Reverse Monte Carlo modelling of crystalline disorder, D. A. Keen, M. G. Tucker and M. T. Dove, *J. Phys. Condens. Matter*, 2005, **17**(5), S15 S22 |
| RMCAW95 | Reverse Monte Carlo modelling of neutron powder diffraction data, A. Mellergård and R. L. McGreevy, *Acta Crystallogr., Sect. A*, 1999, **55**, 783 789 |

*IUCr Commission on Powder Diffraction Newsletter* elaborated on the availability of Fourier Map software based around MPF Maximum-entropy-method Profile Fitting, which also offers an alternative to conventional Rietveld refinement for the solution and refinement of difficult crystal structures from powder diffraction data (Table 17.29).

**Table 17.28** Available hydrogen placement software.

| *Software* | *References* |
|---|---|
| Crystals | CRYSTALS version 12: software for guided crystal structure analysis, P. W. Betteridge, J. R. Carruthers, R. I. Cooper, K. Prout and D. J. Watkin, *J. Appl. Crystallogr.*, 2003, **36**, 1487 |
| Hydrogen/CalcOH | Modeling hydroxyl and water H atoms, M. Nardelli, *J. Appl. Crystallogr.*, 1999, **32**, 563 571 |
| Platon/System S | Single crystal structure validation with the program PLATON, A. L. Spek, *J. Appl. Crystallogr.*, 2003, **36**, 7 13 |
| Shelxl97 | SHELX97 Programs for Crystal Structure Analysis (Release 97 2). G. M. Sheldrick, Institüt für Anorganische Chemie der Universität, Tammanstrasse 4, D 3400 Göttingen, Germany, 1998 |
| Sir2002/CAOS | SIR2004: an improved tool for crystal structure determination and refinement, M. C. Burla, R. Caliandro, M. Camalli, B. Carrozzini, G. L. Cascarano, L. De Caro, C. Giacovazzo, G. Polidori and R. Spagna, *J. Appl. Crystallogr.*, 2005, **38**, 381 388 |
| Xhydex | Indirect Location of Hydride Ligands in Metal Cluster Complexes, A. G. Orpen, *J. Chem. Soc., Dalton Trans.*, 1980, 2509 2516 |
| Xtal (GPL'd) | Xtal3.7 System. S. R. Hall, D. J. du Boulay and R. Olthof Hazekamp, Eds., University of Western Australia. (2000) http://xtal.sourceforge.net/ |
| WinGX: GUI Hydrogen/ CalcOH; GUI Xhydex | WinGX suite for small molecule single crystal crystallography, L. J. Farrugia, *J. Appl. Crystallogr.* 1999, **32**, 837 838 |

### 17.3.25 Quantitative Phase Analysis

Nearly every Rietveld program in existence will also perform quantitative phase analysis, though some manual calculations may be required for some programs. Thus Table 17.30 mainly concentrates on programs that are more focused on quantitative phase analysis, both Rietveld and non-Rietveld based.

### 17.3.26 Powder Pattern Calculation

While most Rietveld programs can calculate powder patterns, it can be easier to use a dedicated program. An excellent program for pattern calculation is the Powder Cell program. However, if attempting to calculate accurate patterns for non-tube wavelengths, the Poudrix software should be considered (Table 17.31).

### 17.3.27 Structure Validation

While computer-based structure validation is integrated in single crystal software, it is somewhat lagging in the powder diffraction community. Ton Spek's

**Table 17.29** Available Fourier Map software.

| *Software* | *References* | *Caveates/features* |
|---|---|---|
| DRAWxtl | DRAWxtl, an open source computer program to produce crystal structure drawings, L. W. Finger, M. Kroeker and B. H. Toby, *J. Appl. Crystallogr.*, 2007, **40**, 188 192 | Views GSAS GRD, Jana, Vasp, Fullprof, CIF FoFc, O, Jana FoFc and Exciting |
| FOUE | FOUE: program for conversion of GSAS binary Fourier Map files to other formats, Scott Belmonte (2000) | Converts GSAS binary Fourier Map files into ASCII DUMP, WinGX and Marching Cubes/ Crystals format files |
| Fox | FOX, 'free objects for crystallography': a modular approach to *ab initio* structure determination from powder diffraction, V. Favre Nicolin and R. Cerný, *J. Appl. Crystallogr.*, 2002, **35**, 734 743 | GSAS Fourier Maps |
| GFourier/ Fullprof Suite | GFourier, J Gonzalez Platas and J. Rodriguez Carvajal, University of La Laguana, Tenerife, Spain and Laboratoire Léon Brillouin, Saclay, France, March 2004 and WinPLOTR: A Windows tool for powder diffraction pattern analysis, T. Roisnel and J. Rodriguez Carvajal, *EPDIC 7: European Powder Diffraction*, Pts 1 and 2 Materials Science Forum 378 3: 118 123, Part 1&2 2001 | Requires hkl's and structure factors in Fullprof format |
| MCE Marching Cubes | MCE program for fast interactive visualization of electron and similar density maps, optimized for small molecules, M. Husák and B. Kratochvíl, *J. Appl. Crystallogr.*, 2003, **36**, 1104 | Views Crystals/ WinGX ASCII FOU, GSAS Fourier and GSAS GRD files |
| OpenDX | 2002 OpenDX.org | General scientific viewer for large amounts of data. Jana can write maps for OpenDX |
| Platon/ Fourier3D | Single crystal structure validation with the program PLATON, A. L. Spek, *J. Appl. Crystallogr.*, 2003, **36**, 7 13 and Fourier3D: visualisation of electron density and solvent accessible voids in small molecule crystallography, D. M. Tooke and A. L. Spek, Fourier3D, *J. Appl. Crystallogr.*, 2005, **38**, 572 573 | Platon requires Shelx format FCF format files to generate maps |
| VENUS | F. Izumi and R. A. Dilanian, "Structure refinement based on the maximum entropy method from powder diffraction data" in *Recent Research Developments* | Includes Maximum Entropy method and can input and output various 3D |

(*Continued*)

**Table 17.29** (*Continued*).

| *Software* | *References* | *Caveates/features* |
|---|---|---|
| | *in Physics*, Transworld Research Network, Trivandrum, 2002, Vol. 3, Part II, pp. 699 726 and F. Izumi, "Beyond the ability of Rietveld analysis: MEM based pattern fitting," *Solid State Ionics*, 2004, **172**, 1 6 | mesh data including: MEED, ALBA, MacMolPlt, SCAT, VASP, VEND 3D, WIEN2k, XSF format of XCrySDen |
| WinGX | WinGX suite for small molecule single crystal crystallography, L. J. Farrugia, *J. Appl. Crystallogr.*, 1999, **32**, 837 838 | Requires Shelx format FCF files to generate the Fourier Map; or a WinGX format MAP file |

**Table 17.30** Available quantitative phase analysis software (also refer to list of Rietveld structure refinement software).

| *Software* | *References* | *Method* | *Freely available?* |
|---|---|---|---|
| BGMN | BGMN a new fundamental parameters based Rietveld program for laboratory X ray sources, its use in quantitative analysis and structure investigations, J. Bergmann, P. Friedel and R. Kleeberg, *Int. Union Crystallogr., Commission Powder Diffr. Newsletter*, 1998, No. 20, pp. 5 8 | Rietveld | |
| Fullpat | FULLPAT: a full pattern quantitative analysis program for X ray powder diffraction using measured and calculated patterns, S. J. Chipera and D. L. Bish, *J. Appl. Crystallogr.*, 2002, **35**, 744 749 | Fullpattern using a corundum internal standard | Yes |
| MAUD | MAUD (Material Analysis Using Diffraction): a user friendly {Java} program for {Rietveld} Texture Analysis and more, L. Lutterotti, S. Matthies and H. R. Wenk, *Proceeding of the Twelfth International Conference on Textures of Materials (ICOTOM 12)*, 1999, Vol. 1, p. 1599 | Rietveld | Yes |
| Quanto | Quanto: a Rietveld program for quantitative phase analysis of polycrystalline mixtures, A. Altomare, M. C. Burla, C. Giacovazzo, | Rietveld | Yes |

(*Continued*)

**Table 17.30** (*Continued*).

| *Software* | *References* | *Method* | *Freely available?* |
|---|---|---|---|
| | A. Guagliardi, A. G. G. Moliterni, G. Polidori and R. Rizzi, *J. Appl. Crystallogr.*, 2001, **34**, 392 397 | | |
| Powder Cell | POWDER CELL a program for the representation and manipulation of crystal structures and calculation of the resulting X ray powder patterns., W. Kraus and G. Nolze, *J. Appl. Crystallogr.*, 1996, **29**, 301 303 | Rietveld | Yes |
| Rietquan | Quantitative analysis of silicate glass in ceramic materials by the Rietveld method, L. Lutterotti, R. Ceccato, R. Dal Maschio and E. Pagani, *Mater. Sci. Forum.*, 1998, **278-281**, 93 98 | Rietveld | Yes |
| RIQAS | RIQAS, Materials Data, Inc., 1224 Concannon Blvd., Livermore, CA 94550, USA | Rietveld | |
| Rockjock | User guide to RockJock A program for determining quantitative mineralogy from X ray diffraction data, D. D. Eberl, USGS Open File Report OF 03 78, (2003) 40p and Quantitative mineralogy of the Yukon River system: Changes with reach and season, and determining sediment provenance, D. D. Eberl, *Am. Mineral.*, 2004, **89**(11 12), 1784 1794 | Fullpattern with the option of using zincite internal standard | Yes |
| Siroquant | Computer Programs for Standardless Quantitative Analysis of Minerals Using the Full Powder Diffraction Profile, J. C. Taylor, *Powder Diffr.*, 1991, **6**, 2 9 | Rietveld | |
| Topas | TOPAS V3: General profile and structure analysis software for powder diffraction data. User's Manual, (2005) Bruker AXS, Karlsruhe, Germany | Rietveld | |

Platon is one of the best programs available for the checking and validation of crystal structures, but tends to be optimized for organics and organometallics. The Addsym function in the Platon program is used for finding missing symmetry and should be considered a mandatory check of all solved and refined structures using powder diffraction data. Platon also includes the Structure-Tidy program of Erwin Parthe (1928–2006), making it easier to compare related structures, and easier to check if polymeric inorganic or intermetallic structures have already been solved. Other programs for geometry checking and bond-valence analysis are also available (Table 17.32).

**Table 17.31** Available powder pattern calculation software (also refer to list of Rietveld structure refinement software).

| *Software* | *References* | *Compatible structure file formats* |
|---|---|---|
| Lazy Pulverix | LAZY PULVERIX, a computer program, for calculating X ray and neutron diffraction powder patterns, K. Yvon, W. Jeitschko and E. Parthé, *J. Appl. Crystallogr.*, 1977, **10**, 73 74 | Lazy Pulverix |
| Lazy Pulverix via the ICSD web interface | LAZY PULVERIX, a computer program, for calculating X ray and neutron diffraction powder patterns, K. Yvon, W. Jeitschko and E. Parthé, *J. Appl. Crystallogr.*, 1977, **10**, 73 74 and ICSD for WWW, Inorganic Crystal Structure Database, Hewat, A. (2002). http://icsd.ill.fr/icsd/ and http://icsdweb.fiz karlsruhe.de/ | CCSL, CIF, ICSD, Shelx, Lazy Pulverix, Rietveld ILL, SERC Cambridge, DBWS, Fullprof, PDB |
| Lazy Pulverix for Windows within WinGX | LAZY PULVERIX, a computer program, for calculating X ray and neutron diffraction powder patterns, K. Yvon, W. Jeitschko and E. Parthé, *J. Appl. Crystallogr.*, 1977, **10**, 73 74 and WinGX suite for small molecule single crystal crystallography, L. J. Farrugia, *J. Appl. Crystallogr.*, 1999, **32**, 837 838 | Shelx, CIF, CSD FDAT, CSSR XR |
| Platon | Single crystal structure validation with the program PLATON, A. L. Spek, *J. Appl. Crystallogr.*, 2003, **36**, 7 13 | Platon, CIF, Shelx, CSD FDAT, PDB |
| Powder Cell for Windows | POWDER CELL a program for the representation and manipulation of crystal structures and calculation of the resulting X ray powder patterns., W. Kraus and G. Nolze, *J. Appl. Crystallogr.*, 1996, **29**, 301 303 | Powder Cell, Shelx, ICSD (TXT) |
| Powdis and Powutl/ ORTEX Suite | POWDIS and POWUTL PC programs for the display and simulation of X ray powder patterns, P. McArdle and D. Cunningham, *J. Appl. Crystallogr.*, 1998, **31**, 826 | Shelx |
| Poudrix for Windows | LMGP Suite Suite of Programs for the interpretation of X ray Experiments, by J. Laugier and B. Bochu, ENSP/Laboratoire des Matériaux et du Génie Physique, BP 46. 38042 Saint Martin d′Hčres, France | Shelx, Powder Cell, Lazy Pulverix LZY, CIF |

**Table 17.32** Available structure validation software.

| *Software* | *References* | *Main feature/caveat* |
|---|---|---|
| Addsym (with Platon) | MISSYM1.1 a flexible new release, Y. Le Page, *J. Appl. Crystallogr.*, 1988, **21**, 983 984, Computer derivation of the symmetry elements implied in a structure description, Y. Le Page, *J. Appl. Crystallogr.*, 1987, **20**, 264 269 and Single crystal structure validation with the program PLATON, A. L. Spek, *J. Appl. Crystallogr.*, 2003, **36**, 7 13 | The benchmark for general validation of crystal structures including the Addsym program for finding missing (higher) symmetry in solved and refined crystal structures |
| Bond Str/Fullprof | Bond Str distances, angles and bond valence calculations, J. Rodriguez Carvajal, Laboratoire Léon Brillouin, Saclay, France, March 2005 and WinPLOTR: A Windows tool for powder diffraction pattern analysis, T. Roisnel and J. Rodriguez Carvajal, *EPDIC 7: European Powder Diffraction*, Pts 1 and 2 Materials Science Forum 378 3: 118 123, Part 1&2 2001 | Bond Valence calculations |
| Bond Valence Wizard | Program for predicting interatomic distances in crystals by the bond valence method, I. P. Orlov, K. A. Popov and V. S. Urusov, *J. Struct. Chem.*, 1998, **39**(4), 575 579 and Predicting bond lengths in inorganic crystals, I. D. Brown, *Acta Crystallogr.*, *Sect. B*, 1977, **33**, 1305 1310 | Bond Valence calculations |
| CHKSYM | CHKSYM a PC program that checks the symmetry properties of the unit cell and its contents, P. McArdle, P. Daly and D. Cunningham, *J. Appl. Crystallogr.*, 2002, **35**, 378 | Checking the symmetry of a refined crystal structure |
| Crystals | CRYSTALS version 12: software for guided crystal structure analysis, P. W. Betteridge, J. R. Carruthers, R. I. Cooper, K. Prout and D. J. Watkin, *J. Appl. Crystallogr.*, 2003, **36**, 1487 | Links to CCDC Mogul |
| dSNAP | dSNAP: a computer program to cluster and classify Cambridge Structural Database searches, G. Barr, W. Dong, C. J. Gilmore, A. Parkin and C. C. Wilson, *J. Appl. Crystallogr.*, 2005, **38**, 833 841 | Checking structures against the CCDC organics and organometallics structure database |
| MISSYM | MISSYM1.1 a flexible new release, Y. Le Page, *J. Appl. Crystallogr.*, | Original algorithm by Y. LePage. |

(*Continued*)

**Table 17.32** (*Continued*).

| *Software* | *References* | *Main feature/caveat* |
|---|---|---|
| | 1988, **21**, 983 984 and Computer derivation of the symmetry elements implied in a structure description, Y. Le Page, *J. Appl. Crystallogr.*, 1987, **20**, 264 269 | Implemented in Addsym within Platon |
| Mogul | Retrieval of Crystallographically Derived Molecular Geometry Information, I. J. Bruno, J. C. Cole, M. Kessler, J. Luo, W. D. S. Motherwell, L. H. Purkis, B. R. Smith, R. Taylor, R. I. Cooper, S. E. Harris and A. G. Orpen, *J. Chem. Inf. Comput. Sci.*, 2004, **44**(6), 2133 2144 | Validation of bond lengths, angles and torsions against the Cambridge database |
| Ortex | ORTEX2.1 a 1677 atom version of ORTEP with automatic cell outline and cell packing for use on a PC, P. McArdle, *J. Appl. Crystallogr.*, 1994, **27**, 438 439 | Includes void finding |
| softBV | Relationship between bond valence and bond softness of alkali halides and chalcogenides, St. Adams, *Acta Crystallogr., Sect. B*, 2001, **57**, 278 287 | Bond Valence calculations with web based input of Shelx and CIF files |
| SVDdiagnostic | SVDdiagnostic, a program to diagnose numerical conditioning of Rietveld refinements, P. H. J. Mercier, Y. Le Page, P. S. Whitfield and L. D. Mitchell, *J. Appl. Crystallogr.*, 2006, **39**, 458 465 | diagnosis of ill conditioned Rietveld refinements |
| Valence | VALENCE: a program for calculating bond valences, I. D. Brown, *J. Appl. Crystallogr.*, 1996, **29**, 479 480 | Bond Valence parameters |
| VaList | VaList, A. S. Wills and I. D. Brown, CEA, France, 1999, Program available from ftp://ftp.ill.fr/pub/dif/valist/ | Bond Valence calculations |
| WinGX | WinGX suite for small molecule single crystal crystallography, L. J. Farrugia, *J. Appl. Crystallogr.*, 1999, **32**, 837 838 | Includes and links to wide variety of validation software including Platon |

### 17.3.28 Crystallographic Structure Visualization: During Structure Solution and Refinement

Unlike modern single crystal suites, most Rietveld programs do not have the ability to graphically track the progress of the refinement by displaying a real-time plot of the structure. Exceptions to this include developments within the Fullprof Suite, MAUD and BRASS. Thus use of a free-standing structure

**Table 17.33** Software for crystallographic structure visualization during structure solution and refinement.

| *Software* | *References* | *Compatible file formats* |
|---|---|---|
| Gretep | LMGP Suite Suite of Programs for the interpretation of X ray Experiments, by J. Laugier and B. Bochu, ENSP/ Laboratoire des Matériaux et du Génie Physique, BP 46. 38042 Saint Martin d′Hčres, France | Poudrix, Shelx, Lazy_Pulvarix, Powder Cell, CIF |
| ORTEP III for Windows | ORTEP 3 for Windows a version of ORTEP III with a Graphical User Interface (GUI), L. J. Farrugia, *J. Appl. Crystallogr*., 1997, **30**, 565 | Shelx, CIF, GX, SPF/ Platon, ORTEP, CSD/CCDC FDAT, CSSR XR, Crystals, GSAS, Sybol MOL/MOL2, MDL MOL, XYZ file, Brookhaven PDB, Rietica LHPM, Fullprof |
| Platon | Single crystal structure validation with the program PLATON, A. L. Spek, *J. Appl. Crystallogr*., 2003, **36**, 7 13 and A. L. Spek, (1998) PLATON, A Multipurpose Crystallographic Tool, Utrecht University, Utrecht, The Netherlands | CIF, Shelx, PDB, Platon SPF |
| Powder Cell | POWDER CELL a program for the representation and manipulation of crystal structures and calculation of the resulting X ray powder patterns, W. Kraus and G. Nolze, *J. Appl. Crystallogr*., 1996, **29**, 301 303 | Powder Cell, Shelx, ICSD TXT |

viewing program may be of assistance. Of the available software, the ORTEP-III for Windows can be effective due to its ability to import various crystal structure formats, including GSAS (Table 17.33).

### 17.3.29 Visualization and Photo Realistic Rendering of Crystal Structures

Most commercial crystal structure viewing software can handle all the requirements that a user may want of them. For freeware software, a collection of programs may be required to match this (*e.g*., one program for annotated ball and stick display, another program for polyhedral structure display). Most structure viewing programs should be able to import CIF files. It is best to check the bond-length and angle output, as well as use different programs to cross-check the correctness of the output. This is especially so with polyhedral structure display software, where possible errors may not be apparent until compared with a similar structure plot generated in a separate program (Table 17.34).

**Table 17.34** Available software for visualization and photo realistic rendering of crystal structures.

| *Software* | *References* | *Ball and Stick* | *ADPs/ ORTEPs* | *Polyhedral* | *Magnetic* | *Freeware* |
|---|---|---|---|---|---|---|
| ATOMS | ATOMS, Shape Software, 521 Hidden Valley Road, Kingsport TN 37663 USA, http://www.shapesoftware.com/ | Yes | Yes | Yes | Yes | |
| Balls and Sticks | Balls&Sticks: easy to use structure visualization and animation program, T. C. Ozawa and S. J. Kang , *J. Appl. Crystallogr*., 2004, **37**, 679 | Yes | | Yes | | Yes |
| BALSAC | BALSAC software by K. Hermann, Fritz Haber Institut der MPG, Berlin (C) Copyright 1991 2004 Klaus Hermann. All Rights Reserved | Yes | | | | Yes |
| Cameron | CAMERON, D. J. Watkin, C. K. Prout and L. J. Pearce, 1996, Chemical Crystallography Laboratory, Oxford, UK | Yes | Yes | | | Yes |
| Carine | CaRIne Crystallography (c)C. Boudias and D. Monceau, 1989 2004: The crystallographic software for research and teaching 3D Modeling: Unit cells, Crystals, Surfaces, Interfaces Simulation and analysis: X Ray diffraction patterns, Stereographic projections, Reciprocal lattices. http://pro.wanadoo.fr/carine.crystallography/ | Yes | | Yes | | |
| Crystallographica | Crystallographica a software toolkit for crystallography, *J. Appl. Crystallogr*. 1997, **30**, 418 419 | Yes | Yes | Yes | | |
| Crystal Maker | CrystalMaker 6 for Mac OS X. CrystalMaker Software Ltd., 5 Begbroke Science Park, Sandy Lane, Yarnton, OX5 1PF, UK | Yes | | Yes | Yes | |

| | | | | | | |
|---|---|---|---|---|---|---|
| Crystal Studio | Crystal Studio Crystallography Software Package, (C)1999 2005, Crystal Systems Co., Ltd., (www.crystalsoftcorp.com), PO Box 7006, Wattle Park, VIC 3128, Australia | Yes | Yes | Yes | | |
| CrystMol | CrystMol, 6209 Litchfield Lane, Kalamazoo, MI, 49009 9159, US | Yes | Yes | | | |
| Diamond | Diamond Crystal and Molecular Structure Visualization Crystal Impact K. Brandenburg and H. Putz GbR, Postfach 1251, D 53002 Bonn | Yes | Yes | Yes | | |
| DrawXTL | DRAWxtl, an open source computer program to produce crystal structure drawings, L. W. Finger, M. Kroeker and B. H. Toby, *J. Appl. Crystallogr.*, 2007, **40**, 188 192 | Yes | Yes | Yes | Yes | Yes |
| FpStudio | FpStudio, L. C. Chapon and J. Rodriguez Carvajal, Rutherford Appleton Laboratory, UK and Laboratoire Léon Brillouin, Saclay, France, March 2005 | Yes | Yes | | Yes | Yes |
| GRETEP | LMGP Suite Suite of Programs for the interpretation of X ray Experiments, by J. Laugier and B. Bochu, ENSP/Laboratoire des Matériaux et du Génie Physique, BP 46. 38042 Saint Martin d′Hčres, France | Yes | Yes | | | Yes |
| Mercury | New software for searching the Cambridge Structural Database and visualising crystal structures, I. J. Bruno, J. C. Cole, P. R. Edgington, M. K. Kessler, C. F. Macrae, P. McCabe, J. Pearson and R. Taylor, *Acta Crystallogr., Sect. B*, 2002, **58**, 389 397 | Yes | Yes | | | Yes |

(*Continued*)

**Table 17.34** (*Continued*).

| *Software* | *References* | *Ball and Stick* | *ADPs/ ORTEPs* | *Polyhedral* | *Magnetic* | *Freeware* |
|---|---|---|---|---|---|---|
| MolXtl | MolXtl: molecular graphics for small molecule crystallography, D. W. Bennett, *J. Appl. Crystallogr.*, 2004, **37**, 1038 | Yes | | | | Yes |
| OLEX | OLEX: new software for visualization and analysis of extended crystal structures, O. V. Dolomanov, A. J. Blakem, N. R. Champness and M. Schröder, *J. Appl. Crystallogr.*, 2003, **36**, 1283 1284 | Yes | | | | Yes |
| ORTEP III | M. N. Burnett and C. K. Johnson, ORTEP III: Oak Ridge Thermal Ellipsoid Plot Program for Crystal Structure Illustrations, Oak Ridge National Laboratory Report ORNL 6895, 1996 | Yes | Yes | | | Yes |
| ORTEP III for Windows | ORTEP 3 for Windows a version of ORTEP III with a Graphical User Interface (GUI), L. J. Farrugia, *J. Appl. Crystallogr.*, 1997, **30**, 565 | Yes | Yes | | | Yes |
| ORTEX/Oscail X | ORTEX2.1 a 1677 atom version of ORTEP with automatic cell outline and cell packing for use on a PC, P. McArdle, *J. Appl. Crystallogr.*, 1994, **27**, 438 439; and "A method for the prediction of the crystal structure of ionic organic compounds? The crystal structures of o toluidinium chloride and bromide and polymorphism of bicifadine hydrochloride", P. McArdle, K. Gilligan, D. Cunningham, R. Dark and M. Mahon, *CrystEngComm*, 2004, **6**, 303 | Yes | Yes | | | Yes |
| Platon/Pluton | Single crystal structure validation with the program PLATON, A. L. Spek, *J. Appl. Crystallogr.*, 2003, **36**, 7 13 and A. L. Spek, 1998, PLATON, A Multipurpose Crystallographic Tool, Utrecht University, Utrecht, The Netherlands | Yes | Yes | | | Yes |

| | | | | | |
|---|---|---|---|---|---|
| Powder Cell | POWDER CELL a program for the representation and manipulation of crystal structures and calculation of the resulting X ray powder patterns., W. Kraus and G. Nolze, *J. Appl. Crystallogr.*, 1996, **29**, 301 303 | Yes | | | Yes |
| PRJMS | "Structure factor of modulated crystal structures" by A. Yamamoto, *Acta Crystallogr. Sect. A*, 1982, **38**, 87 92 | Yes | | | Yes |
| Schakal | "SCHAKAL 99, a computer program for the graphic representation of molecular and sold state structure models", E. Keller, Universitaet Freiburg, Germany, 1999 | Yes | Yes | | Yes |
| Struplo | STRUPLO 2003. A new program for crystal structure drawing., R. X. Fischer and T. Messner, Ber. DMG, Beih. z. *Eur. J. Mineral.*, 2003, **15**(1), 54 | Yes | Yes | Yes | Yes |
| Struplo for Windows | STRUPLO84, a Fortran plot program for crystal structure illustrations in polyhedral representation, R. X. Fischer, *J. Appl. Crystallogr.*, 1985, **18**, 258 262; VRML as a tool for exploring complex structures, A. Le Bail, *Acta Crystallogr.*, *Sect. A*, 1996, **52**, suppl. C78, and WinGX suite for small molecule single crystal crystallography, L. J. Farrugia, *J. Appl. Crystallogr.*, 1999, **32**, 837 838 | | | Yes | Yes |
| Struvir | VRML as a tool for exploring complex structures, A. Le Bail, *Acta Crystallogr.*, *Sect. A*, 1996, 52, suppl. C78. and STRUPLO84, a Fortran plot program for crystal structure illustrations in polyhedral representation, R. X. Fischer, *J. Appl. Crystallogr.*, 1985, **18**, 258 262 | | | Yes | Yes |

(*Continued*)

**Table 17.34** (*Continued*).

| *Software* | *References* | *Ball and Stick* | *ADPs/ ORTEPs* | *Polyhedral* | *Magnetic* | *Freeware* |
|---|---|---|---|---|---|---|
| Venus (includes PRIMA) | Structure refinement based on the maximum entropy method from powder diffraction data, F. Izumi and R. A. Dilanian, in *Recent Research Developments in Physics*, Transworld Research Network, Trivandrum, 2002, Vol. 3, Part II, pp. 699 726 and Beyond the ability of Rietveld analysis: MEM based pattern fitting, F. Izumi, *Solid State Ionics*, 2004, **172**, 1 6 | Yes | Yes | Yes | Yes | Yes |
| XmLmctep | LMCTEP: software for crystal structure representation, A. Soyer, *J. Appl. Crystallogr.*, 1993, **26**, 495 | Yes | Yes | | | Yes |
| X Seed | X Seed A software tool for supramolecular crystallography, L. J. Barbour, *J. Supramol. Chem.*, 2001, **1**, 189. and Molecular graphics: from science to art, J. L. Atwood and L. J. Barbour, *Cryst. Growth Des.* 2003, **3**, 3 | Yes | Yes | | | |
| Xtal 3D | Databases linked to electronic publications, A. Hewat, *Acta Crystallogr. Sect. A*, 2002, **58**, (Supplement), C216 | Yes | Yes | Yes | Yes | Yes |
| XtalDraw | The American Mineralogist Crystal Structure Database. R. T. Downs and M. Hall Wallace, *Am. Mineral.*, 2003, **88**, 247 250 | Yes | Yes | Yes | | Yes |

**Table 17.35** Miscellaneous Internet based resources useful to powder diffractionists.

| *Software* | *Overview (web links are included in Apendix to this chapter)* |
|---|---|
| CCP14 (Collaborative Computational Project Number 14 for Single Crystal and Powder Diffraction) | A first port of call for checking out available crystallographic software. Links to and mirrors of single crystal and powder crystallographic software. Includes tutorials for some of the software and lists of available software |
| Crystallographic Nexus CD ROM for crystallographers isolated from the internet | Free CD ROM containing various Internet available single crystal and powder diffraction software and resources. Mainly intended for academics and students in the developing world |
| Google Search Engine | Currently, the best internet search engine in terms of giving relevant hits (providing your scientific keyword is not associated with a more mainstream non scientific topic) |
| Internet course: Powder Diffraction Course | Internet course teaching powder diffraction from fundamentals through to Rietveld refinement |
| Internet course: Quantitatively Determine the Crystallographic Texture of materials | Internet course teaching materials analysis by texture methods |
| Internet course: Structure Determination by Powder Diffractometry (SDPD) | Internet course teaching the solving of crystal structures from powder diffraction data |
| IUCr (International Union of Crystallography) | Main umbrella organization for crystallographers (including powder diffractionists) |
| IUCr Commission on Powder Diffraction Newsletter | Free on line and hardcopy newsletter for powder diffractonists. Each issue normally has a theme, as well as attracting general announcements and articles of interest |
| IUCr Commission on Crystallographic Computing Newsletter | A free on line newsletter for those who are (or wish to) develop crystallographic software, as well as those who like to see what is under the hood of existing crystallographic software |
| IUCr Sincris Crystallographic Software Library | Links to a very wide variety of crystallographic software (not just single crystal and powder diffraction) |
| IUCr Crystallography World Wide Educational Resources | Links to various crystallographic educational resources |
| IUCr Crystallography World Wide Employment Resources | A first port of call for those interested in crystallographic employment |
| | Free Linux based single crystal and powder crystallographic software on |

(*Continued*)

**Table 17.35** (*Continued*).

| *Software* | *Overview (web links are included in Apendix to this chapter)* |
|---|---|
| Kcristal Linux versions and ports of powder diffraction software on free downloadable CD | CD ROM. Includes a surprisingly wide variety of crystallographic programs, and ports of DOS/Windows programs to Linux.; Ref: Kcristal: Linux 'live CD' for powder crystallography, V. H. S. Utuni, A. V. C. Andrade, H. P. S. Correa and C. O. Paiva Santos, *J. Appl. Crystallogr.*, 2005, **38**, 706 707 |
| Rietveld Users Mailing List | Not only a good place for learning about available Rietveld software, jobs and, answering of general queries: but also to observe the cut, thrust and parry of crystallographic argument |
| Sci.techniques.xtallography Internet newsgroup | General crystallography, which includes powder diffraction. Quite sparse in activity but a good place to check for software announcements, jobs on offer and communal problem software |
| SDPD (Structure Determination by Powder Diffractometry) mailing list | A good mailing list for advice and hints on structure solution, as well as announcements on new software updates and jobs on offer |
| Strategies in Structure Determination from Powder Data by Armel Le Bail | Advice and examples from one of the world experts and developers of structure solution from powder diffraction data |

### 17.3.30 Miscellaneous Resources

Some useful resources are listed in the Table 17.35, including Internet based discussion lists, employment, tutorials and training courses.

## APPENDIX 1: INTERNET LINKS FOR CITED SOFTWARE AND RESOURCES

Absen: http://www.nuigalway.ie/cryst/software.htm
ADM-connect: http://www.RMSKempten.de/ and http://freenet-homepage.de/RMSKempten/admvbal.html
Addsym: is implemented within Platon
American Mineralogist Crystal Structure Database: http://www.geo.arizona.edu/AMS/
ARITVE: http://sdpd.univ-lemans.fr/aritve.html
ATOMS: http://www.shapesoftware.com/
AUTOX: included with VMRIA http://www.ccp14.ac.uk/ccp/web-mirrors/vmria/

AXES: http://www.physic.ut.ee/~hugo/axes/
BABEL: refer to OpenBabel
Balls and Sticks: http://www.toycrate.org/
BALSAC: http://www.fhi-berlin.mpg.de/~hermann/Balsac/
BGMN: http://www.bgmn.de/
BEARTEX: http://eps.berkeley.edu/~wenk/TexturePage/beartex.htm
Bede Search/Match: http://www.bede.co.uk/
Bilbao Crystallographic Server: http://www.cryst.ehu.es/
Bond Str: within the Fullprof Suite
Bond Valence Wizard: http://orlov.ch/bondval/
BRASS: http://www.brass.uni-bremen.de/
BREADTH: http://www.du.edu/~balzar/breadth.htm
Cameron: within Crystals and WinGX
CAOS: within Sir2004 and freestanding at http://www.ic.cnr.it/caos/
Carine: http://pros.orange.fr/carine.crystallography/
CCDC/Cambridge Structure Database: http://www.ccdc.cam.ac.uk/
CCP14 (Collaborative Computational Project Number 14 for Single Crystal and Powder Diffraction): http://www.ccp14.ac.uk/
cctbx-sgtbx Explore symmetry: http://cci.lbl.gov/cctbx/explore_symmetry. html
CDS (EPSRC funded Chemical Database Service): http://cds.dl.ac.uk/
Celref: http://www.ccp14.ac.uk/tutorial/lmgp/#celref and http://www.ccp14.ac.uk/ccp/web-mirrors/lmgp-laugier-bochu/
Chekcell: http://www.ccp14.ac.uk/tutorial/lmgp/#chekcell and http://www. ccp14.ac.uk/ccp/web-mirrors/lmgp-laugier-bochu/
CHKSYM: http://www.nuigalway.ie/cryst/software.htm
CMPR & Portable LOGIC: http://www.ncnr.nist.gov/xtal/software/cmpr/
CMWP-fit: http://www.renyi.hu/cmwp/
COD (Crystallography Open Database): http://www.crystallography.net/
ConTEXT: http://www.context.cx/
ConvX: http://www.ccp14.ac.uk/ccp/web-mirrors/convx/
Crisp: http://xtal.sourceforge.net/
Crunch: http://www.bfsc.leidenuniv.nl/software/crunch/
Cryscon: http://www.shapesoftware.com/
Crysfire: http://www.ccp14.ac.uk/tutorial/crys/ and http://www.ccp14.ac.uk/ccp/web-mirrors/crys-r-shirley/
Crystallographic Nexus CD-ROM for crystallographers isolated from the Internet: http://lachlan.bluehaze.com.au/stxnews/nexus/
Crystal Maker: http://www.crystalmaker.co.uk/
Crystals: http://www.xtl.ox.ac.uk/
Crystal Studio: http://www.crystalsoftcorp.com/CrystalStudio/
CRYSTMET: http://www.tothcanada.com/
Crystallographica and Crystallographica Search-Match: http://www.crystallographica.co.uk/
CrystMol: http://www.crystmol.com/
DANSE: http://wiki.cacr.caltech.edu/danse/index.php/Main_Page
Dash: http://www.ccdc.cam.ac.uk/products/powder_diffraction/dash/

Datasqueeze: http://www.datasqueezesoftware.com/
DBWS: http://www.physics.gatech.edu/downloads/young/DBWS.html
DEBVIN: http://users.uniud.it/bruckner/debvin.html
DERB and DERFFT: http://www.ccp14.ac.uk/ccp/web-mirrors/derb-derfft/
DDM: http://icct.krasn.ru/eng/content/persons/Sol_LA/ddm.html
Diamond: http://www.crystalimpact.com/
Dicvol 91: various internet sites including http://sdpd.univ-lemans.fr/ftp/dicvol91.zip
Dicvol 2004: http://www.ccp14.ac.uk/ccp/web-mirrors/dicvol/
Dicvol 2006: http://www.ccp14.ac.uk/ccp/web-mirrors/dicvol/
DIFFaX+: E-mail Matteo Leoni (matteo.leoni@unitn.it)
DIFFRAC$^{plus}$ SEARCH: http://www.bruker-axs.de/
Dirdif: http://www.xtal.science.ru.nl/documents/software/dirdif.html
DISCUS: http://www.uni-wuerzburg.de/mineralogie/crystal/discus/ and ftp://ftp.lanl.gov/public/tproffen/
DPLOT: http://www.dplot.com/
DrawXTL: http://www.lwfinger.net/drawxtl/
DRXWin: http://icmuv.uv.es/drxwin/
dSNAP: http://www.chem.gla.ac.uk/snap/
DS*SYSTEM: http://www.ccp14.ac.uk/ccp/web-mirrors/okada/
Eflect/Index: http://www.bgmn.de/related.html
Endeavour: http://www.crystalimpact.com/endeavour/
Eracel: http://sdpd.univ-lemans.fr/ftp/eracel.zip
Explore symmetry: refer to cctbx
EXPGUI: http://www.ncnr.nist.gov/programs/crystallography/software/expgui/
EXPO/EXPO2004: http://www.ic.cnr.it/
EXTRACT: http://www.crystal.mat.ethz.ch/Software/XRS82/
Extsym: http://www.markvardsen.net/projects/ExtSym/main.html
FIT2D: http://www.esrf.fr/computing/scientific/FIT2D/
Fjzn: http://www.ccp14.ac.uk/tutorial/crys/ and http://www.ccp14.ac.uk/ccp/web-mirrors/crys-r-shirley/
Fityk: http://www.unipress.waw.pl/fityk/
Focus: http://olivine.ethz.ch/LFK/software/ and http://cci.lbl.gov/~rwgk/focus/
FOUE: http://www.ccp14.ac.uk/ccp/web-mirrors/scott-belmonte-software/foue/
Fourier3D: http://www.cryst.chem.uu.nl/tooke/fourier3d/
Fox: http://objcryst.sourceforge.net/Fox/
FpStudio: within the Fullprof Suite
Fullpat: http://www.ccp14.ac.uk/ccp/web-mirrors/fullpat/
Fullprof Suite: http://www.ill.fr/dif/Soft/fp/
GeneFP: http://crystallography.zhenjie.googlepages.com/GeneFP.html
GEST: http://crystallography.zhenjie.googlepages.com/GEST.html
GETSPEC: http://www.ccp14.ac.uk/ccp/web-mirrors/i_d_brown/getspec/ (see Wgetspec for Windows binary)
Gfourier: within the Fullprof Suite and freestanding via http://www.ill.fr/dif/Soft/fp/
Google Search Engine: http://www.google.com/

Gretep: http://www.ccp14.ac.uk/tutorial/lmgp/#gretep and http://www.ccp14.ac.uk/ccp/web-mirrors/lmgp-laugier-bochu/
GRINSP: http://sdpd.univ-lemans.fr/grinsp/ and http://www.cristal.org/grinsp/
GSAS: http://www.ncnr.nist.gov/xtal/software/downloads.html; http://www.ccp14.ac.uk/solution/gsas/; http://www.ccp14.ac.uk/ccp/ccp14/ftp-mirror/gsas/public/gsas/
Hydrogen/CalcOH: http://www.ccp14.ac.uk/ccp/ccp14/ftp-mirror/nardelli/pub/nardelli/ and GUI version within WinGX
Hypertext Book of Crystallographic Space Group Diagrams and Tables: http://img.chem.ucl.ac.uk/sgp/
ICDD Powder Diffraction Files on CD-ROM: http://www.icdd.com/
IC-POWLS: E-mail Winfried Kockelmann (W.Kockelmann@rl.ac.uk)
ICSD (Inorganic Crystal Structure Database): http://www.fiz-informationsdienste.de/en/DB/icsd/ and http://icsd.ill.fr/
Incommensurate phases database: http://www.mapr.ucl.ac.be/~crystal/
International Tables vol A.: http://it.iucr.org/
Internet course: Powder Diffraction Course: http://pd.chem.ucl.ac.uk/pd/welcome.htm
Internet course: Quantitatively Determine the Crystallographic Texture of materials: http://www.ecole.ensicaen.fr/~chateign/qta/
ISOTROPY: http://stokes.byu.edu/isotropy.html
Ito: various internet sites including http://sdpd.univ-lemans.fr/ftp/ito13.zip
IUCr (International Union of Crystallography): http://www.iucr.org/
IUCr Commission on Crystallographic Computing Newsletter: http://www.iucr.org/iucr-top/comm/ccom/newsletters/
IUCr Commission on Powder Diffraction Newsletter: http://www.iucr.org/iucr-top/comm/cpd/html/newsletter.html and http://www.iucr-cpd.org/Newsletters.htm
IUCr Sincris Crystallographic Software Library: http://www.iucr.org/sincris-top/
IUCr Crystallography World Wide Educational Resources: http://www.iucr.org/cww-top/edu.index.html
IUCr Crystallography World Wide Employment Resources: http://www.iucr.org/cww-top/job.index.html
Jade: http://www.materialsdata.com/products.htm
Jana: http://www-xray.fzu.cz/jana/Jana2000/jana.html and ftp://ftp.fzu.cz/pub/cryst/jana2000/
Kcristal – Linux versions and ports of powder diffraction software on free downloadable CD.: http://labcacc.iq.unesp.br/kcristal/
Koalariet: No longer developed. http://www.ccp14.ac.uk/ccp/web-mirrors/xfit-koalariet/ Sequel is the Topas Rietveld program.
Kohl/TMO: http://www.ccp14.ac.uk/ccp/web-mirrors/kohl-tmo/
LABOTEX: http://www.labosoft.com.pl/
LAMA Incommensurate Structures Database: http://www.cryst.ehu.es/icsdb/
LAPOD: http://www.ccp14.ac.uk/ccp/web-mirrors/lapod-langford/
LAPODS: http://www.ccp14.ac.uk/ccp/web-mirrors/powderx/lapod/

Lazy Pulverix: Erwin Parthe (1928-2006). Software is also available within various programs including WinGX and the ICSD for Web.
LinGX: http://www.xtal.rwth-aachen.de/LinGX/
Lzon: http://www.ccp14.ac.uk/tutorial/crys/ and http://www.ccp14.ac.uk/ccp/web-mirrors/crys-r-shirley/
MacDiff: http://servermac.geologie.uni-frankfurt.de/Staff/Homepages/Petschick/RainerE.html
MacPDF: http://www.esm-software.com/macpdf/
MATCH!: http://www.crystalimpact.com/match/
MAUD: http://www.ing.unitn.it/~maud/
MCE-Marching Cubes: http://www.vscht.cz/min/mce
MCGRtof: E-mail Matt Tucker at m.g.tucker@rl.ac.uk
McMaille: http://sdpd.univ-lemans.fr/McMaille/
MDI DataScan: http://www.materialsdata.com/ds.htm
Mercury: http://www.ccdc.cam.ac.uk/products/mercury/
MINCRYST: http://database.iem.ac.ru/mincryst/
Mogul: http://www.ccdc.cam.ac.uk/products/csd_system/mogul/
MolXtl: http://www.uwm.edu/Dept/Chemistry/molxtl/
Momo: http://www.chemie.uni-frankfurt.de/egert/html/momo.html
MS Excel: http://office.microsoft.com/
MudMaster: ftp://brrcrftp.cr.usgs.gov/pub/ddeberl/MudMaster/
MXD (MiXeD crystallographic executive for diffraction): http://cristallo.grenoble.cnrs.fr/LDC/PRODUC_SCIENTIFIQUE/Programme_Wolfers/ProgCristallo.html
Missym: implemented within NRCVax. There is also an enhanced implementation of Missym within Platon under the name of Addsym
Nickel–Nichols Mineral Database: http://www.materialsdata.com/MINERALS.htm
NIH-Image: http://rsb.info.nih.gov/nih-image/
NRCVax: contact Peter White by E-mail: pwhite@unc.edu
OLEX: http://www.ccp14.ac.uk/ccp/web-mirrors/lcells/
OpenBabel: http://openbabel.sourceforge.net/
OpenDX: http://www.opendx.org/
OpenGenie: http://www.isis.rl.ac.uk/OpenGENIE/
Organa: Contact René Peschar by E-mail: rene@science.uva.nl
ORTEP III: http://www.ornl.gov/ortep/ortep.html
ORTEP III for Windows: http://www.chem.gla.ac.uk/~louis/software/
ORTEX/Oscail X: http://www.nuigalway.ie/cryst/software.htm
Overlap: http://sdpd.univ-lemans.fr/ftp/overlap.zip
Patsee: http://www.chemie.uni-frankfurt.de/egert/html/patsee.html
Pauling File: http://www.asminternational.org/
PC-1710 for Windows/PC-1800 for Windows: http://www.clw.csiro.au/services/mineral/products.html
PDB (Protein Data Bank): http://www.rcsb.org/pdb/
PDFFIT: http://sourceforge.net/projects/discus/
PDFFIT2/PDFgui: http://www.diffpy.org

PDFgetN: http://sourceforge.net/projects/pdfgetn/
PDFgetX2: http://www.pa.msu.edu/cmp/billinge-group/programs/PDFgetX2/
PDFgui: http://www.diffpy.org
PFE: http://www.ccp14.ac.uk/ccp/web-mirrors/pfe/people/cpaap/pfe/
PFLS: http://www.crl.nitech.ac.jp/~toraya/software/
Platon/System S: http://www.cryst.chem.uu.nl/platon/ UNIX: ftp://xraysoft.chem.uu.nl/pub/ Win: http://www.chem.gla.ac.uk/~louis/software/
Platon/Fourier3D: Refer to Fourier3D
Pluton: implemented within Platon. Some free-standing versions are still available via various software distributions.
POFINT: http://www.ecole.ensicaen.fr/~chateign/qta/pofint/
PopLA: http://www.lanl.gov/orgs/mst/cms/poplalapp.html
Poudrix for Windows: http://www.ccp14.ac.uk/tutorial/lmgp/#gretep and http://www.ccp14.ac.uk/ccp/web-mirrors/lmgp-laugier-bochu/
Powder3D: http://www.fkf.mpg.de/xray/html/powder3d.html
Powder Cell: http://www.ccp14.ac.uk/ccp/web-mirrors/powdcell/a_v/v_1/powder/e_cell.html and ftp://ftp.bam.de/Powder_Cell/
Powder Solve: http://www.accelrys.com/products/cerius2/
Powder v4: http://www.ccp14.ac.uk/ccp/web-mirrors/ndragoe/html/software. html
PowderX: http://www.ccp14.ac.uk/ccp/web-mirrors/powderx/Powder/
Powdis and Powutl: http://www.nuigalway.ie/cryst/software.htm
PowDLL: http://users.uoi.gr/nkourkou/
POWF: http://www.crystal.vt.edu/crystal/powf.html
PREMOS: http://quasi.nims.go.jp/yamamoto/
PRIMA: refer to VENUS
PRODD: http://www.ccp14.ac.uk/ccp/web-mirrors/prodd/~jpw22/
Profil: http://img.chem.ucl.ac.uk/www/cockcroft/profil.htm and ftp://img. cryst.bbk.ac.uk/
PRO-FIT: http://www.crl.nitech.ac.jp/~toraya/software/
Pulwin: http://users.uniud.it/bruckner/pulwin.html
PW1050: E-mail Prof. Juergen Kopf at kopf@xray.chemie.uni-hamburg.de, http://aclinux1.chemie.uni-hamburg.de/~xray/
Quanto: http://www.ic.cnr.it/
RAD: http://www.pa.msu.edu/~petkov/software.html
RayfleX: http://www.geinspectiontechnologies.com/
Refcel: http://img.chem.ucl.ac.uk/www/cockcroft/profil.htm and ftp://img.cryst.bbk.ac.uk/
Riet7/SR5/LHPM: ftp://ftp.minerals.csiro.au/pub/xtallography/sr5/ and http://www.ccp14.ac.uk/ccp/ccp14/ftp-mirror/csirominerals-anon-ftp/pub/xtallography/sr5/
RIETAN: http://homepage.mac.com/fujioizumi/rietan/angle_dispersive/angle_ dispersive.html
Rietica: http://www.rietica.org/
Rietquan: http://www.ing.unitn.it/~luttero/
Rietveld Users Mailing List: http://lachlan.bluehaze.com.au/stxnews/riet/welcome.htm

RIQAS: http://www.materialsdata.com/ri.htm
RMC: via ISIS website: http://www.isis.rl.ac.uk/
RMC++: http://www.szfki.hu/~nphys/rmc++/opening.html
RMCAW95: http://sdpd.univ-lemans.fr/glasses/rmca/rmcaw95.html
RMCPOW: via ISIS website: http://www.isis.rl.ac.uk/
RMCprofile: E-mail Matt Tucker at m.g.tucker@rl.ac.uk
Rockjock: ftp://brrcrftp.cr.usgs.gov/pub/ddeberl/RockJock/
PRJMS: http://quasi.nims.go.jp/yamamoto/
Ruby: http://www.materialsdata.com/products.htm
SARAh: http://www.chem.ucl.ac.uk/people/wills/ and ftp://ftp.ill.fr/pub/dif/sarah/
Schakal: http://www.krist.uni-freiburg.de/ki/Mitarbeiter/Keller/
Sci.techniques.xtallography Internet newsgroup: news:sci.techniques.xtallography ; Homepage: http://lachlan.bluehaze.com.au/stxnews/stx/welcome.htm
SDPD (Structure Determination by Powder Diffractometry) mailing list: http://www.cristal.org/sdpd/
SGInfo: http://cci.lbl.gov/sginfo/
sgtbx Explore symmetry: refer to cctbx
SHADOW: Various old copies on the internet including http://www.ccp14.ac.uk/ccp/ccp14/ftp-mirror/snyder/SOURCE/SHADOW/ and http://www.du.edu/~balzar/breadth.htm. Commercial version sold by Materials Data Inc: http://www.materialsdata.com/
Shake'n'Bake (SnB): http://www.hwi.buffalo.edu/SnB/
ShakePSD: http://www.ccp14.ac.uk/ccp/web-mirrors/okada/
Shelxl97/Shelxs86/Shelxs97/ShelxD: http://shelx.uni-ac.gwdg.de/SHELX/
Simref: http://www.uni-tuebingen.de/uni/pki/simref/simref.html
SimPA: http://www.science.uottawa.ca/phy/eng/profs/desgreniers/SImPA/simpa.htm
Simpro: http://www.uni-tuebingen.de/uni/pki/simref/simpro.html
Sir92/Sir97/Sir2004/CAOS: http://www.ic.cnr.it/
Siroquant: http://www.sietronics.com.au/products/siroquant/sq.htm
SIeve: http://www.icdd.com/
SoftBV: http://kristall.uni-mki.gwdg.de/softbv/
Space Group Explorer: http://www.calidris-em.com/archive.htm
Space Group Info: is within the Fullprof Suite
SPEC: http://www.certif.com/
STEREOPOLE: http://www.if.tugraz.at/amd/stereopole/
Strategies in Structure Determination from Powder Data by A. Le Bail: http://sdpd.univ-lemans.fr/iniref/tutorial/indexa.html
Structure Tidy: Erwin Parthe (1928-2006). Software also included within Platon
Struplo: latest version now within the BRASS Rietveld suite : http://www.brass.uni-bremen.de/
Struplo for Windows: http://www.chem.gla.ac.uk/~louis/software/
Struvir: http://sdpd.univ-lemans.fr/vrml/struvir.html and http://www.cristal.org/vrml/struvir.html

Supercell: http://www.ill.fr/dif/Soft/fp/
Superflip: http://superspace.epfl.ch/superflip/
Superspace groups for 1D and 2D Modulated Structures: http://quasi.nims.go.jp/yamamoto/spgr.html
SVDdiagnostic: http://www.tothcanada.com/software_exe/SVDdiagnostic. exe
Taup/Powder: http://www.ccp14.ac.uk/ccp/ccp14/ftp-mirror/taupin-indexing/pub/powder/
Topas/Topas SVD Indexing: http://www.dur.ac.uk/john.evans/topas_academic/topas_main.htm ; http://members.optusnet.com.au/~alancoelho/ and http://www.bruker-axs.de/index.php?id=topas
TexTools: http://www.resmat.com/
TexturePlus: http://www.ceramics.nist.gov/webbook/TexturePlus/texture. htm
Traces: http://www.gbcsci.com/
Treor90: various internet sites including http://sdpd.univ-lemans.fr/ftp/treor90.zip
Treor 2000: within EXPO2000: http://www.ic.cnr.it/
TXRDWIN: http://www.omniinstruments.com/txrd.html and http://www.omniinstruments.com/demos.html
UNITCELL (Holland and Redfern): http://www.esc.cam.ac.uk/astaff/holland/UnitCell.html and ftp://www.esc.cam.ac.uk/pub/minp/UnitCell/
UNITCELL (Toraya): http://www.crl.nitech.ac.jp/~toraya/software/
VALENCE: http://www.ccp14.ac.uk/ccp/web-mirrors/i_d_brown/bond_valence_param/
VALIST: http://www.chem.ucl.ac.uk/people/wills/ and ftp://ftp.ill.fr/pub/dif/valist/
VCTCONV: http://www.ccp14.ac.uk/ccp/web-mirrors/convx/
VENUS (includes PRIMA): http://homepage.mac.com/fujioizumi/visualization/VENUS.html
VMRIA: http://www.ccp14.ac.uk/ccp/web-mirrors/vmria/
Wgetspec: http://www.ccp14.ac.uk/tutorial/lmgp/index.html#pdw and http://www.ccp14.ac.uk/ccp/web-mirrors/lmgp-laugier-bochu/
WinCSD/CSD: http://imr.chem.binghamton.edu/zavalij/CSD.html
WinDust32: http://www.italstructures.com/
WinFIT: http://www.geol.uni-erlangen.de/index.php?id=58&L=3 and http://www.geol.uni-erlangen.de/fileadmin/template/Geologie/software/windows/winfit/winfit.zip
WinGX: http://www.chem.gla.ac.uk/~louis/software/
Winplotr: is within the Fullprof Suite (and freestanding)
$WinX^{Pow}$ : http://www.stoe.com/
WinXRD: http://www.thermo.com/
WPPF: http://www.crl.nitech.ac.jp/~toraya/software/
Xcell: http://www.accelrys.com/
XFIT: No longer developed: http://www.ccp14.ac.uk/tutorial/xfit-95/xfit.htm and download from http://www.ccp14.ac.uk/ccp/web-mirrors/xfit-koalariet/
Xhydex: http://xray.chm.bris.ac.uk/software/XHYDEX/ and GUI version within WinGX

XLAT: http://ruppweb.dyndns.org/; http://ruppweb.dyndns.org/new_comp/xlat_new.htm and http://ruppweb.dyndns.org/ftp_warning.html
XmLmctep: http://www.lmcp.jussieu.fr/~soyer/Lmctep_en.html
XND: ftp://ftp.grenoble.cnrs.fr/xnd/
X'Pert HighScore: http://www.panalytical.com/
Xplot for Windows: http://www.clw.csiro.au/services/mineral/xplot.html
Xpowder: http://www.xpowder.com/
Xdrawchem: WinDrawChem and Build3D: http://xdrawchem.sourceforge.net/
XRD2Dscan: http://www.ugr.es/~anava/xrd2dscan.htm
XRS-82/DLS-76: http://www.crystal.mat.ethz.ch/Software/XRS82/
X-Seed: http://x-seed.net/
XSPEX: http://www.dianocorp.com/software.htm
Xtal : http://xtal.sourceforge.net/
Xtal-3D: http://www.ill.fr/dif/3D-crystals/xtal-3d.html
XtalDraw: http://www.geo.arizona.edu/xtal/xtaldraw/xtaldraw.html
ZDS System: http://krystal.karlov.mff.cuni.cz/xray/zds/zdscore.htm
ZEFSA II: http://www.mwdeem.rice.edu/zefsaII/
Zeolite Structures Database: http://www.iza-structure.org/databases/

# *Subject Index*


2D to 3D model generation software 534, 540
2θ calibration, internal standards 128–30

ab initio nanostructure, modeling 489–91
absolute phase abundances, Rietveld analysis QPA 327–8
absorption
  data acquisition 44
  instrumental function 189–91
  scattering in polycrystalline powders 86–7
acentric structures probability distribution 233–4
accuracy of QPA 308–15
  error 314–15
  microabsorption 312–13
  orientation 310–12
  particle statistics 308–10
  precision 314–15
algebraic expressions for crystal systems 208–9
algorithms for peak-searching 105–11
alkali sulfates, QPA 325–6
ALLHKL software 154
aluminium pressure–volume relationship 450
amorphous content, Rietveld analysis QPA 328–9
angle between two planes, conic/receiving slit intersection 178–9
angle dispersive diffraction 443
angle transformation, diffraction geometry 422–6
anisotropic sample broadening 148–51
anomalous scattering factors 60
anti-phase domain boundaries (APBs) 384–6
APBs *see* anti-phase domain boundaries
area detectors, X-rays 32–3
asymmetry, shift, diffraction peak widths, Bragg angles 181
atmosphere, background 91–2
atoms, centro/non-centro symmetric arrangements 65
axial aberration in instrumental function 186–9
azimuth angles in spherical harmonics 342–4

background data reduction 89, 91–3
ball milling of metal powders 399–1
bending magnets 27–8
Bessel function 69–70
bismuth high pressure powder diffraction 454–5
Born–Mayer potential 248
Bragg angles
  asymmetry, shift, diffraction peak widths 181
  conic/receiving slit intersection 180
Bragg cones diffraction geometry 418
Bragg equation
  derivation 3–6
  derivatives 15–17
  reciprocal lattice 6–10
  scattering 8

Bragg reflections
  crystal lattice scattering 63–83
  instrumental aberrations 136–41
  peak fitting/line profile analysis 151–3
  peak profile functions 135–6
  polycrystalline powder 83–7
  sample broadening 141–51
  single atom scattering theory 58–63
Bragg's Law 17–19, 142
Bragg–Brentano geometry 33–6, 41–2
  diffractometers 175–9
  Dollase–March model 338–9
  instrumental profiles 167–8
  mathematical basis 300–1
  metal powders 400
Brillouin zone (BZ) 73, 77
Bromba–Ziegler filters 97
brucite 130–1, 311
BZ *see* Brillouin zone

caesium high pressure powder diffraction 455–6
Cagliotti law 157
calcite 319–20
calcium sulphate 441
calculation time in instrumental profiles 192–4
calibration of detectors 33
capillaries for sample holders 41–3
CCD *see* charge-coupled devices
cell restrained WPPD 153–4
  Le Bail method 155–6
  Pawley Method 154–5
centric structures probability distribution 233–4
centrosymmetric arrangements of atoms 65
cerium oxide powder, WPPM 402–5
CF *see* cost function
Chadwick, James 46
charge-coupled devices (CCD) 20–1, 32, 415–18
chemical constraints in modeling 489
co-ordinate systems for spherical harmonics 342–4
Cochran reliability parameter 236
collimated beams, Lorentz corrections 432–3
Commission on Powder Diffraction (CPD) 299
complex modeling of pair distribution function 486–7
Compton scattering 59
computer software
  location/testing 494–5
  programs 495–562
  summary 494
configuration of Markov chains 243–4
conic equations
  diffractometers 173–5
  sample surface planes 177
  vectors 173
conic sections, diffraction angle transformation 423–4
conic/receiving slit intersection
  Bragg angles 180
  Bragg–Brentano geometry 178–9, 186
  degenerated cone 181
  equations 176–7, 179–80
  non-convolution calculation of observed profile 181–2
constraints in Rietveld refinement 271–4
convolution approach for line profiles 168
corundum 308–10, 313, 316–18
cost function (CF)
  direct-space techniques 243
  genetic algorithms 252
  hybrid approach 250, 254–5
  simulated annealing 250–1
CPD *see* Commission on Powder Diffraction
Crab nebula supernova 25
Cryscon software 503
crystal lattices 206–11
  scattering 63–82
  thermal motion effects 65–6
crystal size in sample broadening 142–6
crystal structure prediction (CSP) 258–60
crystal structures
  algebraic expressions 208–9
  database software 498, 501–2

direct methods (DM) 230–42
powder neutron data 242–3
vizualization software 555, 556–60
crystallinity in phase structure 306–8
crystallographic structure
visualization software 554–5
CSP *see* crystal structure prediction
Cu atom energy levels 23–4

DAC *see* diamond anvil cell (DAC)
Dandelin sphere 172
Darwinian theory of evolution 252–3
DASH software 221–2, 250, 253, 255
data
acquisition measurements 44
reduction methods summary 89–90
data smoothing
data reduction 89, 93–100
digital low pass filters 96–100
sliding polynomials 91–7
DBWS software 336
DE *see* differential evolution (DE) algorithm
de Broglie relation 46, 62
Debye scattering equation 141, 147
Debye–Scherrer
cones 12–14, 21, 308
diffraction 49
geometry 40–1, 338–9, 418, 479–80
rings 444
Debye–Waller factor 66
deformed metals WPPM analysis 396–402
degenerated cones, conic/receiving slit intersection 177–8, 181
derivative difference minimization (DMM) 291–5
composition procedure 285–8
data 288–91
mesoporous silicates 292–4
principle 283–5
summary 282–3
tests 288–91
derivatives in Bragg equation 15–17
detective quantum efficiency (DQE) 414–15
detectors
calibration 33
systems 20–1
two dimensional 414–18
X-rays 31–3
diamond anvil cell (DAC) techniques 450, 451–3
*DICVOL04* indexing program 218–20
*DICVOL91* indexing program 216–17
differential evolution (DE) algorithm 254
diffracted beams, plane crystal monochromators 197–200
diffraction geometry 418–26
FWHM 419–222
incident angle 426
ray distance 426
resolution 419–222
transformations 426–9
diffractometers, Bragg–Brentano geometry 175–9, 192–4
DIFPATAN profile fitting program 103
digital low pass filters, data smoothing 96–100
Dirac peak profiles 134
direct methods (DM)
crystal structure 240–2
crystal structures 230–42
figure of merit 239–40
normalization of structure factors 232–3
phase analysis 299–300
preliminary refinement 240–2
procedures 239
scaling of observed intensities 232–3
structure invariants 233–8
direct-space techniques (DST)
crystal structure prediction 258–60
*DICVOL04* indexing program 218–19
genetic algorithms 219, 252–4
grid search 245
hybrid approach 254–7
Monte Carlo approach 219
Monte Carlo methods 245–9
real structures 257–8
simulated annealing 249–52
summary 243–5
dislocation densities, WPPM 399–401

DM *see* direct methods
DMM *see* derivative difference minimization
Dollase–March model 336, 337–99
domain size
  summary 376–9
  WPPM 399–401
DQE *see* detective quantum efficiency
DST *see* direct-space techniques
dynamic powder diffraction 440
dynamic range, two dimensional detectors 415

ECMR *see* experimentally constrained molecular relaxation
EDM *see* electron density modification
elastic strain/stress mathematics 349–2
electromagnetic (EM) waves 1
electron density modification (EDM) 240
EM *see* electromagnetic waves
empirical potential modeling 487–9
Empirical Potential Structure Refinement (EPSR) 487–9
ENDEAVOUR software 251
energy dispersive X-ray diffraction (EDXRD) 45–6, 442–3
EPSR *see* Empirical Potential Structure Refinement
equation aberrations, instrumental function 182–91
errors
  accuracy of QPA 314–15
  Rietveld analysis QPA 327–9
ES *see* Extinction Symbol
ESPOIR software 157, 252
Ewald
  circle 12
  construction 11–15
  spheres 379, 456
EWDXRD *see* energy dispersive X-ray diffraction
EXAFS *see* X-ray absorption fine structure
experimentally constrained molecular relaxation (ECMR) 488
EXPO2004 procedure, space group determination 222–4
external standards
  QPA powder diffraction 319–22
  systematic errors 126–7
Extinction Symbol (ES) 207–8

Faber–Ziman scheme 473
fake reflections 89, 90–1
fan radiation from magnets 27
faulting, line broadening 384
$FeCl_4$ anion, rigid body refinement 274–5
$Fe_{1.5}Mo$ iron alloy 396–9
$Fe[OP(C_6H_5)_3]_4Cl_2FeCl_4$ structure 274–7, 278–9
FHWM *see* full widths at half maximum
figure of merit
  cost function 243
  direct methods (DM) 239–40
  powder patterns 213–14
film transistor arrays (TFT) 416–17
filters for X-rays optics 29
finite size crystallites, Bragg's Law 17–19
flat panel detectors 416–17
fluorite 316–18
fluorphlogopites 122–3
form factors 60
Fourier maps, single crystal software 541, 549–50
Fourier methods, line broadening 389–94
Fourier recycling 228, 241–2
Fourier transforms 60, 64, 407–11
FOX software 252, 534, 536–8
FPA *see* Fundamental Parameters Approach
Fraunhofer approximation 3
free standing powder diffraction software 541
Friedel law 334
Friedel pair overlap 84
full profile fitting software 523, 528–30
full widths at half maximum (FWHM)
  crystallite size 142, 145
  data reduction 89
  largest size 137–8
  peak search 106, 109, 110, 112
  Rietveld refinement 168

size broadening 378
two dimensional diffraction 419–22
WPPD 157
FULLPROF software 156
Fundamental Parameters Approach (FPA)
Bragg–Brentano geometry 167
instrumental aberrations 136, 141
line broadening 387
peak fitting 152

GA *see* genetic algorithms
genetic algorithms (GA) 219, 252–4
GEOMET software 138–40
gibbsite 319–20
global optimization algorithms 243
goniometers 447–8
grid search in direct-space methods 245
GRINSP software 260
GSAS software 274, 336, 355
Guinera camera 128
GULP software 260

Harker sections 228
hematite 320
hen egg white lysosyme (HEWL) X-ray powder pattern 58–9
high pressure powder diffraction 450–61
Hill average, stress/strain in isotropic samples 360
home laboratory X-ray sources 444–5
hybrid pixel detectors 417–18
hydrogen placement with single crystal software 541, 548
hydrostatic pressure in isotropic polycrystals 363–4
IB *see* integral breadth
ICDD *see* International Centre for Diffraction Data
ILL *see* Institut Laue Langevin
imaging plate detectors 416
in operando see in situ
*in situ* powder diffraction 440–9
incident angle
diffraction geometry 426
intensity in two-dimensional diffraction 435–7
transformations 427
indexing powder patterns 211–20
indexing programs for powder diffraction patterns 214–17, 217–20
indirect methods for phase analysis 299
industrial systems, QPA 322–6
Institut Laue Langevin (ILL) 48, 52
instrument configurations
laboratory 33–7
synchroton 37–41
instrumental aberrations
Bragg reflections 136–41
largest size 137–8
Monte Carlo Ray-tracing 138–41
instrumental function
absorption 189–91
axial aberration 186–9
equation aberrations 182–91
misalignment 194
monochromators 196–8
plane monochomator 200–1
Soller slits 194–6
instrumental profiles
Bragg–Brentrano geometry 167-8, 192-4
line broadening 386
integral breadth (IB) methods, line broadening 387–9
intensity in two-dimensional diffraction 429–37
incident angle correction 435–7
Lorentz correction 430
polarization correction 434–5
intensity/position extraction, peak fitting 151
intergranular strain/stress 354
internal degrees of freedom, torsion angles 243–4
internal standards
QPA powder diffraction 318–19
systematic errors 127–30
International Centre for Diffraction Data (ICDD) 89
International Union of Crystallography (IUCr) 299

internet sources for powder diffraction software 561–2, 562–70
inverse Monte Carlo analysis 488–9
iron ore sinter phases (SFCA) 319–22
isomorphous replacement methods 227
isotropic polycrystals, hydrostatic pressure 363–4
isotropic samples, stress/strain analysis 357–63
*ITO* indexing program 214–15
IUCr *see* International Union of Crystallography

Jacobi–Anger expressions 68–9

K stripping data reduction 89, 100–5, 130
Kapton polymer 43
$K(C_2H_3N_8O_2)$ derivative difference minimization 291–2
kieserite 319
Kroner model for stress/strain in isotropic samples 360–2, 364

Laboratory methods
  instrument configurations 33–7
  X-rays sources 21–5
largest size of instrumental aberrations 137–8
lattices
  Bragg equation 6–10
  constants and systematic errors 130–1
  crystalline 206–11
  defects summary 376–7
  plane vectors 9
  strain in sample broadening 146–8
Laue classes
  elastic stress/strain 351
  hydrostatic pressure 364
  Reuss model 359
  spherical harmonics 344–6
  strain expansion in spherical harmonics 367–70, 372
  symmetry 210, 220
Le Bail method
  cell restrained WPPM 155–6
  software 523, 528, 529–30, 540
  structure factors 233
lead myristate 123
lead stearate 125
least squares analysis in Rietveld refinement theory 268–71
Leonard–Jones potential 248
line broadening 377–81, 384–7
  faulting 384
  Fourier methods 389–94
  Fundamental Parameters approach 387
  instrumental profile 386
  integral breadth methods 387–9
line profile analysis (LPA) 166–7, 376–7
  Bragg reflections 151–3
  convolution approach 168
  profile fitting 394–6
linear detectors for X-rays 31
lithium high pressure powder diffraction 455–7
lizardite 319
Lorentz factor 66–7, 430, 432–3
Lorentz-polarization factor 66
LPA *see* line profile analysis

macroscopic strain/stress 348–9, 354
magnetic structures
  examples 74–6, 78–9
  factors 77–9
  neutron scattering 81–3
  propagation vectors 73–7
  symmetry 79–81
magnets, fan radiation 27
March–Dollase model 311–12
Markov chains 243–4
mathematical basis for QPA 300–3
MC *see* Monte Carlo
MD *see* molecular dynamics
measurements
  data acquisition 44
  high pressure powder diffraction 454–7
  powder diffraction 41–4
mesoporous silicates, derivative difference minimization 292–4
metal powders, WPPM analysis 396–402
Metropolis criterion 249

microabsorption, accuracy of QPA 312–13
Miller indices 89
mineralogical systems, QPA 315–22
mirrors in X-ray optics 30–1
misalignment, instrumental function 194
ML *see* modified Lorentz curve (ML)
model independent structures
  Pair distribution function 481–2
  total scattering 481–2
modeling
  ab initio nanostructure 489–91
  chemical constraints 489
  empirical schemes 487–9
  pair distribution function 482–5
  total scattering 485–6
modified Lorentz curve (ML) 101, 108, 120
modulated crystal lattices scattering 67–71
molecular dynamics (MD) techniques 254
molecular replacement method 227
monochromators
  instrumental function 196–8
  plane crystal 197–200
  powder neutron diffraction 50–3
  X-rays 29–30
Monte Carlo (MC) methods
  direct-space techniques 219, 245–9, 255–6
  ray-tracing 138–41
Morningstar–Warren approximation 474–5
multicomponent systems, pair distribution function 473–8
multiple diffraction effect 227
Mylar polymer 43

*N-TREOR* indexing program 217–18
nanocrystalline cerium oxide powder, WPPM 402–5
National Institute of Standards and Technology (NIST) 122
neutrons
  detection 49–50
  diffraction 445–6
  magnetic moment scattering 71–83
  properties 46–8
  scattering by single atom 62–3
  scattering lengths 47
  scattering in magnetic structures 81–3
  sources 48–9
nickel laterite ores 318–19
NIST *see* National Institute of Standards and Technology
no cell restraint WPPM 153
non-ambient conditions, powder diffraction, summary 439–40
non-centrosymmetric arrangements, atoms 65
non-convolution of profile in conic intersection 181–2
nontronite 308–10
normalization, structure factors 232–3

observed intensities, crystal structure 232–3
observed profiles, X-rays 169–71, 171–2
OCTOPUS software 247–8
ODF *see* orientation distribution function
optics of X-rays 29–31
organic structures, global optimization methods 258–9
orientation, accuracy of QPA 210–312
orientation distribution function (ODF), texture 332–5, 335–7, 339–40, 356
outliers *see* fake reflections
pair distribution function (PDF)
  Bragg reflection 134
  complex modeling 486–7
  methods 479–81
  model independent structures 481–2
  modeling 482–5
  multicomponent systems 473–8
  peaks 481–2
  single component systems 470–3
  software 541, 547
  structural modeling 481–91

structurally determined function 472–3
summary 464–70
PAL *see* pressure acid leaching
parallel tempering 252
parallel-beam instruments 38–40
parameters
diffraction angle transformation 423
diffraction geometry transformations 428–9
partial pair distribution function 473
particle statistics, accuracy of QPA 308–10
patterns
figures of merit 213–14
indexing programs 214–17
powder diffraction software 548, 552–4
Patterson function 228–30
Paul Scherrer Institute (PSI) 50, 417
Pawley method
cell restrained WPPM 154–5
software 154, 528, 530, 540
structure factors 233
PDF *see* pair distribution function
peak-searching
algorithms 105–11
data reduction 89
predefined peak shape 110–11
second derivatives 107–10
peaks
finding/profiling software 510, 515–18
intensity/position extraction 151
line profile analysis, Bragg reflections 151–3
pair distribution function 481–2
profile functions in Bragg reflections 135–6
size/distribution extraction 152
spherical harmonics 372–3
Pearson VII profile 96–7, 111–14, 116–18
perovskite structures 149–50
phase
analysis 299–300
crystal structure problem 227–8
crystalline structure 306–8
identification software 496–500
shift in sine waves 2
photo realistic rendering of crystal structures software 555, 556–60
photoconductors for flat panel detectors 417
plane monochromators
diffracted beams 197–200
instrumental function 200–1
reflection cones 198–9
Platoon software 551
point detectors, X-rays 31
point spread function (PSF) 415, 419
polar angles, spherical harmonics 342–4
polarization, intensity correction 434–5
polycrystalline powders, Bragg reflection 83–7
polymers for sample holders 43
Portland cement 322–5, 325–6, 441
position-sensitive detector (PSD) 21
powder diffraction software
data conversion 500, 503–9
free standing 541
general 531, 535
indexing 510, 519–22
internet sources 561–2, 562–70
pattern 504, 510, 513–14
pattern calculation 548, 552–4
single crystal 530, 534
structure solution 531, 534, 536–8
powder neutron diffraction 46–56
pre-sample optics in synchroton instrument configurations 37–8
precision, instrumental profiles 192–4
precision and accuracy, QPA 314–15
predefined peak shape 110–11
pressure acid leaching (PAL) 318–19
pressure measurement, powder diffraction 453–4, 457–9
probability distribution, structure invariants 233–4
profile components, Fourier transforms 407–11
profile fitting
data reduction 90, 111–19
line profile analysis 394–6
profile shape functions (PSFs) 111–12
propagation vectors 73–7

protein powder refinement 279–80
PSD *see* position-sensitive detector
PSF *see* point spread function; profile shape function
PSI *see* Paul Scherrer Institute

quantitative phase analysis (QPA)
  industrial systems 322–6
  mathematical basis 300–3
  mineralogical systems 315–22
  Rietveld based error analysis 327–9
  software 548, 550–1
  summary 298–9, 326

rapid acquisition pair distribution function (RAPDF) 479–81
ray distance, diffraction geometry 426
reaction cells, *in situ* powder diffraction 446–9
real space Rietveld approach 483
real structures, direct-space techniques (DST) 257–8
receiving slit plane
  conic equations 176–7, 178–80
  diffraction/reflection conic intersection 199–200
  reflection cone intersection 199–200
reciprocal lattices, Bragg equation 6–10
reference intensity ratio (RIR) methods, QPA 303–4
reflection
  geometry 33–6
  plane crystal monochromators 198–9
  receiving slit intersection 199–200
  scattering in polycrystalline powders 83–7
relative Lorentz factor 432–3
relative phase abundances, errors in Rietveld analysis QPA 327
resolution
  powder diffractometers 53
  two dimensional diffraction 419
resonance scattering factors 60
restraints
  Rietveld refinement 271–4
  stereochemical refinement 277–9
Reuss model, stress/strain in isotropic samples 358–60, 364
reverse Monte Carlo (RMC) modeling 148, 485–6
Rietveld analysis
  errors in QPA 327–9
  industrial systems 323–5
  instrumental aberrations 136
  pair distribution function 483
  programs 166–8
  quantitative phase analysis304–8 317–18
  spherical harmonics 346–8, 373
Rietveld refinement
  constraints/restraints 271–4
  hybrid approach 255
  internal standards 130
  software 541, 542–6
  summary 266–8
  theory 268–71
rigid body refinement
  FeCl anion 275
  Fe[OP(CH)]ClFeCl 274–7
  Rietveld theory 271–4
RIR *see* reference intensity ratio
RMC *see* reverse Monte Carlo
rocks texture 332–48
rubies high pressure powder diffraction 458

SA *see* simulated annealing
sample broadening
  Bragg reflection 141–51
  crystallite size 142–6
  lattice strain 146–8
sample holders
  diffraction patterns 91
  measurements 41–3
sample surface planes, conic equations 177
Savitsky–Golay method 89, 93–6
scaling, observed intensities 232–3
scattering
  Bragg equation 8
  crystal lattices 63–82
  factors 60

intensity 65
lengths of neutrons 47
modulated crystal lattices 67–71
neutron magnetic moment 71–83
polycrystalline powders 83–7
single atom theory 58–63
Scherrer equation 142, 145
SDPD *see* structure determination by powder diffractometry
search-match software 496–500
second derivatives, peak-searching 107–10
SFCA *see* iron ore sinter phases
silicates, derivative difference minimization 292–4
silicon pressure–volume relationship 450
simulated annealing (SA), direct-space techniques 249–52, 257–8
sine waves phase shift 2
single atom scattering theory 58–63
single component systems, pair distribution function 470–3
single crystal elastic constants, stress/strain in isotropic samples 362–3
single crystal software
Fourier maps 541, 549–50
hydrogen replacement 541, 548
powder diffraction 530–1, 533–4
refinement 538, 540
structure solution 534, 539
sintered plates for external standards 126
size
broadening, line broadening 377–81
two dimensional detectors 415
size/distribution extraction, peak fitting 152
size/strain analysis software 528, 532
sliding polynomials, data smoothing 91–7
SLS *see* Swiss Light source
sodium pressure–volume relationship 450
software *see* computer software
Soller collimators 33
Soller slits, instrumental function 194–6
space group
determination 220–4
software 521, 523–6
spallation sources 48, 50
spatial response in two dimensional detectors 415
SPDP *see* structure determination from powder diffraction data
speed in two dimensional detectors 415
spherical harmonics
peak shift 372–3
texture analysis 339–48
SRMs *see* standard reference materials
standard reference materials (SRMs) 122
standard samples 43–4
stereochemical restraint refinement, Fe[OP(CH)]ClFeCl 278–9
strain broadening, line broadening 381–4
strain expansion, spherical harmonics 366–7
strain/stress
averages in spherical harmonics 370–2
diffraction analysis 355–6
elastic 349–2
hydrostatic pressure 363–5
isotropic samples 357–63
macroscopic 348–9
polycrystalline samples 352–4, 352–5
spherical harmonics 365–73
structural modeling
pair distribution function 481–91
pair distribution function (PDF) 481–91
total scattering 481–91
structure
data conversion and transformation software 503, 511–12
invariants in direct methods 233–8
normalization 232–3
validation software 548, 553–4
structure determination from powder diffraction data (SDPD) 153–4, 166
structure solution software
powder diffraction 531, 534, 536–8
single crystal 534, 539
*SVD-INDEX* indexing program 219–20

Swiss Light source (SLS) 417–18
symmetry of magnetic structure factors 79–81
synchroton
  instrument configurations 37–41
  storage ring 26
  X-rays 25–9, 442–4, 454
systematic errors
  data reduction 90, 119–31
  external standards 126–7
  internal standards 127–30
  lattice constants 130–1

tangent formula 238–9
texture analysis 332–5, 335–7
  scattering in polycrystalline powders 84–6
  software 528, 531
TFT *see* film transistor arrays
thermal motion effects in crystal lattices 65–6
thermodynamics in high pressure powder diffraction 459–61
third party diffractometer control software 495–6
Thompson scattering formula 58–61, 67
three phase mixtures, QPA powder diffraction 315–18
tilt, diffraction angle transformation 425
time-of-flight (TOF) techniques for powder neutron diffraction 53–6
TOPAS software 251–2
torsion angles, internal degrees of freedom 243–4
total scattering
  model independent structures 481–2
  modeling 485–6
  muticomponent systems 475–7
  summary 464–70
transformations, diffraction geometry 426–9
trend oriented peak search 105–7
*TREOR* indexing program 215–16
tricalcium aluminate 441
two-dimensional diffraction
  detectors 414–18
  FWHM 419–222
  intensity 429–37
  resolution 419–222

unit cell refinement software 522–3, 537–8
UPACK software 260

variable count time 496
VCT *see* variable count time
vectors
  conic equations 173
  lattice plane 9
VNI powder diffraction pattern 212–13
Voigt model, stress/strain in isotropic samples 357–8, 364

Warren–Averbach (WA) method 389–94
Weissenberg camera 418
WH *see* Williamson–Hall
Whole Powder Pattern Decomposition (WPPD) 148, 153–8
  applications 156–8
  cell restrained 153–4
  no cell restraint 153
whole powder pattern fitting (WPPF) 394–5
whole powder pattern modelling (WPPM)
  cerium oxide powder 402–5
  deformed metal powders 396–402
  dislocation densities 399–401
  domain size 399–401
  LPA 395–6
Wilkens parameter 400–1
Wilkens–Krivoglaz approach 400
Williamson–Hall (WH) method 387–9
Wilson plots 232–3
WIMV method 335–7, 356
WPPD *see* whole powder pattern decomposition
WPPF *see* whole powder pattern fitting
WPPM *see* whole powder pattern modelling

*X-CELL* indexing program 220
X-ray absorption fine structure (EXAFS) 475, 487
X-rays
  area detectors 32–3
  definition 1
  detectors 31–3
  diffraction 2–3
  experimental setups 20
  filters 29
  fluorescence 60
  hen egg white lysosyme powder pattern 8–9
  home laboratory sources 444–5
  laboratory sources 21–5
  mirrors 30–1
  monochromators 29–30
  optics 29–31
  radiation in observed profiles 169–71, 171–2
  scattering 58–62, 63
  sources 21–9
  spectra 21–3

zeolite 449
zincite 316–18
ZIP-PROMET software 260
$Zn_4Sb_3$ pair distribution function 469